Évolution de la dénudation et contexte géomorphologique des minéralisations cuprifères supergènes dans le district Centinela, désert d'Atacama, Chili, à partir de la thermochronologie et des nucléides cosmogéniques

Caroline Sanchez

THÈSE

En vue de l'obtention du

DOCTORAT DE L'UNIVERSITÉ DE TOULOUSE

Délivré par :

Université Toulouse 3 Paul Sabatier (UT3 Paul Sabatier)
en co-tutelle avec la Universidad Católica del Norte, Antofagasta, Chili

Présentée et soutenue par :
Caroline Sanchez

Le Jeudi 29 Juin 2017

Titre :

Denudation evolution and geomorphic context of supergene copper mineralization in Centinela District, Atacama Desert, Chile, from thermochronology and cosmogenic nuclides

École doctorale et discipline ou spécialité :
ED SDU2E : Sciences de la Terre et des Planètes Solides

Unité de recherche :
UMR 5563

Jury

Stéphanie Duchêne	Professeur, Université Paul Sabatier, Toulouse	Présidente
Cécile Gautheron	Professeur, Université Paris Sud, Orsay	Rapporteur
Carole Petit	Professeur, Université Sophia Antipolis, Nice	Rapporteur
Riccardo Vassallo	Maître de conférences, Université Savoie Mont-Blanc, Chambéry	Rapporteur
Eduardo Campos	Associate professor, Universidad Catolica del Norte, Antofagasta	Examinateur
Rodrigo González	Research associate, Universidad Catolica del Norte, Antofagasta	Examinateur
Sébastien Carretier	Directeur de recherche IRD, GET, Toulouse	Directeur
Rodrigo Riquelme	Associate professor, Universidad Catolica del Norte, Antofagasta	Directeur
Stéphanie Brichau	Chargée de recherche IRD, GET, Toulouse	Invitée
Vincent Regard	Maître de conférences, Université Paul Sabatier, Toulouse	Invité

Directeurs de thèse :
Sébastien Carretier (GET, France)
Rodrigo Riquelme (UCN, Chili)

Co-encadrants de thèse :
Stéphanie Brichau (GET, France)
Vincent Regard (GET, France)

Abstract: During the Middle Eocene in the Atacama Desert region (northern Chile), the intrusion of porphyries and the synchronous deformation of the Precordillera resulted in the formation of important clusters of supergene and exotic copper ore deposits that are currently exploited. Such metal ore deposits result of the interaction of tectonics, erosion and climate, for which both timing and relations remain debated. This PhD study focuses on the quantification of geomorphological, tectonic and erosive processes to understand their relationship in the Andean western slope around 23°S in the Centinela district in the Precordillera. Twenty-nine new low-temperature thermochronological data and their modelling indicate that shallow porphyry copper emplaced during mid-Eocene were quickly exhumed near the surface by the early Oligocene. There is a five million years-long time gap between the exhumation of primary source of copper and the ~25-12 Ma range of existing $^{40}Ar/^{39}Ar$ and K/Ar ages of secondary mineralization in the District. This suggests that supergene copper related deposits occurred when the reliefs where already flattened. A syn-sedimentary exotic copper mineralization was deposited in an intra-mountainous basin in the Centinela District. We sampled sand at different depths between 135 and 13 meters in the Tesoro and Mirador open-pit mines, one of them including this exotic deposit. The ^{10}Be and ^{21}Ne concentrations of fourteen new samples were used to determine the exotic deposit age and to constrain the paleo-sedimentation rate for the last 14 Ma. The study dates the exotic deposit at ~12 Ma and suggests that this mid-Miocene exotic layer occurred during an erosive quiescence, confirming the view that supergene copper mineralization occurs during a stage of slower geomorphic activity in arid environments. The results also confirm that the erosion rates drastically dropped after 10-12 Ma, when the hyperaridity was established. This study highlights the necessary balance between exhumation and precipitation rates required to form secondary copper.

Key words: Supergene copper ore deposit, low-temperature thermochronology, Atacama Desert, cosmogenic nuclides.

Résumé : Pendant l'Eocene Moyen, dans la région du désert d'Atacama, Nord Chili, la mise en place de porphyres et la déformation synchrone de la Précordillère aboutissent à la formation de clusters importants de dépôts de cuivre supergènes et exotiques, actuellement en cours d'exploitation. La formation de ces dépôts métallifères résulte de l'interaction entre la tectonique, l'érosion et le climat. La nature et la chronologie de ces interactions sont encore débattues. Ce travail de doctorat se concentre sur la quantification des processus géomorphologiques, tectoniques et érosifs, sur le versant ouest des Andes, autour de 23°S dans le District minier Centinela situé dans la Précordillère. Vingt-neuf nouvelles données thermochronologiques basse-température et leur modélisation indiquent que les porphyres cuprifères mis en place à faible profondeur durant l'Eocène moyen étaient déjà exhumés près de la surface à l'Oligocène moyen. Il existe un intervalle de temps de cinq millions d'années entre l'exhumation du porphyre qui constitue la source primaire de cuivre et le dépôt secondaire de cuivre dans le district de Centinela daté par les méthodes $^{40}Ar/^{39}Ar$ et K/Ar. Cette relation suggère que les dépôts de cuivre secondaires ont eu lieu lorsque les reliefs étaient déjà aplanis. Un dépôt exotique cuprifère syn-sédimentaire s'est formé dans le bassin continental du district Centinela. Des échantillons de sable ont été prélevés entre 135 et 13 mètres de profondeur dans les mines El Tesoro et Mirador. Les concentrations en ^{10}Be et ^{21}Ne de quatorze nouveaux échantillons ont permis de déterminer l'âge du dépôt et de contraindre les paléo taux de sédimentation des derniers 14 Ma. L'étude permet de dater le dépôt exotique à ~12 Ma et suggère qu'il a eu lieu lors d'une quiescence des taux d'érosion, confirmant l'idée que les dépôts supergènes de cuivre en milieu aride ont lieu après l'aplanissement des reliefs. Ces résultats confirment aussi que les taux d'érosion ont drastiquement chuté après 10-12 Ma, quand l'hyperaridité s'est établie. Ce travail de thèse illustre la balance nécessaire entre l'exhumation et les taux de précipitation pour former des minéralisations secondaires de cuivre et les conserver.

Mots-clés : Dépôt de cuivre supergène, thermochronologie basse-température, désert d'Atacama, nucléides cosmogéniques.

Resumen: Durante el Eoceno medio, en la región del desierto de Atacama, en el norte de Chile, la ubicación y deformación sincrónica de la Precordillera generó la formación de depósitos significativos de cobre, ambos supergénicos y exóticos, los que se encuentran actualmente en explotación. Tales formaciones de metales resultan de la interacción de procesos tectónicos, erosivos y climáticos por los cual aún se debaten la sincronización y las interacciones que los produjeron. Esta tesis doctoral se enfoca en la cuantificación de los procesos geomorfológicos, tectónicos y erosivos, y sus interacciones, en la vertiente occidental de los Andes, alrededor de 23°S en el Distrito Minero Centinela, situado en la Precordillera. Veintinueve nuevos datos termocronológicos de baja temperatura y sus modelados indican que los porfiros cupríferos se emplazaron a poca profundidad en el Eoceno medio y que se habrían exhumado cerca la superficie en el Oligoceno medio. Existe un período de tiempo de cinco millones de años entre la exhumación de la fuente primaria de cobre y el rango de edades $^{40}Ar/^{39}Ar$ y K/Ar de los depósitos secundarios de cobre en el distrito Centinela. Esta relación sugiere que los depósitos de cobre secundario tuvieron lugar cuando los relieves ya estaban aplanados. Un depósito de cobre sin-sedimentaria de cobre exótico ocurrió en los sedimentos de la cuenca continental del distrito Centinela. Para determinar la edad del depósito y cuantificar la velocidad de paleo-sedimentación, se recogieron muestras de arena entre 135 y 13 metros en las minas El Tesoro y Mirador. Las concentraciones de ^{10}Be y ^{21}Ne de catorce nuevas muestras se utilizaron para datar el deposito exótico y cuantificar las paleo tasas de sedimentación de los últimos 14 Ma. El estudio nos permite datar el depósito exótico a ~12 Ma, sugiriendo que pasó por un momento de quietud erosiva, lo que confirma la hipótesis de que en ambientes áridos, los depósitos de cobre exóticos se producen durante la etapa de baja actividad geomorfológica. Estos resultados también confirman que las tasas de erosión se han reducido drásticamente después de 10-12 Ma, cuando empezó la hiperaridez en el desierto de Atacama. Este trabajo ilustra el equilibrio necesario entre la exhumación y la tasa de precipitación para formar mineralización de cobre secundario.

Palabras claves: Depositos supergenos de cobre, termocronología baja-temperatura, Desierto de Atacama, nucleídos cosmogenicos, Andes

Acknowledgments

Contents

English version

The geomorphologic processes forming the landscapes result from interactions between tectonic, erosion and climate (Molnar and England, 1990). Landscape evolution models have been proposed for two centuries and are still debated. In particular, the Critical Zone has been the focus of numerous recent researches in geomorphology (e.g. Riebe et. al., 2016). The Critical Zone is the weathered layer above fresh substratum. Its depth and composition reflect the tectonics, landscape and global climate evolutions. For example, the chemical weathering of silicate rocks consumes atmospheric CO_2 over millions of years, thus influencing the global climate over the Earth history (Raymo and Ruddiman, 1992). The evolution of the Critical Zone thickness and composition is tightly linked to uplift, climate and erosion, but in a non-straightforward relationship (Riebe et. al., 2016). For example, a more humid climate favors dissolution and accelerates the weathering front advance, but at the same time it fosters the physical erosion, removing the weathered material. Whether the weathered profile thickens or becomes thinner in response to an increase of humidity is not easily predictable. This response will depend, among other parameters, on the topographic slope, which is in turns the result of a combination of tectonics, climate and lithology.

During this complex evolution, some metal elements initially disseminated within an intrusive body can be transported by meteoritic water, be washed out or precipitate deeper in the weathering profile or be laterally transported downslope from the source. Copper is one of these elements. The precipitation and concentration of copper in the Critical Zone is referred as supergene copper mineralization.

In the Atacama Desert, in northern Chile, the supergene copper mineralization formed world-class ore deposits, among which the largest open-pit mine in the world, the Chuquicamata mine. The uppermost part of a porphyry copper is the argillic lithocap, which contains pyrite. When the lithocap reaches several tens to hundreds of meters below the ground surface, the dissolution of pyrite by meteoritic water decreases the pH of groundwater. Acid water circulating in the vadose zone dissolves primary copper sulfides. After downwards vertical transport, the solute copper precipitates as copper oxides above the water table in the oxidation zone. Below the water table, secondary supergene copper sulfides precipitate and concentrate the copper, forming the enriched ore deposits that are the main economic ores. Sometimes, part of the copper-rich solute migrates laterally and the copper minerals

precipitate at several kilometers from the porphyry copper (Münchmeyer, 1996; Bouzari and Clark, 2002). This kind of deposit is called exotic copper deposit.

The formation of supergene copper deposits probably results from a subtle balance between uplift, erosion and climate (Figure 1.1).
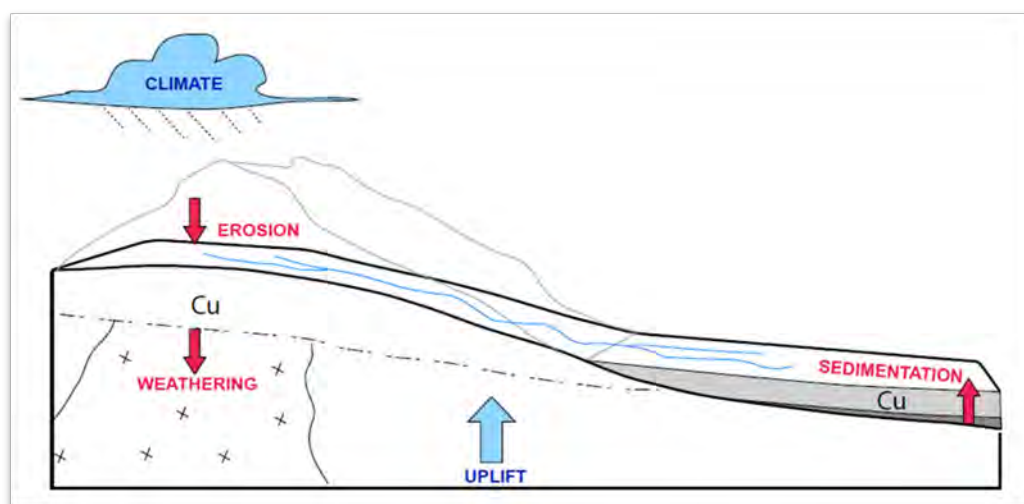
Figure 1.1 − Relationship between geomorphologic, climatic and tectonic processes controlling the supergene and exotic copper mineralization (COPEDIM LMI final report). Supergene copper mineralization results from the chemical weathering of porphyry copper ore deposits, when their depth is sufficiently shallow to allow meteoritic water circulation to dissolve and redistribute copper through the weathering profile. The generation of supergene copper deposits requires a subtle balance between uplift, erosion, and precipitation rates, all of these controlling the thickness of the weathered profile.

The supergene enrichment requires rainfall and circulation of meteoritic water. However, if the climate is too humid, the dissolved copper will be diluted and will be washed away. A humid climate increases also erosion, which tends to destroy the weathered profile. Ideal conditions where low available water circulates and low erosion rates may explain that supergene copper deposits are found in the arid areas of southern Peru and northern Chile (Sillitoe, 2005). Nevertheless, supergene copper enrichment in deep profiles are also found under humid climates, such as the Ok Tedi mine in New Guinea (Chivas et al., 1984) or the Boyongan and Bayugo mines in the Philippines (Braxton and Mathur, 2011), where exhumation rates are higher than in northern Chile. The thickening of the weathered profile and the degree of copper enrichment thus depends probably on a subtle balance between the precipitation rate and the exhumation rate of a porphyry copper, both controlling the residence times of water in the vadose and saturated zones (Brimhall et al., 1985).

This ratio between erosion and precipitation is poorly known. In northern Chile, chemical modelling based on chemical mass balance, which considers constant erosion rates, have explored the relationship between the grade and thickness of the copper depleted and enriched layers (Brimhall et al., 1985). Nevertheless, the landscape is dynamical, and denudation rates have changed through the Cenozoic in response to tectonic and climatic variations.

The dating of supergene minerals showed that supergene copper mineralization mainly occurred between ~36 and 9 Ma in the Atacama Desert, millions of years after the main exhumation period of porphyries copper documented by few low-temperature thermochronological ages in Atacama (Maksaev et al., 1999; Arancibia et al., 2006; Reich et al., 2009). Nevertheless, the erosion rates during the supergene copper enrichment periods is poorly constrained. In northern Chile, the landscape evolution has led to widely distributed low relief surfaces or pediments. Their relationship with supergene copper mineralization has been discussed for a long time (e.g. Mortimer, 1973; Clark et al., 1990; Quang et al. 2005). These authors suggested that supergene mineralization occurred during this pedimentation stage, and thus during "low denudation" periods. Nevertheless, the timing of the formation of these surfaces and the evolution of the denudation during this relief evolution is poorly constrained.

The main issue of this thesis focused on the quantitative denudation rates during the Late Cenozoic geologic evolution of the Atacama Desert, in northern Chile, on what can we learn about the timings and rates of the controlling processes for supergene mineralization in this place.

I raise the following specific questions in this context:

1. When did the porphyry copper ore deposits exhume during the Cenozoic and how did this exhumation can be related to the landscape evolution of the Atacama forearc region?

2. What is the temporal relationship between exhumation and supergene copper mineralization?

3. Do exotic copper deposits occur in some specific erosive context?

4. What are optimum erosive and climatic conditions for supergene copper mineralization?

In order to address these issues, I carried out an approach based on field observations, low-temperature thermochronology, geochronology and cosmogenic nuclides, in the Centinela Mine district (~23° Lat S, Antofagasta Region). This district includes porphyry copper ore deposits and sedimentary succession that host supergene exotic mineralization. It offers the possibility to document the formation of supergene copper mineralization within the temporal frame of the denudation and sedimentation histories. I used the low-temperature thermochronology data to constrain the porphyry copper ore deposits exhumation of this area, and to propose an unroofing history of these ores considering the geologic regional evolution. I used the cosmogenic nuclides contained in sediment that host syn-sedimentary exotic copper mineralization exposed at great depth (0 to 300 m) in open pit mines. We

attempt to date the Miocene exotic copper sediments but also to evidence if such a mineralization responds to variation of the sedimentation rate.

This last approach constitutes one of the first attempt to use cosmogenic nuclides for paleo-erosion or sedimentation rates over such old periods. We take advantage of the exceptional access to deep samples exposed only recently by mining.

This thesis is organized in the following order.

After a first introductive chapter, I review the state of the art of the different disciplines involved in this thesis in the second chapter, including landscape evolution models, copper deposits models and the geology of northern Chile. In the third chapter, I present the methods used during this thesis. In the fourth chapter, I propose an integrated evolution model for the Chilean forearc since the Late-Cretaceous based on existing data and my new thermochronological data. In the fifth chapter, I constrain the relationship between porphyry copper exhumation and supergene copper mineralization based on my new thermochronological data. This chapter is presented with the format of the paper I submitted to Terra Nova. The sixth chapter presents the application of cosmogenic nuclides: the first burial dating of exotic copper mineralization and the first quantification of paleo-sedimentation rate in the last ~14 Ma. In the seventh chapter, I will briefly discuss the general results and possible perspectives before concluding.

Version en français

Les processus géomorphologiques qui modèlent les paysages sont consécutifs aux interactions entre la tectonique, l'érosion et le climat (Molnar and England, 1990). Pour les expliquer, des modèles d'évolution du paysage ont été proposés pendant près de deux siècles et sont encore débattus. La zone critique, qui est la couche altérée au-dessus de la roche mère, a fait l'objet de nombreuses recherches récentes en géomorphologie (Riebe et al., 2016). Par définition, c'est donc la couche altérée au-dessus du substrat non altéré. Sa profondeur et sa composition reflètent l'évolution de la tectonique, des paysages récents, et du climat mondial. Par exemple, l'altération chimique des roches silicatées consomme du CO_2 atmosphérique pendant des millions d'années, influençant ainsi le climat mondial à l'échelle géologique de la Terre (Raymo et Ruddiman, 1992). L'évolution de l'épaisseur et de la composition de la zone critique est étroitement liée à l'altitude, au climat, et dans une moindre mesure à l'érosion (Riebe et al., 2016). Par exemple, un climat plus humide favorise la dissolution et accélère le développement du front d'altération en profondeur, mais en même temps il favorise l'érosion physique, érodant le régolithe. Le fait de savoir si le profil d'altération s'épaissit ou devient plus mince en réponse à une augmentation de l'humidité n'est pas facilement prévisible. Cette réponse dépendra, notamment, de la pente topographique, qui résulte-de l'interaction entre la tectonique, le climat, et la lithologie.

Au cours de cette évolution complexe, certains éléments métalliques initialement disséminés dans un corps intrusif peuvent, (1) être transportés par de l'eau météoritique et exportés en solution, et/ou (2) précipiter en profondeur dans le profil d'altération ou latéralement par rapport à la source. Le cuivre est l'un de ces éléments. La précipitation et la concentration de cuivre dans la zone critique définissent la minéralisation du cuivre supergène.

Dans le désert d'Atacama, au nord du Chili, se sont formés des gisements de cuivre supergène de premier ordre, parmi lesquels la plus grande mine à ciel ouvert du monde, la mine Chuquicamata. La partie supérieure du gisement supergène, le lithocap, contient de la pyrite. Lorsque le lithocap atteint plusieurs dizaines à centaines de mètres sous la surface du sol, la dissolution de la pyrite par l'eau météorique diminue le pH des eaux souterraines. L'eau acide circulant dans la zone vadose dissout les sulfures primaires de cuivre. Après infiltration, le cuivre initialement en solution précipite sous forme d'oxydes de cuivre au-dessus de la nappe phréatique dans la zone d'oxydation. Au-dessous de la nappe phréatique, les sulfures de cuivre supergène secondaires précipitent et concentrent le cuivre, formant les gisements de minerai enrichis qui sont ensuite exploités. Parfois, une partie du soluté riche en cuivre migre latéralement et la minéralisation du cuivre se trouve à plusieurs kilomètres du porphyre cuprifère (Münchmeyer, 1996 ; Bouzari et Clark, 2002). Ce type de dépôt est appelé dépôt « cuprifère exotique ».

La formation de cuivre supergène résulte d'un équilibre subtil entre soulèvement, l'érosion et le climat (figure 1.1).
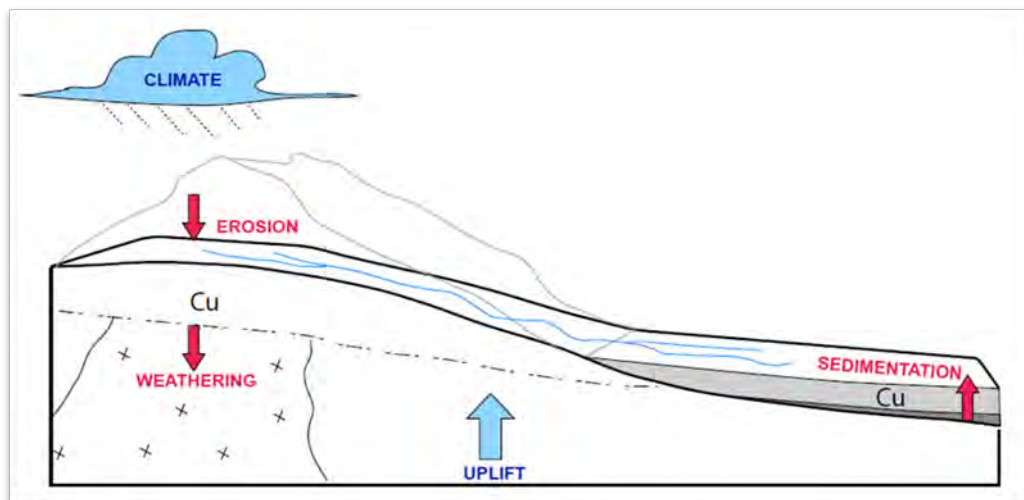
Figure 1.1 – Relation entre les processus géomorphologiques, climatiques et tectoniques, impliqués dans la minéralisation de cuivre supergène et exotique (rapport final COPEDIM LMI). La minéralisation du cuivre supergène se produit pendant l'altération chimique des porphyres cuprifères, lorsque leur profondeur est suffisamment grande pour que la circulation de l'eau météoritique dissolve et reprécipite le cuivre le long d'un profil d'altération vertical ou latéral. La formation de gisements de cuivre supergène requiert un équilibre subtil entre le taux de soulèvement, le taux d'érosion et le taux de précipitation, contrôlant l'épaisseur du profil enrichi et le temps de résidence des eaux souterraines.

L'enrichissement supergène nécessite la présence de pluie et la circulation de l'eau météoritique. Cependant, si le climat est trop humide, le cuivre dissous ne précipitera pas et sera évacué vers l'océan. Un climat humide a pour conséquence d'augmenter les taux d'érosion, ce qui tend à détruire le profil résistant. Des conditions climatiques semi-arides vont induire de faibles taux de précipitation et donc de faibles taux d'érosion, ce qui favorise la formation de ce type de dépôt. Cela peut expliquer que des dépôts de cuivre se trouvent dans les régions arides du sud du Pérou et du nord du Chili (Sillitoe, 2005). Néanmoins, l'enrichissement en cuivre supergène dans des profils épais se produit également dans des climats humides, tels que dans la mine Ok Tedi en Nouvelle-Guinée (Chivas et al., 1984) ou les mines Boyongan et Bayugo aux Philippines (Braxton et Mathur, 2011), où les taux d'exhumation sont probablement plus élevés que dans le nord du Chili. L'épaississement du profil et le degré d'enrichissement en cuivre dépendent probablement d'un subtil équilibre entre le taux de précipitation et le taux d'exhumation d'un porphyre cuprifère, contrôlant à la fois les temps de résidence de l'eau dans les couches vadoses et saturées (Brimhall et al., 1985).

Ce rapport nécessaire entre l'érosion et les précipitations pour former des dépôts supergènes est peu connu. Dans le nord du Chili, la modélisation géochimique, (à taux d'érosion constant), a permis une première estimation de la relation entre la concentration en cuivre, l'épaisseur, et les processus des couches enrichies en cuivre (Brimhall et al., 1985).

Néanmoins, la dynamique du paysage et les taux de dénudation varient pendant le cénozoïque en réponse aux variations tectoniques et climatiques. La datation des minéraux supergènes a montré que les minéralisations du supergène cuprifère ont principalement lieu entre ~ 36 et 9 Ma en Atacama, des millions d'années après la période d'exhumation principale des porphyres de cuivre documentée par quelques âges thermochronologiques basse température (Maksaev et al., 1999; Arancibia et al., 2006; Reich et al., 2009). Il en résulte que les taux d'érosion pendant les périodes d'enrichissement en cuivre supergène ne sont pas contraints. Dans le nord du Chili, l'évolution du paysage a conduit à la formation de surfaces à faible relief de grandes extension géographique, aussi appelées pédiments. La relation entre les paysages et la minéralisation du cuivre supergène a été discutée depuis longtemps (e.g. Mortimer, 1973; Clark et al., 1990 ; Quang et al., 2005). Ces auteurs ont suggéré que la minéralisation du cuivre supergène s'est produite au cours de cette étape de pédimentation, et donc pendant les périodes de faible dénudation. Néanmoins, la formation des surfaces et l'évolution des taux de dénudation sont peu contraints dans le nord du Chili.

Dans cette thèse, je me suis concentrée sur l'évolution du taux de dénudation dans le désert d'Atacama, dans le nord du Chili, près de 23 ° S, dans la région d'Antofagasta.

Je soulève les questions spécifiques suivantes dans le contexte du désert d'Atacama :

1. Comment et quand est-ce que l'avant-arc du désert d'Atacama s'est exhumé pendant le Cénozoïque et comment le paysage a-t-il évolué?

2. Quelle est la relation temporelle entre l'exhumation et la minéralisation de cuivre supergène?

3. Un dépôt de cuivre exotique se produit-il dans un contexte érosif spécifique?

4. Quelles sont les conditions érosives et climatiques optimales pour la minéralisation du cuivre supergène?

Afin d'aborder ces problèmes, j'ai procédé à une approche multiple basée sur les observations sur le terrain, la thermochronologie basse température, et l'application des nucléides cosmogéniques, dans le district de Centinela. Ce district comprend des porphyres de cuivre et un bassin sédimentaire dont le remplissage contient des dépôts exotiques et supergènes cuprifères. Il offre la possibilité de documenter la chronologie de formation de la minéralisation de cuivre supergène au cours de l'évolution de la dénudation et de la sédimentation. J'ai utilisé la thermochronologie basse température pour contraindre l'exhumation des porphyres de cette zone et proposer un scenario d'évolution du paysage depuis le Crétacé de façon régionale. J'ai utilisé la quantification de nucléides cosmogéniques dans les sédiments échantillonnés à grande profondeur dans les mines ouvertes afin de contraindre l'évolution du taux de sédimentation pendant le Miocène, en particulier lors des dépôts de cuivre exotique.

Cette dernière approche constitue l'une des premières tentatives d'utilisation de nucléides cosmogéniques pour estimer les taux d'érosion ou de sédimentation sur des périodes si anciennes, et a été rendu possible par l'accès exceptionnel aux échantillons qui affleurent grâce à l'industrie minière.

Après une brève introduction dans le premier chapitre, le deuxième chapitre de cette thèse est consacré à l'état de l'art des différentes disciplines impliquées dans cette thèse, y compris les modèles d'évolution du paysage, les modèles de dépôts de cuivre et la géologie du nord du Chili. Dans le troisième chapitre, je présente les méthodes utilisées lors de cette thèse. Le quatrième chapitre propose un modèle d'évolution intégré pour l'avant-arc chilien autour de 23°S depuis le Crétacé supérieur à partir des données existantes et de mes nouvelles données thermochronologiques. Dans le cinquième chapitre, je contrains la relation entre l'exhumation des porphyres et la minéralisation du cuivre supergène à partir de mes nouvelles données thermochronologiques. Ce chapitre se présente sous la forme d'un article publié dans le journal *Terra Nova*. Il est mis en parallèle avec un article répondant à la même question scientifique mais avec une méthode différente, dont les résultats concordent, ajouté en annexes. Le sixième chapitre présente l'application des nucléides cosmogéniques pour réaliser la première datation de minéralisation exotique de cuivre ainsi que la quantification du taux de paléo-sédimentation depuis ~ 14 Ma. J'y discute les résultats de façon générale et y expose les possibles perspectives avant de conclure dans le septième chapitre 7.

References for Chapter 1

Arancibia, G., Matthews, S.J., de Arce, C.P., 2006. K–Ar and ^{40}Ar/^{39}Ar Geochronology of supergene processes in the Atacama Desert, northern Chile: Tectonic and climatic relations. Journal of the Geological Society 163, 107–118.

Bouzari, F., Clark, A.H., 2002. Anatomy, evolution, and metallogenic significance of the supergene orebody of the Cerro Colorado porphyry copper deposit, I Región, northern Chile. Economic Geology 97, 1701–1740.

Braxton, D., Mathur, R., 2011. Exploration applications of copper isotopes in the supergene environment: A case study of the Bayugo porphyry copper-gold Deposit, southern Philippines. Economic Geology 106, 1447–1463.

Brimhall, G.H., Alpers, C.N., Cunningham, A.B., 1985. Analysis of supergene ore-forming processes and ground-water solute transport using mass balance principles. Economic Geology 80, 1227–1256.

Chivas, A.R., O'Neil, J.R., Katchan, G., 1984. Uplift and submarine formation of some Melanesian porphyry copper deposits: stable isotope evidence. Earth and Planetary Science Letters 68, 326–334.

Clark, A.H., Tosdal, R.M., Farrar, E., Plazolles, A., 1990. Geomorphologic environment and age of supergene enrichment of the Cuajone, Quellaveco, and Toquepala porphyry copper deposits, southeastern Peru. Economic Geology 85, 1604–1628.

Maksaev, V., Zentilli, M., 1999. Fission track thermochronology of the Domeyko Cordillera, northern Chile: Implications for Andean tectonics and porphyry copper metallogenesis. Exploration and Mining Geology 8, 65–90.

Molnar, P., England, P., 1990. Late Cenozoic uplift of mountain ranges and global climate change: chicken or egg? Nature 346, 29–34.

Mortimer, C., 1973. The Cenozoic history of the southern Atacama Desert, Chile. Journal of the Geological Society 129, 505–526.

Quang, C.X., Clark, A.H., Lee, J.K., Hawkes, N., 2005. Response of supergene processes to episodic Cenozoic uplift, pediment erosion, and ignimbrite eruption in the porphyry copper province of southern Peru. Economic Geology 100, 87–114.

Raymo, M.E., Ruddiman, W.F., 1992. Tectonic forcing of late Cenozoic climate. Nature 359, 117–122.

Reich, M., Palacios, C., Alvear, M., Cameron, E.M., Leybourne, M.I., Deditius, A., 2009. Iodine-rich waters involved in supergene enrichment of the Mantos de la Luna argentiferous copper deposit, Atacama Desert, Chile. Mineralium Deposita 44, 719.

Riebe, C.S., Hahm, W.J., Brantley, S.L., 2016. Controls on deep critical zone architecture: a historical review and four testable hypotheses. Earth Surface Processes and Landforms.

Sillitoe, R.H., 2005. Supergene oxidized and enriched porphyry copper and related deposits. Economic Geology 100th Anniversary Volume 29, 723–768.

<div align="right">

Chapter 2

State of the art

</div>

Abstract

In the "state of the art" chapter, I present an introduction to the four main different disciplines necessary to the understanding of supergene copper mineralization. In the first part I will present the general geology of southern central Andes, more specifically, the northern Chile geology of the Atacama Desert and its evolution since the Cretaceous. Secondly, I will present the climatic evolution of the Atacama Desert, and the possible reasons which can explain the aridity onset and the timing proposed for it, by the numerous studies performed in this region. The content of the third part of the chapter will present the geomorphology of the Atacama Desert and more generally the different models proposed for the formation of flat landscapes like the one encountered in the Atacama Desert. Finally, I will describe the present state of knowledge concerning the conditions to form and preserve copper-rich minerals associated with supergene copper enrichment processes, and especially in the Atacama Desert.

2.1 Geology of the Andes and the Atacama Desert

2.1.1 Generalities

The subduction of the Nazca oceanic plate below the South American continental plate (Dewey and Bird, 1970) erects the longest mountain range known as the Andes (Figure 2.1), approximately 7000 km long, and rising up to ~7000 m high.
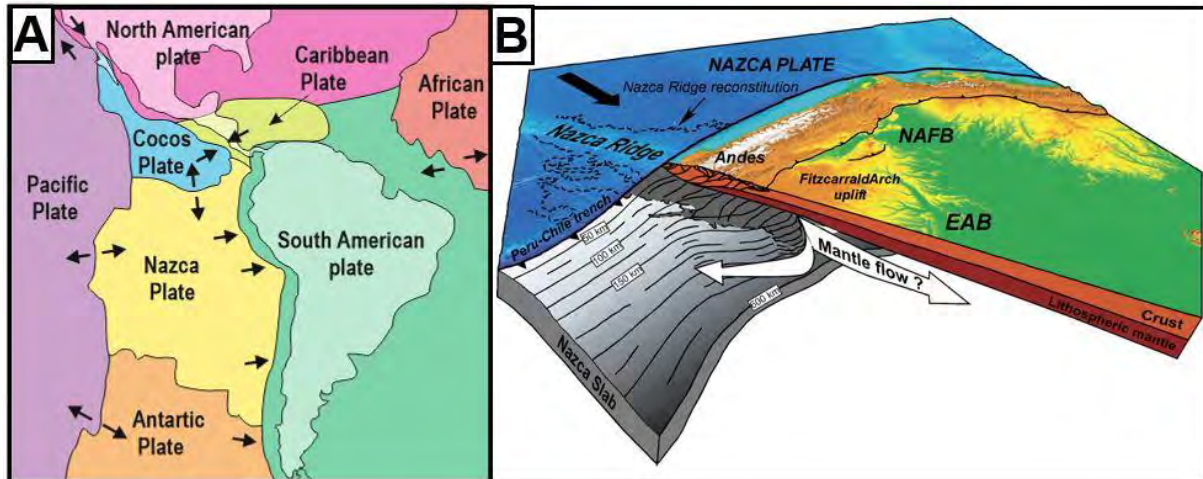
Figure 2.1 – Plate subduction in South America. **A**. Plate tectonics in the American southern hemisphere with direction of plate migration (USGS). **B**. 3D representation of the Andean subduction, NAFB North Amazonian Foreland Basin, EAB: East Amazonian Basin after Espurt et al. (2007).

One of the most significant expression of the coupling between these plates is the seismic activity, all along the subduction zone (Figure 2.1). Inter-plate friction is responsible for destructive earthquakes like the Chilean one described by Charles Darwin in 1846, the Mw~9.5 Valdivia earthquake in 1960 or the Mw~8.8 Maule earthquake in Chile in 2010 (Figure 2.2).

The tectonic regime type has varied over time according to several parameters such as the obliquity of the subducting plate, the convergence rate, the plate velocity, the subduction of oceanic plateaus as well as the quantity of sediments in the trench (e.g. Isaacks 1988; Lamb and Davis, 2003; Martinod et al., 2010; Martinod et al., 2016). The diversity of subduction cases is illustrated by profiles of the coupling plates along the Andes (Figure 2.3). The slab slope can change through time and space as illustrated in Figure 2.3. This generates different type of magmatic activity, and in case of flat slab, it even causes magmatic activity migration or even its possible cessation (Gutscher at al., 2000a, 2000b).
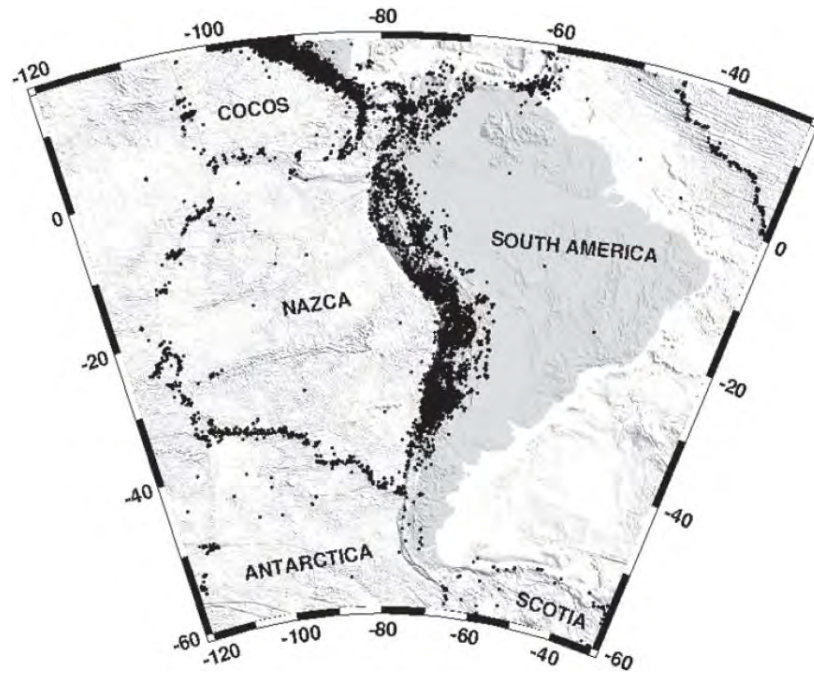
Figure 2.2 – Seismicity map in southern America, reflecting plate boundaries (Barrientos, 2007), from data. Black points represent seismicity reported by NEIC for the period 1973–2004
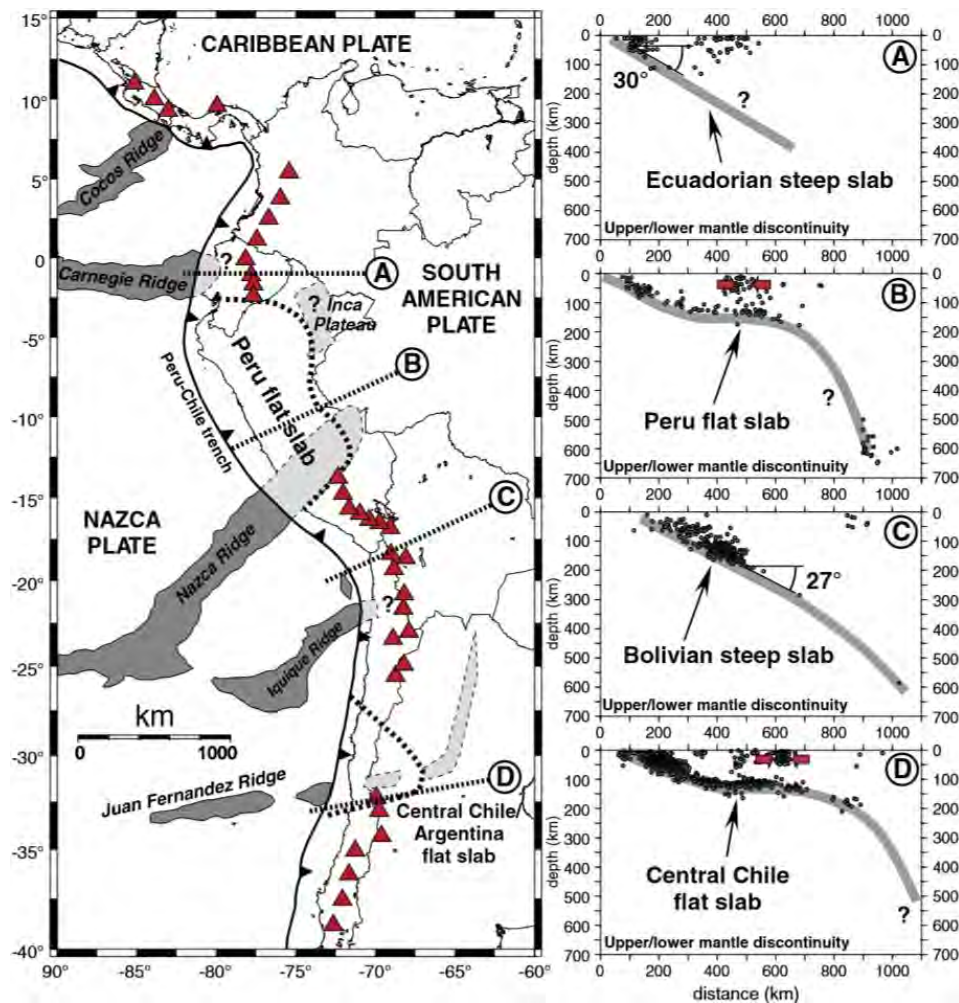
Figure 2.3 – Slab present-day configuration of the Andean cordillera, after Espurt et al. (2008). Triangles mark active volcanoes. Flat-slab segments and oceanic ridges have been reported (Martinod et al., 2010).

2.1.2 Andean segmentation

The Andean physiography has been divided into three latitudinal segments which differ from each other on width and elevation criteria (e.g. Sempere et al., 2002). Namely the northern Andes from 12°N to 4°S is constituted by the Ecuadorian, Columbian and Venezuelan range, the Central Andes 4°S-35°S in Peru, Bolivia and Chile, and the Southern Andes from ~35°S to ~55°S in Chile (Figure 2.4). The Central Andes can be subdivided itself into three parts: the northern segment from ~4°S to ~13°S mainly located in Peru, the so-called Central Andean Orocline between ~13°S and ~28°S including part of Peru and Chile in its western flank and finally the southern Central Andes from ~28°S to ~35°S located in Chile and Argentina.

Figure 2.4 – Segmentation of the Andes at different latitudes, after Sempere et al. (2002).

2.1.3 Geology of northern Chile in the region of Antofagasta

In the Central Andean Orocline from 23°S to 28°S (Figure 2.4) the Chilean forearc can be divided from west to east into the Coastal Cordillera, the Central Depression, the Precordillera, the Western Cordillera and the Altiplano (Jordan et al., 1983; Borgel, 1983).

These units correspond to different lithologies, which are going to be described in the following. In northern Chile the Coastal Cordillera reaches up to ~1500 m.a.s.l. and is characterized by an abrupt cliff (e.g. Paskoff, 1977; Macharé and Ortlieb, 1992; Regard et al., 2010). The Central Depression is located between 1000 to 2000 m.a.s.l while the Precordillera, the western Cordillera and the Altiplano correspond to elevations between ~2500 and ~4000 m.a.s.l. (Figure 4.5).

I will first present lithology and then present the deformation and exhumation evidences identified in the Precordillera, which will be the focus of this work.
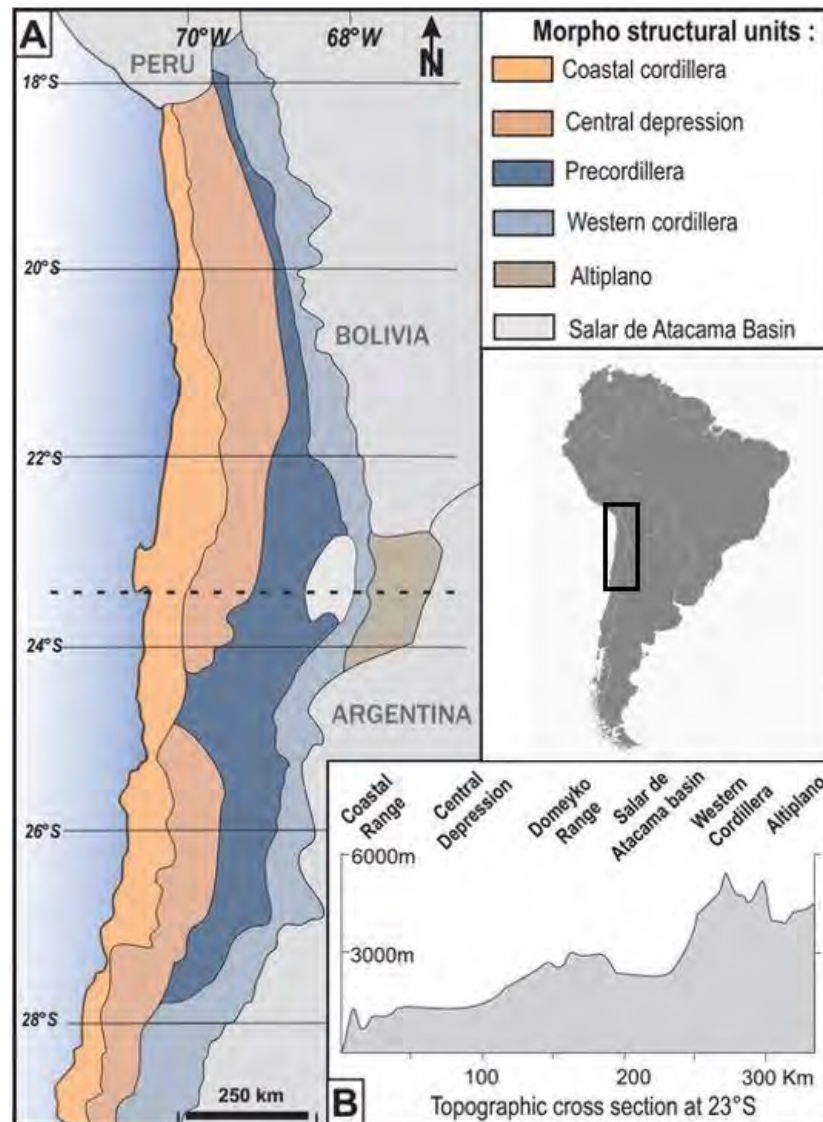
Figure 2.5 – A. Morpho-structural in northern Chile B. Topographic profile of the forearc at 23°S, after Valero-Garcés et al. (1999).

2.1.3.1 Lithology

The northern Chilean geology in the region of Antofagasta reflects many geologic events associated with variations in the subduction dynamics.

The geology is characterised by terranes accreted to the South American margin during the Paleozoic constituting the basement, old magmatic arcs and active magmatic arcs, wide Jurassic marine incursions, and finally Neogene continental sediments (Figure 2.6).
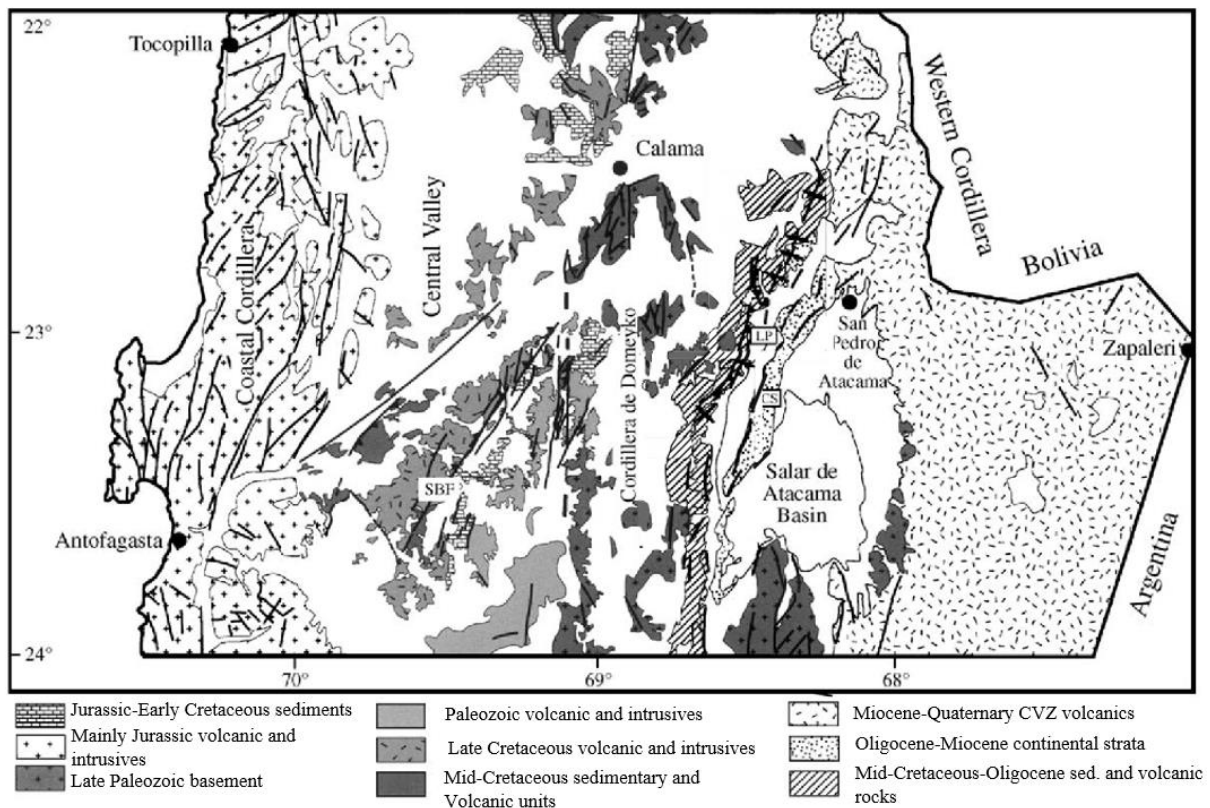
Figure 2.6 – Geological map of the Antofagasta region between 22°S to 24°S., after Mpodozis et al., (2005).

Volcanic units show the progressive migration of the volcanic arc toward the east from the Jurassic to present day (Figure 2.7), and form four large north-south oriented distinct ancient arcs (Scheuber et al., 1994). In the Coastal cordillera, the Jurassic arc corresponds to the broadly distributed La Negra volcanic formation. Huge plutonic gabbroic and granodioritic bodies intruded these volcanic deposits through NS and NW-SE sinistral strike-slip and normal faults in a context of intra-arc controlled by oblique subduction (e.g. Parada et al. 2007; Grocott and Taylor, 2002). In the Central Depression, Late Cretaceous plutons of andesitic and rhyolitic-dacitic nature correspond to migration of the magmatic arc towards the East. This period is characterised by a major plate reorganization and by a phase of shortening in the Andes ("Peruvian" phase, Charrier and Vincente 1972; Charrier et al., 2007; Charrier et al., 2009). A foreland basin developed to the east of the arc, in which the Purilactis formation deposited during the Late Cretaceous to Eocene and that is nowadays located in eastern border of the Salar de Atacama (e.g. Arriagada, 1999; Mpodozis et al., 1999).

In the Precordillera, called the Domeyko range in this region, Paleocene and Eocene intrusions and calderas testify of a new eastward migration of the arc during the Incaic phase.

Paleomagnetism shows that most of the bloc rotations occurred by that time and no major rotation is recognized after 25 Ma (Arriagada et al., 2000, 2003, 2008; Narea et al., 2015).

36

A notable volcanic gap occurred between 38 and 26 Ma, a quiescence interpreted as a flat slab period (Soler and Jimenez, 1993). No intrusions younger than 37 Ma have been observed around 23°S in the Precordillera, but ignimbrites of about 10 and 5 Ma in age have been recognized (Da Silva, 1989). Finally, the active arc is located in the Western Cordillera.
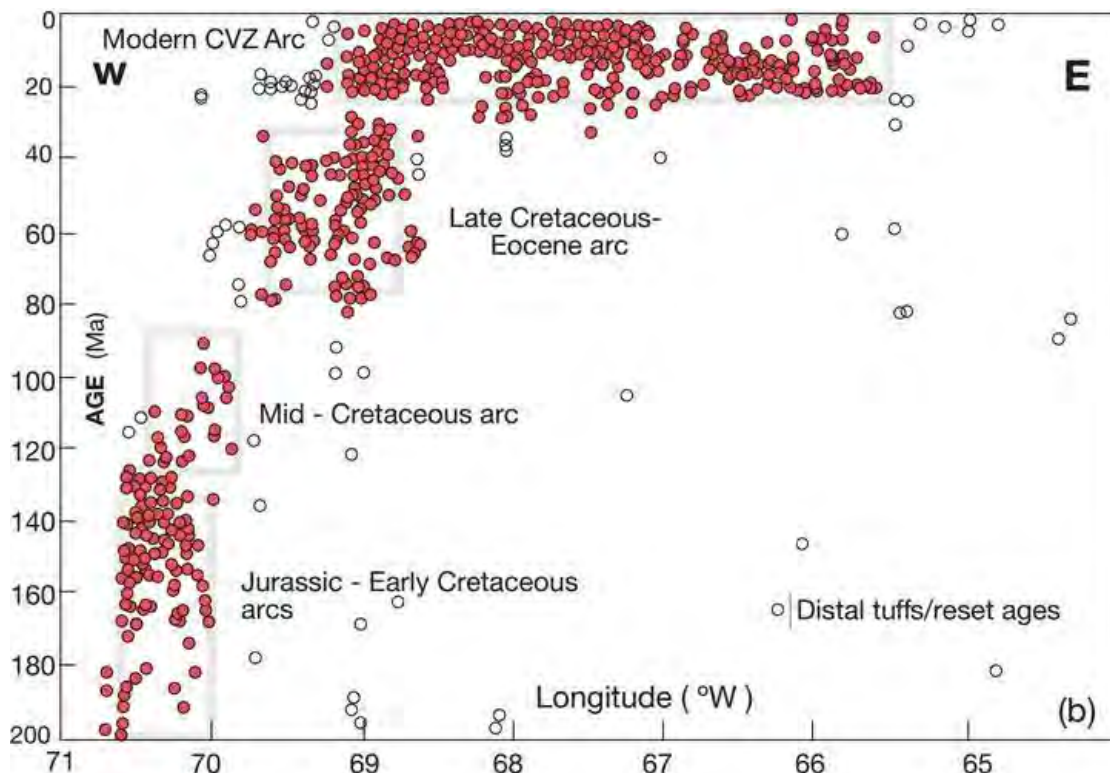
Figure 2.7 – Migration of the magmatic arc to the east through time (Mpodozis and Cornejo, 2012 after Haschke et al., 2002), illustrated by volcanic rock ages vs longitude.

The deposit of Mesozoic marine and continental sediments in this region began in the Sinemurian to Kimmeridgian, in a context of back-arc extension. At that time, the arc was located in the Coastal Cordillera. The corresponding geological groups were called Quinchamale and Caracoles. The ~5000 m thick Bajocian to Kimmeridgian Caracoles group deposited on the eastern flank of the Jurassic back-arc basin is now found in the Pre-Cordillera, on the western flank of the Domeyko range (Figure 2.8).

During the Late Cretaceous and Early Cenozoic shortening phase, as indicated above, a foreland basin has developed to form the Purilactis sedimentological series, nowadays located in the Salar de Atacama western border. The base of this series is constituted of marine limestones, which argue for a contemporary rifting context.

Above, the continental terrigenous series is mainly composed of conglomerates and coarse sandstone with some volcanic intercalations (Muñoz et al., 2002; Mpodozis et al., 2005; Bascuñan et al., 2015).

There is no unanimity between scientists about the tectonic control on deposition of these sediments (see Charrier et al., 2010). Some authors argue for an extensional context (somehow related with opening of the Atlantic Ocean (Macellari et al.; 1991; Hartley et al., 1992 and Flint et al., 1993), whereas others assert that a first period of extension followed by a tectonic inversion in the Late Cretaceous, led to the eastward thrusting of the Pre-Cordillera over the Salar de Atacama basin (Figure 2.8) (Bascuñan et al., 2016; Mpodozis et al., 2005).

Sedimentation continued overlying the Purilactis group up to the Pliocene and probably Pleistocene, with the deposition of evaporites (e.g. Muñoz et al., 2002). In total, the Salar de Atacama infill reaches ~9000 m.
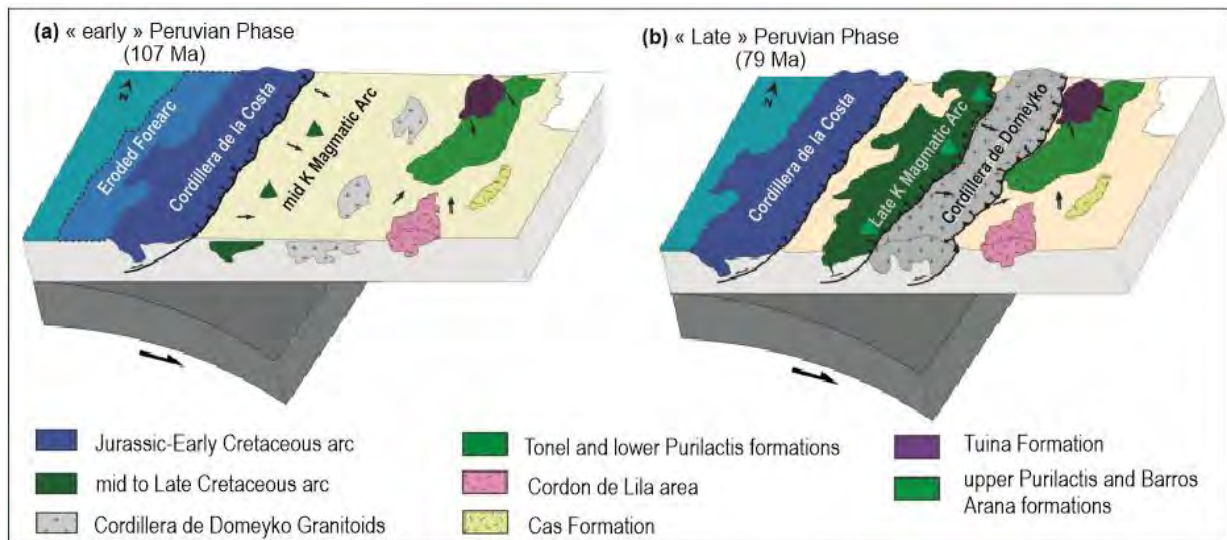
Figure 2.8 – Schematic cross-section of northern Chile between 22°–23°S, showing basin and orogenic wedge evolution. The figure also shows a hypothetical eroded forearc (Bascuñan et al., 2015).

Between the Coastal Cordillera and the Salar de Atacama, Eocene-Oligo-Miocene gravel constitutes most of sedimentary cover. Their thickness reaches from several tens of meters to ~1000 m. Two basins were particularly well studied in this region, the Calama Basin, and the Centinela Basin. As the deposition time of these sediments encompass the period studied in this manuscript, (Eocene to present), I recall here the main units.

The Calama basin is located in the northern border of the studied region. It contains several hundred meters of sediments from the Eocene to Late Pliocene-Pleistocene with four different identified depo-centres (Jordan et al., 2015). There seems to be no agreement about the stratigraphic subdivision of this basin (Hartley and Evenstar, 2010 and Jordan et al., 2014). The most recent compilation of sedimentological data can be found in Jordan et al. (2014).

A simplified stratigraphy may include the Eocene Calama formation (conglomerates), the Oligocene Yalqui formation (sandstones and conglomerates), the Miocene El Loa group (ignimbrite, sediment breccias, sandstone) and the Plio-Pleistocene Opache and Chiu-Chiu formations (sandstones and limestone) (e.g. Blanco et al., 2003; May et al., 2005, Mpodozis et al., 2005; Jordan et al., 2014).

The Centinela basin records a similar time period as the Calama basin in a ~1000 m thick infill. It is mainly filled by alluvial deposits with few intercalated sandstones, limestones and paleosoils, with only two ash deposits at ~37 Ma and ~10 Ma (Figure 2.9). This makes the dating of the different formations difficult (Mora et al., 2004; Tapia et al., 2012; Oerter et al., 2016; Riquelme et al., 2017).

The lowest member of the Centinela basin is the Eocene Esperanza formation. Then comes the El Tesoro formation, up to 700 m thick. This formation hosts exotic copper and has been assigned to Oligocene. Eocene zircons present in these sediments indicate that porphyry copper of the Domeyko range were massively eroding at that time and provided the sediment filling the basin. The upper part of the infill is the Arrieros formation, a widely extended late Miocene gravel cover corresponding to a widening of the basin, interpreted by Riquelme et al. (2017), as a pedimentation stage, which appears consistent with new results presented in the following chapters. The ~10 Ma ignimbrite seals the present-day topography in many places, signing a sudden stop in the sedimentation. However, younger sediments testify of an ongoing, although very slow, sedimentation in valleys (Davis et al., 2014).
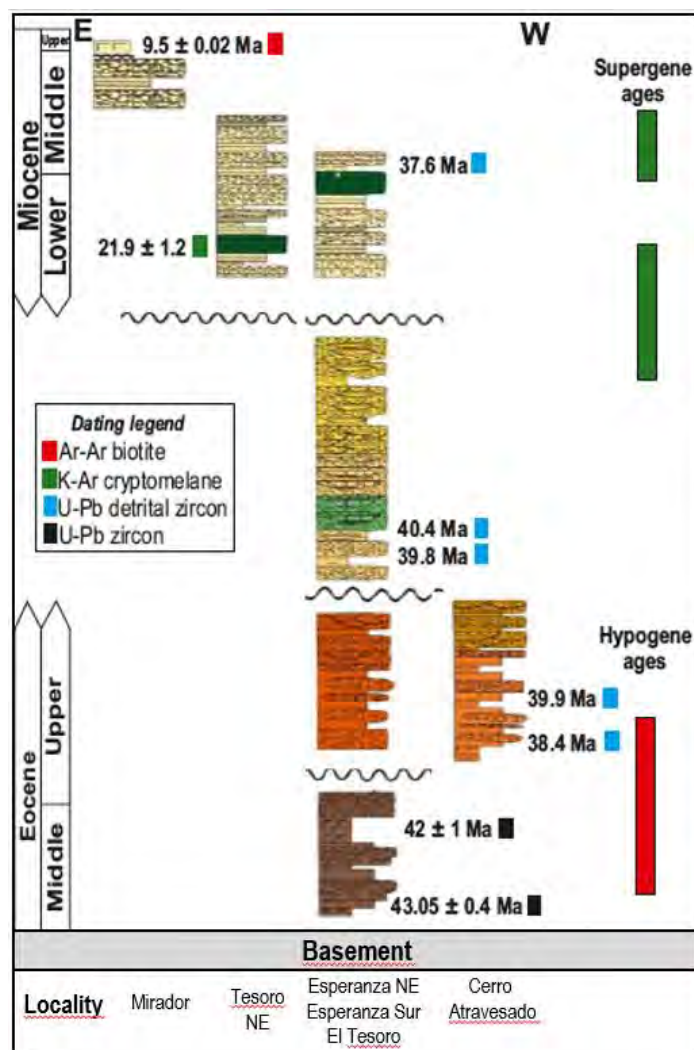
Figure 2.9 – Centinela basin stratigraphy along a ~8 km latitudinal transect along with detrital Ar-Ar biotite age in red, U-Pb detrital zircon ages, in blue, cryptomelane age, in green and U-Pb zircon ages in black after Riquelme et al. (2017).

In the Calama and Centinela basins, both infills indicate an arid climate from the Eocene to hyper-arid current climate. These sediments reflect the uplift and erosion of the adjacent Domeyko range during the so-called Eocene Incaic phase, with depo-centers probably influenced by faulting. Then the Oligo-Miocene sedimentation area is widened in absence of significant creation of accommodation space (Riquelme et al., 2017).

2.1.3.2 Structural framework

In addition to the subduction thrust, two main fault systems have controlled the fore-arc deformation in the studied region since the Jurassic (Figure 2.10). These fault systems are roughly parallel to the subduction trench.

The westernmost fault system is the Atacama Fault System (AFS) whose activity started in the Early Jurassic probably with the initiation of the South American subduction and the beginning of the Andean Orogeny (Scheuber et al., 1994). It has been active during the Neogene (Riquelme et al., 2003) with some strike-slip and mainly vertical movements (e.g. Gonzalez et al., 2003; 2006).
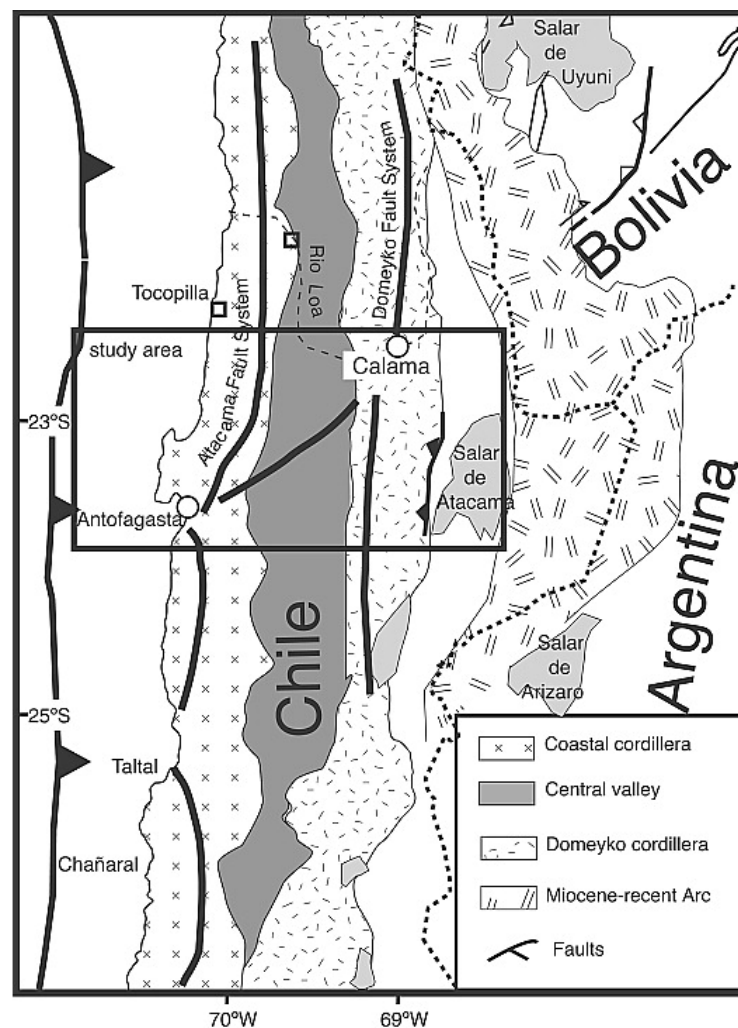
Figure 2.10 – Simplified structural geological map of northern Chile between 27°S-21°S, (Arriagada, 2003) with Atacama Fault System (AFS) and Domeyko Fault System (DFS).

The second notable fault system, to the east, is a strike-slip system called the Domeyko Fault System (DFS) occurring in the Precordillera. The DFS is also parallel to the coastal border which activity begun during the Eocene (Mpodozis et al., 1993). The DFS is of a particular interest for this PhD thesis because it controlled both the sedimentation in the Centinela basin and the exhumation of the studied porphyry-copper deposits.

Note that the region of Antofagasta seems to not correspond to the model by Armijo et al. (2015), arguing that the West Andean Thrust system (WAT) is the main fault system controlling the westward thrusting of all the Central Andes over the forearc. Although the WAT has been recognized for many years in many places along the Chilean (and Peruvian) Andes (Charrier et al., 2009), it seems absent in this region. Actually, the main deformation seems to have occurred in the Pre-Cordillera since the Late Cretaceous along strike-slip and east-vergent faults (e.g. Muñoz et al., 2002; Bascuñan et al., 2016).

2.1.3.3 Exhumation quantification

Several decades ago, the large deformation of the central and southern Andes was classified through three phases. That classification includes: Peruvian phase (inversion in the Late Cretaceous, Pfiffner and Gonzalez. 2013, Mora et al., 2010), Incaic phase (Eocene compressional phase) and Quechua phase (Miocene reactivation of Eocene faults), which were recognized in southern Peru phases. The ubiquity of these past deformations all over the Andes is still debated. Additionally, to the differentiated manifestation of these deformation phases along the Andes, there is also a debate about the duration of the phases. For example, concerning the Incaic Eocene phase, several studies point out very punctual deformations (Hammerschmitd et al., 1994) whereas other authors propose a long deformation phase (Maksaev and Zentilli, 1990, Jaillard et al., 1996).

To study the vertical deformation, structural analysis was carried out (Mpodozis et al., 1993) on one hand, and on the other hand rock path exhumation quantification of rock has been determined in some places through low-temperature thermochronology methods (specific details are described in the following chapters).

In the three last decades, thermochronology has been applied in the northern Atacama Desert (Figure 2.11), starting with Maksaev's PhD thesis, 1990. Maksaev and Zentilli (1999)'s publication was the first to quantify the Precordillera exhumation and timing using the fission track on apatite method. The authors suggest that before 30 Ma, exhumation rates were about 200-100 m.My^{-1} and dropped to 50 m.My^{-1} after 30 Ma. A study of the major Chuquicamata copper ore deposit was published the same year (McInnes et al.,1999) showing the cooling history of the ore deposit. Then thermochronological data (U-Th)/He obtained on apatite and zircon from the coast to the western Cordillera at ~26°-27°S, were presented in 2007 in which the authors suggest different steps for the forearc exhumation (Nalpas et al., 2007), with younger ages moving to the east. This was confirmed by the dataset from Reiners et al. (2015) on at the forearc larger scale.

Even though significant works were performed, the studied objects were really local or very large scale (McInnes et al., 1999; Campos et al., 2009; Maksaev et al., 2010), mainly to constrain the cooling history of the porphyres. There is a lack of thermochronological study at the scale of mountain-plus-basin systems which appear necessary to better understand the formation of supergene copper ore deposit (McInnes et al., 2005). Furthermore, previous studies did not allow the paleo relief and its relation with the formation of supergene copper to be really defined.
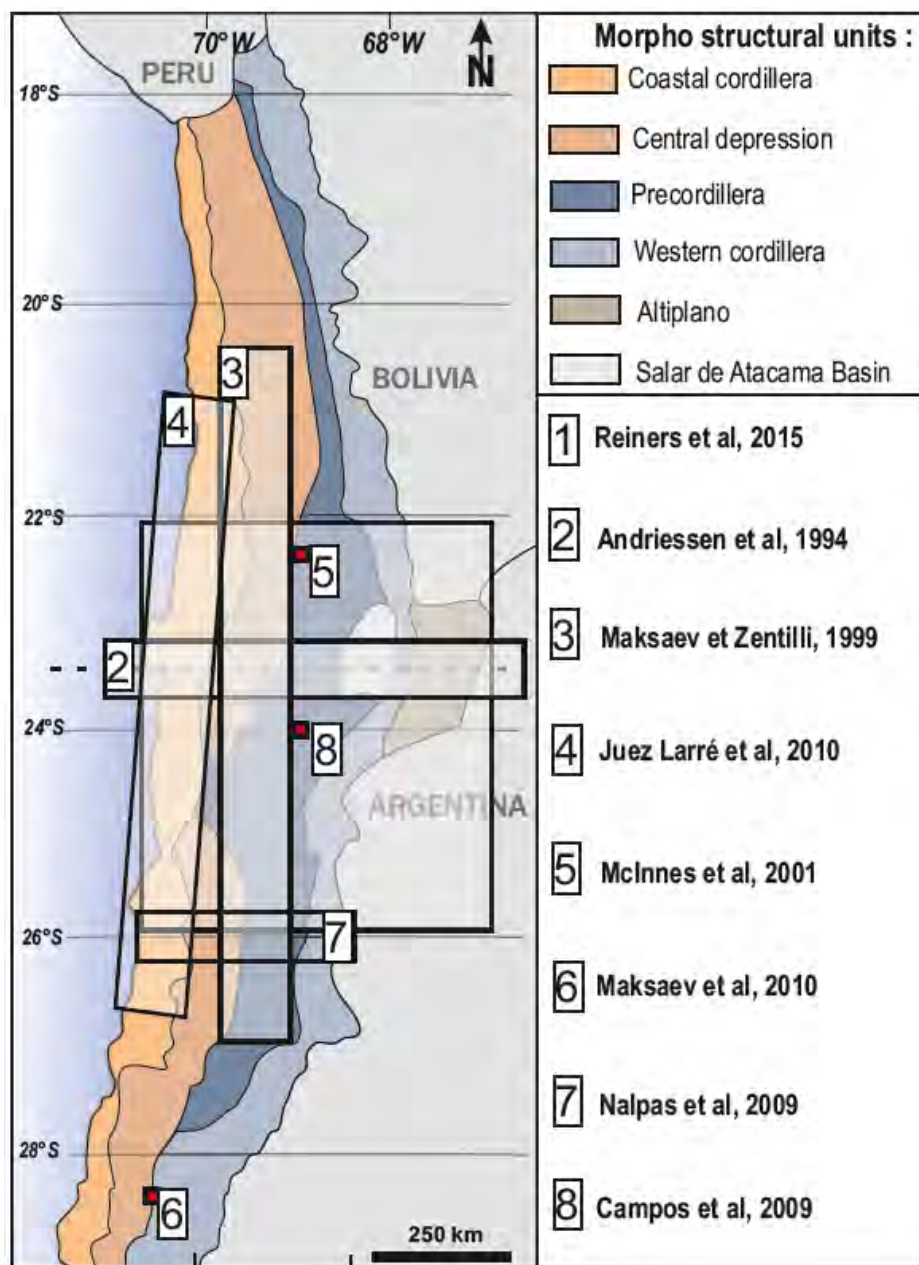
Figure 2.11 – Low-temperature thermochronologic study zone in the Atacama Desert from 28°S to 18°S (Maksaev et al., 1990; Andriessen et al., 1994; Reiners et al., 2015; McIness et al., 1999).

2.2 Climate of the Atacama Desert

2.2.1 Definition

The Atacama Desert, which extends from ~30°S in Chile to 10°S in Peru is the driest non-polar desert on the planet (New, 2002; McKay et al., 2003). As one can see in Figure 2.12, the rainfall distribution shows the transition between arid and Mediterranean climate at 30°S.

Present-day precipitations of this Desert, defined as hyper arid, are inferior to 20 mm.yr^{-1} (Houston, and Hartley, 2003) with areas of extreme hyperaridity where precipitations are inferior at <1 mm.yr^{-1} (Garreaud et al., 2009). The precipitation rate spatial variations in the Desert are mainly related to altitudes. The rare precipitation events are generally related to El Niño events.
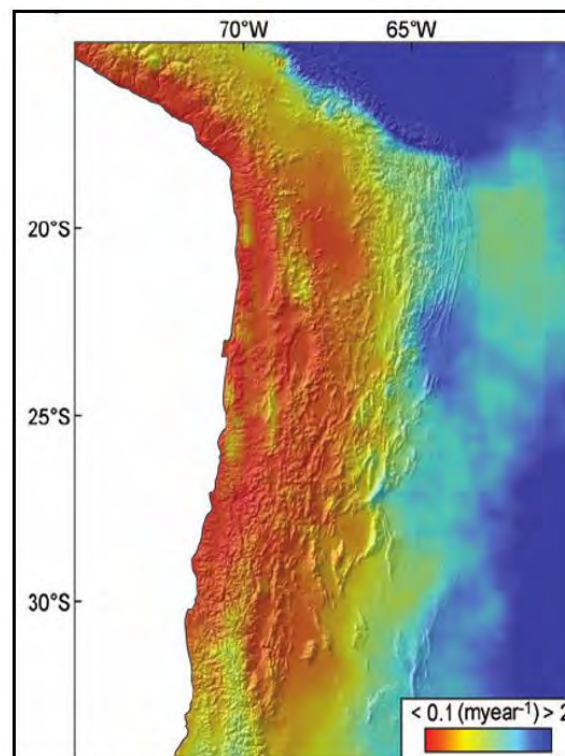
Figure 2.12 – Rainfalls rate in the Norther Chile, Atacama Desert, **from ~15°S to 35°S** (m.yr^{-1}), (Strecker et al., 2007).

2.2.2 Why is northern Chile a desert?

The different mechanisms suggested by Hare (1961) to explain the Atacama Desert formation are depicted in Figure 2.13. They are displayed together with precipitation rates and altitude in the forearc between Arica and Belen, near 18°S in northern Chile (Figure 2.14).

First of all, a strong control is exerted by the presence of the subtropical ridge which is a significant high atmospheric pressure belt at 30°S, as witnessed by the presence of major deserts (Namib Desert, Australian Desert…) on Earth.

The southern pacific anticyclone prevents moisture formation on the west coast of Chile and provides atmospheric stability. A second reason relies on the influence of the Humboldt oceanic cold current, which originates near the Antarctic since Drake's passage.

This cold current refreshes the marine air mass and prohibits the generation of water vapour, and thus inhibits precipitation on the continent (Houston and Hartley, 2003). The third major mechanism is the elevation of the Andes forming a physical barrier to hotter and wetter air masses coming from the Amazonian basin. All the water driven southwards the Amazonian basin is dropped when air masses rise, condense and discharge on the Bolivian side of the Andes (Zhou and Lau, 1998; Vuille and Amman, 1997). This effect is also called the orographic rain shadow effect. Despite those hyper-arid conditions, rare and catastrophic rainfall events occur during El Niño and la Niña periods in the Atacama Desert (Ortlieb et al., 1994; McKay et al., 2003; Houston et al., 2006).
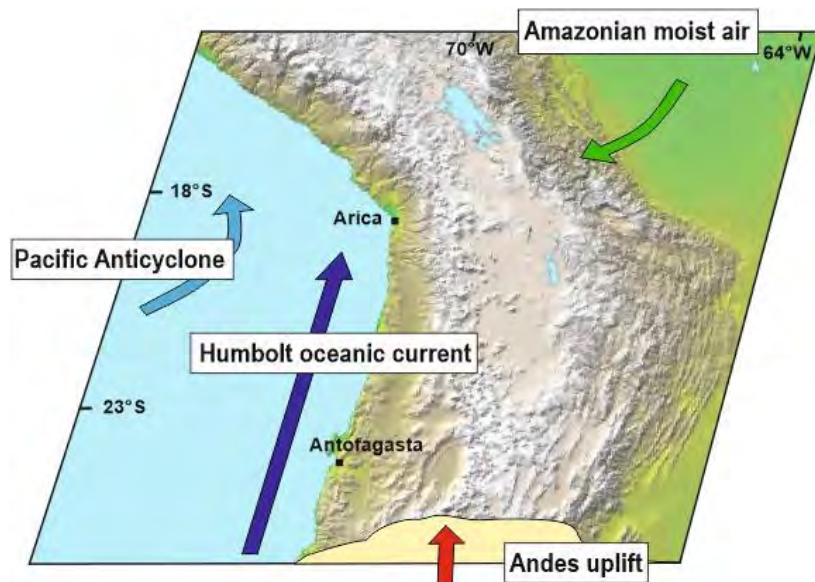
Figure 2.13 – Possible mechanisms responsible for low precipitations in the Atacama Desert. DEM from http://photojournal.jpl.nasa.gov/jpeg.
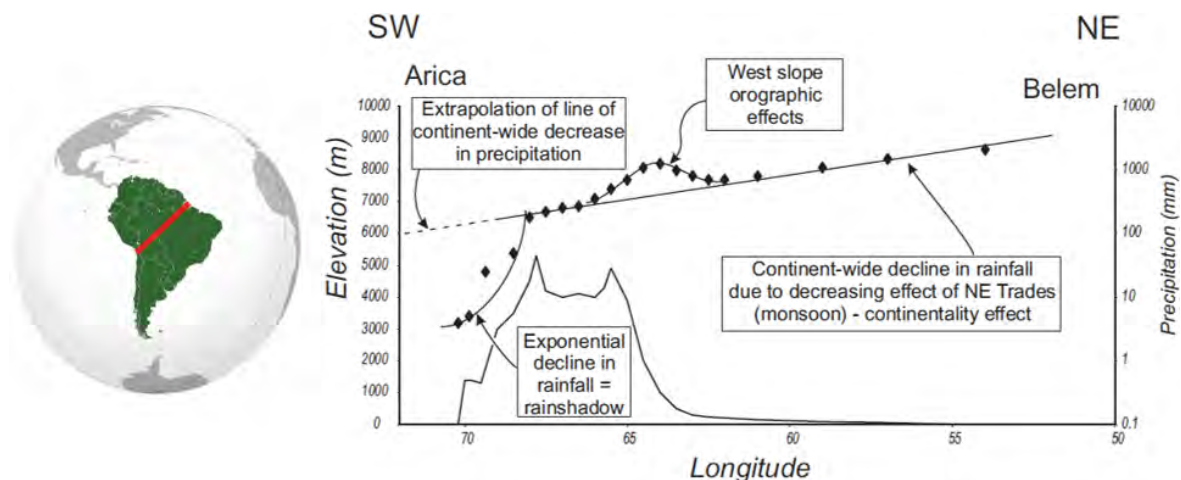
Figure 2.14 – Generalized latitudinal section of precipitation and elevation from 70 to 50°W based on Philip's World Atlas Fullard and Darby (2001), Lizarazu et al., (1997), Dirección General de Aguas de Chile and Houston and Hartley (2003).

The potential coupling between the rising of the Andes and a major climate change has been invoked to explain the Late Miocene surface uplift of the Andes (e.g. Lamb and Davis, 2003). Furthermore, the Andes relief influence on the southern atmospheric circulation is thought to have controlled Andean erosion and morphology (Montgomery et al., 2001).

Yet, the causality or synchronicity between the uplift and the rain shadow effect is debated. (U-Th)/He geochronology on hematite to recover the incision timing in northern Chile suggest that aridity is posterior to the main Andean uprising episode (Cooper et al., 2016). Numerical modelling of global ocean circulation concludes that decreasing the elevation of the Andes does not increase the rainfall in the Atacama region (Garreaud et al., 2010). This result suggests that the Andean uplift was not the driver of Atacama hyper-aridity, which should be rather associated with a strengthening of the Humbold current (Garreaud et al., 2010)

2.2.3 Since when?

To date the onset of aridity, a panel of different approaches exist such as sedimentological study, soil analysis, surface exposure dating, copper supergene mineralization and stable isotope analysis on sediments. All these methods have been applied with a large panel of results and ages (Figure 2.15).
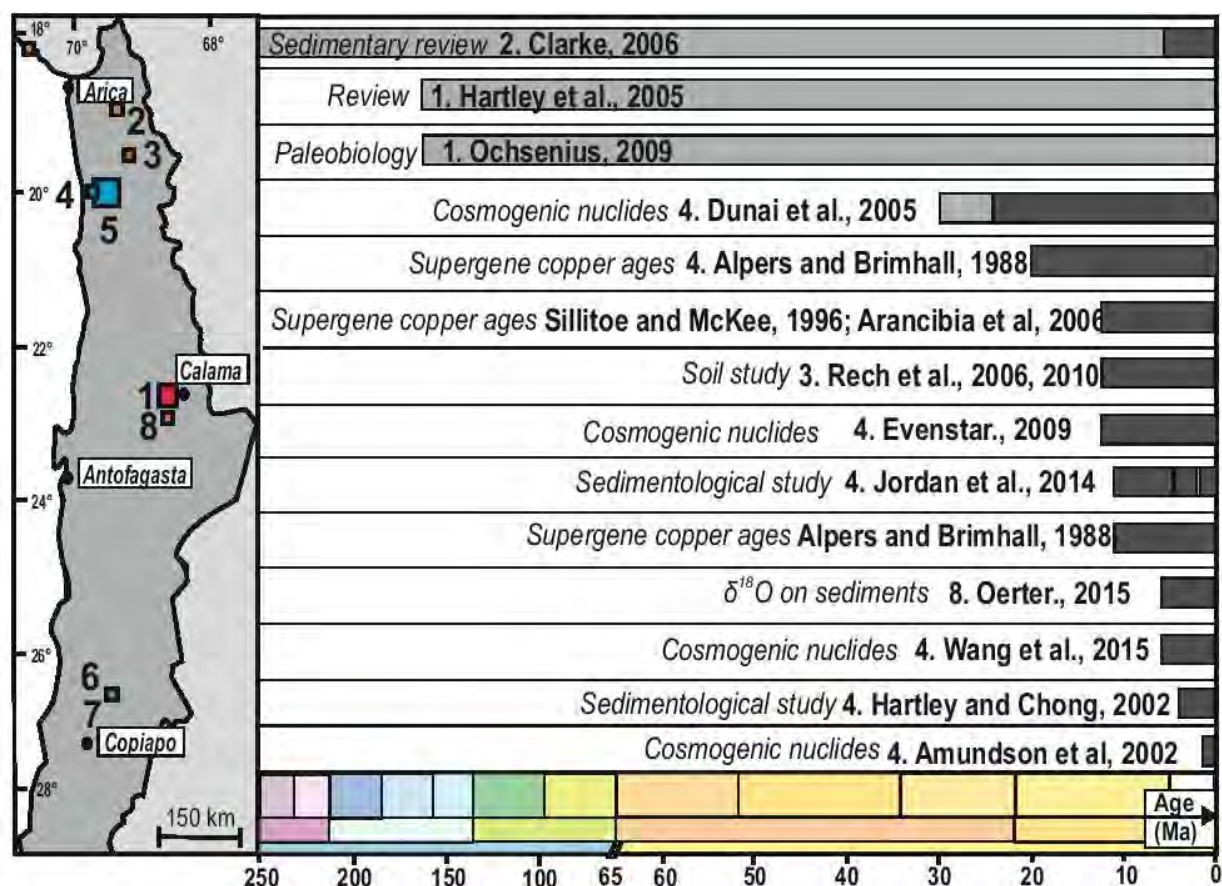
Figure 2.15 – Summary of aridity ages proposed for the Atacama Desert, the tool used to obtain the age and references. Variation in precipitation rates >100 mm.y^{-1} in dark grey and <100 mm.y^{-1} in light grey.

Those age variations can also be explained by spatial repartition in different morpho-structural units. For example, the altitude or the proximity to the coast can generate different moisture conditions and thus different precipitation rates and erosion rates. The difference in ages can also arise from inherited paleo-surfaces which do not always reflect average erosion rates but local events. Hence, we chose to make a difference between different grades of aridification with 100 mm annual rain precipitation and of hyper-aridification with precipitation <100 mm.y^{-1}. This range is presented in Figure 2.15.

Triassic and Jurassic ages have been proposed (Hartley et al., 2005; Clarke et al., 2006) for the Atacama Desert aridification. These old ages were justified by the absence of significant latitudinal movements of the South American plate (accorded to paleo-magnetic data). Most of the studies consider younger ages, relying on different types of dating methods, mostly applied to sediments or surface bedrock (Figure 2.15).

Surface exposure ages derived from cosmogenic nuclides have been proposed as a proxy for the Atacama aridity onset, but show a strong scatter (see Chapter VI). Even when applied to one geomorphic surface, the dating based on cosmogenic nuclides leads generally to a large range (several million years) of ages (Evenstar et al., 2009).

Oligocene-Miocene ages have been proposed for the onset of the aridity, derived from surface ages by Dunai et al. (2005) using ^{21}Ne clast exposure dating in the Precordillera and consistent with supergene alteration in cerro Colorado at 34-35 Ma (Bouzari and Clark; 2002; Sillitoe and Mckee, 1996). Other surfaces ages (Evenstar et al., 2009) have been proposed with a large span from 0.1 to 22 Ma.

These older ages support the idea that aridity is a cause for the Andes elevation more than a consequence. The formation of some ore deposit (as supergene Cu-related) can be used as a climate proxy: their formation (see section 4.1) requires precipitation rates lower than 100 mm.y^{-1}. Thus, several authors based their study on this assumption (e.g. Alpers and Brimhall, 1988; Sillitoe and McKee, 1996), showing that the aridity in the Atacama Desert occurred 12 Ma ago with the cessation of supergene alteration ages in the Precordillera, in northern Chile.

As illustrated in Figure 2.15, the majority of the ages advanced for the Atacama Desert aridity onset are Miocene ages. Indeed surface exposure dating (Nishiizumi, 2005) and sedimentological studies (Jordan et al., 2014) suggest Miocene ages. The change of soils in Miocene to Pliocene sediments interpreted as precipitation drop from semiarid to hyperarid climate between 19 and 13 Ma matches results from stable isotopic studies (Rech et al., 2006, 2010, Oether et al., 2015) which also suggests Mid-Miocene ages.

Other studies, such as Hartley and Chong, (2002) based on sedimentological investigations proposed upper Miocene-Pliocene ages, meanwhile 6 Ma old to actual variations were highlighted by ^{10}Be variation in soils (Wang et al., 2015).

2.3 Atacama geomorphology

2.3.1 Atacama pediplain

The Atacama Desert is known as being the world's non-polar driest and oldest rock desert. In terms of geomorphology, an important proportion of it is considered as flat. A hanging cliff at 1000 m a.s.l. form the costal line, extending over 1600 km from southern Peru (18°S) to northern Chile (26°-27°S).

In the Atacama Desert, the pediplain/peneplain/pediments have been studied for a long period. They have been identified in the late 19th century by Darwin, followed since by pioneer geomorphologists. Mortimer (1973), which worked on geomorphology-ore deposit relationship named this region the Atacama Pediplain.

Figure 2.16 –View to the south of the pediment in Centinela District at 23°S, 69°, at 2500 m.

In the Centinela district and around, the Atacama Pediplain is composed of bare-bedrock low relief surfaces, covered in some places by an alluvial cover (Figure 2.16). We called these surfaces "pediments" in the following. The thickness of the cover reaches locally up to several hundreds of meters, as in the Calama or Centinela basins, but it generally does not exceed a dozen meters. This is a very different situation compared to the northernmost Chile where up to several kilometres of Cenozoic sediments are deposited in the forearc.

As in the classical definition, the morphometry of each pediment constituting this vast peneplain can be described by different zones: a degradation zone, a zone of transport and a zone of aggradation (Figure 2.17).

2.3.2 Geomorphological models of pediments under arid climate

As illustrated in Figure 2.16, the Atacama Desert slopes are usually weak. These low relief features represent the last stage of the geomorphological cycle (Davis, 1889). Thus, a lot of questions about the origin and the formation of such flat surfaces remain. Through time, low relief erosive landforms have been named differently as peneplains, pediplains, glacis or pediments (Tricart et al., 1972; Dohenweren et al., 2009).
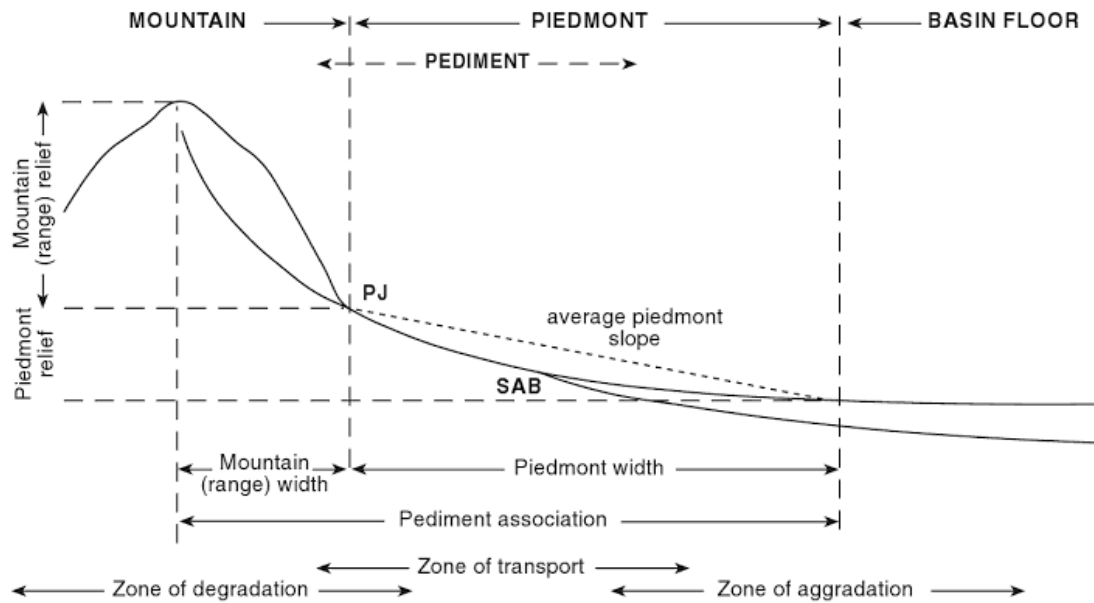
Figure 2.17 –Representation of a pediment association, after Cooke (1970) in Dohrenwend et al. (2009). PJ: piedmont junction; SAB: subaerial alluvial boundary.

The difference between each term is still indecisive but some generic meaning has been proposed: a pediplain describes an extensive low relief surface, mostly erosive, that brings together various pediments (e.g. Twidale, 1992). Other authors differentiated them according to their surface area. The term peneplain assumes that various pediplains can form at the same time at different elevations, meaning that base level changes are not necessary to explain these different levels (Migon, 2004). To avoid any misunderstanding in the nomenclature, from now on we use the term pediment to describe an extensive erosion low relief surface, partially covered by alluvial sediment.

Different models have been proposed to establish which main factor was responsible for the formation of the pediments as illustrated in Figure 2.18.
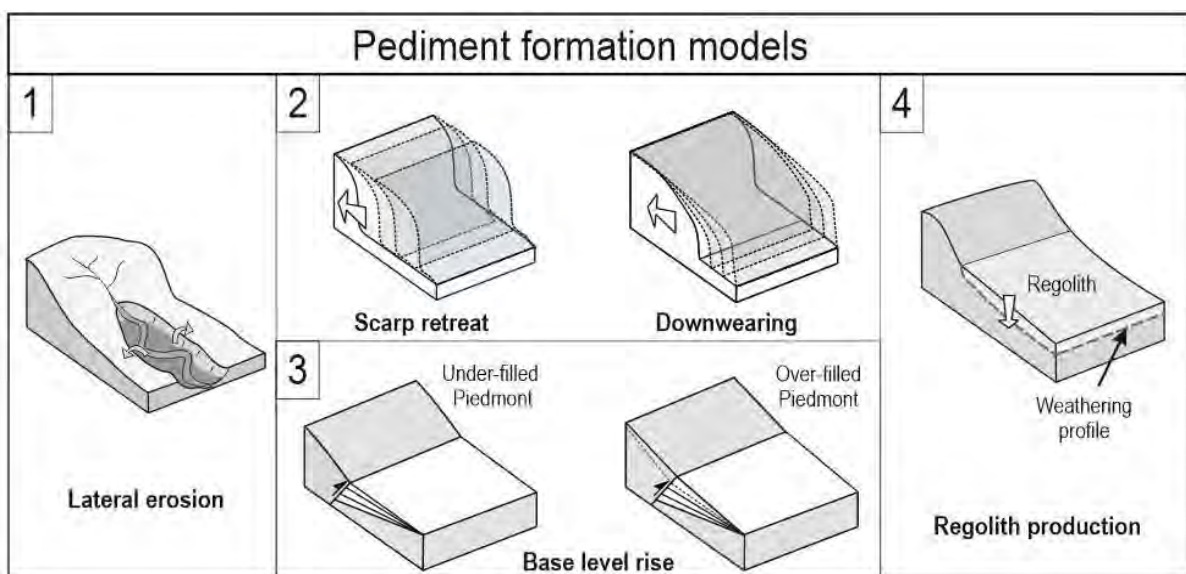
Figure 2.18 – Pediment formation models. 1. Lateral erosion. 2. The scarp retreat versus downwearing. 3. The relation piedmont/mountain. 4. Etching.

The first example (Figure 2.18.1), given in 1877 by Gilbert took place in the Henry Mountains, Utah, USA, suggested that the main process for the pediment formation was lateral erosion, considering the widening of pre-existent streams by river divagation, (also called lately pedi-valleys) (Guillocheau et al., 2015). This lateral erosion process was also called "lateral corrosion" (e.g. Johnson, 1931). Another explanation was proposed by Davis (1938): where the main process would be the downwearing, namely the reduction of the relief by regional diminution of the altitude by erosion processes. Davis (1938) argued that the borders of valley outlets do not usually show evidence of active lateral erosion. He suggested that the relief reduction was dominated by overland sheet-flow. Nevertheless, sheet-flow occurs when the topography has a low roughness, and thus appears as a consequence rather than a cause.

This type of vertical relief decay was then challenged by the concept of scarp retreat (King, 1949, Fig 2.18.2), which is characterised by a parallel erosive front retreat, separating the pediment surface downstream from a backscarp upstream.

A third model (Figure 2.18.3) is linked to the base level rise of a relief during piedmont sedimentation at the foot of a mountain. Such a base level rise decreases the erosion rate of the adjacent relief, lowering the slopes and possibly forming pediments within the mountain bedrock (Babault et al., 2005; Carretier and Lucazeau, 2005).

Finally, the last main process proposed for pedimentation deals with the development of a regolith by weathering, also referred as etching (Figure 2.18.4). It corresponds to the development of an erodible regolith which may foster the erosion above a roughly planar bedrock-regolith interface at a regional scale.

The production of this erodible material may favour the lateral migration of river and parallel retreat (Oberlander, 1974), and thus may act against relief growth by river incision (Strudley et al., 2006a).

In addition to those models, other factors have been pointed out. Pelletier (2010) proposed, through numerical modelling, that the main pedimentation processes could be the production of regolith by weathering and a flexural isostatic response of the lithosphere to denudation.

Few recent modelling studies tried to put theoretical basis for these different processes (Tucker and Whipple, 2002; Strudley et al., 2006a, 2006b; Pelletier 2010). Nevertheless, deciphering between the different causes in specific examples has not succeeded. For example, Braun et al. (2004) tried to determine which of downwearing or scarp retreat models fits the evolution of the southern Australian passive margin the best. They used landscape evolution modelling and a set of low thermochronological data (Persano et al., 2002) in an original approach, but their results permit to demonstrate that "*there are situations where thermochronological data sets do not provide constraints on the mode of escarpment migration (…) where migration has possibly been very rapid*".

In northern Chile along the Andes the pedimentation presents important variations: the thickness of Oligocene to Miocene continental sediment accumulation varies significantly in northern Chile. At latitude lower than 23°S, a large repartition of a thousand-meter-thick, refills the Central Depression. At the south of 23°S, these deposits are not present. It has also been observed that to the north of 23°S the drainage is mostly exoreic while in the southern part of the Atacama Desert it is endoreic. In the northern Atacama region, Riquelme et al. (2003) proposed three possible causes for the pedimentation that occurred in the Central Depression and the Precordillera: first the blocking of the valleys by the uplift of the Coastal Cordillera (Juez-Larré et al., 2010), then the deposit of an abundant gravel sequence associated with relief reduction, and finally the fossilisation of the topography by Mid-Miocene hyper-aridification.

A consequence of the relief flattening problem is the time needed to decay the relief, and by extension, the response time of erosion to an episode of uplift. Actually, the response time to the uplift is a main clue to specify the relief evolution model as proposed by Davis (1889), Penck (1953) and Hack (1975)(Figure 2.19).

From a general point of view, relief reduction leading to pediments is possible if the erosion response time is shorter than the period between two significant surface uplifts. Determining this response time would thus allow pediments to be interpreted in terms of uplift "phases".
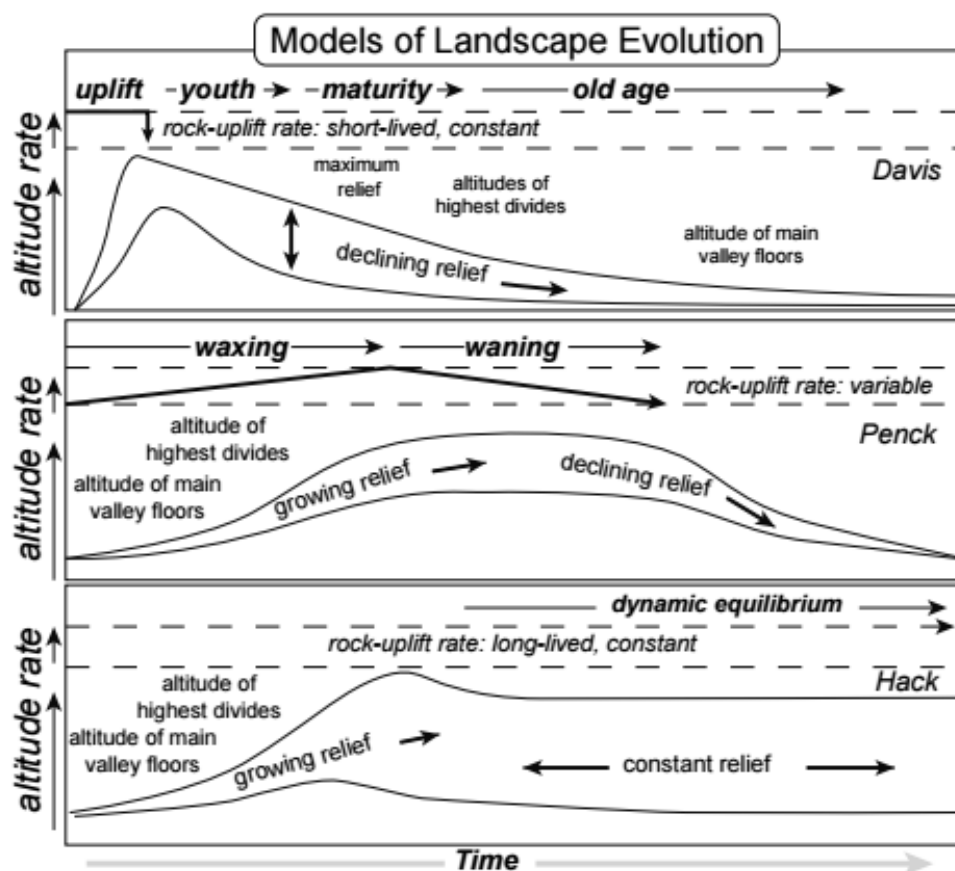
Figure 2.19 – Classical models of tectonic forcing and landscape responses, based on landscape response theories: Davis (1889), Penck (1953) and bottom Hack (1975). After Summerfield (1991).

2.3.3 Methods that permit to date landscapes

To assess the geomorphology state of a landscape, the capacities to quantify the forming processes and also to date it, have represented a crucial point. In the northern Chile, several methods have been applied. The oldest methods applied to date the surfaces are isotopic methods as $^{40}Ar/^{39}Ar$ dating or U-decay series methods. They present the advantage of being highly reliable but present an important drawback: they require the presence of specific minerals, not always present. $^{40}Ar/^{39}Ar$ datings on ignimbrites allow the age of paleo-reliefs like pediplains to be estimated (Mortimer 1973, Tosdal et al., 1984).

The last two decades saw the emergence of new surface dating methods. The major ones rely on cosmogenic nuclides. As these methods are mainly applied to quartz minerals with exception on pyroxene, sanidine (Kober et al., 2005; Ivy-Ochs et al., 2007), they can be applied on nearly all rocks, both bedrock or detrital, and all types: plutonic, metamorphic or sedimentary rocks. Cosmogenic nuclide methods present the great advantage of estimating erosion rates in both bedrock and sediments (e.g. Gosse and Philips, 2001; von Blanckenburg et al., 2005).

The first studies pertaining to surface exposure dating in the Atacama Desert (Mortimer, 1973; Clark et al., 1990), show that a relationship is observed between geomorphology and economic geology. Indeed, subplanar erosion markers sometimes covered by ignimbrites where often encountered near copper related ore deposit minerals.

2.4   Copper Supergene mineralization

2.4.1 Principles

Copper is rarely found in its native phase but often joins other elements and requires enrichment processes to be economically profitable. The copper-related ore deposits can be classified in two types, occurring at different time: hypogene (primary source) and supergene (secondary source). These two deposits are differentiated by the depth and consequently at the time at which they occur. Hypogene ore deposits occur deep under the surface whereas supergene ore deposits form near or at the surface.

2.4.1.1 Hypogene mineralization

Hypogene hydrothermal alteration is the source of primary copper deposits related to magma chambers and their degassing, in subduction zones. The magma will intrude upper rocks, forming porphyritic intrusive rock, several kilometers below the Earth's surface. The partial melting processes in the chamber will lead to the rise of volatiles, sulphur and incompatible elements in the magma (Richards et al., 2003). After emplacement, during the cooling and crystallisation phases, meteoritic fluids may interact with magmatic fluids.
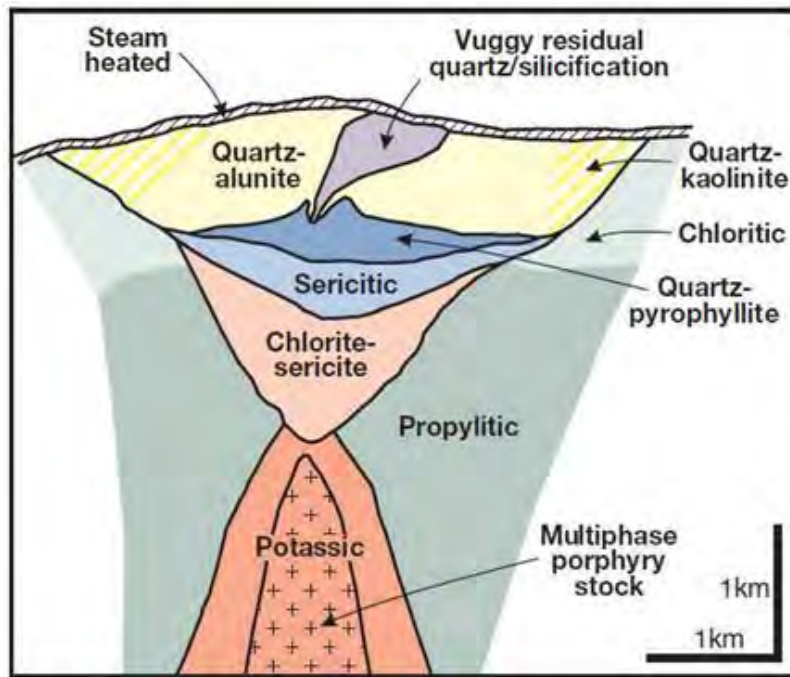
Figure 2.20 – Schematic cross-section of epithermal and alteration types in a porphyry copper (Sillitoe, 2010).

The successive alterations caused by fluids form a hydrothermal alteration profile with ore enriched layers (Figure 2.20). Such concentrated ore deposit can lead to economic viability (Cooke et al., 2005).

Thermal fluid circulations form enriched deposits and series of alteration profiles, from potassic, propylitic, sericitic to chloritic, each alteration type presenting its own mineral association and associated copper grade (Figure 2.20).

In terms of repartition, copper porphyry deposits are often related to magmatic arcs in subduction zones. They seem to have appeared in clusters parallel to the trench as in the Andes (Sillitoe, 2010; Mpodozis and Cornejo, 2012).

2.4.1.2 Supergene mineralization

Supergene mineralization results from secondary processes superimposed on pre-existing hypogene primary minerals in porphyry copper. Conceptual models have been proposed, the interested reader could refer to Chapter V for a more complete review. They occur near the surface (in the first hundred of meters) because of meteoritic fluid circulations (Sillitoe, 2005). First, the meteoritic fluids circulation dissolves the primary sulfide minerals, leaving a leached cap at the surface (Figure 2.21). As the water table with the metal in solution migrates downwards and encounters fresh rocks or sediments, pH conditions change and minerals can precipitate by reduction-oxidation reactions in two different layers.
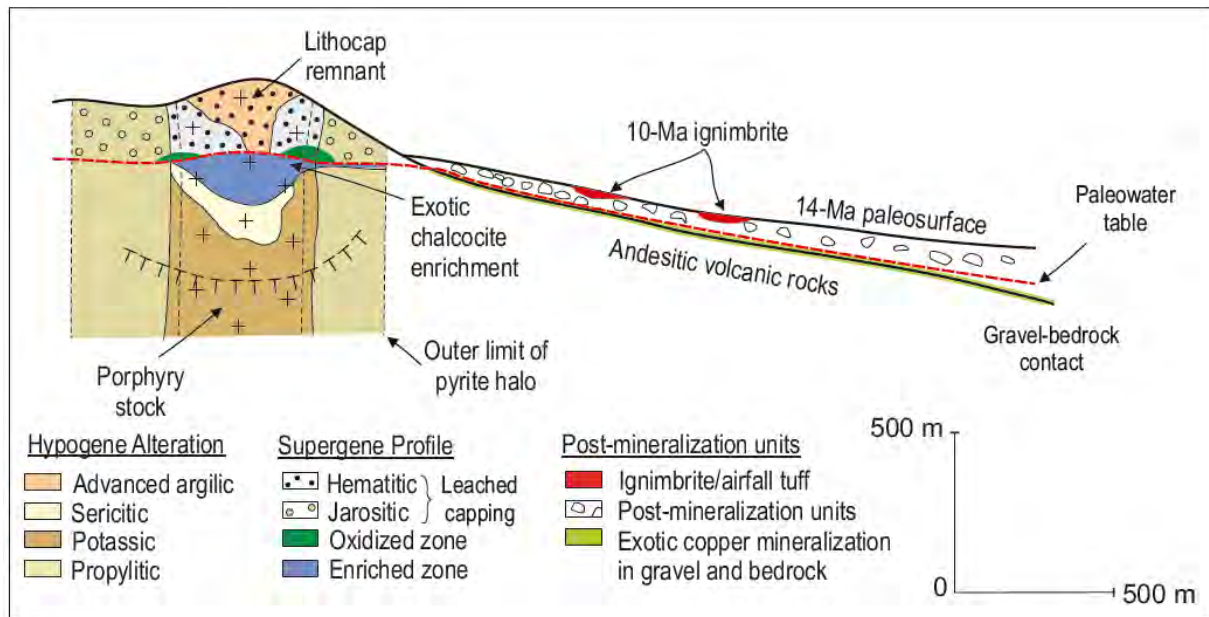
Figure 2.21 – Schematic view of supergene formation with the hypogene alteration and supergene profile series Sillitoe (2005).

The first zone above the water table is the oxidized zone where occurs solution and removal of the copper. Below the water table reduction conditions allow the precipitation of secondary sulphures enriched in copper. (Figure 2.21). Each zone contains particular minerals corresponding to these two reduction-oxidation conditions.

This process occurs mainly vertically. However, in some cases, supergene copper mineralization may result from lateral migration of fluids, leading to mineralization within the sediment (Münchmeyer, 1996). In this case, supergene ore deposits are called exotic deposits.

Even if some of the minerals found in the supergene mineralization sequence are not copper-bearing minerals as it can not be processed to extract copper, they can require similar conditions as copper-bearing minerals to precipitate and thus can be used to date their formation.

For example, supergene alunite, which did not present any interest in the beginning of economic geology, started to attract the attention several decades ago, when it has been proved that the conditions necessary for its formation were analogue to the oxidation conditions for copper-bearing minerals in the oxidation zone. As a hydrated aluminium and potassium sulfate mineral ($K\ Al_3\ (SO_4)_2\ (OH)_6$), the high potassium content of the alunite makes its dating possible.

Other potassium manganese oxides such as cryptomelane ($K(Mn^{4+},Mn^{2+})_8O_{16}$) have been successfully dated (Vasconcelos et al., 2015; Beauvais et al., 2016). Jarosite ($KFe^{3+}_3(OH)_6(SO_4)_2$) is also a sulfate mineral part of the alunite mineral group but with additional iron. Jarosite is typically present in the shallowest part of the leached cap of the supergene alteration profile (Figure 2.21).

Clark et al. (1990) proposed that supergene copper minerals needed at least 100 mm of annual precipitation to form. Their formation conditions are still unclear.

General models call upon a certain combination of erosion, uplift and precipitations. Theoretically, the development of a significant supergene ore deposit requires a precise balance between the residence times of meteoritic water in the lixiviation layer and then in the aquifer. Very little rainfall inhibits lixiviation. Too much rainfall may prevent secondary sulphurs to precipitate, the copper remains in the solution and is transported by rivers. Furthermore, heavy rainfall drives erosion which removes the eventual copper-enriched layer. Based on observations, Hartley et al. (2005) proposed three requirements for supergene formation. First a tectonically induced uplift. Secondly, they proposed moderate precipitation to maintain a favourable balance between dissolution in the lixiviation zone and precipitation in the layer below, and finally a lack of burial by subsequent sediments.

On the other hand, Sillitoe (2005) stated that *"Subplanar erosion surfaces, such as pediplains, are not considered to be a requirement for efficient supergene activity"*. This statement questions the landscape stage during which the supergene mineralization occurs.

Different periods of supergene copper mineralization have been observed in the Atacama Desert, in northern Chile and Southern Peru, so we will present in the following the range of supergene mineralization dating obtained in these regions.

2.4.2 Supergene mineralization in the Atacama Desert

Due to the specific hydro-chemical balance required to form copper supergene mineralization, some environments are more likely to the ore formation. Mainly present in semi-arid to hyper arid climates, they were nevertheless also observed in the tropical environment of the Philippines and Indonesia

In this case, the exhumation rates were very rapid, and thus able to compensate the downward rates of the water table so that the time residence of meteoritic water remained favourable to dissolve and then precipitate copper-bearing minerals (Braxton et al., 2009; 2011). Since the mid-1960s, supergene mineralization have been observed in the Atacama Desert (Figure 2.22). Chile is hosting 30% of the known worldwide copper reserves (USGS, 2013), being the first world copper producer.

In northern Chile it has been pointed out that the main supergene ore deposits are aligned in metallogenic belts of different ages (Sillitoe 2005, Mpodozis and Cornejo, 2012) and their distribution is visible in Figure 2.22. Dating of supergene mineralization started approximately three decades ago and nowadays presents an important number of data (Gustasfon and Hunt, 1975; Alpers and Brimhall, 1988; Sillitoe and McKee, 1996; Marsh et al., 1997; Arancibia, 2006; Bouzari and Clark, 2002; Quang et al., 2003-2005; Mote et al., 2001, Reich et al., 2009) with ages spanning from 45 to 5 Ma ages (Figure 2.23). Arancibia et al. (2006) reviewed all the supergene copper mineralization dating performed in northern Chile to this date.

They compared low-temperature thermochronology ages to these supergene copper mineralization ages. A time shift of ~ 20 Ma was observed between both populations, suggesting that supergene enrichment occurred later after the main exhumation associated with the Incaic deformation period in northern Chile (Figure 2.23).
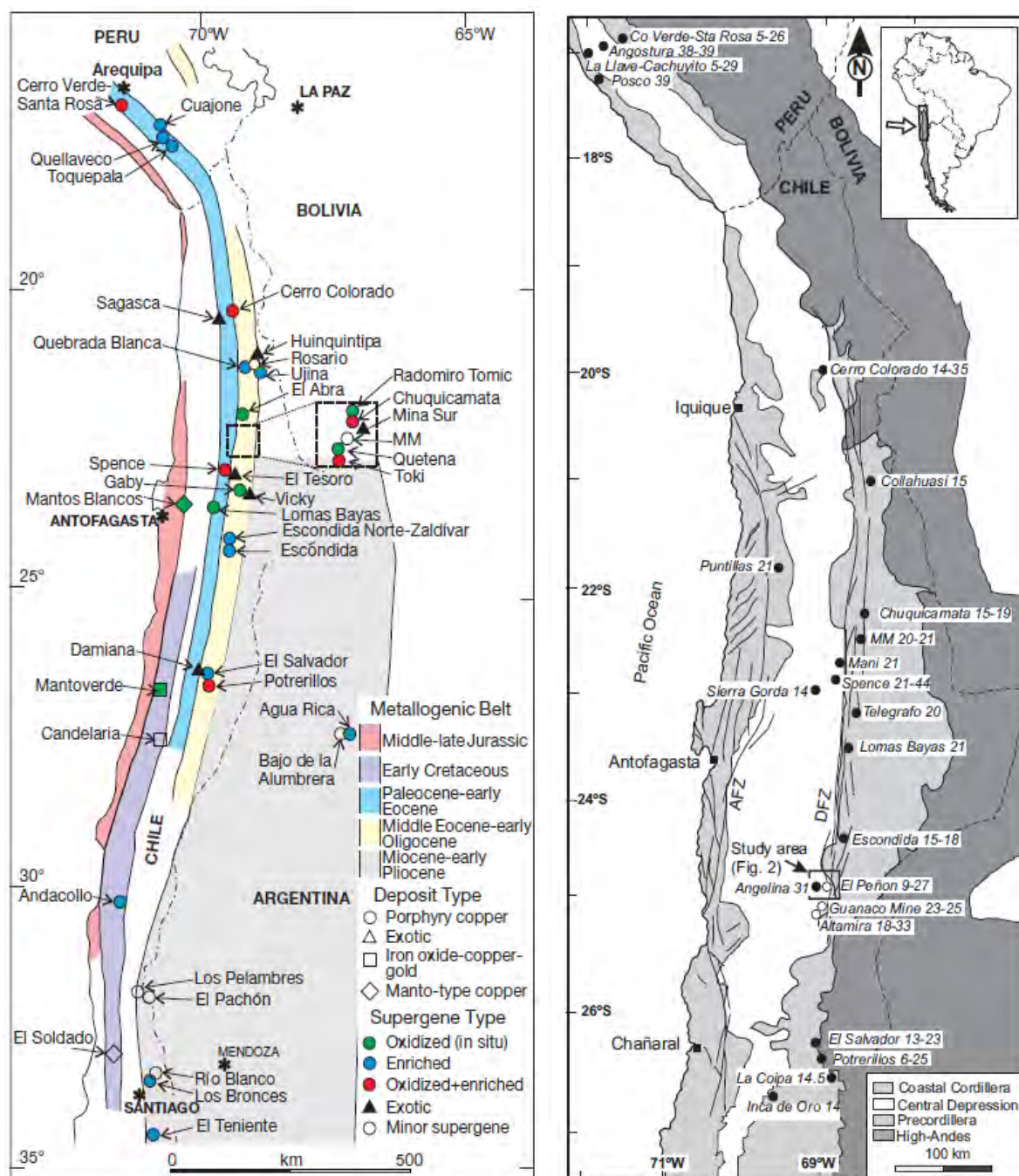
Figure 2.22 – A. Porphyries emplacement metallogenic belts in northern Chile (Sillitoe, 2005) **B. ^{40}Ar/^{39}Ar and K/Ar supergene mineralization precise ages in Ma and morpho-structural units in the Andes**.
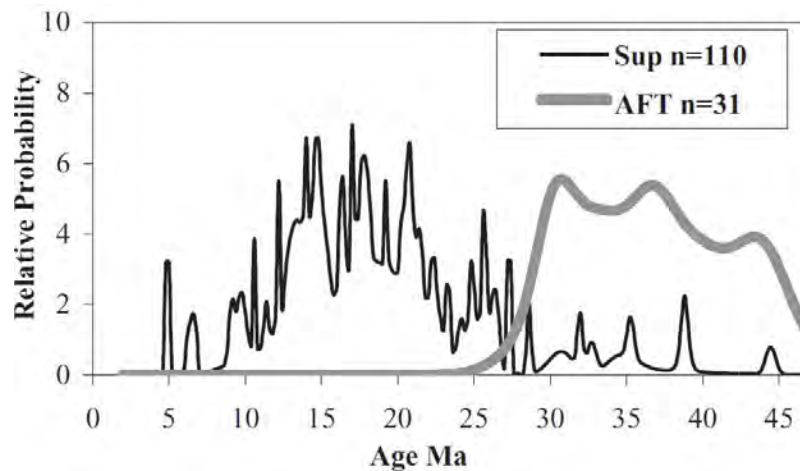
Figure 2.23 – Probability, after Deino and Potts (1992), of supergene mineral (Sup) and apatite fission track (AFT) age distribution in northern Chile (from Maksaev and Zentilli, 1999, Arancibia et al., 2006).

Nevertheless, this comparison suffers from two limitations to be conclusive about the genetic link between period of uplift and period of supergene copper enrichment. Firstly, the closure temperature of apatite fission track may be too high to identify uplift-related exhumation events younger than 25 Ma. Secondly, the comparison at a regional scale may hamper uplift-exhumation-supergene couplings acting at the scale of a specific porphyry-copper. Low-temperature thermochronological data at the scale of a mining district are thus strongly required to understand the relationship between the different stages of relief evolution and the mineralisation of copper by supergene processes. This lack motivated my work synthesised in Chapter 5.

References for Chapter 2

Alpers, C.N., Brimhall, G.H., 1988. Middle Miocene climatic change in the Atacama Desert, northern Chile: Alpers, C.N., Brimhall, G.H., 1988. Middle Miocene climatic change in the Atacama Desert, northern Chile: Evidence from supergene mineralization at La Escondida. Geological Society of America Bulletin 100, 1640–1656.

Andriessen, P.A.M., Reutter, K.-J., 1994. K-Ar and fission track mineral age determination of igneous rocks related to multiple magmatic arc systems along the 23 S latitude of Chile and NW Argentina, in: Tectonics of the Southern Central Andes. Springer, pp. 141–153.

Armijo, R., Lacassin, R., Coudurier-Curveur, A., Carrizo, D., 2015. Coupled tectonic evolution of Andean orogeny and global climate. Earth-Science Reviews 143, 1–35.

Arancibia, G., Matthews, S.J., de Arce, C.P., 2006. K–Ar and ^{40}Ar/^{39}Ar Geochronology of supergene processes in the Atacama Desert, northern Chile: Tectonic and climatic relations. Journal of the Geological Society 163, 107–118.

Arriagada, C., 1999. Geología y paleomagnetismo del borde Oriental de la Cordillera de Domeyko, entre los 22 45'y 23 30'Latitud Sur, II Región, Chile. Memoria de Título (Inédito), Universidad de Chile, Departamento de Geología.

Arriagada, C., Roperch, P., Mpodozis, C., 2000. Clockwise block rotations along the eastern border of the Cordillera de Domeyko, northern Chile (22 45′–23 30′ S). Tectonophysics 326, 153–171.

Arriagada, C., Roperch, P., Mpodozis, C., Dupont-Nivet, G., Cobbold, P.R., Chauvin, A., Cortés, J., 2003. Paleogene clockwise tectonic rotations in the forearc of central Andes, Antofagasta region, northern Chile. Journal of Geophysical Research: Solid Earth 108.

Arriagada, C., Roperch, P., Mpodozis, C., Cobbold, P.R., 2008. Paleogene building of the Bolivian Orocline: Tectonic restoration of the central Andes in 2-D map view. Tectonics 27.

Babault, J., Van Den Driessche, J., Bonnet, S., Castelltort, S., Crave, A., 2005. Origin of the highly elevated Pyrenean peneplain. Tectonics 24.

Barrientos, S., 2007. Earthquakes in Chile. The geology of Chile. The Geological Society, London 263–287.

Bascuñán, S., Arriagada Ortega, C., Le Roux, J., Deckart, K., 2016. Unraveling the Peruvian Phase of the Central Andes: stratigraphy, sedimentology and geochronology of the Salar de Atacama Basin (22 degrees 30-23 degrees S), northern Chile.

Beauvais, A., Bonnet, N.J., Chardon, D., Arnaud, N., Jayananda, M., 2016. Very long-term stability of passive margin escarpment constrained by ^{40}Ar/^{39}Ar dating of K-Mn oxides. Geology 44, 299–302.

Bissig, T., Riquelme, R., 2010. Andean uplift and climate evolution in the southern Atacama Desert deduced from geomorphology and supergene alunite-group minerals.

Blanco, N., Tomlinson, A., Mpodozis, C., Pérez de Arce, C., Matthews, Y., 2003. Formación Calama, Eoceno, II Región de Antofagasta (Chile): estratigrafía e implicancias tectónicas, in: Congreso Geológico Chileno.

Borgel, R., 1983. Geomorfologia. Geografia de Chile, tomo II. Santiago.

Bouzari, F., Clark, A.H., 2002. Anatomy, evolution, and metallogenic significance of the supergene orebody of the Cerro Colorado porphyry copper deposit, I Región, northern Chile. Economic Geology 97, 1701–1740.

Braun, J., Van Der Beek, P., 2004. Evolution of passive margin escarpments: What can we learn from low-temperature thermochronology? Journal of Geophysical Research: Earth Surface 109.

Braxton, D. P., Cooke, D. R., Ignacio, A. M., Rye, R. O., Waters, P. J. 2009. Ultra-deep oxidation and exotic copper formation at the late Pliocene Boyongan and Bayugo porphyry copper-gold deposits, Surigao, Philippines: geology, mineralogy, paleoaltimetry, and their implications for geologic, physiographic, and tectonic controls. Economic Geology, 104(3), 333-349.

Braxton, D., Mathur, R., 2011. Exploration applications of copper isotopes in the supergene environment: A case study of the Bayugo porphyry copper-gold Deposit, southern Philippines. Economic Geology 106, 1447–1463.

Campos, E., Wijbrans, J., Andriessen, P.A., 2009. New thermochronologic constraints on the evolution of the Zaldívar porphyry copper deposit, northern Chile. Mineralium Deposita 44, 329.

Carretier, S., Lucazeau, F., 2005. How does alluvial sedimentation at range fronts modify the erosional dynamics of mountain catchments? Basin research 17, 361–381.

Charrier, R., Vicente, J.-C., 1972. Liminary and geosyncline Andes: major orogenic phases and synchonical evolution of the central and autral sectors of the Southern Andes: conferencia sobre problemas de la tierra solida Buenos Aires, Argentina, 26-31 octubre de 1970. Buenos aires comite argentino del manto superior, 1972. V. 2, PP. 451-470.

Charrier, R., Pinto, L., Rodriguez, M.P., 2007. Tectonostratigraphic evolution of the Andean Orogen in Chile. The Geology of Chile 21–114.

Charrier, R., Farías, M., Maksaev, V., 2009. Evolución tectónica, paleogeográfica y metalogénica durante el Cenozoico en los Andes de Chile norte y central e implicaciones para las regiones adyacentes de Bolivia y Argentina. Revista de la Asociación Geológica Argentina 65, 05–35.

Clark, Alan H, Tosdal, R.M., Farrar, E., Plazolles, A., 1990. Geomorphologic environment and age of supergene enrichment of the Cuajone, Quellaveco, and Toquepala porphyry copper deposits, southeastern Peru. Economic Geology 85, 1604–1628.

Clarke, J.D.A., 2006. Antiquity of aridity in the Chilean Atacama Desert. Geomorphology 73, 101–114.

Cooke, D.R., Hollings, P., Walshe, J.L., 2005. Giant porphyry deposits: characteristics, distribution, and tectonic controls. Economic Geology 100, 801–818.

Cooke, R.U., 1970. Morphometric analysis of pediments and associated landforms in the western Mohave Desert, California. American Journal of Science 269, 26–38.

Cooper, F.J., Adams, B.A., Blundy, J.D., Farley, K.A., McKeon, R.E., Ruggiero, A., 2016. Aridity-induced Miocene canyon incision in the Central Andes. Geology 44, 675–678.

Davis, M., Matmon, A., Placzek, C. J., McIntosh, W., Rood, D. H., Quade, J. 2014. Cosmogenic nuclides in buried sediments from the hyperarid Atacama Desert, Chile. Quaternary Geochronology, 19, 117-126

Davis, W.M., 1889. The rivers and valleys of Pennsylvania. National Geographic Society.

Davis, W.M., 1938. Sheetfloods and streamfloods. Geological Society of America Bulletin 49, 1337–1416.

De Silva, S.L., 1989. Geochronology and stratigraphy of the ignimbrites from the 21 30′ S to 23 30′ S portion of the central Andes of northern Chile. Journal of Volcanology and Geothermal Research 37, 93–131.

Dewey, J.F., Bird, J.M., 1970. Mountain belts and the new global tectonics. Journal of Geophysical Research 75, 2625–2647.

Dohrenwend, J.C., Parsons, A.J., 2009. Pediments in arid environments, in: Geomorphology of Desert Environments. Springer, pp. 377–411.

Donelick, R.A., O'Sullivan, P.B., Ketcham, R.A., 2005. Apatite fission-track analysis. Reviews in Mineralogy and Geochemistry 58, 49–94.

Dunai, T.J., López, G.A.G., Juez-Larré, J., 2005. Oligocene–Miocene age of aridity in the Atacama Desert revealed by exposure dating of erosion-sensitive landforms. Geology 33, 321–324.

Espurt, N., Funiciello, F., Martinod, J., Guillaume, B., Regard, V., Faccenna, C., Brusset, S., 2008. Flat subduction dynamics and deformation of the South American plate: Insights from analog modelling. Tectonics 27.

Espurt, N., Baby, P., Brusset, S., Roddaz, M., Hermoza, W., Regard, V., Antoine, P.-O., Salas-Gismondi, R. Bolaños, R. 2007. How does the Nazca Ridge subduction influence the modern Amazonian foreland basin? Geology, 35(6), 515-518.

Eude, A.A., 2014. The Growth of the Centrales Andes of northern Peru (5 to 9 °S): Orogenic wedge propagation in context of inheritance tectonics and flat slab subduction (Theses). Université Toulouse III Paul Sabatier.

Evenstar, L.A., Hartley, A.J., Stuart, F.M., Mather, A.E., Rice, C.M., Chong, G., 2009. Multiphase development of the Atacama Planation Surface recorded by cosmogenic 3He exposure ages: Implications for uplift and Cenozoic climate change in western South America. Geology 37, 27–30.

Flint, S., Turner, P., Jolley, E.J., Hartley, A.J., 1993. Extensional tectonics in convergent margin basins: An example from the Salar de Atacama, Chilean Andes. Geological Society of America Bulletin 105, 603–617.

Fullard, H., Darby, H. C., 2001. Philip's World Atlas, 2001.

Garreaud, R.D., Molina, A., Farias, M., 2010. Andean uplift, ocean cooling and Atacama hyperaridity: a climate modelling perspective. Earth and Planetary Science Letters 292, 39–50.

Garreaud, R.D., Vuille, M., Compagnucci, R., Marengo, J., 2009. Present-day South American climate. Palaeogeography, Palaeoclimatology, Palaeoecology 281, 180–195.

González, G., Cembrano, J., Carrizo, D., Macci, A., Schneider, H., 2003. The link between forearc tectonics and Pliocene–Quaternary deformation of the Coastal Cordillera, northern Chile. Journal of South American Earth Sciences 16, 321–342.

Gonzalez, L., Dunai, T., Carrizo, D., Allmendinger, R., others, 2006. Young displacements on the Atacama Fault System, northern Chile from field observations and cosmogenic 21Ne concentrations. Tectonics 25.

Gosse, J.C., Phillips, F.M., 2001. Terrestrial in situ cosmogenic nuclides: theory and application. Quaternary Science Reviews 20, 1475–1560.

Grocott, J., Taylor, G.K., 2002. Magmatic arc fault systems, deformation partitioning and emplacement of granitic complexes in the Coastal Cordillera, north Chilean Andes (25 30′ S to 27 00′ S). Journal of the Geological Society 159, 425–443.

Guillocheau, F., Chelalou, R., Linol, B., Dauteuil, O., Robin, C., Mvondo, F., Callec, Y., Colin, J.-P., 2015. Cenozoic landscape evolution in and around the Congo Basin: constraints from sediments and planation surfaces, in: Geology and Resource Potential of the Congo Basin. Springer, pp. 271–313.

Gustafson, L.B., Hunt, J.P., 1975. The porphyry copper deposit at El Salvador, Chile. Economic Geology 70, 857–912.

Gutscher, M.-A., Maury, R., Eissen, J.-P., Bourdon, E., 2000a. Can slab melting be caused by flat subduction? Geology 28, 535–538.

Gutscher, M.-A., Spakman, W., Bijwaard, H., Engdahl, E.R., 2000b. Geodynamics of flat subduction: Seismicity and tomographic constraints from the Andean margin. Tectonics 19, 814–833.

Hack, J.T., 1975. Dynamic equilibrium and landscape evolution. Theories of landform development 1, 87–102.

Hare, F.K., 1961. The causation of the arid zone L.D. Stump (Ed.), A History of Land Use in Arid Lands, UNESCO, Paris (1961), pp. 25 – 30 25–30.

Hartley, A.J., Jolley, E.J., Turner, P., 1992. Paleomagnetic evidence for rotation in the Precordillera of northern Chile: Structural constraints and implications for the evolution of the Andean forearc. Tectonophysics 205, 49–64.

Hartley, A.J., Chong, G., 2002. Late Pliocene age for the Atacama Desert: Implications for the desertification of western South America. Geology 30, 43–46.

Hartley, A.J., Chong, G., Houston, J., Mather, A.E., 2005. 150 million years of climatic stability: evidence from the Atacama Desert, northern Chile. Journal of the Geological Society 162, 421–424.

Hartley, A. J., Evenstar, L. 2010. Cenozoic stratigraphic development in the north Chilean forearc: Implications for basin development and uplift history of the Central Andean margin. *Tectonophysics*, *495*(1), 67-77.

Haschke, M., Siebel, W., Günther, A., Scheuber, E., 2002. Repeated crustal thickening and recycling during the Andean orogeny in north Chile (21–26 S). Journal of Geophysical Research: Solid Earth 107.

Houston, J., Hartley, A.J., 2003. The central Andean west-slope rainshadow and its potential contribution to the origin of hyper-aridity in the Atacama Desert. International Journal of Climatology 23, 1453–1464.

Houston, J., 2006. Variability of precipitation in the Atacama Desert: its causes and hydrological impact. International Journal of Climatology 26, 2181–2198.

Isacks, B.L., 1988. Uplift of the central Andean plateau and bending of the Bolivian orocline. Journal of Geophysical Research: Solid Earth 93, 3211–3231.

Ivy-Ochs, S., Kober, F., Alfimov, V., Kubik, P. W., Synal, H. A. 2007. Cosmogenic [10]Be, [21]Ne and [36]Cl in sanidine and quartz from Chilean ignimbrites. Nuclear Instruments and Methods in Physics Research Section B: Beam Interactions with Materials and Atoms, 259(1), 588-594.

Jaillard, E., Soler, P., 1996. Cretaceous to early Paleogene tectonic evolution of the northern Central Andes (0–18 S) and its relations to geodynamics. Tectonophysics 259, 41–53.

Johnson, D., 1931. Planes of lateral corrasion. Science 73, 174–177.

Jordan, T.E., Isacks, B., Ramos, V.A., Allmendinger, R.W., 1983. Mountain building in the Central Andes. Episodes 3, 20–26.

Jordan, T.E., Kirk-Lawlor, N.E., Blanco, N.P., Rech, J.A., Cosentino, N.J., 2014. Landscape modification in response to repeated onset of hyperarid paleoclimate states since 14 Ma, Atacama Desert, Chile. Geological Society of America Bulletin 126, 1016–1046.

Juez-Larré, J., Kukowski, N., Dunai, T.J., Hartley, A.J., Andriessen, P.A.M., 2010. Thermal and exhumation history of the Coastal Cordillera arc of northern Chile revealed by thermochronological dating. Tectonophysics 495, 48–66.

Kesler, S.E., Wilkinson, B.H., 2008. Earth's copper resources estimated from tectonic diffusion of porphyry copper deposits. Geology 36, 255–258.

King, L.C., 1949. The Pediment Landform: Some Current Problems. Geological Magazine 86, 245–250.

Kober, F., Ivy-Ochs, S., Schlunegger, F., Baur, H., Kubik, P. W., Wieler, R. 2007. Denudation rates and a topography-driven rainfall threshold in northern Chile: Multiple cosmogenic nuclide data and sediment yield budgets. Geomorphology, 83(1), 97-120.

Lamb, S., Davis, P., 2003. Cenozoic climate change as a possible cause for the rise of the Andes. Nature 425, 792–797.

Lizarazu J, Soria A, Cortes L., 1997. Mapa Hidrogeológico de Bolivia.

Macellari, C.E., Su, M.J., Townsend, F., 1991. Structure and seismic stratigraphy of the Atacama Basin, Northern Chile, in: Proc. VI Congr. Geol. Chileno. pp. 133–137.

Macharé, J., Ortlieb, L., 1992. Plio-Quaternary vertical motions and the subduction of the Nazca Ridge, central coast of Peru. Tectonophysics 205, 97–108.

Maksaev, V., 1990. Unpublished Ph. D. thesis.

Maksaev, V., Zentilli, M., 1999. Fission track thermochronology of the Domeyko Cordillera, northern Chile: Implications for Andean tectonics and porphyry copper metallogenesis. Exploration and Mining Geology 8, 65–90.

Maksaev, V., Munizaga, F., Zentilli, M., Charrier, R., 2010. Fission track thermochronology of Neogene plutons in the Principal Andean Cordillera of central Chile (33-35 S): Implications for tectonic evolution and porphyry Cu-Mo mineralization. Andean Geology 36, 153–171.

Marsh, T.M., Einaudi, M.T., McWilliams, M., 1997. [40]Ar/[39]Ar geochronology of Cu-Au and Au-Ag mineralization in the Potrerillos District, Chile. Economic Geology 92, 784–806.

Martinod, J., Husson, L., Roperch, P., Guillaume, B., Espurt, N., 2010. Horizontal subduction zones, convergence velocity and the building of the Andes. Earth and Planetary Science Letters 299, 299–309.

Martinod, J., Regard, V., Riquelme, R., Aguilar, G., Guillaume, B., Carretier, S., Cortés-Aranda, J., Leanni, L., Hérail, G., 2016. Pleistocene uplift, climate and morphological segmentation of the northern Chile coasts (24° S–32° S): Insights from cosmogenic [10]Be dating of paleoshorelines. Geomorphology 274, 78–91.

May, G., Hartley, A.J., Chong, G., Stuart, F., Turner, P., Kape, S.J., 2005. Litoestratigrafía, cronoestratigrafía durante el Eoceno al Pleistoceno y evolución tectono-sedimentaria de la Cuenca de Calama, norte de Chile. Revista geológica de Chile 32, 33–58.

McInnes, B.I.A., Farley, K.A., Sillitoe, R.H., Kohn, B.P., 1999. Application of apatite (U-Th)/He thermochronometry to the determination of the sense and amount of vertical fault displacement at the Chuquicamata porphyry copper deposit, Chile. Economic Geology 94, 937–947.

McInnes, B.I.A., Farley, K.A., Sillitoe, R.H., Kohn, B.P., 2001. Application of apatite (U-Th)/He thermochronology to the determination of the sense and amount of vertical displacement at the Chuquicamata porphyry copper district, Chile-A Reply. Economic Geology 96, 1310–1310.

McInnes, B.I.A., 2005. Application of Thermochronology to Hydrothermal Ore Deposits. Reviews in Mineralogy and Geochemistry 58, 467–498.

McKay, C.P., Friedmann, E.I., Gómez-Silva, B., Cáceres-Villanueva, L., Andersen, D.T., Landheim, R., 2003. Temperature and moisture conditions for life in the extreme arid region of the Atacama Desert: four years of observations including the El Nino of 1997–1998. Astrobiology 3, 393–406.

Mercier, J., Braun, J., Guillocheau, F., Robin, C., Simon, B., 2016. A simple model for pediment formation. In: EGU General Assembly Conference Abstracts. p. 17615.

Montgomery, D.R., Balco, G., Willett, S.D., 2001. Climate, tectonics, and the morphology of the Andes. Geology 29, 579–582.

Mora, R., Artal, J., Brockway, H., Martinez, E., Muhr, R., 2004. El Tesoro exotic copper deposit, Antofagasta region, northern Chile. Society of Economic Geologists, Special Publication 11, 187–197.

Mora, A., Baby, P., Roddaz, M., Parra, M., Brusset, S., Hermoza, W., Espurt, N., 2010. Tectonic history of the Andes and sub-Andean zones: implications for the development of the Amazon drainage basin. Amazonia, Landscape and Species Evolution: A Look into the Past. Blackwell-Wiley, Hoboken 38–60.

Mortimer, C., 1973. The Cenozoic history of the southern Atacama Desert, Chile. Journal of the Geological Society 129, 505–526.

Mote, T.I., Brimhall, G.H., Tidy-Finch, E., Muller, G., Carrasco, P., 2001. Application of mass-balance modelling of sources, pathways, and sinks of supergene enrichment to exploration and discovery of the Quebrada Turquesa exotic copper orebody, El Salvador district, Chile. Economic Geology 96, 367–386.

Mpodozis, C., Marinovic, N., Smoje, I., 1993. Eocene left lateral strike slip faulting and clockwise block rotations in the Cordillera de Domeyko, west of Salar de Atacama, northern Chile.

Mpodozis, C., Arriagada, C., Roperch, P., 1999. Cretaceous to Paleogene geology of the Salar de Atacama basin, northern Chile: a reappraisal of the Purilactis Group stratigraphy.

Mpodozis, C., Arriagada, C., Basso, M., Roperch, P., Cobbold, P., Reich, M., 2005. Late Mesozoic to Paleogene stratigraphy of the Salar de Atacama Basin, Antofagasta, northern Chile: implications for the tectonic evolution of the Central Andes. Tectonophysics 399, 125–154.

Mpodozis, C., Cornejo, P. 2012. Cenozoic tectonics and porphyry copper systems of the Chilean Andes. *Society of Economic Geologists Special Publication*, *16*, 329-360.

Münchmeyer, C., Camus, F., Sillitoe, R.M., Petersen, R., 1996. Exotic deposits-products of lateral migration of supergene solutions from porphyry copper deposits. Andean Copper Deposits 43–58.

Muñoz, N., Charrier, R., Jordan, T., 2002. Interactions between basement and cover during the evolution of the Salar de Atacama Basin, northern Chile. Revista geológica de Chile 29, 55–80.

Nalpas, T., Hérail, G., Mpodozis, C., Riquelme, R., Clavero, J., Dabard, M.-P., 2007a. Thermochronologicals data and denudation history along a transect between Chañaral and Pedernales ($\approx 26^{\circ}$ S), north Chilean Andes: orogenic implications, in: 3rd Meeting of the ILP Task Force on Sedimentary Basin.

Narea, K., Peña, M., Bascuñán, S., Becerra, J., Gómez, I., Deckart, K., Munizaga, F., Maksaev, V., Arriagada, C., Roperch, P., 2015. Paleomagnetism of Permo-Triassic and Cretaceous rocks from the Antofagasta region, northern Chile. Journal of South American Earth Sciences, Tectonics of the Argentine and Chilean Andes 64, Part 2, 261–272.

Nishiizumi, K., Caffee, M.W., Finkel, R.C., Brimhall, G., Mote, T., 2005. Remnants of a fossil alluvial fan landscape of Miocene age in the Atacama Desert of northern Chile using cosmogenic nuclide exposure age dating. Earth and Planetary Science Letters 237, 499–507.

Oberlander, T.M., 1974. Landscape inheritance and the pediment problem in the Mojave Desert of southern California. American Journal of Science 274, 849–875.

Oerter, E., Amundson, R., Heimsath, A., Jungers, M., Chong, G., Renne, P., 2016. Early to Middle Miocene climate in the Atacama Desert of northern Chile. Palaeogeography, Palaeoclimatology, Palaeoecology 441, 890–900.

Ortlieb, L., 1995. Eventos El Niño y episodios lluviosos en el desierto de Atacama: el registro de los últimos dos siglos. Bull. Inst. fr. études andines 24, 519–537.

Parada, M.A., López-Escobar, L., Oliveros, V., Fuentes, F., Morata, D., Calderón, M., Aguirre, L., Féraud, G., Espinoza, F., Moreno, H., Others, 2007. Andean magmatism. The geology of Chile 115–146.

Paskoff, R.P., 1977. Quaternary of Chile: the state of research. Quaternary Research 8, 2–31.

Pelletier, J.D., Rasmussen, C., 2009. Quantifying the climatic and tectonic controls on hillslope steepness and erosion rate. Lithosphere 1, 73–80.

Pelletier, J.D., 2010. How do pediments form? A numerical modelling investigation with comparison to pediments in southern Arizona, USA. Geological Society of America Bulletin 122, 1815–1829.

Penck, W., 1953. Morphological analysis of land forms: a contribution to physical geology. MacMillan and Company.

Persano, C., Stuart, F. M., Bishop, P., and Barford, D. N. (2002). Apatite (U-Th)/He age constraints on the development of the Great Escarpment on the southeastern Australian passive margin. Earth and Planetary Sciences Letters

Pfiffner, O.A., Gonzalez, L., 2013. Mesozoic–Cenozoic evolution of the western margin of South America: Case study of the Peruvian Andes. Geosciences 3, 262–310.

Quang, C.X., Clark, A.H., Lee, J.K.W., Guillén, J., 2003. ^{40}Ar-^{39}Ar ages of hypogene and supergene mineralization in the Cerro Verde-Santa Rosa porphyry Cu-Mo cluster, Arequipa, Peru. Economic Geology 98, 1683–1696.

Quang, C.X., Clark, A.H., Lee, J.K.W., Hawkes, N., 2005. Response of supergene processes to episodic Cenozoic uplift, pediment erosion, and ignimbrite eruption in the porphyry copper province of southern Peru. Economic Geology 100, 87–114.

Rech, J.A., Currie, B.S., Michalski, G., Cowan, A.M., 2006. Neogene climate change and uplift in the Atacama Desert, Chile. Geology 34, 761–764.

Rech, J.A., Currie, B.S., Shullenberger, E.D., Dunagan, S.P., Jordan, T.E., Blanco, N., Tomlinson, A.J., Rowe, H.D., Houston, J., 2010. Evidence for the development of the Andean rain shadow from a Neogene isotopic record in the Atacama Desert, Chile. Earth and Planetary Science Letters 292, 371–382.

Regard, V., Saillard, M., Martinod, J., Audin, L., Carretier, S., Pedoja, K., Riquelme, R., Paredes, P., Hérail, G., 2010. Renewed uplift of the Central Andes Forearc revealed by coastal evolution during the Quaternary. Earth and Planetary Science Letters 297, 199–210.

Reich, M., Palacios, C., Vargas, G., Luo, S., Cameron, E.M., Leybourne, M.I., Parada, M.A., Zúñiga, A., You, C.-F., 2009. Supergene enrichment of copper deposits since the onset of modern hyperaridity in the Atacama Desert, Chile. Mineralium Deposita 44, 497–504.

Reiners, P.W., Thomson, S.N., Vernon, A., Willett, S.D., Zattin, M., Einhorn, J., Gehrels, G., Quade, J., Pearson, D., Murray, K.E., others, 2015. Low-temperature thermochronologic trends across the central Andes, 21 S–28 S. Geological Society of America Memoirs 212, 215–249.

Richards, M.P., Fuller, B.T., Sponheimer, M., Robinson, T., Ayliffe, L., 2003. Sulphur isotopes in palaeodietary studies: a review and results from a controlled feeding experiment. International Journal of Osteoarchaeology 13, 37–45.

Riquelme, R., Martinod, J., Hérail, G., Darrozes, J., Charrier, R., 2003. A geomorphological approach to determining the Neogene to Recent tectonic deformation in the Coastal Cordillera of northern Chile (Atacama). Tectonophysics 361, 255–275.

Riquelme, R., Hérail, G., Martinod, J., Charrier, R., Darrozes, J., 2007. Late Cenozoic geomorphologic signal of Andean forearc deformation and tilting associated with the uplift and climate changes of the Southern Atacama Desert (26°S–28°S). Geomorphology 86, 283–306.

Riquelme, R., Tapia, M., Campos, E., Mpodozis, C., Carretier, S., González, R., Muñoz, S., Fernandez-Mort, A., Sanchez, C., Marquardt, C. 2017. Supergene and exotic Cu mineralization occur during periods of landscape stability in the Centinela Mining District, Atacama Desert. Basin Research, 1, 31.

Scheuber, E., Bogdanic, T., Jensen, A., Reutter, K.-J., 1994. Tectonic development of the north Chilean Andes in relation to plate convergence and magmatism since the Jurassic, in: Tectonics of the Southern Central Andes. Springer, pp. 121–139.

Scheuber, E., González, G., 1999. Tectonics of the Jurassic-Early Cretaceous magmatic arc of the north Chilean Coastal Cordillera (22°–26°S): A story of crustal deformation along a convergent plate boundary. Tectonics 18, 895.

Schildgen, T.F., Ehlers, T.A., Whipp, D.M., Van Soest, M.C., Whipple, K.X., Hodges, K.V., 2009. Quantifying canyon incision and Andean Plateau surface uplift, southwest Peru: A thermochronometer and numerical modelling approach. Journal of Geophysical Research: Earth Surface 114, 1–22.

Sempere, T., Carlier, G., Soler, P., Fornari, M., Carlotto, V., Jacay, J., Arispe, O., Néraudeau, D., Cárdenas, J., Rosas, S., others, 2002. Late Permian–Middle Jurassic lithospheric thinning in Peru and Bolivia, and its bearing on Andean-age tectonics. Tectonophysics 345, 153–181.

Sillitoe, R.H., McKee, E.H., 1996. Age of supergene oxidation and enrichment in the Chilean porphyry copper province. Economic Geology 91, 164–179.

Sillitoe, R.H., 2005. Supergene oxidized and enriched porphyry copper and related deposits. Economic Geology 100th Anniversary Volume 29, 723–768.

Sillitoe, R.H., Perelló, J., 2005. Andean copper province: Tectonomagmatic settings, deposit types, metallogeny, exploration, and discovery. Economic Geology 100th Anniversary Volume 845–890.

Sillitoe, R.H., 2010. Porphyry copper systems. Economic geology 105, 3–41.

Soler, P., Jiménez, C., others, 1993. Magmatic constraints upon the evolution of the Bolivian Andes since late Oligocene times.

Strecker, M.R., Alonso, R.N., Bookhagen, B., Carrapa, B., Hilley, G.E., Sobel, E.R., Trauth, M.H., 2007. Tectonics and climate of the southern central Andes. Annu. Rev. Earth Planet. Sci. 35, 747–787.

Strudley, Mark W., Murray, A.B., Haff, P.K., 2006a. Regolith thickness instability and the formation of tors in arid environments. Journal of Geophysical Research: Earth Surface 111.

Strudley, Mark W., Murray, A.B., Haff, P.K., 2006b. Emergence of pediments, tors, and piedmont junctions from a bedrock weathering–regolith thickness feedback. Geology 34, 805–808.

Summerfield, M.A., 1991. Tectonic geomorphology. Progress in Physical Geography 15, 193–205.

Tapia, M., Riquelme, R., Marquardt, C., Mpodozis, C., Mora, R. (2012). Estratigrafía y sedimentología de la Cuenca El Tesoro, Distrito Centinela (región de Antofagasta) y su relación con la mineralización exótica de cobre. In En XII Congreso Geológico Chileno, Antofagasta.

Thiry, M., Coincon, R.S., 2009. Palaeoweathering, Palaeosurfaces and Related Continental Deposits (Special Publication 27 of the IAS). John Wiley & Sons.

Tosdal, R.M., Clark, A.H., Farrar, E., 1984. Cenozoic polyphase landscape and tectonic evolution of the Cordillera Occidental, southernmost Peru. Geological Society of America Bulletin 95, 1318–1332.

Tricart, J., Raynal, R., Besançon, J., 1972. Cônes rocheux, pédiments, glacis, in: Annales de Géographie. JSTOR, pp. 1–24.

Tucker, G.E., Whipple, K.X., 2002. Topographic outcomes predicted by stream erosion models: Sensitivity analysis and intermodel comparison. Journal of Geophysical Research: Solid Earth 107.

Twidale, C.R., 1992. King of the plains: Lester King's contributions to geomorphology. Geomorphology 5, 491–509.

Valero-Garcés, B.L., Grosjean, M., Kelts, K., Schreier, H., Messerli, B., 1999. Holocene lacustrine deposition in the Atacama Altiplano: facies models, climate and tectonic forcing. Palaeogeography, Palaeoclimatology, Palaeoecology 151, 101–125.

Vasconcelos, P.M., Reich, M., Shuster, D.L., 2015. The paleoclimatic signatures of supergene metal deposits. Elements 11, 317–322.

Von Blanckenburg, F. 2005. The control mechanisms of erosion and weathering at basin scale from cosmogenic nuclides in river sediment. *Earth and Planetary Science Letters*, *237*(3), 462-479.

Vuille, M., Ammann, C., 1997. Regional snowfall patterns in the high, arid Andes, in: Climatic Change at High Elevation Sites. Springer, pp. 181–191.

Wang, F., Michalski, G., Seo, J.-H., Granger, D.E., Lifton, N., Caffee, M., 2015. Beryllium-10 concentrations in the hyper-arid soils in the Atacama Desert, Chile: Implications for arid soil formation rates and El Niño driven changes in Pliocene precipitation. Geochimica et Cosmochimica Acta 160, 227–242.

Zachos, J., Pagani, M., Sloan, L., Thomas, E., Billups, K., 2001. Trends, rhythms, and aberrations in global climate 65 Ma to present. Science 292, 686–693.

Zachos, J.C., Shackleton, N.J., Revenaugh, J.S., Pälike, H., Flower, B.P., 2001. Climate response to orbital forcing across the Oligocene-Miocene boundary. Science 292, 274–278.

Zhou, J., Lau, K.M., 1998. Does a monsoon climate exist over South America? Journal of climate 11, 1020–1040.

Table of Figures for Chapter 2

<div align="right">

Chapter 3

Methodology

</div>

Abstract

In this thesis, analytic data acquisition has been an important part of the work. This chapter will introduce the different principles and specificities of the techniques used for this study (Figure 3.1). As the aim is to reconstruct the relief denudation, reliable methods applicable on long-term and on several kilometres exhumation scale are required. As all methods have their own limits, various ones were combined.

After an introduction, will be presented the different methods relative to U-chronometry, such as low-temperature thermochronology and U-Pb dating which permit to quantify exhumation processes at a large temporal and spatial scale. In a second part, will be presented the possible applications of cosmogenic nuclides for dating and geomorphologic process quantification.

3.1. Introduction

To retrace the exhumation and erosion of reliefs, several methods were employed in this work from thermobarometry, to thermochronologie and cosmogenic nuclides. As illustrated in Figure 3.1, geochronology as well as U-Pb method combined to thermobarometry allow to date the crystallization and to constrain the temperature and pression of crystallization conditions, which can be interpreted as emplacement depth.
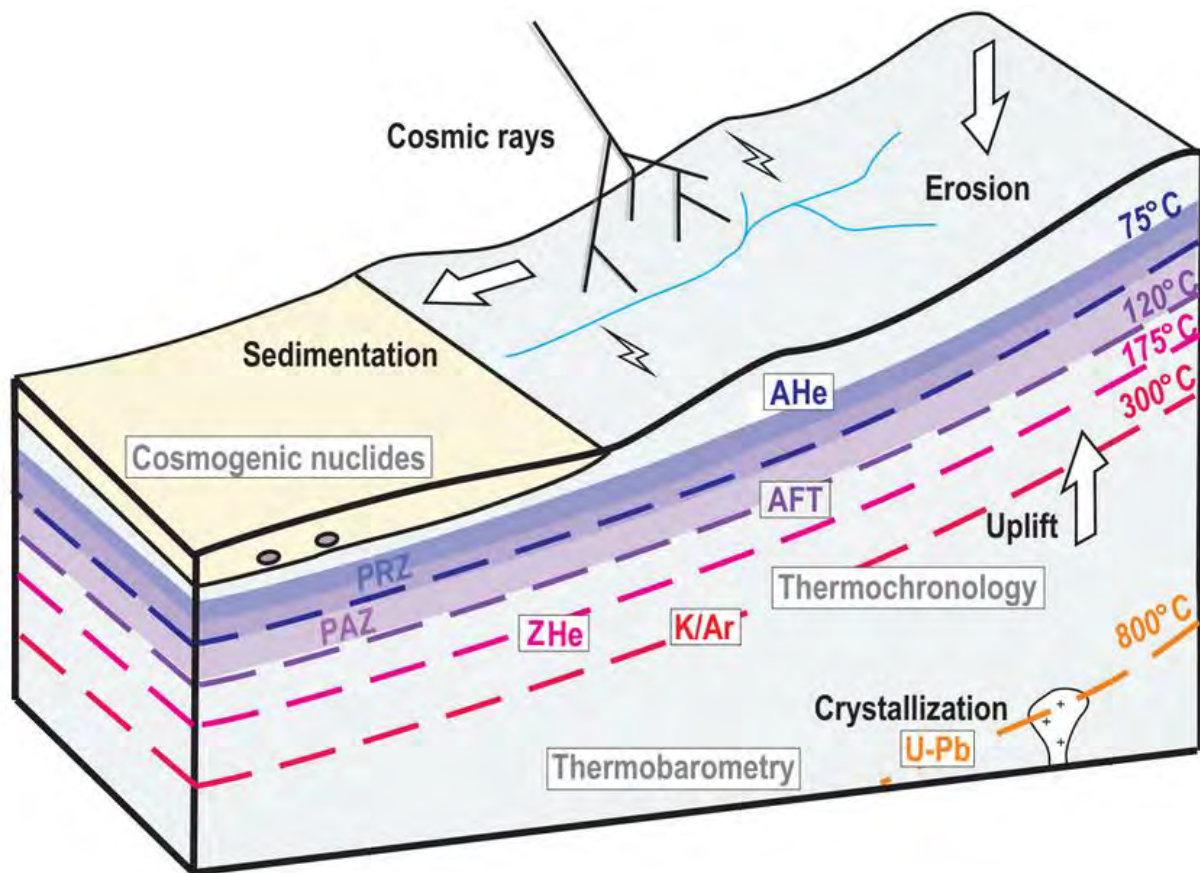
Figure 3.1 – Summary of the methods, cosmogenic nuclides, thermochronology and thermobarometry presented in this chapter and their relationship with the quantified processes of the geomorphological cycle (crystallization, uplift, erosion and sedimentation). **AHe**: Helium on apatite; **AFT**: apatite fission tracks, **ZHe**: Helium on zircon. Each dotted line corresponds to the closure temperature of the associated system, explications further in the chapter.

Thermochronology methods allow to retrace the thermal evolution of the rocks. Thus, the different methods have their specificities and limits on time and temperature range (Figure 3.2). On one hand, thermochronological methods can be applied to study thermal events between ~120 to 40°C and on 100 of millions to the million scale time to study at several kilometres deep. On the other hand cosmogenic nuclides can be applied to quantify younger time scale geomorphological processes on the surface.
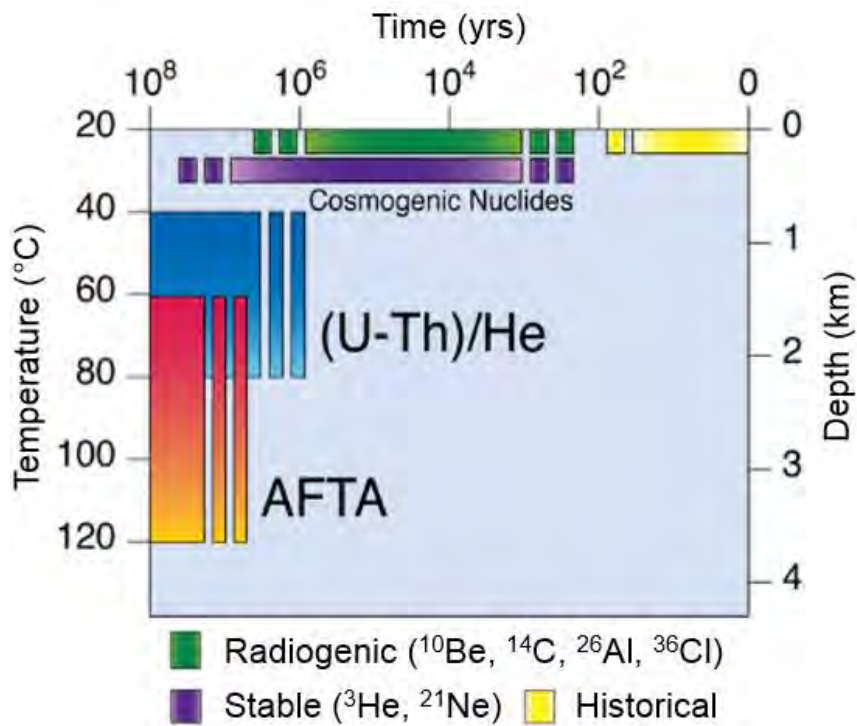
Figure 3.2 – Temperature-Time-Depth thermochronological and cosmogenic nuclides application possibilities. AFTA: apatite fission track ages, (U-Th)/He: temperature range on apatite mineral. Image of Roderick Brown shared on Codilean's (2009) webpage (https://serc.carleton.edu/).

3.2 Thermochronology

"Thermochronology" from "thermos" and "cronos" ancient greek terms, is the method which dates sample path through a certain temperature. All thermochronological techniques employed in this thesis are related to two basic concepts: 1. the radioactive decay of a parent nuclide (the fission of ^{238}U) and/or 2. the notion of closure temperature (Dodson, 1973). Thermochronometers allow to date the moment (time) at which a sample in a system has cooled enough to ensure that neither parent nor daughter isotopes diffuse out of the system (Figure 3.3). As the isotope production by radioactive decay is a function of time, measuring the isotopic ratio allows to date the last time the sample underwent a specific temperature (called closure temperature T°C) depending of the thermochronometer (e.g. Braun et al., 2006; Reiners and Brandon, 2006).
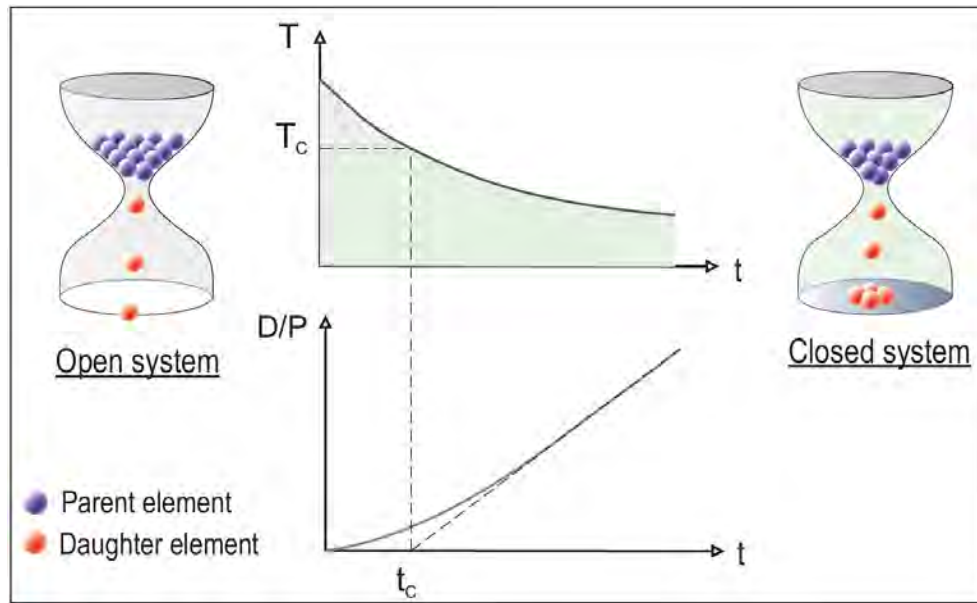
Figure 3.3 – Radioactive decay explicative cartoon (Braun et al., 2006). "T" stands for temperature, "t" stands for time, "Tc" stands for closure temperature, "D" stands for daughter, and "P" stands for parent. The hour glasses represent a mineral system.

The number of parent elements decreases (Figure 3.2), and the decay rate dN/dt is proportional to the number of N atoms present at *t* time. The half-life is the time necessary to reduce to half its initial value.

$$\frac{dN}{dt} = -\lambda N$$

$$N_{daughter} = N_{parent}\,(e^{\lambda t} - 1)$$

with $N_{daughter/parent}$ as atom numbers, λ for decay constant (or half-life) in s^{-1} and t stands for the time in seconds.

In the frame of this thesis, the following methods have been used zircon : uranium-lead dating (U-Pb), apatite fission track analysis (AFT) and apatite uranium, thorium-helium method (AHe). These methods will be presented in the ongoing section.

Low-temperature thermochronology methods have has been widely applied to quantify orogeny exhumation, to date thermal event and also to better understand geomorphological process (Braun et al., 2006).
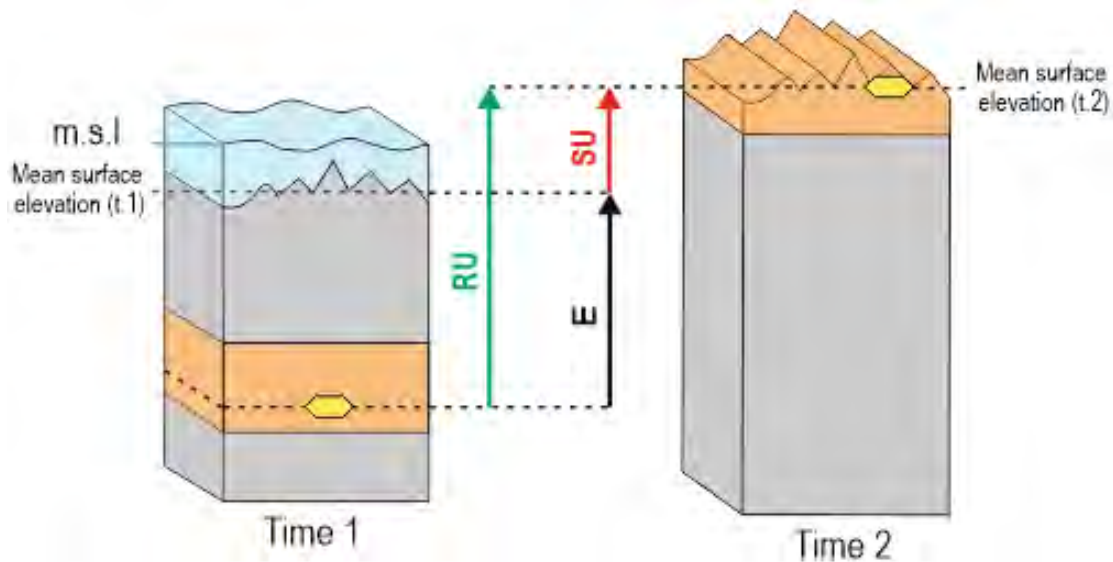
Figure 3.4 – Uplift evolution illustration, between two different times of the vertical uplift. Modified from Molnar and England (1990) and Eude (2015); RU: rock uplift, E: exhumation and SU: surface uplift.

For each method and each mineral on which the method is applied corresponds a particular closing temperature (Figure 3.3). Applied on a same sample, different thermochronometers allow to reconstruct its cooling history from its emplacement to its actual position for intrusive rocks or often more complex histories for detrital samples. In this thesis I will only focus on intrusive rocks.

3.2.1 Sample preparation

Five to twelve kg of fresh intrusive rocks in the Atacama Desert have been collected during three missions between 2012 and 2013. I processed the different steps of the sample preparation to recover zircons and apatites, both heavy minerals, in the laboratoire Geosciences Environnement Toulouse (GET) and the different steps are illustrated in the Figure 3.5. First, I crushed and sieved the samples at a fraction inferior to 400 µm. Then I used a Wilfley type shaking table to remove ultra-fine fraction (as the clays), and low-density minerals. Finally, I performed gravity separation using heavy liquids such as tetrabromoethane (d=2.967) followed by diiodomethane (d=3.325) for the heaviest fraction after the elimination of oxides using a Frantz magnetic separator.

The aim was to recover apatites and zircons but also to separate them. Since apatites have a density of approximately 3.2 and zircons a density varying from 3.9 to 4.8, the methylene iodide allowed us to set them apart.
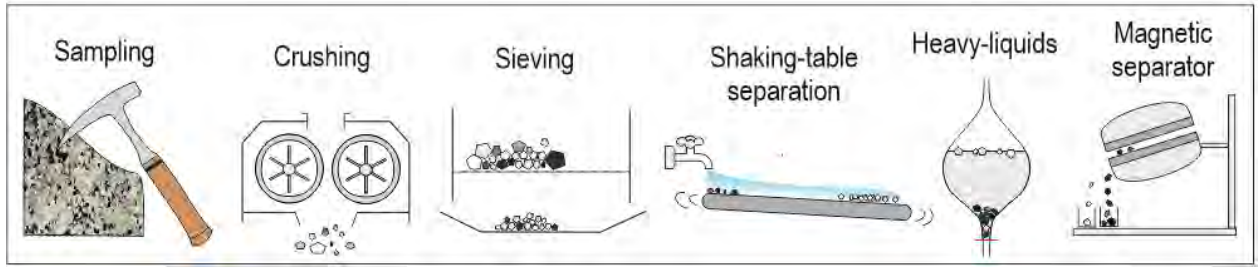
Figure 3.5 – Mineral separation methodology: from sampling to separated minerals.

3.2.2 U-Pb dating

Among the radiometric systems employed in geology U-Pb dating applied on zircons is one of the most widespread method, allowing to date intrusive rock emplacement since its closure temperature is $T°_C > 800°C$. After mineral separation, the zircons were mounted in epoxy and polished in GET lab.

The main advantage of this method is that it associates three different parent isotopes of two elements, [235]U and [238]U, and the [232]Th that decay according to radioactive decay laws into three daughter isotopes, [207]Pb, [206]Pb and [208]Pb. Therefore, U concentration decreases meanwhile the concentration in Lead rises proportionally with time. Nevertheless, the Lead isotopic composition also changes, so can be extracted three different ages from the different radiogenic isotopic ratios:

$$^{206}Pb_{act} = \ ^{206}Pb_i + \ ^{238}U\left(e^{\lambda_{238}t} - 1\right)$$

$$^{207}Pb_{act} = \ ^{207}Pb_i + \ ^{235}U\left(e^{\lambda_{235}t} - 1\right)$$

$$^{208}Pb_{act} = \ ^{208}Pb_i + \ ^{232}Th\left(e^{\lambda_{238}t} - 1\right)$$

With act = current, i = initial, t = time; λ_N = N half life

Analytically, the spectrometer does not measure concentration but signals. The half-life of [232]Th is too long to be taken into account (1.405×10^{10} years). If the equations are divided by the non-radiogenic [204]Pb can be obtained the following equations:

$$\left(\frac{^{206}Pb}{^{204}Pb}\right)_{act} = \left(\frac{^{206}Pb}{^{204}Pb}\right)_i + \frac{^{238}U}{^{204}Pb}\left(e^{\lambda_{238}t} - 1\right)$$

$$\left(\frac{^{207}Pb}{^{204}Pb}\right)_{act} = \left(\frac{^{207}Pb}{^{204}Pb}\right)_i + \frac{^{235}U}{^{204}Pb}\left(e^{\lambda_{235}t} - 1\right)$$

In the case of U-enriched minerals (as zircons), where usually Pb radiogenic daughter quantity is high compared to Pb radiogenic mother; the Pb radiogenic mother elements can be neglected so that the first term of equations can be removed:

$$\left(\frac{^{206}Pb}{^{204}Pb}\right)_{act} = \left(e^{\lambda_{238}t} - 1\right)$$

$$\left(\frac{^{207}Pb}{^{204}Pb}\right)_{act} = \left(e^{\lambda_{235}t} - 1\right)$$

Analysis were performed at the Birkbeck College of London on a New Wave NWR 193 nm laser ablation system coupled with an Agilent 7700 quadrupole-based ICP–MS. The ablation signal was processed with the GLITTER program against repeated measurement of Temora, GJ-2, 91500 and Plesovice zircon as standards correcting instrumental mass bias and depth-dependent inter-element fractionation of Pb, Th and U.

3.2.3 Fission track analyses

3.2.3.1 Principles

The low-temperature thermochronology fission track method, proposed by Price and Walker (1963), is based on the spontaneous fission of natural uranium present in U-enriched minerals as zircon, apatite or titanite (Fleischer et al., 1965). Natural uranium presents 3 natural isotopes, ^{238}U, ^{235}U and ^{234}U with respective abundances of 99.3%, 0.72% and <0.01%. Due to the extremely low ^{234}U abundances, only ^{238}U and ^{235}U are considered in this system.

They both decay through alpha ejection, emitting a ^{4}He atom (see (U-Th)/He method part) but only ^{238}U present the specificity to experience both α-ejection and spontaneous nuclear fission measurable at the geological time scale (Donelick et al., 2005). During spontaneous fission the initial nucleus splits in two fragments emitting two high energy neutrons. Those two daughter elements ionized leave a latent trace after the emission. Steps of their formation are resumed in Figure 3.6. Unusually in geochronological systems, the daughter element measured is an optical mineral defect.
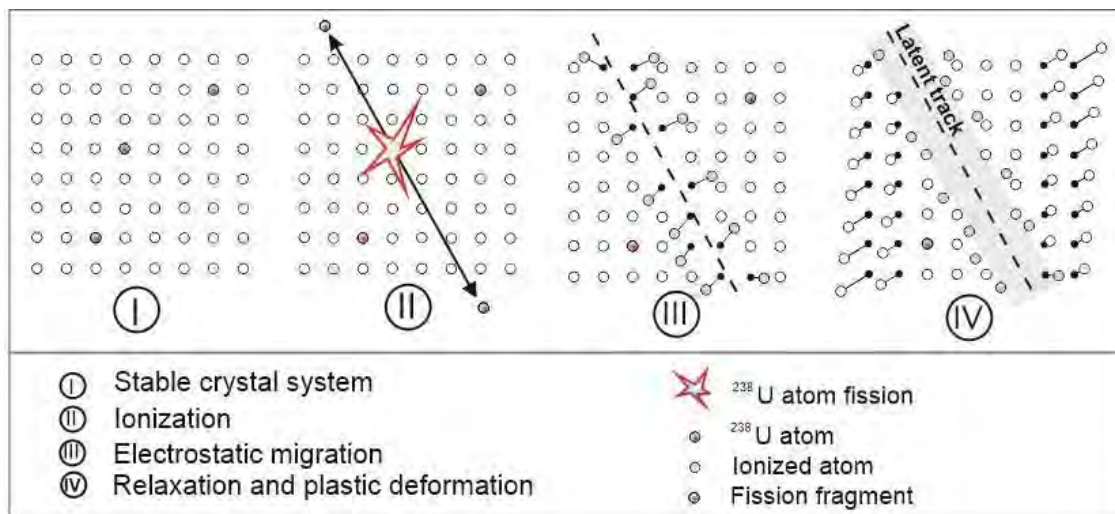
Figure 3.6 – Fission track formation due to ion spike explosion model. FromTagami and O'Sullivan (2005) after Fleischer et al. (1975).

This defect called fission track is the proxy to the daughter element from ^{238}U that is measured in this method. To complete the pair of parents and daughter element, the parent's element concentration need to be assessed. To this aim is used the ^{235}U isotope that is sensible to reaction causing fission useful to recover the concentration of ^{238}U knowing the ^{238}U/^{235}U ratio (137.88, Steiger and Jäger, 1977). Bombing the grains with a neutron flow in a nuclear reactor with an external detector as a muscovite sheet that registers induced fissions in its structure, provokes the apparition of induced fission tracks in the structure of this muscovite sheet. The ionization flow of the nuclear reactor is quantified using dosimeters (CN5 in this study).

This method provides two elements of information: 1. an age of the closure of the mineral system (by density counting of both spontaneous fission tracks on the grain and induced fission tracks in the external detector) and 2. a cooling speed pattern (by fission track length measurement).

3.2.3.2 Fission track annealing

Fission tracks are only retained in the grain when the temperature of the sample is below the closure temperature. This temperature varies depending on which mineral it is performed. In the case of apatite, the T°C is about 110 ± 10°C. If the sample stayed a significant time below the T°C and above 60°C, fission tracks length can be reduced, this is called the partial annealing process (Naeser, 1979).

Fission tracks are not naturally visible. They need to be etched with acids (nitric or fluoric regarding if it is applied to apatite or muscovite) to be revealed. When a track intercepts the surface, it forms a "hole" called etch pit and its measure is called the Dpar. The counting and measuring will only be performed on grains that are upon the c-axis in the mount, which is the largest axis of the grain and the only permitting the measure of Dpar. In the other axes of the grain the intersection of the fission track with the surface would result in non-measurable and distinguishable shapes. The counted tracks are those intersecting the polished grain surface.

The fission tracks measured to apprehend the annealing processes are the one parallel to the surface (Figure 3.7) that intersect cleavage (TINCLE, tracks in cleavage) or other tracks (TINTS, tracks in tracks).
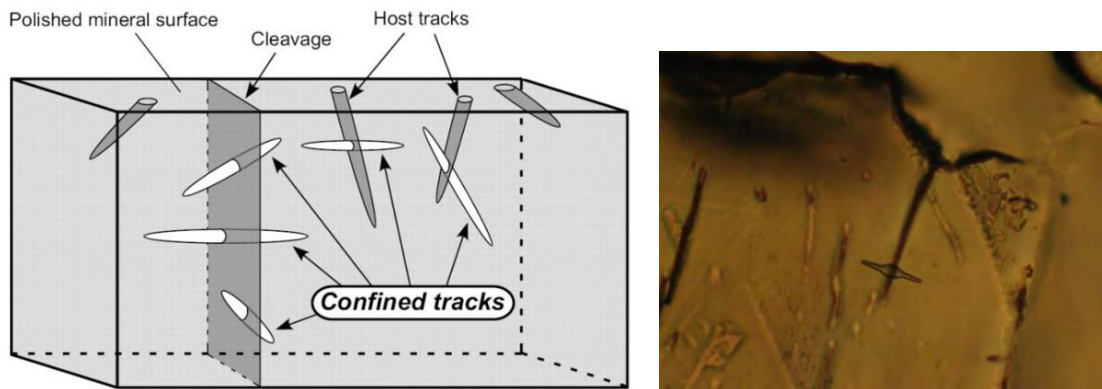
Figure 3.7 – A. Cartoon of confined fission tracks and illustration (Tagama and Sullivan, 2005) where the surface is parallel to the c-axis of the grain, with different interceptions between countable tracks and confined tracks, and illustrative picture of a track in cleavage (TINC).

The measure of a hundred confined-track length (Green, 1985; Laslett et al., 1982) and their distribution permits to acquire more information about the complexity of sample thermal history (Figure 3.8). This technique can be performed on intrusive and on detrital samples. In the second case, we can recover the thermal history of basins can be recovered or also process to sedimentary sourcing by detrital ages distribution analysis.
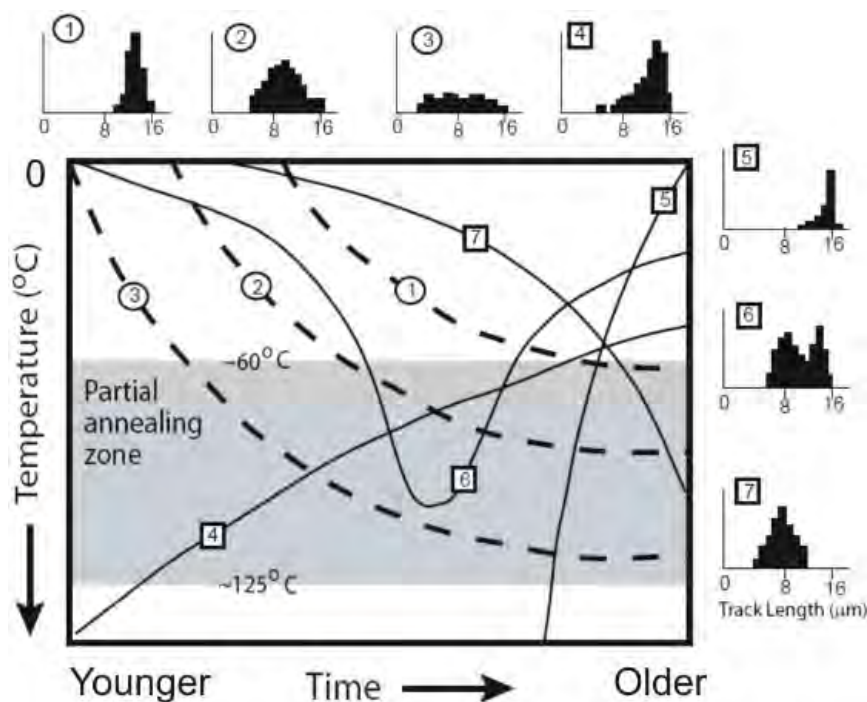
Figure 3.8 – Diagram showing the different track length histograms possible (Armstrong, 2005) depending on the exhumation or burial history for detrital samples for example. In rapid exhumation context (path 5) the distribution will be narrow (standard deviation (<1.5 μm) with larger length (<14 μm) in case of slow exhumation and a longer period in the PAZ, the dispersion will be higher (>2 μm) and the track length will be shorter (10-13μm). (Gleadow et al. 1986; Carter, 1999; Armstrong, 2005). After Gleadow et al. (1983).

One of the major factor influencing the annealing process, is the chemical composition of the apatite (Green et al., 1986; Carlson et al., 1999; Barbarand et al., 2003; Ketcham et al., 2007). Chlorine and Rare Earth Elements are elements influencing the closure temperature of the system.

An alternative to the chemical composition measurement using microprobe is the measure of the etch pit size named Dpar which is a proxy of the mineral composition (Barbarand et al., 2003).

3.2.3.3 Counting specificities

After irradiation both spontaneous in the grain mount (ρ_s) and induced in the muscovite sheet (ρ_i) fission tracks density are measured by counting each track into a specific surface on 20 grains from the same sample in the case of crystalline rocks and 100 grains for detrital rocks. The fission track age can be calculated with the following formula:

$$ t = \frac{1}{\lambda_\alpha} \ln\left(\frac{\rho_s}{\rho_i} . \lambda\alpha. \rho_d. g. \zeta + 1 \right) $$

with t standing for the time (Ma), λ_α standing for the α particle decay constant (s^{-1}), ρ_s, ρ_i and ρ_d for the spontaneous, induced and dosimeter induced track density (tracks.surface unit), g as a non-dimensional geometrical factor and ζ as the non-dimensional zeta parameter

The actual fission track counting method with the external detector is based on the zeta method (Hurford and Green, 1983). Every analyst needs to calculate his own ζ (Hurford, 1990) which is a personal experimental parameter obtained by calibration on standards. Here is the formula for its calculation:

$$ \zeta = \frac{e^{\lambda_\alpha t} - 1}{\lambda_\alpha \frac{\rho_s}{\rho_i} \, g \, \rho_d} $$

The different standards are Durango from the Cerro Mercado in Mexico (31.4 ± 0.5 Ma; Naeser and Fleischer, 1975; Steigner and Jäger, 1977; McDowell et al., 2005) and the Fish Canyon Tuff from Colorado in USA (27.8 ± 0.2 Ma: Stevens et al., 1967; Hurford and Hammerschmidt, 1985; Kunk et al., 1985). My mean zeta calibration is presented in the Table 1.

Once all the densities are defined on grains from a single sample, a chi-squared (χ^2) test is performed to test the homogeneity of the ages obtained on every grain (Galbraith, 1981).

If $P(\chi^2) > 5\%$ then the repartition of ages is considered homogeneous $P(\chi^2)$ is the probability for the chi-squared for n degrees of freedom, n corresponding to the number of crystals measured minus 1 (Galbraith and Laslett, 1993).

Irradiation	Standard	ȝ Apatite ±1σ
IR-TLS-12	DUR	292.13 ± 16,23
ORE5	DUR	228,90 ± 23,71
ORE5	DUR	279,38 ± 24,86
ORE5	FC	271,83 ± 22,47
ORE6	FC	289,23 ± 21,52
ORE6	FC	262,50 ± 22,76
ORE5	FC	311,72 ± 27,29
ORE5	FC	246,56 ± 25,30
IR-STG-14	FC	269,97 ± 26,03
IR-STG-14	DUR	327,06 ± 20,41
ORE5	DUR	246,35 ± 31,86
Mean ȝ (WMZ) =		279,02 ± 8,36

Table 3.1 – Zeta measurements from Durango (DUR) and Fish Canyon (FC) standard apatites for Caroline Sanchez.

The fission track ages can also be represented with radial plot (Figure 3.9). The radial plot was first proposed by Galbraith (1988) and is a graphic way to represent different population of individual grain ages and and associate incertainties.
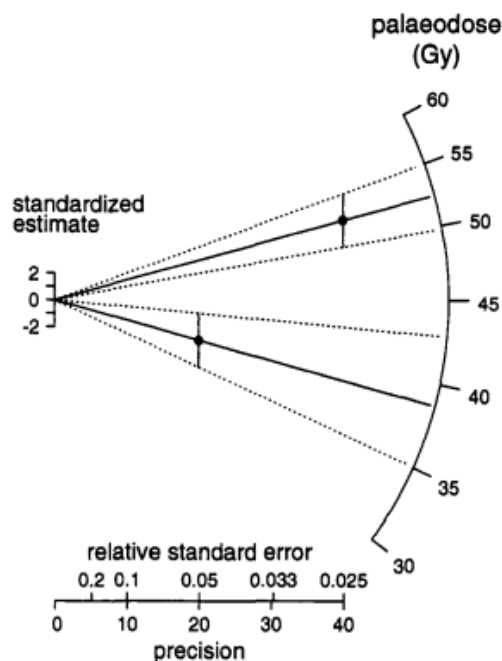
Figure 3.9 – Radial plot representation of two different fission track ages (52.5 and 38 Ma) and their associated uncertainties (Galbraith et al., 1999)

The calculated central age is the origin of the ordinate axis. Each age is then plotted on an original line (x = 0, y = 0) and directed to the value of the age on the circular axis.

According to its precision, the point is located more or less (depending of the uncertainty) close to the origin.

The minimum and maximum ages of the circular axis depend on the dispersion of the ages of each grain. If 95% of the individual ages are in the uncertainty range $\pm 2\sigma$ (ordinate), then the central age is validated. All the radial plots of the fission track ages in this thesis generated with the RadialPlotter application (Vermeesch, 2009) are reported in the Annexes section.

3.2.3.4 Fission track mount preparation

For the fission track method, apatites were mounted in epoxy (all the different steps of the preparation before analyses are summarized in the Figure 3.10). As defined before, the spontaneous tracks resulting from ^{238}U radioactive decay need to be etched to be seen. I used HNO_3 5N for 20 seconds at 20°C (Green et al., 1986). Then mica sheets were adjoined to the mount before irradiation in the Cchen nuclear reactor of Santiago de Chile, during 25 minutes with a neutronic flux at 1.10^{12} n.cm^{-2}.s^{-1}.
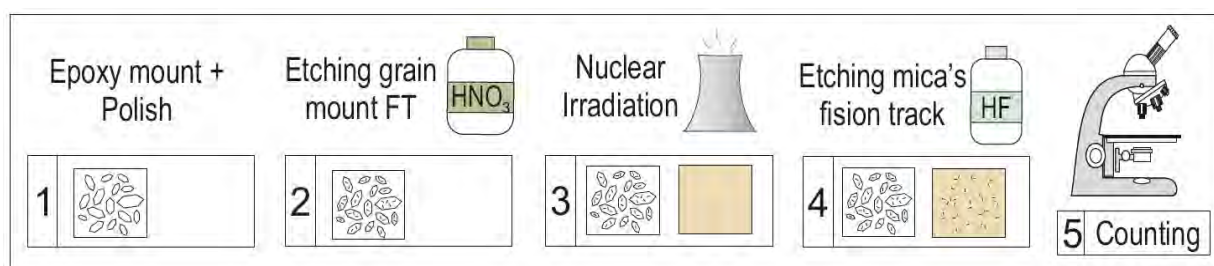
Figure 3.10 – Summary of different step in the apatite fission track mounts preparation, between polish, etching, and nuclear irradiation to finally count and measure the confined tracks.

Once irradiated and the security time laps for the decrease of remnant radioactivity respected, induced fission tracks on the mica were also etched with hydrofluoric acid (48% during 25 minutes).

Both grain and mica mounts were positioned for counting and measuring (Figure 3.10) with a BX-61 Olympus microscope (GET) or a Zeiss Axio Imager (Santiago de Chile Universidad) at a magnification of 1250x.

3.2.4 (U-Th)/He

3.2.4.1 Principles

Production

(U-Th)/He is a low thermochronology method based on the emission and accumulation of α particles (helium nucleus) during radioactive decay and their diffusion in a mineral (Rutherford, 1905; Zeitler et al., 1987; Wolf et al., 1998). In this system the daughter element is the He atom.

On Earth, ten radionuclides produce helium. For the helium thermochonology methods, only the four with heavier mass number ^{238}U, ^{235}U, ^{232}Th and the lighter one ^{147}Sm are taken into account, also called parent elements.

As He diffusion depends on temperature it permits to apprehend the thermal history of the sample. The precise measure of ^{4}He, ^{238}U, ^{235}U and ^{232}Th at t time, allows to calculate an age correspond to the time elapsed since the mineral diffusive system closed (Figure 3.3). This thermo-chronometer has a closure temperature lower than AFT, at ~75°C (Farley et al., 2002).

$$^4He = \ 8\ ^{238}U\left(e^{-\lambda_{238}\,t} - 1\right) + 7\ \frac{^{238}U}{137.88}\left(e^{-\lambda_{235}\,t} - 1\right) + 6\ ^{232}Th\left(e^{-\lambda_{232}\,t} - 1\right)$$

λ_{238}, λ_{235}, and λ_{232} are the respective decay constant of ^{238}U, ^{235}U and ^{235}Th, t is the time and ^{4}He, ^{238}U, ^{232}Th are the concentration of the respective elements.

This method requires to be applied on minerals with a minimum U and Th concentration as apatites (Farley, 2000), zircons (Tagami et al., 2003), titanites (Reiners et Farley, 1999; Pik et al., 2003) and monazites (Gleadow et al., 2005).

He diffusion

Helium presents various specific characteristics, in addition to his gaseous state. First of all, ^{238}U, ^{235}U and ^{232}Th all produce (or eject) a He atom with a specific kinetic energy (Ec, Farley et al., 1996), which defines its stopping distance, when the particules travels into the mineral structure and slows down. On average the stopping distance for all 3 elements is ~20µm. This characteristic involves that at the crystal edge a α particle presents an equal possibility to stay in the crystal or to be ejected. Ejection can happen but also implantation from surrounding uranium rich minerals. This possibility implies that the size of the grain as his shape are important parameters (Figure 3.11). To overcome this, AHe analyses should only be performed on crystals exceeding 60µm wide (Farley, 2002).
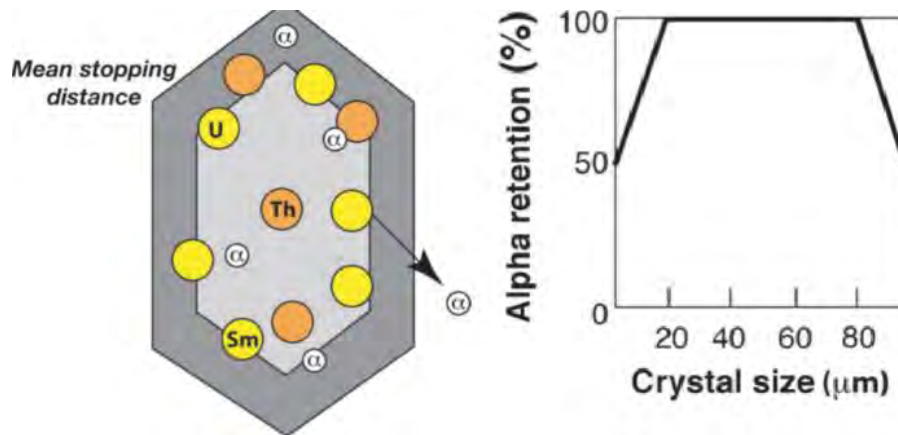
Figure 3.11 – Representation of the possibility of an α particles ejection at the border of the grain and the illustrated effect of the size of the crystal on the He retention probability (α particles) after Gautheron et al. (2012).

Additionally, to the possibility to lose or gain external He due to the simple geometry of the grain, this element presents the characteristic to be retained in the mineral in given thermal conditions.

The thermal zone called the He Partial Retention Zone (He-PRZ) is defined by the zone in which 10 to 90 % of the total production of He is retained in the crystal (Dodson, 1986). He diffusion coefficient is defined by the Arrhenius law below:

$$\frac{D}{a^2} = \frac{D_0}{a^2} e^{\frac{-Ea}{RT}}$$

with D_0 and D standing for the initial diffusion coefficient frequency factor and the diffusion coefficient at t time (cm².s⁻¹); "a" standing for the size of diffusion domain (µm); "R" standing for the ideal gas constant (R = 9.314J.mol⁻¹.K); "T" standing for the temperature (Kelvin) and E_a standing for the activation energy (kj.mol ⁻¹)

In this system the T_C refers to the temperature at which the fraction of helium emitted out of the crystal is equal as the one retained in the crystal. In the example illustrated in the Figure 3.12 the T_C value is about 70°C.
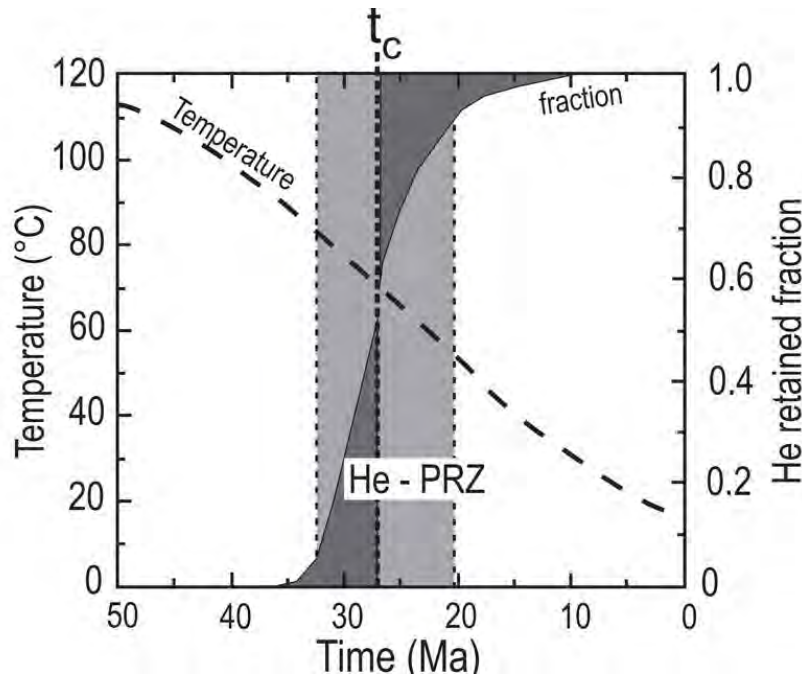
Figure 3. 12 – Diffusion results, knowing E_a and D_o for a 60µm wide crystal, through a Monte Carlo simulation applied for a geometric sphere (Gautheron and Tassan-Fot, 2010). Simulation is realized for a specific thermic history (represented by the dotted line). The partial retention zone (He-PRZ) is represented in light grey. The grey line represents the fraction of the he kept in the mineral.

To estimate the correction needed due to ejection and the geometry of the grain also, a correction factor called F_T is calculated with a software provided by Gautheron et al. (2012) and Ketcham et al. (2011) (Figure 3.13). The algorithm of this software is based on a random mother element draw of (U-Th) in a defined volume of the sampled crystal and the geometry of the grain.

The crystal volume is simplified in an equivalent-sphere volume, F_T idealizes the shape of the crystal, taking into account the major characteristics of the geometry as the radius and the height of each crystal (Gautheron and Tassan-Got, 2010). After each draw is calculated its position, knowing the stopping length, it is possible to estimate the zone outside which He particles could be ejected.

Figure 3.13 – Interface of the Ft-ejection calculator (Gautheron and Tassan-Got, 2010).

The corrected age is the raw age obtained with chemical measures divided by the correction factor that takes into account the He diffusion.

$$Corrected\ age = \frac{Raw\ age}{F_T}$$

With FT the correction parameter obtained with the FT ejection calculator, Raw age, the age obtained after analyses.

3.2.4.2 Measurement

After mineral separation (Figure 3.5), grains were selected non-broken, inclusion free, and superior to 60µm wide crystals (Figure 3.11).

Then the selected minerals are introduced into a small platinum tube to be degassed by heating. The shape of the tube allows the heat to be homogeneously distributed within and an easy handling and recuperation of the grain. All the different steps of the analysis are shown in simplified form in Figure 3.14.
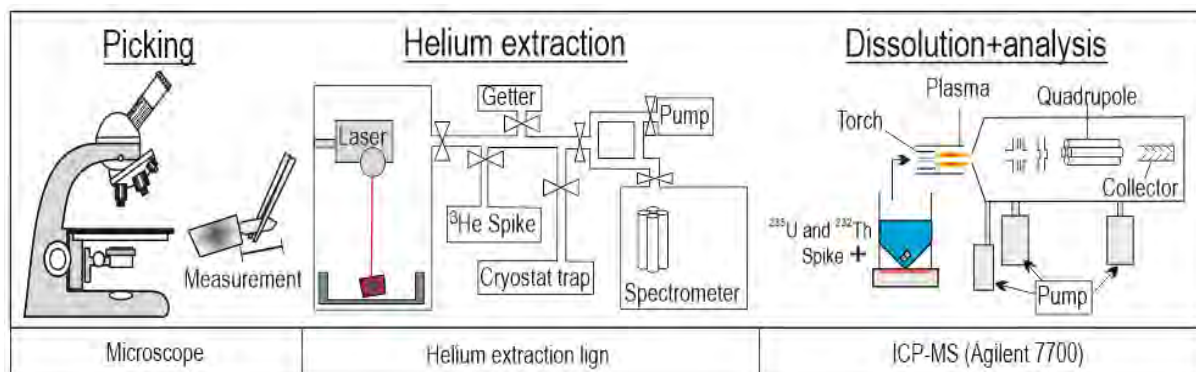
Figure 3.14 – (U-Th)/He analysis steps, picking, helium extraction and dissolution plus analysis. Chemistry protocol, dissolution with addition of a ^{235}U and ^{230}Th spike and ICPMS analysis.

Then each individual platinum packet is heated using a 1090nm diode laser at about 950°C to extract the ^{4}He. Then the ^{4}He is spiked with ^{3}He, purified by SAES getters and trapped in a JANIS cryostat (Figure 3.15).

Afterwards, the ratio between the two isotopes is measured during the slow temperature rise of the cryostat and then analyzed by a PrismaPLus QMG 220 Quadrupole mass spectrometer. For every ~six aliquots a double heating was practiced to make sure no more ^{4}He was kept trapped in the mineral.

Figure 3.15 – Picture of the Helium line (http://www.gm.univ-montp2.fr) in the Laboratoire Geosciences Montpellier. The black box is where is placed the laser, and at the end of the line the quadrupole mass spectrometer.

He was trapped in the grain. Every four aliquots was placed a Durango standard (the isotopic results with associate errors are visible in Figure 3.16).

Finally, the apatite grains were dissolved in HNO_3 13N during an hour at around 100°C, added a double spike of ^{235}U and ^{230}Th to be able to measure ^{238}U and the ^{232}Th concentration using a ICP-MS, Agilent 7700. All these analyses have been carried out at the Laboratoire Geosciences Montpellier.
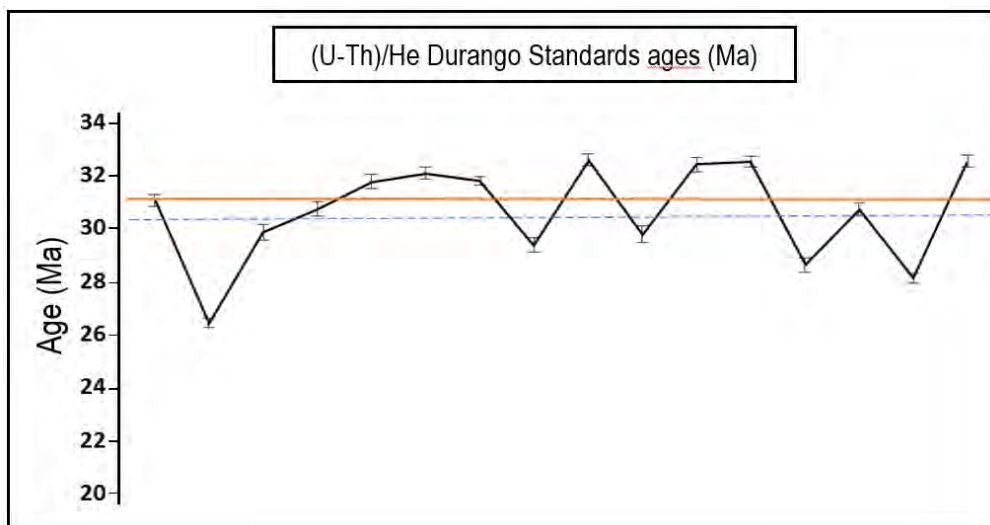
Figure 3.16 – (U-Th)/He Durango standards ages with errors (dotted line in blue represents the Durango age McDowell et al. (2005) orange line stands for the mean of all the obtained ages).

While it is generally admitted that single grain analyses are better than multigrain analyses, in the case of young samples, the low He concentration can be problematic. Therefore, in our study, both mono and multi-grain aliquot were realized for each sample to avoid any analytical problems due to low signal. For each sample between two to four analyses were performed (Farley, 2002).

3.2.5 Modelling the temperature-time cooling path

To reconstruct the cooling history of the samples, all informations extracted from the different thermochronometers were used, as well as geological setting information.

Since each method provides numerous information about ages, temperatures, specific thermal behaviors, composition to He diffusion and fission track annealing kinematic process, all those data were computed through a numerical model for each sample (Figure 3.17).

In this study we used the HeFty program (Ketcham, 2005) to realize inverse modelling working with present day data obtained with the thermochronometers and assumptions of emplacement conditions. Inverse modelling requires different features such as a theoretical annealing T-temperature model, an algorithmic means of calculating model evolution and statistical means for comparing the model calculation to measurement. But this model also proposes to show a range of possible time-temperature path and to search for the best or mean fit between the possibilities.

HeFty interface (Figure 3.17) is based on time-temperature constraints (black boxes) that represent regions in which the thermal model history must pass, which can either be geological or purely geochronological constraints.
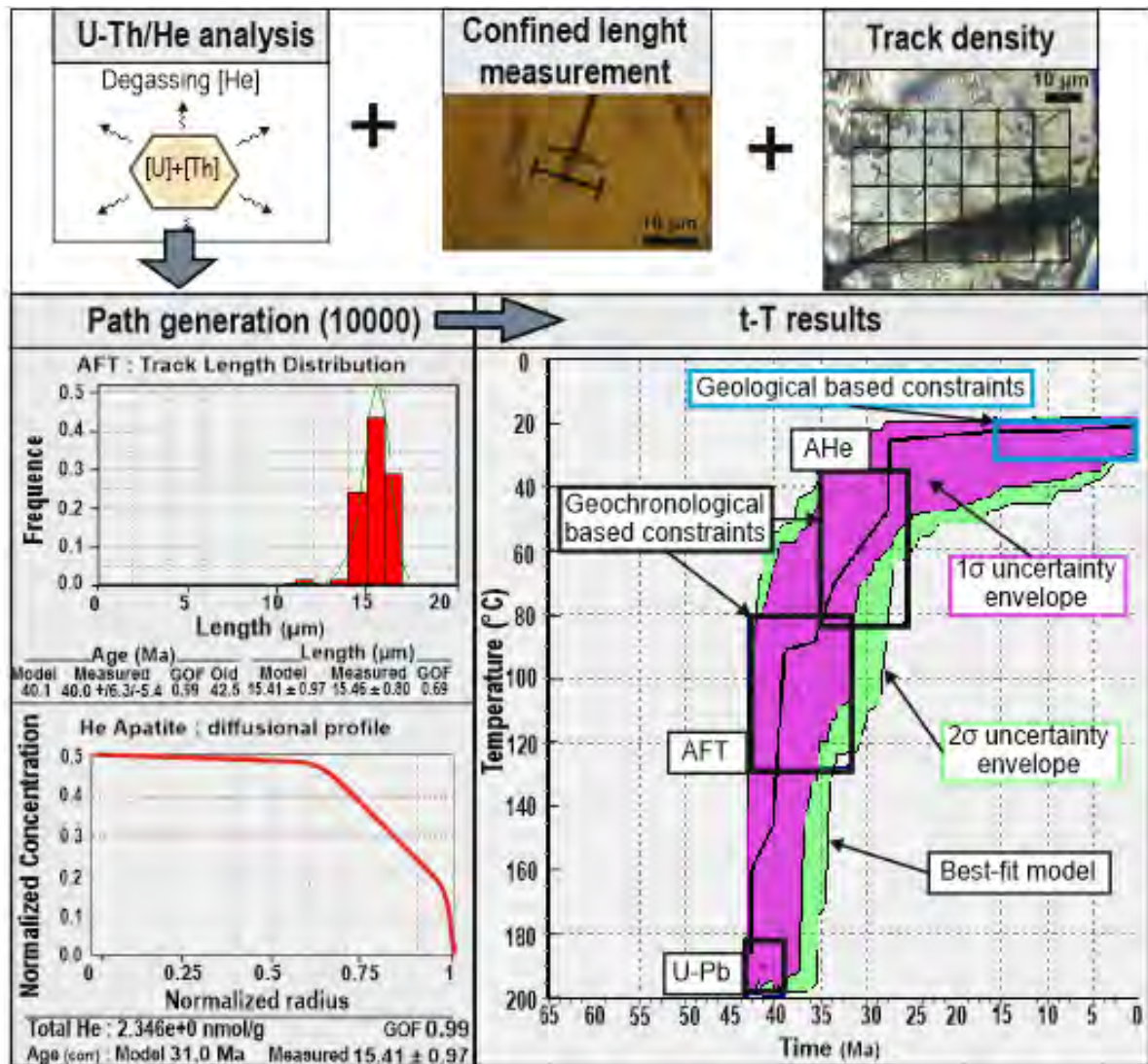
Figure 3.17 – Result of t-T path realized with HeFty simulation. Different type of possible inputs as track density, confined tracks lengths and (U-Th)/He concentrations. Results as the track length distribution and He apatite diffusion profile (modified after http://ivan.bour.over-blog.com/page-5341403.html).

This is the base on which random Time-temperature exploration starts with tests, each one compared to the analytical data. A Goodness Of Fit (GOF) criterion ranging from 0 to 1, 1 being the best, is used to value this comparison. GOF>0.5 are good fits (in pink, with 1 sigma error), 0.05<GOF<0.5 are acceptable fits (in green, with 2 sigma error).

3.3 Cosmogenic nuclides

The earth surface and atmosphere are constantly bombed by charged particles whose fluxes are called cosmic rays (Lal and Peters, 1967). Cosmogenic nuclides are the result of the interaction between these particles (and secondary particles, see below) and nucleus in the atmosphere and in the minerals of the Earth surface. For almost three decades their concentration in rocks has been used to quantify earth surface processes. Here will be presented what are the cosmic rays, how cosmogenic nuclides are produced and some applications for quantifying geomorphologic processes.

84

3.3.1 What are cosmic rays?

Cosmic rays consist in high-energy particles like neutrons, protons, alpha-particles but also electrons, positrons and other subatomic particles (Siame et al., 2001). They originate from galactic and solar rays but the quantity of solar rays arriving to the Earth's surface is considered to be as negligible in comparison to the galactic component (Masarik and Reedy, 1995).

Primary cosmic-ray particles hit nuclei present in the atmosphere and start chain reactions down to the Earth's surface. However, only 0.1% of initial cosmic-rays flux reaches the Earth's surface as secondary particles as their interaction with atmospheric atoms decreases their energy level. In this long reaction cascade, cosmic rays can be divided and classified in three flux components (Figure 3.18): The different components are defined below.
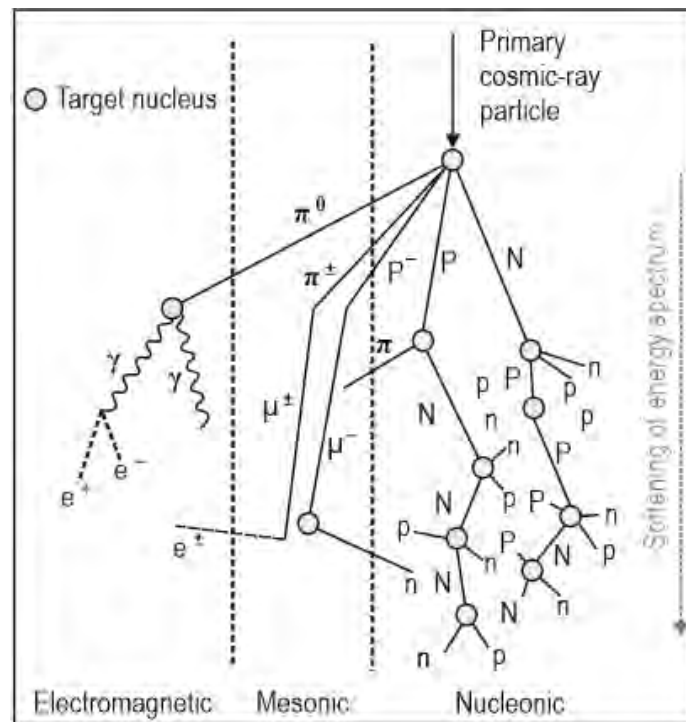
Figure 3.18 – Schematic representation of the cosmic ray cascade. N: secondary neutrons; P: high energy secondary protons; n: thermal neutrons; p: thermal protons; π, μ: muonic component; γ, e+, e- : gamma rays, positrons, electrons, after Lal (1991), Dunai (2010).

It is currently admitted that particles from the electromagnetic groups do not reach the Earth's Surface, so that only nucleonic and mesonic components will be considered from now on (Gosse and Phillips, 2001; Mewaldt et al., 1994).

The nucleonic component is mainly constituted of neutrons and protons which are ejected of target elements by neutron percussion (Figure 3.18), the latter being characterized by conserving the direction of the initial high energy element (Siame et al., 2001). Neutrons being less sensitive than proton to ionic loss, the cosmic flux of this component is neutron-dominated. Neutrons present a large speed spectrum depending on the neutron energy level, ranging from fast, high-energy neutrons to slow and epithermal ones (Dunai, 2010).

The mesonic component is constituted of elements named mesons, which are subatomic particles also resulting of the collision of high-energy cosmic rays and atoms. They decay in elements called muons which have their own decay chain too.

The principal difference between nucleonic and mesonic components is the penetration depth of their product: as muons interact less with the surrounding matter, they penetrate deeper underground.

3.3.2 How cosmogenic nuclides are produced?

At the ground level, various types of interactions between cosmic rays and nucleus generate so-called cosmogenic nuclides, which are defined in the next paragraphs. Each type of cosmogenic nuclide produces different elements on specific target elements.

The first way to produce cosmogenic nuclides at Earth's surface is the spallation. It occurs when an atomic nucleus is hit by an incident particle which can be a neutron or a proton, or even a high-energy electromagnetic wave. The target nucleus decomposes producing lighter particles as neutrons or protons and, after the hit, presents an atomic mass inferior to the initial one.

Secondly, thermal neutron capture happens when neutrons originating from the nuclear cascade transform into thermal neutrons, with a lower energy. They are in a minority compared to other types of production but play an important role in specific cosmogenic nuclides production, like for ^{36}Cl.

Finally, the last two types of production are related to muons and their abundance is generally low at the surface level. The first is the stopping negative muon capture "μ_" (Eidelman et al., 2004) where captured muons neutralize one proton, which delivers a high energy quantity to the nucleus target possibly leading to nuclear evaporation of several nucleons. In the second production type the fast muons rise of decelerating radiation (Bremstrahlung effect) to produce secondary neutrons. Those neutrons can cause all the neutrons reactions presented in this chapter (Groom et al., 2001).

Muons still have a non-negligible contribution at larger depths where spallation contribution can be considered as negligible. Figure 3.19 depicts the respective contribution of the different physical processes involved (described below) in the formation of ^{10}Be cosmogenic nuclides.
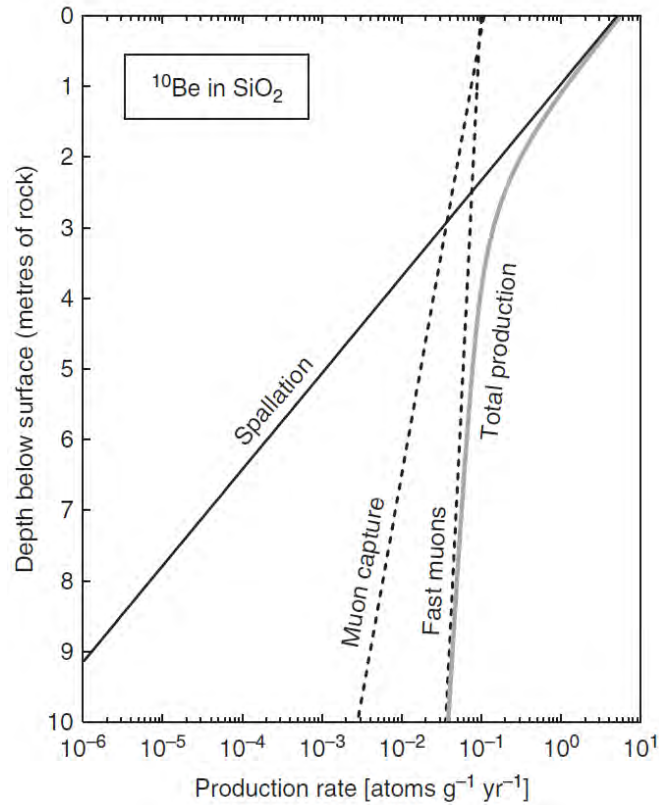
Figure 3.19 – Respective contribution of spallation, muon capture and fast muon processes in the ^{10}Be production as a function of depth beneath surface (Heisenger, 2002a, 2002b).

The different flux input of each type production type at sea level varies strongly for each isotope and are represented in table 1. At sea level, 98% of the cosmic ray flux is made up of neutrons and muons (Masarik and Beer, 1999).

3.3.3 Cosmogenic nuclides diversity and characteristics.

Most cosmogenic nuclides are produced in the atmosphere but this work will focus on Terrestrial Cosmogenic Nuclides (TCN), which are formed inside minerals. Cosmogenic nuclides can be either radiogenic or stable and each element requires specific target elements (Si, N, O, Mg for example for ^{10}Be…), which are present in main target minerals (^{3}He, ^{21}Ne, ^{10}Be, ^{26}Al, ^{36}Cl, ^{14}C) (Table 3.2).

To be used in dating or any process quantification TCNs have to fulfil some conditions (Dunai et al., 2010). First, they have to be naturally rare in the rock to avoid interferences with background. Secondly, they have to be either stable or to present a long half-life, comparable to the processes investigated. Finally, the production mechanism of the nuclide and its type has to be enough understood and constrained. The nuclide should also be retained in a common mineral that is resistant to alteration.

The most used target mineral is the quartz, which presents the advantage to be resistant, physically abundant at the earth surface and also chemically pure of Si and O. Besides, being the most widespread, the ^{10}Be cosmogenic nuclide is the most used and best constrained. His different production aspects are generally well constrained. His half-life is the longest of the radiogenic cosmogenic nuclides that are found in quartz (Table 3.2).

Isotope (half-life)	Main target minerals	Predominant target elements	Reaction pathways (SLHL)
^{3}He (stable)	Olivine, Pyroxene, other He-retentive minerals	All major elements and Li	Spallation: 100% Muons: negligible Thermal neutrons produce ^{3}He on Li, via precursor ^{3}H ($T_{1/2} = 12.3$ a)
^{10}Be (1.36 ± .07 Ma)	Quartz (rarely Pyroxene and Olivine)	O, Si (Mg)	Spallation: 96.4% Muons: 3.6%
^{14}C (5730 ± 30 a)	Quartz	O, Si	Spallation: 82% Muons: 18%
^{21}Ne, ^{22}Ne (stable)	Quartz, Pyroxene, Olivine	Mg, Al, Si	Spallation: >96.4% Muons: ≤3.6%
^{26}Al (708 ± 17 ka)	Quartz	Si	Spallation: 95.4% Muons: 4.6%
^{36}Cl (301 ± 2 ka)	Carbonates, Feldspar, Whole rock	K, Ca, Cl (Fe, Ti)	K: spallation 95.4%; muons 4.6% Ca: spallation 86.6%; muons 13.4% Fe, Ti: spallation presumed 100% Thermal neutrons produce ^{36}Cl from Cl and K.
^{36}Ar, ^{38}Ar (stable)	Feldspar, Amphibole, Pyroxene	K, Ca,	Spallation: up to 100% Muons: not determined Thermal neutrons produce ^{36}Ar from Cl and K, via precursor ^{36}Cl ($T_{1/2} = 301$ ka).
^{41}Ca (104 ± 4 ka)	Fe–Ti oxides	Fe, Ti, (Ca)	Fe, Ti: spallation 100% Thermal neutrons produce ^{41}Ca on ^{40}Ca
^{53}Mn (3.7 ± .4 Ma)	Fe-bearing minerals	Fe, Mn	Fe: spallogenic 90.2%; muons 9.8% Mn: not determined.

Table 3.2 – Principal cosmogenic nuclides produced in situ in rocks characteristics, isotope half-life (Nishiizumi et al.; 2007), main target minerals together with their target elements and the reactions pathways leading to TCN production.

3.3.4 Production rates

The nuclide production rates is influenced by the following main five main parameters:

1. The Earth geomagnetic inclination (Legrand and Simon, 1985) and its temporal variation (Wagner et al., 2000), as it interacts as a shield with the reception of cosmic rays (more rays hit the earth surface near the poles, Niedermann et al., 2002).

2. The altitude (atmospheric pressure), as the production rate increases with altitude and decrease through the atmosphere, as the nuclear cascade activity basically presents an exponential attenuation (Lal, 1988).

3. The topography also impacts the production rate, as the incident rays do not reach all the surfaces with the same intensity, due to shielding effect of surrounding reliefs.

4. Time, as the intensity of the primary cosmic ray flux is not stable through time.

5. The depth at which the sample is located is a major issue. As energy dissipates through mass the cosmogenic nuclide production rate decreases exponentially with the mass of overlying material (Gosse and Phillips, 2001). The attenuation length is the distance that has to cross a particle through material before the production of this particle is considered as null.

The material can either be sediments, water (through liquid form or snow). The attenuation is strongly depending on the material density (Dunne et al., 1999).

Production rates have been calibrated analogically and experimentally for current rates (Dunai, 2000).

Attenuation depth also differs according to the physical type of the particle: for example, in the case of ^{10}Be ~150 g.cm^{-2} for the neutrons and ~1300 g.cm^{-2} for muons (Brown et al., 1995; Braucher et al., 2003; 2011; 2013).

Production rate at z depth can be calculated if the initial production rate is known at the surface:

$$P_{(z)} = P_o e^{\frac{-\rho z}{\wedge}}$$

with P(z) the production rate at x depth (at.g^{-1}.yr^{-1}), ρ the density (g.cm^{-3}), z the depth (cm), ∧ the attenuation length (g.cm^{-2}).

Several production models have been proposed since 1998 (Stone et al., 1998). All the details will be presented in the Chapter 4.

To establish a production rate calibration on samples taking into account the correction due to each parameter previously mentioned (latitude, altitude, etc…) in this subchapter, I used the CRONUS-Earth online calculator (http://hess.ess.washington.edu/) elaborated by Balco et al. (2008).

3.3.5 Acquisition

3.3.5.1 Sampling and quartz separation

In this study, the samples were prepared for ^{10}Be and ^{21}Ne analysis. The aim of the preparation is to obtain pure quartz sand prior to dissolution (for ^{10}Be) or heating (for ^{21}Ne). The different steps of the preparation are represented in a simplified way in the Figure 3.20.
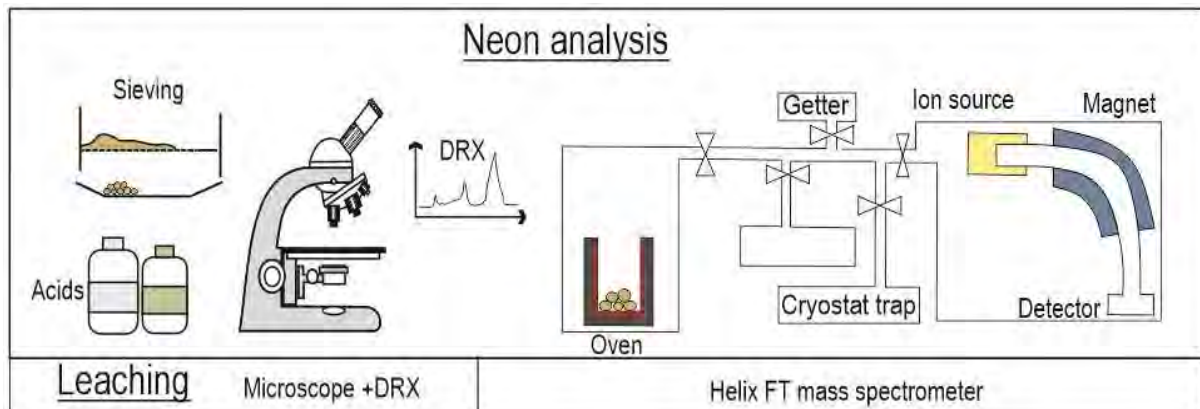
Figure 3.20 – Schematic simplified protocol of separation and ^{21}Ne analysis from sample preparation to spectrometer analysis.

The sampling in the open mine pit in the Atacama Desert (Figure 3.21) was performed on the sedimentary levels presenting millimetre scale quartz grains. Approximately 50 grams of each sample were collected with a fraction from 0.5 mm to 1 mm.

Figure 3.21 – Picture of sand sampled in the Tesoro open mine, Atacama Desert, northern Chile.

Then the samples were leached with hydrochloric acid in independent bottles, to dissolve every carbonate present in the sediments. This operation was repeated until the end of degassing for high carbonate content samples. After this step were performed three hexafluorosilicic acid leaching baths plus mechanical shaking on a shaker, which attack the surface of the grains to eliminate possible atmospheric ^{10}Be contamination.

The purification was realized in the Geosciences Environnement Toulouse (GET) laboratory and in the Centre Européen de Recherche et d'Enseignement en Géosciences de l'Environnement (CEREGE) by the ASTER team.

After the separation in the GET, quartz minerals of some samples were analysed through DRX to verify their purity and discard the presence of inclusions. Before performing the separation of the elements by ion chromatography column chemistry for the ^{10}Be the samples were separated in two. 50 to 100 g were kept for the ^{10}Be measurements and 1g was kept for the ^{21}Ne measurements in the Centre de Recherche Pétrographiques et Géochimiques (CRPG) at Nancy with Pierre Henri-Blard.

The quality of the quartz grain was doubled cheked by manual optic separation of ~120 mg of quartz for each sample.

3.3.5.2 Measurement

^{10}Be measurements by Accelerator Mass Spectrometry (AMS) were performed at ASTER AMS at the CEREGE by local staff (Figure 3.22). The AMS combined a mass spectrometer and an accelerator that permits to differentiate and spare atoms with neighbouring masses. As the Beryllium in unstable it requires to be injected under the oxide state BeO$^-$. In this process is measured the ^{10}Be/^{9}Be ratio of the sample, by number of beam hits on the detector and compared to a standard with known ^{10}Be/^{9}Be ratio.

Figure 3.22 – Picture of the Accelerator Mass Spectrometer of the CEREGE, Aix in Provence, France (picture from www.cerege.com).

In the case of ^{21}Ne which is a gas, its extraction is proceeded by step heating in an oven to a temperature higher than 900°C, 600°C being the degassing temperature of neon (Niedermann, 2002). This step heating is preferential to only eject the ^{21}Ne comprised in the lattice and not in inclusions that require higher temperatures to be released. A HELIX SFT™ static vacuum mass spectrometer which is a magnetic sector mass spectrometer was used to perform the analysis. This mass spectrometer is specific to the noble gases isotopic analysis quantification (working for ^{3}He too).

After precise weighing of each sample, they were packed in tin foils before deposition in the loading platform. CREU standards were also analysed during the ^{21}Ne analyses (Vermeesch et al., 2015). During this analysis, we measured ratios between the three Ne isotopes: ^{21}Ne/^{20}Ne, ^{22}Ne/^{20}Ne. Neon is naturally present in the atmosphere with known abundance ratio: ^{21}Ne/^{20}Ne = 0.00296 and ^{22}Ne/^{20}Ne = 10.20 (Eberhardt et al. 1965).

The ratios measured are compared with the one of the atmosphere to determine the origin of the Ne isotopes measured. They have to be higher than the one of the air. Then a calculation must be performed to retrieve the ^{21}Ne concentration of the sample (formula below).

$$^{21}Ne^* = R_c \times \ ^{20}Ne_m * \frac{R_m - R_a}{R_c - R_a}$$

Where ^{20}Ne $_m$ is the measured ^{20}Ne, R $_c$ is the cosmogenic ^{21}Ne/^{20}Ne ratio (R $_c$ = 0.8; Niedermann, 2002) R$_m$ is the measured ^{21}Ne/^{20}Ne-ratio, and R$_a$ is the atmospheric ^{21}Ne/^{20}Ne-ratio (R $_a$ = 0.00296).

3.3.6 Geomorphological quantifications

3.3.6.1 Dating surfaces.

To apply TCN to date surface exposure, the environment in which the study is realized has to undergo relatively low erosion rates. Strong erosion rates will limit a lot the possible time scale on which the method is accurate. The first application of TCN to geomorphology was to date surfaces (Klein et al., 1986; Nishiizumi et al., 1986; Granger et al., 2013).

This method relies on the accumulation of TCN in the surface material, making the assumption that no erosion did occur on that surface and that the concentration is only proportional to the production without considering radioactive decay.

As few perfect cases occur with no erosion two cosmogenic nuclides on same samples and their ratios can be used to verify if any more complex scenario than simple surface exposure occurred, comparing the two elements ratio (see figure 3.23).
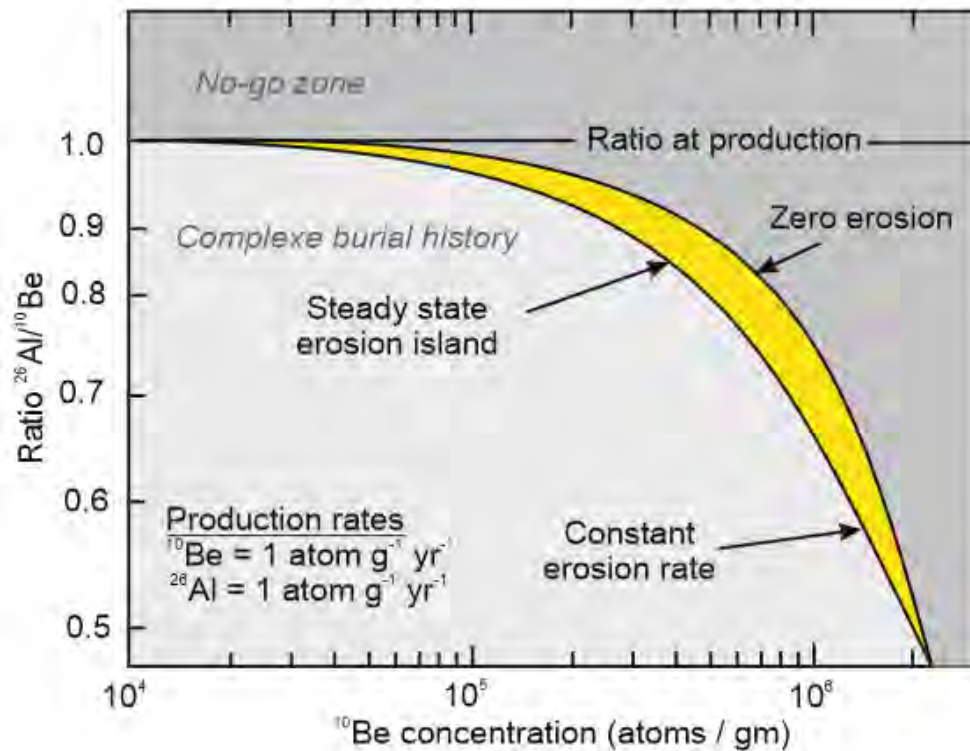
Figure 3.23 – The "banana plot" modified after Lal (1991). Evolution of the[10]Be concentration plotted ratio [26]Al/[10]Be. In this figure is illustrated the possible expected range (in yellow) of [26]Al and [10]Be concentrations for an exposed surface. Further explication in the paragraph below.

This "banana" is limited by an upper bound curve which is traced by the irradiation of a rock of zero erosion and the lower bound is [26]Al/[10]Be ratio line in case of constant erosion rate.

The island represents the steady state erosion possible range where would be plotted the results for rocks of different erosion rates, in case of constant erosion rates. The dark grey zone represents represented the zone were the results are not possible to obtain and the light grey zone is where the concentrations should be the result of burial process, explained in the further 3.2.5.3 section.

Since these pioneer works, other applications have been developed to quantify geomorphic processes as including exposure histories on surfaces (Vassallo et al., 2011) but also catchment scale erosion rate (Von Blanckenburg, 2005), river incision rates (Saillard et al., 2014) and burial ages of sediment (Davis et al., 2014).

As our work in this thesis is mainly focused on erosion and burial processes, I only introduce the use of TCN to document these processes in the following.

3.3.6.2 Local Erosion rate quantification

Despite some limitations, cosmogenic nuclides provide the most accurate erosion rate evaluation when required conditions are respected (Granger et al., 1996; Dunai, 2010). The possibility of their application varies depending on the tectonic settings and climatic zones. Indeed the application is depending on the magnitude of erosion rates.

Slow erosion rates permit to retrieve older erosion timescales (von Blanckenburg, 2005). At steady state and at the Earth surface, the cosmogenic nuclide concentration represents a balance between production via cosmic ray interactions (in yellow) and the losses (in grey) by erosion and radioactive decay.

$$\frac{dC}{dt} = P_0 e^{\left(-\frac{\rho z}{\wedge}\right)} + \varepsilon \frac{dC}{dz} - \lambda . C$$

with P_0 as surface production rate (at.g^{-1}.yr^{-1}), z as the depth (cm), C standing for the concentration (at.g^{-1}), $\wedge$ standing for attenuation depth (g.cm^{-2}), and ε standing for erosion rate (cm.a^{-1}).

Active landscape supplies sediments from the bedrock/regolith downstream the corresponding catchment. As TCN concentrations are inversely proportional to erosion rates, flux weighted concentrations reflect spatially averaged erosion rates (Granger et al., 1996; Brown et al., 1995: Schaller et al., 2002; Codilean et al., 2008, Granger and Schaller, 2014) yielding basin-wide erosion rates (Figure 3.24). The TCN production rate depends on elevation.
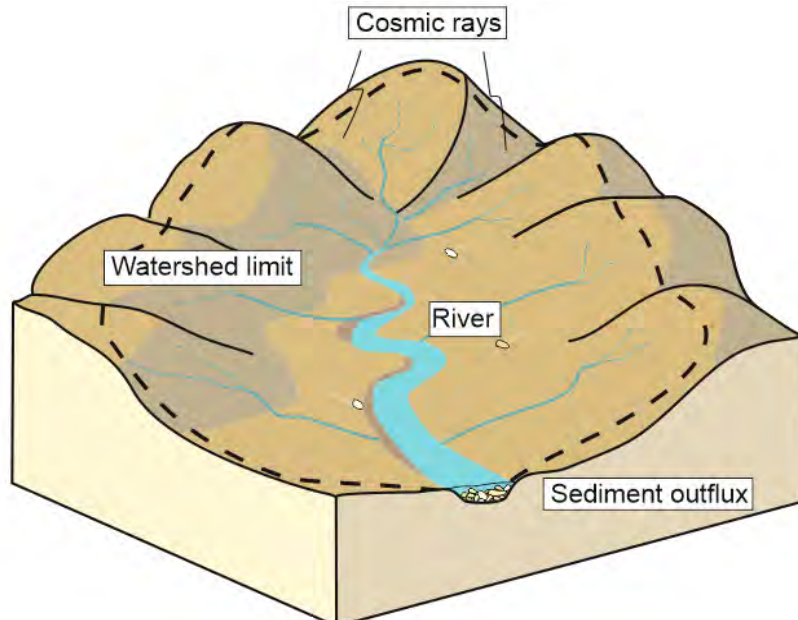
Figure 3.24 – Simplified watershed scale catchment and cosmic rays' interaction. Sediments must be carried by active channels at the outlet of the catchment to yield the average denudation rates of this catchment.

The catchment mean production rate in the next equation is computed by averaging the local TCN production rates within the catchment.

$$\overline{C} = \frac{\overline{P}}{\lambda + \rho \ \overline{\varepsilon}/\Lambda}$$

with C standing for the mean concentration of the catchment (at.g^{-1}), P the mean production (at.g^{-1}.yr^{-1}), ρ the density (g.cm^{-3}), ∧ the attenuation length (g.cm^{-2}), $\overline{\varepsilon}$ standing for the mean erosion of the catchment

Such averaging is usually done using a Geographical Information System in which the TCN production is calculated for each pixel and then averaged (e.g. Mudd et al., 2016).

The precedent equation assumes that the target mineral is spread homogeneously in the parent rock of the catchment (Granger and Schaller, 2014). This situation is not always verified, in particular for large catchments. The variation in the proportion of the target mineral can be partially taken into account to calculate the mean TCN production rate (e.g., Safran et al., 2005; Carretier et al., 2015).

Depending on the type of Environnement, the mass loss in the basin can occur by physical surface lowering and also by deep chemical weathering, deep meaning depth superior to the attenuation depth (Brown et al., 1995; Granger et al., 1996; Riebe and Granger, 2013; Regard et al., 2016) .

3.3.6.3 Burial dating

The concept of burial dating is based on the shielding of sediments and the stop of TCN production. It requires the use of at least one pair of cosmogenic nuclides with different decay constants but produced in the same mineral (as quartz). At the surface, when minerals are exposed, TCN concentrations in the mineral will be proportional to the production ratios. Once sediments cover the surface, the production will decrease exponentially with the burial depth. When the sediment layer above the minerals reach a depth of 2 m, which represents about 3 times the attenuation length of neutrons (about 60 cm for quartz), the TCN production due to spallation is only ~5% of that at the Earth surface. The TCN production becomes then dominantly controlled by the muons.

Then the ratio between the two radiogenic nuclides will change. In case of stable isotopes, the concentration will not change for that element meanwhile the concentration of radiogenic nuclide will keep on decreasing by radioactive decay.

$$R_{AB}(t_b) = \frac{C_A(t_b)}{C_B(t_b)} = R_{AB}(0) \ e^{-t_b(\lambda_A - \lambda_B)}$$

With A and B for two cosmogenic nuclides, RAB, the ratio between their content, tb, burial time, CA and CB the concentration of the A and B TCN, λ_A and λ_B.

The measurements of the ratio between both elements indicate the length of time the sediments have been buried. To calculate the burial time in a case with two cosmogenic TCN the following formula can be used:

$$t_b = \frac{-\ln\left(\frac{R_{AB}(t_b)}{R_{AB}(0)}\right)}{(\lambda_A - \lambda_B)}$$

The first descriptive models applied to burial dating were performed with ^{26}Al/^{10}Be (Lal, 1991; Granger and Muzikar, 2001; Granger, 2006). The results can be represented in burial dating plots as in Figure 3.25.
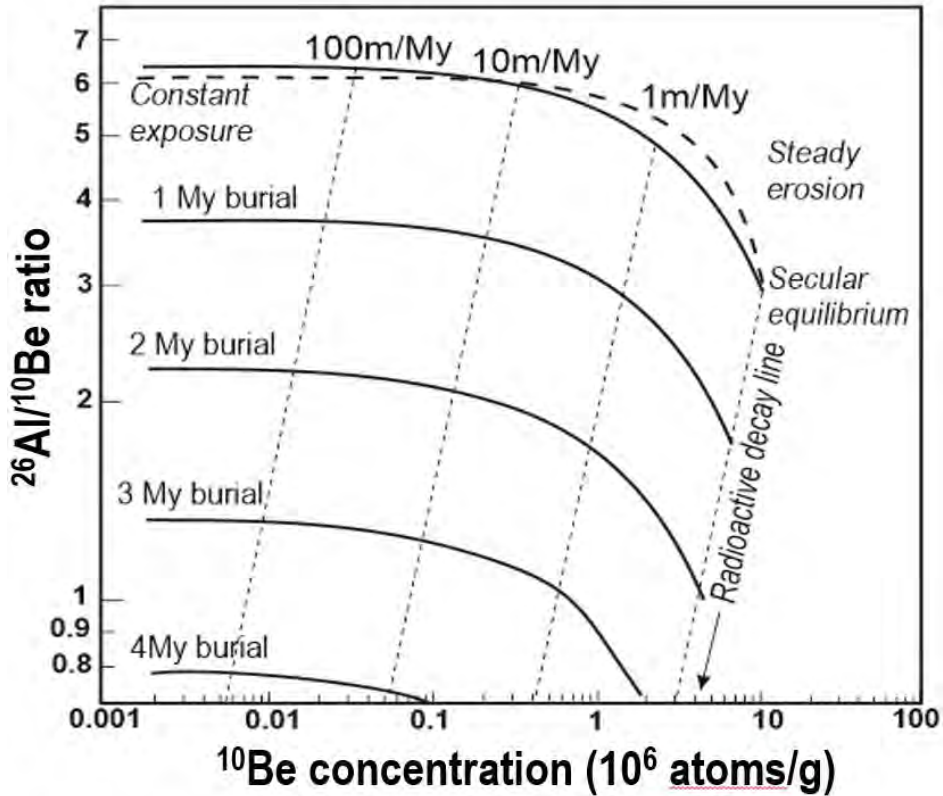
Figure 3.25 – Burial diagram plotted ^{10}Be concentration in function of the ^{26}Al/^{10}Be where production rates of ^{26}Al and ^{10}Be are fixed at 1 at.g^{-1}.yr^{-1}. The horizontal parallel lines represent burial isochrones.

The dashed line represents constant exposure meanwhile the top continuous line represents steady erosion (cf. figure 3.25). Continuous lines below represent million years' isochrones for sediment burial following steady erosion. Sub vertical dashed lines are radioactive decay lines. When the sediments are suddenly shielded from TCN production at a depth superior to the attenuation length, their ^{10}Be and ^{26}Al content evolve along a "Radioactive decay line" originating at the point corresponding to its surface-acquired content, generally lying on the steady erosion line. The top right corner of the figure, over the steady erosion line, is the "impossible" zone where results would not have any meaning (cf. figure 3.23).

Balco et al. (2008) stipulated that the *"useful range of ^{26}Al–^{10}Be burial dating is ca. 0.5–6Ma"* considering the radioactive decay constant but older burial ages have been found with this method as in Davis et al., (2014), in the Atacama Desert in which post deposit production did occur.

In their study, Davis et al., (2014) applied burial dating with the ^{26}Al and ^{10}Be cosmogenic nuclide couple, to a post 10 Ma 25 m high sedimentary sequence in a paleo channel. The authors relied on the ages of an interbedded ignimbrite and the possible correlations they made with other ignimbrites in the zone. They also realized simulations of the variations of ^{26}Al/^{10}Be ratios according to ^{10}Be concentrations to see the impact of three different muon schemes. In terms of possible application range for burial dating Balco and Shuster (2009) also proposed that the ^{10}Be-^{21}Ne couple could permit to cover all the Miocene. This will be presented in the Chapter 6.

3.4   Thermobarometry

Thermobarometry is a science applied in order to better constrain temperature and pressure history, possibly on both igneous and metamorphic rocks during crystallization. Several methods have been developed in the last decades on different minerals (Berman, 1991; Anderson, 1996; Ernst and Liu, 1998; Anderson et al., 2008; etc...).

Studies focused on thermobarometry applied on amphibole on igneous rocks (Ague, 1997; Stein and Dietl, 2001; Zhang et al., 2006). A novative thermobarometry method (Ridolfi et al., 2010; Ridolfi and Renzulli, 2012) has been proposed, calibrated for `calc-alkaline and alkaline igneous rocks`. This method was applied to Mg-rich amphiboles and is based on their composition in nine main chemical elements which are `Si, Ti, Al, Fe, Mn, Mg, Ca, Na and K` (Ridolfi et al., 2010). The Ridolfi and Renzulli (2012) method has also been applied to recover magmatic crystallization conditions of magmatic rocks (Erdmann et al., 2014).

After many calibration on amphiboles of different geological environnements (Costa et al., 2013; Leuthold et al., 2014; Ridolfi et al., 2016) this method has successfully been applied to quantify emplacement depths on Andean igneous rocks from the White Cordillera in Bolivia (Margirier et al., 2016), combined with low-temperature thermochronology methods.

First step of the procedure, igneous rocks containing amphiboles were sampled. Then to perform the analyses, the development of polished thin section was required. Then, a petrological analyse allowed to recognize the presence of amphiboles and their state of alteration. Indeed, the mineral chemistry would be modified if any sign of alteration was visible, so they need to be unaltered. The chemical analyses were performed with a microprobe on the minerals, along a transect from the border to the center of the mineral. By that, it is possible to verify that the chemical composition is homogeneous in all the grain.

With the concentration of these different elements, pressure and temperature conditions were calculated for each point measured as described by Ridolfi et al. (2010) and Ridolfi and Renzulli (2012).

References for Chapter 3

Ague, J. J. 1997. Thermodynamic calculation of emplacement pressures for batholithic rocks, California: Implications for the aluminum-in-hornblende barometer. *Geology*, *25*(6), 563-566.

Anderson, J. L. 1996. Status of thermobarometry in granitic batholiths. *Geological Society of America Special Papers*, *315*, 125-138.

Anderson, J. L., Barth, A. P., Wooden, J. L., & Mazdab, F. 2008. Thermometers and thermobarometers in granitic systems. *Reviews in Mineralogy and Geochemistry*, *69*(1), 121-142.

Armstrong, P.A., 2005. Thermochronometers in sedimentary basins. Reviews in Mineralogy and Geochemistry 58, 499–525.

Balco, G., Stone, J.O., Lifton, N.A., Dunai, T.J., 2008. A complete and easily accessible means of calculating surface exposure ages or erosion rates from ^{10}Be and ^{26}Al measurements. Quaternary geochronology 3, 174–195.

Balco, G., Shuster, D. L. 2009. ^{26}Al–^{10}Be–^{21}Ne burial dating. Earth and Planetary Science Letters, 286(3), 570-575.

Barbarand, J., Carter, A., Wood, I., Hurford, T., 2003. Compositional and structural control of fission-track annealing in apatite. Chemical Geology 198, 107–137.

Berman, R. G. 1991. Thermobarometry using multi-equilibrium calculations; a new technique, with petrological applications. *The Canadian Mineralogist*, *29*(4), 833-855.

Braucher, R., Bourlès, D., Merchel, S., Romani, J.V., Fernadez-Mosquera, D., Marti, K., Leanni, L., Chauvet, F., Arnold, M., Aumaître, G., others, 2013. Determination of muon attenuation lengths in depth profiles from in situ produced cosmogenic nuclides. Nuclear Instruments and Methods in Physics Research Section B: Beam Interactions with Materials and Atoms 294, 484–490.

Braucher, R., Brown, E.T., Bourlès, D.L., Colin, F., 2003. In situ produced ^{10}Be measurements at great depths: implications for production rates by fast muons. Earth and Planetary Science Letters 211, 251–258.

Braucher, R., Merchel, S., Borgomano, J., Bourlès, D.L., 2011. Production of cosmogenic radionuclides at great depth: a multi element approach. Earth and Planetary Science Letters 309, 1–9.

Braun, J., der Beek, P., Batt, G., 2006. Quantitative thermochronology: numerical methods for the interpretation of thermochronological data. Cambridge University Press.

Brown, E.T., Stallard, R.F., Larsen, M.C., Raisbeck, G.M., Yiou, F., 1995. Denudation rates determined from the accumulation of in situ-produced ^{10}Be in the Luquillo Experimental Forest, Puerto Rico. Earth and Planetary Science Letters 129, 193–202.

Carlson, W.D., Donelick, R.A., Ketcham, R.A., 1999. Variability of apatite fission-track annealing kinetics: I. Experimental results. American mineralogist 84, 1213–1223.

Carretier, S., Regard, V., Vassallo, R., Martinod, J., Christophoul, F., Gayer, E., Audin, L., Lagane, C., 2015. A note on ^{10}Be-derived mean erosion rates in catchments with heterogeneous lithology: examples from the western Central Andes. Earth Surface Processes and Landforms 40, 1719–1729.

Carter, A., 1999. Present status and future avenues of source region discrimination and characterization using fission track analysis. Sedimentary Geology 124, 31–45.

Codilean, A.T., Bishop, P., Stuart, F.M., Hoey, T.B., Fabel, D., Freeman, S.P., 2008. Single-grain cosmogenic ^{21}Ne concentrations in fluvial sediments reveal spatially variable erosion rates. Geology 36, 159-162.

Codilean, A.T., 2009 https://serc.carleton.edu/

Davis, M., Matmon, A., Placzek, C. J., McIntosh, W., Rood, D. H., Quade, J. (2014). Cosmogenic nuclides in buried sediments from the hyperarid Atacama Desert, Chile. Quaternary Geochronology, 19, 117-126.

Dodson, M.H., 1986. Closure profiles in cooling systems, in: Materials Science Forum. Trans Tech Publ, pp. 145–154.

Dodson, M.H., 1973. Closure temperature in cooling geochronological and petrological systems. Contributions to Mineralogy and Petrology 40, 259–274.

Donelick, R.A., O'Sullivan, P.B., Ketcham, R.A., 2005. Apatite Fission-Track Analysis. Reviews in Mineralogy and Geochemistry 58, 49–94.

Dunai, T.J., 2010. Cosmogenic nuclides: principles, concepts and applications in the earth surface sciences. Cambridge University Press.

Dunai, T.J., 2000. Scaling factors for production rates of in situ produced cosmogenic nuclides: a critical reevaluation. Earth and Planetary Science Letters 176, 157–169.

Dunne, J., Elmore, D., Muzikar, P., 1999. Scaling factors for the rates of production of cosmogenic nuclides for geometric shielding and attenuation at depth on sloped surfaces. Geomorphology 27, 3–11.

Eberhardt, P., Eugster, O., Marti, K. 1965. A redetermination of the isotopic composition of atmospheric neon. Zeitschrift für Naturforschung A, 20(4), 623-624.

Eidelman, S., Hayes, K.G., Olive, K. ea, Aguilar-Benitez, M., Amsler, C., Asner, D., Babu, K.S., Barnett, R.M., Beringer, J., Burchat, P.R., others, 2004. Review of particle physics. Physics Letters B 592, 1–5.

Erdmann, S., Martel, C., Pichavant, M., & Kushnir, A. 2014. Amphibole as an archivist of magmatic crystallization conditions: problems, potential, and implications for inferring magma storage prior to the paroxysmal 2010 eruption of Mount Merapi, Indonesia. *Contributions to Mineralogy and Petrology*, *167*(6), 1016.

Ernst, W. G., & Liu, J. 1998. Experimental phase-equilibrium study of Al-and Ti-contents of calcic amphibole in MORB—a semiquantitative thermobarometer. *American mineralogist*, *83*(9-10), 952-969.

Eude, A. 2014. La croissance des Andes centrales du nord du Pérou (5-9°S): Propagation d'un prisme orogénique dans un contexte d'héritage tectonique et de subduction plane. Géologie appliquée. Université Toulouse III Paul Sabatier, 2014.

Farley, K.A., Wolf, R.A., Silver, L.T., 1996. The effects of long alpha-stopping distances on (U-Th)/He ages. Geochimica et cosmochimica acta 60, 4223–4229.

Farley, K.A., 2000. Helium diffusion from apatite: General behavior as illustrated by Durango fluorapatite. Journal of Geophysical Research B 105, 2903–2914.

Farley, K. A. 2002. (U-Th)/He dating: Techniques, calibrations, and applications. Reviews in Mineralogy and Geochemistry, 47(1), 819-844.

Fleischer, R.L., Price, P.B., Walker, R.M., 1975. Nuclear tracks in solids: principles and applications. Univ of California Press.

Fleischer, R.L., Price, P.B., Walker, R.M., 1965. Ion explosion spike mechanism for formation of charged-particle tracks in solids. Journal of applied Physics 36, 3645–3652.

Galbraith, R. F. 1981. On statistical models for fission track counts. Mathematical Geology, 13(6), 471-478.

Galbraith, R. F. 1988. Graphical display of estimates having differing standard errors. Technometrics, 30(3), 271-281.

Galbraith, R.F., Laslett, G.M., 1993. Statistical models for mixed fission track ages. Nuclear tracks and radiation measurements 21, 459–470.

Galbraith, R. F., Roberts, R. G., Laslett, G. M., Yoshida, H., Olley, J. M. 1999. Optical dating of single and multiple grains of quartz from Jinmium rock shelter, northern Australia: Part I, experimental design and statistical models. Archaeometry, 41(2), 339-364.

Gautheron, C., Tassan-Got, L., 2010. A Monte Carlo approach to diffusion applied to noble gas/helium thermochronology. Chemical Geology 273, 212–224.

Gautheron, C., Tassan-Got, L., Ketcham, R. A., Dobson, K. J. 2012. Accounting for long alpha-particle stopping distances in (U–Th–Sm)/He geochronology: 3D modeling of diffusion, zoning, implantation, and abrasion. Geochimica et Cosmochimica Acta, 96, 44-56.

Gleadow, A. J. W., Duddy, I. R., Lovering, J. F. 1983. Fission track analysis: a new tool for the evaluation of thermal histories and hydrocarbon potential. The APPEA Journal, 23(1), 93-102.

Gleadow, A.J.W., Duddy, I.R., Green, P.F., Lovering, J.F., 1986. Confined fission track lengths in apatite: a diagnostic tool for thermal history analysis. Contributions to Mineralogy and Petrology 94, 405–415.

Gleadow, A.J.W., Raza, A., Kohn, B.P., Spencer, S.A., 2005. The potential of monazite for fission-track dating, in: Geochimica et Cosmochimica Acta. Pergamon-Elsevier science ltd the boulevard, Langford Lane, Kidlington, Oxford ox5 1gb, England, p. A21—-A21.

Gosse, J.C., Phillips, F.M., 2001. Terrestrial in situ cosmogenic nuclides: theory and application. Quaternary Science Reviews 20, 1475–1560.

Granger, D.E., Kirchner, J.W., Finkel, R., 1996. Spatially averaged long-term erosion rates measured from in situ-produced cosmogenic nuclides in alluvial sediment. The Journal of Geology 104, 249–257.

Granger, D. E., Muzikar, P. F. 2001. Dating sediment burial with in situ-produced cosmogenic nuclides: theory, techniques, and limitations. Earth and Planetary Science Letters, 188(1), 269-281.

Granger, D. E. 2006. A review of burial dating methods using 26Al and ^{10}Be. Geological Society of America Special Papers, 415, 1-16.

Granger, D.E., Lifton, N.A., Willenbring, J.K., 2013. A cosmic trip: 25 years of cosmogenic nuclides in geology. Geological Society of America Bulletin 125, 1379–1402.

Granger, D.E., Schaller, M., 2014. Cosmogenic nuclides and erosion at the watershed scale. Elements 10, 369–373

Green, P.F., 1985. Comparison of zeta calibration baselines for fission-track dating of apatite, zircon and sphene. Chemical Geology: Isotope Geoscience section 58, 1–22.

Green, P.F., Duddy, I.R., Gleadow, A.J.W., Tingate, P.R., Laslett, G.M., 1986. Thermal annealing of fission tracks in apatite: 1. A qualitative description. Chemical Geology: Isotope Geoscience section 59, 237–253.

Groom, D.E., Mokhov, N.V., Striganov, S.I., 2001. Muon stopping power and range tables 10 MeV–100 TeV. Atomic Data and Nuclear Data Tables 78, 183–356.

Heisinger, B., Lal, D., Jull, A.J.T., Kubik, P., Ivy-Ochs, S., Knie, K., Nolte, E., 2002a. Production of selected cosmogenic radionuclides by muons: 2. Capture of negative muons. Earth and Planetary Science Letters 200, 357–369.

Heisinger, B., Lal, D., Jull, A.J.T., Kubik, P., Ivy-Ochs, S., Neumaier, S., Knie, K., Lazarev, V., Nolte, E., 2002b. Production of selected cosmogenic radionuclides by muons: 1. Fast muons. Earth and Planetary Science Letters 200, 345–355.

Hurford, A.J., 1990. Standardization of fission track dating calibration: Recommendation by the Fission Track Working Group of the IUGS Subcommission on Geochronology. Chemical Geology: Isotope Geoscience Section 80, 171–178.

Hurford, A.J., Green, P.F., 1983. The zeta age calibration of fission-track dating. Chemical Geology 41, 285–317.

Hurford, A.J., Hammerschmidt, K., 1985. ^{40}Ar/^{39}Ar and K/Ar dating of the Bishop and Fish Canyon Tuffs: Calibration ages for fission-track dating standards. Chemical Geology: Isotope Geoscience section 58, 23–32.

Ketcham, R.A., 2005. Forward and inverse modelling of low-temperature thermochronometry data. Reviews in mineralogy and geochemistry 58, 275–314.

Ketcham, R. A., Carter, A., Donelick, R. A., Barbarand, J., Hurford, A. J. (2007). Improved modeling of fission-track annealing in apatite. American Mineralogist, 92(5-6), 799-810.

Ketcham, R. A., Gautheron, C., Tassan-Got, L. (2011). Accounting for long alpha-particle stopping distances in (U–Th–Sm)/He geochronology: Refinement of the baseline case. Geochimica et Cosmochimica Acta, 75(24), 7779-7791.

Klein, J., Giegengack, R., Middleton, R., Sharma, P., Underwood, J.R., Weeks, R.A., 1986. Revealing histories of exposure using in situ produced ^{26}Al and ^{10}Be in Libyan desert glass. Radiocarbon 28, 547–555.

Kunk, M.J., Sutter, J.F., Naeser, C.W., 1985. High-precision/sup ^{40}Ar/^{39}Ar ages of sanidine, biotite, hornblende, and plagioclase from the Fish Canyon Tuff, San Juan volcanic field, south-central Colorado. Geol. Soc. Am., Abstr. Programs; (United States) 17.

Lal, D., 1991. Cosmic ray labeling of erosion surfaces: in situ nuclide production rates and erosion models. Earth and Planetary Science Letters 104, 424–439.

Lal, D., Peters, B., 1967. Cosmic ray produced radioactivity on the earth, in: Kosmische Strahlung II/Cosmic Rays II. Springer, pp. 551–612.

Laslett, G.M., Kendall, W.S., Gleadow, A.J.W., Duddy, I.R., 1982. Bias in measurement of fission-track length distributions. Nuclear Tracks and Radiation Measurements (1982) 6, 79–85.

Legrand, J. P., Simon, P. A. 1985. Some solar cycle phenomena related to the geomagnetic activity from 1868 to 1980. I-The shock events, or the interplanetary expansion of the toroidal field. Astronomy and Astrophysics, 152, 199-204.

Masarik, J., Beer, J., 1999. Simulation of particle fluxes and cosmogenic nuclide production in the Earth's atmosphere. Journal of Geophysical Research: Atmospheres 104, 12099–12111.

Masarik, J., Reedy, R.C., 1995. Terrestrial cosmogenic-nuclide production systematics calculated from numerical simulations. Earth and Planetary Science Letters 136, 381–395.

McDowell, F.W., McIntosh, W.C., Farley, K.A., 2005. A precise ^{40}Ar–^{39}Ar reference age for the Durango apatite (U–Th)/He and fission-track dating standard. Chemical Geology 214, 249–263.

Mewaldt, R.A., 1994. Galactic cosmic ray composition and energy spectra. Advances in Space Research 14, 737–747.

Molnar, P., England, P., 1990. Late Cenozoic uplift of mountain ranges and global climate change: chicken or egg? Nature 346, 29–34.

Mudd, S., Hurst, M., Grieve, S., Clubb, F., Milodowski, D., Attal, M., 2016. Detecting geomorphic processes and change with high resolution topographic data, in: EGU General Assembly Conference Abstracts. p. 13431.

Naeser, C. W., Fleischer, R. L. 1975. Age of the apatite at Cerro de Mercado, Mexico: A problem for fission-track annealing corrections. Geophysical Research Letters, 2(2), 67-70.

Naeser, C. W. 1979. Fission-track dating and geologic annealing of fission tracks. In Lectures in isotope geology (pp. 154-169). Springer, Berlin, Heidelberg.

Niedermann, S., 2002. Cosmic-ray-produced noble gases in terrestrial rocks: dating tools for surface processes. Reviews in Mineralogy and Geochemistry 47, 731–784.

Nishiizumi, K., Imamura, M., Caffee, M.W., Southon, J.R., Finkel, R.C., McAninch, J., 2007. Absolute calibration of ^{10}Be AMS standards. Nuclear Instruments and Methods in Physics Research Section B: Beam Interactions with Materials and Atoms 258, 403–413.

Nishiizumi, K., Lal, D., Klein, J., Middleton, R., Arnold, J.R., 1986. Production of ^{10}Be and ^{26}Al by cosmic rays in terrestrial quartz in situ and implications for erosion rates.

Pik, R., Marty, B., Carignan, J., Lavé, J., 2003. Stability of the Upper Nile drainage network (Ethiopia) deduced from (U–Th)/He thermochronometry: implications for uplift and erosion of the Afar plume dome. Earth and Planetary Science Letters 215, 73–88.

Price, P.B., Walker, R.M., 1963. Fossil tracks of charged particles in mica and the age of minerals. Journal of Geophysical Research 68, 4847–4862.

Regard, V., Carretier, S., Boeglin, J.-L., Ndam Ngoupayou, J.-R., Dzana, J.-G., Bedimo Bedimo, J.-P., Riotte, J., Braun, J.-J., 2016. Denudation rates on cratonic landscapes: Comparison between suspended and dissolved fluxes, and ^{10}Be analysis in the Nyong and Sanaga River basins, South Cameroon. Earth Surface Processes and Landforms 41, 1671–1683.

Reiners, P.W., Brandon, M.T., 2006. Using thermochronology to understand orogenic erosion. Annu. Rev. Earth Planet. Sci. 34, 419–466.

Reiners, P.W., Farley, K.A., 1999. Helium diffusion and (U–Th)/He thermochronometry of titanite. Geochimica et Cosmochimica Acta 63, 3845–3859.

Ridolfi, F., Renzulli, A., & Puerini, M. 2010. Stability and chemical equilibrium of amphibole in calc-alkaline magmas: an overview, new thermobarometric formulations and application to subduction-related volcanoes. *Contributions to Mineralogy and Petrology*, *160*(1), 45-66.

Ridolfi, F., & Renzulli, A. 2012. Calcic amphiboles in calc-alkaline and alkaline magmas: thermobarometric and chemometric empirical equations valid up to 1,130°C and 2.2 GPa. *Contributions to Mineralogy and Petrology*, *163*(5), 877-895.

Riebe, C.S., Granger, D.E., 2013. Quantifying effects of deep and near-surface chemical erosion on cosmogenic nuclides in soils, saprolite, and sediment. Earth Surface Processes and Landforms 38, 523–533.

Rutherford, E., 1905. Bakerian lecture: the succession of changes in radioactive bodies. Philosophical Transactions of the Royal Society of London. Series A, Containing Papers of a Mathematical or Physical Character 204, 169–219.

Safran, E.B., Bierman, P.R., Aalto, R., Dunne, T., Whipple, K.X., Caffee, M., 2005. Erosion rates driven by channel network incision in the Bolivian Andes. Earth Surface Processes and Landforms 30, 1007–1024.

Saillard, M., Petit, C., Rolland, Y., Braucher, R., Bourlès, D. L., Zerathe, S. Jourdon, A. (2014). Late Quaternary incision rates in the Vésubie catchment area (Southern French Alps) from in situ-produced 36Cl cosmogenic nuclide dating: Tectonic and climatic implications. Journal of Geophysical Research: Earth Surface, 119(5), 1121-1135.

Schaller, M., Von Blanckenburg, F., Veldkamp, A., Tebbens, L.A., Hovius, N., Kubik, P.W., 2002. A 30 000 yr record of erosion rates from cosmogenic ^{10}Be in middle European river terraces. Earth and Planetary Science Letters 204, 307–320.

Siame, L.L., Braucher, R., Bourles, D.L., Bellier, O., Sebrier, M., 2001. Datation de surfaces geomorphologiques reperes par le ^{10}Be produit in-situ; implications tectoniques et climatiques. Bulletin de la Société Géologique de France 172, 223–236.

Steiger, R., Jäger, E., 1977. Subcommission on geochronology: convention on the use of decay constants in geo- and cosmochronology. Earth and planetary science letters 36, 359–362.

Stein, E., & Dietl, C. 2001. Hornblende thermobarometry of granitoids from the Central Odenwald (Germany) and their implications for the geotectonic development of the Odenwald. *Mineralogy and Petrology*, *72*(1), 185-207.

Steven, T.A., Mehnert, H.H., Obradovitch, J.D., 1967. Juan Mountains, Colorado. Geological Survey Research 1967 575, 47.

Tagami, T., Farley, K.A., Stockli, D.F., 2003. (U–Th)/He geochronology of single zircon grains of known Tertiary eruption age. Earth and Planetary Science Letters 207, 57–67.

Tagami, T., O'Sullivan, P.B., 2005. Fundamentals of fission-track thermochronology. Reviews in Mineralogy and Geochemistry 58, 19–47.

Vassallo, R., Ritz JF., Carretier, S. 2011 Control of geomorphic processes on ^{10}Be concentrations in individual clasts: Complexity of the exposure history in Gobi-Altay range (Mongolia). Geomorphology, *Geomorphology*, *135*(1), 35-47.

Vermeesch, P. 2009. RadialPlotter: A Java application for fission track, luminescence and other radial plots. Radiation Measurements, 44(4), 409-410.

Vermeesch, P., Balco, G., Blard, P.-H., Dunai, T.J., Kober, F., Niedermann, S., Shuster, D.L., Strasky, S., Stuart, F.M., Wieler, R., others, 2015. Interlaboratory comparison of cosmogenic ^{21}Ne in quartz. Quaternary Geochronology 26, 20–28.

Von Blanckenburg, F., 2005. The control mechanisms of erosion and weathering at basin scale from cosmogenic nuclides in river sediment. Earth and Planetary Science Letters 237, 462–479.

Wagner, G., Masarik, J., Beer, J., Baumgartner, S., Imboden, D., Kubik, P.W., Synal, H.-A., Suter, M., 2000. Reconstruction of the geomagnetic field between 20 and 60 kyr BP from cosmogenic radionuclides in the GRIP ice core. Nuclear Instruments and Methods in Physics Research Section B: Beam Interactions with Materials and Atoms 172, 597–604.

Wolf, R.A., Farley, K.A., Kass, D.M., 1998. Modelling of the temperature sensitivity of the apatite (U–Th)/He thermochronometer. Chemical Geology 148, 105–114.

Zeitler, P.K., Herczeg, A.L., McDougall, I., Honda, M., 1987. U-Th-He dating of apatite: A potential thermochronometer. Geochimica et Cosmochimica Acta 51, 2865–2868.

Zhang, S. H., Zhao, Y., & Song, B. 2006. Hornblende thermobarometry of the Carboniferous granitoids from the Inner Mongolia Paleo-uplift: implications for the tectonic evolution of the northern margin of North China block. *Mineralogy and Petrology*, *87*(1), 123-141.

Table of Figures for Chapter 3

Chapter 4

Forearc cooling history at 23°S and geomorphic implications

Abstract

Tectonism and climate lead to the deformation and formation of the reliefs, and also to the supergene copper hosting environements. To understand the actual landscape, it is crucial to seize each process involved in its modelling. In this chapter, I attempt to understand the evolution of the relief in northern Chile (at around 23°S) from the late Cretaceous to nowadays in the Western Cordillera. As the long-term climate history in the Atacama Desert is relatively well constrained, I focused on the tectonic parameter, to quantify vertical rock movements along the forearc. In this context I addressed several questions: when did the major flat surfaces form in the Forearc? Does an eastward propagating deformation signal in the Forearc exist?

For this, I combined low-temperature thermochronology, geochronology and modelling. I provided 25 new thermochronological data. To better estimate the emplacement depth of the intrusive rocks, the timing and the cooling history of the samples, I added thermobarometric constraints. I made a review of previous low-temperature thermochronology performed over the three last decades from the Coast to the Atacama Salar border. I added new data in some specific locations since previous results were sparse.

The data evidences the following conclusion:
1. Progressive eastward rejuvenation of ages towards the main Cordillera.
2. The Coastal Cordillera Jurassic to Cretaceous rocks were mainly exhumed at 40-50 Ma even though Neogene activities have been observed.
3. The Precordillera early Paleogene and Eocene rocks present a similar main exhumation signal around 40 Ma from the Central Depression border to the Salar de Atacama western border.
4. The results show a previously undocumented post-10 Ma increasing cooling near the Quimal Mount which can be attributed to volcanic activity or to the Precordillera uplift above the Salar de Atacama.

4.1 Introduction

Tectonic and erosion processes have shaped the relief of the Andes (Reutter et al., 1988; Jordan et al., 1983). In this study, I will focus on understanding and quantifying the exhumation of the western slope of the Andes at a regional scale. This will allow us to improve the Cenozoic tectonic evolution understanding and the geomorphic framework in which porphyry copper and the subsequent supergene copper enrichment took place (Mpodozis and Cornejo, 2012). Since the Andes are divided into several morpho-structural units, one approach to constrain the surface processes consists in apprehending the rock vertical movements at a large scale by quantifying the exhumation of each domain of the western slope of the Andean Cordillera. These morpho-structural units of the forearc are roughly parallel to the subduction trench and the shortening (Jordan et al., 1983; Allmendinger et al., 2005). This evolution led to the formation and preservation of supergene copper deposits at some particular periods of this evolution (Mortimer et al., 1973; Alpers and Brimhall, 1988). Porphyry copper supergene enrichment periods are specific and correspond to a balance between climatic, tectonic, and geomorphic conditions (Sillitoe, 2005). Some of these ore deposits enriched during supergene processes were probably eroded and deposited in basins or washed away towards the Pacific Ocean. Constraining this evolution requires to develop an approach reconsidering paleo-topography and exhumation of the distinct morpho-structural units of the forearc, using here thermochronology, geochronology and modelling.

I carried out a regional sampling of the studied area (see Figure 4.2 - Figure 4.5). Twenty sites were sampled from the Coastal Cordillera to the Salar de Atacama western limit near 23°S. This transect includes the Centinela District (see chapter 5). Reiners et al. (2015) published a review of thermochronological data from 28° to 20°S that I used in combination with other low-temperature thermochronological studies performed on the Western slope of the Andes and ages from ignimbrites, to propose a Cenozoic exhumation review of the forearc.

As presented in chapter 3 section 1, low-temperature thermochronology provides cooling path history of samples from which exhumation information can be extracted. Post emplacement cooling can result from erosional or tectonic exhumation. To explain the present high altitude of the Andes, several authors have proposed alternative scenarii, ranging from pure tectonic shortening and thickening (e.g. Isacks, 1988; Baby et al., 1997; McQuarrie, 2002) to magmatic underplating (e.g. Kay and Coira, 2009).

On the western side of the Andes, tectonic shortening has been invoked, but different interpretations were given for the deep rooting of the main structures. The west slope Andean uplift has been accommodated by a west verging thrust system bordering the pre-Cordillera is described by different authors around 33.5°S latitude and to the north of our study area (Muñoz and Charrier, 1996; Garcia and Hérail, 2005; Charrier et al., 2007; Armijo et al., 2010; Jordan et al., 2010), but it seems not applicable to the Antofagasta region with the border of the Salar de Atacama latitude where the thrusting occurs towards the east (Jordan et al., 2010).

4.2 Geological setting

4.2.1 Regional Scale

At 23°S, the Chilean forearc is composed of four parallel morpho-structural units (see Figure 4.1 - 4.2; Jordan et al., 1983; Isacks; 1988; Niemeyer et al. 1996), from west to east, the Coastal Cordillera or Coastal range, the Central depression, the Precordillera also known as the Cordillera de Domeyko and the Atacama Salar. More at the East, is present the Western Cordillera and the Altiplano. In this chapter is presented briefly the geology of each morpho-structural unit from the Coastal Cordillera to the Atacama Salar.
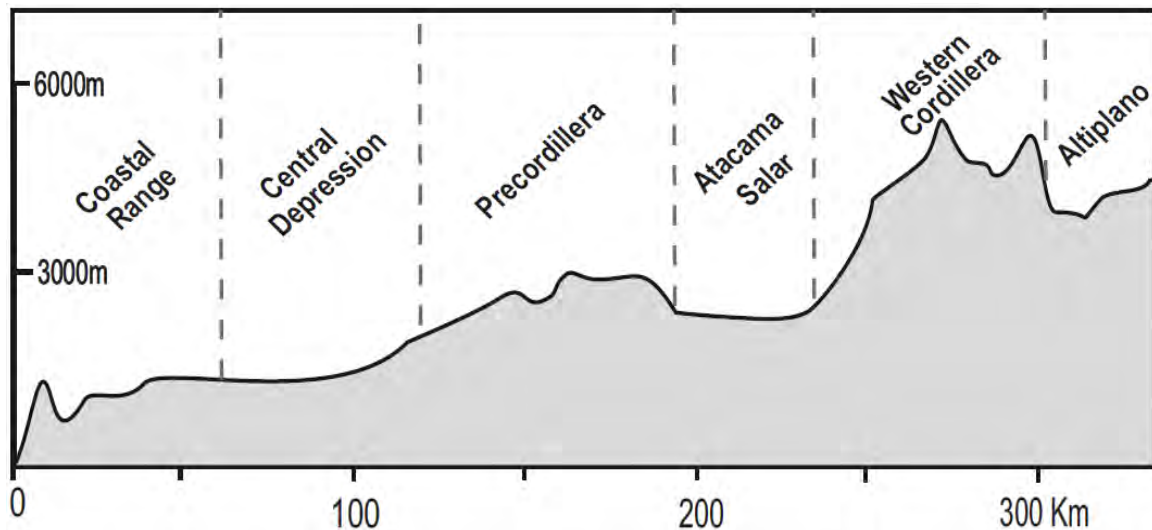
Figure 4.1 – Morpho-structural units at 23°S across the forearc topographic profile, from the coast to the Altiplano.

In northern Chile, the Andean cycle is characterized by an eastward magmatic and volcanic arc migration (Coira et al., 1982; Mpodozis and Ramos, 1990; Kay et al., 2005). Since the Jurassic, four distinctive paleo-arcs locations were identified (Kay et al., 2005; Grocott and Taylor, 2002; Scheuber and Reutter; 1992; Scheuber et al., 1994): a first Jurassic-early Cretaceous arc was located at the present Coastal Cordillera, then a mid-Cretaceous arc at the place of the Central Depression, a late Cretaceous-early Paleogene in the Precordillera, and finally mid-Oligocene-early Eocene arc also in the Precordillera. The actual active volcanic arc is located in the Western Cordillera.

107
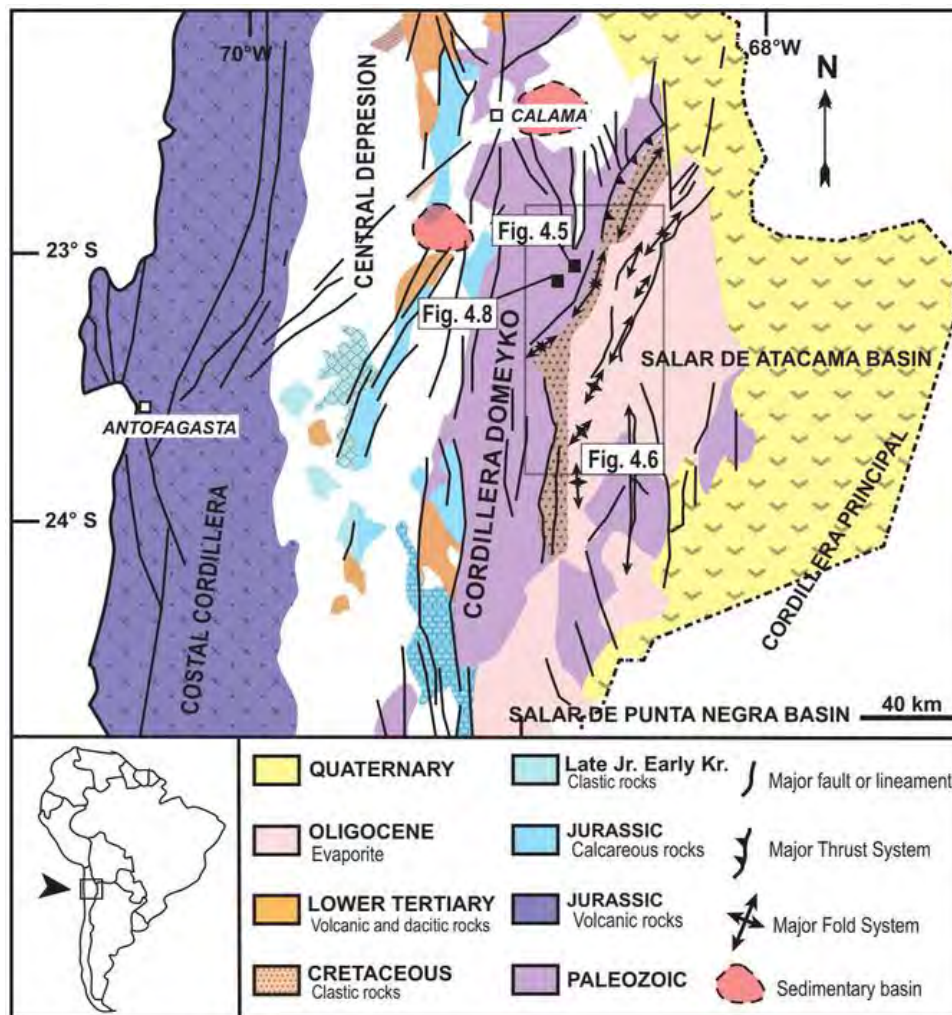
Figure 4.2 – Simplified geological map of northern Chile and location of morpho-structural units, after Muñoz et al. (2002).

Westward tilting at the forearc scale (Figure 4.3), has been proposed by several authors to explain the accommodation of the Andean uplift in the forearc deformation at different latitudes along northern Chile around 18°S (Isacks, 1988; Lamb et al., 1997; Garcia, 2001; Garcia and Hérail, 2005; Farias et al., 2005). In the region of the Atacama region, the tilting would be linked to the Atacama Fault system extensive activity and the Domeyko fault system (both fault systems are described in the 2.2 section) and occur counter clockwise direction.

The situation may have been different in the Antofagasta region, where the pre-Cordillera structure is mostly composed of Eocene to Oligocene "Incaic" strike-slip fault systems where large scale morphology is rather compatible with eastward thrusting (Mpodozis et al., 1993; Muñoz, 2002; Jordan et al., 2010). In addition to the horizontal component, vertical motion must be responsible for rock uplift and formation of adjacent basins (Figure 4.2).
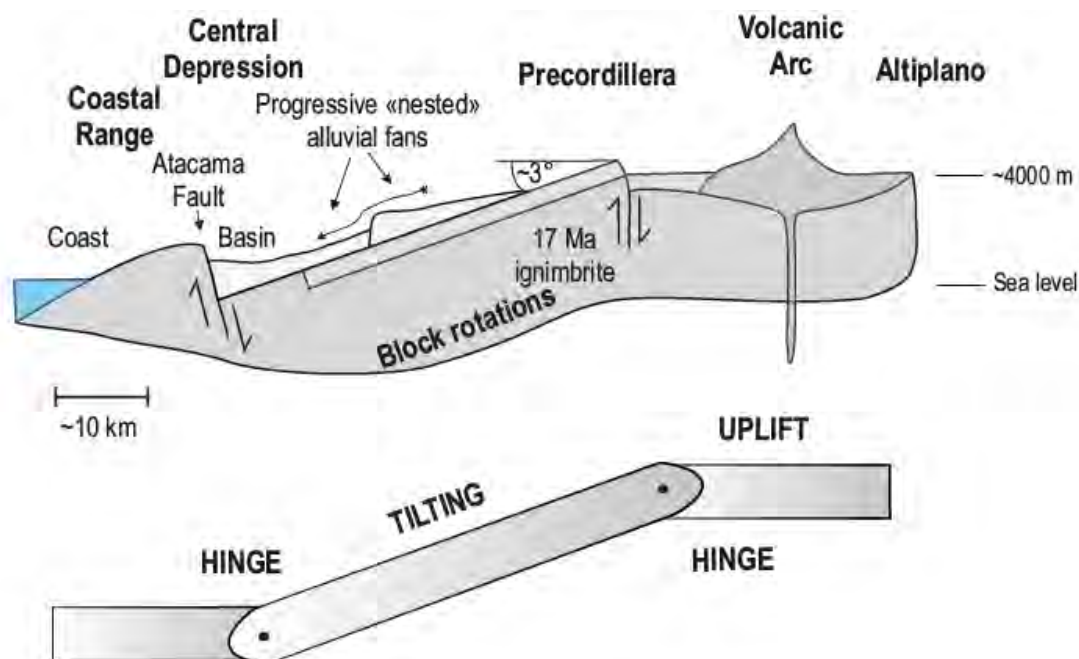
Figure 4.3 – Cartoon explaining the "Tilting" concept of the forearc in northern Chile, after Lamb et al. (1997).
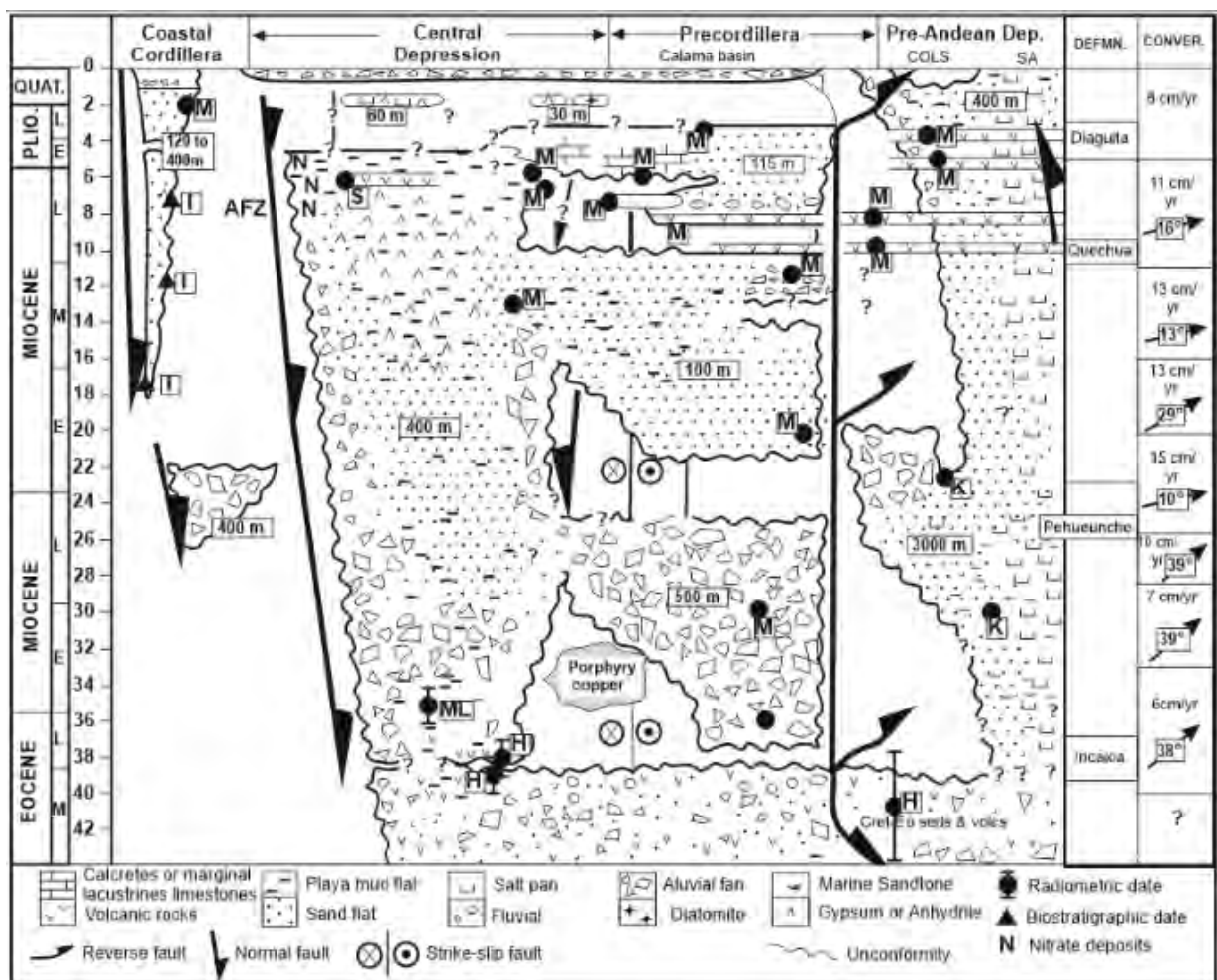
Figure 4.4 – Eocene to actual filling of the continental forearc, with sediment lithology, faulting indication, convergence rates and radiometric/biostratigraphic datings, May et al. (1999) after Hartley et al. (2000).

Since the Eocene, gravels have filled intramountane, endorheic basins (Figure 4.4). The thickest gravels layer (almost 1000 m) was found in depocenters in the Calama and Centinela Basins (e.g. Jordan et al., 2014), whereas much thinner layers (<100 m) were found in the Coastal Cordillera.

In the following, I will-briefly describe in more details the geology of each morpho-structural unit and the published thermochronological data.

4.2.2 Morpho-structural unit scale

4.2.2.1 The Costal Cordillera

The Coastal Cordillera is composed of Triassic volcanic rocks, covered by volcano- sedimentary Jurassic rocks of the Negra Formation, and intruded by Jurassic plutonic rocks (Scheuber et al., 1994). Juez Larré et al. (2010) published apatite fission track and (U-Th)/He ages obtained on sample from the coastal scarp at different elevations of the coastal scarp of the Coastal Cordillera (Figure 4.1). A major cooling period recorded in the Jurassic plutonic rocks between 60 and 80 Ma, was interpreted as a compressive phase ("Peruvian phase"). These authors proposed that a younger cooling event in the Coastal Cordillera around 40-50 Ma deduced from apatite (U-Th)/He ages was related to the Farellones Phoenix ridge subduction. Strike slip deformation of the Coastal Cordillera and activity of the Atacama Fault system over 1000 km kept going on from Late Jurassic-early Cretaceous to Quaternary, which has been attributed to the beginning of the Farallon plate subduction under the South American plate (Arabazs, 1971; Scheuber y Andriessen, 1990; Scheuber y González, 1999; Riquelme et al., 2007; Allmendinger and Gonzalez, 2010).

Regional geology indicate that paleocene pyroclastic products are continuously exposed from the eastern border of the Coastal Cordillera to the Paleocene emission structures in the Precordilleran structures suggesting that no major vertical movements relative the different morpho-structural unit did occur after the Paleocene.

4.2.2.2 The Central Depression.

The origin of the Central Depression has been discussed, either it has formed by erosive or structural processes or structural as the expression of a rift for example. In northern Chile, at the 18°S latitude, there is no evidence of significant subsidence to explain this basin (Farias et al., 2005). The Central Depression around 23°S forms a basin, currently endorheic, with a gentle slope toward the west, covered with patchy Oligo-Miocene fluvio-volcaniclastic deposits (Parraguez, 1998).

Sediments deposited in accommodation spaces mainly related to previous erosion, in particular within very large valleys (~40 km large) (Farias et al., 2005a). At this latitude, in the Central Depression, there is no record of previous published thermochronological data, probably due to poor access to intrusive outcrops as most of the landscape is covered by gravels.

4.2.2.3 The Precordillera

The Precordillera is composed of Paleozoic-Triassic volcanic and intrusive bodies, Jurassic to Cretaceous volcano-sedimentary rocks, which were deformed and exhumed during the Cretaceous back arc tectonic inversion (Mpodozis et al., 2005), and several Paleocene volcanic nested caldera complexes.

These rocks were deformed again later, during the Eocene Incaic phase (Charrier *et al.,* 2009), along the transpressive and transtensive Domeyko Fault System (DFS) (Mpodozis et al., 1993; Amilibia et al., 2008; Mpodozis et Cornejo, 2012). During the Eocene activity of the DFS, important porphyry copper emplaced. Intramountane basins associated with fault systems formed at this period, like the Calama Basin (May et al., 2005; Jordan et al., 2014) and the Centinela Basin. These basins have hosted the sediment eroded from the Incaic range (see Figure 4.5), sometimes also contain exotic supergene copper mineralization, and possibly covered by ignimbrites level as in Figure 4.5.

At the Eastern border of the Precordillera stands the Quimal Mount. The Quimal is the highest mountain of the area overhanging the Atacama Salar at the top of the ~1000 m El Bordo escarpment, 2000 m when taking into account the Quimal relief. El Bordo escarpment is associated with a thrust fault (Bascuñan et al., 2016) which has uplifted the Precordillera over the Atacama Salar (Figure 4.2).

Figure 4.5 – Picture of a paleochannel north east to the base of the Quimal Mountain during the sampling of an ignimbrite level (localization on Figure 4.2).

The thermochronological data in this zone are quite numerous, indeed since the late 90's, most of the low-temperature thermochronological studies have been performed in the Precordillera where copper ore deposit are located. They were performed either focusing on specific intrusive as that exposed at the Chuquicamata open mining pit (McInnes et al., 2001) or either at a very large 1000 km long scale in north-south direction resolution scale (Maksaev and Zentilli, 1999).

The major low-temperature thermochronological study was realized at the scale of the all Precordillera from 20°S to 28°S and to led to exhumation rates estimation from 100 to 200 m.My^{-1} from 50 to 30 Ma then dropping to 50 m.My^{-1} after 30 Ma.

4.2.2.4 Pre-Andean Depression or Salar de Atacama

The pre-Andean Depression at 23°S also known as the Atacama Salar is a basin currently in a forearc position. Its nine kilometres thick of sediment infill includes rock from Jurassic to Miocene age, (Macellari et al.; 1991; Arriagada et al., 2006; Bascuñan et al., 2016) which have been described with western border outcropping deformed sediments and seismic data.

The type and timing of successive tectonic events has been debated from seismic profile interpretation as both extensive and compressive structures have been identified, nearly all interpretation realized with seismic profiles Jordan et al. (2002, 2007), Muñoz et al. (2002) and Panamount et al. (2004) describe extensive features during Oligocene (the Salar Fault system) in the Atacama Salar. On the other hand, Arriagada et al. (2006) points out exclusively compressive features in the Cretaceous to Paleogene sedimentary outcrops which represent a 5-km thickness of continental sediments, with several growth strata inter-bedded on the western border of the Salar since the Cretaceous (Figure 4.6).

Jordan et al. (2007) recognises the presence of normal Oligocene faults (as the Patiencia fault) between the Bordo Escarpment and the Cordillera de la sal (Figure 4.6) from the seismic data. The authors also identify a vertical offset in this region that they dated mid-Miocene with the presence of the 10 Ma and 5 Ma ignimbrite series present at this latitude of the Precordillera

Detrital low-temperature thermochronology was applied on sediments from the Purilactis group by Reiners et al. (2015). They interpreted the pre-Neogene Naranja and Loma Amarilla formations (Figure 4.6) as representative of a progressive Cretaceous to Eocene unroofing of a magmatic crustal section.
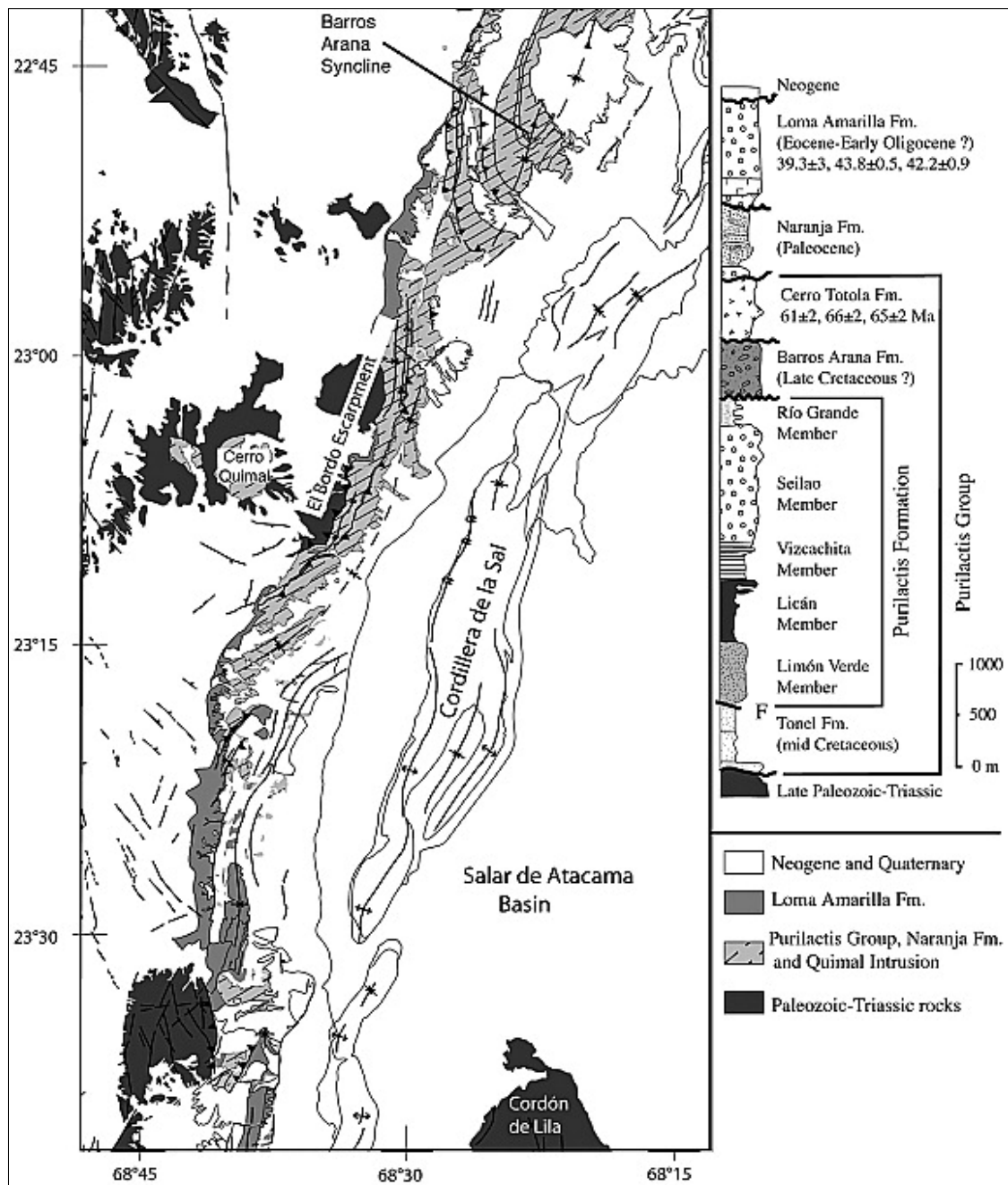
Figure 4.6 – Geology of Western border of the Atacama Salar, with major features as the El bordo escarpment, Cordillera de la Sal and the Quimal Mountain and the sedimentary log. After Arriagada et al. (2006) see Figure 4.2 for location.

4.3   Methods

Details of the analytical procedures and equipment used have been previously explained in chapter 3.1 and the details of the new results are in the corresponding annexes section. I will first recall the principles and the possible applications of the several methods.

4.3.1 Sampling
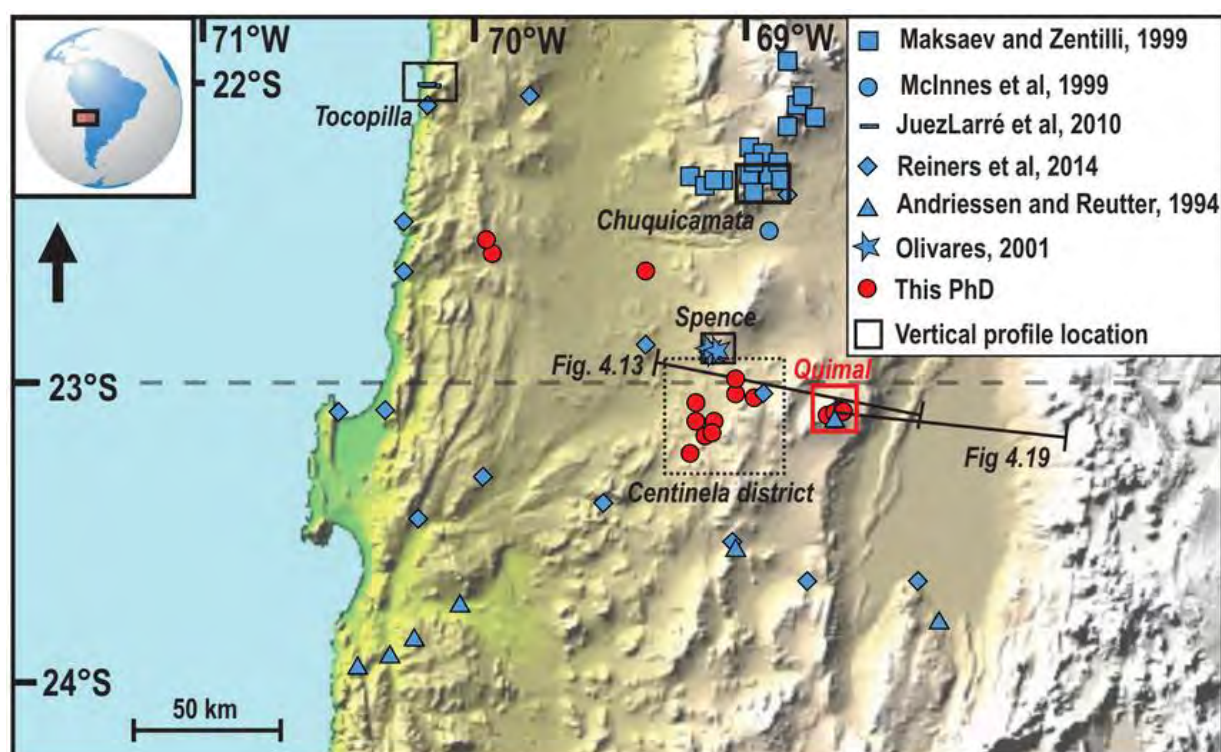
Figure 4.7 –S**ample location from this study and previous studies** from Maksaev and Zentilli (1999); McInnes et al. (2001); Juez Larré et al. (2010); Reiners et al. (2015); Andrienssen and Reutter (1994). The black lines represent cross-sections in Figures 4.13 and 4.19.

I attempted to sample all possible rocks containing apatites, including granodiorite, diorites and dacitic rocks (Figure 4.7). I present 14 new AHe ages and 13 new AFT ages. It was not always possible to apply both methods on every sample due to the quality and abundance of apatite. I also present 7 new zircon U-Pb dating from granodiorites.

Figure 4.8: Picture of the Eastern face of the Quimal Mountain before sampling, base level at ~3200m (Location Figure 4.2).

4.3.2 Low thermochronology methodology

Low-temperature thermochronology methods allow to obtain information about cooling ages and rates that I used to quantify exhumation rates (Gallagher et al. 2005). At the exception of the Coastal Cordillera and the Quimal, most of the samples have been collected in a pediplanated bedrock surface. Due to the lack of canyon in the region, the granodioritic Quimal mount were the only location where a sampling along a vertical profile was possible (Figure 4.7 and 4.8). As it will be seen later, sample from the Quimal recorded the most recent cooling event of the forearc in the area.

4.3.3 Thermobarometry

Thermobatometry combined with low-temperature thermochronology is a powerful association to recover the thermal history of a rock from its emplacement throught its exhumation to the surface. Amphibole crystals were only abundant and unaltered in the Quimal Mountain rock samples (see location Figure 4.7). Samples, QUI13-02 and QUI13-07 of a ~65 Ma gabbro were choosed. In the Centinela district, the samples did either not present amphiboles or the amphiboles were altered in the copper porphyries.

The samples were analyzed with the CAMECA SXFive microprobe in the Geosciences Environnement Toulouse laboratory (Figure 4.9) on at least 3 amphiboles by sample from border to core of the minerals.
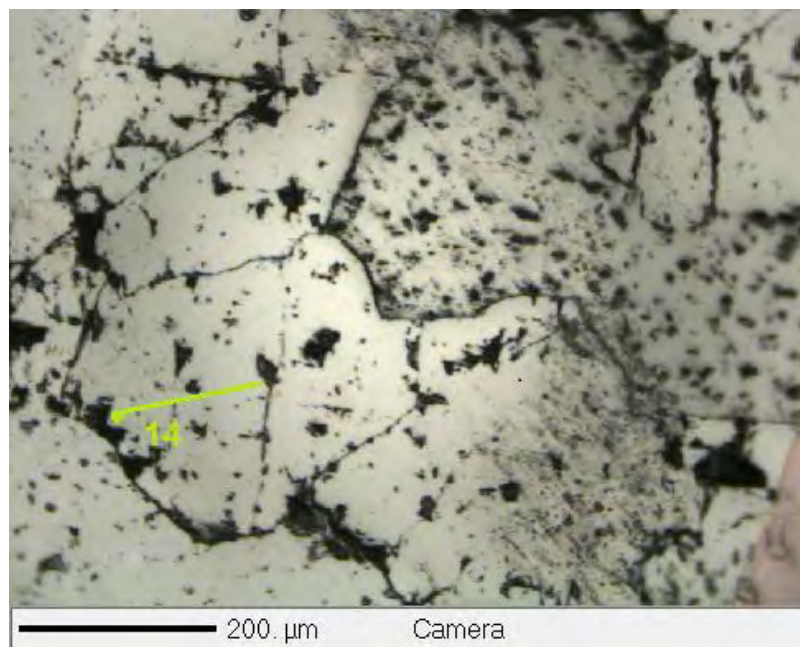
Figure 4.9 – Image of the profile edge to core of an amphibole with the microprobe on the QUI13-02 sample, Performed in GET lab.

In addition, bulk rock analyses in major and trace elements were also performed in the Centre des Recherches Pétrologique et Géochimiques in Nancy.

4.4 Results

4.4.1 Age results

Table 4.1 summarizes all the results obtained during this thesis (raw results are available in the annexes, page 11). Most of the results are consistent with rock ages and follow the logical order of closure temperatures of the thermochronometers used (Rock age > AFT age > AHe age). Two samples (QUI13-02 and DC12-08) do not obey to this logic. In the case of QUI13-02 the AFT age is significantly older than other AFT ages from the Quimal Mountain profile samples. The [U] content estimation from the fission track sugest that the grains present an important dispersion in [U] content from 10 to 100 ppm which does not fit with the U content measurements during the AHe analyses by ICP-MS ([U] are reported in the annexes).

Sample	Long. (E)	Lat. (S)	Alt. (m)	Rock age	Error (2σ)	AFT (Myrs)	Error (1σ)	Length	Error (1σ)	AHe (Myrs)	Error (2σ)
DC12-01	69.19	23.24	2323	42.7	0.7	40.6	3.3	14	1.28	29.85	1.7
DC12-03	69.02	22.95	2226	39.7	1.1	40	2.7	14.99	1.04	31.18	1.8
DC12-06	68.96	23.04	2955	40.3	1.3	36.6	5.2	14.84	1.04	29.11	2.1
DC12-08	69.16	23.02	2653	64.3	1.2	41.1	4.7	15.37	1.3	52.4	5.2
DC12-09	69.19	23.03	2012	-	-	46.1	4.8	14.96	1.55	22.42	1.1
DC12-10	69.17	23.07	2082	64.4	1.4	-	-	-	-	45.00	2.3
DC12-12	69.10	23.15	2611	68.5	-	-	-	-	-	35.80	2.5
DC12-13	69.11	23.12	2847	57.7	-	-	-	-	-	43.1	1.6
DC12-14	69.14	23.16	2375	43.9	1.3	-	-	-	-	16.20	1.1
DC12-15	69.18	23.13	2183	65.2	-	42.5	3.4	13.96	1.28	-	-
PV13-02	69.93	22.55	1598	136.4	2.4	96.1	12.2	13.6	1.02	-	2.5
PV13-03	69.95	22.53	1531	-	-	90.5	11	15.44	0.96	-	-
PV13-04	69.37	22.59	1462	69.4	0.9	-	-	-	-	-	-
PV13-05	69.35	22.62	1529	-	-	-	-	13.26	1.3	36.8	2.8
QUI13-01	68.75	23.30	3408	66.8	1.3	45.1	2.6	12.07	0.83	-	-
QUI13-02	68.63	23.09	3596	66.8	1.3	52.1	15.3	13.07	1.3	30.57	2.1
QUI13-03	68.64	23.10	3818	66.8	1.3	45.7	2.3	12.88	1.37	40.60	2.8
QUI13-05	68.66	23.11	4286	66.8	1.3	38.5	3.7	14.84	0.9	36.80	2.3
QUI13-06	68.65	23.11	4089	66.8	1.3	41.1	3.1	13.25	1.3	35.48	2.2
QUI13-07	68.65	23.11	3860	66.8	1.3	45.3	3.2	12.97	1.59	34.58	2.4

Table 4.1 - Table summary of sample, coordonates, U-Pb, AFTA, AHe and track lengths of the analysis realized during this thesis.

This dispersion was not observed in the other samples. Even though all the samples are granodiorites, the QUI13-02 petrology seems different.

Thus, I propose that this sample may be a secondary dike which would explain non-homogeneous content and the U dispersion. No zonation has been observed on the grains neither on the mica sheets after irraidation.

In the case of the DC12-08 AHe ages, between the four aliquots, only two present measurable He content, and among these two aliquots, one led to a AHe age twice the U-Pb rock age. In the case of the two other aliquots case it can be considered that either He concentration were really low and at the limit of measurable concentration, which does not fit with the U and Th concentrations, or either AHe ages were really young which seems poorly suitable with the geology.

Of all the samples, U-Pb results vary between 136.4 ± 2.4 Ma for the PV13-02 from the Coastal Cordillera to 39.7 ± 1.1 Ma for the Mirador porphyry in the Centinela District of the Precordillera. AFT results vary from 96.1 ± 12.2 Ma to 90.5 ± 11 Ma in the Coastal Cordillera, from 46.1 to 36.6 Ma in the Precordillera, and from 52.1 ± 15.3 Ma to 38.5 ± 3.7 Ma in the Quimal profile. All confined track length distributions display normal distribution and not bimodal distribution (see length measurement histograms in Figure 4.14 - 4.16). This suggests that no significant reheating occurred during the long-term cooling of the samples (Figure 4.14-4.16). The AFT results are plotted among the other AFT results from previous studies in the Figure 4.10, by projecting the data along a WE axis from the Coastal Cordillera to the Atacama Salar. AHe results vary from 45.0 ± 2.3 Ma to 16.2 ± 1.1 Ma in the Precordillera and more locally from 40.6 ± 2.1 Ma to 30.6 ± 2.8 Ma in the Quimal Cerro. The AHe results are plotted among the other AHe results from previous studies in Figure 4.11.
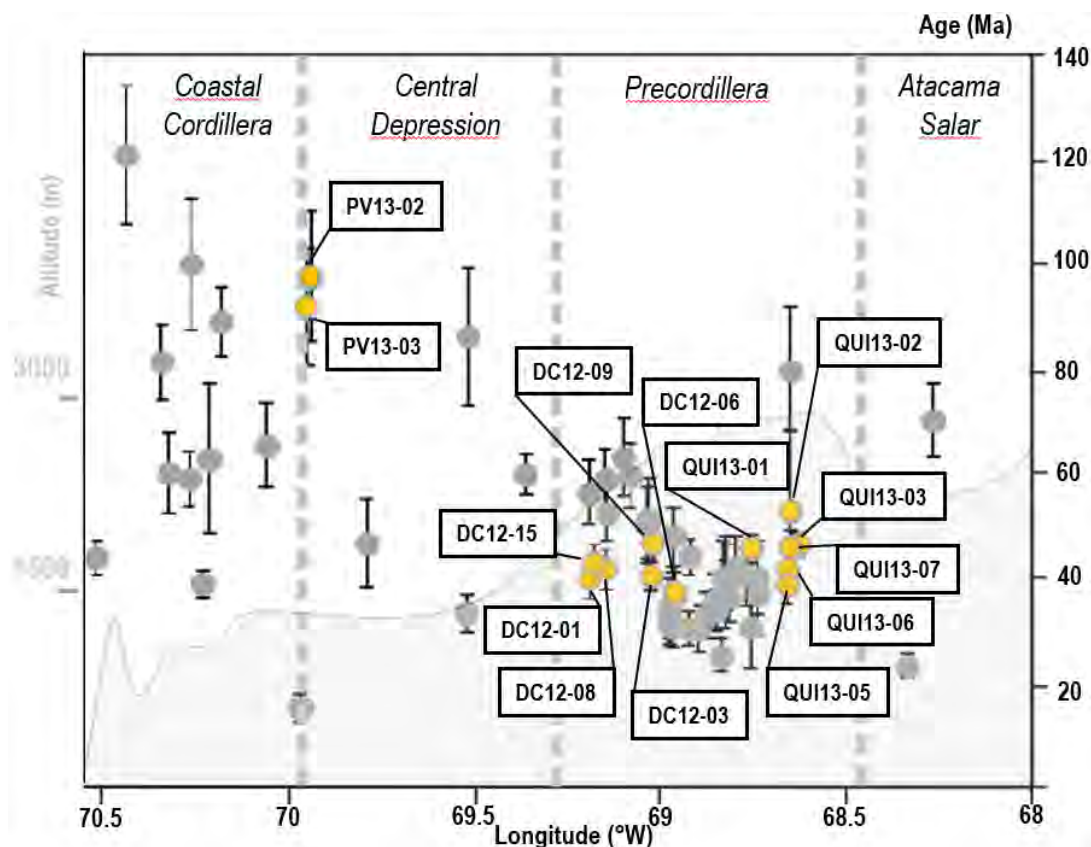
Figure 4.10 – **AFT ages in the 23°S range transect in northern Chile** (including from 22°S to 24°S) from the compilation
of ages mentioned above. In yellow, results from this PhD and in grey from, others as Andriessen and Reutter (1994);
Maksaev and Zentilli (1999), McInnes et al. (2001).
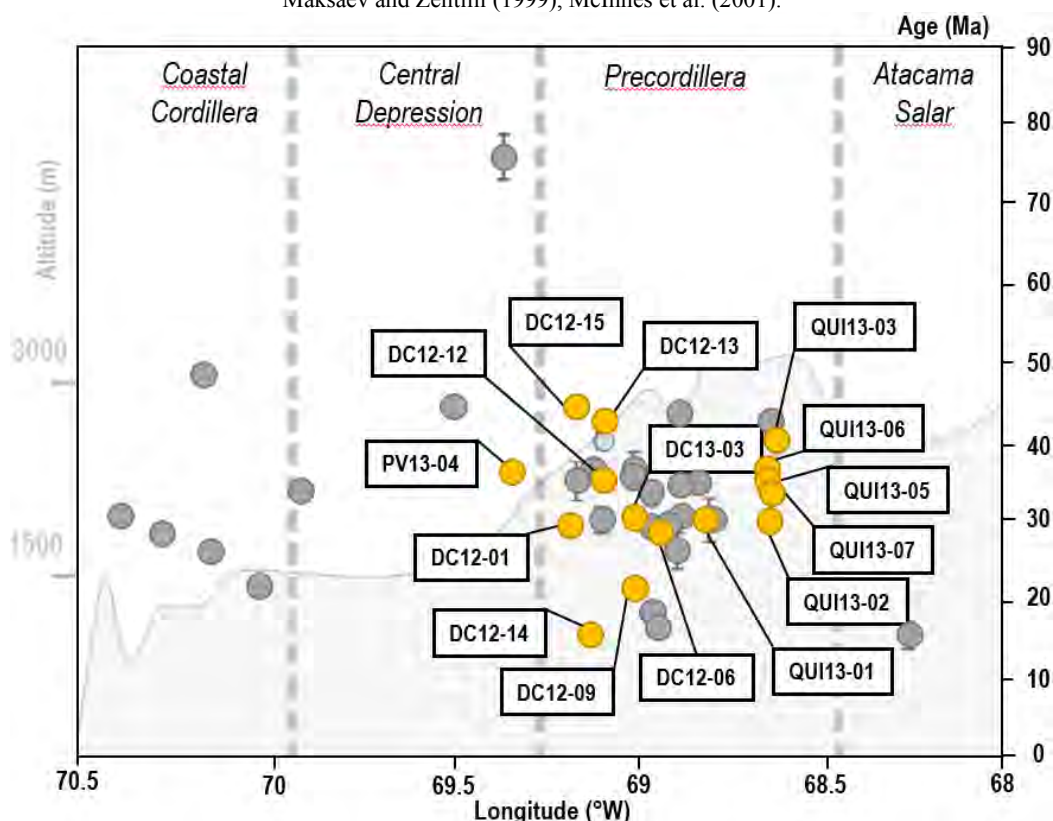
Figure 4.11 – **AHe ages in the 23°S range transect in northern Chile** (including from 22°S to 24°S). In yellow, results
from this PhD and in grey from Andriessen et al. (1994); Maksaev and Zentilli (1999), McInnes et al. (1999); Juez-Larré et
al., (2010); Reiners et al., (2015).

U-Pb and K-Ar ages suggest Upper Cretaceous/Early Paleogene (66.4 ± 1.4 Ma and 64.6 ± 1.1
Ma; Ramirez and Gardeweg, 1982) for the Quimal rock age. The low-temperature thermochronology
ages in the vertical profile suggests a main cooling event between 35-45 Ma (Figure 4.12) without
significant variation related to elevation.
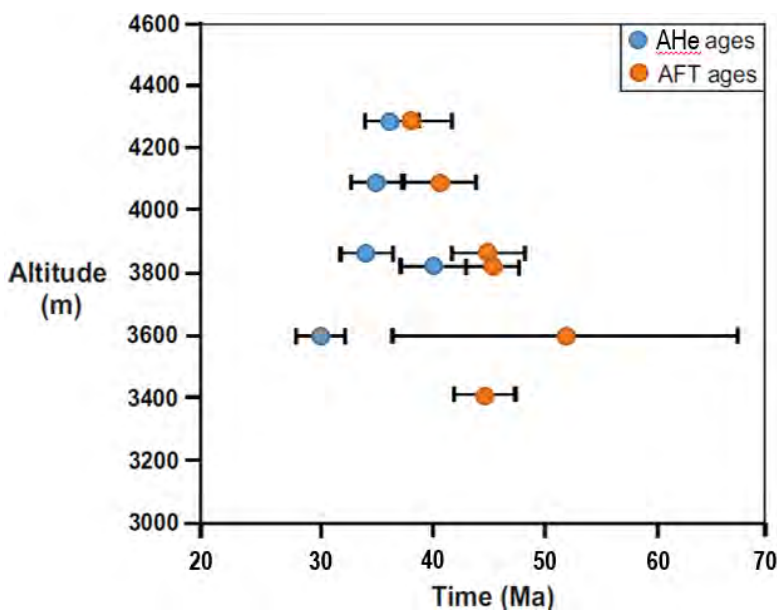
Figure 4.12 – **Cerro Quimal vertical profile: altitude vs AHe-AFT ages**, errors at 2 sigmas.

118

Next page: **Figure 4.13 – Simplified structural profile of the Precordillera and the Central Depression** after Lopez (2016) and the projection of the low-temperature thermochronological results from this thesis (Localization is visible on Figure 4.5).
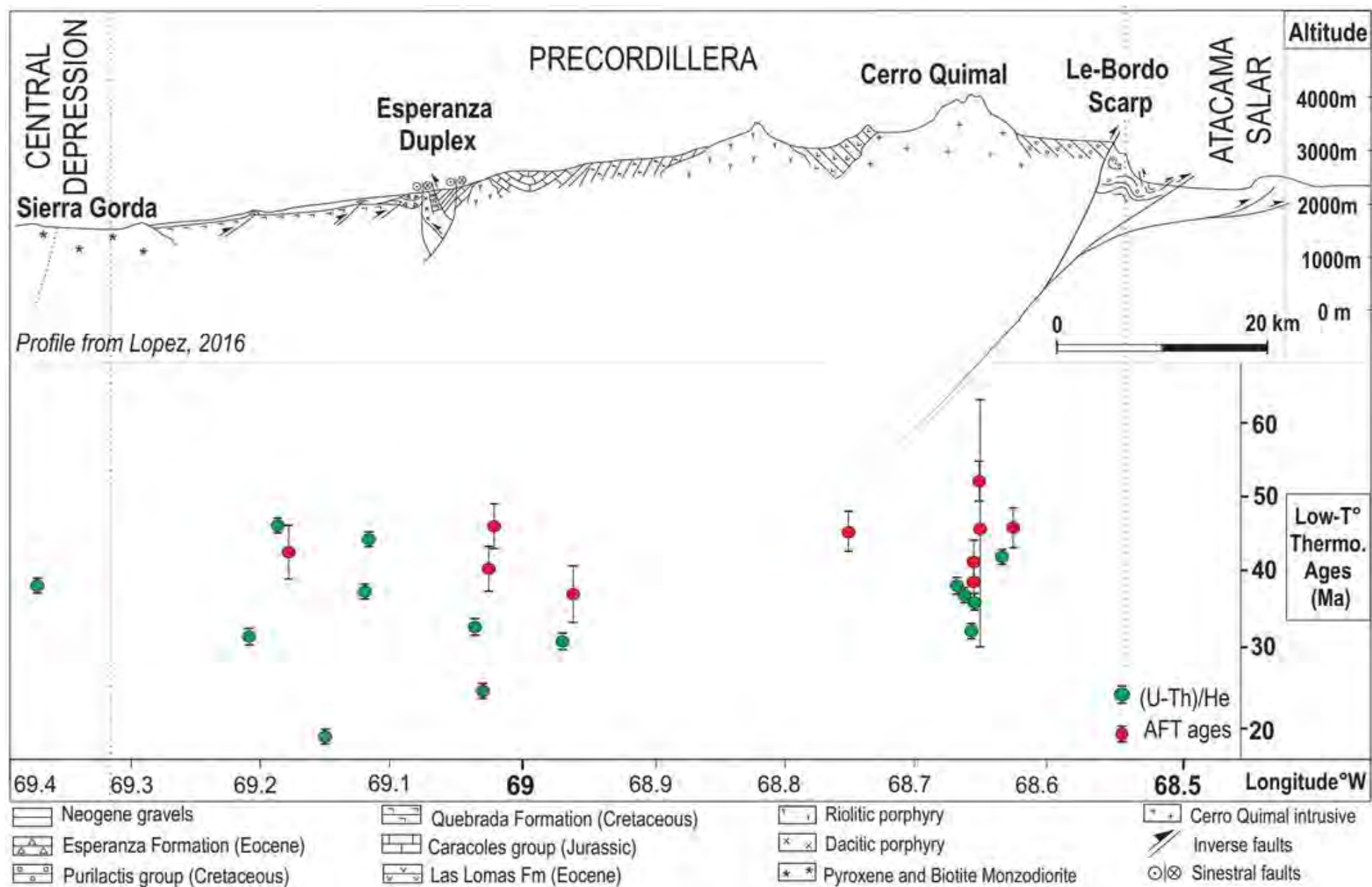
4.4.3 Thermal modelling

All U-Pb, AFT and AHe ages provided information about temperature thresholds but do not reconstruct the exhumation history. To do so, it is necessary to model additional information such as track lengths measurement. To model such data set I used HeFty software (Ketcham, 2005; see Chapter 3.1).

4.4.3.1 The Coastal Cordillera sample modelling

Two samples (PV13-02 and PV13-03) from the eastern border of the Coastal Cordillera suggest a relatively rapid cooling since the emplacement to 90 Ma followed by a progressive cooling story to actual. The length distribution is a normal distribution suggesting a simple exhumation history, without any evident posterior heating.
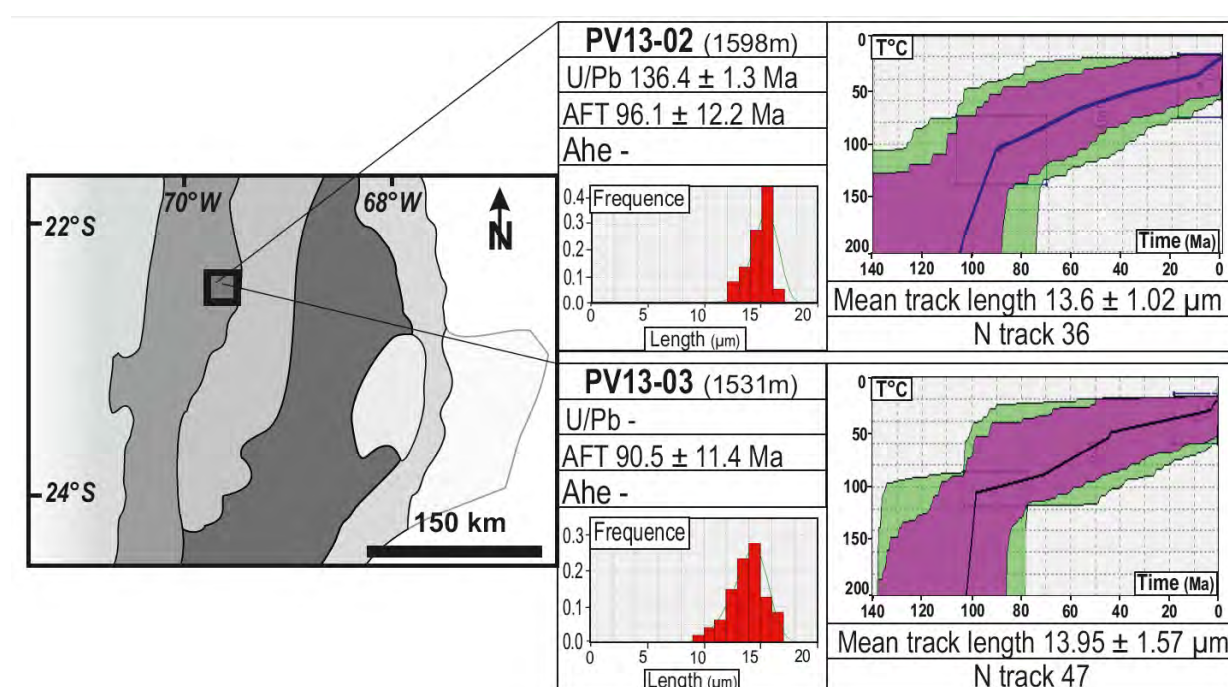
Figure 4.14 – Low-temperature thermochronological modelling of the samples from the coastal range with HeFty, U/Pb, AFT and AHe ages and fission track lengths data (number and mean track length).

4.4.3.2 Precordillera sample modelling

The following figures (Figure 4.15 and 4.16) display the modelling results for all the samples from the Precordillera. It can be divided in two groups: 1) the Centinela District and 2) the Quimal Mountain.

.
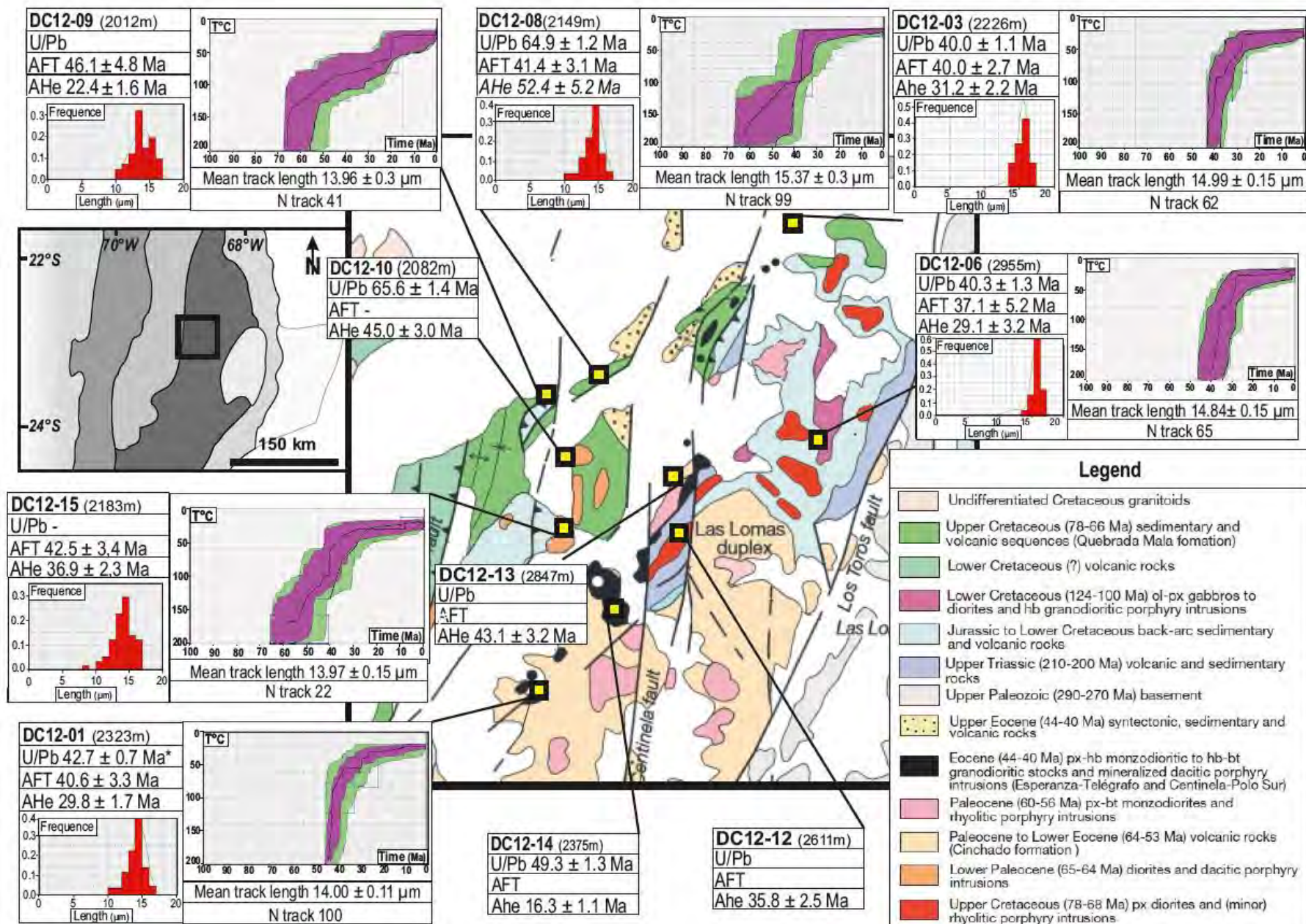
Figure 4.15 – Modelling results obtained with HeFty of the Precordillera in the Centinela District, U/Pb, AFT and AHe ages and fission track lengths data (number and mean track length). Geological map after Mpodozis et al. (2012).
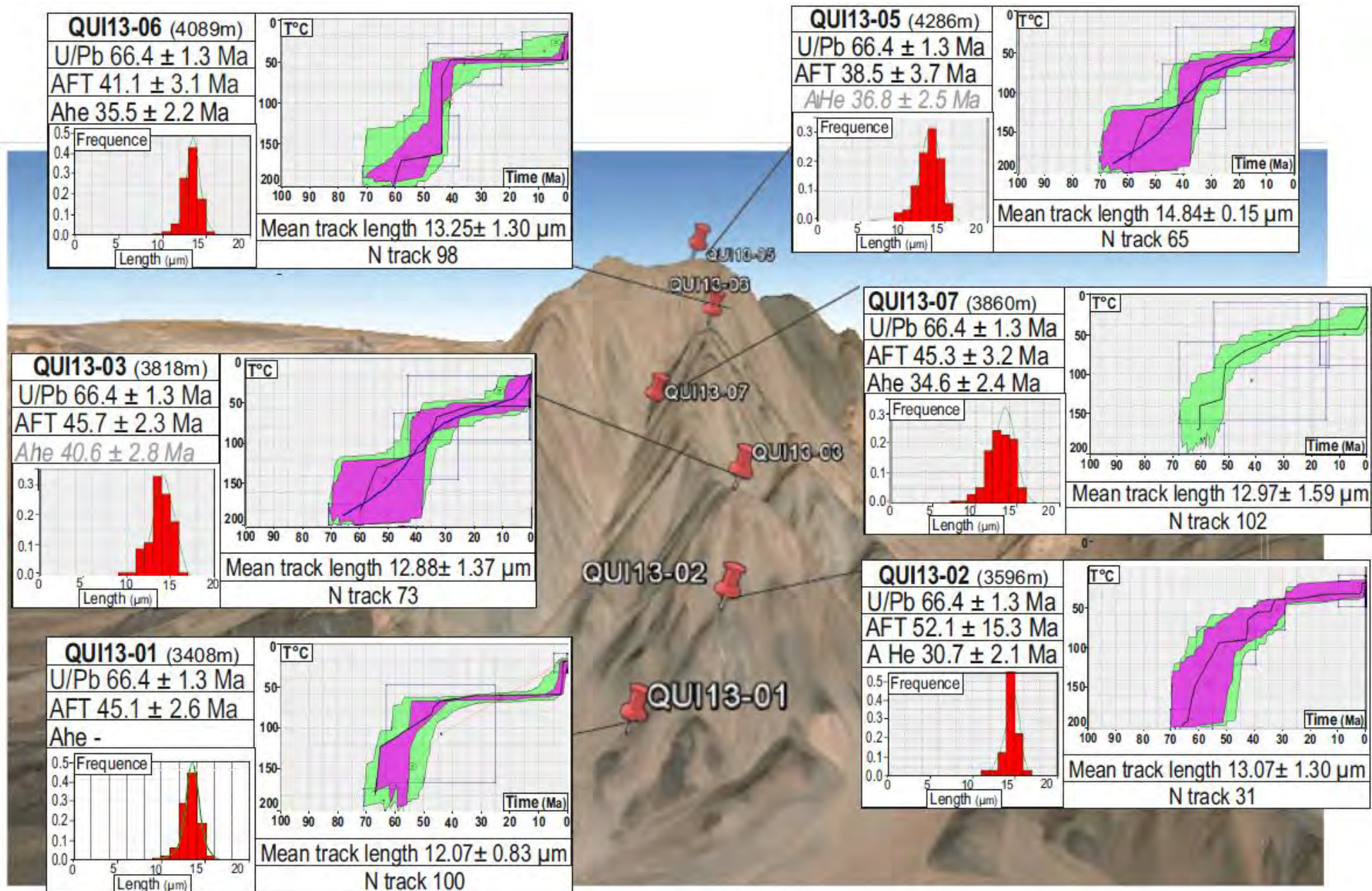
Figure 4.16 – HefTy modelling of data from the Quimal Mountain, U/Pb, AFT and AHe ages and fission track lengths data (number and mean track length). Localization on a googlemaps image of the Quimal Mountain, view to the West.

4.4.3.3 Centinela District:

In the Centinela District, six Late Paleogene and Eocene samples have been modelled. They nearly all suggest a rapid cooling from their emplacement until 30 Ma for the Eocene samples and before 40 Ma for the Late Paleogene samples, and for all ending before 30 Ma. Then the cooling is really slow to reach 20°C from 30 to 10 Ma. DC12-09 display a slightly different cooling pattern probably due to FT length modelling but also to a lower He age. This younger cooling could be related to the fault located nearby this sample. His younger age could be related to a nearby local fault reactivation where thermal fluid circulation could have occured.

4.4.3.4 Quimal Mountain:

Among the six samples of the Quimal for which both AHe and AFT analyses were performed, two samples were impossible to model with both type of data (QUI13-03 and QUI13-05). I chose to model them with AFT ages, tracks lengths and the Dpar measured and still take them into account as all six samples present similar and consistent time-temperature path (Figure 4.17).

In the case of the Quimal samples, a rapid cooling occurred mainly between 60 and 35 Ma, consistently with the cooling observed at this period for the samples of the Centinela District of the Precordillera. After this main event, the modelled temperature of all six samples present a "plateau" from ~35 to ~10 Ma before showing a significant cooling post 10 Ma. This is the first time that such a young cooling event is evidenced in this region. I will debate the possible interpretations in the discussion section.

4.4.4 Thermobarometry results

The pressures and temperature acquired by calculation on amphibole chemical composition after micro probe analyses display high apparent pressures, principally between 12 to 22 kbar at ~950°C (Figure 4.17). The QUI13-02 sample present temperatures between 930°C and 980°C and pressures between 12 kbar and 20 kbar and the QUI13-07 sample present higher temperatures between 920 to 1020°C and pressures 12 kbar and 22 kbar.

These pressures (which would represent depths between 30 and 60 km if converted into depth) are much higher than other paleo-pressures obtained in the Andes (Margirier et al., 2016). The bulk rock major and trace elements geochemistry is visible in the A.2 section of the annexes.
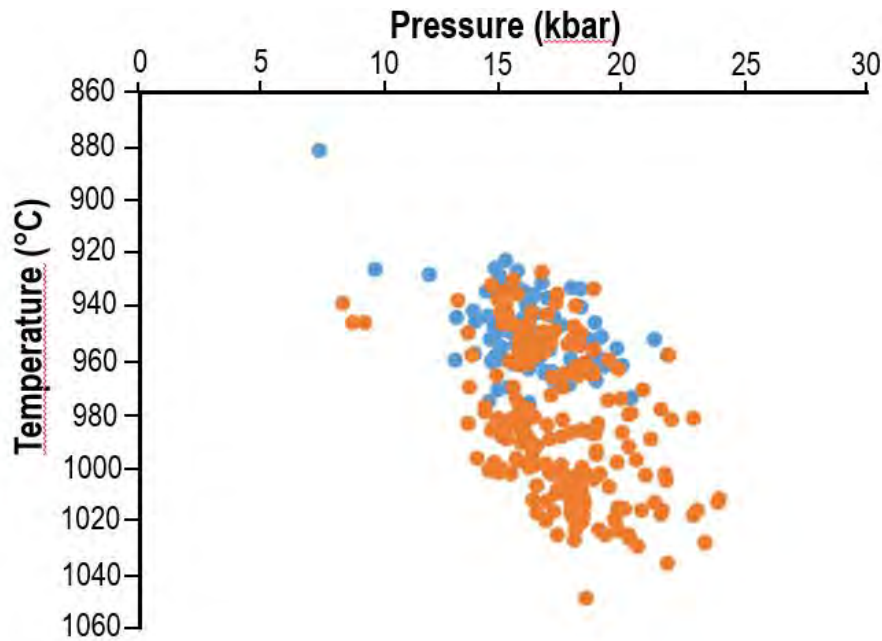
Figure 4.17 – Temperature vs Pressure from amphiboles thermobarometry on Quimal Mountain granodiorite according to the method of Ridolfi and Renzulli (2012). Each point represents the analyses on one point of an amphibole: QUI13-02 results in orange and QUI13-07 results in blue.

4.5   Discussion

4.5.1   Eastward migration of the deformation?

This new dataset is consistent with previous thermochronological ages. Results show a decrease in ages towards the east across the whole Andes at these latitudes. Reiners et al. (2015) concluded that this trend is consistent with a simple kinematic model in which the deformation has propagated eastwards at a nearly continuous rate of 6-10 km.My^{-1}.

At the scale of the forearc, results from this study are mainly agreeing to the previous statement of eastward migration of the cooling ages as AFT ages are older in the Coastal Cordillera than in the Precordillera. These results are concordant with AFT ages of Juez-Larré et al. (2010). Along the Chilean Coastal Cordillera these ages are mostly Cretaceous and classically associated with the cooling and exhumation of the Cretaceous arc during the "Peruvian phase" (e.g. Bascuñan et al., 2016).

Nevertheless, at the scale of the Central Depression and Precordillera this eastern cooling pattern is not obvious (low-temperature thermochronological results are between ~46 to 16 Ma) and their HeFty modelling are consistent, suggesting a main cooling event between 45-35 Ma in all the morpho-structural unit, from the border eastern border of the Central Depression to the western limit of the Atacama Salar. This 45-35 Ma cooling period is thus much younger compared to the results in the Coastal Cordillera from Juez-Larré et al., 2010 (152 Ma to 60 Ma). In this paper has been discussed its possible origin.

Although they did not discard totally the possibility that this cooling period resulted from a significant erosion period (0.24-0.36 km.My^{-1}), this possibility does not seem to be consistent with the absence of thick contemporaneous sedimentary basins offshore, and onshore.

They support the theory of the subduction of a hypothetical Farallon-Phoenix ridge during the Eocene-Oligocene flat-slab period. The eastward movement of this ridge would have rapidly heated and then cooled the lithosphere above, explaining the Eocene cooling event in the Coastal Cordillera. According to Juez-Larré et al. (2010), the migration of the ridge may have weakened the lithosphere below the Precordillera, and would have been the main driver of the Eocene Incaic deformation and emplacement of porphyry cooper. However, two major points seem to contradict this interpretation.

The first one is that the Eocene location of the Farallon-Phoenix ridge is very poorly known and probably much more to the south (Somoza and Ghidella, 2012). Secondly, if the eastward motion of the ridge would have controlled the cooling history of pre-Eocene intrusives, the data will show that should have obtained an eastward trend toward younger ages. Yet our cooling data on Paleogene and Cretaceous intrusive of the Precordillera do not show such pattern.

A third explanation may justify the coastal 40-30 Ma cooling. It was envisaged but rejected by Juez-Larré et al., (2010), namely the erosion of several kilometers of the cliff by marine erosion. The retreat of an Eocene paleo-cliff would have forced the isotherms to go down and deviate toward the sea. A Late Eocene cliff would be consistent with a regional Incaic surface uplift including the Coastal Cordillera, possibly driven by the flattening of the slab and the fall in the velocity convergence rate (Martinod et al., 2016). Such a surface uplift would have fostered marine erosion and the retreat of a cliff. Nevertheless, to date, there is no direct evidence for or against such a Late Eocene cliff.

4.5.2 Time varying geothermal gradient?

Thermal fluxes can vary significantly along the magmatic arc, for a given time period (Hyndman et al., 2005), or over time when the magmatic arc evolves (Noury et al., 2017; Simon-Labric et al., 2013). The previous discussion points out towards a possible variation in the geothermal gradient through time in our study area. The actual geothermal gradient varies between 10°C/km in the Coastal Cordillera to 30°C/km in the Precordillera, and locally 50°C/km 100 km to the north of our study zone in the Precordillera (Springer and Foerster, 1998). During the Late Eocene-Oligocene flat-slab period (37-26 Ma), as the arc migrated to the actual position of the Precordillera and later farther east, the geothermal gradient probably decreased to the west, in the Coastal Cordillera and increased in the Precordillera. The question is how much this cooling may explain our data?

Even if true, this Late Eocene cooling would be unlikely to explain the mid-Eocene in the Precordillera ages as it would have occurred afterwards. Hence, the cooling pattern extracted from our data is rather explained by denudation or tectonic exhumation.

4.5.3 Emplacement depths of the Quimal rocks?

The amphibole thermo-barometrical data obtained on the Quimal Mount rock samples indicate pressures and temperatures during their crystallization associated to the upper mantle conditions (Ridolfi and Renzulli, 2012) with temperatures ranging between 900°C and 1000°C. As they do not present any growth ring chemical modification (Figure 4.9), high temperature suggest that they initially crystalized in the mantle followed by a rapid ascension, so that no amphibole with crust conditions pressure could crystalise. Their composition reflect more the magma crystallization conditions than a precise emplacement depth.

In addition, the depth corresponding to the calculated pressure between 30 and 60 km would mean that several dozens of kilometers would have been exhumed since the beginning of the Cenozoic in the Precordillera. This suggestion is incompatible with the geology observed and the low-temperature thermochronology results. Indeed with apatite fission tracks around 40 Ma no more than 5 km where exhumed since 40 Ma (emplacement depth inferred by thermochronology methodology are developpement in Sanchez et al., in press in chapter 5). This is why it seems that the pressure calculated on the Quimal amphiboles only reflect crystallisation conditions that seem to correspond to lower crust-upper mantle conditions.

Many other studies in the southern and central Andes, as Mamani et al. (2010) and Demouy (2012) used geochemistry to trace magma sources. In addition to the pressure and temperature conditions, the geochemical concentrations in La and Sm of the Quimal rocks in whole rock samples suggest a mantle source composition compared to Peruvian igneous rocks composition (Mamani et al., 2010) (Figure 4.18). To explain the suggested mantellic source and amphibole crystallization place can also be proposed a rapid rise through the crust. This could suggest that the rapid rise was facilitated by a thin crust during the Paleogene instead of a thickened crust like encountered nowadays in the Bolivian orocline.
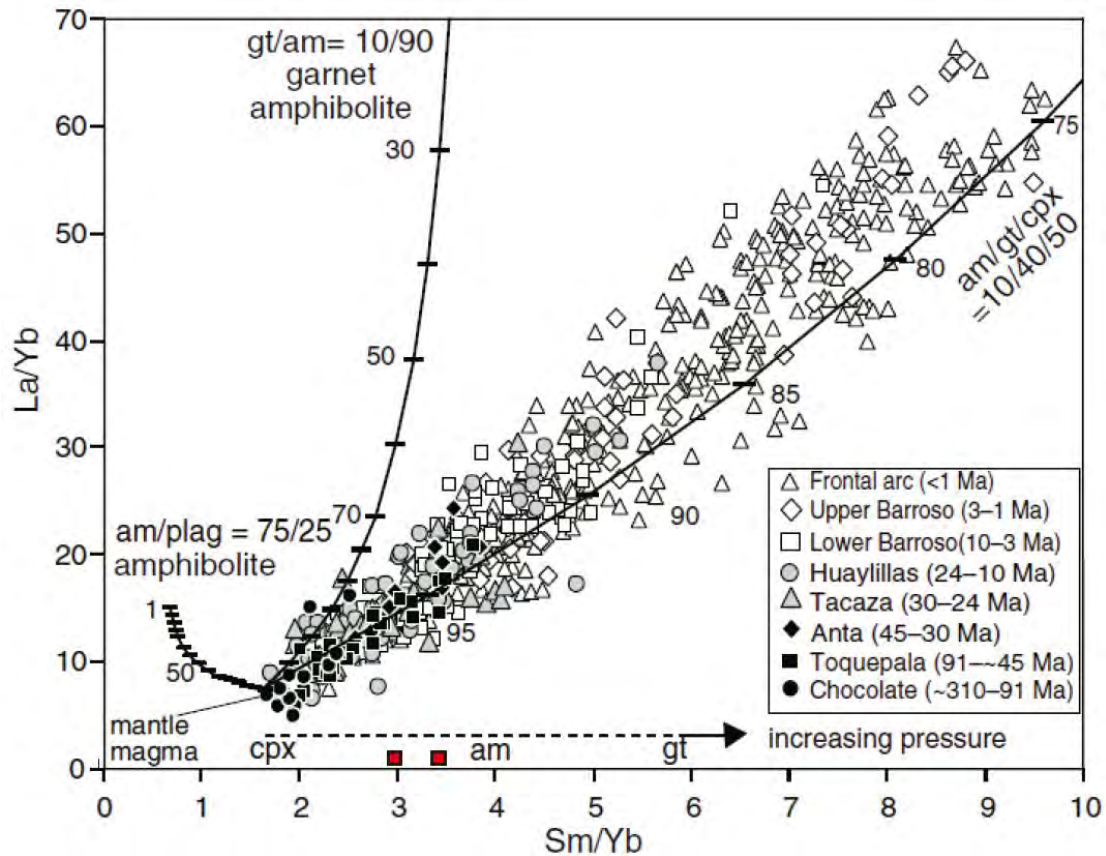
Figure 4.18 – QUI13-02 and QUI13-07 La/Yb and Sm/Yb ratios (in red) compared to magmatic arc composition in Peru, after Mamani et al. (2010)

4.5.4 A young cooling event recorded by the Quimal samples

All the Quimal samples modelling yielded two cooling periods (Figure 4.15). A first one between 45 and 35 Ma from the Incaic deformation of the Precordillera, identified in all the samples of the Precordillera, and a second one, post 10 Ma.

As older thermochronological ages exist even more at the east in the main cordillera, the post 10 Ma cooling seems secondary to the eastward migration of the cooling evoked by Reiners et al., (2015).

The potential reasons of the later cooling are multiple. I discuss the possibility that this Late Mio-Pliocene cooling results from denudation or to a local readjustment of the isotherms due to a differential uplift between the Precordillera and the Atacama Salar. I discard a post 10 Ma cooling which would have occurred after a heating event like the magmatic arc activity.

The reason is related to the distance (~100 km) with the actual magmatic arc in the Western Cordillera (Figure 4.19). Additionally, no warming event is clearly visible on the cooling paths models, only cooling.
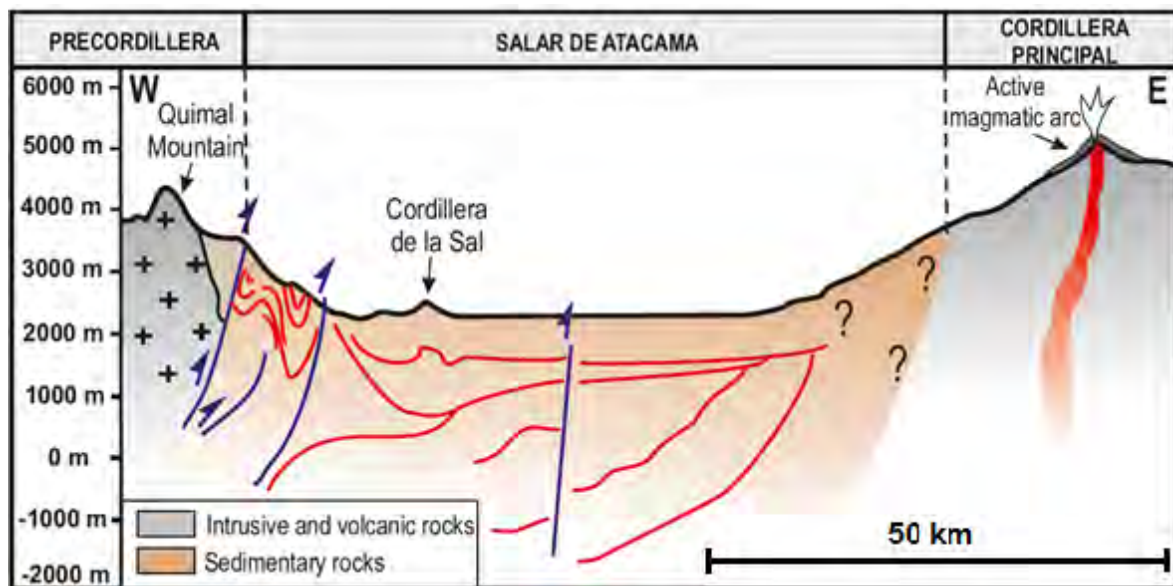
Figure 4.19 – Profile and actual situation of the Quimal Mountain towards the Atacama Salar and the active magmatic arc, after Panamont et al., (2004).

If I use the closest geothermal gradient of 30°C/km used in this area (Springer and Foerster, 1998), then the ~50 -40 Celsius degrees of cooling in the last 10 Ma would correspond to maximum 1.5 km of erosion.

Such a Late Miocene uplift would also be consistent with the tectonic inversion of the Atacama Salar from the Mid-Miocene (J-F. Rubilar, Master's thesis, University of Chile, 2015), and the shortening of the Cordillera de la Sal during the same period as it folds Oligocene to Pliocene deposits (Arriagada et al., 2006).

An argument in favor of tectonic uplift and not regional denudation is the weak thickness of sediments encountered. Only few meters of sediments over the 10 Ma tuff exists on the plain surface at the base of the Quimal Mountain, which suggest that the cooling event is in relation to a block uplift in an arid context and not to an erosion that would have affected the whole Precordillera.

A surface uplift of 1000-2000 m may have forced the isotherms to go down in the uplifted block, and particularly near the scarp within the Quimal Mountain (Figure 4.19).

The post-10 Ma cooling inferred from the Quimal samples may thus correspond to this differential surface uplift between the Precordillera and the Atacama salar. As temperatures require several 100 kyr to several Myrs to decrease to roughly steady values, the uplift may have begun several 100 krs to Myrs before the rapid Late Miocene-Pliocene cooling period evidenced by the Hefty thermal modelling.

The relationship between AHe and AFT ages and elevation does not show any clear correlation, which are necessary to highlight a progressive denudation. The absence or inverse correlations could be

explained by decreasing relief (Braun et al., 2002) but only for long wave-length alternations (~100 km) of hills and valleys, which does not hold in the pediplain context of the fore-arc.

This data may thus constitute the first thermochronological evidence of the Late Miocene-Pliocene thrusting of fore-arc above the Atacama Salar that supports previous structural observations made from seismic data (Jordan et al., 2007).

I note that Late Miocene uplift event is demonstrated in many other places of the Central Andes and is known as the Quechua phase (e.g. Mégard et al., 1984; reviews in Barnes and Ehlers (2009); Jordan et al. (2010)). The difference here is that this uplift occurred on a westward dipping thrust fault system, whereas it was associated with eastward dipping thrusts to the north and to the south of the Atacama Salar region (e.g. review in Charrier et al., 2007).

This young exhumation event suggests that the westward tilting of the Precordillera may have occurred after 10 Ma and may be associated to the thrust system bordering the western side of the Atacama Salar. Tilting has already been supported by interpretations of sedimentological columns (Houston et al., 2008).

4.5.5 Summary

On the basis of previous published results and combined with my new dataset, I propose a simplified history including different steps during the exhumation (Figure 4.20):

95 Ma:

The Coastal Cordillera was already exhuming around 90 Ma and if a ~25°C/km gradient is considered our thermochronological data suggest that less than 4 km were exhumed since 90 Ma (see Figure 4.14). The ~66.3 Ma tuff encountered near the surface suggests that most of this exhumation occurred before this date, and thus, that the surface of the Coastal Cordillera has remained almost non-deformed and poorly eroded since that time.

These results are consistent with thermochronological data located 1000 km to the south (at ~35°S-40°S) showing that the Coastal Cordillera experienced a period of rapid cooling ~100 Ma (Cembrano et al., 2002; Arancibia et al; 2004; Parada et al; 2005).The volcanic arc was located in the Central Depression-Precordillera and a back-arc basin existed to the east, including the region encompassing nowadays the eastern border of the Precordillera and the Atacama Salar.

65 Ma:

During the Late Cretaceous-Early Paleogene, inversion of the back-arc basin began and a mountain front developed to the east of the current Precordillera. The Atacama Salar was a foreland basin where the Purilactis formation accumulated. Several Late Cretaceous-Early Paleogene porphyry

emplaced in the Precordillera. This data confirm that the western Precordillera was exhuming in the Early Paleogene as suggested by Bascuñan et al. (2016).

45-35 Ma:

Both AHe and AFT ages and modelling suggest that most of the late Cretaceous and early Paleogene intrusive rocks were already exhuming. Other Eocene porphyries emplaced at this time lapse and most of their exhumation occurred before 30 Ma. Paleo-thermobarometry data in amphiboles suggest a relatively thinned crust when the Early Paleogene and Eocene intrusive were emplacing, which may be consistent with the back-arc extension which affected this region during the Cretaceous.

This exhumation data confirm previous local studies with the same range of ages in the Precordillera, but the additional point here is the spatial extension of these ages all over the Central Depression and Precordillera, from the border of the Coastal Cordillera to the Pre-Andean Depression.

30 Ma:

Between 37 and 26 Ma, there is no evidence of volcanic activity. The modelling of low-temperature thermochronological data show that most of the porphyries cooling occurred before 35 Ma. Remaining relief of the Precordillera were probably declining more and more slowly and after 26 Ma. Assuming a temperature for the partial retention zone between 80°C and 40°C for (U-Th)/He in apatites, and a constant geothermal gradient between 20 and 30° C/km, the AHe ages around 35 Ma imply a denudation of 1 to 2 km between 35 Ma and now. Given that Eocene calderas are still outcropping in the Precordillera, the true denudation is probably closer to 1 km.

10-0 Ma

A significant uplift (possibly up to 1000 m) of the fore-arc was associated with the thrusting of the Precordillera over the Atacama Salar. This uplift produced a westward tilting, which reversed the regional slope, at least on the eastern side of the Precordillera near the el Bordo Escarpment.

After a long period between 35 and 10 Ma, this regional tilting seems to be the main deformation event of this area. Other Late Miocene vertical faults were recognized in the Precordillera but displaced less than several tens of meters.

4.6 Conclusion

These new thermochronologic data confirms previous findings and provide new insights about the recent deformation of the fore-arc. These thermochronological ages and modelling confirm first that the exhumation of the Coastal Cordillera preceeded the exhumation of the Precordillera. In the Precordillera the main cooling period span between 65 and 35 Ma.

This cooling mainly corresponds to denudation, which did not exceed several kilometers and probably close than 1 km. Such values suggest an Incaic paleogeography characterized by 20-50 km wide mountains with a modest relief corresponding to tectonic duplexes and volcanoes, and separated by shallow sedimentary basins.

The eastern border of the Precordillera, at the limit of the Atacama Salar, where stands the Quimal mountain presents the first thermochronological record of a mid-Miocene significant exhumation phase, supporting the idea of an westward tilting of the Forearc and an west-verging thrusting at 23°S.

References for Chapter 4

Allmendinger, R.W., González, G., Yu, J., Hoke, G., Isacks, B., 2005. Trench-parallel shortening in the northern Chilean Forearc: Tectonic and climatic implications. Geological Society of America Bulletin 117, 89–104.

Allmendinger, R.W., González, G., 2010. Invited review paper: Neogene to Quaternary tectonics of the coastal Cordillera, northern Chile. Tectonophysics 495, 93–110.

Alpers, C. N., Brimhall, G. H. 1988. Middle Miocene climatic change in the Atacama Desert, northern Chile: Evidence from supergene mineralization at La Escondida. *Geological Society of America Bulletin*, *100*(10), 1640-1656.

Amilibia, A., Sàbat, F., McClay, K.R., Muñoz, J.A., Roca, E., Chong, G., 2008. The role of inherited tectono-sedimentary architecture in the development of the central Andean mountain belt: Insights from the Cordillera de Domeyko. Journal of Structural Geology 30, 1520–1539.

Andriessen, P.A., Reutter, K.-J., 1994. K-Ar and fission track mineral age determination of igneous rocks related to multiple magmatic arc systems along the 23 S latitude of Chile and NW Argentina, in: Tectonics of the Southern Central Andes. Springer, pp. 141–153.

Arabasz, W.J., 1971. Geological and geophysical studies of the Atacama fault zone in northern Chile. California Institute of Technology.

Arancibia, G., 2004. Mid-Cretaceous crustal shortening: evidence from a regional-scale ductile shear zone in the Coastal Range of central Chile (32°S). Journal of South American Earth Sciences 17, 209–226.

Armijo, R., Rauld, R., Thiele, R., Vargas, G., Campos, J., Lacassin, R., Kausel, E., 2010. The West Andean thrust, the San Ramon fault, and the seismic hazard for Santiago, Chile. Tectonics 29.

Armijo, R., Lacassin, R., Coudurier-Curveur, A., Carrizo, D., 2015. Coupled tectonic evolution of Andean orogeny and global climate. Earth-Science Reviews 143, 1–35.

Arriagada, C., Roperch, P., Mpodozis, C., Fernandez, R., 2006. Paleomagnetism and tectonics of the southern Atacama Desert (25–28 S), northern Chile. Tectonics 25.

Baby, P., Rochat, P., Mascle, G., Hérail, G., 1997. Neogene shortening contribution to crustal thickening in the back arc of the Central Andes. Geology 25, 883–886.

Barnes, J. B., Ehlers, T. A. 2009. End member models for Andean Plateau uplift. *Earth-Science Reviews*, *97*(1), 105-132.

Bascuñán, S., Arriagada Ortega, C., Le Roux, J., Deckart, K., 2016. Unraveling the Peruvian Phase of the Central Andes: stratigraphy, sedimentology and geochronology of the Salar de Atacama Basin (22 degrees 30-23 degrees S), northern Chile.

Braun, J., 2002. Quantifying the effect of recent relief changes on age–elevation relationships. Earth and Planetary Science Letters 200, 331–343.

Cembrano, J., Lavenu, A., Reynolds, P., Arancibia, G., López, G., Sanhueza, A., 2002. Late Cenozoic transpressional ductile deformation north of the Nazca–South America–Antarctica triple junction. Tectonophysics 354, 289–314.

Charrier, R., Pinto, L., Rodríguez, M.P., 2007. Tectonostratigraphic evolution of the Andean Orogen in Chile. The Geology of Chile 21–114.

Charrier, R., Farías, M., Maksaev, V., 2009. Evolución tectónica, paleogeográfica y metalogénica durante el Cenozoico en los Andes de Chile norte y central e implicaciones para las regiones adyacentes de Bolivia y Argentina. Revista de la Asociación Geológica Argentina 65, 05–35.

Coira, B., Davidson, J., Mpodozis, C., Ramos, V., 1982. Tectonic and magmatic evolution of the Andes of northern Argentina and Chile. Earth-Science Reviews 18, 303–332.

Costa, F., Andreastuti, S., de Maisonneuve, C.B., Pallister, J.S., 2013. Petrological insights into the storage conditions, and magmatic processes that yielded the centennial 2010 Merapi explosive eruption. Journal of Volcanology and Geothermal Research 261, 209–235.

Demouy, S. 2012. La naissance des Andes au Crétacé supérieur: origine et construction du Batholite côtier sud-péruvien (région d'Arequipa) (Doctoral dissertation, Université de Toulouse, Université de Toulouse III-Paul Sabatier).

Farías, M., Charrier, R., Comte, D., Martinod, J., Hérail, G., 2005. Late Cenozoic deformation and uplift of the western flank of the Altiplano: Evidence from the depositional, tectonic, and geomorphologic evolution and shallow seismic activity (northern Chile at 19°30′S). Tectonics 24, TC4001.

Gallagher, K., Stephenson, J., Brown, R., Holmes, C., Fitzgerald, P. 2005. Low temperature thermochronology and modeling strategies for multiple samples 1: Vertical profiles. Earth and Planetary Science Letters, 237(1), 193-208.

Garcia, M. 2001. Evolution oligo-miocène de l'Altiplano occidental (arc et avant arc du nord du Chili, Arica): tectonique, volcanisme, sédimentation, géomorphologie et bilan érosion-sédimentation (Doctoral dissertation, Université Joseph-Fourier-Grenoble I).

Garcia, M., Hérail, G., 2005. Fault-related folding, drainage network evolution and valley incision during the Neogene in the Andean Precordillera of northern Chile. Geomorphology 65, 279–300.

Grocott, J., Taylor, G.K., 2002. Magmatic arc fault systems, deformation partitioning and emplacement of granitic complexes in the Coastal Cordillera, north Chilean Andes (25 30′ S to 27 00′ S). Journal of the Geological Society 159, 425–443.

Hartley, A.J., May, G., Chong, G., Turner, P., Kape, S.J., Jolley, E.J., 2000. Development of a continental forearc: A Cenozoic example from the Central Andes, northern Chile. Geology 28, 331–334.

Houston, J., Hart, D., Houston, A. 2008. Neogene sedimentary deformation in the Chilean forearc and implications for Andean basin development, seismicity and uplift. Journal of the Geological Society, 165(1), 291-306.

Isacks, B.L., 1988. Uplift of the central Andean plateau and bending of the Bolivian orocline. Journal of Geophysical Research: Solid Earth 93, 3211–3231.

Jordan, T.E., Isacks, B., Ramos, V.A., Allmendinger, R.W., 1983. Mountain building in the Central Andes. Episodes 3, 20–26.

Jordan, T.E., Nester, P.L., Blanco, N., Hoke, G.D., Dávila, F., Tomlinson, A.J., 2010a. Uplift of the Altiplano-Puna plateau: A view from the west. Tectonics 29, TC5007.

Jordan, T.E., Kirk-Lawlor, N.E., Blanco, N.P., Rech, J.A., Cosentino, N.J., 2014. Landscape modification in response to repeated onset of hyperarid paleoclimate states since 14 Ma, Atacama Desert, Chile. Geological Society of America Bulletin 126, 1016–1046.

Juez-Larré, J., Kukowski, N., Dunai, T.J., Hartley, A.J., Andriessen, P.A., 2010. Thermal and exhumation history of the Coastal Cordillera arc of northern Chile revealed by thermochronological dating. Tectonophysics 495, 48–66.

Kay, S.M., Godoy, E., Kurtz, A., 2005. Episodic arc migration, crustal thickening, subduction erosion, and magmatism in the south-central Andes. Geological Society of America Bulletin 117, 67–88.

Kay, S. M., Coira, B. L. 2009. Shallowing and steepening subduction zones, continental lithospheric loss, magmatism, and crustal flow under the Central Andean Altiplano-Puna Plateau. *Geological Society of America Memoirs*, *204*, 229-259.

Ketcham, R.A., 2005. Forward and inverse modelling of low-temperature thermochronometry data. Reviews in mineralogy and geochemistry 58, 275–314.

Lamb, S., Hoke, L., Kennan, L., Dewey, J., 1997. Cenozoic evolution of the Central Andes in Bolivia and northern Chile. Geological Society, London, Special Publications 121, 237–264.

Leuthold, J., Müntener, O., Baumgartner, L.P., Putlitz, B., 2014. Petrological constraints on the recycling of mafic crystal mushes and intrusion of braided sills in the Torres del Paine mafic complex (Patagonia). Journal of Petrology 55, 917–949.

Macellari, C. E., Su, M. J., Townsend, F. 1991. Structure and seismic stratigraphy of the Atacama Basin, Northern Chile. In *Proc. VI Congr. Geol. Chileno* (Vol. 1, pp. 133-137).

Maksaev, V., Zentilli, M., 1999. Fission track thermochronology of the Domeyko Cordillera, northern Chile: Implications for Andean tectonics and porphyry copper metallogenesis. Exploration and Mining Geology 8, 65–90.

Mamani, M., Wörner, G., Sempere, T. 2010. Geochemical variations in igneous rocks of the Central Andean orocline (13°S to 18°S): Tracing crustal thickening and magma generation through time and space. *Geological Society of America Bulletin*, *122*(1-2), 162-182.

Margirier, A., Audin, L., Robert, X., Herman, F., Ganne, J., Schwartz, S., 2016. Time and mode of exhumation of the Cordillera Blanca batholith (Peruvian Andes). Journal of Geophysical Research: Solid Earth 121, 6235–6249.

Martinod, J., Regard, V., Letourmy, Y., Henry, H., Hassani, R., Baratchart, S., Carretier, S. 2016. How do subduction processes contribute to forearc Andean uplift? Insights from numerical models. Journal of Geodynamics, 96, 6-18.

May, G., Hartley, A. J., Stuart, F. M., Chong, G. 1999. Tectonic signatures in arid continental basins: an example from the Upper Miocene–Pleistocene, Calama Basin, Andean forearc, northern Chile. Palaeogeography, Palaeoclimatology, Palaeoecology, 151(1), 55-77.

McInnes, B.I., Farley, K.A., Sillitoe, R.H., Kohn, B.P., 2001. Application of apatite (u-th)/he thermochronology to the determination of the sense and amount of vertical displacement at the Chuquicamata porphyry copper district, Chile–a reply. Economic Geology 96, 1310–1310.

McQuarrie, N., 2002. Initial plate geometry, shortening variations, and evolution of the Bolivian orocline. Geology 30, 867–870.

Mégard, F., Noble, D. C., McKee, E. H., Bellon, H. 1984. Multiple pulses of Neogene compressive deformation in the Ayacucho intermontane basin, Andes of central Peru. Geological Society of America Bulletin, 95(9), 1108-1117.

Mortimer, C. 1973. The Cenozoic history of the southern Atacama Desert, Chile. Journal of the Geological Society, 129(5), 505-526.

Mpodozis, C., Ramos, V., 1990. The Andes of Chile and Argentina.Mpodozis, C., Marinovic, N., Smoje, I., 1993. Eocene left lateral strike slip faulting and clockwise block rotations in the Cordillera de Domeyko, west of Salar de Atacama, northern Chile.

Mpodozis, C., Arriagada, C., Basso, M., Roperch, P., Cobbold, P., Reich, M. 2005. Late Mesozoic to Paleogene stratigraphy of the Salar de Atacama Basin, Antofagasta, Northern Chile: implications for the tectonic evolution of the Central Andes. Tectonophysics, 399(1), 125-154.

Mpodozis, C., Cornejo, P., 2012. Cenozoic tectonics and porphyry copper systems of the Chilean Andes. Society of Economic Geologists Special Publication 16, 329–360.

Muñoz, N., Charrier, R., 1996. Uplift of the western border of the Altiplano on a west-vergent thrust system, northern Chile. Journal of South American Earth Sciences 9, 171–181.

Muñoz, N., Charrier, R., Jordan, T. 2002. Interactions between basement and cover during the evolution of the Salar de Atacama Basin, northern Chile. *Revista geológica de Chile*, *29*(1), 55-80.

Nalpas, T., Hérail, G., Mpodozis, C., Riquelme, R., Clavero, J., Dabard, M.-P., 2007. Thermochronologicals data and denudation history along a transect between Chañaral and Pedernales (≈ 26ºS), north Chilean Andes: orogenic implications, in: 3 Rd Meeting of the ILP Task Force on Sedimentary Basin.

Niemeyer, H., Gonzalez, G., Martinez-De Los Rios, E., 1996. Evolución tectónica cenozoica del margen continental activo de Antofagasta, norte de Chile. Andean Geology 23, 165–186.

Noury, M., Philippon, M., Bernet, M., Paquette, J. L., Sempere, T. 2017. Geological record of flat slab–induced extension in the southern Peruvian forearc. *Geology*, G38990-1.

Pananont, P., Mpodozis, C., Blanco, N., Jordan, T.E., Brown, L.D., 2004. Cenozoic evolution of the northwestern Salar de Atacama Basin, northern Chile. Tectonics 23, TC6007.

Parada, M.A., Féraud, G., Fuentes, F., Aguirre, L., Morata, D., Larrondo, P., 2005. Ages and cooling history of the Early Cretaceous Caleu pluton: testimony of a switch from a rifted to a compressional continental margin in central Chile. Journal of the Geological Society 162, 273–287.

Parraguez, G.V., 1998. Sedimentologia y geomorphologia producto de la tectonica Cenozoica, en la Depresion Central, Pampa de Chaca, 1 Region Tarapaca, Chile. Departamento de Geologia, Universidad de Chile, Santiago, Chile 108.

Reiners, P.W., Thomson, S.N., Vernon, A., Willett, S.D., Zattin, M., Einhorn, J., Gehrels, G., Quade, J., Pearson, D., Murray, K.E., others, 2015a. Low-temperature thermochronologic trends across the central Andes, 21 S–28 S. Geological Society of America Memoirs 212, 215–249.

Reutter, K.-J., Giese, P., Götze, H.-J., Scheuber, E., Schwab, K., Schwarz, G., Wigger, P., 1988. Structures and crustal development of the Central Andes between 21 and 25 S, in: The Southern Central Andes. Springer, pp. 231–261.

Ridolfi, F., Renzulli, A., Puerini, M., 2010. Stability and chemical equilibrium of amphibole in calc-alkaline magmas: an overview, new thermobarometric formulations and application to subduction-related volcanoes. Contributions to Mineralogy and Petrology 160, 45–66.

Ridolfi, F., Renzulli, A., 2012. Calcic amphiboles in calc-alkaline and alkaline magmas: thermobarometric and chemometric empirical equations valid up to 1,130° C and 2.2 GPa. Contributions to Mineralogy and Petrology 163, 877–895.

Ridolfi, F., Braga, R., Cesare, B., Renzulli, A., Perugini, D., Del Moro, S., 2016. Unravelling the complex interaction between mantle and crustal magmas encoded in the lavas of San Vincenzo (Tuscany, Italy). Part I: Petrography and Thermobarometry. Lithos 244, 218–232.

Riquelme, R., Hérail, G., Martinod, J., Charrier, R., Darrozes, J., 2007. Late Cenozoic geomorphologic signal of Andean forearc deformation and tilting associated with the uplift and climate changes of the Southern Atacama Desert (26 S–28 S). Geomorphology 86, 283–306.

Rubilar, J. F., Becerra, J., Arriagada, C. 2015. Structure of the Cordillera de la Sal: A key tectonic feature for the Oligocene-Neogene evolution of the Salar de Atacama basin, Central Andes of Northern Chile. In This congress.

Scheuber, E., Andriessen, P.A., 1990. The kinematic and geodynamic significance of the Atacama fault zone, northern Chile. Journal of Structural Geology 12, 243–257.

Scheuber, E., Reutter, K.-J., 1992. Magmatic arc tectonics in the Central Andes between 21 and 25 S. Tectonophysics 205, 127–140.

Scheuber, E., Bogdanic, T., Jensen, A., Reutter, K.-J., 1994. Tectonic development of the north Chilean Andes in relation to plate convergence and magmatism since the Jurassic, in: Tectonics of the Southern Central Andes. Springer, pp. 121–139.

Scheuber, E., Gonzalez, G. 1999. Tectonics of the Jurassic-Early Cretaceous magmatic arc of the north Chilean Coastal Cordillera (22°–26°S): A story of crustal deformation along a convergent plate boundary. Tectonics, 18(5), 895-910

Sillitoe, R.H., 2005. Supergene oxidized and enriched porphyry copper and related deposits. Economic Geology 100th Anniversary Volume 29, 723–768.

Simon-Labric, T., Brocard, G. Y., Teyssier, C., Beek, P. A., Fellin, M. G., Reiners, P. W., Authemayou, C. 2013. Preservation of contrasting geothermal gradients across the Caribbean-North America plate boundary (Motagua Fault, Guatemala). Tectonics, 32(4), 993-1010.

Somoza, R., Ghidella, M. E. (2012). Late Cretaceous to recent plate motions in western South America revisited. Earth and Planetary Science Letters, 331, 152-163.

Springer, M., Förster, A., 1998. Heat-flow density across the Central Andean subduction zone. Tectonophysics 291, 123–139.

Table of Figures for Chapter 4

Chapter 5

Exhumation history and timing of the supergene copper mineralization

Abstract

The Centinela District in the Precordillera, in the Atacama Desert, northern Chile, exposes various mid-late Eocene porphyry Cu deposits affected by supergene mineralization and also provides access to a record of gravel deposits that host syn-sedimentary exotic Cu mineralized layers. The presence of both type of features allows to study the temporal relationship between the exhumation processes leading to the exposition of the primary source of copper to the surface and then to date the secondary mineralization deposits.

Late-Cretaceous to mid-Oligocene intrusive rocks present at the surface in the district were sampled to determine the exhumation through cooling path with two different low-temperature thermochronology methods, as apatite fision track (AFT) and U-Th/He (AHe) on apatite. Sixteen new AFT and AHe and four zircon U/Pb dating on the same intrusive rocks which remained undated were produced. The results provided cooling patterns we interpreted as exhumation signals.

The patterns are similar for all the intrusive rocks, they indicate a rapid cooling since the rock age emplacement to early Oligocene ~30 Ma. They also permit to constrain an emplacement depth range for Cu-porphyry between ~2 and 3 km deep. After 30 Ma we consider that the denudation rates dropped drastically like suggested by Maksaev and Zentilli (1999) at the scale of the Precordillera. This drop is associated to the flattening of the landscape as a response of an initial uplift (the rapid pre-30 Ma cooling event).

The results of this study have been published in Terra Nova (Sanchez et al., in press).

In order to relate the gravel deposition episodes with the timing of the supergene mineralization, we provide new $^{40}Ar/^{39}Ar$ and K-Ar ages on both exotic and supergene minerals. An integrated study based on stratigraphic and sedimentological data, lithology clast counts, $^{40}Ar/^{39}Ar$ and U/Pb from interbedded tuff layers and U/Pb detrital zircon geochronology. Added to pre-existent ages, the new supergene and exotic copper mineral ages form a range of ~25 to 12 Ma ages. The five million years gap between the drop of erosion rates and the range of supergene copper ages strongly support that low denudation rates concord with the formation of ore deposit. The description and dating of the facies is exposed in Riquelme et al., 2017 (in annexes).

Both paper do corroborate that landscape pediplanation favors supergene mineralization and helps preserve the former supergene mineralized zones from significant erosion.

Pediplanation requires the prevalence of a relative wetter climate (semiarid) condition to efficiently allow the supergene mineralization processes to occur. Thus, the drastic drop of precipitation rates is also necessary to the preservation of the supergene mineralization deposits. Low erosion rates during pediplantation may constitute a necessary condition for the efficiency of the supergene processes arid conditions.

Article published in Terra Nova (Sanchez et al., in press)

PAPER

Exhumation history and timing of supergene copper mineralisation in an arid climate: New thermochronological data from the Centinela District, Atacama, Chile

Caroline Sanchez[1,2] | Stéphanie Brichau[2] | Rodrigo Riquelme[1] | Sébastien Carretier[2] | Thomas Bissig[3] | Cristopher Lopez[1] | Constantino Mpodozis[4] | Eduardo Campos[1] | Vincent Regard[2] | Gérard Hérail[2] | Carlos Marquardt[5]

[1]Depto. Ciencias Geológicas, Universidad Católica del Norte, Antofagasta, Chile

[2]Géosciences Environnement Toulouse (GET), Université de Toulouse, UPS, CNRS, IRD, CNES, Toulouse, France

[3]Mineral Deposit Research Unit, Department of Earth, Ocean and Atmospheric Sciences, University of British Columbia, Vancouver, BC, Canada

[4]Antofagasta Minerals S.A., Las Condes, Santiago, Chile

[5]Departamento de Ingeniería en Minería, Pontificia Universidad Católica de Chile, Santiago, Chile

Correspondence
Miss Caroline Sanchez, Depto. Ciencias Geológicas, Universidad Catolica del Norte, Antofagasta, Chile. Geosciences Environnement Toulouse (GET), Universite de Toulouse, UPS, CNRS, IRD, CNES, Toulouse, France
Email: csanchez@get.obs-mip.fr

Abstract

Supergene copper mineralisation (SCM) processes occur during the unroofing of porphyry copper deposits. However, the geomorphological stage during which the main mineralisation occurs is still under debate. Here, we present 24 new thermochronological data from Cenozoic intrusives and compare them with the evolution of supergene mineralisation from the Centinela Mining District in the Atacama Desert. Our results indicate a two-step cooling path: a rapid Late Eocene exhumation followed by a slow denudation. Previously published supergene mineralisation ages cluster after the main Upper Oligocene exhumation period. Ours is the first study that establishes the relationship between exhumation and supergene processes on the scale of a single mining district. It confirms that SCM took place during pediplanation, likely a required condition for efficient SCM under arid climatic conditions, in contrast to wet tropical environments where SCM occurs during rapid relief growth but has limited preservation potential.

1 | INTRODUCTION

Porphyry copper deposits are genetically linked to the emplacement of shallow intrusions (<5 km deep: Richards, 2011; Wilkinson, 2013), on which hypogene sulphide mineralisation precipitates from magmatic–hydrothermal fluids (Seedorff et al., 2005), but copper grades may increase substantially after exhumation when sulphides are exposed to oxidation and leaching. Leached copper may precipitate as either copper oxides or secondary enriched sulphides depending on whether precipitation occurs above or below the water table (Chávez, 2000; Sillitoe, 2005).

Climatic and geomorphologic conditions favouring supergene copper mineralisation (SCM) are still a matter of debate (Reich & Vasconcelos, 2015). SCM is thought to be particularly efficient under semi-arid climates, where moderate precipitation provides high water-to-rock ratios and denudation is limited, preserving the weathering profile (e.g. Clark, Tosdal, Farrar, & Plazolles, 1990; Hartley & Rice, 2005; Vasconcelos, 1999). However, rare SCM examples have been documented in tropical rapidly uplifted environments (Bamford, 1972; Braxton & Mathur, 2011).

SCM requires an equilibrium between denudation and water-table descent rates, which can be encountered at different stages of
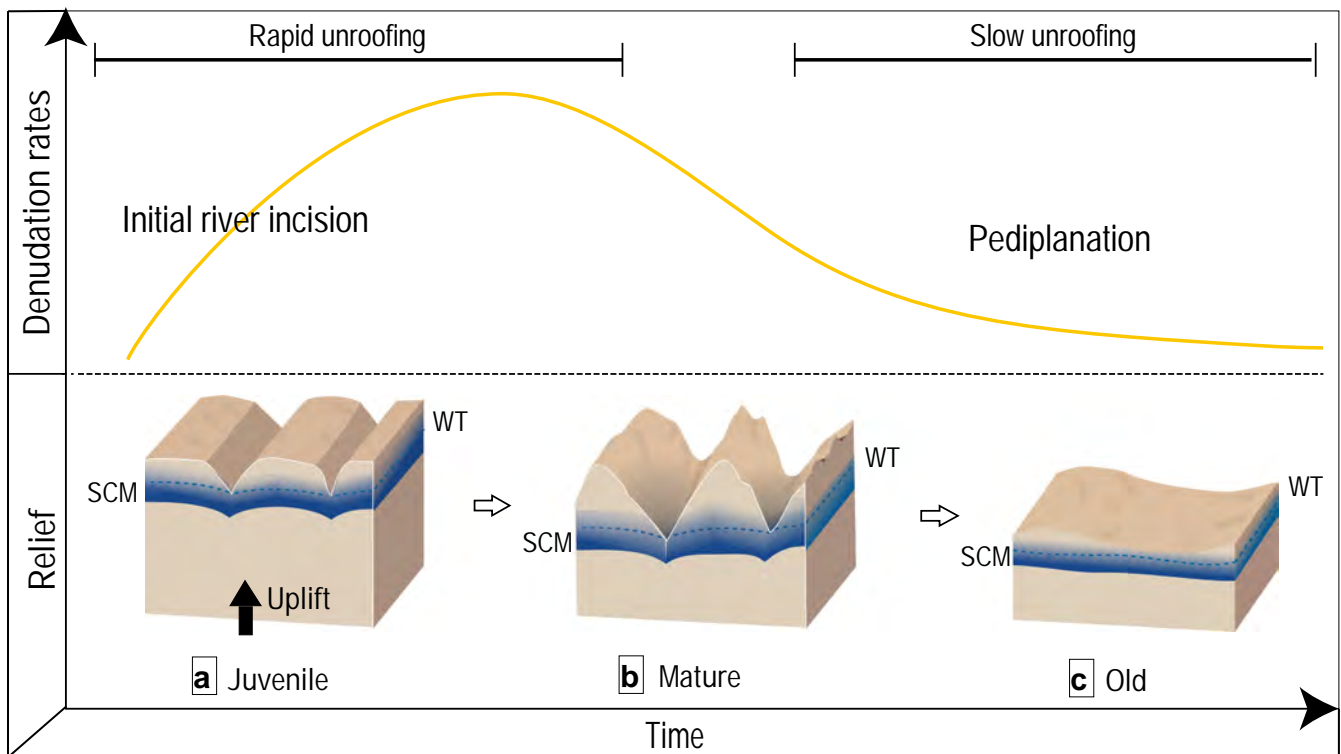
FIGURE 1 Schematic evolution of the denudation rate through time in response to a period of surface uplift. WT, water table (dashed line); SCM, supergene copper mineralisation (blue layer)

the landscape evolution in response to surface uplift (Alpers & Brimhall, 1988; Bouzari & Clark, 2002; Mortimer, 1973). During this cycle, illustrated in three stages, the erosion rate follows a "humped" curve (e.g. Kooi & Beaumont, 1996; Figure 1).

Previous studies have proposed that SCM may occur: (1) during the increasing relief, denudation and river incision phase (Figure 1a) (Bissig & Riquelme, 2009, 2010; Sillitoe & Perelló, 2005); (2) during the maximum hillslope angle and denudation rate period (Figure 1b; Braxton, Cooke, Ignacio, Rye, & Waters, 2009) or (3) during landscape pediplanation (Figure 1c) when denudation and slopes decrease (Bouzari & Clark, 2002; Clark et al., 1990; Mortimer, 1973; Quang, Clark, Lee, & Hawkes, 2005).

In the Atacama Desert, the SCM development in numerous Cenozoic porphyry copper deposits has been placed within the physiographic context of Upper Oligocene–Lower Miocene erosional pediments (e.g. Alpers & Brimhall, 1988; Mortimer, 1973). The role of pediment formation in SCM remains unclear. Distinct supergene episodes have been correlated with brief intervals of uplift and pediment incision (e.g. Bissig & Riquelme, 2010; Bouzari & Clark, 2002; Quang et al., 2005), whereas Sillitoe (2005) argued that thick SCM develop during major surface uplift events, implying that pediplanation is not required for efficient supergene formation. Conversely, Hartley and Rice (2005) proposed that the influence of regional pediplain formation on SCM is not well established, mainly due to the lack of landform ages. To tackle this issue, we focused on the Centinela District (CD) in northern Chile (Figure 2a,b), where most of the world-class SCMs are hosted beneath pediplains (Mortimer, 1973; Segerstrom, 1963).

We performed a thermochronological study to identify when in the geomorphological cycle SCM took place. Four zircon U–Pb, six apatite fission-track (AFT) and 10 apatite helium (AHe) ages were obtained and compared with published supergene minerals' $^{40}Ar/^{39}Ar$ and K–Ar ages (see supporting information; Sillitoe & McKee, 1996; Perelló et al., 2010; Riquelme et al., 2017). In northern Chile, low-temperature thermochronological studies have been conducted on specific porphyries (Campos, Wijbrans, & Andriessen, 2009; Maksaev et al., 2010; McInnes, Farley, Sillitoe, & Kohn, 1999) to constrain their cooling/exhumation history, yet none has been performed at a mining-district scale. The CD is a key area including both exhumed porphyries and SCMs. Our samples were taken from both mineralised and non-Cu-mineralised intrusions. Their denudation is recorded in the mid-Eocene to Upper Miocene gravel deposits that constitute the CD sedimentary cover (Mora, Artal, Brockway, Martinez, & Muhr, 2004; Riquelme et al., accepted).

2 | GEOLOGICAL BACKGROUND

The CD is located 60 km south of Calama (Figure 2b) on the western limb of the Precordillera. The district includes outcrops of Palaeozoic basement, Mesozoic volcanic and sedimentary rocks, and Palaeocene volcanic rocks (Mpodozis & Cornejo, 2012; Figure 2c). These rocks are intruded by Lower Cretaceous–Upper Eocene diorites and rhyolitic and dacitic porphyry intrusions (Marinovic & García, 1999; Mpodozis & Cornejo, 2012).
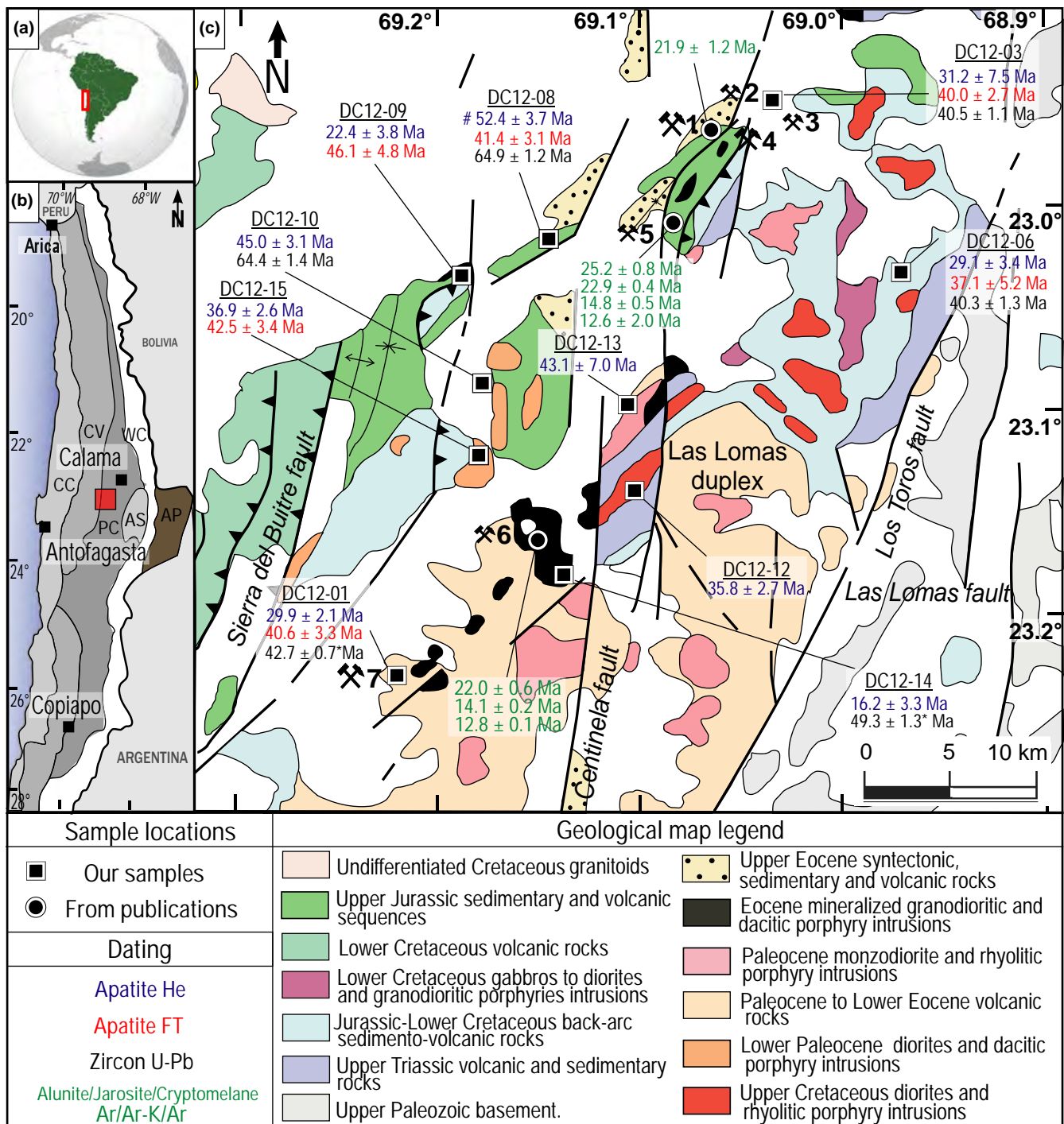
FIGURE 2 (a) Location of the studied area in the South American continent. (b) Morpho-structural map of northern Chile (CC, Coastal Cordillera; CV, Central Valley; PC, Precordillera; AS, Atacama Salar; AP, Altiplano after Jordan, Isacks, Ramos, & Allmendinger, 1983). Red square marks the location of the Centinela District. (c) Detailed Centinela District map after Mpodozis and Cornejo (2012), showing sample locations and ages (^{40}Ar/^{39}Ar – K/Ar are from Sillitoe & McKee, 1996; Perelló et al., 2010; and Riquelme et al., accepted). *Zircon U–Pb ages from Antofagasta Mineral SA, personal communication

Two regional-scale tectonic phases affected the CD during the Cenozoic. The first phase, characterised by crustal shortening and labelled K–T, occurred at ~60 Ma and was accompanied by Palaeocene intrusions (Cornejo, Matthews, & Pérez de Arce, 2003; Mpodozis & Cornejo, 2012), whereas porphyry-Cu mineralisation is related to intrusions emplaced between 45 and 41 Ma, during the Incaic orogenic phase (Mpodozis, Cembrano, & Mora, 2009; Perelló et al., 2004). The Incaic phase activated the 800 km long N-trending transpressive Domeyko Fault System in the Precordillera, upthrowing porphyry-Cu intrusions to the west and allowing the formation of structurally controlled basins (Figure 2c) to the east (Amilibia et al., 2008; Mpodozis & Cornejo, 2012; Mpodozis, Marinovic, & Smoje,

TABLE 1 Global dataset. Altitude, sample location, rock type and zircon U–Pb, AFT and AHe age results; track measurement details (number measured, Dpar = etch pit width). Asterisks indicate unpublished ages from Antofagasta Minerals

Name	Altitude (m)	Latitude	Longitude	Rock type	Age U–Pb (Ma)	Age FT (Ma)	Track lengths N tracks	Dpar (StD)	Age He (Ma)
DC12-01	2323	23°14′23″	69°11′52″	Dacitic	42.7* ± 0.7	40.6 ± 3.3	14.00 ± 0.11100	2.7 ± 0.37	29.9 ± 2.1
DC12-03	2226	22°56′44″	69°01′32″	Dacitic, mineralised	40.5 ± 1.1	40.0 ± 2.7	14.99 ± 0.1562	2.9 ± 1.30	31.2 ± 7.5
DC12-06	2955	23°02′34″	68°57′41″	Dacitic	40.3 ± 1.3	37.1 ± 5.2	14.84 ± 0.1559	2.6 ± 1.56	29.1 ± 3.4
DC12-08	2149	23°01′22″	69°09′40″	Granodiorite	64.9 ± 1.2	41.4 ± 3.1	13.98 ± 0.3099	1.8 ± 0.86	52.4 ± 3.7
DC12-09	2012	23°01′56″	69°11′26″	Granodiorite	–	46.1 ± 4.8	13.96 ± 0.3041	3.9 ± 0.90	22.4 ± 3.8
DC12-10	2082	23°07′31″	69°10′37″	Granodiorite	64.4 ± 1.4	–	–	–	45.0 ± 3.1
DC12-12	2611	23°04′23″	69°10′26″	Granodiorite	–	–	–	–	35.8 ± 2.7
DC12-13	2847	23°08′60″	69°06′03″	Granodiorite	–	–	–	–	43.1 ± 7.0
DC12-14	2375	23°07′22″	69°06′26″	Dacitic	49.3* ± 1.3	–	–	–	16.2 ± 3.3
DC12-15	2183	23°09′50″	69°08′27″	Dacitic	–	42.5 ± 3.4	13.96 ± 0.3058	2.3 ± 0.26	36.9 ± 2.6

1993). In the CD, Precordilleran erosion and denudation in response to the Incaic phase resulted in the deposition of up to ~800 m of mid-late Eocene to Late Miocene gravel and sand deposits with scarce interbedded volcanic and evaporitic layers (Mora et al., 2004; Riquelme et al., accepted).

In the Atacama Desert, most supergene mineralisation ages range from ~25 to 13 Ma (Arancibia, Matthews, & Pérez de Arce, 2006; Bissig & Riquelme, 2010; Perelló et al., 2010; Reich et al., 2009; Riquelme et al., accepted; Sillitoe & McKee, 1996). In northern Chile, supergene mineralisation ages are generally younger than exhumation ages (Arancibia et al., 2006; Maksaev & Zentilli, 1999) but precise SCM onset remains difficult to date. In the CD, supergene alunite and jarosite $^{40}Ar-^{39}Ar$ and K–Ar ages range from 25 to 13 Ma, matching previously obtained SCM ages and the age of hyperaridity onset in the area (Alpers & Brimhall, 1988; Dunai, López, & Juez-Larré, 2005).

3 | METHODS

Ten Palaeogene–Upper Eocene equigranular granodioritic and sub-volcanic dacitic porphyry intrusives were sampled in the CD (Table 1). Apatite and zircon were extracted from the samples using conventional mineral separation techniques at the Geosciences Environnement Toulouse (GET) laboratory (France).

AFT analyses were jointly carried out at GET and Universidad de Chile, while irradiations were performed in the Chilean CCHEN nuclear reactor; AHe analyses were performed at the Geosciences Montpellier laboratory, France, and zircon U–Pb dating was performed at Birbeck College, London, UK. Detailed laboratory procedures are described in Witt, Rangin, Andreani, Olaez, and Martinez (2012), Eude et al. (2015) and Wu et al. (2016). Results are summarised in Table 1.

To extract thermal histories from the six samples providing both AFT and AHe ages, we used Ketcham's HeFTy modelling package (Ketcham, 2005). For visual representation, we extracted two cooling histories representing good paths and the average best fit for each

sample from Lower Palaeogene granodiorite and Middle Eocene dacitic intrusions (Figure 3; see details in supporting information section 2).

4 | RESULTS

Our new AFT and AHe ages provide evidence of two intrusive cooling histories. Lower Palaeocene granodiorites display zircon U–Pb ages of 64.4 ± 1.4 Ma and 64.9 ± 1.2 Ma, AFT ages from 46.1 ± 4.8 Ma to 41.1 ± 3.1 Ma, and AHe ages ranging from 45.0 ± 2.3 Ma to 22.4 ± 1.1 Ma (Figure 3). Mid-Eocene dacitic samples yielded zircon U–Pb ages from 42.7 ± 1.1 Ma to 39.7 ± 1.1 Ma, AFT ages of 46.1 ± 4.8 Ma to 41.1 ± 3.1 Ma, and AHe ages between 40.6 ± 3.3 Ma and 37.9 ± 5.2 Ma. Modelling of these data suggest rapid cooling between ~60 and 35 Ma for the granodiorites and even faster cooling between ~40 and 30 Ma for the dacitic samples, followed, in both cases, by minor cooling (Figure 3).

5 | DISCUSSION

5.1 | New constraints on emplacement depth

To estimate Lower Palaeocene and middle Eocene porphyry copper emplacement depths, we divided the AFT (110°C, Gunnell, 2000) and AHe (75°C, Farley, 2002) closure temperatures by a geothermal gradient estimated for the area at ~30–25°C/km (Morgan, 1984). This suggests closure-temperature depths of 4.5–3.7 km for the AFT chronometer and 2.5–3 km for the AHe system. Lower Palaeocene granodiorite displays zircon U–Pb emplacement ages ~20 Ma older than the AFT ages, suggesting a minimum emplacement depth of 4.5–3.7 km. Eocene dacitic samples have emplacement ages that are similar to AFT ages but ~10 Ma older than the AHe ages, suggesting an emplacement depth between 4.5–3.7 km and 2.5–3 km. This difference is consistent with sample petrographic characteristics (Perelló et al., 2004). This suggests that Lower Palaeocene

FIGURE 3 Temperature vs. time paths, modelled from HeFTy (Ketcham, 2005), U–Pb dating (from this study and geological map) and $^{40}Ar/^{39}Ar$ and K/Ar supergene ages (see tables in the supporting information) of six samples. The envelopes represent the possible "good paths" obtained for 10000 Monte Carlo simulations for each sample. We superimposed the envelopes for the six samples providing AFT and AHe ages, and added mean best-fit paths for the Palaeocene and Eocene sample groups (three samples in each)
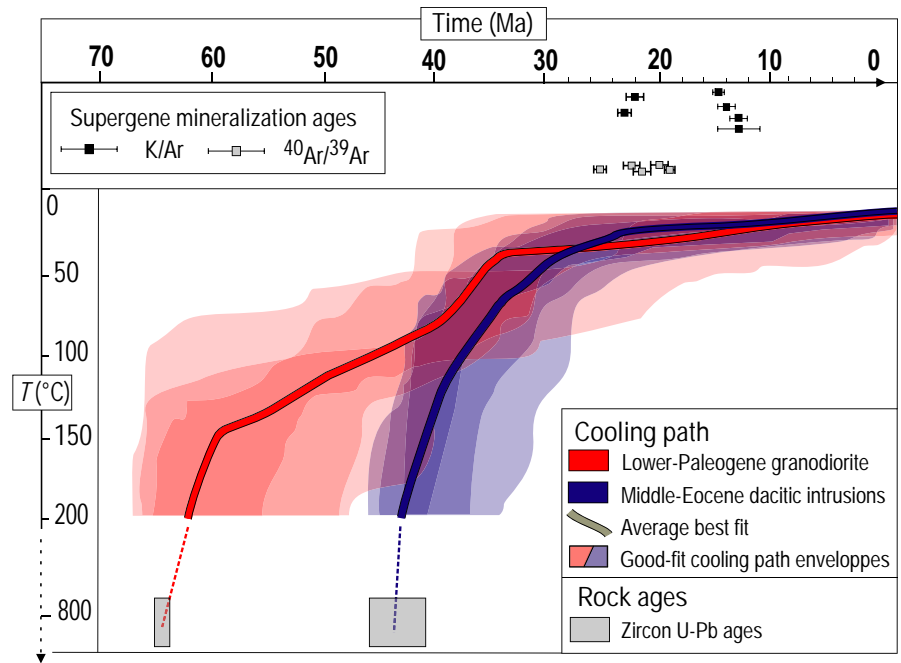
granodiorite exhumation started before and from a greater depth than the exhumation of the Eocene dacitic bodies.

5.2 | Tectonic implications

The low-temperature thermochronology results indicate a protracted cooling phase in all samples. Lower Palaeocene intrusions experienced a rapid cooling from ~65 Ma to ~30 Ma, which may have been initiated by a rock exhumation episode during the K–T tectonic phase (Cornejo et al., 2003; Mpodozis & Cornejo, 2012). On the other hand, Eocene dacitic intrusions have similar zircon U–Pb and AFT ages, and display a rapid cooling from 40 to ~30 Ma. This fast cooling is consistent with emplacement during the Incaic tectonic phase (Charrier, Pinto, & Rodríguez, 2007; Noble, McKee, & Mégard, 1979; Steinmann, Stappenbeck, Sieberg, & Lissón, 1929). The duration of this major tectonic phase is the subject of debate. Hammerschmidt, Döbel, and Friedrichsen (1992) and Tomlinson and Blanco (1997) considered it a short tectonic contractile event at about 42 Ma, whereas Maksaev and Zentilli (1999) and Jaillard et al. (2000) proposed a duration from ~55 to ~30 Ma. Our results support the latter scenario.

After the Incaic tectonic phase, Eocene and Palaeocene intrusions exhibit a slow cooling path suggesting only minor exhumation not exceeding 2.5 km since the Early Oligocene. This can be related to the generalised landscape pediplanation reported for the Atacama Desert during Oligocene–Miocene time (Evenstar et al., 2009; Isacks, 1988; Mortimer, 1973; Riquelme, Hérail, Martinod, Charrier, & Darrozes, 2007).

5.3 | Relationship between exhumation and supergene mineralisation

The relationship between exhumation and the onset of SCM has previously been studied at the El Salvador deposit, 400 km south

of CD (Bissig & Riquelme, 2010; Mote, Becker, Renne, & Brimhall, 2001). There, supergene mineralisation initiated at ~35 Ma, some 6 Ma after hypogene mineralisation, suggesting rapid exhumation. However, the exhumation history of the porphyries is not constrained by thermochronology, and it is not known whether supergene mineralisation occurred during relief growth or pediplanation. Similarly, at La Escondida mine, 200 km south of CD, Alpers and Brimhall (1988) found that hypogene hydrothermal alteration occurred around ~34–31 Ma, while SCM was active at ~18–14 Ma. Using mass balance calculations (Brimhall et al., 1985) and taking the unmineralised lithocap as a reference surface, Alpers and Brimhall (1988) discussed scenarios linking denudation history and SCM. However, uncertainties about the timing of the onset of SCM combined with a lack of exhumation data prevented them from determining whether supergene mineralisation occurred after a rapid denudation period or during a constant, slow denudation phase.

This study provides new constraints on the relationship between SCM and pediplanation. Specifically, the difference between the timing of exhumation and the SCM ages (Figure 3) indicates that supergene mineralisation (25–13 Ma data from Sillitoe & McKee, 1996; Perelló et al., 2004 and Riquelme et al., accepted) occurred between 5 and 15 Ma after the end of rapid exhumation of the porphyry copper mineralisation (~40–30 Ma). The relative tectonic quiescence inferred from the low exhumation rates after 30 Ma (Figure 3) suggests that the district landscape was already in the pediplanation stage when supergene mineralisation occurred (Figure 1c). For other areas of the Atacama Desert, Arancibia et al. (2006) proposed that older SCM may have been eroded away. If so, SCM could have formed during the main unroofing period associated with the Incaic deformation and not only during pediplanation. However, for the CD, we regard this as unlikely since no evidence of SCM detrital

clasts older than ~25 Ma has been found in Centinela Basin sediments (Riquelme et al., accepted). Thus, low erosion rates and low relief are conducive not only to preservation but also to SCM in arid climates.

5.4 | Climatic and tectonic controls on SCM

Wetter periods during the Oligo-Miocene may have controlled SCM periods in northern Chile's planar landscapes (Alpers & Brimhall, 1988; Reich et al., 2009; Sillitoe & McKee, 1996) as well as in other climatic zones (Feng & Vasconcelos, 2007; Vasconcelos, Reich, & Shuster, 2015).

The apparent difficulty of developing significant SCM during rapid exhumation may not apply to humid environments where extensive SCM during rapid exhumation has been documented (Bamford, 1972; Braxton et al., 2009, 2012). Transport-reactive models may help to clarify the differences between northern Chile and tropical examples (Mathur & Fantle, 2015). Under arid climates, primary copper dissolution may be limited by slow diffusion of copper species into the interstitial fluid (Lebedeva, Fletcher, & Brantley, 2010). The weathered-layer thickening rate may be too slow to outpace the denudation rate during the main exhumation period. Even if there are more humid periods, the runoff excess may foster erosion on steep slopes and prevent the weathered layer from thickening. Once the slopes are gentle during pediplanation, the weathering profile can thicken. More humid periods will then favour groundwater infiltration, with a limited impact on erosion, favoring leaching as well as SCM at depth (Palacios, Rouxel, Reich, Cameron, & Leybourne, 2011). In humid environments, sulphide dissolution may be controlled more by the groundwater velocity and thus may be rapid (Maher, 2010). While leaching is more efficient, chemical saturation requires in turn great groundwater penetration depths (Mathur & Fantle, 2015), limiting the SCM in stable landscapes (Carajás Mountains, Brazil – Vasconcelos et al., 2015). Nevertheless, if the protolith is exhuming fast (Boyongan and Bayugo deposits), the vertical supply of primary copper sulphides allows the Cu concentration in the descending groundwater to increase, so SCM saturation and precipitation may occur in the vadose (Cu oxide minerals, Boyongan and Bayugo) or saturated (enriched sulphides, Ok Tedi) zone. Although other factors locally control the SCM (pyrite content, bacteria, initial rock porosity etc.; Braxton et al., 2009), such a process may explain the difference in optimum exhumation–climate combinations between the humid cases and the CD.

The time required to form a mature supergene profile most likely depends on the balance between exhumation and precipitation rates. In the case of the Ok Tedi, Boyongan and Bayugo districts, high exhumation rates are balanced by high precipitation rates (2,000–4,000 mm/a) allowing a mature supergene profile to form within a few hundreds of thousands of years. In contrast, when primary ore is subjected to low exhumation and precipitation rates, the formation of mature supergene profiles may require more than 10 Ma, as is suggested by the supergene mineralisation ages of the CD.

6 | CONCLUSION

Our data from the CD intrusions suggest that two important tectonic phases can be identified from the intrusive paths: the K–T tectonic phase (Cretaceous–Palaeogene limits) followed by the Incaic deformation (mid-Eocene and Early Oligocene). From the Incaic phase to the present day, slow cooling paths can be related to landscape pediplanation. Our results provide quantitative support to previous interpretations suggesting that low denudation rates and low relief are favourable for SCM in arid environments.

ORCID

Caroline Sanchez [iD] http://orcid.org/0000-0002-9526-4759

REFERENCES

Alpers, C. N., & Brimhall, G. H. (1988). Middle Miocene climatic change in the Atacama Desert, northern Chile: Evidence from supergene mineralization at La Escondida. *Geological Society of America Bulletin*, *100*, 1640–1656.

Amilibia, A., Sàbat, F., McClay, K. R., Muñoz, J. A., Roca, E., & Chong, G. (2008). The role of inherited tectono-sedimentary architecture in the development of the central Andean mountain belt: Insights from the Cordillera de Domeyko. *Journal of Structural Geology*, *30*, 1520–1539.

Andriessen, P., & Reutter, K.-J. (1994). K-Ar and fission-track mineral age determination of igneous rocks related to multiple magmatic arc system along the 23°S latitude of Chile and NW Argentine. In K.-J., Reutter, E. Scheuber & P. Wigger (Eds.), *Tectonics of the Southern Central Andes* (pp. 141–153), Berlin: Springer-Verlag.

Arancibia, G., Matthews, S. J., & Pérez de Arce, C. (2006). K–Ar and 40Ar/39Ar geochronology of supergene processes in the Atacama Desert, Northern Chile: Tectonic and climatic relations. *Journal of the Geological Society*, *163*, 107–118.

Bamford, R. W. (1972). The Mount Fubilan (Ok Tedi) Porphyry Copper Deposit, Territory of Papua and New Guinea. *Economic Geology*, *67*, 1019–1033.

Bissig, T., & Riquelme, R. (2009). Contrasting landscape evolution and development of supergene enrichment in the El Salvador porphyry Cu and Potrerillos-El Hueso Cu-Au districts, northern Chile. In: S. Titley (Ed.), *Supergene environments, processes and products. Society of Economic Geologists Special Publication*, *14*, 59–68.

Bissig, T., & Riquelme, R. (2010). Andean uplift and climate evolution in the southern Atacama Desert deduced from geomorphology and supergene alunite-group minerals. *Earth and Planetary Science Letters*, *299*, 447–457.

Bouzari, F., & Clark, A. H. (2002). Anatomy, evolution, and metallogenic significance of the supergene orebody of the Cerro Colorado porphyry copper deposit, I Región, northern Chile. *Economic Geology*, 97, 1701–1740.

Braxton, D. P., Cooke, D. R., Dunlap, J., Norman, M., Reiners, P., Stein, H., & Waters, P. (2012). From crucible to graben in 2.3 Ma: A high-resolution geochronological study of porphyry life cycles, Boyongan-Bayugo copper-gold deposits, Philippines. *Geology*, 40, 471–474.

Braxton, D. P., Cooke, D. R., Ignacio, A. M., Rye, R. O., & Waters, P. J. (2009). Ultra-deep oxidation and exotic copper formation at the late Pliocene Boyongan and Bayugo porphyry copper-gold deposits, Surigao, Philippines: Geology, mineralogy, paleoaltimetry, and their implications for geologic, physiographic, and tectonic controls. *Economic Geology*, 104, 333–349.

Braxton, D., & Mathur, R. (2011). Exploration applications of copper isotopes in the supergene environment: A case study of the Bayugo porphyry copper-gold Deposit, southern Philippines. *Economic Geology*, 106, 1447–1463.

Brimhall, G. H., Alpers, C. N., & Cunningham, A. B. (1985). Analysis of supergene ore-forming processes and ground-water solute transport using mass balance principles. *Economic Geology*, 80, 1227–1256.

Campos, E., Wijbrans, J., & Andriessen, P. A. (2009). New thermochronologic constraints on the evolution of the Zaldívar porphyry copper deposit, Northern Chile. *Mineralium Deposita*, 44, 329.

Charrier, R., Pinto, L., & Rodríguez, M. P. (2007). Tectonostratigraphic evolution of the Andean Orogen in Chile. *The Geology of Chile*, 21–114.

Chávez, W. X. Jr. (2000). Supergene oxidation of copper deposits: Zoning and distribution of copper oxide minerals. *Society of Economic Geologists Newsletter*, 41, 10–21.

Clark, A. H., Tosdal, R. M., Farrar, E., & Plazolles, A. (1990). Geomorphologic environment and age of supergene enrichment of the Cuajone, Quellaveco, and Toquepala porphyry copper deposits, southeastern Peru. *Economic Geology*, 85, 1604–1628.

Cornejo, P., Matthews, S., & Pérez de Arce, C. (2003). The "K-T" Compressive Deformation Event in Northern Chile (24–27°). 10° Congreso Geológico Chileno, Concepción.

Dunai, T. J., López, G. A. G., & Juez-Larré, J. (2005). Oligocene–Miocene age of aridity in the Atacama Desert revealed by exposure dating of erosion-sensitive landforms. *Geology*, 33, 321–324.

Eude, A., Roddaz, M., Brichau, S., Brusset, S., Calderon, Y., Baby, P., & Soula, J.-C. (2015). Controls on timing of exhumation and deformation in the northern Peruvian eastern Andean wedge as inferred from low-temperature thermochronology and balanced cross section. *Tectonics*, 34, 715–730.

Evenstar, L. A., Hartley, A. J., Stuart, F. M., Mather, A. E., Rice, C. M., & Chong, G. (2009). Multiphase development of the Atacama Planation Surface recorded by cosmogenic 3He exposure ages: Implications for uplift and Cenozoic climate change in western South America. *Geology*, 37, 27–30.

Farley, K. A. (2002). (U-Th)/He dating: Techniques, calibrations, and applications. *Reviews in Mineralogy and Geochemistry*, 47, 819–844.

Feng, Y.-X., & Vasconcelos, P. (2007). Chronology of Pleistocene weathering processes, southeast Queensland, Australia. *Earth and Planetary Science Letters*, 263, 275–287.

Gunnell, Y. (2000). Apatite fission track thermochronology: An overview of its potential and limitations in geomorphology. *Basin Research*, 12, 115–132.

Hammerschmidt, K., Döbel, R., & Friedrichsen, H. (1992). Implication of 40Ar39Ar dating of Early Tertiary volcanic rocks from the north-Chilean Precordillera. *Tectonophysics*, 202, 55–81.

Hartley, A. J., & Rice, C. M. (2005). Controls on supergene enrichment of porphyry copper deposits in the Central Andes: A review and discussion. *Mineralium Deposita*, 40, 515–525.

Isacks, B. L. (1988). Uplift of the central Andean plateau and bending of the Bolivian orocline. *Journal of Geophysical Research: Solid Earth*, 93 (B4), 3211–3231.

Jaillard, E., Hérail, G., Monfret, T., Díaz-Martínez, E., Baby, P., Lavenu, A., & Dumont, J. F. (2000). Tectonic evolution of the Andes of Ecuador, Peru, Bolivia and northernmost Chile. *Tectonic Evolution of South America*, 31, 481–559.

Jordan, T. E., Isacks, B., Ramos, V. A., & Allmendinger, R. W. (1983). Mountain building in the Central Andes. *Episodes*, 3, 20–26.

Ketcham, R. A. (2005). Forward and inverse modeling of low-temperature thermochronometry data. *Reviews in Mineralogy and Geochemistry*, 58 (1), 275–314.

Kooi, H., & Beaumont, C. (1996). Large-scale geomorphology: Classical concepts reconciled and integrated with contemporary ideas via a surface processes model. *Journal of Geophysical Research: Solid Earth*, 101, 3361–3386.

Lebedeva, M. I., Fletcher, R. C., & Brantley, S. L. (2010). A mathematical model for steady-state regolith production at constant erosion rate. *Earth Surface Processes and Landforms*, 35, 508–524.

Maher, K. (2010). The dependence of chemical weathering rates on fluid residence time. *Earth and Planetary Science Letters*, 294, 101–110.

Maksaev, V., Almonacid, T. A., Munizaga, F., Valencia, V., McWilliams, M., & Barra, F. (2010). Geochronological and thermochronological constraints on porphyry copper mineralization in the Domeyko alteration zone, northern Chile. *Andean Geology*, 37, 144–176.

Maksaev, V., & Zentilli, M. (1999). Fission track thermochronology of the Domeyko Cordillera, northern Chile: Implications for Andean tectonics and porphyry copper metallogenesis. *Exploration and Mining Geology*, 8, 65–90.

Marinovic, N., & García, M. (1999). Hoja Pampa Unión, Región de Antofagasta. Escala 1:100.000, Servicio Nacional de Geología y Minería, Mapas Geológicos, N° 9, Santiago.

Mathur, R., & Fantle, M. S. (2015). Copper isotopic perspectives on supergene processes: Implications for the global Cu cycle. *Elements*, 11, 323329.

McInnes, B. I., Farley, K. A., Sillitoe, R. H., & Kohn, B. P. (1999). Application of apatite (U-Th)/He thermochronometry to the determination of the sense and amount of vertical fault displacement at the Chuquicamata porphyry copper deposit, Chile. *Economic Geology*, 94, 937–947.

Mora, R., Artal, J., Brockway, H., Martinez, E., & Muhr, R. (2004). El Tesoro exotic copper deposit, Antofagasta region, northern Chile. *Society of Economic Geologists, Special Publication*, 11, 187–197.

Morgan, P. (1984). The thermal structure and thermal evolution of the continental lithosphere. *Physics and Chemistry of the Earth*, 15, 107–193.

Mortimer, C. (1973). The Cenozoic history of the southern Atacama Desert, Chile. *Journal of the Geological Society*, 129, 505–526.

Mote, T. I., Becker, T. A., Renne, P., & Brimhall, G. H. (2001). Chronology of exotic mineralization at El Salvador, Chile, by 40 Ar/39 Ar dating of copper wad and supergene alunite. *Economic Geology*, 96, 351–366.

Mpodozis, C, Cembrano, J., & Mora, R. (2009). *Deformación compresiva-oblicua polifásica y pórfidos cupríferos eocenos en el Sistema de Fallas de Domeyko: la región de Esperanza-Caracoles (Distrito Centinela)*. En XII Congreso Geológico Chileno, Santiago, Actas S11-062.

Mpodozis, C., & Cornejo, P. (2012). Cenozoic tectonics and porphyry copper systems of the Chilean Andes. *Society of Economic Geologists Special Publication*, 16, 329–360.

Mpodozis, C., Marinovic, N., & Smoje, I. (1993). Eocene left lateral strike slip faulting and clockwise block rotations in the Cordillera de Domeyko, west of Salar de Atacama, northern Chile. Géodynamique Andine: Symposium International II.

Noble, D. C., McKee, E. H., & Mégard, F. (1979). Early Tertiary "Incaic" tectonism, uplift, and volcanic activity, Andes of central Peru. *Geological Society of America Bulletin*, 90, 903–907.

Palacios, C., Rouxel, O., Reich, M., Cameron, E. M., & Leybourne, M. I. (2011). Pleistocene recycling of copper at a porphyry system, Atacama Desert, Chile: Cu isotope evidence. *Mineralium Deposita*, *46*, 1–7.

Perelló, J., Brockway, H., & Martini, R. (2004). Discovery and geology of the Esperanza porphyry copper-gold deposit, Antofagasta region, northern Chile. In R. H. Sillitoe, J. Perello & C. E. Vidal (Eds.), *Andean Metallogeny: New Discoveries, Concepts and Updates. Society of Economic Geologists, Special Publication 11*, 167–186.

Perelló, J., Muhr, R., Mora, R., Martinez, E., Brockway, H., Swaneck, T., ... Argandona, R. (2010). Wealth Creation through Exploration in a Mature Terrain: The Case History of the Centinela District, Northern Chile Porphyry Copper Belt. *Society of Economic Geologists, Special Publication*, *15*, 229–252.

Quang, C. X., Clark, A. H., Lee, J. K., & Hawkes, N. (2005). Response of supergene processes to episodic Cenozoic uplift, pediment erosion, and ignimbrite eruption in the porphyry copper province of southern Peru. *Economic Geology*, *100*, 87–114.

Reich, M., Palacios, C., Vargas, G., Luo, S., Cameron, E. M., Leybourne, M. I., ... You, C.-F. (2009). Supergene enrichment of copper deposits since the onset of modern hyperaridity in the Atacama Desert, Chile. *Mineralium Deposita*, *44*, 497–504.

Reich, M., & Vasconcelos, P. M. (2015). Geological and economic significance of supergene metal deposits. *Elements*, *11*, 305–310.

Richards, J. P. (2011). Magmatic to hydrothermal metal fluxes in convergent and collided margins. *Ore Geology Reviews*, *40*, 1–26.

Riquelme, R., Hérail, G., Martinod, J., Charrier, R., & Darrozes, J. (2007). Late Cenozoic geomorphologic signal of Andean forearc deformation and tilting associated with the uplift and climate changes of the Southern Atacama Desert (26 S–28 S). *Geomorphology*, *86*, 283–306.

Riquelme, R., Tapia, M., Campos, E., Mpodozis, C., Carretier, S., Gonzalez, R., ... Marquardt, C. (2017). Supergene and exotic Cu mineralization occur during periods of landscape stability in the Centinela Mining District, Atacama Desert. *Basin Research*, https://doi.org/10.1111/bre.12258.

Seedorff, E., Dilles, J. H., Proffett, J. M., Einaudi, M. T., Zurcher, L., Stavast, W. J. A., ... Barton, M. D. (2005). Porphyry deposits: Characteristics and origin of hypogene features. In: J. W. Hedenquist, J. F. H. Thompson, R. J. Goldfarb & J. P. Richards (Eds.), *Economic Geology 100th Anniversary Volume. Society of Economic Geologists, Inc.*, 251–298.

Segerstrom, K. (1963). Matureland of northern Chile and its relationship to ore deposits. *Geological Society of America Bulletin*, *74*(4), 513–518.

Sillitoe, R. H. (2005). Supergene oxidized and enriched porphyry copper and related deposits. In: J. W. Hedenquist, J. F. H. Thompson, R. J. Goldfarb & J. P. Richards (Eds.), *Economic Geology 100th Anniversary Volume. Society of Economic Geologists, Inc.*, 723–768.

Sillitoe, R. H., & McKee, E. H. (1996). Age of supergene oxidation and enrichment in the Chilean porphyry copper province. *Economic Geology*, *91*, 164–179.

Sillitoe, R. H., & Perelló, J. (2005). Andean copper province: Tectonomagmatic settings, deposit types, metallogeny, exploration, and discovery. In: J. W. Hedenquist, J. F. H. Thompson, R. J. Goldfarb & J. P. Richards (Eds.), *Economic Geology 100th Anniversary Volume. Society of Economic Geologists, Inc.*, 845–890.

Steinmann, G., Stappenbeck, R., Sieberg, A. H., & Lissón, C. I. (1929). *Geologie von Perú: mit 9 Tafeln, 271 Textabbildungen und Geologischer Karte 1: 3000000*. Heildelberg: Carl Winters Universitätsbuchhandlung.

Tomlinson, A. J., & Blanco, N. (1997). Structural evolution and displacement history of the West Fault System, Precordillera, Chile: Part 2, postmineral history. In *Congreso Geológico Chileno* (Vol. 8, pp. 1878–1882). Antofagasta.

Vasconcelos, P.-M. (1999). K-Ar and 40Ar/39Ar geochronology of weathering processes. *Annual Review of Earth and Planetary Sciences, 27*, 183–229.

Vasconcelos, P. M., Reich, M., & Shuster, D. L. (2015). The paleoclimatic signatures of supergene metal deposits. *Elements*, *11*, 317–322.

Wilkinson, J. J. (2013). Triggers for the formation of porphyry ore deposits in magmatic arcs. *Nature Geoscience*, *6*, 917.

Witt, C., Rangin, C., Andreani, L., Olaez, N., & Martinez, J. (2012). The transpressive left-lateral Sierra Madre de Chiapas and its buried front in the Tabasco plain (southern Mexico). *Journal of the Geological Society*, *169*, 143–155.

Wu, L., Monié, P., Wang, F., Lin, W., Ji, W., Bonno, M., ... Wang, Q. (2016). Cenozoic exhumation history of Sulu terrane: Implications from (U–Th)/He thermochrology. *Tectonophysics*, *672*, 1–15.

SUPPORTING INFORMATION

Additional Supporting Information may be found online in the supporting information tab for this article.

FIGURE S1 U–Pb concordia spots for samples DC12-03, DC12-06, DC12-08 and DC12-10.

FIGURE S2 HeFty modelling.

TABLE S1 $^{39}Ar/^{40}Ar$ and K/Ar supergene and exotic ages of the Centinela District.

TABLE S2 Zircon U–Pb data.

TABLE S3 Apatite fission track data.

TABLE S4 Apatite (U–Th)/He data.

Using cosmogenic nuclides to reconstruct the Miocene evolution of the Centinela basin

Abstract

In the hyperarid Atacama Desert, northern Chile, Neogene sediments host copper enriched layers (supergene and exotic mineralization). The environmental conditions of their formation are still debated. Current mines are excavated into relatively thin (<200 m) Neogene basins whose infill chronology is poorly constrained. We took advantage of two of these mining pits, and sampled for ^{10}Be and ^{21}Ne cosmogenic nuclide analysis at depths between ~150 m and ~65 m in the El Tesoro pit and between ~67 m and ~12 m in the Mirador pit. Some of the samples were taken within the copper rich layers. Basin sediments are deposited with a prior cosmogenic nuclide content acquired on hillslopes. Then during the sedimentation in the basin, cosmogenic nuclide concentrations evolve through the competing production (decreasing with depth) and disintegration (except for ^{21}Ne). Previous works on Plio-Pleistocene sediment showed that the different evolution of ^{10}Be and ^{21}Ne allow the burial age to be determined. In our case, applying cosmogenic nuclides to document the burial evolution of these Cenozoic sediments and at such large depths constituted a challenge. Nevertheless, we hypothesized that cosmogenic nuclides may help to constrain the sedimentation chronology in this particular environment because erosion and sedimentation processes are *a priori* slow and prior concentrations high.

We obtained measurable cosmogenic concentrations for 14 samples. The ratio between the two cosmogenic nuclides indicate a maximum burial age of 12 Ma (minimal erosion rate of 15 m.My^{-1}) in the El Tesoro pit. The burial age is surprisingly similar from bottom to top, indicating a probable rapid infilling. This age is much younger than previously inferred by lateral correlation of another K/Ar (22 Ma) and corresponds to the age of another exotic mineralization event recognized in this region. Assuming a two-step scenario composed of source erosion and basin stochastic sedimentation, we processed a Monte-Carlo inversion to find the best-fit (χ2 minimization) sedimentation scenario. We found that inversion results are strongly dependent on the muonic production scheme. Interestingly, the similarity in concentrations from bottom to top pleads for a quite low production at depth. Our data finally indicates a quick infill between 12.5 and 10 Ma accounting for ~100 m of deposition. Such a high sedimentation rate may be explained by Miocene faults that blocked sediment routing. In the El Tesoro pit, the exotic copper layer deposited during a decrease of the sedimentation rate.

6.1 Introduction

During the past decades, major improvements have been realized to quantify geomorphologic processes, especially thanks to the use of cosmogenic nuclides. Cosmogenic nuclides are commonly used to date Quaternary events and processes. The limits of the methods have been pushed (e.g. Granger et al., 2013) to document glacier erosion and moraine ages (Fabel and Harbor, 1999; Brook et al., 1995; Putkonen and Swanson, 2003) or to date remnant Miocene to Pleistocene surfaces (Hancock et al., 1999; Dunai et al., 2005). Nevertheless, determining older surfaces or sediment ages and erosion-sedimentation rates (>> 1 Ma) still represents an important challenge, peculiarly because of the many limits imposed by the initial erosion rates of the source, by the radiogenic decay or because of uncertainties relative to production rates (Gosse and Phillips, 2001; Granger et al., 1996).

Long-term geomorphic processes are commonly studied through landscape evolution models (e.g. Tucker and Hancock, 2010) or using experimental device (Babault et al., 2005), as resumed in Bishop (2007). Low-temperature thermochronology provide information about denudation and sedimentation rates with a time resolution which exceeds 100 ka periods. Recent paleo-erosion rate estimates in Tien Shan showed the potential of cosmogenic nuclides to reconstruct the variations of some catchment denudation over the last 9 Ma (Charreau et al., 2011). Cosmogenic nuclides have been also used to date the burial age and rate of Late Miocene sediment in Atacama over the last 10 Ma (Davis et al. 2014). To date, these studies encompass the oldest periods over which denudation or sedimentation were estimated using cosmogenic nuclides, with a time resolution which approaches the global climate change period (<< 1 Ma).

Documenting paleo-denudation rates and paleo-sedimentation rates associated with gravel deposits in which supergene exotic copper mineralization is hosted would provide valuable data to constrain the paleo-environmental conditions in which these kinds of ore deposit are formed. Indeed, it is thought, although debated, that supergene enrichment of copper occurs during low erosion periods, when the topography is relatively stable for enriched soil layers to thicken. A preliminary sedimentological study carried out in the Tesoro mine, in the Centinela District, seems to show that supergene enrichment of copper occurs during low erosion periods, when the topography is relatively stable for enriched soil layers to thicken (Fernandez-Mort et al., 2015).

Contrastingly, other authors proposed that such enrichment occurs during a renewed surface uplift, possibly associated with increased denudation and sedimentation rates, see review in Sillitoe (2005). To date, there is no paleo-denudation or sedimentation data allowing to decipher between these two end-member models.

To study the geomorphologic conditions for supergene copper mineralization, we applied a new cosmogenic nuclides related approach to the natural case of the Centinela district in Atacama, where the access to supergene copper mineralization hosted within sediments was possible.

Atacama Desert, the world's driest Desert (Clark, 2006) is one of the best places on Earth to use cosmogenic nuclides to resolve such problem. Due to absence or really low precipitation rates, erosion rates are one of the lowest in the world, presenting the advantage to show high cosmogenic nuclides concentrations. Such high concentrations are favorable to measure radioactive cosmogenic nuclides in Miocene sediments and use them to obtain information about ages, paleo-denudation or sedimentation rates over that period (see Figure 6.1). Other cosmogenic studies took advantage of these very low landscape evolution rates in Atacama to date Neogene surfaces and quantify post 10 Ma sedimentation rates (Dunai et al., 2005; Davis et al., 2014; Evenstar et al., 2009; Kober et al., 2007; Nishiizumi et al., 2005; Placzek et al., 2010; Jungers et al., 2013; Owen et al., 2013; Wang et al., 2015, Placzek et al., 2014; Cesta and Ward, 2016).
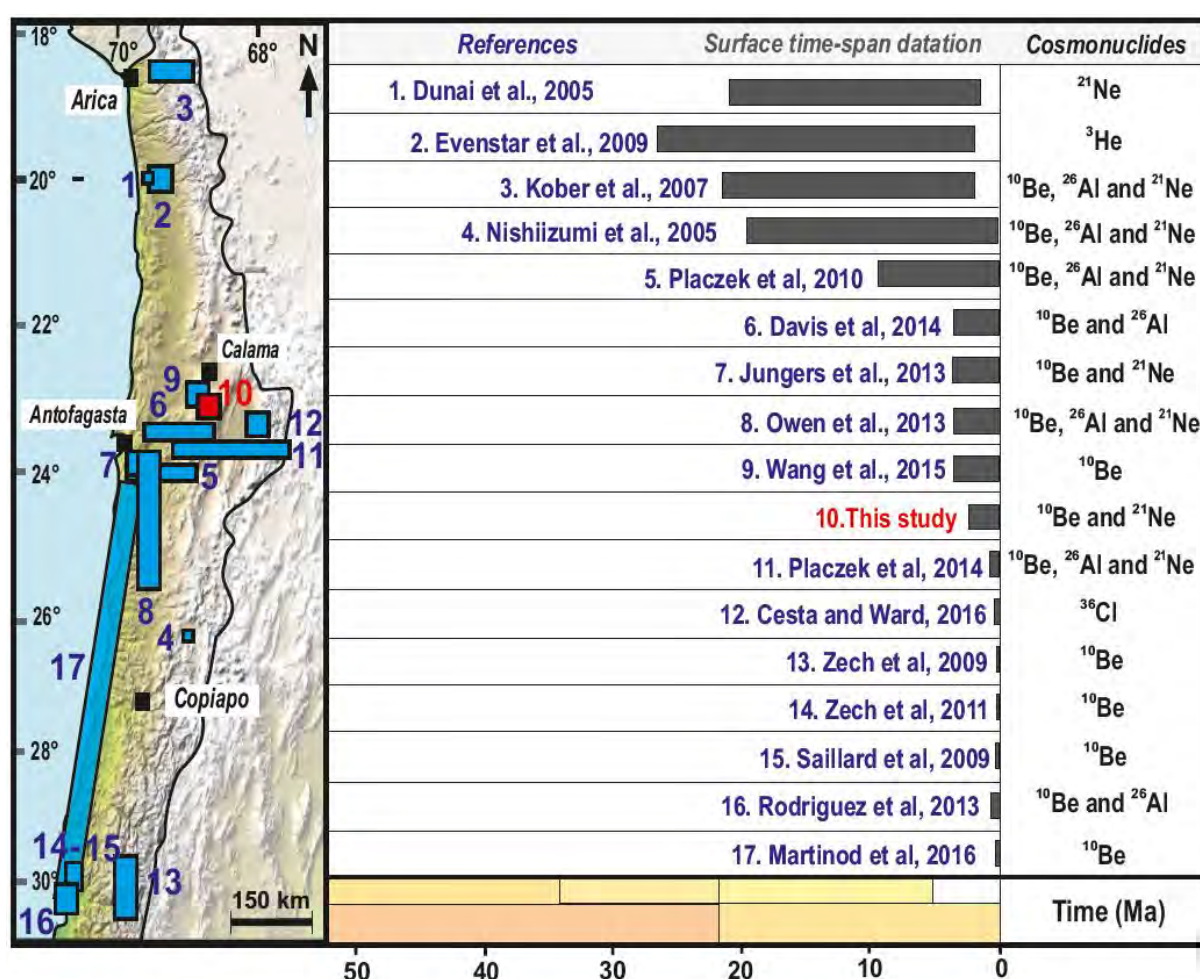
Figure 6.1 – Location of previous studies using cosmogenic nuclides to date surfaces from 18°to 31°S, as pediments and marine terraces encountered in northern Chile.

Yet, no one of these studies refer to denudation or sedimentation rates over periods older than 10 Ma. Thanks to open-pit mines of the Centinela mining district it was possible to sample sediment hosting supergene exotic copper at different depths between the surface and ~150 m below the surface in two pits.

These sediments are poorly dated (Riquelme et al., 2017), but are older than ~9.5 Ma, the age of an ignimbrite interbedded in the upper part of the sedimentary association covering the regional surface. By coupling [10]Be and [21]Ne, we aimed at dating and quantifying the sediment rate variations before, during and after the exotic copper ore deposit.

Considering that sedimentologic evidence indicate that exotic Cu formation is syn-sedimentary, we aim at answering a simple question: does the exotic Cu mineralization precipitated during a period of low or high sedimentation rate?

In this work we pushed the limits of the burial dating method and applied it to date especially "ancient" old sediments, estimated to be early Miocene (Tapia et al., 2012; Oether et al., 2016; Riquelme et al., 2017). On the same samples we also quantified erosion rates at deeper depths than done before. We thus needed to adapt the burial method as the ½ life of the [26]Al/[10]Be doesn't allow to access older burial than 6 Ma (Balco and Shuster, 2008).

The cosmogenic nuclides concentration encountered in a basin at z depth is the results of three step: (i) bedrock source erosion; (ii) transport; (iii) and finally the deposition in the basin. The resulting cosmogenic concentrations depend on the source erosion rate, transit velocity, and sedimentation rate.
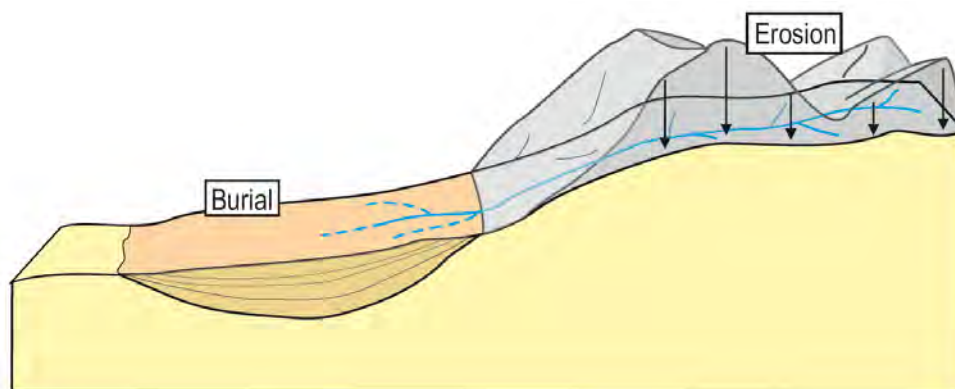
Figure 6.2 – Schematic representation of the relationship between a watershed where occur erosive processes and his associated basin where occurs the sediment burial (Regard, personal com.).

Vincent Regard developed a new two steps source-to-sink model allowing to predict [10]Be and [21]Ne concentrations for different scenarios of source denudation and basin sedimentation, assuming that the time of sediment transport duration is negligible (Figure 6.2). I used this model in a Monte Carlo approach to explore the possible paleo-environmental scenarios explaining the cosmogenic concentrations measured in the sediment of two open pits of the Centinela district.

This model is similar to a two-box system. The first box represents the caracteritics of the eroding basin (watershed) and the second box, the sedimentary basin where burial occurs (Figure 6.3). In the the first one is fixed several informations as the mean altitude of the eroding watershed and his supposed erosion rates.

In the second box are fixed the sediment pile thickness through time but the sedimentary rates are "opened" meaning that they should reflect the concentration evolution through the pile. In both case, the production rates are fixed by the user and the concentration measured used.
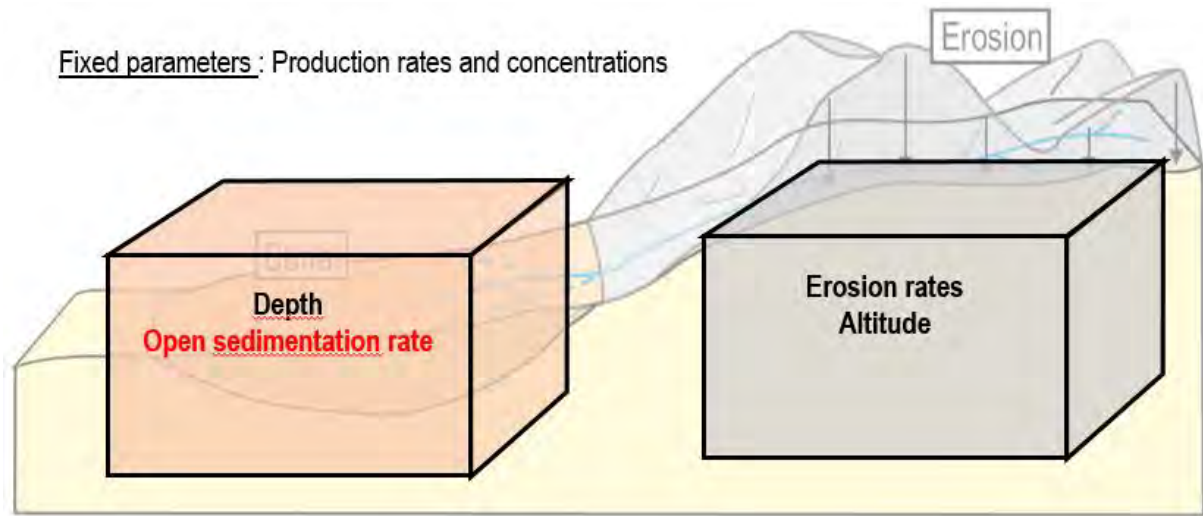
Figure 6. 3 – Schematic representation of the relationship between a watershed and his associated basin (Regard, personal com.).

In the following of this chapter will be explained the testing of this method with pre-10 Ma data, obtained at 50 km south this PhD study zone, to verify its possible application with ^{26}Al and ^{10}Be. Then will be presented the different ages calculated with raw cosmogenic nuclides concentrations, then with one calculated with the model as the tested erosion rates scenariies aand sedimentation rates obtained.

6.2 Geological Settings.

The Centinela District is located in the Precordillera of the Andean fore-arc, in northern Chile at approximately 23°S (Figure 6.1). The Domeyko Fault System is an Eocene strike-slip faults system, constituting the Precordilla at these latitudes (Mpodozis et al., 2012).

The movements along this fault system allowed the shallow emplacement of Eocene porphyry copper. Their exhumation drove the supergene weathering responsible for the formation of supergene copper ore deposits found in this area. Supergene enrichment took place between ~25 and ~12 Ma (Riquelme et al., 2017). The mines exploited in the northern part of the Centinela District are El Tesoro, El Tesoro Norte-este and Mirador (Figure 6.4).

A poorly consolidated gravel cover has been deposited since the Late Eocene to nowadays (Mora et al., 2004, Perello et al., 2010; Riquelme et al., 2017). The gravels have been divided into 4 different units (Riquelme et al., 2017): the Esperanza gravels at the base, over it the Tesoro gravels and the Atravesado gravels, and finally the Arrieros gravels, which form an extensive developed blanket of sediment (Figure 6.4).
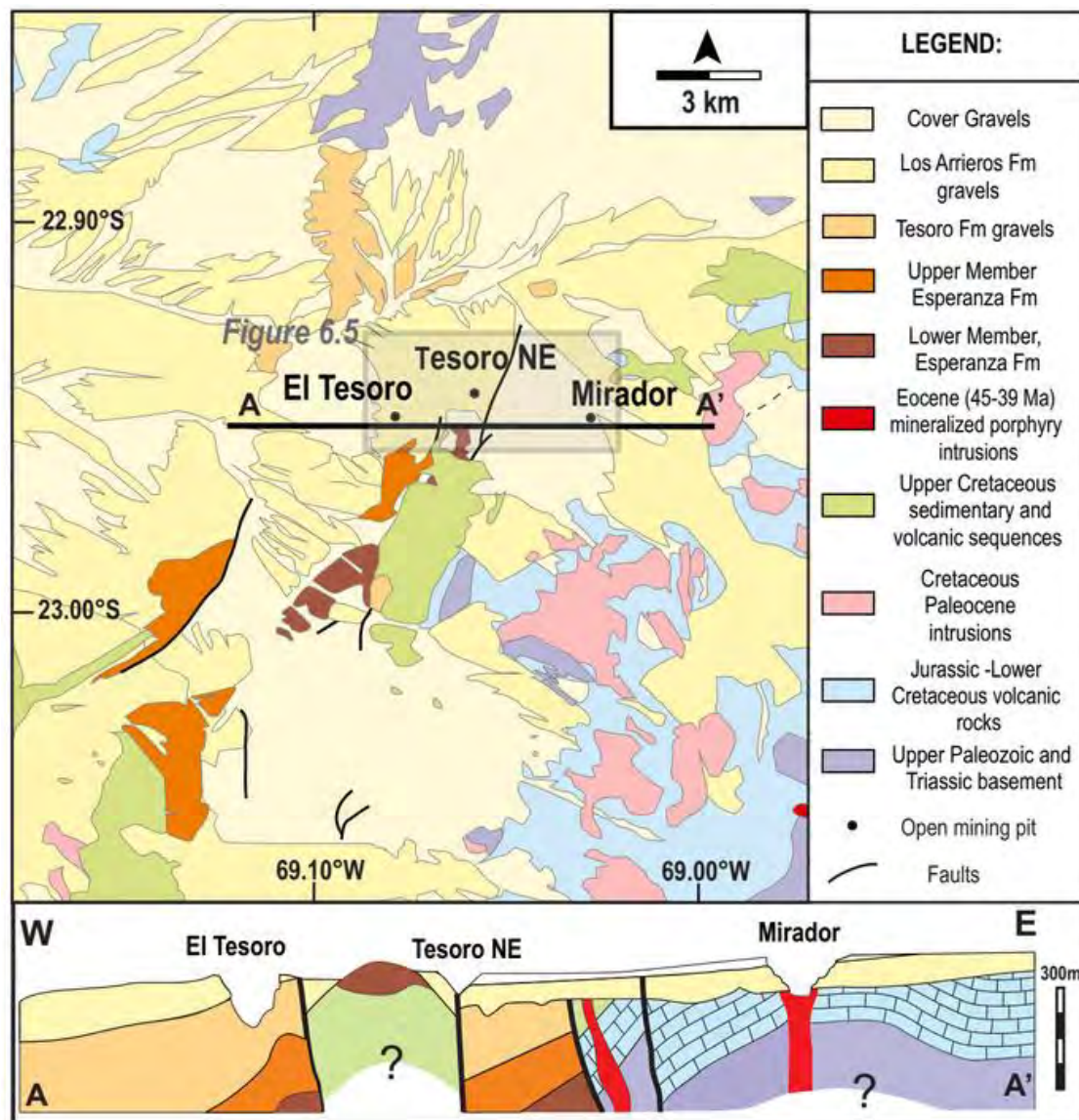
Figure 6.4 – Geological map of the Centinela District and geological profile of the northern section of the district with location of the open mining pits and profile (Tapia et al., 2012).

In this district two types of secondary copper ore deposits are currently exploited. The first type of copper ore deposit is developed at the top of the Eocene Mirador porphyry Cu and results from "in situ" supergene enrichment (Figure 6.4). The second type are the two exotic "*mantos*" exposed within the approximately 200 m thick of gravel succession in which El Tesoro open pit is mining (Figure 6.5).

The Mirador porphyry is covered by ~60 m thick gravel. These gravel include a 9.5 Ma ignimbrite which constitutes the unique direct reference of age of this sequence (Riquelme et al., 2017).

156

Figure 6.5 – View of Tesoro, Tesoro-NE and Mirador open mining pits (Google images 2016), localization figure 6.4

The sediment provenance directions of the sediments infill of the two open mining pits has been described in an internal AMSA report (Blanco and Tomlinson, 2002). On the basis of clast imbrication measuring and the study of sedimentary features, this report points out that in the Tesoro mine, sediment come from the east, whereas sediment located to the east in the Mirador open pit, could come from the north.

6.3 Methods

6.3.1 Analytical methods

6.3.1.1 Sampling

An exceptional access to the sedimentary columns of the El Tesoro and Mirador active mining pits was permitted by Antofagasta Minerals S.A. Company for sampling in December 2013 (location in table 1). Elevations a.s.l. were obtained using a hand GPS, for which we infer and uncertainty of +/- 5m.

Sample	Location			Comments
	Est (UTM)	West (UTM)	Alt (m)	
ET13-01	491816	7462568	2196	
ET13-02	491785	7462578	2198	
ET13-03	491861	7462539	2192	
ET13-04	492007	7462482	2171	
ET13-05	492262	7462376	2139	
ET13-06	492262	7462376	2138,5	
ET13-07	492262	7462376	2137,7	Mineralized blanket
ET13-08	492262	7462376	2137	
ET13-09	492262	7462376	2133	
MIR13-01	496859	7462263	2337	Above 9.5 Ma ignimbrite
MIR13-04	496852	7462258	2342	
MIR13-05	496848	7462256	2343	
MIR13-10	497435	7462048	2310	
MIR13-11	497123	7462010	2292	

Table 6.1 – Location in Universal Transverse Mercator UTM 19S zone and altitude in meters of the samples, (ET: El Tesoro and MIR: Mirador). In grey, samples comprised in the Cu exotic enriched layer.

In the case of El Tesoro, a total of nine samples were collected, five of which at different depth of the exotic copper *manto* (Figure 6.5).
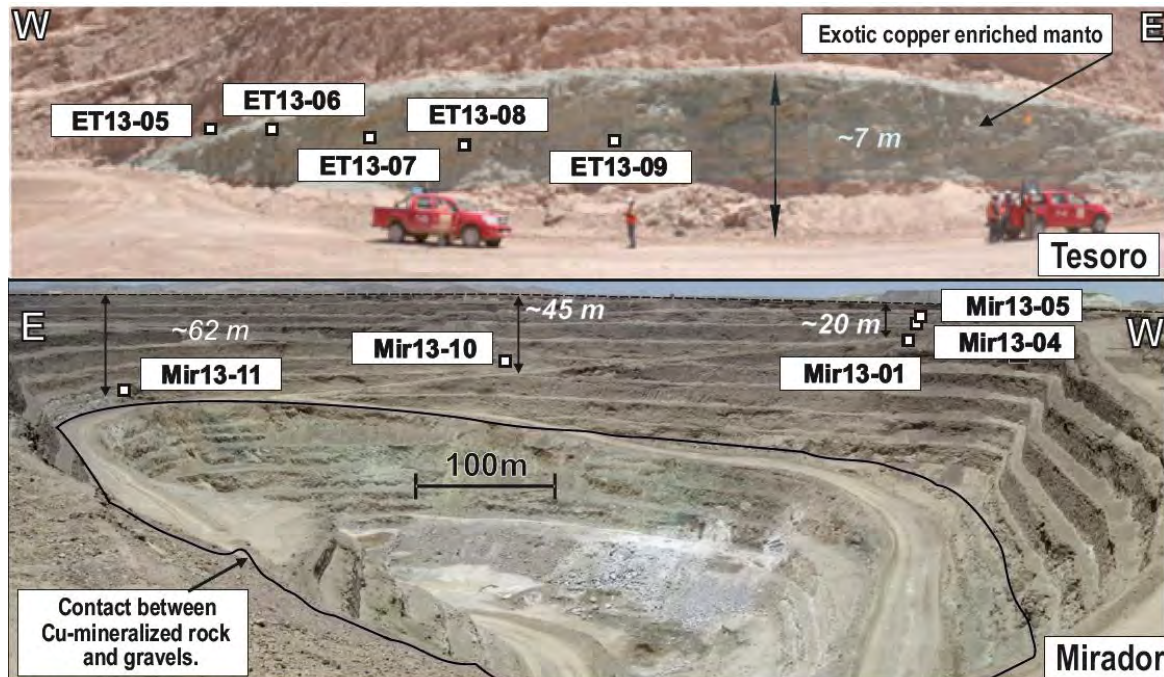
Figure 6.6 – Sampling in the Mirador open pit. The superior mineralized manto in the El Tesoro Mine at 110 m depth in the open pit mine and the sampling Mirador open mine pit.

For the Mirador pit, five samples were gathered from the contact of the porphyry up to the surface.

In the case of MIR13-01 sample, taken just above a reworked ignimbrite dated at 9.5 Ma, we observed that the quartz were probably of volcanic origin, coming from the Mirador tuff (Figure 6.6). Fresh biotites were also found, which reinforces the suggestion that those quartz come from the tuff.

Figure 6.7 – Bipyramidal neoformed quartz found in reworked tuff MIR13-01 dated at 9.5 Ma.
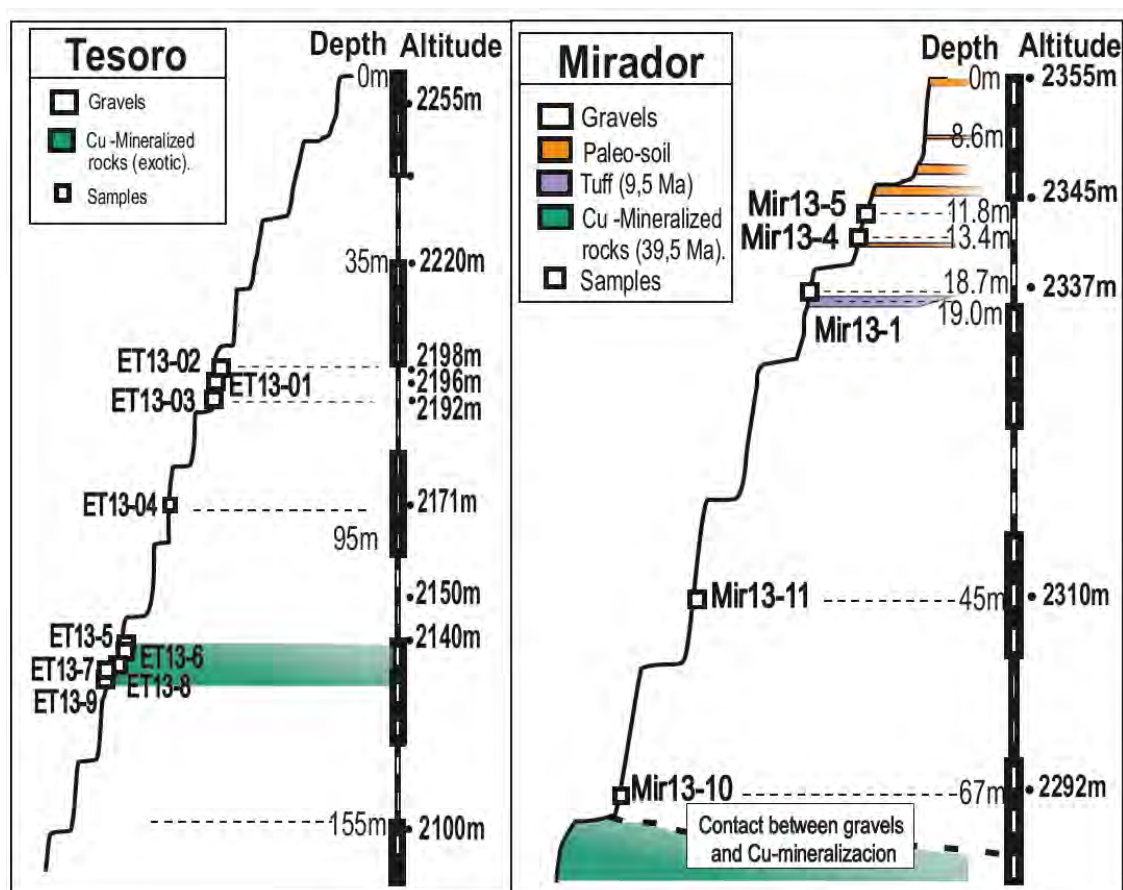
Figure 6.8 – Sample position and major notable features in the Tesoro and Mirador sedimentary columns.

6.3.1.2 Concentration analyses

We selected the sand fraction between 0.5 and 1 mm. The sieving and purification of quartz were realized in the Geosciences Environment Toulouse (GET) laboratory. From an average of 300g of sand the purification ended by 66g of quartz.

The purity of five samples was also verified using X-Ray Diffraction in the GET laboratory. The two only clear visible peaks at ~4.26 and ~3.34 Å are characteristic of the quartz mineral, confirming the purity of the prepared quartz for analyses (Figure 6.8). The chemical separation Be was performed in the CEREGE, in Aix en Provence following the protocol described in Braucher et al. (2011) and in the GET for five samples following the protocol described in Von Blanckenburg et al. (1996).

159
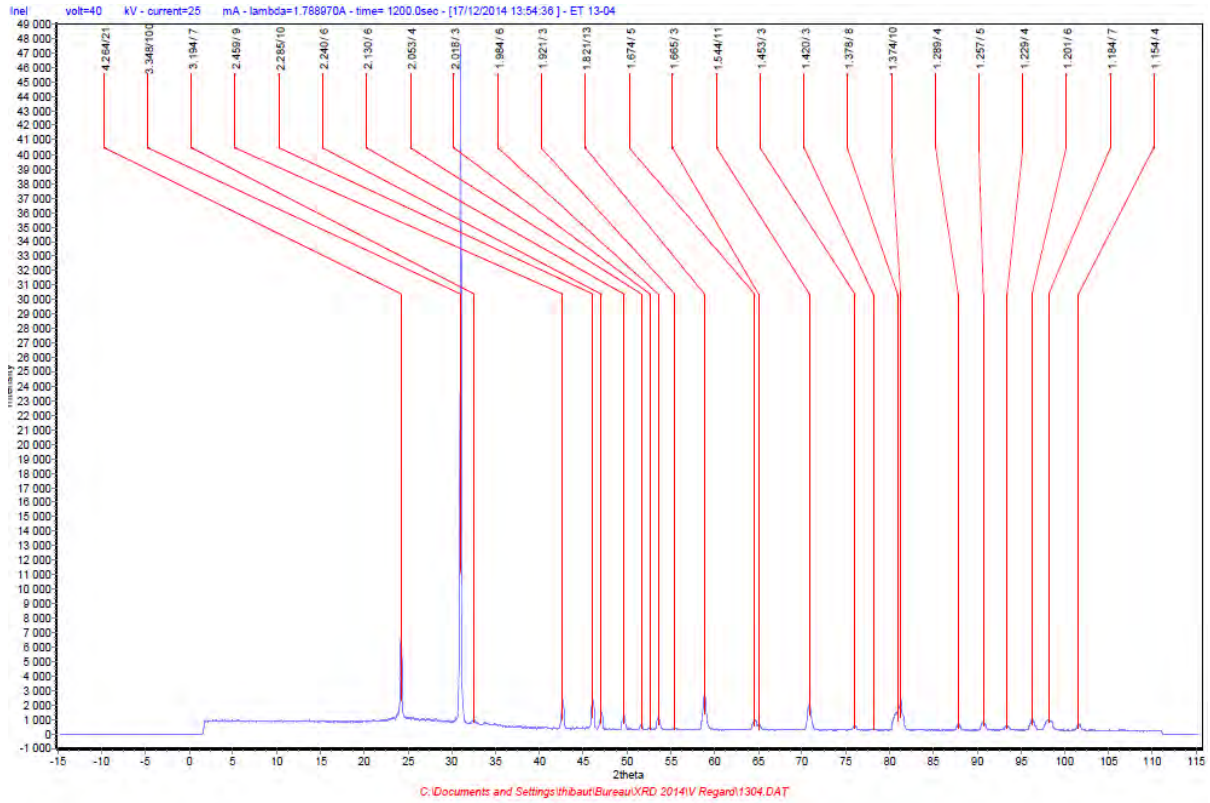
Figure 6.9 DRX of ET13-04, intensity vs 2theta angle. In the upper part of the figure, the values are corresponding to the inter-reticular distances (see annexes for better quality).

[10]Be analyses were performed at the CEREGE (Arnold et al., 2010) meanwhile [21]Ne analyses were performed on the SFT Helix in the CRPG in Nancy, both in France (for further details refer to the Chapter 2.2).

6.3.2 Numerical methods

6.3.2.1 Burial age

For each sample, it is possible to estimate a burial age. This age is based on the following assumptions: 1- Before entering the basin, [10]Be and [21]Ne concentrations correspond to secular equilibrium between production and loss by radioactive decay (for [10]Be only) and erosion, 2- once deposited, the sediments are instantaneously buried, the production in [10]Be and [21]Ne is null, and the [10]Be concentration decreases by radioactive decay.

In order to calculate the theoretical pre-burial [10]Be concentration ($[^{10}Be]_{th}$), we use the [21]Ne concentration, assumed to result from exposure in the source only, and the ratio between [10]Be and [21]Ne $P^{21}Ne/P^{10}Be$, which equals 4.23, 4.08 ± 0.37 or 4.31 ± 0.17 according to, respectively, Kober et al. (2011), Balco and Shuster (2009) and Goethals et al. (2009). Following this consideration, [10]Be concentration before burial is thus given by:

$$[^{10}Be_{th}] = \left. [^{21}Ne] \middle/ \frac{P^{10}Be}{P^{21}Ne} \right.$$

Then the ^{10}Be concentration after burial ^{10}Be$_m$ has been reduced by radioactive decay:

$$[^{10}Be_m] = {}^{21}Ne_{th}e^{-\lambda t}$$

Where lambda is the ^{10}Be half-life $(1.387 \pm 0.012) \times 10^6$ yr (Korschinek et al., 2010; Chmeleff et al. 2010).

Thus, the apparent burial duration is:

$$t = \frac{1}{\lambda} \ln \frac{^{10}Be_{th}}{^{10}Be_m}$$

This burial duration or burial age is only an estimate that depends on the initial assumptions. Indeed, part of the ^{21}Ne concentration used to calculate the pre-burial ^{10}Be concentration ($[^{10}$Be$]_{th}$) may result from acquisition during sedimentation in the basin. The true pre-burial ^{10}Be concentration is thus lower than $[^{10}$Be$]_{th.}$. On the other hand, the measured ^{10}Be concentration does not result from radioactive decay only. Part of this concentration has been acquired by ^{10}Be production during sedimentation. Neglecting this burial ^{10}Be concentration production leads to underestimate the true age. We see that the two assumptions made to calculate the burial age tend to overestimate or underestimate the true age. A better estimate of the burial age will result from the inversion of data by considering ^{10}Be and ^{21}Ne production during sedimentation. At this stage, we can only predict that deviation between the true and calculated burial ages will increase with decreasing sedimentation rate.

Preliminary tests show that for sedimentation rates larger than 20 m.My^{-1}, the difference between true and calculated age is lower than 1 Ma.

6.3.2.2 Modelling

The code used to predict ^{10}Be and ^{21}Ne concentrations at depth in sediment was written by Vincent Regard, under the R program. We assume a two-box model constituted of an erosive source and a basin (Figure 6.3). In order to simplify the nature of the system, the assumption has been made that the transport duration between source and basin is negligible.

The acquisition of cosmogenic nuclide during this transport is finally implicitly included in the acquisition during the surface exposure of a sediment layer before its burial by the following one.

The forward model generates values of ^{10}Be and ^{21}Ne concentrations at different depths in the basin for different time steps. The basin is progressively filled by sediment layers of randomly chosen thickness between a specified min and max.

The constant time step is imposed as model parameter. The ^{10}Be and ^{21}Ne concentrations are calculated at each time step in each layer according to their previous values and to the thickness of sediment above the considered layer. For a new layer, the initial ^{10}Be and ^{21}Ne concentrations correspond to source concentrations. These concentrations depend on an imposed elevation and a specified erosion rate. The main model parameters are thus: the source erosion rate, possibly variable with time, and the sedimentation rate (sediment layer divided by time step), possibly variable with time.

Precision

The accuracy of the models includes the error about AMS measurement and chemical preparation, of the duration of initial exposure and the uncertainties about the cosmogenic nuclide production (Granger and Muzikar, 2001).

Production rates

A good knowledge of the cosmogenic nuclide production rates is essential to accurately predict the cosmogenic nuclide concentrations in sediment. The production rate at the surface, mostly produced by spallation, is relatively well known (e.g. Martin et al., 2017). On the other hand, the production rates at depth are harder to calibrate and there are different models of cosmogenic nuclide production by muons at depth (e.g. Heisenberg, 1998; Gosse and Phillips, 2001; Braucher et al., 2011).

In the late nineties several projects were carried out to quantify the muonic flux deep beneath the surface (Bilokon et al., 1989; Berger et al., 1989; Ambrosio et al., 1995; Heisenberg, 1998).

Nucleonic production rates at the surface have been expressed as a function of depth, modeled by a simplistic exponential law:

$$P_{X,n}(z) = A_0 e^{\frac{-z}{L_0}}$$

With P for cosmogenic nuclide production (at.g^{-1}.yr^{-1}) at depth z (cm), L_0 the nucleon decay length (cm) (Reedy et al., 1994), with $A_0 \sim 5$ at.g^{-1}.yr^{-1} for the quartz.

The muonic production rate cannot be expressed as simply as the nucleonic component. Granger and Smith (2000) proposed the sum of three exponential terms to model the production by neutrons, fast muons and stop muons.

$$P_{X,\mu}(z) = A_1 e^{-z/L1} + A_2 e^{-z/L2} + A_3 e^{-z/L3}$$

With P for cosmogenic nuclide production (at.g^{-1}.yr^{-1}) at depth z (cm), A as surface production by neutrons (1) fast muons (2) and stop muons (3), and L the attenuation depths for the three particles, respectively (cm).

Several other models were proposed either based on calculations (Heisenger et al., 2002a, 2002b), or by determining the relative contributions and attenuation lengths of the different particles from site calibration (Braucher et al., 2003, 2011, 2013; Kim and Englert, 2004; Lupker et al., 2013; Phillips et al., 2015).

In our study three different models were considered, which present different attenuation lengths. The respective attenuation lengths and production ratios for the different are exposed in table 6.2 and table 6.3.

Studies	Attenuation length (cm)		
	Neutrons (L_1)	Negative muons (L_2)	Fast muons (L_3)
Granger and Muzikar, (2001)	160	738	2688 - 4360
Braucher et al. (2003 ; 2011)	160	1500	5300
Lupker Pers. Com.	160	1500	4320

Table 6.2 – Attenuation length (cm) from Granger and Muzikar, (2001); Braucher et al., (2003, 2011); Lupker, personal communication.

In the case of Granger and Muzikar; 2001 the authors propose two different attenuation lengths.

Studies	Production coefficients (at.g^{-1}.yr^{-1})		
	Negative muons (A_1)	Fast muons 1 (A_2)	Fast muons 2 (A_3)
Granger and Muzikar, (2001) ^{10}Be	0.09	0.16	0.19
^{26}Al	0.72	0.02	0.02
Braucher et al. (2003; 2011)	0.015	0.0065	

Table 6.3 – Production coefficients from Granger and Muzikar, (2001) and Braucher et al., (2003, 2011).

In the case of Lupker the calculation of the production rate is calculated in a different way than Granger and Muzikar (2001) and Braucher et al. (2003), the production rate is recalculated for each depth. Surface production rates were calculated with the CRONUS calculator (Balco et al., 2008) at source elevation separately for neutrons and muons. In the case of El Tesoro (latitude 23.5°S and elevation 2300 m) the ^{10}Be production rates are 16.5 at.g^{-1}.yr^{-1} for the neutron production rate and 0.38 at.g^{-1}.yr^{-1} for the total muon production rate and in the case of Mirador.

Inversion models

The inversion model is based on a Monte Carlo simulation and on χ^2 test statistics. One run of the Monte Carlo simulation corresponds to a forward simulation with a given sedimentation scenario, namely a random succession of sediment layer of different thicknesses. The χ^2 is calculated separately for each cosmogenic nuclide at the end of each run.

$$\chi^2 = \sum_{i=1}^{k} \left(\frac{X_i - \mu_i}{\sigma_i} \right)^2$$

With X_i the values obtained by the model, μ_i the obtained analytical values and σ_i the values incertainties

By varying the sedimentation scenario, we search to have the lowest χ^2 for each element. The lowest χ^2 defines the best fit scenario. This scenario may be different for [10]Be and [21]Ne. We also define a bestfit scenario corresponding to the minimum of the sum between the two χ^2.

Application of the inversion to data in the Atacama Desert

The present inversion model has been tested with the [10]Be and [26]Al raw data of the Davis et al. (2014), see location on the Figure 4.1, 50 km south to this PhD study zone. These authors used pairs of [10]Be and [26]Al in different sand samples of a natural depth profile at a place nearby our study site. The sediments sampled by Davis et al. (2014) are located above the ~9.5 Ma ignimbrite, and thus are younger than ~9.5 Ma. In order to model their data, we used the same surface production rates as Davis et al. (2014), and we used the cosmogenic depth production model of Lupker (see further section for details). We imposed a constant source erosion rate of 3m.My[-1]. Then we varied the sedimentation scenario in the Monte-Carlo simulation. The results of the inversion are shown on Figures 6.10, 6.11 and 6.12.
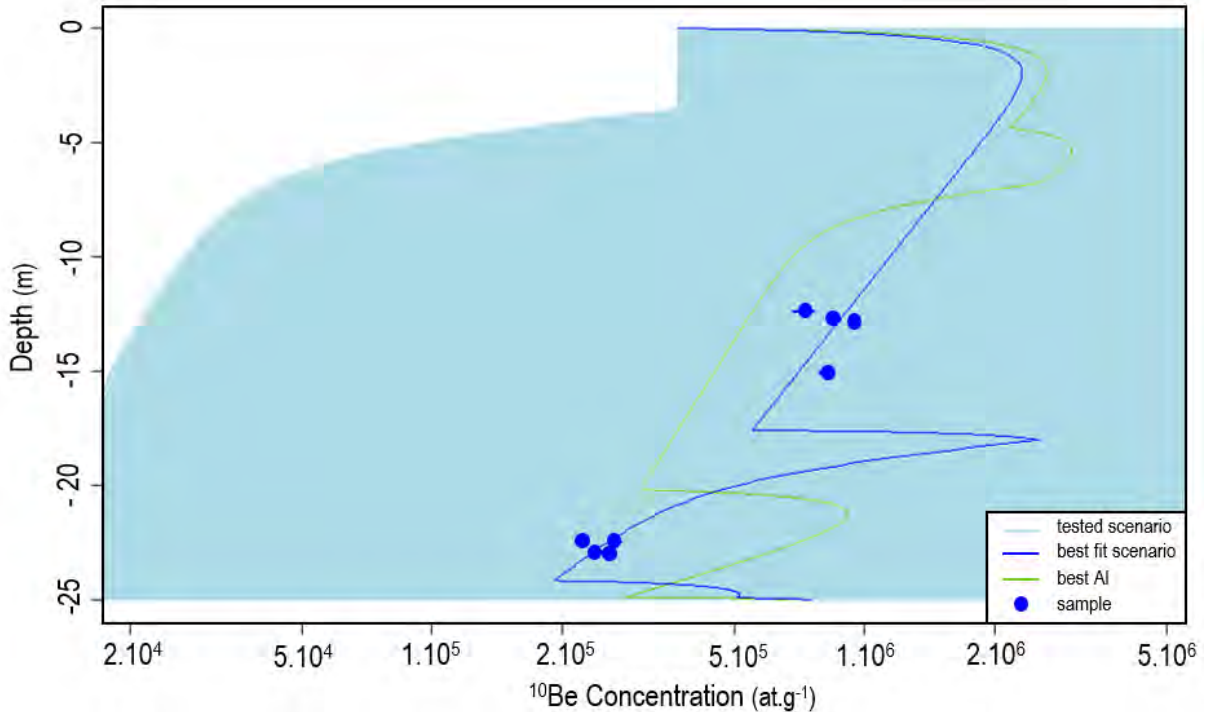
Figure 6.10 – Modeling [10]Be concentration compared with data from Davis et al., (2014). Each path represents a tested scenario. In green, the best [26]Al fit scenario.
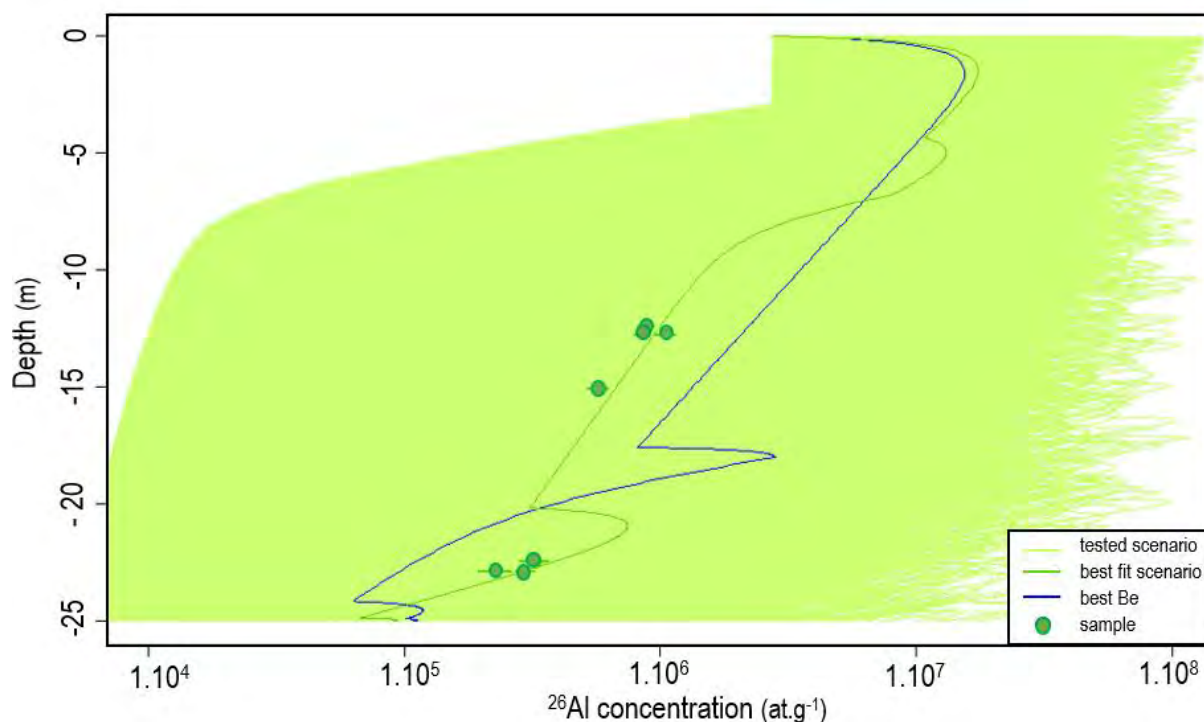
Figure 6.11 – Modeling [26]Al concentration compared with data from Davis et al. (2014). Each path represents a tested scenario. In blue, the best [10]Be fit scenario.

Both inversions for [26]Al and [10]Be concentrations yield a similar best fit sedimentation scenario illustrated on Figure 6.12. Sedimendation rates seem relatively low between 12 to 5 Ma. After 5 Ma sedimentation rates seem to increase (Figure 6.12) with a sedimentation rate of ~ 5 m.My[-1], consistent with the value determined by Davis et al. (2014).
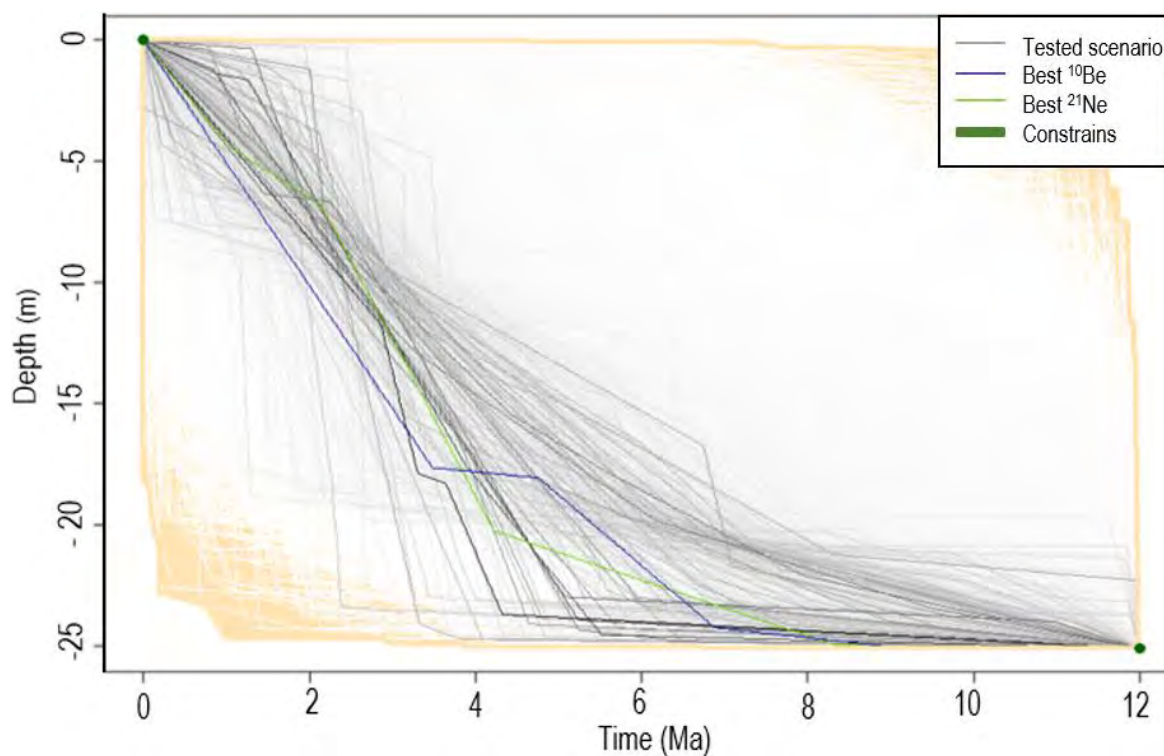
Figure 6.12 – Depth vs Time scenariis determined from data of Davis et al. (2014). The tested scenaris are visible in grey, the darkest the path are the more confident they are, with smallests χ^2.

6.4 Results.

6.4.1 Raw results

6.4.1.1 Concentrations

First of all, all the samples present a measurable ^{10}Be concentration, and, except for the ET13-01 sample, they also all present a measurable ^{21}Ne concentration, with sometime significant associated errors (see Figures 6.13 and 6.14).

The ^{10}Be concentrations of the El Tesoro samples vary from 1.98 10^3 to 7.98 10^3 at.g^{-1} and the ^{21}Ne concentrations vary from 1.4 10^6 to 121 10^6 at.g^{-1}. In the case of the samples of the Mirador open pit, the ^{10}Be concentrations vary from 4.3 10^3 to 9.7 10^3 at.g^{-1} and the ^{21}Ne concentration from 10.3 10^6 at.g^{-1} to 140.10^6 at.g^{-1}.

Sample	Cosmogenics nuclides concentration (at.g^{-1})			
	^{10}Be (10^3)	± (10^3)	^{21}Ne (10^6)	± (10^6)
ET13-01	8,0	3,3	-	-
ET13-02	7,8	4,0	5,7	2,7
ET13-03	5,2	2,6	6,5	4,6
ET13-04	3,6	1,7	121	3,9
ET13-05	7,5	1,8	8,0	4,3
ET13-06	6,2	7,1	7,2	6,3
ET13-07	3,9	1,9	7,4	3,7
ET13-08	2,0	0,9	5,5	3,5
ET13-09	3,9	1,8	1,4	3,5
MIR13-01	68,0	6,2	10,3	3,1
MIR13-04	657,0	32,3	118	4,5
MIR13-05	969,8	46,8	140	6,8
MIR13-10	4,3	2,1	17,4	4,4
MIR13-11	5,1	8,4	50,2	5,1

Table 6.4 – Concentrations in ^{10}Be and ^{21}Ne in at.g^{-1} for the El Tesoro (ET) and Mirador (MIR) samples

In comparison to the data from Davis et al. (2014), in the El Tesoro samples the ^{10}Be concentrations are two orders of magnitude lower meanwhile in the case of the Mirador, the post 10 Ma (cf. position relative to the 9.5 Ma-old ignimbrite) samples show ^{10}Be concentrations ten times more enriched in ^{10}Be. The post 10 Ma samples (MIR13-04 and MIR13-05) from Mirador show similar ^{21}Ne concentrations to the surface samples from Dunai et al. (2005) and from Jungers et al. (2013) (see location in Figure 6.1).
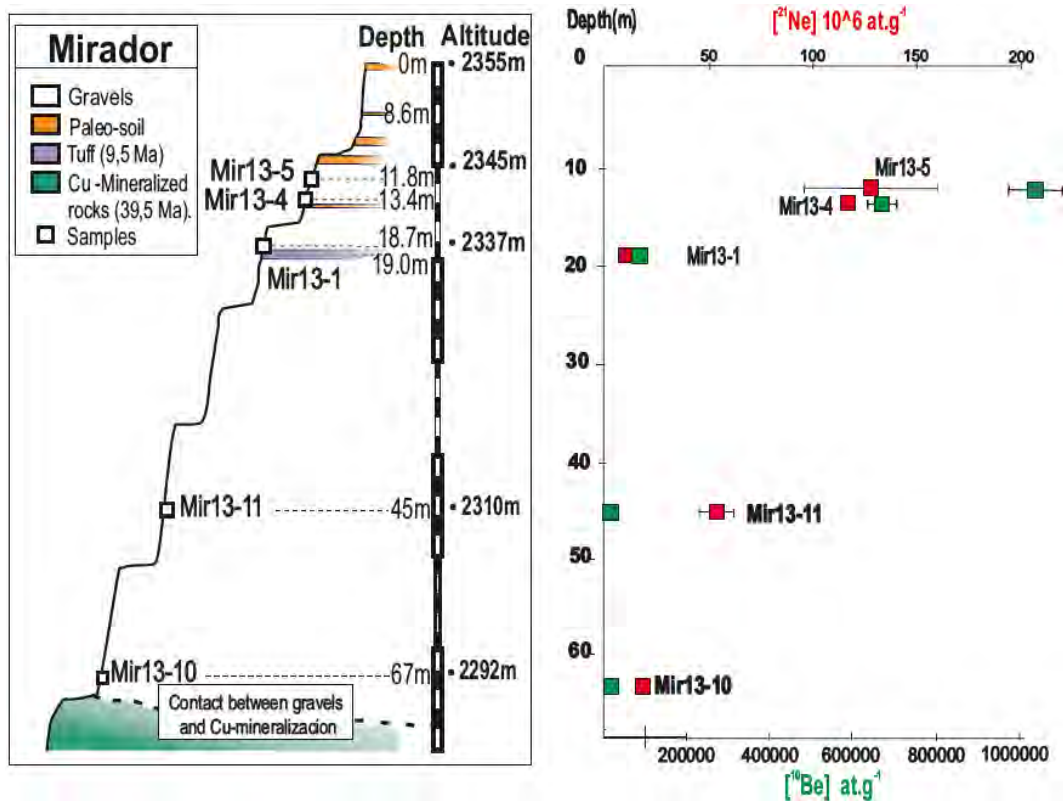
Figure 6.13 – ^{21}Ne and ^{10}Be concentrations at depth in the Mirador pit.
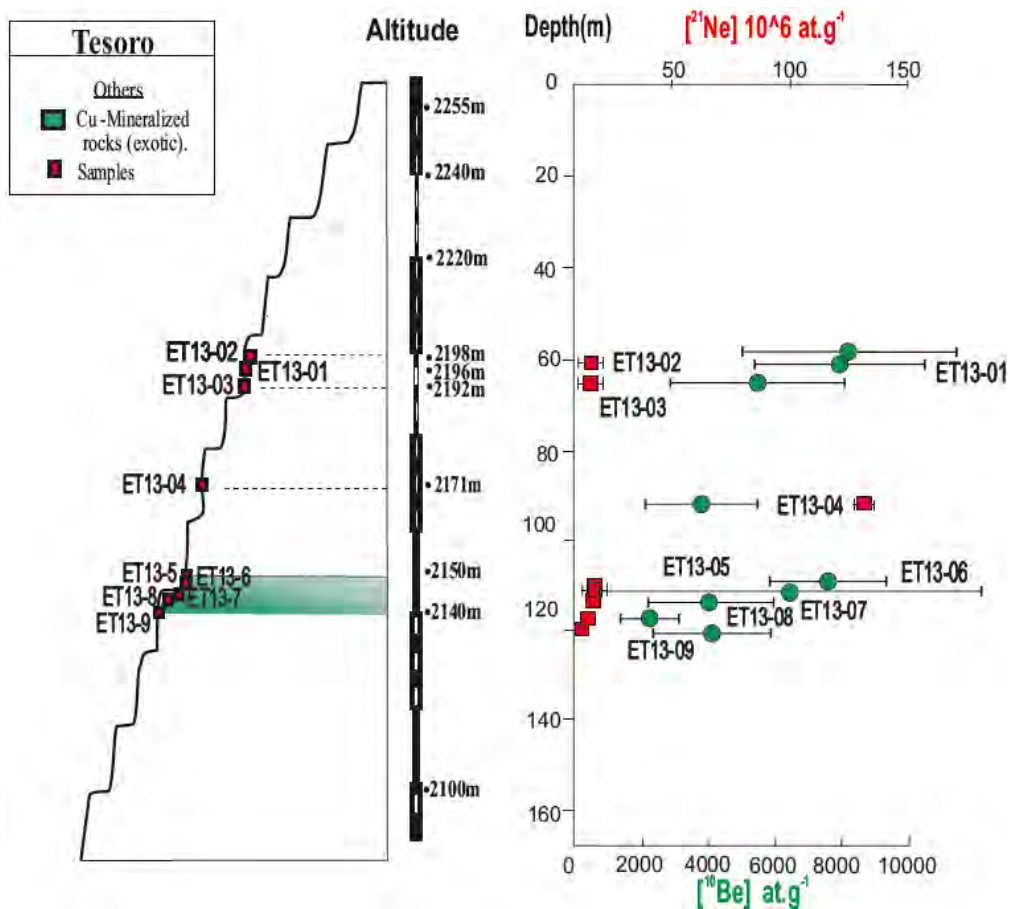
Figure 6.14 – ^{21}Ne and ^{10}Be concentrations in El Tesoro at depth.

6.4.1.2 Burial dating ages

In the case of the Tesoro samples, the minimum deposit ages range between 8.9 ± 0.6 and 13.0 ± 3.2 Ma with a slight decrease in the ages towards the surface (Figure 6.14).
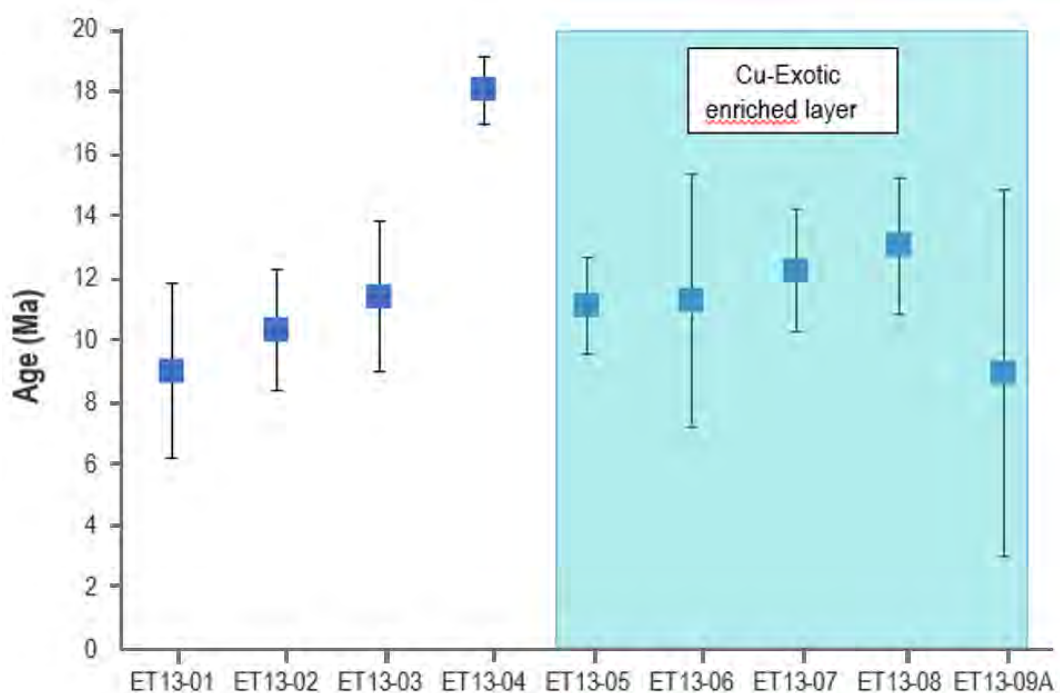
Figure 6.15 – Ages calculated for each Tesoro sample with associated errors.

In the case of the Mirador samples (Figure 6.15), maximum deposit ages range from 7.1 ± 0.2 Ma to 15.6 ± 3.5 Ma. Those ages do coincide with the only absolute dating of the Mirador column: the 9.5 Ma ignimbrite which separates the samples with a maximum age lower than 9 Ma from those which have an older maximum age.
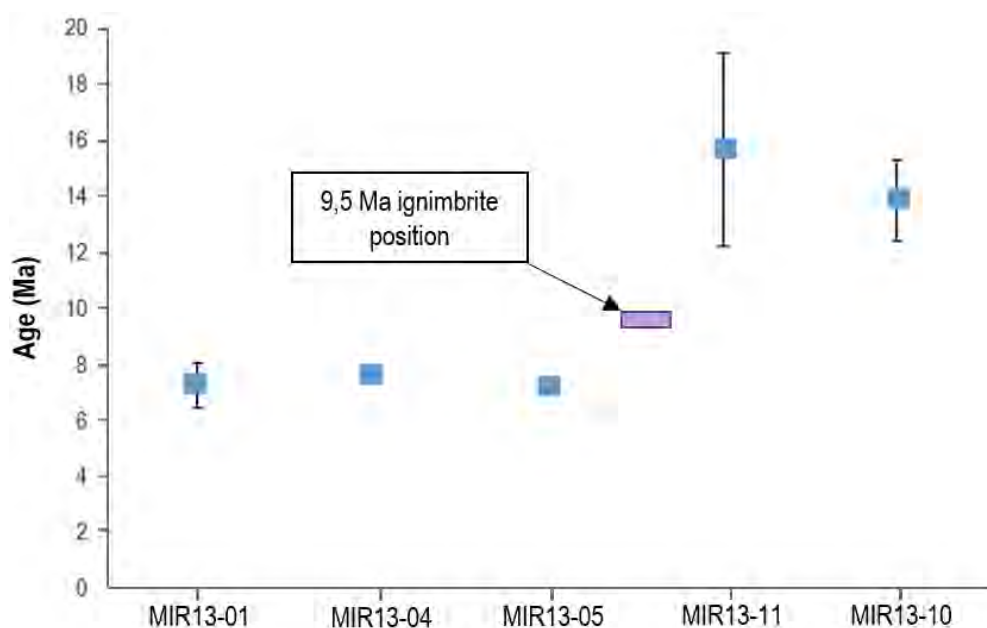
Figure 6.16 – Ages calculated for each Mirador sample with associated errors.

6.4.2 Modelling results

To establish which model fit best the results obtained in the Centinela District we present the results of model runs realized making variations with two parameters: the muon production (the values corresponding to those models are presented in chapter 4) and the erosion rates of the watershed.

6.4.2.1 Model of muon production

The considered models are Granger and Muzikar (2001) (Gr); Braucher et al. (2003) (Br) and Lupker from personal communication (Lu.e) to Vincent Regard.

In this section are presented the χ^2 results (Figure 6.17-6.19) of the modeling of the results according to the erosion rates variation of the initial source in Tesoro and Mirador mines for the samples located beneath the 9.5 Ma ignimbrite (see figure 6.7). Initial erosion rates vary from 50 m.My^{-1} to 1000 m.My^{-1}, with a different try every 50 m.My^{-1}. The blue points represent the $\chi^2(^{10}Be)$ and the pink points the $\chi^2(^{21}Ne)$.
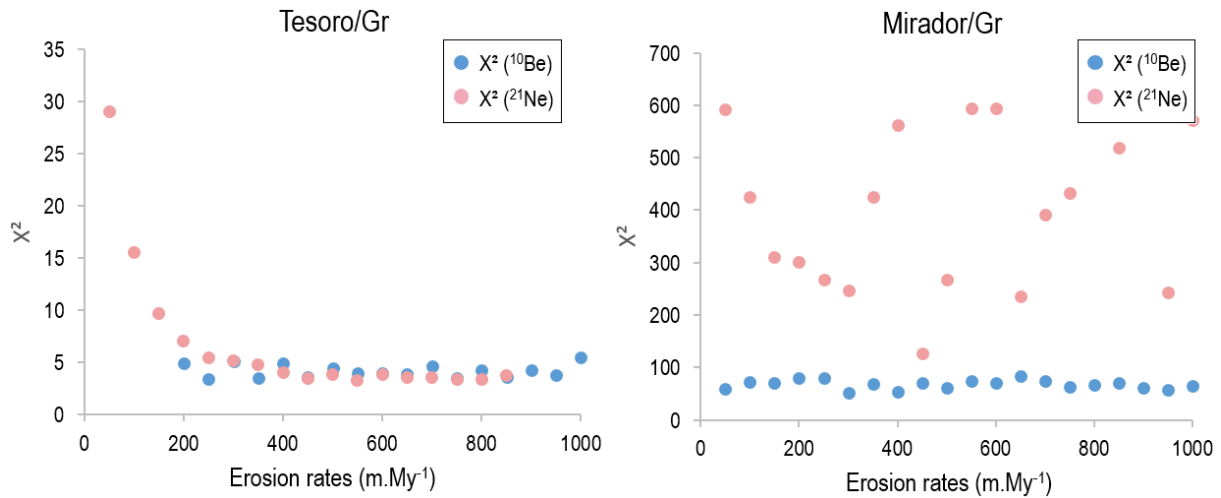
Figure 6.17 – χ^2 results according to erosion rates of the initial source in Tesoro and Mirador mines with the Granger and Muzikar (2001) production model.
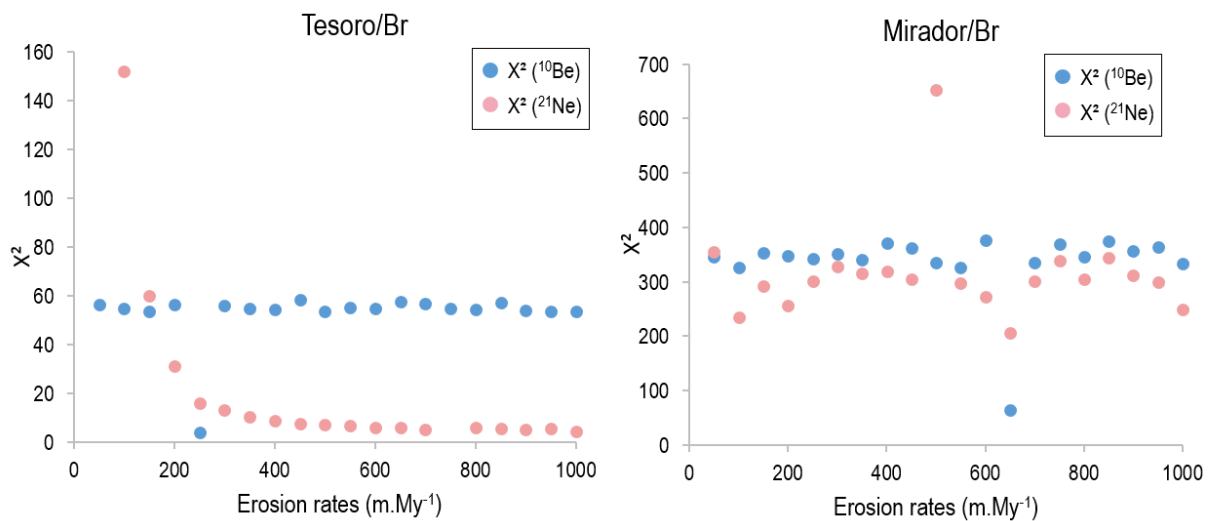
Figure 6.18 – χ^2 results according to erosion rates of the initial source in Tesoro and Mirador mines with the Braucher et al., (2003) production model.
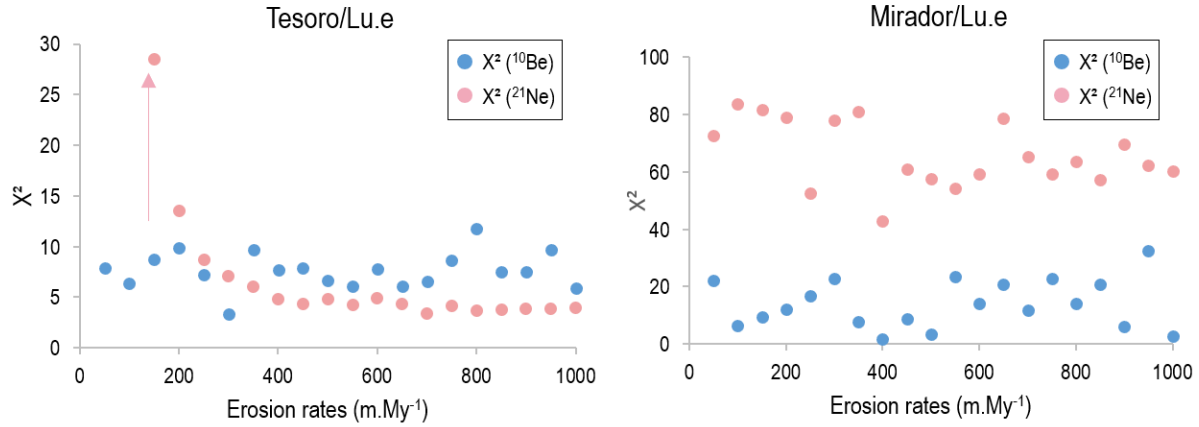
Figure 6.19 – χ^2 results according to erosion rates of the initial source in Tesoro and Mirador mines with the Lupker, personal com. production model.

Globally the patters of χ^2 distribution for both mines data set are qualitatively similar. In the three production model cases the $\chi^2(^{10}Be)$ patterns present an exponential decrease, before forming an abscissa parallel line around 400 m.My^{-1}. The real difference between the models is visible by the mean of the "plateau" formed by the results. Whereas the means of $\chi^2(^{10}Be)$ values are similar for the Tesoro/Gr and Tesoro/Br production mode (~5 and ~8) it it significantly higher for the Tesoro/Lu.e (~60). In the case of $\chi^2(^{21}Ne)$ for Tesoro's modeling, the mean of the "plateau" is ~5 for all the production models. In the Mirador case the mean $\chi^2(^{10}Be)$ values are vary a lot between respectively ~80, ~300 and ~10 for Mirador/Gr, Mirador/Br and Mirador/Lu.e. In the case of $\chi^2(^{21}Ne)$ for Tesoro's modeling, the mean of the "plateau" are respectively 400, 300 and 70 for Mirador/Gr, Mirador/Br and Mirador/Lu.e. In conclusion, $\chi^2(^{21}Ne)$ are higher than $\chi^2(^{10}Be)$ values for Mirador samples and more difficult to model. The models fit best for Tesoro models. The production model which seems to better fit both Tesoro and Mirador samples is Lupker's production model, which will be used for the following models presented in this work.

In addition, the "plateau" values for $\chi^2(^{10}Be)$ and $\chi^2(^{21}Ne)$ seem to indicate that the model manages to fit the data once the erosion rate values are superior to 400 m.My^{-1}.

In the next figures 6.20 to 6.22, is illustrated the incidence of the models on the concentration inversion of ^{21}Ne in the Tesoro samples with initial erosion rates at 400 m.My^{-1}, and how they fit with the data. When a model is presented, it is based on one cosmogenic nuclide either ^{10}Be or ^{21}Ne. In case it is tested for ^{21}Ne, the scenariis will be visible in light pink. The best fitting ^{21}Ne scenario will be visible in red. Meanwhile ^{10}Be scenariis will also be calculated based on the ratio known between the two elements, the best ^{10}Be scenario will be visible in blue. The best fit scenario for both element will be visible in purple. In case the scenario is based on the ^{10}Be (scenariis in cyan blue) the colours will stay the same.
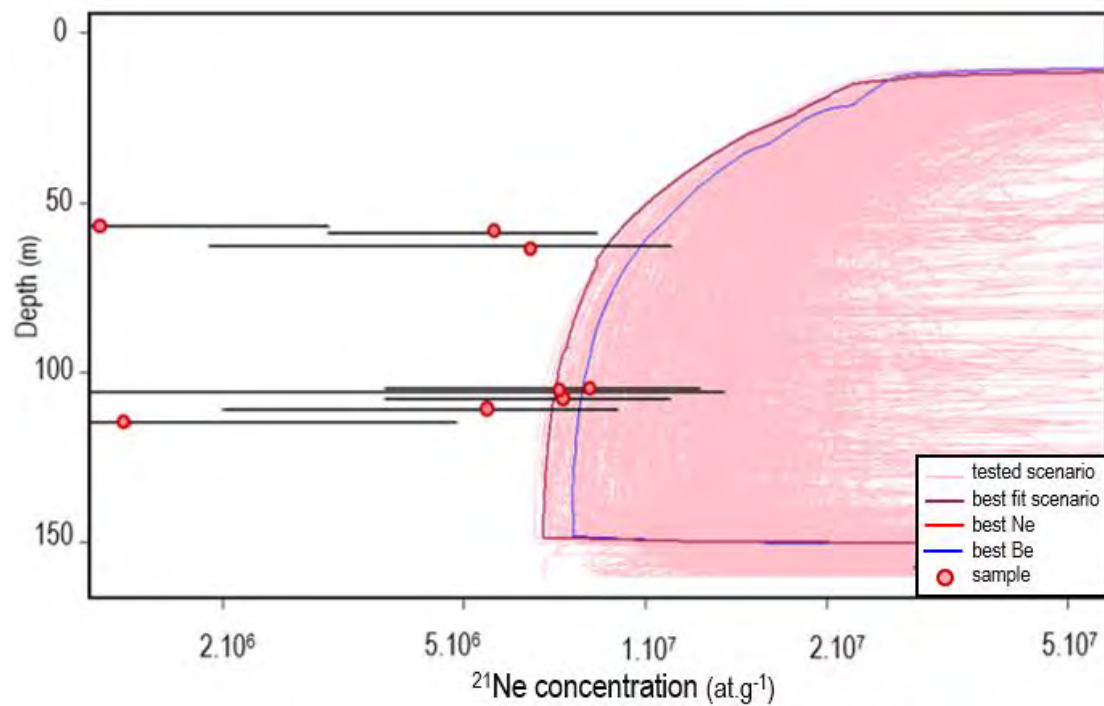
Figure 6.20 – Bestfit models for ^{21}Ne concentration (at. g^{-1}) with erosion rate of 400 m.My^{-1} for the Tesoro samples using Braucher et al. (2003) muonic production model.
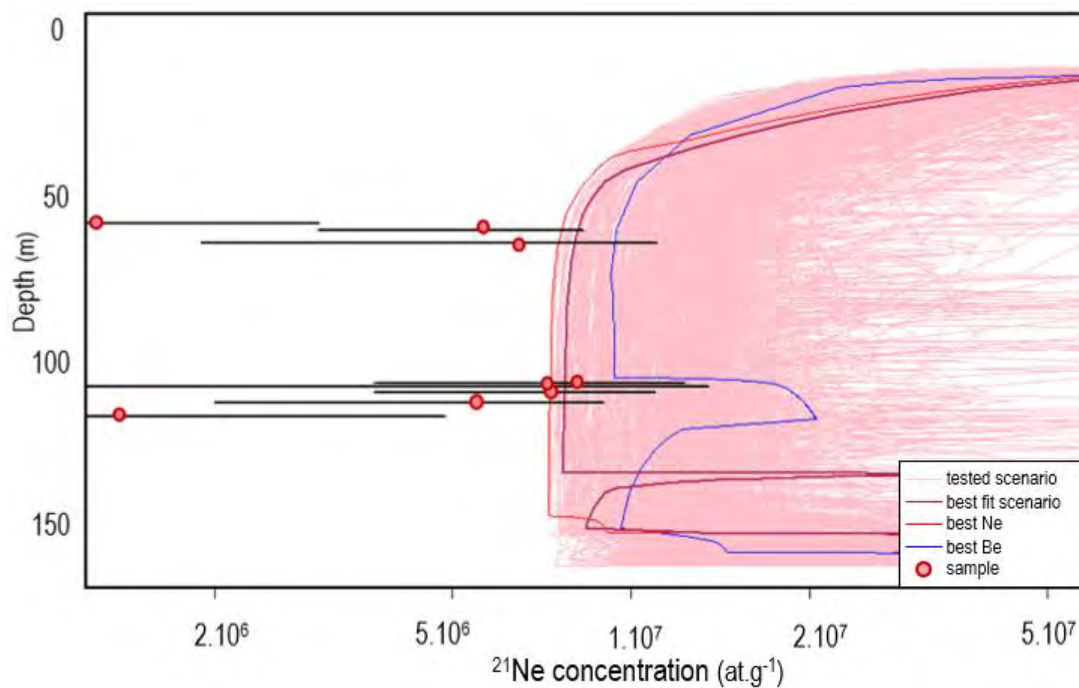
Figure 6.21 – Bestfit models for ^{21}Ne concentration (at. g^{-1}) with erosion rates of 400 m.My^{-1} for the Tesoro samples using the Granger and Muzikar (2001) muonic production model.
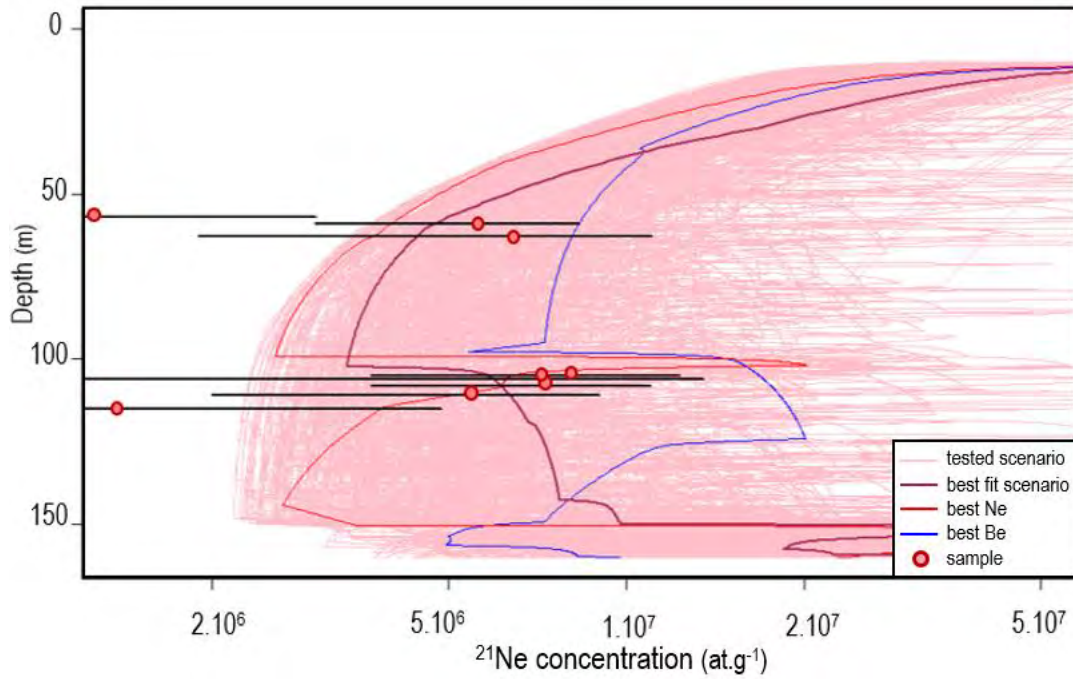
Figure 6.22 – Bestfit models for ^{21}Ne concentration (at. g^{-1}) with erosion rate of 400 m.My^{-1} for the Tesoro samples using the Lupker (personal com.), muonic production model.

In the Tesoro/Br ^{21}Ne inversion model (Figure 6.20) is visible the scenarios rarely fit with the data and that the modeled ^{21}Ne concentrations are higher than the measured ones. No major rapid concentration variation is visible meanwhile in the Tesoro/Gr ^{21}Ne inversion model (Figure 6.21) an increase and drop in ^{21}Ne concentrations appears below and above the ~110m deep samples. Despite this, the scenariis do not fit with the measured concentrations.

The Tesoro/Lu.e ^{21}Ne inversion model (Figure 6.22) presents the best fitting of the data between the three different production model, showing variation like in Figure 6.21 an increase and decrease in the ^{21}Ne concentration.

6.4.2.2 Concentration inversions

In a first attempt, I present the results in the case of low constant erosion rate (Figure 6.23-6.26). Present day and late Miocene erosion rates estimated in the Atacama Desert are commonly below 10 m.My^{-1} (Placzek et al., 2010; 2014; Owen et al., 2013; Martinod et al., 2016). Nevertheless, the majority of the sediments sediment in the mining pits are older than 10 Ma, they are older than the hyper-aridification of the Atacama Desert (Riquelme et al., 2017). Consequently, I consider larger erosion rates as plausible. Low-temperature thermochronological data in the Precordillera suggest denudation rates on the order of 50 m.My^{-1} (e.g. Maksaev and Zentilli, 1999) from 30 Ma to now on.

In all the following inversions I use the initial erosion rates of 50 m.My^{-1} from 30 to 10 Ma and then 10 m.My^{-1} from 10 Ma to nowadays. The changes from 50 m.My^{-1} to 400 m.My^{-1} in the following example will only be applied to the 30 to 10 Ma period.

El Tesoro
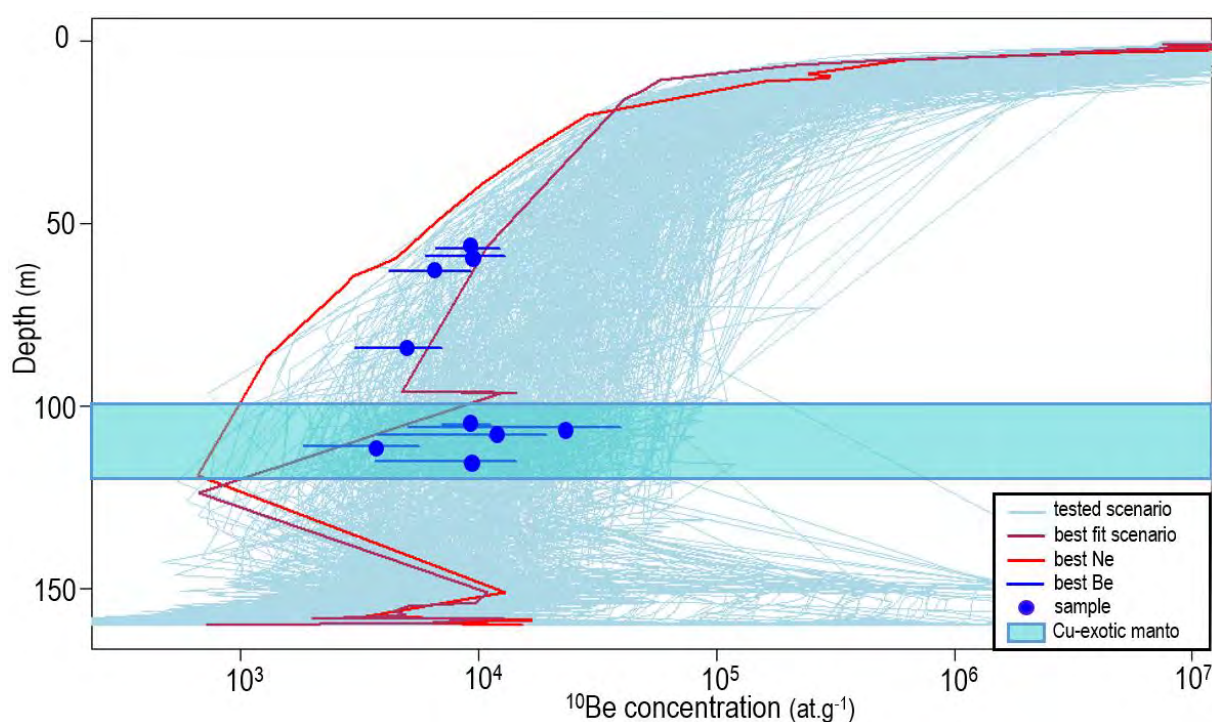
Figure 6.23 – Bestfit models for ^{10}Be concentration (at.g^{-1}) in El Tesoro. Sediment source erosion rate is fixed at 50 m.My^{-1}.
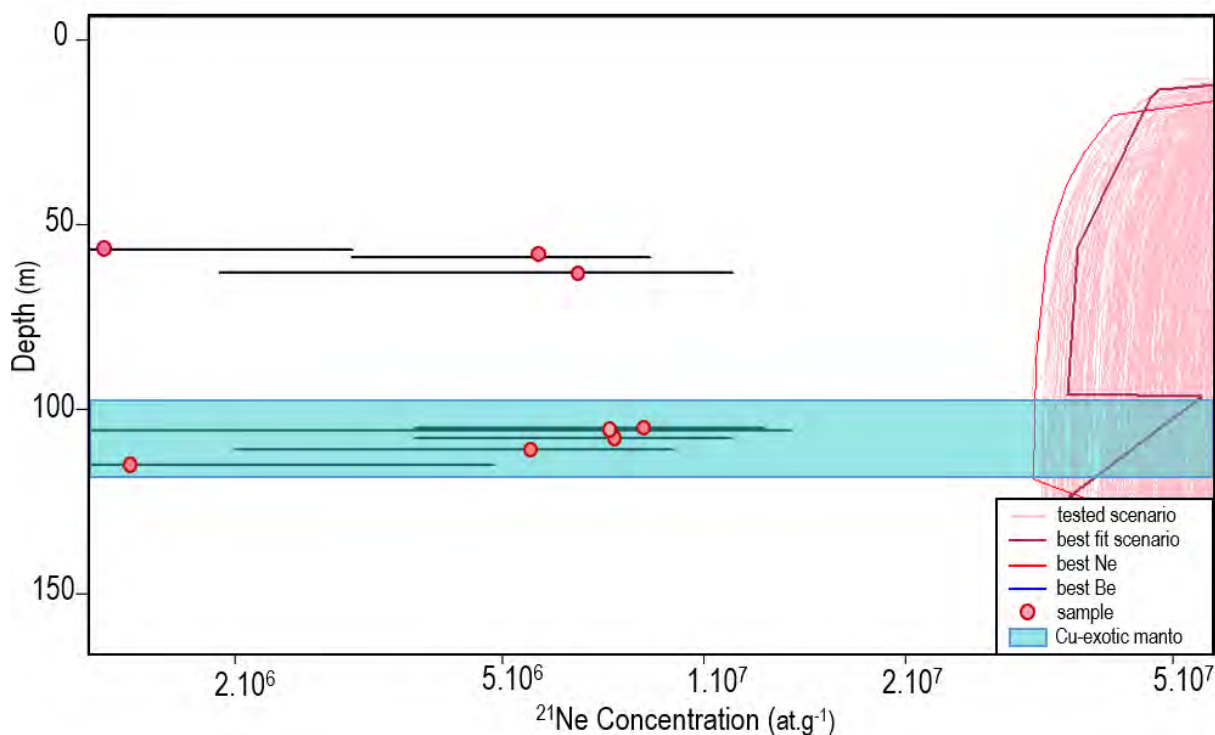
Figure 6.24 – Bestfit models for ^{21}Ne concentration (at.g^{-1}) in El Tesoro Sediment source erosion rate is fixed at 50 m.My^{-1}.

Using a constant denudation rate of 50 m.My^{-1}, the inversion yields a best fit profile which fits ^{10}Be but not the ^{21}Ne concentrations. The best fit model predicts 10 times higher concentrations than the observed ones. fit the data, I use an initial erosion rate of 400 m.My^{-1} for both El Tesoro and Mirador pit samples (Figure 6.25-6.26).

173
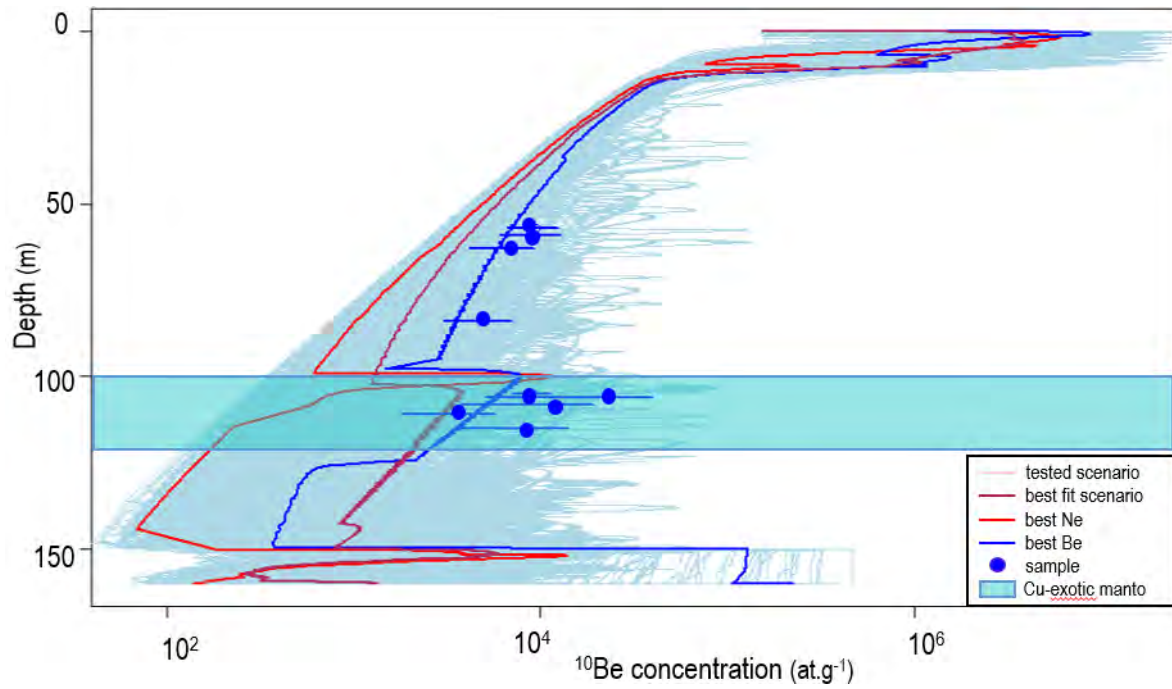
Figure 6.25 – Inversion of ^{10}Be concentrations (at.g^{-1}) of the Tesoro samples, depth according to ^{10}Be with erosion rate of 400 m.My^{-1}.
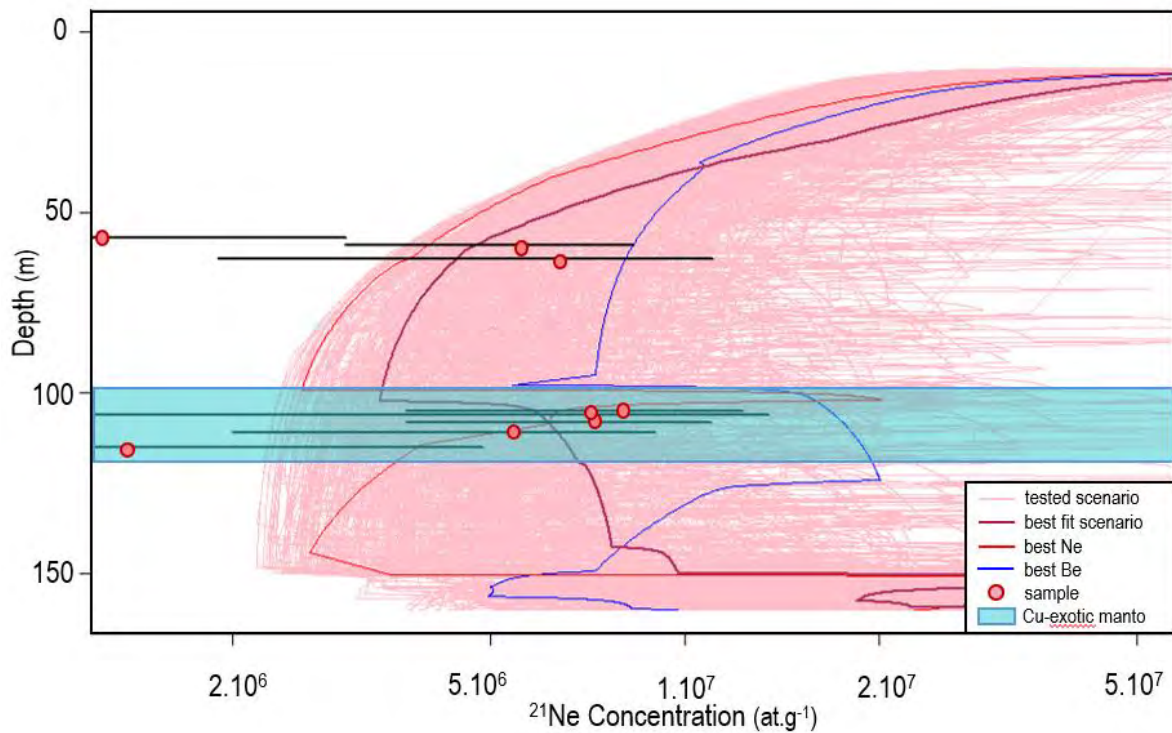
Figure 6.26–Inversion of ^{21}Ne concentrations (at.g^{-1}) of the Tesoro samples, depth according to ^{21}Be with erosion rate of 400 m.My^{-1}.

When initial erosion rates are fixed at 400 m.My^{-1} instead of 50 m.My^{-1} the ^{21}Ne based inversion is fitting with the data (except with the lowest values, which could be attributed to an analytical problem).

Mirador
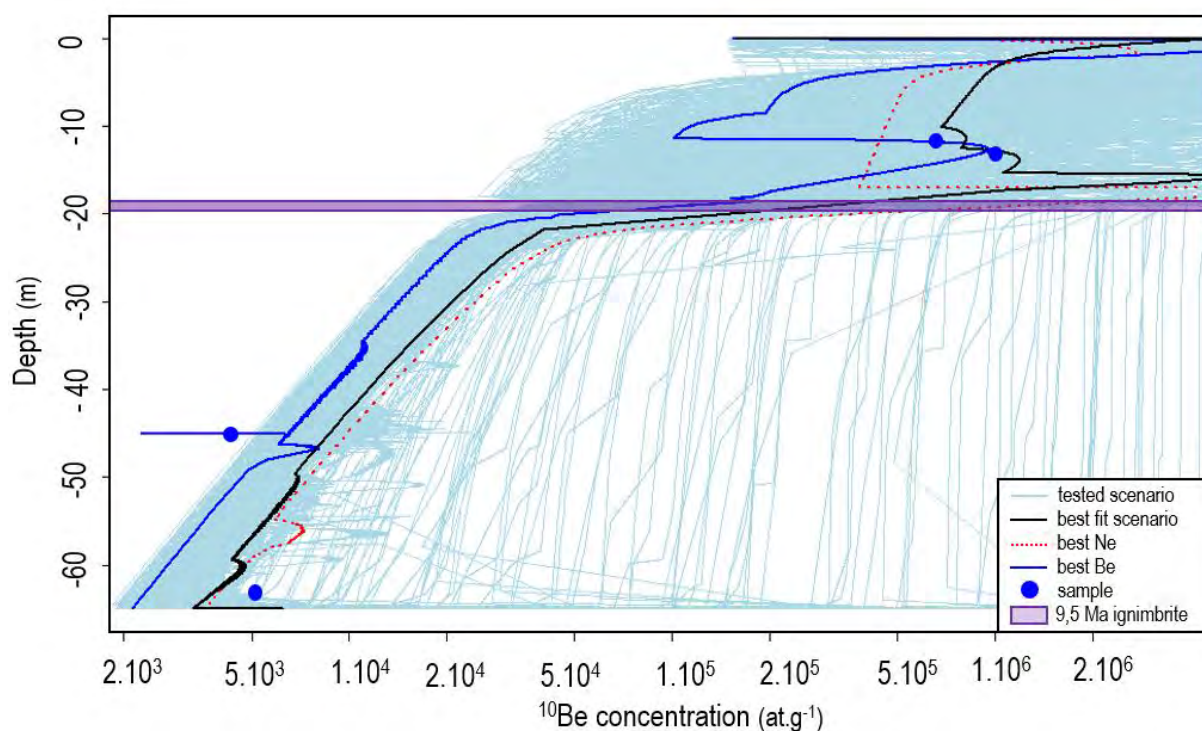
Figure 6.27 – Bestfit models for ^{10}Ne concentration (at.g^{-1}) in Mirador. Sediment source erosion rate is fixed at 50 m.My^{-1}.
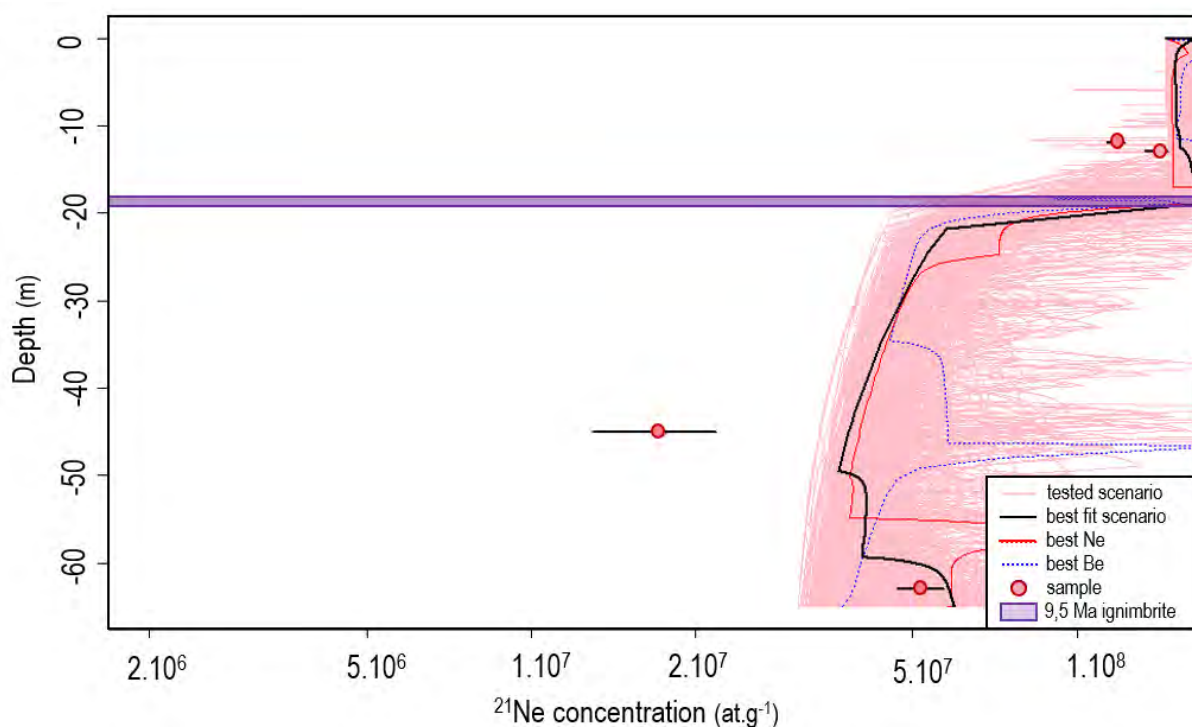
Figure 6.28 – Bestfit models for ^{21}Ne concentration (at.g^{-1}). Sediment source erosion rate is fixed at 50 m.My^{-1}.

The inversion leads to a reasonable fit for ^{10}Be, whereas the fit of ^{21}Ne concentrations is very poor, the bestfit model overestimating the concentrations as in the El Tesoro case.

175
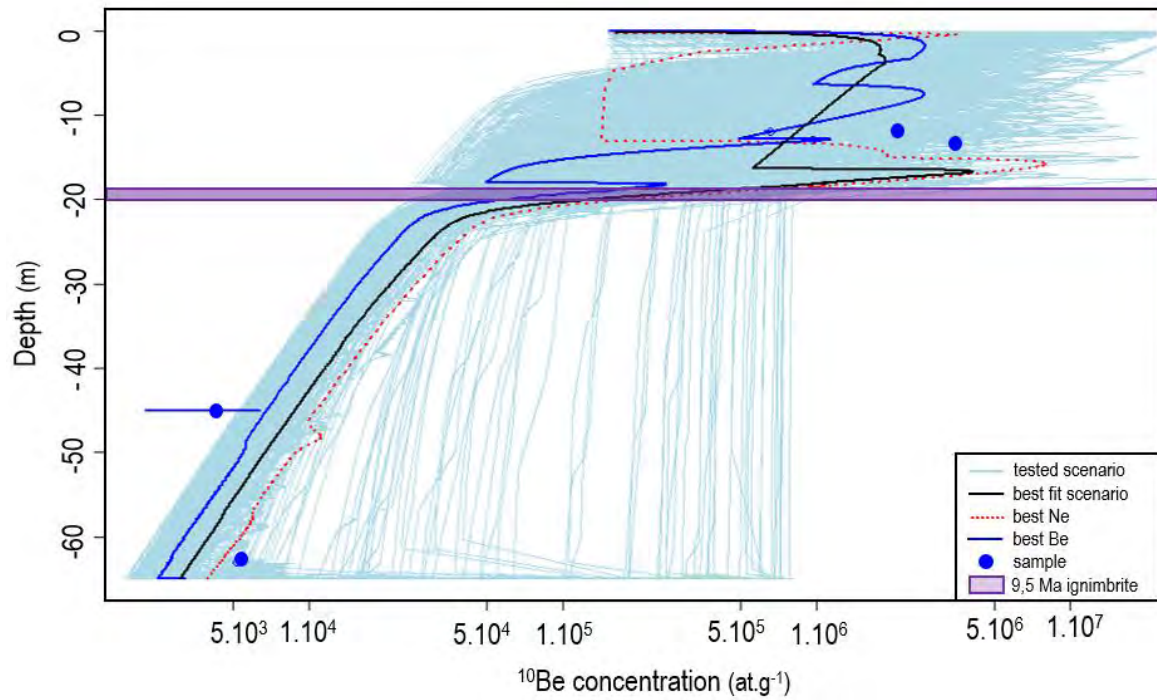
Figure 6.29–Inversion of concentrations of the Mirador samples, depth according to ^{10}Be with erosion rate of 400 m.My^{-1}
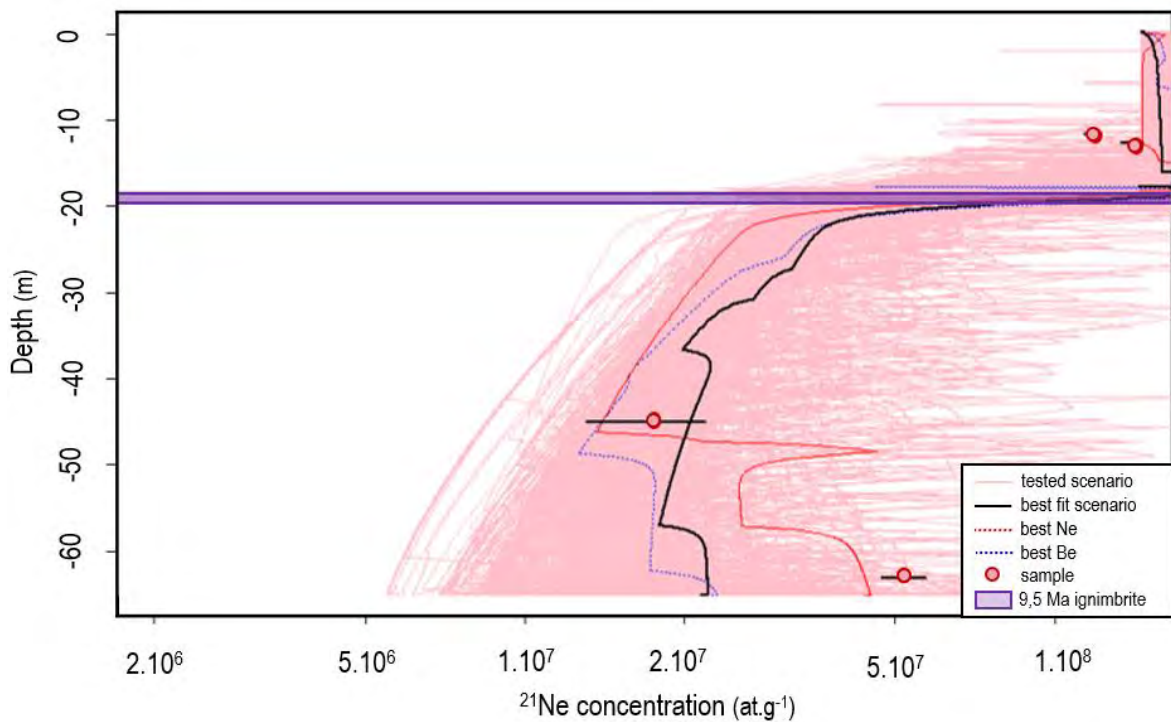
Figure 6.30 – Inversion of concentrations of the Mirador samples, depth according to ^{21}Ne with erosion rate of 400 m.My^{-1}

In Mirador case, the fit between the bestfit model and ^{21}Ne concentrations is significantly improved (Figures 6.28, 6.30), while the fit between the model and ^{10}Be concentrations is not significantly modified (Figures 6.27, 6.29). In all the models an important decrease of the concentration is observed in the sediments above the 9.5 Ma ignimbrite.

6.4.2.3 Filling scenarios.

The model inversion permits also to reconstruct the timing of the sedimentary infilling of the Tesoro (Figure 6.31) and Mirador (Figure 6.32) mines. In the next figure they are represented for 18000 iterations in the case of Tesoro samples and 1000 for the Mirador samples. They are represented with 98% and 68% confidence envelopes with are constituted of all the best scenarios tested.

El Tesoro
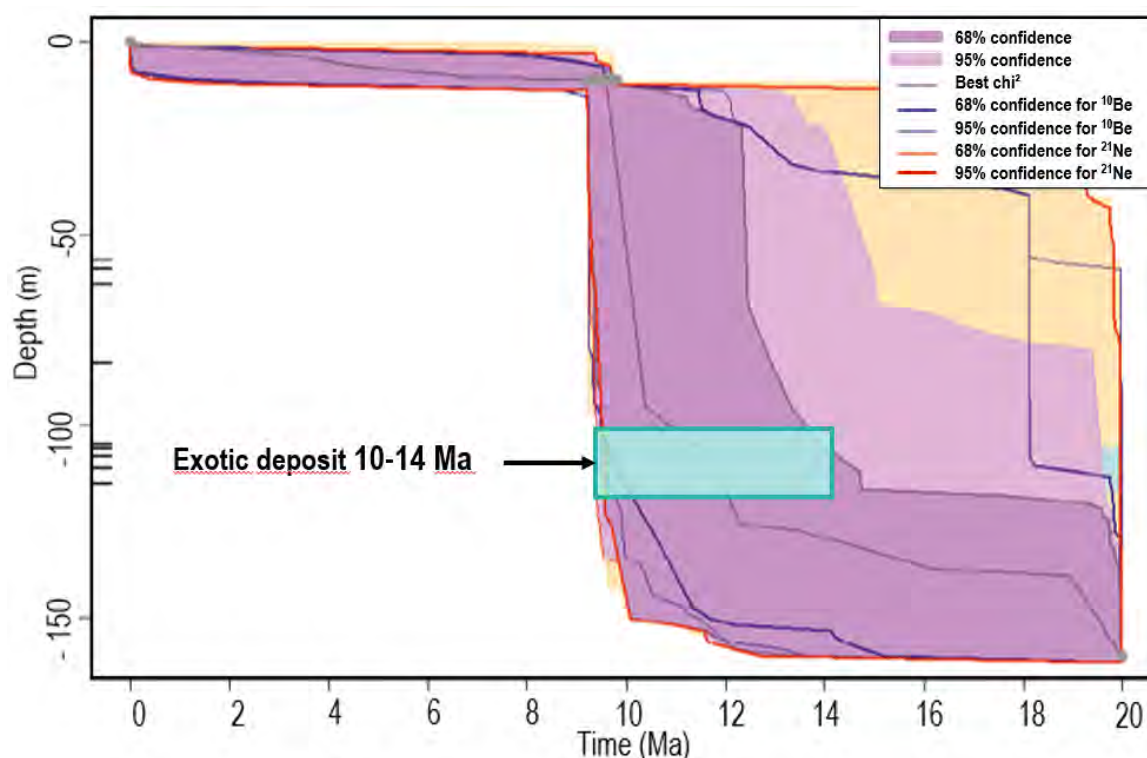
Figure 6.31 – Filling scenarios of the Tesoro samples, depth according to Time.

The filling scenarios suggest that sedimentation rates where low between 20 and ~14 Ma, deeper than 100 m. Then the infill rates seem rapid between 14 and 10 Ma, to finally slow down from 10 Ma to nowadays.

Mirador

In the case of the Mirador mine (Figure 6.32), the filling scenario suggests that the sedimentation rate kept decreasing from 20 Ma to 10 Ma, below the 9.5 Ma ignimbritic level. Then, above the ignimbrite leven, the sedimentation rates dropped before rising again around 4 Ma. This last results concords with to the sedimentation scenario tested with the Davis et al. (2014) data where sedimentation rates started to rise 5 Ma.
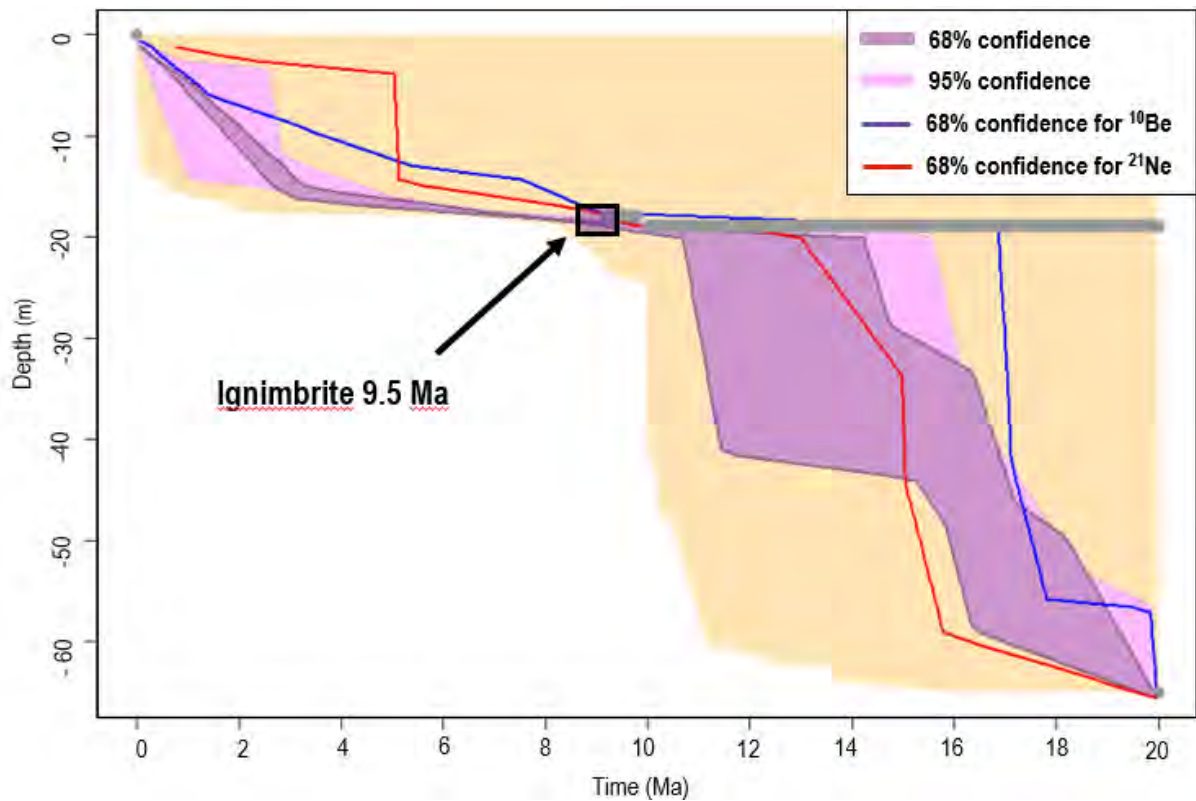
Figure 6.32 – Filling scenarios of the Mirador samples, depth (m) according to time (Ma).

6.4.2.5 Exotic Cu-enriched layer dating

The deposit of exotic Cu has never been dated in situ. Until now the supergene copper deposit have not been dated in the literature. The ages attributed to them are in fact the ages of supergene minerals that precipitate in similar conditions than supergene copper minerals.

As presented in the 4.1.2 Burial dating ages from this chapter, we calculated the ages for the burial of each sample contained in the exotic copper layer, see location Figure 6.5. In the Figure 6.33 are presented the concentrations from the left to right, respectively ET13-05 to ET13-09. The concentrations in both elements are decreasing towards the surface.
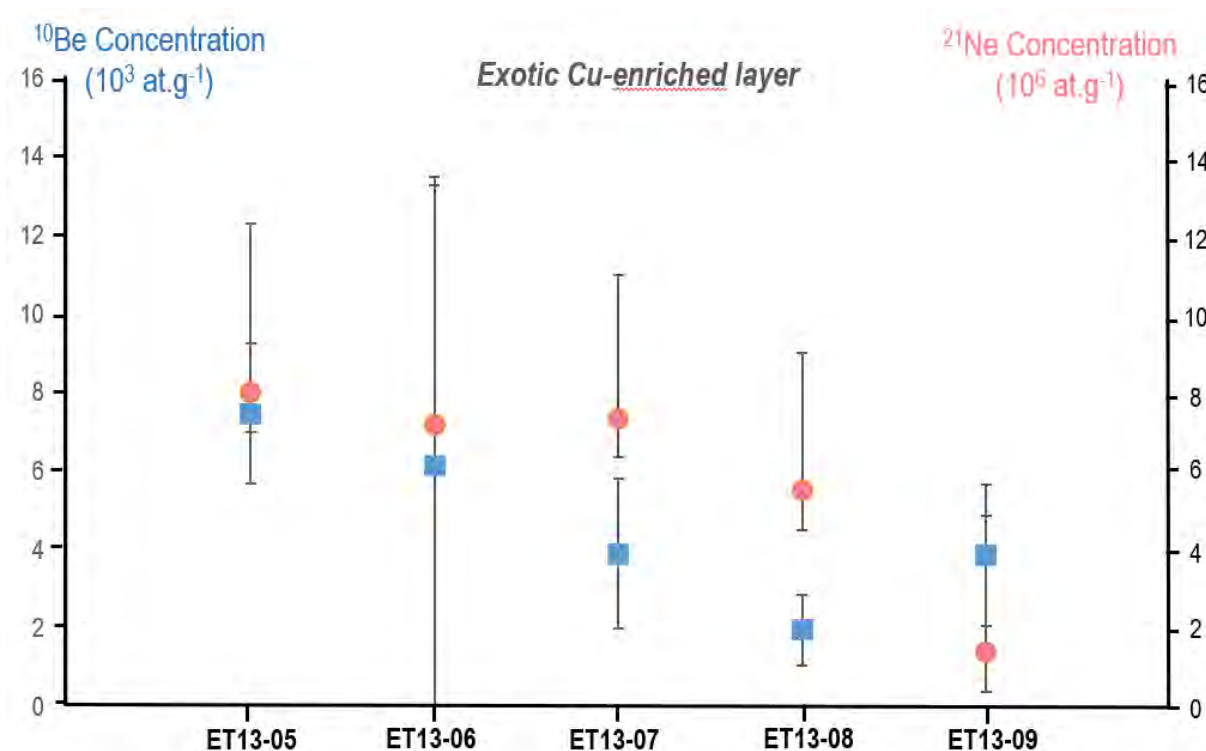
Figure 6.33 – ¹⁰Be and ²¹Ne concentrations of the Cu-enriched layer in the Tesoro mine.

This trend is visible in the inversion of the concentration inversions as in Figure 6.27 where the concentration decreases right above the Cu-exotic layer.

6.5   Discussion

6.5.1 Source erosion/basin infilling history

Erosion rates in the samples of the Mirador site suggest a drastic erosion fall around 10 Ma which is coincident in both El Tesoro and Mirador modeled scenariis.

In case of the Tesoro Mine, the sediment deposit seems really fast around 14-12 Ma.

When focusing on the initial concentrations and the concentration inversion in both elements, the results both suggest that this quick infill would have occurred just after the deposit of the enriched layer, suggesting a post-Miocene event as the activity of the Tesoro fault at the west of the deposit generating a 100m deposit of sediments nearby.

The inversions of the Mirador sedimentary infill suggest a continuous decrease of the erosion rates in this column with relative high sedimentation rates before 10 Ma and an important decrease above the 9.5 ignimbrite.

6.5.2 Robustness of the results

The model assumes an instantaneous transfer from the hillslopes of the denuding source to the basin. In the reality, sediment transfer along the fluvial system may modify the CN concentrations when sediment enter the basin. This may increase the ²¹Ne concentrations (e.g. Carretier et al., 2009; Yanites

179

et al., 2009) and thus underestimate the source denudation rate. The transfer through the fluvial system may change the ^{10}Be concentration in a non-straightforward manner. Radioactive decay and production at shallow depth within sediment in transit may compensate one each other in case of the ^{10}Be.

In the Mirador case, the deposit ages calculated for the sediments underneath and over the ignimbrite are respectively older and younger than the age of the 9.5 Ma ignimbrite obtained with ^{40}Ar/^{39}Ar. This consistency between deposition ages and ignimbrite age determined by an independent method tends to give confidence in the measured CN concentrations and in the calculated ages.

6.5.3 Atacama hyper-aridity onset

This age is in agreement with a recent compilation of sedimentological arguments dating the hyper-aridification of the Atacama Desert around 12 Ma (Jordan et al., 2014). The previous literature gave a large range of ages for this major climatic change between 15 and 9 Ma, some of the ages reaching even the Pleistocene (Hartley et al., 2003; Reich et al., 2009; Arancibia et al., 2006… see chapter 2). Our results thus provide the first direct evidence of a drastic fall in denudation rate at 10-12 Ma, confirming sedimentological evidence for a hyper aridification of the Atacama Desert at this time.

The inversion results suggest that 100 m of sediments were deposited in less than ~2 Ma. Such a relatively high sedimentation rate ($>=50$ m.My^{-1}) contrasts with sedimentation and denudation rates inferred for the Neogene period time in the Atacama Desert (Maksaev and Zentilli, 1999; Alpers and Brimhall, 1988). A higher erosion from the source and the blocking by Miocene fault reactivity as the Llano o Tesoro fault, that disrupted the topography with vertical displacements of several tens of meters may explain this sedimentation event. This high sedimentation rate ceased by 10 Ma, consistently with the hyper-aridification by that time.

6.5.4 Supergene and exotic copper deposit ages

This study provides the first age estimation of the uppermost exotic copper deposits in the El Tesoro open mine and challenges previous estimations.

These previous estimations for this age were made by correlation with a K/Ar 22 Ma cryptomelane age obtained in the Tesoro Norte Este mine in the Centinela District (Figure 6.3). This age has been reused afterward by Oerter et al. (2016) to propose a scenario for the paleo-environmental evolution of these deposits.

The late Miocene age 10-14 Ma range obtained with cosmogenic nuclides suggests a much younger age. This age corresponds to the younger cluster of ages of supergene copper mineralization found in the region (e.g. Arancibia et al., 2006; Riquelme et al., 2017). This first direct age shows that the sediment hosting this exotic layer are much younger than previously thought. This result also indicates that the ~22 Ma old exotic deposit may be present deeper in this pit, although it was dated a

couple of kilometers from this place. The exotic deposits are thus patchy in this region and their lateral correlation may be highly hazardous.

Exotic supergene mineralization occurred during this period of relatively high mean sedimentation rate, but probably during a short event of decreased sedimentation rate at some moment between 12 and 10 Ma (Figure 6.34). This short event of sedimentation rate fall is a result of the data inversion. This decrease in sedimentation rate is inevitable to explain the CN concentrations measured within the exotic layer.

It is striking to see that the best-fit model predicts this sedimentation fall even in absence of concentration data few meters above the exotic layer. The sensibility of the CN concentration in this case demonstrates that this approach is promising.

6.5.5 Muonic production rate versus high erosion rate

The estimation of muonic production rates at depth suffers uncertainties. The muonic contribution varies according to the authors (Heisenger et al., 2002a, 2002b; Braucher et al., 2003, 2011, 2013; Kim and Englert, 2004; Lupker 2013; Phillips et al., 2015). The formalism of the physics of production at depth was simplified by summing exponential functions, which remains an approximation. The *in-situ* calibration of this exponential model was realized over depth with only one example deeper than 25 m (Braucher et al., 2003, 2011, 2013). In our study, samples were gathered much deeper, so that the extrapolation of existing models is hazardous. The results of inversion of ^{21}Ne concentrations show that the predicted ^{21}Ne concentrations are too high. This misfit suggests either that the published models overestimate the ^{21}Ne production by muons at great depth (>> 20 m), or that the erosion of the source was much higher than the value obtained for the last 10 Ma on gentle surfaces of the Atacama Desert (e.g. Kober et al., 2007; Nishizumi et al., 2005; Aguilar et al., 2011; Placzek et al., 2014).

With high erosion rates (>>10 m.My^{-1}), the ^{21}Ne concentration acquired at the source would be much lower. With a much smaller muonic contribution, the acquisition of ^{21}Ne in the basin would be smaller. At this stage, our dataset cannot be used to improve or calibrate a muonic production model, and we let this issue for future research.

The alternative hypothesis of a high erosion rate seems unrealistic, but it cannot be totally discarded. It is possible that erosion has been high during several periods of hundreds of thousand years, alternating with intervals of low erosion rate without significant sediment volume deposited in the basin. In our modellings, we have tested constant erosion rates.

Scenarios with variable erosion rates deserve to be tested in future works, although the number of available data is probably not sufficient to constrain the timing of these variations.

6.6   Conclusion

We developed and applied a new source-to-sink model to predict CN concentrations within a sedimentary sequence at depths of tens of meters in Atacamean sediments. For the first time, we demonstrate that Miocene sediments contain measurable ^{10}Be concentrations. Coupling ^{10}Be and ^{21}Ne we show that the exotic deposit of El Tesoro previously estimated at 22 Ma is actually no older than 14 Ma. By inverting the depth data, we show a sharp change in denudation and sedimentation rates between 12 and 10 Ma, consistent with the hyper-aridification of the Atacama Desert. The result of the inversion, although preliminary given the limited set of data, clearly shows that the exotic deposit formed during a pronounced decrease in sedimentation rate. This result is consistent with a view that supergene enrichment occurs during erosion stability periods.

References for Chapter 6

Aguilar, G., Riquelme, R., Martinod, J., Darrozes, J., Maire, E., 2011. Variability in erosion rates related to the state of landscape transience in the semi-arid Chilean Andes. Earth Surface Processes and Landforms 36, 1736–1748.

Alpers, C.N., Brimhall, G.H., 1988. Middle Miocene climatic change in the Atacama Desert, northern Chile: Evidence from supergene mineralization at La Escondida. Geological Society of America Bulletin 100, 1640–1656.

Ambrosio, M., Antolini, R., Auriemma, G., Baker, R., Baldini, A., Barbarino, G.C., Barish, B.C., Battistoni, G., Bellotti, R., Bemporad, C., others, 1995. Vertical muon intensity measured with MACRO at the Gran Sasso laboratory. Physical Review D 52, 3793.

Arancibia, G., Matthews, S.J., Arce, C.P. de, 2006. K–Ar and ^{40}Ar/^{39}Ar geochronology of supergene processes in the Atacama Desert, northern Chile: tectonic and climatic relations. Journal of the Geological Society 163, 107–118.

Arnold, M., Merchel, S., Bourlès, D.L., Braucher, R., Benedetti, L., Finkel, R.C., Aumaître, G., Gottdang, A., Klein, M., 2010. The French accelerator mass spectrometry facility ASTER: improved performance and developments. Nuclear Instruments and Methods in Physics Research Section B: Beam Interactions with Materials and Atoms 268, 1954–1959.

Babault, J., Van Den Driessche, J., Bonnet, S., Castelltort, S., Crave, A., 2005. Origin of the highly elevated Pyrenean peneplain. Tectonics 24.

Balco, G., Stone, J.O., Lifton, N.A., Dunai, T.J., 2008. A complete and easily accessible means of calculating surface exposure ages or erosion rates from ^{10}Be and ^{26}Al measurements. Quaternary geochronology 3, 174–195.

Balco, G., Shuster, D.L., 2009a. ^{26}Al–^{10}Be–^{21}Ne burial dating. Earth and Planetary Science Letters 286, 570–575.

Balco, G., Shuster, D.L., 2009b. Production rate of cosmogenic ^{21}Ne in quartz estimated from ^{10}Be, ^{26}Al, and ^{21}Ne concentrations in slowly eroding Antarctic bedrock surfaces. Earth and Planetary Science Letters 281, 48–58.

Berger, C., Fröhlich, M., Mönch, H., Nisius, R., Raupach, F., Schleper, P., Benadjal, Y., Blum, D., Bourdarious, C., Dudelzak, B., others, 1989. Experimental study of muon bundles observed in the Fréjus detector. Physical Review D 40, 2163.

Bilokon, H., Castagnoli, G.C., Castellina, A., Piazzoli, B.D., Mannocchi, G., Meroni, E., Picchi, P., Vernetto, S., 1989. Flux of the vertical negative muons stopping at depths 0.35–1000 hg/cm2. J. Geophys. Res. 94, 12145–12152.

Bishop, P., 2007. Long-term landscape evolution: Linking tectonics and surface processes. Earth Surface Processes and Landforms 32, 329–365.

Blanco, N.; Tomlinson, A. 2002. Estudio estratigrafico y sedimentologico del Distrito Minero El Tesoro. Unplublished report, 29 pp.

Braucher, R., Brown, E.T., Bourlès, D.L., Colin, F., 2003. In situ produced ^{10}Be measurements at great depths: implications for production rates by fast muons. Earth and Planetary Science Letters 211, 251–258.

Braucher, R., Merchel, S., Borgomano, J., Bourlès, D.L., 2011. Production of cosmogenic radionuclides at great depth: a multi element approach. Earth and Planetary Science Letters 309, 1–9.

Braucher, R., Bourlès, D., Merchel, S., Romani, J.V., Fernandez-Mosquera, D., Marti, K., Leanni, L., Chauvet, F., Arnold, M., Aumaître, G., others, 2013. Determination of muon attenuation lengths in depth profiles from in situ produced cosmogenic nuclides. Nuclear Instruments and Methods in Physics Research Section B: Beam Interactions with Materials and Atoms 294, 484–490.

Brook, E.J., Brown, E.T., Kurz, M.D., Ackert, R.P., Raisbeck, G.M., Yiou, F., 1995. Constraints on age, erosion, and uplift of Neogene glacial deposits in the Transantarctic Mountains determined from in situ cosmogenic ^{10}Be and ^{26}Al. Geology 23, 1063–1066.

Carretier, S., Regard, V., Soual, C., 2009. Theoretical cosmogenic nuclide concentration in river bed load clasts: Does it depend on clast size? Quaternary Geochronology 4, 108–123.

Cesta, J.M., Ward, D.J., 2016. Timing and nature of alluvial fan development along the Chajnantor Plateau, northern Chile. Geomorphology 273, 412–427.

Charreau, J., Blard, P.-H., Puchol, N., Avouac, J.-P., Lallier-Verges, E., Bourlès, D., Braucher, R., Gallaud, A., Finkel, R., Jolivet, M., others, 2011. Paleo-erosion rates in Central Asia since 9Ma: A transient increase at the onset of Quaternary glaciations? Earth and Planetary Science Letters 304, 85–92.

Chmeleff, J., von Blanckenburg, F., Kossert, K., Jakob, D., 2010. Determination of the ^{10}Be half-life by multicollector ICP-MS and liquid scintillation counting. Nuclear Instruments and Methods in Physics Research Section B: Beam Interactions with Materials and Atoms 268, 192–199.

Clarke, J.D., 2006. Antiquity of aridity in the Chilean Atacama Desert. Geomorphology 73, 101–114.

Davis, M., Matmon, A., Placzek, C.J., McIntosh, W., Rood, D.H., Quade, J., 2014. Cosmogenic nuclides in buried sediments from the hyperarid Atacama Desert, Chile. Quaternary Geochronology 19, 117–126.

De Silva, S.L., 1989. Geochronology and stratigraphy of the ignimbrites from the 21 30′ S to 23 30′ S portion of the central Andes of northern Chile. Journal of Volcanology and Geothermal Research 37, 93–131.

Dunai, T.J., López, G.A.G., Juez-Larré, J., 2005. Oligocene–Miocene age of aridity in the Atacama Desert revealed by exposure dating of erosion-sensitive landforms. Geology 33, 321–324.

Evenstar, L.A., Hartley, A.J., Stuart, F.M., Mather, A.E., Rice, C.M., Chong, G., 2009. Multiphase development of the Atacama Planation Surface recorded by cosmogenic ^{3}He exposure ages: Implications for uplift and Cenozoic climate change in western South America. Geology 37, 27–30.

Fabel, D., Harbor, J., 1999. The use of in-situ produced cosmogenic radionuclides in glaciology and glacial geomorphology. Annals of Glaciology 28, 103–110.

Fernández-Mort, A., Riquelme, R., Alonso-Zarza, A.M., Campos, E., Tapia, M., Sola, S., 2015. Sedimentary controls on the formation of gravel-hosted exotic-Cu deposits. Examples from El Tesoro Basin, northern Chile. Presented at the XIV Congreso Geológico Chileno, 4-8 Octob.

Goethals, M.M., Hetzel, R., Niedermann, S., Wittmann, H., Fenton, C.R., Kubik, P.W., Christl, M., Von Blanckenburg, F., 2009. An improved experimental determination of cosmogenic ^{10}Be/^{21}Ne and ^{26}Al/^{21}Ne production ratios in quartz. Earth and Planetary Science Letters 284, 187–198.

Gosse, J.C., Phillips, F.M., 2001. Terrestrial in situ cosmogenic nuclides: theory and application. Quaternary Science Reviews 20, 1475–1560.

Granger, D.E., Kirchner, J.W., Finkel, R., 1996. Spatially averaged long-term erosion rates measured from in situ-produced cosmogenic nuclides in alluvial sediment. The Journal of Geology 104, 249–257.

Granger, D.E., Smith, A.L., 2000. Dating buried sediments using radioactive decay and muogenic production of ^{26}Al and ^{10}Be. Nuclear instruments and methods in physics research section B: beam interactions with materials and atoms 172, 822–826.

Granger, D.E., Muzikar, P.F., 2001. Dating sediment burial with in situ-produced cosmogenic nuclides: theory, techniques, and limitations. Earth and Planetary Science Letters 188, 269–281.

Granger, D.E., Lifton, N.A., Willenbring, J.K., 2013. A cosmic trip: 25 years of cosmogenic nuclides in geology. Geological Society of America Bulletin 125, 1379–1402.

Hancock, G.S., Anderson, R.S., Chadwick, O.A., Finkel, R.C., 1999. Dating fluvial terraces with ^{10}Be and ^{26}Al profiles: Application to the Wind River, Wyoming. Geomorphology 27, 41–60.

Hartley, A., 2003. Andean Uplift and Climate Change. Journal of the Geological Society, London 160, 7–10.

Heisinger, B. P., 1998. Myonen-induzierte produktion von radionukliden [Ph. D. thesis]: Munich. Technischen Universität München.

Heisinger, B., Lal, D., Jull, A.J.T., Kubik, P., Ivy-Ochs, S., Knie, K., Nolte, E., 2002a. Production of selected cosmogenic radionuclides by muons: 2. Capture of negative muons. Earth and Planetary Science Letters 200, 357–369.

Heisinger, B., Lal, D., Jull, A.J.T., Kubik, P., Ivy-Ochs, S., Neumaier, S., Knie, K., Lazarev, V., Nolte, E., 2002b. Production of selected cosmogenic radionuclides by muons: 1. Fast muons. Earth and Planetary Science Letters 200, 345–355.

Jordan, T.E., Kirk-Lawlor, N.E., Blanco, N.P., Rech, J.A., Cosentino, N.J., 2014. Landscape modification in response to repeated onset of hyperarid paleoclimate states since 14 Ma, Atacama Desert, Chile. Geological Society of America Bulletin 126, 1016–1046.

Jungers, M.C., Heimsath, A.M., Amundson, R., Balco, G., Shuster, D., Chong, G., 2013. Active erosion–deposition cycles in the hyperarid Atacama Desert of northern Chile. Earth and Planetary Science Letters 371, 125–133.

Kim, K.J., Englert, P.A.J., 2004. Profiles of in situ ^{10}Be and ^{26}Al at great depths at the Macraes Flat, East Otago, New Zealand. Earth and Planetary Science Letters 223, 113–126.

Kober, F., Ivy-Ochs, S., Schlunegger, F., Baur, H., Kubik, P.W., Wieler, R., 2007. Denudation rates and a topography-driven rainfall threshold in northern Chile: Multiple cosmogenic nuclide data and sediment yield budgets. Geomorphology 83, 97–120.

Kober, F., Alfimov, V., Ivy-Ochs, S., Kubik, P.W., Wieler, R., 2011. The cosmogenic ^{21}Ne production rate in quartz evaluated on a large set of existing ^{21}Ne–^{10}Be data. Earth and Planetary Science Letters 302, 163–171.

Korschinek, G., Bergmaier, A., Faestermann, T., Gerstmann, U.C., Knie, K., Rugel, G., Wallner, A., Dillmann, I., Dollinger, G., Von Gostomski, C.L., others, 2010. A new value for the half-life of ^{10}Be by heavy-ion elastic recoil detection and liquid scintillation counting. Nuclear Instruments and Methods in Physics Research Section B: Beam Interactions with Materials and Atoms 268, 187–191.

Lupker, M., Hippe, K., Kober, F., Wacker, L., Braucher, R., Bourlès, D., Vidal Romani, J., Wieler, R., 2013. Depth-dependence of the production rate of in-situ 14-C in quartz, in: EGU General Assembly Conference Abstracts. p. 2185.

Maksaev, V., Zentilli, M., 1999. Fission track thermochronology of the Domeyko Cordillera, northern Chile: Implications for Andean tectonics and porphyry copper metallogenesis. Exploration and Mining Geology 8, 65–90.

Martinod, J., Regard, V., Riquelme, R., Aguilar, G., Guillaume, B., Carretier, S., Cortés-Aranda, J., Leanni, L., Hérail, G., 2016. Pleistocene uplift, climate and morphological segmentation of the northern Chile coasts (24° S–32° S): Insights from cosmogenic ^{10}Be dating of paleoshorelines. Geomorphology 274, 78–91.

Mora, R., Artal, J., Brockway, H., Martinez, E., Muhr, R., 2004. El Tesoro exotic copper deposit, Antofagasta region, northern Chile. Society of Economic Geologists, Special Publication 11, 187–197.

Mpodozis, C., Cornejo, P., 2012. Cenozoic tectonics and porphyry copper systems of the Chilean Andes. Society of Economic Geologists Special Publication 16, 329–360.

Nishiizumi, K., Caffee, M.W., Finkel, R.C., Brimhall, G., Mote, T., 2005. Remnants of a fossil alluvial fan landscape of Miocene age in the Atacama Desert of northern Chile using cosmogenic nuclide exposure age dating. Earth and Planetary Science Letters 237, 499–507.

Oerter, E., Amundson, R., Heimsath, A., Jungers, M., Chong, G., Renne, P., 2016. Early to Middle Miocene climate in the Atacama Desert of northern Chile. Palaeogeography, Palaeoclimatology, Palaeoecology 441, 890–900.

Owen, J.J., Dietrich, W.E., Nishiizumi, K., Chong, G., Amundson, R., 2013. Zebra stripes in the Atacama Desert: Fossil evidence of overland flow. Geomorphology 182, 157–172.

Perelló, J., Muhr, R., Mora, R., Martínez, E., Brockway, H., Swaneck, T., Artal, J., Mpodozis, C., Münchmeyer, C., Clifford, J., others, 2010. Wealth Creation through Exploration in a Mature Terrain: The Case History of the Centinela District, northern Chile Porphyry Copper Belt. Economic Geology. Special Publication 15, 229–252.

Phillips, F.M., Hinz, M., Marrero, S.M., Nishiizumi, K., 2015. Constraints on cosmogenic nuclide production rates by samples from the Sierra Nevada, California: II. Sample sites and evaluation. Quat. Geochronol.

Placzek, C.J., Matmon, A., Granger, D.E., Quade, J., Niedermann, S., 2010. Evidence for active landscape evolution in the hyperarid Atacama from multiple terrestrial cosmogenic nuclides. Earth and Planetary Science Letters 295, 12–20.

Placzek, C., Granger, D.E., Matmon, A., Quade, J., Ryb, U., 2014. Geomorphic process rates in the central Atacama Desert, Chile: Insights from cosmogenic nuclides and implications for the onset of hyperaridity. American Journal of Science 314, 1462–1512.

Putkonen, J., Swanson, T., 2003. Accuracy of cosmogenic ages for moraines. Quaternary Research 59, 255–261.

Reedy, R. C., Nishiizumi, K., Lal, D., Arnold, J. R., Englert, P. A. J., Klein, J., Middleton, R.; Jull, A.J.T., Donahue, D. J. (1994). Simulations of terrestrial in-situ cosmogenic-nuclide production. *Nuclear Instruments and Methods in Physics Research Section B: Beam Interactions with Materials and Atoms*, *92*(1-4), 297-300

Reich, M., Palacios, C., Vargas, G., Luo, S., Cameron, E.M., Leybourne, M.I., Parada, M.A., Zúñiga, A., You, C.-F., 2009. Supergene enrichment of copper deposits since the onset of modern hyperaridity in the Atacama Desert, Chile. Mineralium Deposita 44, 497–504.

Riquelme, R., Tapia, M., Campos, E., Mpodozis, C., Carretier, S., González, R., Muñoz, S., Fernandez-Mort, A., Sanchez, C., Marquardt, C. (2017). Supergene and exotic Cu mineralization occur during periods of landscape stability in the Centinela Mining District, Atacama Desert. Basin Research, 1, 31.

Schaller, M., Von Blanckenburg, F., Veldkamp, A., Tebbens, L.A., Hovius, N., Kubik, P.W., 2002. A 30 000 yr record of erosion rates from cosmogenic ^{10}Be in middle European river terraces. Earth and Planetary Science Letters 204, 307–320.

Sillitoe, R.H., 2005. Supergene oxidized and enriched porphyry copper and related deposits. Economic Geology 100th Anniversary Volume 29, 723–768.

Stone, J.O.H., Evans, J.M., Fifield, L.K., Allan, G.L., Cresswell, R.G., 1998. Cosmogenic chlorine-36 production in calcite by muons. Geochimica et Cosmochimica Acta 62, 433–454.

Tapia, M., Riquelme, R., Marquardt, C., Mpodozis, C., Mora, R., 2012. Estratigrafía y sedimentología de la Cuenca El Tesoro, Distrito Centinela (región de Antofagasta) y su relación con la mineralización exótica de cobre, in: En XII Congreso Geológico Chileno, Antofagasta.

Tucker, G.E., Hancock, G.R., 2010. Modelling landscape evolution. Earth Surface Processes and Landforms 35, 28–50.

Von Blanckenburg, F., Belshaw, N.S., O'Nions, R.K., 1996. Separation of 9Be and cosmogenic ^{10}Be from environmental materials and SIMS isotope dilution analysis. Chemical Geology 129, 93–99.

Wang, F., Michalski, G., Seo, J.-H., Granger, D.E., Lifton, N., Caffee, M., 2015. Beryllium-10 concentrations in the hyper-arid soils in the Atacama Desert, Chile: Implications for arid soil formation rates and El Niño driven changes in Pliocene precipitation. Geochimica et Cosmochimica Acta 160, 227–242.

Yanites, B.J., Tucker, G.E., Anderson, R.S., 2009. Numerical and analytical models of cosmogenic radionuclide dynamics in landslide-dominated drainage basins. Journal of Geophysical Research 114.

Table of Figures and tables for Chapter 6

Chapter 7

General discussion

Abstract

In this general discussion, I discuss implications of the results obtained in the context of the Centinela District.

First, I recall erosion rates of the Centinela District, obtained from the different methods in this PhD. Then I discuss the main implications of such results at the scale of the district and at the scale of the entire Precordillera of the Atacama Desert.

In a second part I review the controls of supergene mineralization and the possible contributions to precedent models with my new data and observations.

Finally, the third part will compare and extend these observations in a general application context, with other metallic supergene known deposits.

7.1 Supergene and exotic copper mineralization formation conditions in the Centinela District and northern Chile.

In chapter 5, the relationship between the exhumation timing of primary hypogene porphyry copper present in the Centinela District and supergene copper mineralization ages was highlighted. Nineteen new low-temperature thermochronological data permitted to model cooling patterns through scenarios for early Paleocene to mid-Eocene intrusive porphyry copper. All the Centinela District samples show similar and coherent modelled cooling patterns. Compared to the timing of supergene Cu-mineralization on the district, our models strongly suggest that supergene processes occurred during the stage of landscape pediplanation.

The Chapter 6 presents the application of ^{10}Be and ^{21}Ne cosmogenic nuclides to estimate the sediment burial age in a Miocene sedimentary column in the Tesoro and Mirador mining pits. The ages obtained allow, in turns, the age of syn-sedimentary exotic Cu-mineralization to be determined. The cosmogenic nuclide concentrations in the copper enriched layer demonstrates that the exotic deposit occurred in a moment of sedimentation quiescence. Nevertheless, this pause of sedimentation occurred during a period of an accelerated sedimentation rate from ~14 to ~10 Ma, probably due to the blocking effect of faulting and before the hyper-aridification of the Atacama Desert. Low-temperature thermochronologic method was applied to the entire Centinela District on intrusive rocks meanwhile the cosmogenic nuclides were applied at the scale of a mine on Miocene gravels. Both methods, which are independent and correspond to different spatial and temporal application scales suggest similar conclusions, namely that supergene copper enrichment occurred during periods of slow landscape evolution.

To illustrate this, I transposed the low-temperature thermochronological and cosmogenic nuclides information into erosion rates (Figure 7.1), at the scale of the District, to which I added information from geological constrains as the presence of the ~10 Ma ignimbrite in the District.
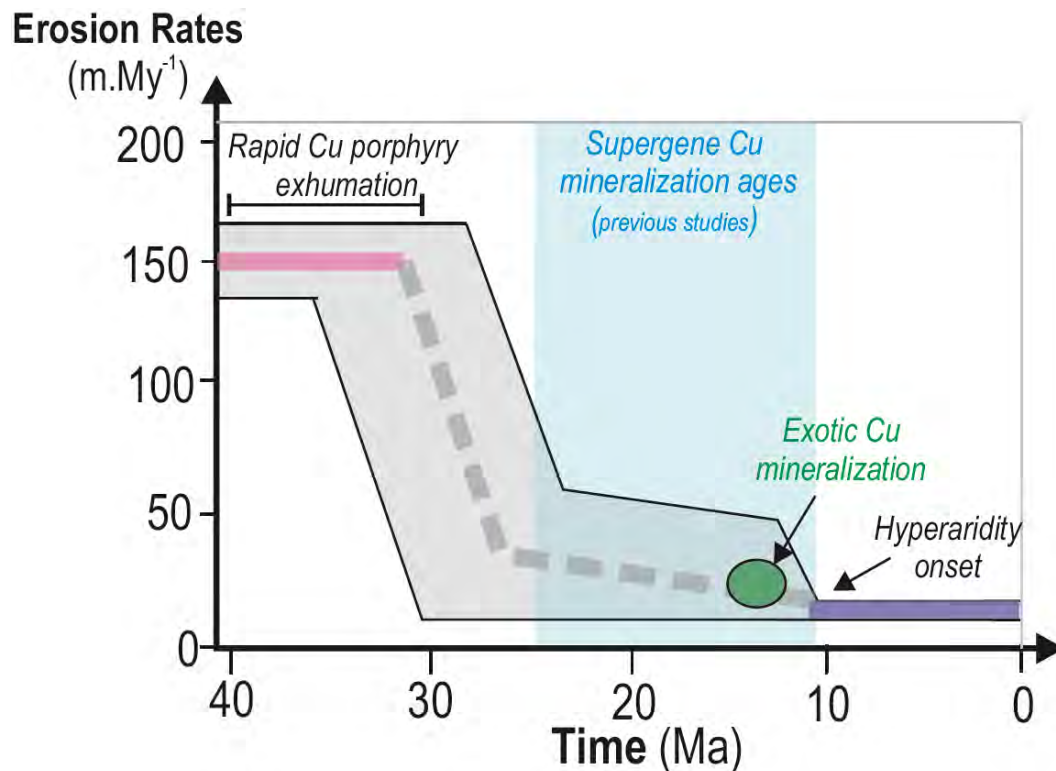
Figure 7.1 – Erosion rates (m.My⁻¹) simplified estimations according to time (Ma) in the Centinela District inferred from low-temperature thermochronology (in pink) and cosmogenic nuclides (in purple). Supergene Cu mineralization age from (Sillitoe and McKee, 1996; Perello et al., 2010; Riquelme et al., 2017)

The only previous quantitative analysis of denudation in an arid context of supergene copper enrichment was realized in the Atacama Desert by Alpers and Brimhall (1988) in the Escondida mine, located 150 km south to the Centinela District (Figure 7.2).

The authors combined hypogene and supergene mineralization dating on K-Ar, estimations of the eroded leached capping thickness and the use of geochemical mass-balance analysis and fluid inclusion geothermobarometry on similar deposits. Because these authors had no direct estimation of the denudation history, they proposed three scenarios A, B and C, each one corresponds to a different hypothesis about the onset of the lithocap thickness erosion. Scenario A is based on high and low estimates of eroded thickness and a constant exhumation since the hypogene alteration of the porphyry copper (~34 Ma). Scenario B assumes that the lithocap erosion begin at ~21 Ma. The last scenario, C, is based on the continuous erosion of leached capping material during supergene enrichment. The evolution of the eroded thickness (in meters) according to time (in million years) are represented in Figure 7.3 for the different scenarios. The alteration timing in the Escondida mine are respectively ~34 Ma and 18 Ma for the hypogene and supergene alteration and the main erosion necessarily occurred in-between, but with a timing which is not constrained and depends on the 3 scenarios
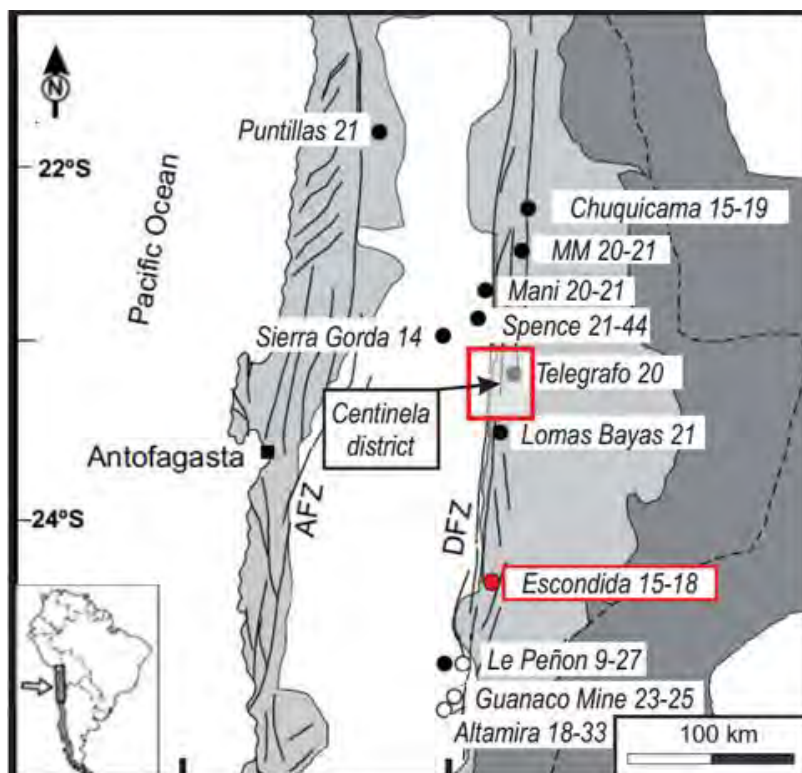
Figure 7. 2 – Localization of the mine in northern Chile from ~26°S to 21°S (modified from Arancibia, 2006).

The different curves illustrate the uncertainties of denudation histories (Figure 7.3) and magnitude between ~34 and ~18 Ma. Based on K/Ar ages for supergene alunite, Alpers and Brimhall (1988) could estimate that at least 140 m was eroded between 18 and 14.7 Ma, which led to a minimum denudation rate during supergene enrichment of 42 m.My^{-1}, possibly larger than 100 m.My^{-1}.

First of all, an interesting observation is that regarding the distance between both mining districts (Escondida and Centinela) the maximum identified eroded thickness (3000 m) between hypogene alteration and supergene alteration in Alpers and Brimhall (1988) corresponds to the emplacement depths range of the Eocene porphyries copper determined in my thesis (~4100-2800 m; see Chapter 5). The timing range of supergene processes are also similar. This suggests that independent methods such as geochemical mass balance and thermochronology coincide in terms of total denudation.

In a second time, this comparison rises up the great advantage of thermochronology that allows us to document the exhumation path history of the porphyries copper. Our exhumation path modelling clearly points to the scenario A of Alpers and Brimhall (1988) of a slow and continuous denudation since ~34 Ma of porphyries and thus disqualifies the hypothesis for the B and C scenarios for the Centinela district. Furthermore, the thermochronology data and modelling indicates that the main exhumation period occurred before ~34 Ma, what Alpers and Brimhall (1988) could not evidence in the Escondidad mine. Finally, Alpers and Brimhall (1988) could only estimate a minimum denudation rate during supergene enrichment. In the Centinela district, our data indicate that this mean denudation rate ranged between several meters per Ma and 50 m.My^{-1} between ~30 Ma and ~10 Ma.
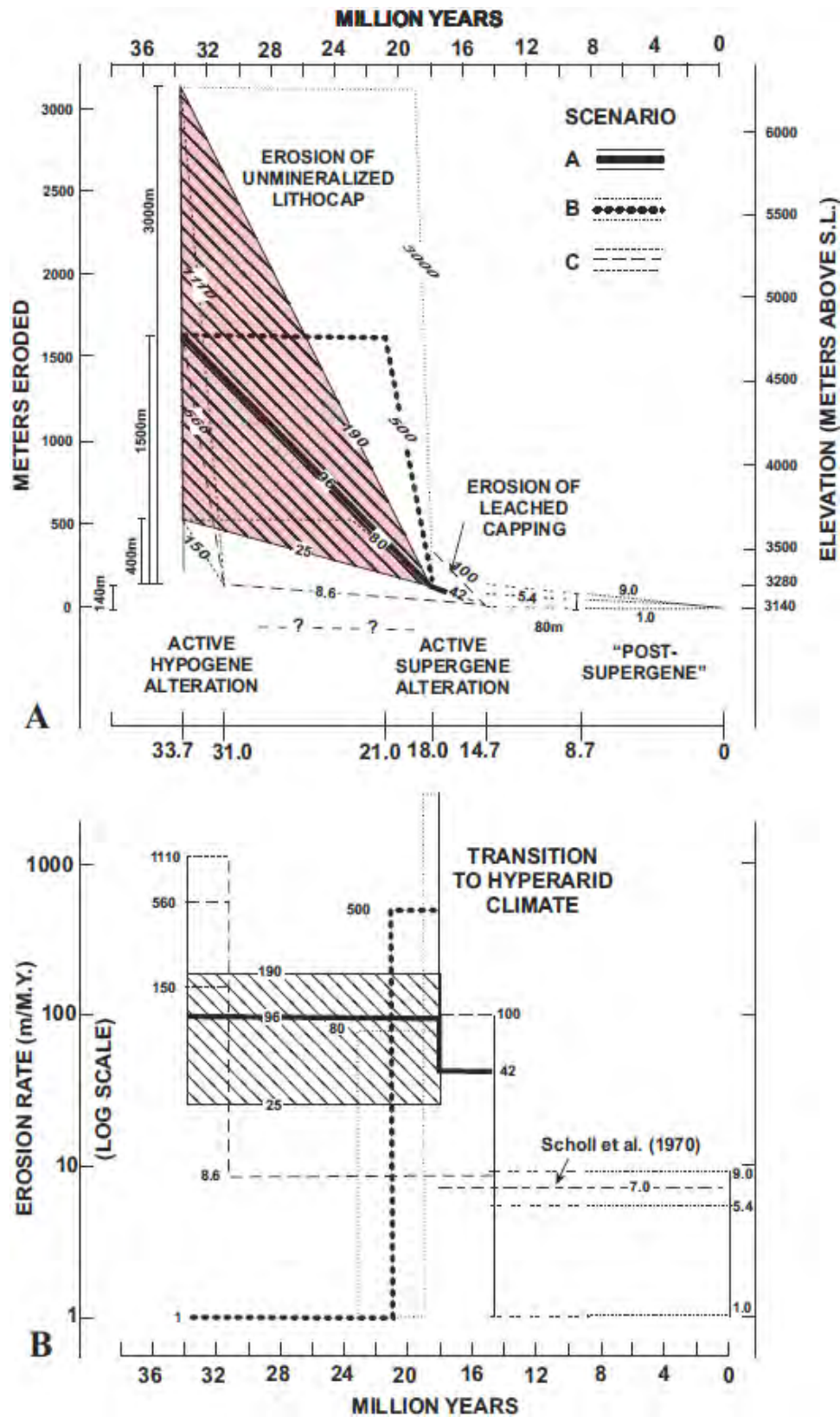
Figure 7.3 – A: Evolution of thickness of eroded meters above the porphyry Cu according to time, since the mid-Eocene in the Escondida Mine, northern Chile. B: Erosion rates of the porphyry Cu system, including the hydrothermal alteration, (m.My^{-1}) according to time (Ma), since the mid-Eocene after Alpers and Brimhall (1988)

195

At the scale of entire northern Chile existent data set (Vasconcelos et al., 2015), the comparison the between the erosion rates at the scale of the Centinela District and the supergene enrichment age spectra suggests that in majority supergene enrichment occurs when erosion rates are the lowest, during the pedimentation phase (Figure 7.4).
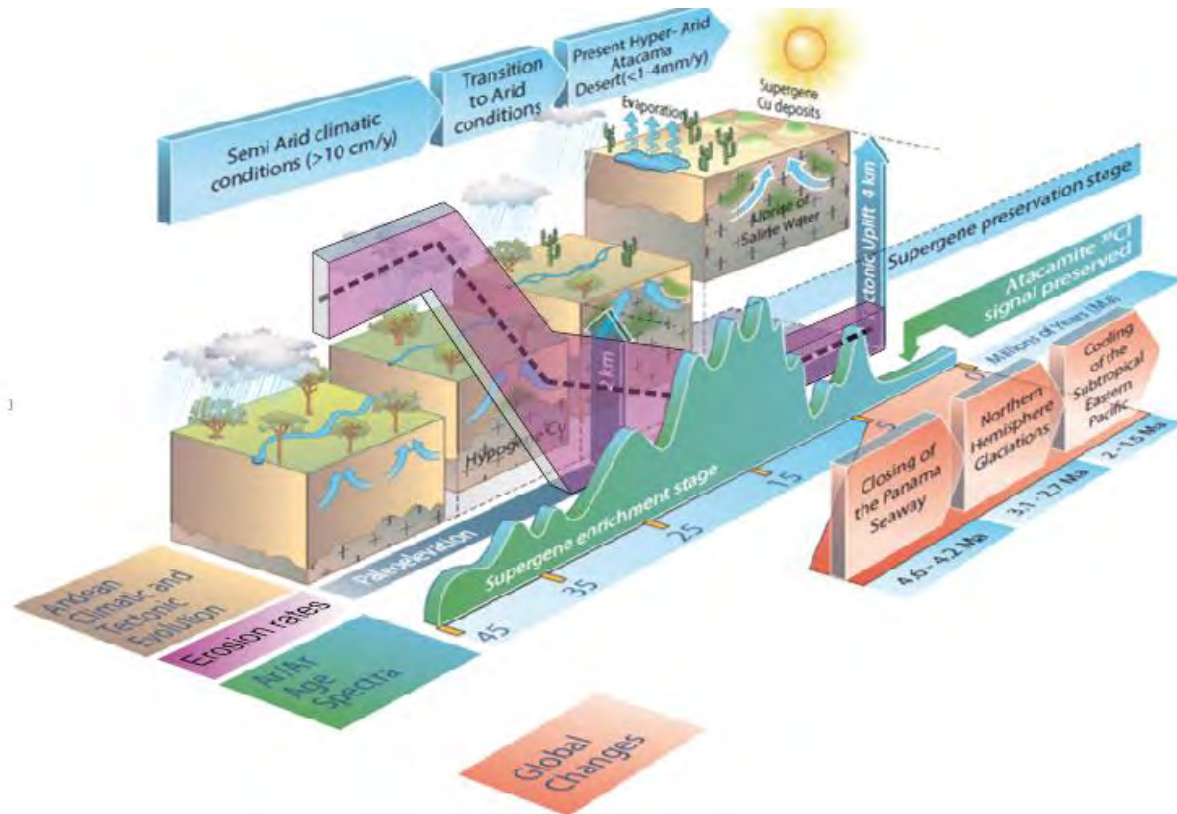
Figure 7.4 – Schematic representation of supergene enrichment processes during the climatic and tectonic evolution of the Andes, after Vasconcelos et al. (2015).

7.2   Supergene mineralization controls.

Copper remobilization and re-precipitation in the supergene environment requires enough groundwater to promote the oxidation and leaching of hypogene sulfides, the transport of copper in solution, the formation of secondary enriched sulfides and/ or copper oxide minerals, and eventually the formation of gravel-hosted exotic Cu deposits related to the lateral migration of the solutions (Clark et al., 1990; Münchmeyer, 1996; Chavez, 2000; Sillitoe, 2005). Several conditions have been advanced in literature as needed to generate supergene minerals from the weathering of a porphyry. Hartley and Rice (2005) summed up those conditions.

Firstly, a moderate precipitation rate, at the very least, is required (>100 mm/year, i.e. a semiarid climate, Clark et al. 1990), to provide high water-to-rock ratios that favor supergene mineral generation (e.g. Vasconcelos, 1999; Chavez, 2000).

Secondly, supergene mineralization requires a water table descent rate that allows for the hypogene sulfides to be gradually exposed to the effects of oxydative weathering (Sillitoe, 2005; Hartley and Rice, 2005; Bissig and Riquelme, 2009, 2010). Thus, the average erosion rate must be in overall balance with the water table descent rate so that the sulfides can undergo significant oxydation before they are removed mechanically (e.g. Emmons, 1917; Ransome, 1919; Brimhall et al., 1985; Sillitoe, 2005).

A third control relies on the absence of burial by superimposed sediments (Hartley and Rice, 2005). Indeed, the presence of gravels could inhibit the efficient descent of the paleo-water table in the Critical zone and unable the oxidative weathering of sulphides (Sillitoe and McKee 1996). Finally, the last constrain concerns the landscape evolution. Sillitoe (2005) suggests that the "*Subplanar erosion surfaces, such as pediplains, are not considered to be a requirement for efficient supergene activity*".

The results obtained during this thesis allow me to discuss some of these different hypothesis, especially the one related to the geomorphology of supergene environment. Indeed, as both low-temperature thermochronology and cosmogenic nuclides seem to indicate that supergene enrichment processes occur during the pedimentation stage, where erosion rates are low, it seems not likely and not compatible with my results that the descent of the water table is produced by a tectonically induced event. My results thus unsettle the last statement from Sillitoe (2005), at least in the case of the Centinela district.

7.3   Global context relationship about metalliferous deposits.

The thickening of the weathered profile and the degree of copper enrichment thus depends probably on a subtle balance between the precipitation rate and the exhumation rate of a porphyry copper, both controlling the residence times of water in the vadose and saturated zones (Brimhall et al., 1985). Even though the balance between geomorphic, climate and tectonic processes seems ideal in the Atacama Desert for the formation of supergene enriched deposit, they do also occur and are being preserved in other environments. Therefore, to quantify the rates of the parameters involved in such a balance, a first approach is to consider this balance as a ratio between erosion rate and precipitation rate.

To illustrate this balance, I choose to represent precipitation rates and erosion rates for three different type of environments in which metalliferous supergene ore deposits have been documented: tropical and tectonically highly active (as in Papua Nueva Guinea), lateritic cratonic environments (as those in Africa or south Brazil) or arid and convergent environments (as in northern Chile and Perú). To allow this comparison between different environments I did not take into account the metal ore deposit type that has or have been concentrated by supergene processes.

The P (precipitation) and E (erosion) values are the following: in tropical active environments: P = 2000-4000 mm.y^{-1} and E = 1000-3000 m.My^{-1} (Braxton et al., 2009) in cratonic contexts: P = 2000-4000 mm.y^{-1} and E =~10 m.My^{-1} (Beauvais et al., 2007), in arid context, precipitations rates < 300 mm.y^{-1} (Clark et al., 1997; Jordan et al., 2014) and erosion exhumation rates 50 m.My^{-1} (Maksaev and Zentilli (1999) and results of this thesis).
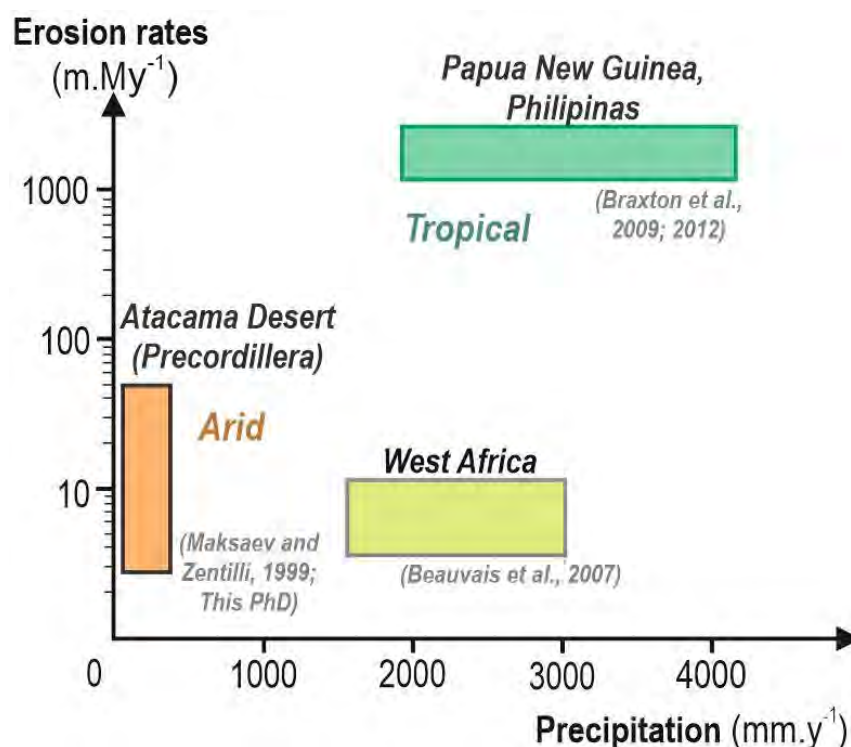
Figure 7.5 – Syn-supergene enrichment conditions Erosion rates (m.My^{-1}) according to precipitation (mm.y^{-1}) for different locations where do occur metallic supergene enrichment.

It would be possible that a range of ratio between erosion rates and precipitation rates of syn-supergene enrichment could be a guideline to discriminate the potential environment where the conditions are brought together (the grey zone in Figure 7.5). This diagram could be refined by plotting many other examples of supergene copper deposits, for example from the USA. Nevertheless, in many cases, the paleo-denudation history is not known, by lack of thermochronological data. Similarly, quantifying the paleo-precipitation rate is a challenge. In the Centinela case, many sedimentological arguments point to an arid climate since the Eocene, with possible more humid periods (Riquelme et al., 2017). The mean paleo-precipitation rate can thus be bounded (<200 mm.yr^{-1}), although paleo peaks of humidity and drought in the Neogene remain difficult to quantify. The first paleo-sedimentation rates obtained with cosmogenic nuclides (Chapter 6) are a first promising step. A denser set of data would probably allow paleo-denudation and sedimentation rates to be estimated over time periods shorter than 1 Myr. This new approach could be developed in other cases to complement Figure 7.5.

Our results and Figure 7.5 show the predictive potential of the approach consisting of quantifying the paleo-denudation rates, as carried out in my PhD.

Following the pioneer works of Alpers and Brimhall (1988), the recent works of Braxton et al. (2009; 2011) and my own work show that such an approach should be carried out systematically in different districts under variable environments. If the favorable denudation-precipitation domain illustrated in Figure 7.5 was confirmed, this plot could also be useful as benchmarks for numerical modelling. For example, a model could be developed by coupling denudation, ground water circulation (e.g. Braun et al., 2016) and chemical weathering along a hill in order to determine the effect of the initial lithology, the condition for lateral flow and the formation of exotic deposits, and the effect of porosity variations associated with supergene mineralization processes. Such a model may also be used to evaluate the pertinence of defining the erosion-weathering balance as a simple ratio between physical erosion and precipitation rate. In order to develop a thick weathering profile, the rate of the downward weathering front advance must equal or exceed the erosion rate. The weathering front advance may depend on the first order on the water flux at the base of the weathering profile (Maher et al., 2010), as well as on the chemical disequilibrium between water and rock. The water flux depends on the precipitation rates which determines the water flux entering the soil, but also on the porosity evolution of the weathering profile, which itself should depend on the leaching and secondary mineralization processes (Brimhall et al., 1985). Linking the precipitation rate and the rate of the weathering front advance thus remains a general challenge.

One of the complications in this kind of study is that in many situations, the syn-supergene enrichment are difficult to recover, especially in environment with high precipitation /erosion rates and post enrichment environment changes. From this point of view, the Atacama Desert is really ideal as many supergene copper ore deposits were "fossilized" after the hyper-aridification of the Atacama climate (Sillitoe, 2005) This doesn't mean that no posterior supergene ore deposit occurred, but that they are really scarce and minor in terms of development of weathering profile (e.g. Reich et al., 2009).

In addition to the erosion and precipitation rates, a third important parameter is the time (Figure 7.6). In comparison, it seems intuitive that the profiles in arid environments take more time to develop. This time may correspond to the response time necessary to thicken the weathering profile. In humid and rapidly uplifting environments, the process controlling the weathering front advance (the rate of conversion of fresh rock into weathered rock) may be the descent of the water table. This descent may be fast because it is driven by relative uplift and high ground water pressure gradient. The resulting high ground water flux may foster the development of the weathering profile (Maher et al., 2010). A large precipitation rate favors this process.

On the contrary, in arid environments with lower ground water fluxes and solutes closer to saturation, the rate of front advance may be more dependent on the kinetics of mineral dissolution at the weathering front.

Such a difference may explain that the humid and rapidly uplifting Ok Tedi supergene copper weathering profile developed in less than 2 Ma, whereas we documented a time shift of 5 to 10 Ma between the beginning of the pedimentation and the formation of supergene copper in the Centinela district.
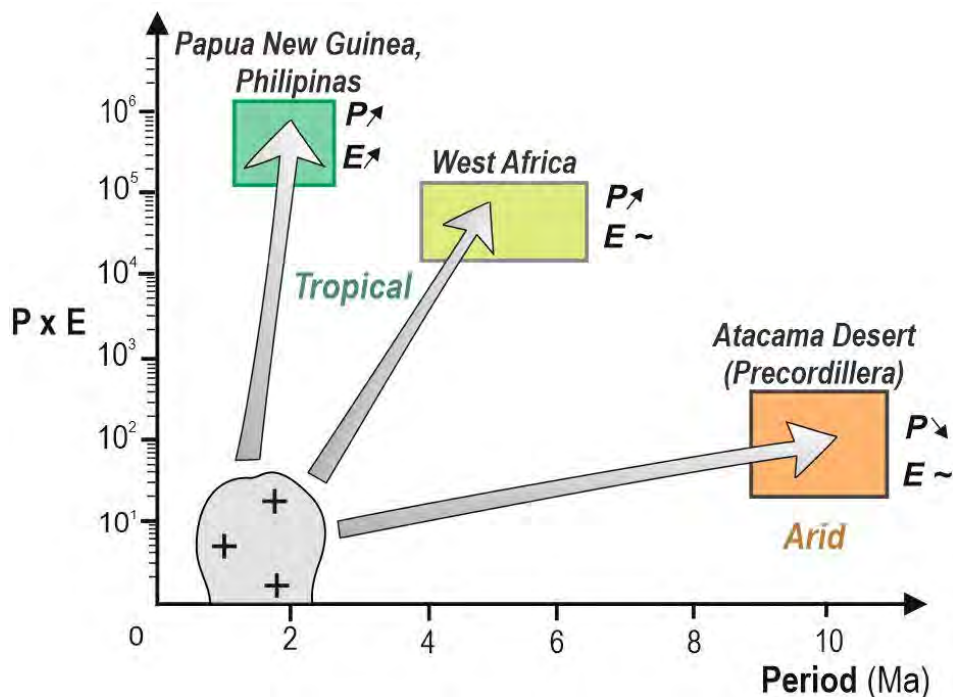
Figure 7. 6 – Qualitative relationship between precipitation rates x erosion according to age range of encountered supergene ages. P: precipitation (mm.y^{-1}); E: exhumation (m.My^{-1}) (References in Figure 7.5).

On the other hand, the precipitation rate seems to be inversely correlated with the thickness of supergene profiles (see Figure 7.7 and review of Braxton et al., 2009). Indeed, the thickest supergene profile (a medium thickness of ~200 m) is reported in arid environment meanwhile thinner (less than ~50 m) profiles were reported in the humid environments. A notable exception corresponds to the Boyongan mine case in Philippines, where both precipitation rates and exhumation rates seem high. In this latter case, the geological structure of the zone (high elevation, rock permeability and uplift) permitted an important drop of the table water (Braxton et al., 2012) and has maintained a thick layer of enriched copper mineralization (Braxton et al., 2009). From a general point of view, the weathered profile thickness depends on the rate of the weathering front advance and the physical erosion of the ground surface. In arid catchments, limited rainfall implies smaller erosion rate and thus favors the thickening of the profile, but it will take more time to develop because weathering front advance is slow. Again, the water circulation at the surface and in the ground, may control the response time, the thickness and the maturity of a weathered profile hosting supergene copper. Consequently, understanding how this water circulation has varied during geological times constitutes a major challenge.
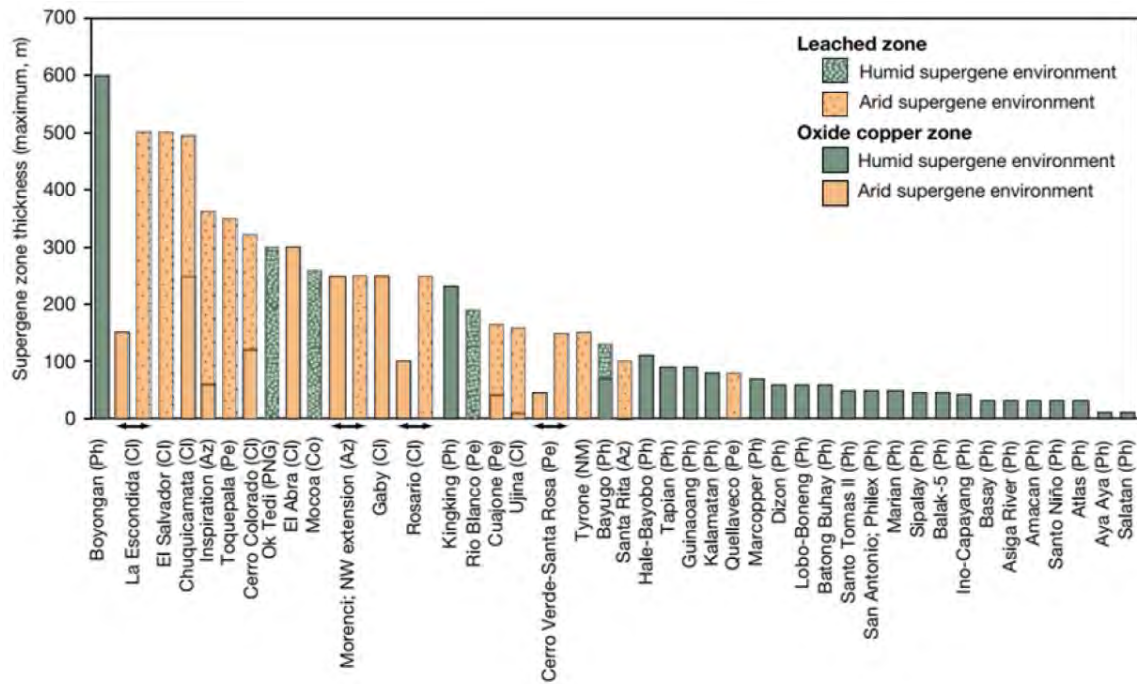
Figure 7.7 – Maximum thickness of the leached zone and/or oxide copper zone for selected porphyries from arid, leached cap portrayed above oxide zone for deposits where these maxima approximately coincide. Az = Arizona (USA); Cl = Chile, Co = Columbia, NM = New Mexico (USA); Pe = Perú; Ph = Philippines; PNG = Papua New Guinea (Braxton et al., 2009).

References for Chapter 7

Alpers, C.N., Brimhall, G.H., 1988. Middle Miocene climatic change in the Atacama Desert, northern Chile: Evidence from supergene mineralization at La Escondida. Geological Society of America Bulletin 100, 1640–1656.

Beauvais, A., 2007. Cenozoic evolution of West Africa scenery from cryptomelane ^{40}Ar-^{39}Ar dating, in: Geophysical Research Abstracts. p. 03191.

Bissig, T., Riquelme, R., 2010. Andean uplift and climate evolution in the southern Atacama Desert deduced from geomorphology and supergene alunite-group minerals. Earth and Planetary Science Letters 299, 447–457.

Bissig, T., Riquelme, R., 2009. Contrasting landscape evolution and development of supergene enrichment in the El Salvador porphyry Cu and Potrerillos-El Hueso Cu-Au districts, northern Chile. Society of Economic Geologists Special Publication 59–68.

Braun, J., Mercier, J., Guillocheau, F., Robin, C., 2016. A simple model for regolith formation by chemical weathering. Journal of Geophysical Research: Earth Surface 121, 2140–2171.

Braxton, D.P., Cooke, D.R., Dunlap, J., Norman, M., Reiners, P., Stein, H., Waters, P., 2012. From crucible to graben in 2.3 Ma: A high-resolution geochronological study of porphyry life cycles, Boyongan-Bayugo copper-gold deposits, Philippines. Geology 40, 471–474.

Braxton, D.P., Cooke, D.R., Ignacio, A.M., Rye, R.O., Waters, P.J., 2009. Ultra-deep oxidation and exotic copper formation at the late Pliocene Boyongan and Bayugo porphyry copper-gold deposits, Surigao, Philippines: geology, mineralogy, paleoaltimetry, and their implications for geologic, physiographic, and tectonic controls. Economic Geology 104, 333–349.

Brimhall, G.H., Alpers, C.N., Cunningham, A.B., 1985. Analysis of supergene ore-forming processes and ground-water solute transport using mass balance principles. Economic Geology 80, 1227–1256.

Chavez, W.X., 2000. Supergene oxidation of copper deposits: zoning and distribution of copper oxide minerals. Society of Economic Geologists Newsletter 41, 10–21.

Clark, A.H., Farrar, E., Kontak, D.J., Langridge, R.J., France, L.J., McBride, S.L., Woodman, P.L., Wasteneys, H.A., Sandeman, H.A., Archibald, D.A., others, 1990. Geologic and geochronologic constraints on the metallogenic evolution of the Andes of southeastern Peru. Economic Geology 85, 1520–1583.

Emmons, W.H., 1917. The enrichment of ore deposits. US Government Printing Office.

Hartley, A.J., Rice, C.M., 2005. Controls on supergene enrichment of porphyry copper deposits in the Central Andes: a review and discussion. Mineralium Deposita 40, 515–525.

Jordan, T.E., Kirk-Lawlor, N.E., Blanco, N.P., Rech, J.A., Cosentino, N.J., 2014. Landscape modification in response to repeated onset of hyperarid paleoclimate states since 14 Ma, Atacama Desert, Chile. Geological Society of America Bulletin 126, 1016–1046.

Maher, K., 2010. The dependence of chemical weathering rates on fluid residence time. Earth and Planetary Science Letters 294, 101–110.

Maksaev, V., Zentilli, M., 1999. Fission track thermochronology of the Domeyko Cordillera, northern Chile: Implications for Andean tectonics and porphyry copper metallogenesis. Exploration and Mining Geology 8, 65–90.

Münchmeyer, C., Camus, F., Sillitoe, R.M., Petersen, R., 1996. Exotic deposits-products of lateral migration of supergene solutions from porphyry copper deposits. Andean Copper Deposits 43–58.

Ransome, F. L. (1919). *The copper deposits of Ray and Miami, Arizona* United states geological survey, professional paper No. 115.

Reich, M., Palacios, C., Vargas, G., Luo, S., Cameron, E.M., Leybourne, M.I., Parada, M.A., Zúñiga, A., You, C.-F., 2009. Supergene enrichment of copper deposits since the onset of modern hyperaridity in the Atacama Desert, Chile. Mineralium Deposita 44, 497–504.

Sillitoe, R.H., 2005. Supergene oxidized and enriched porphyry copper and related deposits. Economic Geology 100th Anniversary Volume 29, 723–768.

Sillitoe, R.H., McKee, E.H., 1996. Age of supergene oxidation and enrichment in the Chilean porphyry copper province. Economic Geology 91, 164–179.

Vasconcelos, P.-M., 1999. K-Ar and ^{40}Ar/^{39}Ar geochronology of weathering processes. Annual Review of Earth and Planetary Sciences 27, 183–229.

Vasconcelos, P.M., Reich, M., Shuster, D.L., 2015. The paleoclimatic signatures of supergene metal deposits. Elements 11, 317–322.

Table of figures for Chapter 7

Conclusion

English version

By combining low-temperature thermochronology and the application of cosmogenic nuclides, I have aimed to constrain the paleo-denudation and geomorphic context of supergene copper mineralization in the Centinela District, in the Atacama Desert of Chile.

At the regional scale, the 29 new low-temperature thermochronology data permitted to quantify the exhumation along the forearc at 23°S, showing the different timing of exhumation between the different morpho-structural units.

It also permitted to confirm and clarify previous studies about the Precordillera timing of exhumation. Indeed, the Precordillera went through a rapid event of exhumation from the mid-Eocene to early Oligocene. The thermochronological results at the eastern border of the Precordillera also suggest a post mid-Miocene rapid cooling affirming the hypothesis that the main structural fault was east verging and not to the west as it is commonly documented in the forearc of the Atacama region.

In the Centinela District, supergene mineralization ^{40}Ar/^{39}Ar and K/Ar dating range from ~25 to ~12 Ma. This time span roughly overlaps the timing of pediplanation stage of the landscape evolution in the Atacama Desert, i.e. the landscape stage where denudational removal and wear of the landscape lead to a flattened landscape surface. From our thermochronological data we show that supergene copper enrichment occurs at least ~5 Ma after the exhumation of the primary source of copper. In terms of geomorphological cycle, this signifies that low reliefs are necessary to the formation of supergene copper mineralization in this particular climatic context, which wasn't demonstrated before.

The cosmogenic nuclides study performed on gravels which resulted from the exhumation of the reliefs in the district since the mid-Eocene, allowed us to refine the quantification of erosive processes during the deposition of an exotic copper mineralization layer. The decreasing concentration towards the top level of the enriched layer of sediments highlights that the deposit occurred during an erosive quiescence before being covered by a hundred meters before the onset of hyperaridity around 10 Ma. We also show that those deposits were datable by a new method. Indeed, coupling ^{10}Be and ^{21}Ne we show that the upper exotic deposit of El Tesoro previously associated to a ~22 Ma event is no older than 12 Ma.

The two methods applied indicate that supergene copper mineralization occur when the landscape is flattened and erosion rates are slow, even though humidity is required to form ore related deposits.

Version en français

En combinant la thermochronologie basse température et l'application des nucléides cosmogéniques, j'ai réussi à contraindre le contexte de la paléo-dénudation et le contexte géomorphologique de la minéralisation de cuivre supergène dans le district de Centinela, dans le désert d'Atacama au Chili.

À l'échelle régionale (~23°S de latitude), les 29 nouvelles données de thermochronologie basse température ont permis de quantifier l'exhumation le long de l'avant-arc, montrant le timing de l'exhumation entre les différentes unités morpho-structurales qui constituent les Andes.

Cette étude a également permis de confirmer et de préciser les études antérieures sur le timing d'exhumation de la Précordillère. En effet, la Précordillère a subi un événement rapide d'exhumation du milieu de l'Eocène au début de l'Oligocène. Les résultats thermochronologiques à la frontière orientale de la Précordillère suggèrent également un refroidissement rapide post- miocène confirmant l'hypothèse selon laquelle la principale faille structurale était de vergence est et non de vergence ouest, comme cela est communément documenté dans l'avant-arc de la région d'Atacama.

Dans le district de Centinela, les minéralisations supergènes ^{40}Ar / ^{39}Ar et K / Ar sont datées de ~25 à ~12 Ma. Cette période s'étend à peu près au stade de pédimentation du paysage dans le désert d'Atacama, c'est-à-dire l'étape du paysage où les taux de dénudation et l'usure des reliefs aboutissent à une surface plane. A l'aide des résultats thermochronologiques, nous montrons que l'enrichissement supergène en cuivre se produit ~5 Ma après l'exhumation de la principale source de cuivre. En termes de cycle géomorphologique, cela signifie que les bas-reliefs sont nécessaires à la formation de la minéralisation du cuivre supergène dans ce contexte climatique particulier, ce qui n'avait jamais été démontré.

L'étude des nucléides cosmogéniques effectuée sur les graves, résultant de l'exhumation des reliefs dans le district depuis le milieu de l'Eocène, a permis d'affiner la quantification des processus érosifs lors du dépôt d'une couche exotique de minéralisation de cuivre. La diminution de la concentration vers le niveau supérieur de la couche de sédiments enrichie en cuivre souligne que le dépôt s'est produit pendant une quiescence érosive avant d'être recouvert d'une centaine de mètres lors du début de l'hyperaridité autour de 10 Ma. Il a également été montré que ces dépôts sont datables par une nouvelle méthode. En effet, en couplant ^{10}Be et ^{21}Ne, nous montrons que l'âge du dépôt exotique d'El Tesoro précédemment associé à un événement daté autour de ~22 Ma, n'est pas supérieur à 14 Ma.

Les deux méthodes appliquées indiquent que la minéralisation du cuivre supergène se produit lorsque le paysage est aplati et les taux d'érosion sont lents, même si un certain niveau d'humidité est nécessaire pour former des gisements cuprifères.

Annexes

A.1 Quimal thermochronological results

A.1.1 Fission track analyses results

Sample no.	No. of crystals	Track density (x10^6 tr.cm-2)			Age dispersion		U	Central age	Mean track length	StD	No. of tracks
		ρd (Nd)	ρs (Ns)	ρi (Ni)	RE (%)	Pχ2 (%)	(ppm)	(Ma ± 1σ)	(μm)	(μm)	measured
QUI13-01	17	0,718	1,082	2,428	0,0	80,46	42,3	45,1 ± 2,6	12,07 ± 0,15	0,83	100
		[11903]	[445]	[1011]							
QUI13-02	11	0,850	0,849	2,187	46,1	0,00	32,2	52,1 ± 15,3	13,70 ± 0,15	1,3	31
		[11903]	[272]	[647]							
QUI13-03	20	0,838	0,933	2,345	0,0	64,27	35	45,7 ± 2,3	12,88 ± 0,15	1,37	73
		[11903]	[562]	[1437]							
QUI13-05	22	0,903	0,552	1,935	9,3	99,83	9,5	38,5 ± 3,7	15,37 ± 0,15	1,3	99
		[11903]	[265]	[952]							
QUI13-06	15	0,879	0,733	2,221	0,0	89,38	31,6	40,6 ± 3.3	14.00 ± 0,15	1,23	100
		[11903]	[247]	[753]							
QUI13-07	20	0,867	0,373	0,957	0,3	78,63	13,8	45,3 ± 3,2	12,96 ± 0,15	1,59	102
		[11903]	[285]	[762]							

Table A1 – Quimal Fission track data. Analyses determined by the external detector method using 0.5 for the 4π/2π geometry correction factor. Apatite fission-track ages were calculated using dosimeter glass CN-5; Analyst Caroline ξ=280±7.8 calibrated by multiple analyses of IUGS apatite age standards (Hurford, 1990). Pχ2 is probability of obtaining χ2 value for ν degrees of freedom, where ν=number of crystals. Central age is a modal age, weighted for different precisions of individual crystals. In track densities (N) shown in brackets is the numbers of tracks counted. ρd is the fission track density of the standard U-glass (CN-5); Ns (spontaneous), Ni (induced) and Nd (dosimeter) are the fission track numbers corresponding to ρs, ρi and ρd respectively.

A.1.2. AHe results.

Sample no.	Aliquot number	Mineral	He nmol/g	U (ppm)	Th (ppm)	FT	He raw age (Ma)	He corr. age (Ma)	error Abs
QUI13-03	A	1	45,06	37,04	152,07	0,70	28,54	40,60	2,80
	B	1	63,72	50,48	208,42	0,67	29,53	44,20	3,10
	D	1	73,41	24,61	305,95	0,59	34,97	59,60	4,20
	E	1	76,46	71,10	344,61	0,63	23,17	36,90	2,60
Mean			64,66	45,81	252,76	0,65	29,05	45,33	3,18
QUI13-02	A	1	14,93	12,63	99,36	0,66	19,11	29,13	2,04
	B	2	13,63	19,08	110,08	0,55	13,98	25,33	1,77
	C	1	14,15	10,56	87,33	0,65	20,96	32,30	2,26
	D	1	9,95	7,42	43,42	0,73	26,02	35,55	2,49
Mean			13,17	12,42	85,05	0,65	20,02	30,57	2,14
QUI13-05	A	1	28,71	22,16	137,49	0,69	24,27	35,17	2,46
	B	1	3,82	3,99	17,65	0,56	21,63	38,42	2,69
Mean			16,26	13,08	77,57	0,63	22,95	36,80	2,58
QUI13-06	A	2	38,97	32,58	236,88	0,59	20,34	34,24	2,40
	B	1	54,97	42,37	245,24	0,68	25,32	37,18	2,60
	C	2	49,92	40,67	247,68	0,62	23,26	37,52	2,63
	D	2	38,92	36,20	225,87	0,61	20,08	32,97	2,31
Mean			45,70	37,96	238,92	0,63	22,25	35,48	2,48
QUI13-07	A	1	21,22	16,11	116,34	0,66	22,49	33,92	2,37
	B	1	19,82	13,06	79,11	0,73	28,84	39,29	2,75
	C	1	24,66	22,18	181,95	0,57	17,49	30,96	2,17
	D	1	69,04	39,63	366,75	0,74	25,25	34,17	2,39
Mean			33,68	22,75	186,04	0,68	23,52	34,58	2,42

Table A2 – AHe raw data. The alpha ejection F_T corrections applied to AHe ages were calculated using the procedure of Gautheron and Tassan-Got (2010).

A.1.3. Radial plots
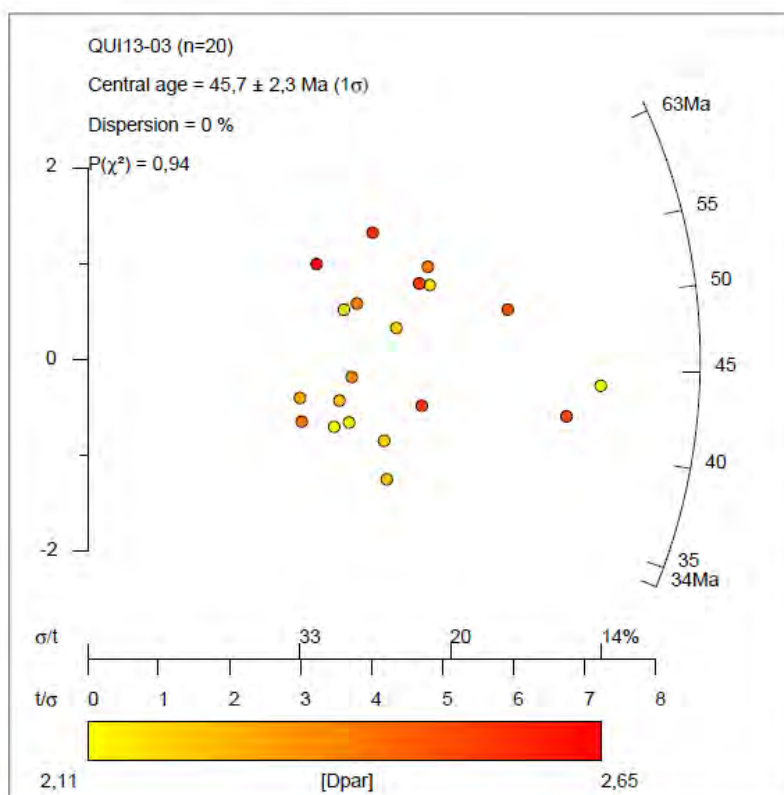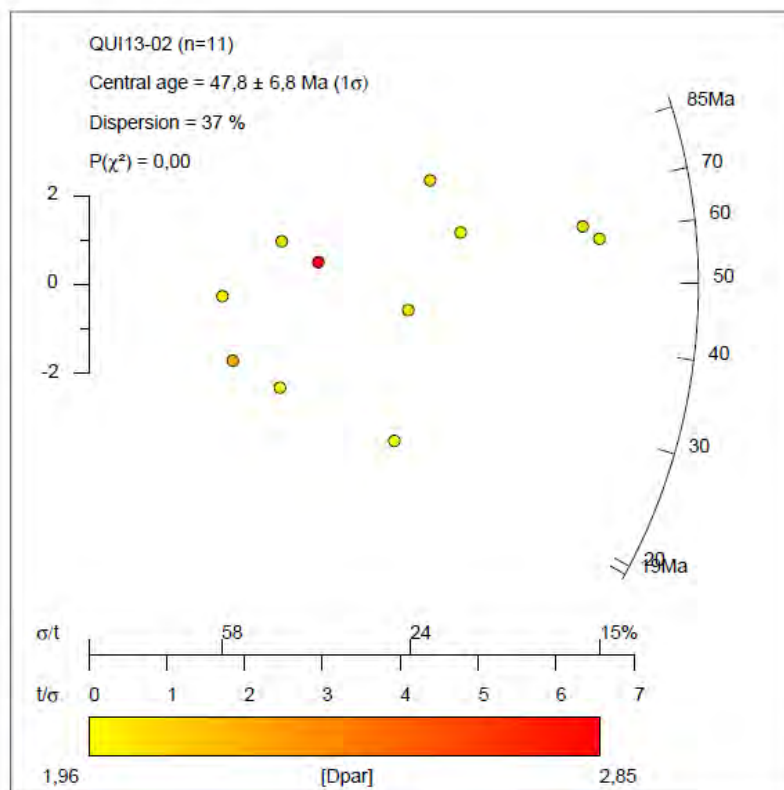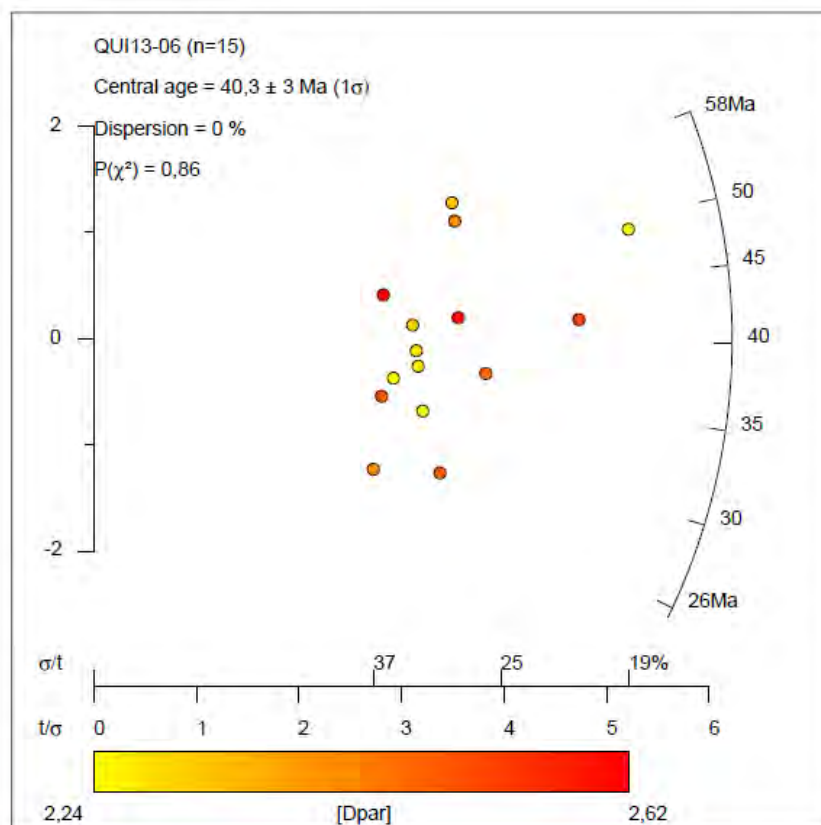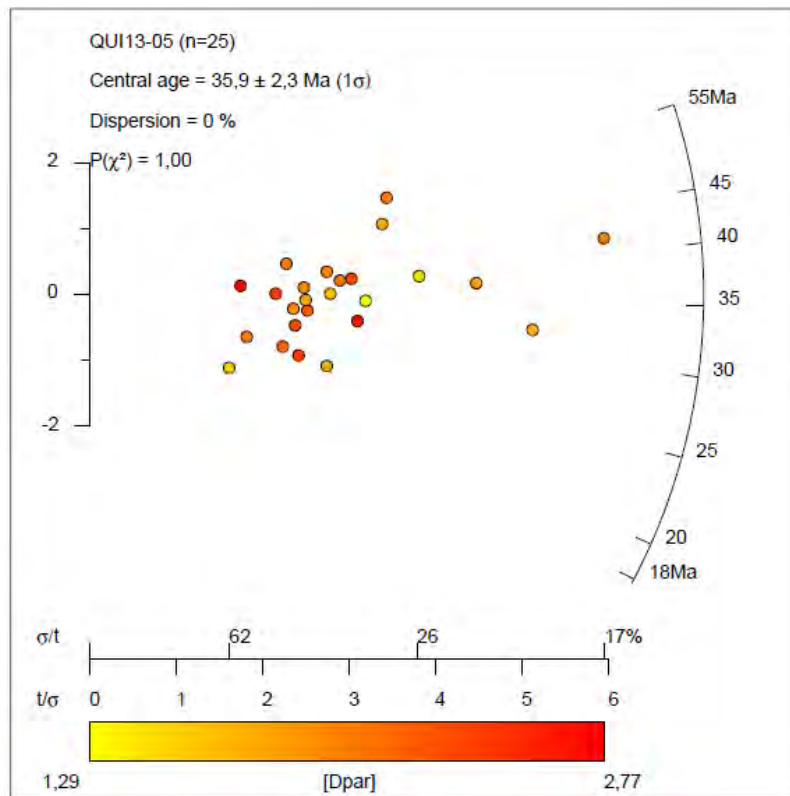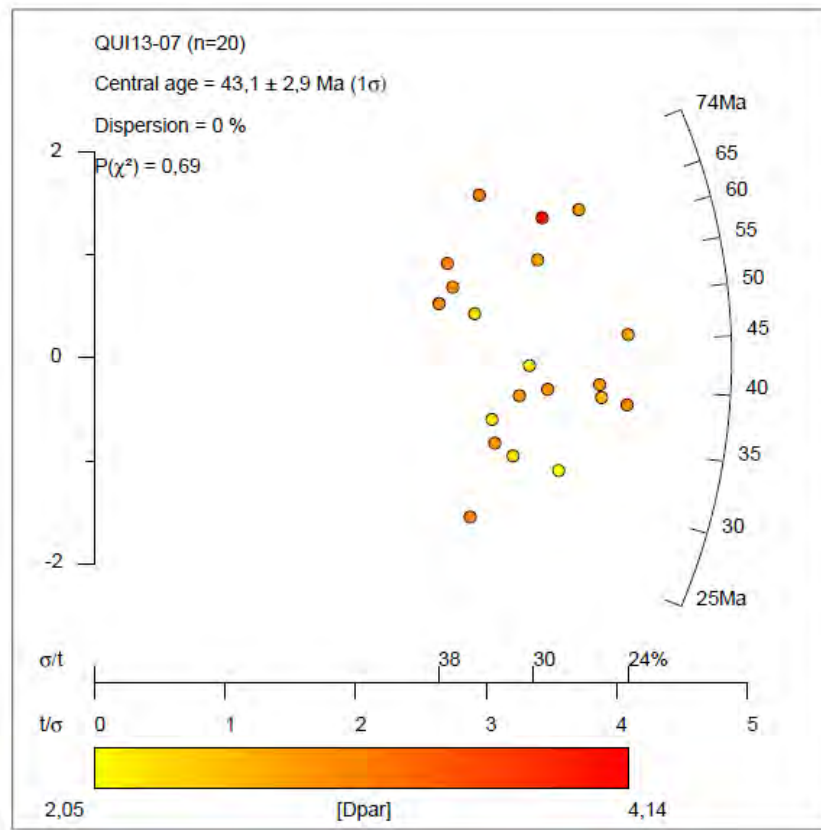
Figure A1 – QUI13-02, QUI13-03, QUI13-05, QUI13-06 and QUI13-07 radial plot.

A.2 Geochemistry

Ref Echantillon	As ppm	Ba ppm	Be ppm	Bi ppm	Cd ppm	Ce ppm	Co ppm	Cr ppm	Cs ppm	Cu ppm	Dy ppm	Er ppm	Eu ppm	Ga ppm	Gd ppm	Ge ppm	Hf ppm	Ho ppm	In ppm	La ppm
QUI13-07	1,574	1247	3,771	< L.D.	0,176	55,43	17,99	16,04	1,88	91,21	4,547	2,311	2,101	21,98	5,622	1,21	3,383	0,902	0,071	28,01
QUI13-02	< L.D.	2167	2,767	< L.D.	0,167	43,22	21,25	82,31	1,513	118,9	3,507	1,67	1,844	16,87	4,571	1,051	2,555	0,672	< L.D.	21,3

Ref Echantillon	Lu ppm	Mo ppm	Nb ppm	Nd ppm	Ni ppm	Pb ppm	Pr ppm	Rb ppm	Sc ppm	Sb ppm	Sm ppm	Sn ppm	Sr ppm	Ta ppm	Tb ppm	Th ppm
QUI13-07	0,339	1,581	6,128	28,48	9,119	12,1952	6,921	86,66	16,26	< L.D.	6,409	1,336	1898	0,491	0,797	3,763
QUI13-02	0,232	7,001	5,545	23,13	42,52	11,0818	5,507	93,41	20,58	< L.D.	5,261	1,202	2152	0,405	0,638	2,191

Ref Echantillon	V ppm	W ppm	Y ppm	Yb ppm	Zn ppm	Zr ppm	SiO2 %	Al2O3 %	Fe2O3 %	MnO %	MgO %	CaO %	Na2O %	K2O %	TiO2 %	P2O5 %	PF %	Total %
QUI13-07	243,4	0,808	24,29	2,169	103	122,2	51,62	18,12	8,35	0,21	2,69	8,28	3,77	4,14	0,84	0,52	0,56	99,09
QUI13-02	216,7	0,803	17,86	1,535	80,5	91,22	51,34	17,06	7,94	0,17	3,62	8,11	3,14	5,46	0,76	0,63	0,79	99,02

Table A3 – Major and traces elements concentration of the QUI13-07 and QUI13-02 samples from the Quimal.

A.3 Mineralogy: DRX diagrams.

C:\Documents and Settings\thibaut\Bureau\XRD 2014\V Regano\1304.DAT

volt=40   kV - current=25   mA - lambda=1.788970A - time= 1200.0sec - [17/12/2014 13:54:36] - ET 13-04
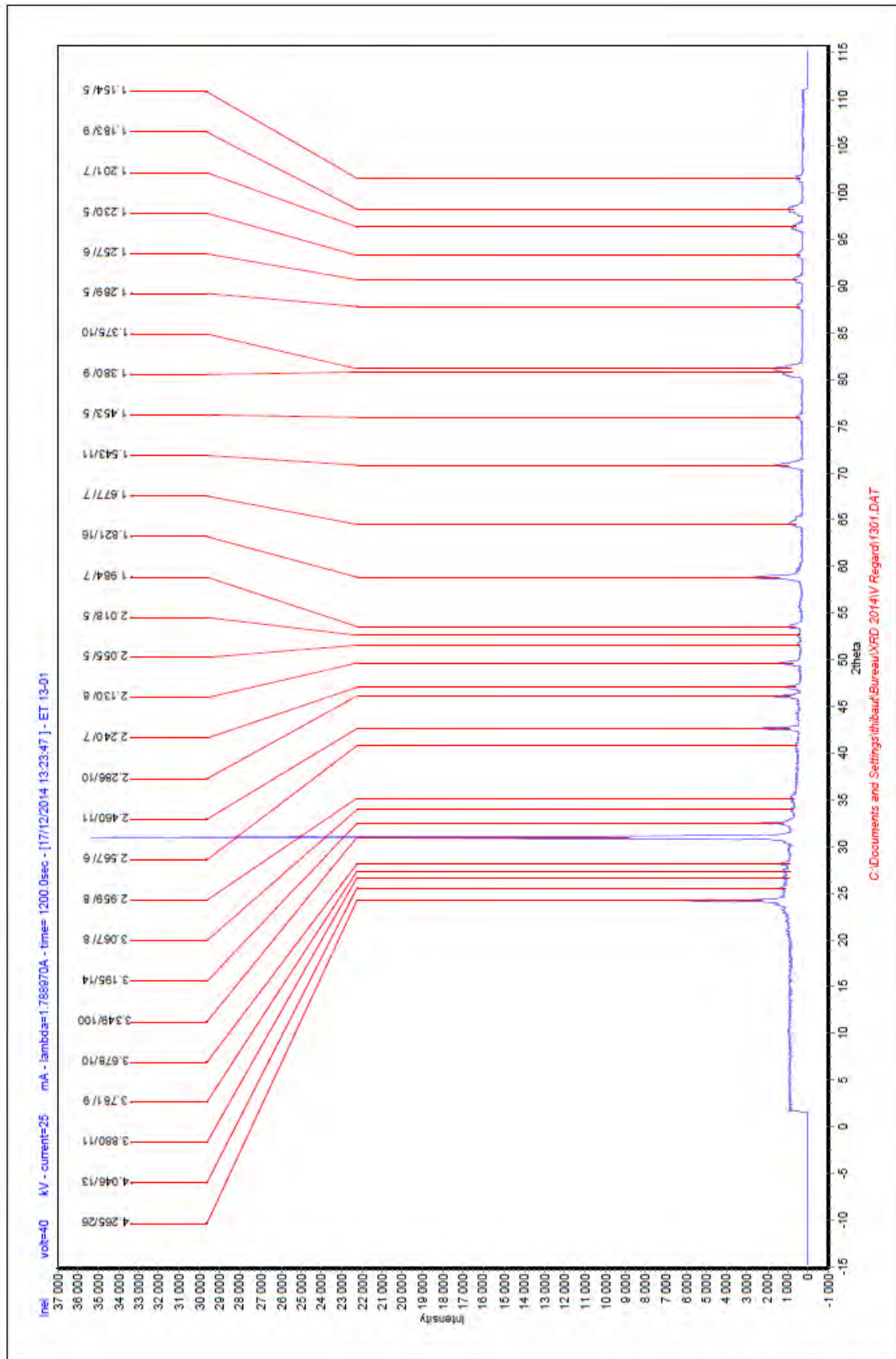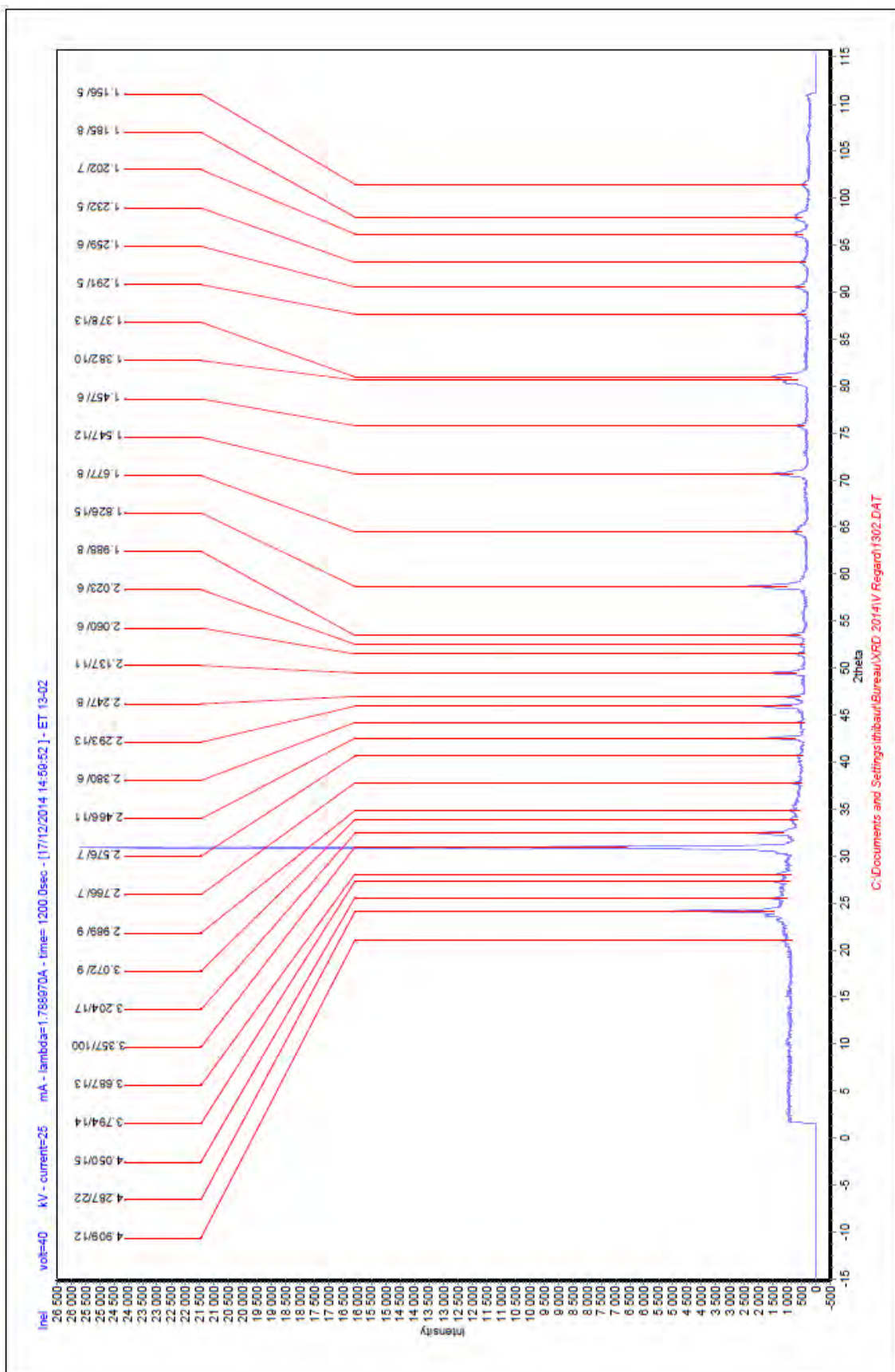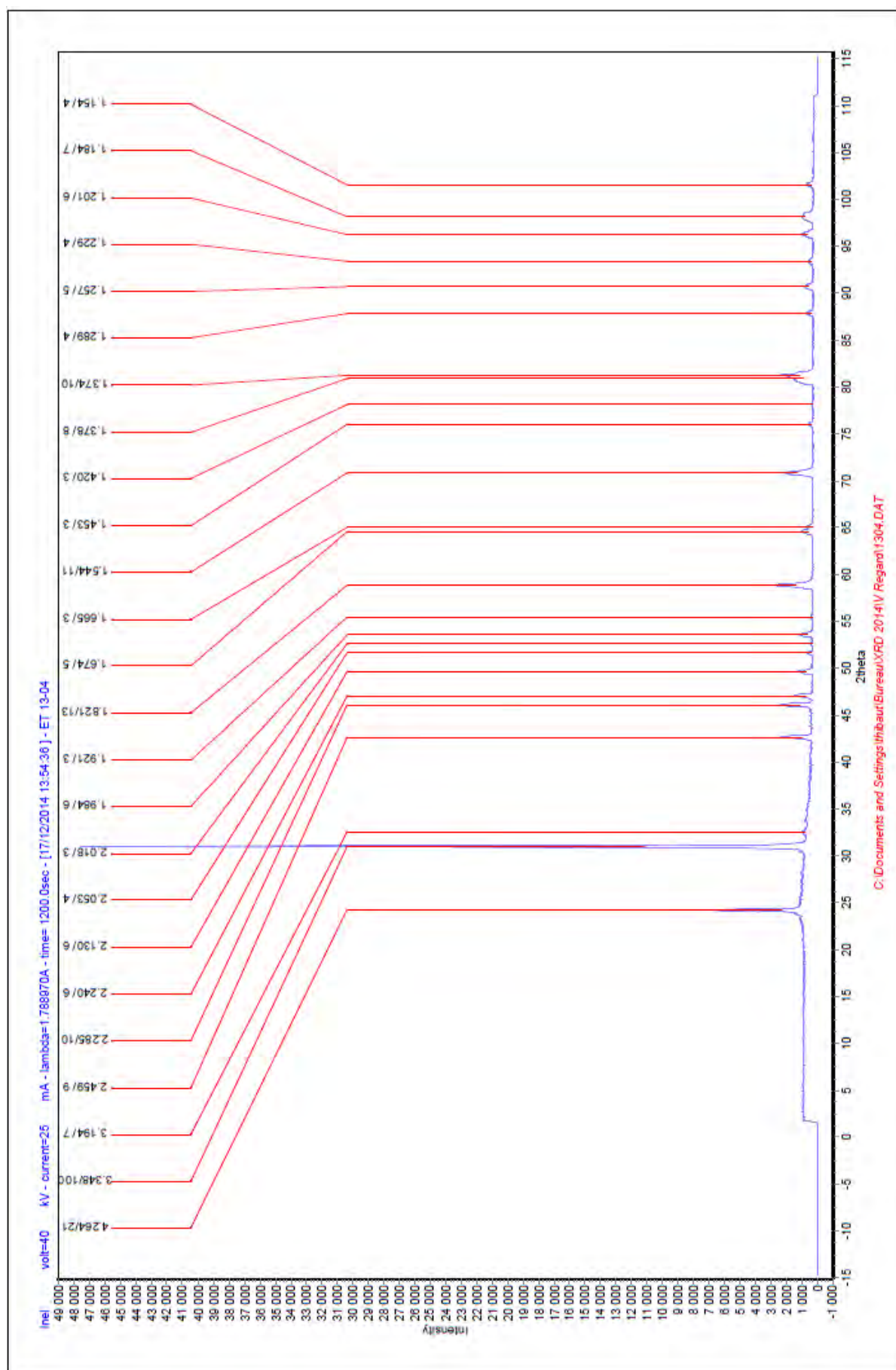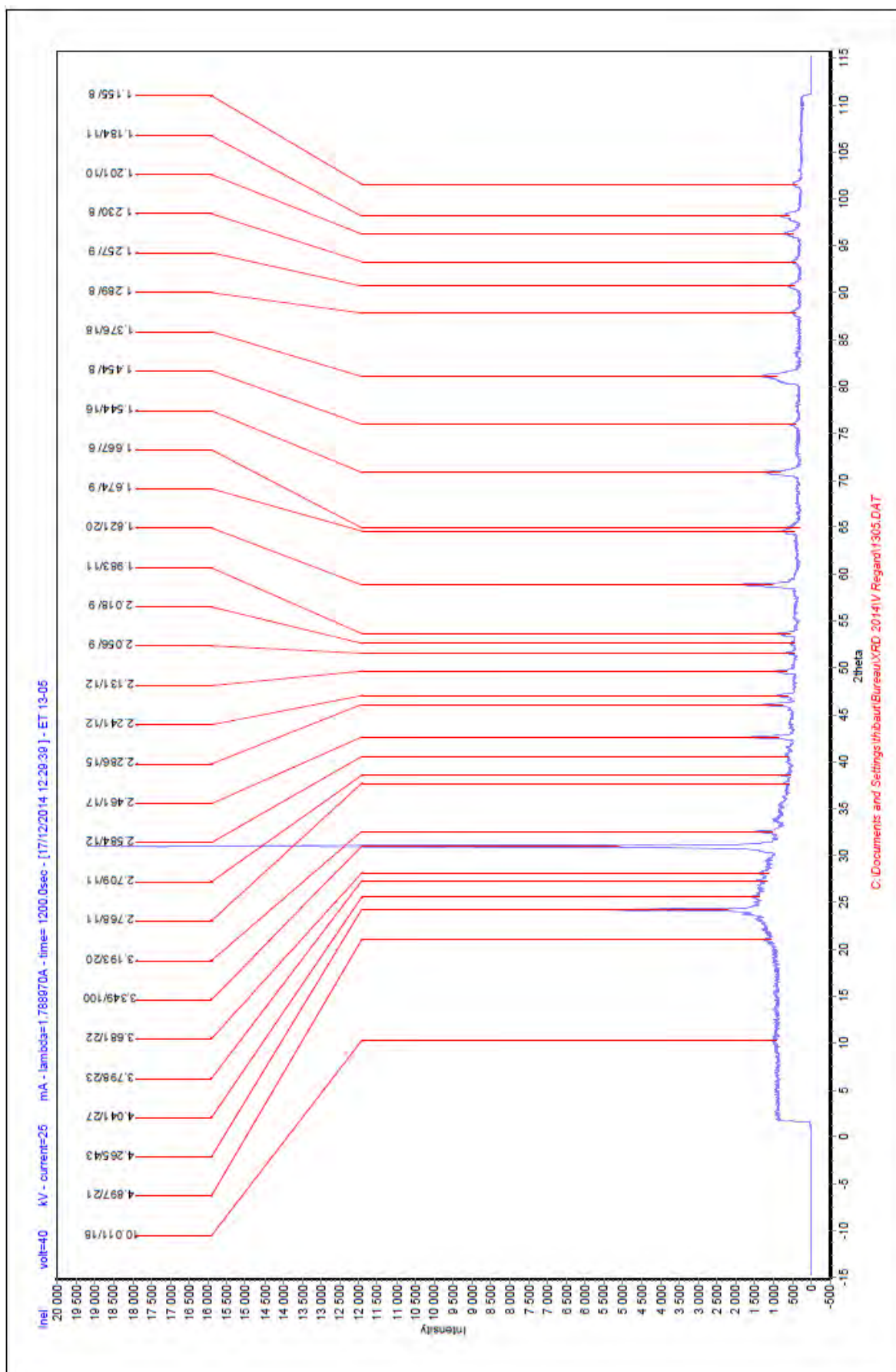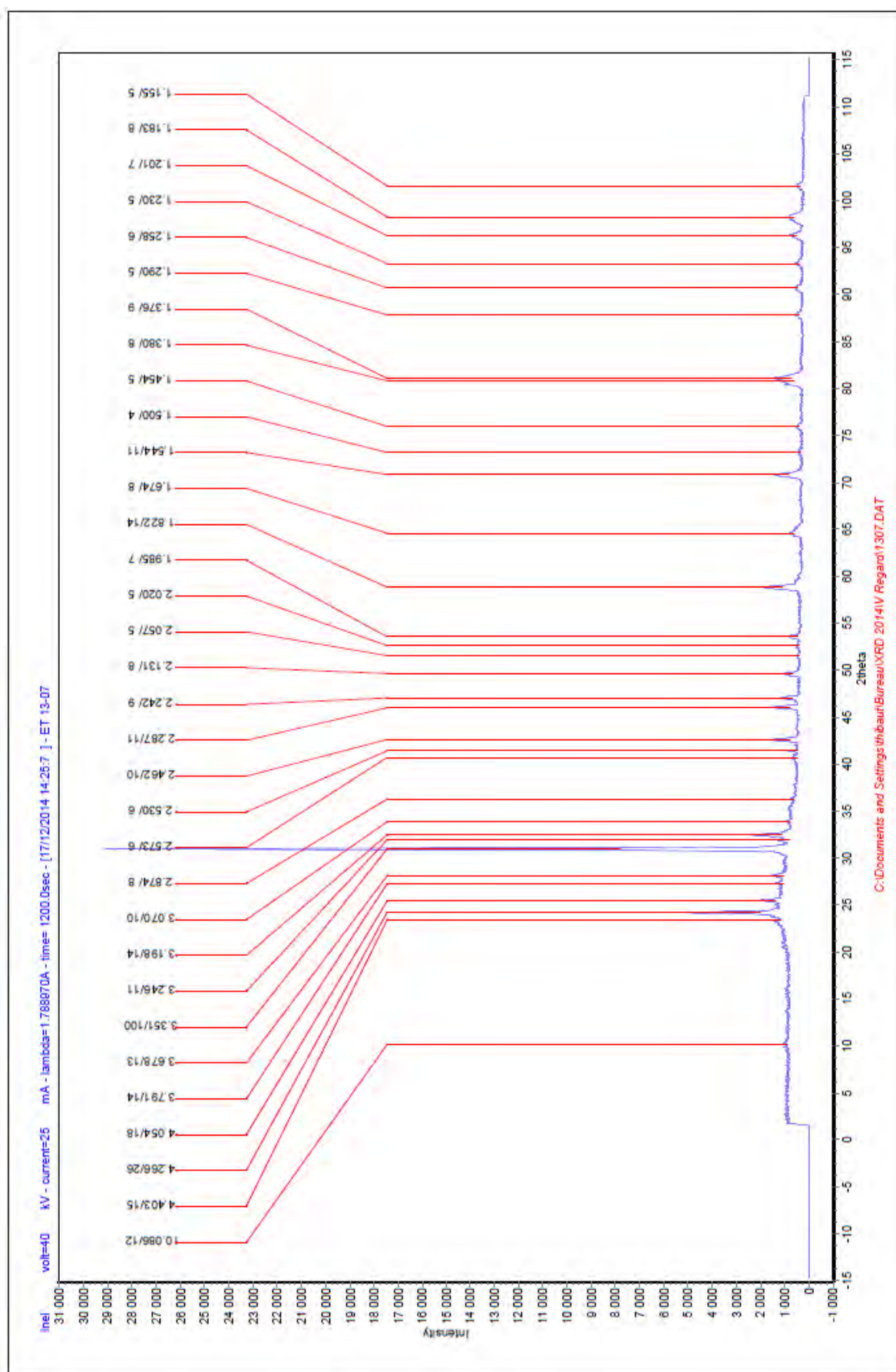
Figure A2 – DRX diagrams for ET13-01, ET13-02, ET13-04, ET13-05 and ET13-07

DATA REPOSITORY

Exhumation history and timing of supergene copper mineralization in arid context: new thermochronological data from the Centinela District, Atacama. Chile.

Caroline Sanchez, Stéphanie Brichau, Rodrigo Riquelme, Sébastien Carretier, Thomas Bissig, Cristopher Lopez, Constantino Mpodozis, Eduardo Campos, Vincent Regard, Gérard Hérail and Carlos Marquardt.

Table A1. ^{39}Ar/^{40}Ar and K/Ar supergene and exotic ages of the Centinela District

Paper	Mining Project	Mineral	Dating Method	PlateauAge (My ± 2s)
Riquelme et al. (2017)	Esperanza Sur	Jarosite	^{39}Ar/^{40}Ar	14.8 ± 0.5
Riquelme et al. (2017)	Esperanza Sur	Supergene alunite	^{39}Ar/^{40}Ar	12.6 ± 2.0
Riquelme et al. (2017)	Penacho Blanco	Supergene alunite	^{39}Ar/^{40}Ar	22.0 ± 0.6
Riquelme et al. (2017)	Penacho Blanco	Jarosite	^{39}Ar/^{40}Ar	14.1± 0.2
Riquelme et al. (2017)	Penacho Blanco	Jarosite	^{39}Ar/^{40}Ar	12.8 ± 0.1
Perelló et al. (2010)	Esperanza (Telegrafo)	Supergene alunite	^{39}Ar/^{40}Ar	22.9 ± 0.4
Riquelme et al. (2017)	Cerro Coronado	Supergene alunite	K/Ar	25.2 ± 0.8
Riquelme et al. (2017)	Tesoro NE	Criptomelane	K/Ar	21.9 ± 1.2
Sillitoe and Mckee (1996)	Telegrafo	Jarosite	K/Ar	20.0 ± 1.0
Perelló et al. (2010)	Esperanza (Telegrafo)	Supergene alunite	K/Ar	21.2 ± 0.2
Perelló et al. (2010)	Esperanza (Telegrafo)	Supergene alunite	K/Ar	19.2 ± 0.2

2   **Table A2.** Zircon U-Pb data.

3

Grain No.	Pb*	U	Atomic Th/U	Measured isotope ratios & 1σ (%) internal errors						Corrected ages (Ma) & absolute internal erros (2 σ)						206*/238-207*/235	206/238-207/235	Best age	Error (±2σ)
				206 Pb/ 238U	±	207 Pb/ 235U	±	207 Pb/ 206U	±	206 Pb*/ 238U	±	207* Pb/ 235U	±	207* Pb/ 206 Pb*	±	Concord. (%)	Concord. (%)		
	(ppm)	(ppm)																(Ma)	(Ma)
DC03-01	1.8	221.9	0.40	0.0076	0.0001	0.0735	0.0026	0.0691	0.0024	49.1	1.0	72.0	5.0	900.5	41.2	31.9	94.6		
DC03-02	1.6	208.4	0.89	0.0063	0.0001	0.0443	0.0024	0.0512	0.0028	40.6	1.2	44.0	4.9	250.7	24.6	7.6	83.8	40.61	1.15
DC03-03	0.5	64.3	0.69	0.0067	0.0002	0.0483	0.0047	0.0509	0.0049	43.2	1.9	47.9	9.1	236.3	41.5	9.6	81.7	43.24	1.92
DC03-04	1.0	130.5	0.78	0.0066	0.0001	0.0432	0.0025	0.0467	0.0027	42.6	1.2	42.9	4.9	36.0	4.7	0.8	-18.5	42.60	1.15
DC03-05	0.8	82.8	0.73	0.0076	0.0002	0.1319	0.0062	0.1301	0.0062	48.9	1.9	125.8	12.5	2099.0	84.6	61.1	97.7		
DC03-06	1.8	248.5	0.78	0.0061	0.0001	0.0428	0.0017	0.0502	0.0020	39.4	0.9	42.5	3.4	202.4	15.0	7.4	80.5	39.40	0.90
DC03-07	3.4	459.9	0.71	0.0065	0.0001	0.0443	0.0014	0.0500	0.0015	41.4	0.8	44.0	2.7	196.4	11.3	5.8	78.9	41.45	0.77
DC03-08	2.5	338.9	0.89	0.0063	0.0001	0.0410	0.0016	0.0472	0.0018	40.5	0.9	40.8	3.2	60.4	5.1	0.7	32.9	40.49	0.90
DC03-09	0.8	118.5	0.68	0.0063	0.0001	0.0522	0.0027	0.0613	0.0031	40.2	1.2	51.7	5.4	650.8	49.2	22.2	93.8		
DC03-10	1.7	171.7	1.12	0.0077	0.0001	0.0638	0.0029	0.0597	0.0027	49.4	1.3	62.8	5.6	593.1	40.6	21.3	91.7		
DC03-11	0.6	78.8	0.55	0.0065	0.0001	0.0430	0.0039	0.0477	0.0043	41.7	1.5	42.8	7.6	83.9	15.1	2.5	50.3	41.70	1.54
DC03-12	0.7	114.0	0.62	0.0065	0.0001	0.3254	0.0113	0.3536	0.0129	41.8	1.8	286.0	20.7	3722.4	72.9	85.4	98.9		
DC03-13	0.5	81.3	0.47	0.0059	0.0001	0.0352	0.0030	0.0424	0.0037	38.2	1.3	35.1	6.0	-202.1	-37.9	-8.7	118.9	38.18	1.28
DC03-14	1.4	198.3	0.73	0.0061	0.0001	0.0420	0.0019	0.0494	0.0022	39.2	0.9	41.8	3.7	168.8	14.2	6.1	76.8	39.20	0.90
DC03-15	0.9	135.6	0.74	0.0058	0.0001	0.0412	0.0030	0.0525	0.0038	37.1	1.4	41.0	6.1	306.4	38.8	9.5	87.9	37.09	1.41
DC03-16	1.0	151.1	0.73	0.0057	0.0001	0.0379	0.0027	0.0482	0.0034	36.8	1.3	37.8	5.5	108.6	15.3	2.6	66.1	36.83	1.28
DC03-17	2.1	253.6	0.85	0.0067	0.0001	0.0444	0.0018	0.0482	0.0019	43.3	0.9	44.1	3.6	107.1	8.8	1.9	59.6	43.30	0.90
DC03-18	1.5	216.9	0.69	0.0060	0.0001	0.0418	0.0018	0.0506	0.0022	38.5	0.9	41.6	3.6	222.2	17.6	7.4	82.7	38.50	0.90
DC03-19	0.8	127.0	0.39	0.0057	0.0001	0.0400	0.0023	0.0507	0.0030	36.8	1.0	39.9	4.7	228.6	24.5	7.6	83.9	36.83	1.03
DC06-03	1.9	239.0	0.73	0.0071	0.0001	0.0421	0.0018	0.0438	0.0018	45.3	0.9	41.9	3.5	-123.1	-10.1	-8.2	136.8	45.29	0.90
DC06-04	0.3	40.7	0.51	0.0059	0.0002	0.0444	0.0060	0.0559	0.0077	37.6	2.3	44.1	12.3	446.8	100.0	14.8	91.6	37.60	2.31
DC06-05	1.2	126.5	0.52	0.0086	0.0001	0.0713	0.0031	0.0577	0.0025	55.1	1.3	70.0	5.8	519.9	35.7	21.2	89.4		
DC06-06	0.6	82.3	0.78	0.0061	0.0001	0.0579	0.0044	0.0670	0.0051	39.1	1.7	57.1	8.6	836.8	87.9	31.6	95.3		
DC06-07	0.7	105.9	0.72	0.0058	0.0001	0.0467	0.0030	0.0581	0.0037	37.4	1.3	46.3	6.0	533.5	53.8	19.3	93.0		
DC06-08	1.1	149.6	1.05	0.0057	0.0001	0.0462	0.0025	0.0591	0.0032	36.7	1.2	45.9	5.1	568.9	48.0	20.0	93.5		
DC06-09	1.6	231.5	1.12	0.0055	0.0001	0.0504	0.0020	0.0656	0.0025	35.2	0.8	50.0	3.8	792.4	42.4	29.5	95.6		

DC06-10	0.7	108.0	0.68	0.0055	0.0001	0.0520	0.0028	0.0701	0.0038	35.4	1.2	51.5	5.7	930.7	65.8	31.3	96.2		
DC06-11	1.2	165.2	0.93	0.0062	0.0001	0.0377	0.0021	0.0440	0.0024	40.0	1.0	37.6	4.2	-113.5	-12.7	-6.4	135.2	39.97	1.03
DC06-12	1.1	165.2	1.01	0.0056	0.0001	0.0409	0.0020	0.0539	0.0026	36.1	0.9	40.7	4.1	368.5	30.5	11.4	90.2	36.06	0.90
DC06-13	1.0	135.1	0.81	0.0064	0.0001	0.0469	0.0025	0.0542	0.0029	41.0	1.2	46.6	5.1	377.7	34.2	12.0	89.1	41.00	1.15
DC06-14	1.0	126.5	0.82	0.0066	0.0001	0.0725	0.0041	0.0803	0.0045	42.4	1.5	71.1	8.2	1204.6	80.2	40.3	96.5		
DC06-15	1.3	161.2	1.02	0.0066	0.0001	0.0428	0.0022	0.0477	0.0024	42.2	1.0	42.5	4.4	83.9	8.8	0.8	49.7	42.21	1.02
DC06-16	3.6	485.5	1.03	0.0059	0.0001	0.0497	0.0017	0.0597	0.0019	37.7	0.8	49.3	3.1	591.3	29.3	23.4	93.6		
DC06-17	1.0	122.0	0.88	0.0064	0.0001	0.0596	0.0031	0.0672	0.0035	41.4	1.3	58.8	6.3	844.6	60.8	29.6	95.1		
DC06-18	1.0	177.7	1.67	0.0055	0.0001	0.0490	0.0026	0.0635	0.0034	35.4	1.2	48.5	5.2	723.3	55.4	27.0	95.1		
DC06-19	0.8	95.9	1.02	0.0066	0.0001	0.1148	0.0042	0.1276	0.0046	42.5	1.2	110.3	8.2	2065.3	64.7	61.4	97.9		
DC06-20	1.1	149.6	0.94	0.0062	0.0001	0.1007	0.0035	0.1168	0.0040	39.5	1.0	97.4	6.6	1907.5	58.8	59.4	97.9		
DC06-21	10.9	283.7	0.86	0.0328	0.0002	0.2320	0.0046	0.0537	0.0009	207.7	2.4	211.9	6.7	356.8	10.1	1.9	41.8	*207.74*	*2.37*
DC08-03	2.8	193.8	0.87	0.0116	0.0001	0.2600	0.0057	0.1655	0.0032	74.5	1.4	234.6	9.1	2512.7	36.1	68.2	97.0		
DC08-04	6.5	481.0	0.99	0.0110	0.0001	0.0726	0.0021	0.0481	0.0013	70.3	1.1	71.1	3.8	105.7	5.9	1.1	33.4	70.33	1.15
DC08-05	3.3	213.4	0.80	0.0124	0.0001	0.2627	0.0059	0.1545	0.0031	79.4	1.4	236.8	9.3	2396.7	37.3	66.5	96.7		
DC08-06	1.8	162.7	0.69	0.0098	0.0001	0.0682	0.0034	0.0517	0.0026	62.8	1.7	67.0	6.8	273.1	24.3	6.2	77.0	62.80	1.66
DC08-07	0.9	74.3	0.68	0.0103	0.0002	0.1347	0.0064	0.0930	0.0044	66.1	2.2	128.3	11.8	1487.9	74.0	48.5	95.6		
DC08-08	3.7	308.8	1.04	0.0097	0.0001	0.0650	0.0018	0.0490	0.0013	62.4	0.9	63.9	3.3	145.9	7.6	2.4	57.3	62.36	0.89
DC08-09	2.9	233.0	0.77	0.0106	0.0001	0.0740	0.0028	0.0505	0.0018	67.9	1.4	72.5	5.2	218.1	14.8	6.3	68.9	67.91	1.40
DC08-10	1.7	150.1	0.52	0.0103	0.0001	0.0712	0.0032	0.0497	0.0022	65.9	1.5	69.8	6.1	180.0	15.2	5.6	63.4	65.93	1.53
DC08-11	2.5	182.3	0.93	0.0112	0.0001	0.0787	0.0035	0.0511	0.0022	71.7	1.8	77.0	6.7	247.1	19.7	6.9	71.0	71.67	1.79
DC08-12	3.7	329.4	0.84	0.0095	0.0001	0.0620	0.0017	0.0476	0.0012	61.1	0.9	61.1	3.2	78.9	4.5	-0.1	22.5	61.14	0.89
DC08-13	12.4	1094.6	0.54	0.0104	0.0001	0.0889	0.0018	0.0622	0.0011	66.6	0.8	86.5	3.0	681.7	17.4	23.0	90.2		
DC08-14	2.2	192.3	0.73	0.0098	0.0001	0.0877	0.0027	0.0641	0.0019	62.5	1.1	85.3	4.9	746.3	31.4	26.7	91.6		
DC08-15	14.7	894.7	1.37	0.0116	0.0001	0.1421	0.0026	0.0824	0.0012	74.6	0.9	134.9	3.8	1254.3	21.9	44.7	94.1		
DC08-16	2.1	193.8	0.78	0.0094	0.0001	0.0817	0.0026	0.0616	0.0019	60.0	1.1	79.8	4.7	660.3	29.9	24.8	90.9		
DC08-17	3.5	262.6	0.93	0.0110	0.0001	0.1105	0.0030	0.0757	0.0019	70.2	1.3	106.5	5.6	1086.9	34.5	34.1	93.5		
DC08-18	5.6	522.2	0.47	0.0101	0.0001	0.0684	0.0017	0.0495	0.0011	64.8	0.9	67.2	3.1	173.0	7.9	3.4	62.5	64.85	0.89
DC08-19	4.0	344.9	1.04	0.0092	0.0001	0.0670	0.0023	0.0525	0.0017	58.8	1.1	65.8	4.3	308.5	17.7	10.6	80.9	58.84	1.15
DC08-20	8.3	754.1	0.75	0.0091	0.0001	0.0892	0.0025	0.0777	0.0021	58.3	1.1	86.7	5.1	1139.7	37.1	32.8	94.9		
DC08-21	2.3	176.2	0.66	0.0108	0.0001	0.1583	0.0039	0.1075	0.0024	69.0	1.3	149.2	6.8	1757.6	38.1	53.8	96.1		
DC08-22	3.0	241.0	1.23	0.0096	0.0001	0.0639	0.0022	0.0487	0.0016	61.3	1.1	62.9	4.1	135.3	8.8	2.6	54.7	61.27	1.15
DC08-23	2.0	161.7	1.00	0.0102	0.0001	0.0640	0.0025	0.0463	0.0018	65.6	1.3	63.0	4.9	13.8	1.7	-4.1	-375.8	65.61	1.28
DC08-24	1.1	95.9	0.92	0.0096	0.0002	0.1113	0.0055	0.0882	0.0043	61.4	2.0	107.1	10.9	1385.8	74.5	42.7	95.6		

DC08-25	1.6	127.5	1.07	0.0098	0.0001	0.0882	0.0037	0.0666	0.0027	62.9	1.5	85.8	7.2	825.6	46.8	26.7	92.4		
DC08-26	1.7	140.6	0.76	0.0103	0.0001	0.0706	0.0028	0.0494	0.0019	65.7	1.4	69.3	5.3	167.3	12.5	5.1	60.7	65.74	1.40
DC08-27	3.9	321.3	1.09	0.0096	0.0001	0.0663	0.0018	0.0501	0.0012	61.8	0.9	65.2	3.2	198.7	9.5	5.2	68.9	61.78	0.89
DC10-03	1.3	99.4	1.01	0.0102	0.0001	0.0982	0.0042	0.0697	0.0029	65.3	1.7	95.1	7.8	919.8	50.6	31.3	92.9		
DC10-04	3.9	299.8	1.22	0.0099	0.0001	0.0648	0.0020	0.0476	0.0014	63.5	1.0	63.8	3.8	78.4	5.1	0.4	19.0	63.51	1.02
DC10-05	1.5	132.1	0.79	0.0099	0.0001	0.0774	0.0033	0.0575	0.0024	63.4	1.5	75.7	6.4	512.3	34.2	16.2	87.6		
DC10-06	2.3	203.3	1.10	0.0091	0.0001	0.0743	0.0023	0.0590	0.0017	58.1	1.0	72.8	4.3	568.6	26.1	20.2	89.8		
DC10-07	1.6	144.1	0.91	0.0090	0.0001	0.0736	0.0025	0.0591	0.0019	57.7	1.2	72.1	4.7	569.3	29.1	20.0	89.9		
DC10-08	1.9	169.2	0.91	0.0091	0.0001	0.0659	0.0023	0.0525	0.0018	58.3	1.1	64.8	4.4	308.1	18.4	9.9	81.1	58.33	1.15
DC10-09	1.2	92.4	0.97	0.0105	0.0002	0.0744	0.0040	0.0519	0.0028	67.1	1.9	72.9	7.8	279.2	26.5	7.8	76.0	67.14	1.91
DC10-10	2.0	151.1	0.99	0.0104	0.0001	0.1172	0.0036	0.0831	0.0024	66.5	1.4	112.5	6.7	1272.5	42.7	40.9	94.8		
DC10-11	1.1	99.9	0.88	0.0095	0.0002	0.0614	0.0038	0.0475	0.0030	61.0	1.9	60.5	7.6	75.4	9.7	-0.8	19.2	60.95	1.92
DC10-12	2.6	200.8	1.03	0.0104	0.0001	0.0674	0.0025	0.0474	0.0017	66.8	1.3	66.2	4.8	70.4	5.5	-0.9	5.1	66.82	1.28
DC10-13	1.0	84.4	0.76	0.0102	0.0002	0.0681	0.0045	0.0479	0.0031	65.6	2.2	66.9	8.7	96.3	12.7	1.9	31.9	65.61	2.17
DC10-14	1.3	74.3	0.81	0.0140	0.0002	0.4998	0.0120	0.2735	0.0059	89.6	2.2	411.6	17.3	3325.9	42.6	78.2	97.3		
DC10-15	3.4	256.6	1.07	0.0107	0.0001	0.0666	0.0024	0.0453	0.0016	68.4	1.3	65.5	4.5	-40.0	-2.2	-4.4	270.8	68.36	1.28
DC10-16	1.5	117.0	0.94	0.0102	0.0001	0.0652	0.0031	0.0471	0.0022	65.5	1.5	64.1	6.1	53.3	5.5	-2.2	-23.0	65.55	1.53
DC10-17	2.5	140.6	0.88	0.0163	0.0002	0.8716	0.0199	0.4051	0.0079	104.0	2.5	636.4	22.3	3928.1	39.5	83.7	97.4		
DC10-18	1.1	96.4	0.80	0.0095	0.0001	0.0737	0.0038	0.0550	0.0028	61.0	1.7	72.2	7.2	413.0	35.4	15.6	85.2		
DC10-19	2.8	224.9	0.75	0.0100	0.0001	0.1589	0.0039	0.1150	0.0025	64.4	1.1	149.8	6.6	1879.3	38.0	57.0	96.6		
DC10-20	3.0	129.0	0.60	0.0210	0.0002	0.2512	0.0074	0.0864	0.0023	133.7	2.7	227.6	11.4	1347.4	40.0	41.3	90.1		

4

5

6   **Figure A1.** U-Pb concordias spots for samples DC12-03, DC12-06, DC12-08, and DC12-10.

7

8
9

10

11

12
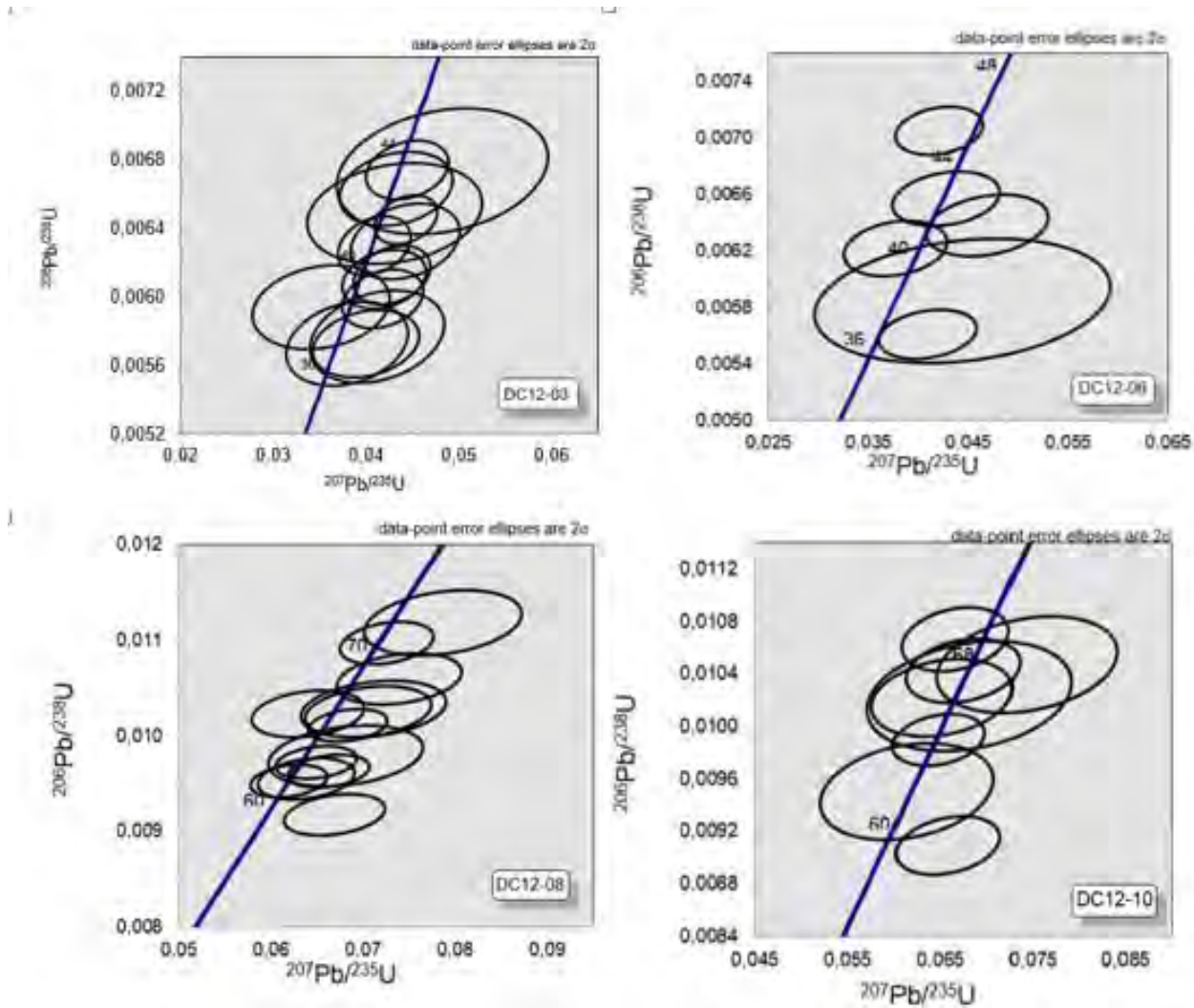
13 **Table A3.** Apatite Fission track data.

14

| Sample no. (Lithology) | No. of crystals | Track density (x10^6 tr.cm^{-2}) | | | Age dispersion | | U (ppm) | Central age (Ma ± 1σ) | Mean track length (μm) | StD (μm) | Dpar (μm) | StD (μm) | No. of tracks measured |
		ρd (Nd)	ρs (Ns)	ρi (Ni)	RE (%)	Pχ2 (%)							
DC12-01	20	0.903 [16983]	0.372 [208]	0.186 [646]	0.0	99.7	16.4	40.6 ± 3.3	14.00 ± 0.11	1.23	2.7	0.19	100
DC12-03	12	0.919 [16983]	0.456 [295]	1.450 [945]	0.0	99.9	19.7	40.0 ± 2.7	14.99 ± 0.15	1.04	2.9	0.26	62
DC12-06	13	0.895 [16983]	0.077 [65]	0.226 [219]	0.0	100.0	3.6	37.1 ± 5.2	14.84 ± 0.15	1.04	2.6	0.36	59
DC12-08	26	0.871 [16983]	0.240 [239]	0.704 [718]	0.0	100.0	10.1	41.4 ± 3.1	13.98 ± 0.3	1.32	1.8	0.22	99
DC12-09	13	0.835 [16983]	0.230 [147]	0.480 [304]	0.0	70.4	7.2	46.1 ± 4.8	13.96 ± 0.3	1.55	3.9	0.92	41
DC12-15	11	0.728 [16983]	0.550 [249]	1.192 [519]	0.3	61.1	20.5	42.5 ± 3.4	13.96 ± 0.3	1.28	2.3	0.26	58

15 Fission track analyses have been determined by the external detector method using 0.5 for the 4π/2π geometry correction factor. Apatite fission-track ages were

16 calculated using dosimeter glass CN-5; Analyst Caroline ξ=280±7.8 calibrated by multiple analyses of IUGS apatite age standards (Hurford. 1990). Pχ2 is probability

17 of obtaining χ2 value for ν degrees of freedom, where ν is the number of crystals. Central age is a modal age weighted for different precisions of individual crystals.

18 In track densities (N) shown in brackets is the numbers of tracks counted. ρd is the fission track density of the standard U-glass (CN-5). Ns (spontaneous), Ni (induced)

19 and Nd (dosimeter) are the fission track numbers corresponding to ρs, ρi and ρd densities of track, respectively.

20

21　**Table A4.** Apatite (U-Th)/He data.

Sample no.	Aliquot number	Mineral	n	He nmol/g	U (ppm)	Th (ppm)	F_T	He raw age (Ma)	He corr. age (Ma)	error Abs	Std dev
DC12-01	A	Apatite	1	13.63	11.83	60.93	0.839	24.01	28.6	2.0	
	B	Apatite	1	7.69	7.58	40.89	0.703	20.61	29.3	2.1	
	E	Apatite	4	9.02	10.34	36.50	0.696	22.00	31.6	2.2	
Mean				**10.11**	**9.92**	**46.11**	**0.75**	**22.21**	**29.9**	**2.1**	**1.6**
DC12-03	A	Apatite	1	6.86	6.68	43.57	0.744	18.69	25.1	1.3	
	B	Apatite	1	11.45	14.89	43.09	0.733	21.13	28.8	2.0	
	C	Apatite	1	9.48	7.84	32.77	0.710	28.12	39.6	2.8	
Mean				**9.27**	**9.80**	**39.81**	**0.73**	**22.65**	**31.2**	**2.2**	**7.5**
DC12-06	D	Apatite	2	2.25	2.16	14.06	0.710	18.96	26.7	1.9	
	E	Apatite	2	2.40	1.90	13.28	0.699	22.03	31.5	2.2	
Mean				**2.33**	**2.03**	**13.67**	**0.70**	**20.50**	**29.1**	**2.0**	**3.4**
DC12-08	A	Apatite	3	17.1	12.8	48.4	0.6	32.7	52.4	3.7	
DC12-09	A	Apatite	1	4.06	3.61	22.81	0.764	20.87	27.3	1.9	
	B	Apatite	1	4.41	4.29	33.25	0.710	16.80	23.7	1.7	
	C	Apatite	1	5.24	5.55	52.90	0.696	13.41	19.3	1.3	
	D	Apatite	1	3.83	4.20	43.69	0.628	12.20	19.4	1.4	
Mean				**4.39**	**4.41**	**38.16**	**0.70**	**15.82**	**22.4**	**1.6**	**3.8**
DC12-10	A	Apatite	1	10.74	7.23	31.01	0.690	34.08	49.4	3.5	
	B	Apatite	1	14.83	11.89	45.43	0.708	30.30	42.8	3.0	
	C	Apatite	1	7.67	4.64	27.52	0.723	31.80	44.0	3.1	
	D	Apatite	1	14.11	8.24	65.36	0.629	27.52	43.8	3.1	
Mean				**11.84**	**8.00**	**42.33**	**0.69**	**30.93**	**45.0**	**3.1**	**3.0**
DC12-12	B	Apatite	1	10.51	9.22	43.73	0.659	24.86	37.7	2.6	
	C	Apatite	1	14.99	13.24	66.29	0.707	23.97	33.9	2.4	
Mean				**12.75**	**11.23**	**55.01**	**0.68**	**24.42**	**35.8**	**2.5**	**2.7**
DC12-13	B	Apatite	1	12.43	8.10	56.70	0.70	26.73	38.13	3.81	
	D	Apatite	1	16.70	6.20	69.55	0.71	33.89	48.00	4.80	
Mean				**14.57**	**7.15**	**63.13**	**0.70**	**30.31**	**43.1**	**3.0**	**7.0**
DC12-14	B	Apatite	1	3.04	4.54	59.07	0.60	7.60	12.77	0.89	
	D	Apatite	1	6.06	6.81	79.60	0.66	10.93	16.61	1.16	
	E	Apatite	1	5.10	3.73	53.86	0.74	14.31	19.31	1.35	
Mean				**4.73**	**5.03**	**64.18**	**0.66**	**10.95**	**16.2**	**1.1**	**3.3**
DC12-15	A	Apatite	3	13.1	34.7	21.8	0.6	23.2	36.9	2.6	

22

23　(U-Th)/He ages were performed by laser heating for He extraction and ICP-MS for U-Th determinations at

24　Géoscience Montpellier, France. The estimated analytical uncertainty for He ages is about 7% (2σ). Alpha

25　ejection F_T corrections applied to raw ages were calculated using the procedure of Gautheron and Tassan-Got

26　(2010). Standard deviation on ages is used as error when higher than the analytical uncertainty.

27　n = number of grain per aliquot.

Figure A2. Hefty modelling.

HeFty program v1.9.1 performs inverses modeling of thermochronological data with a Monte Carlo search for better fitting cooling paths through a set of user-defined t–T boxes that rely on analytical results and geological observations (Ketcham 2005; Witt *et al.*, 2012). The inversion code incorporates He diffusion kinetic models in apatite (Farley 2000; Flowers *et al.,* 2009). AFT annealing multi-kinetic model (Ketcham *et al.*, 2007a) and c-axis projection of track lengths (Ketcham *et al.*, 2007b). Input parameters used to model each sample are central AFT ages, track length measurements of individual track, Dpar values and AHe ages including grain sizes and chemical characteristics. The program statistically compares the models and analytical dataset (10^4–10^5 Monte Carlo trials) to establish a Chi-square goodness-of-fit (GOF) test for each path processed. Probability values are either highlighted in green (> 0.05 acceptable) or pink (> 0.5 good). For each sample modeled. The following figures display A: show T-t path modeled; B: display the track length distributions compare to modeled distributions (green curve) and C: He diffusional profiles. Geological constraint used for model is the presence of the Artola ignimbrite dated at 9.5 Ma covering a large part of the Centinela district (Riquelme *et al.*, 2017)
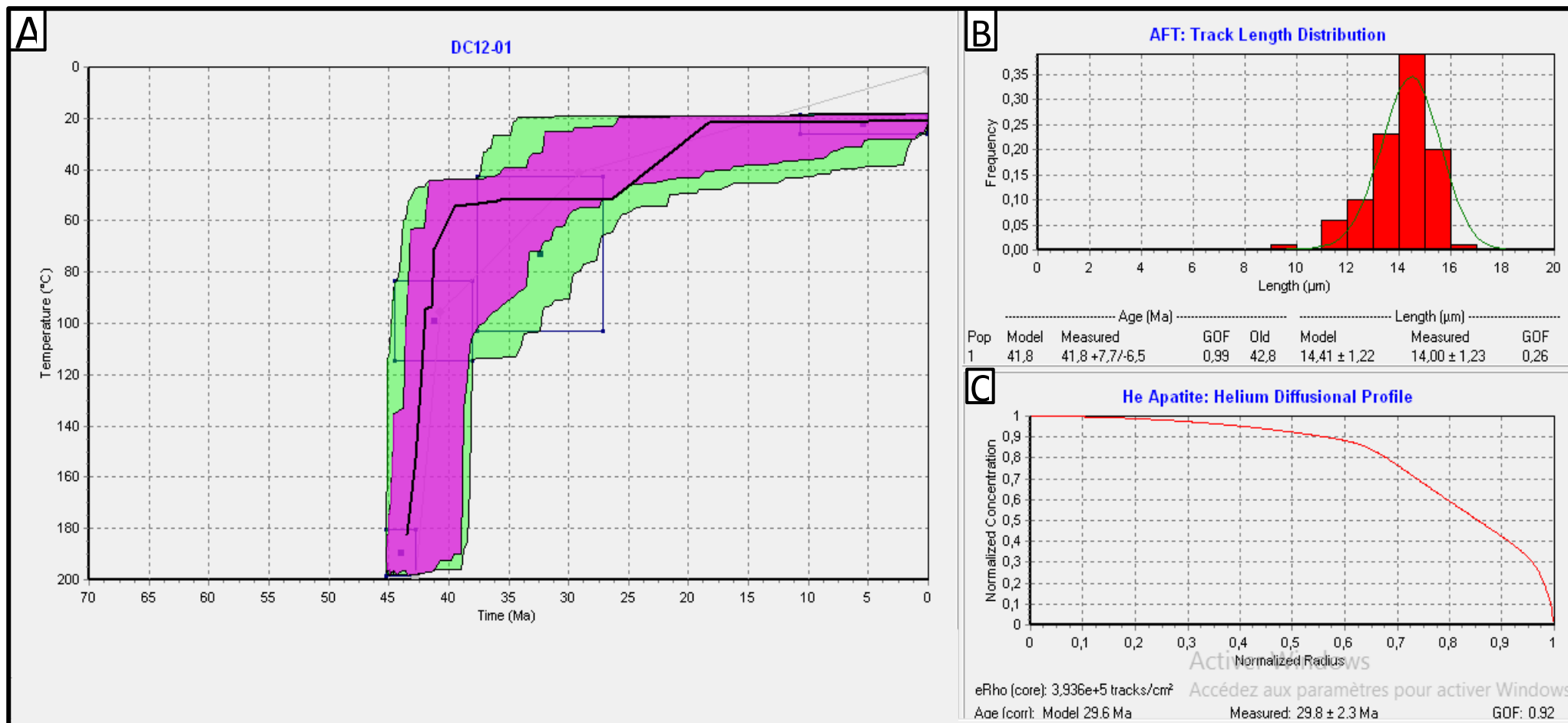
Figure A2- A. DC12-01 sample HeFty modeling.
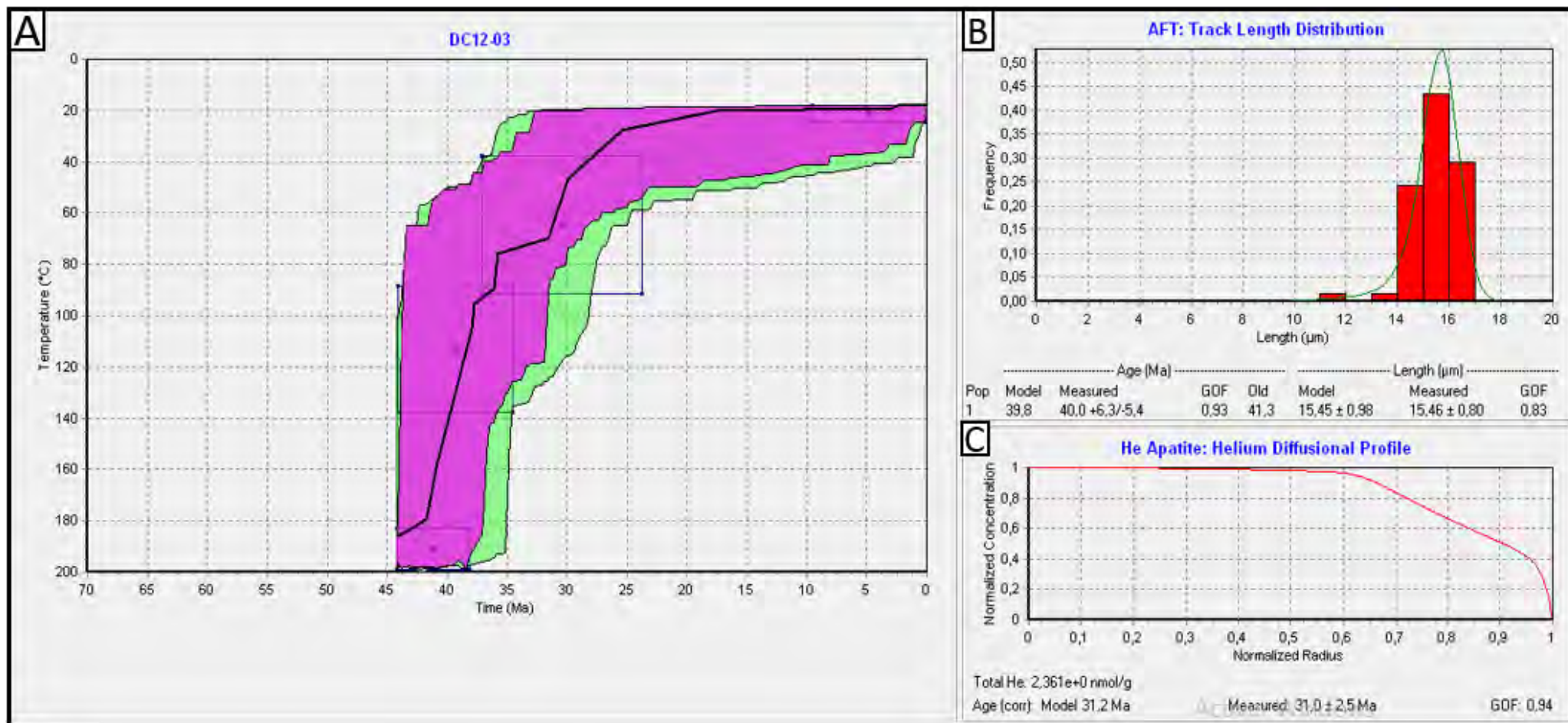
Figure A2- B. DC12-03 sample HeFty modeling.
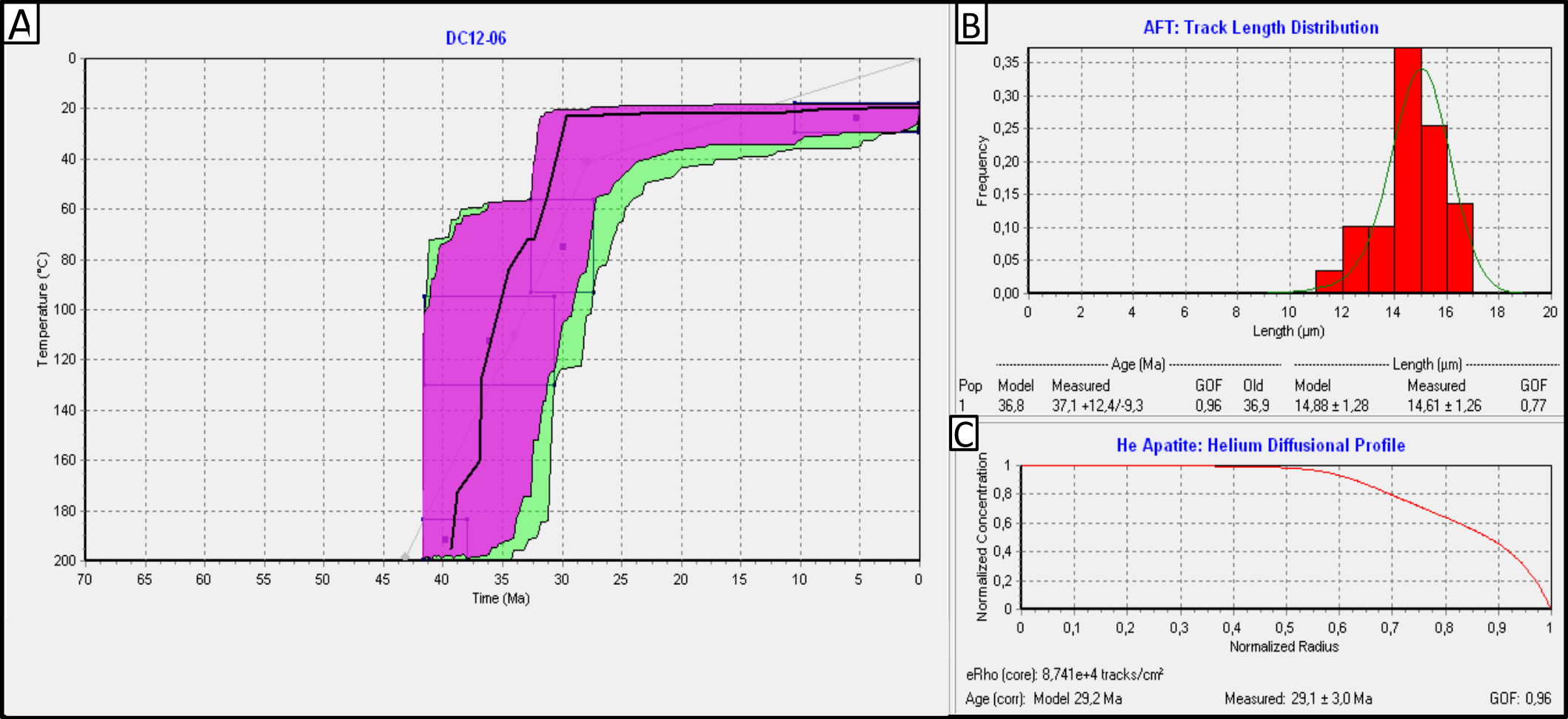
Figure A2- C. DC12-06 sample HeFty modeling.

51
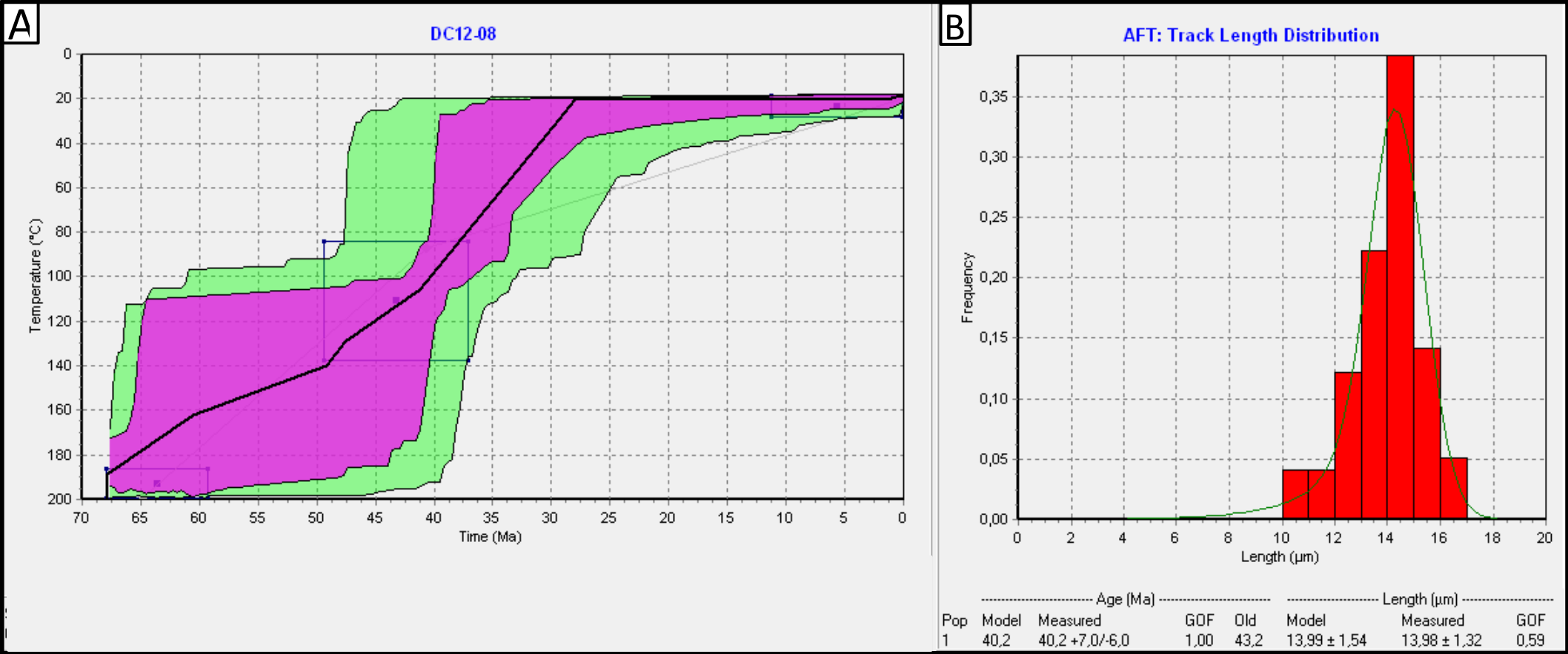
Figure A2- D. DC12-08 sample HeFty modeling. In this model, we didn't include the AHe parameters as the AHe is older that the AFT age.
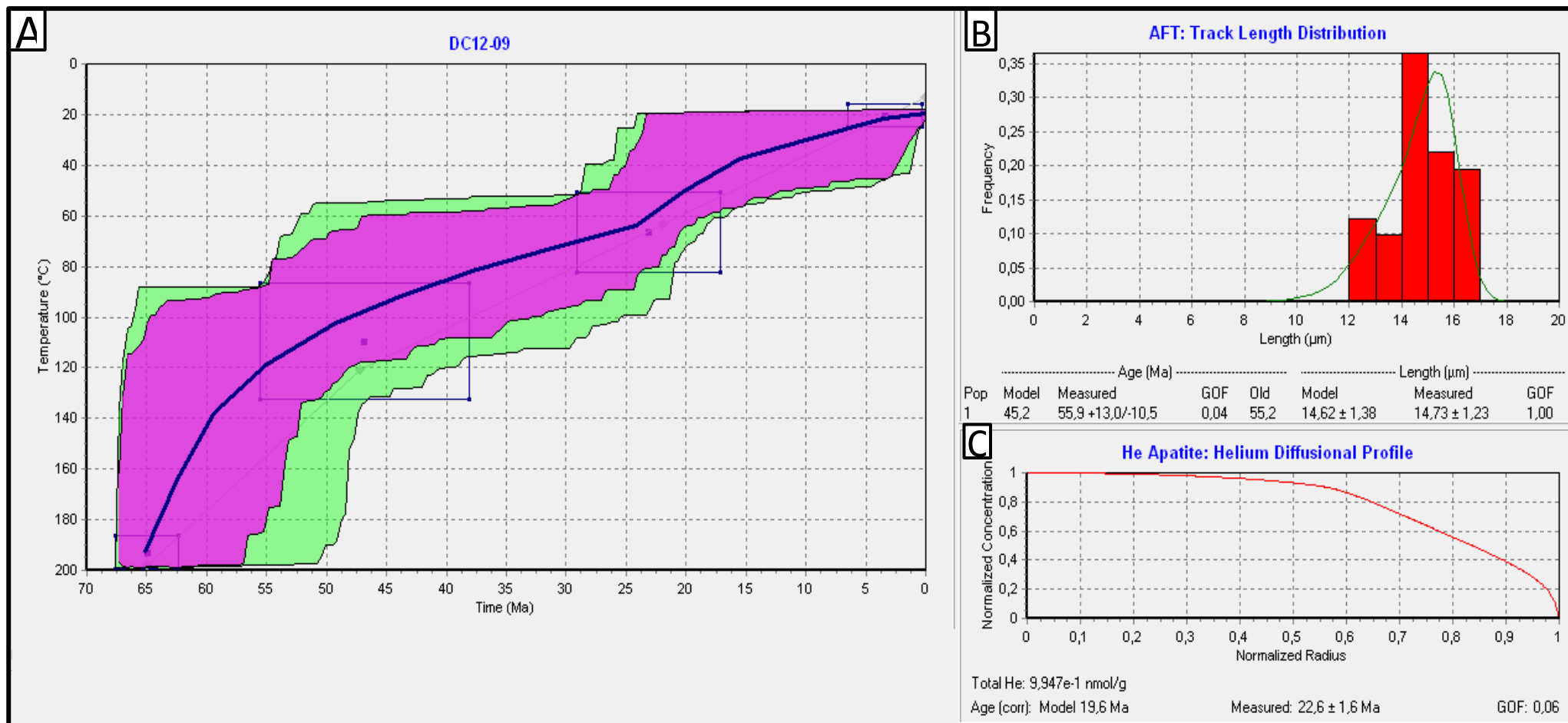
Figure A2- E. DC12-09 sample HeFty modeling.

60
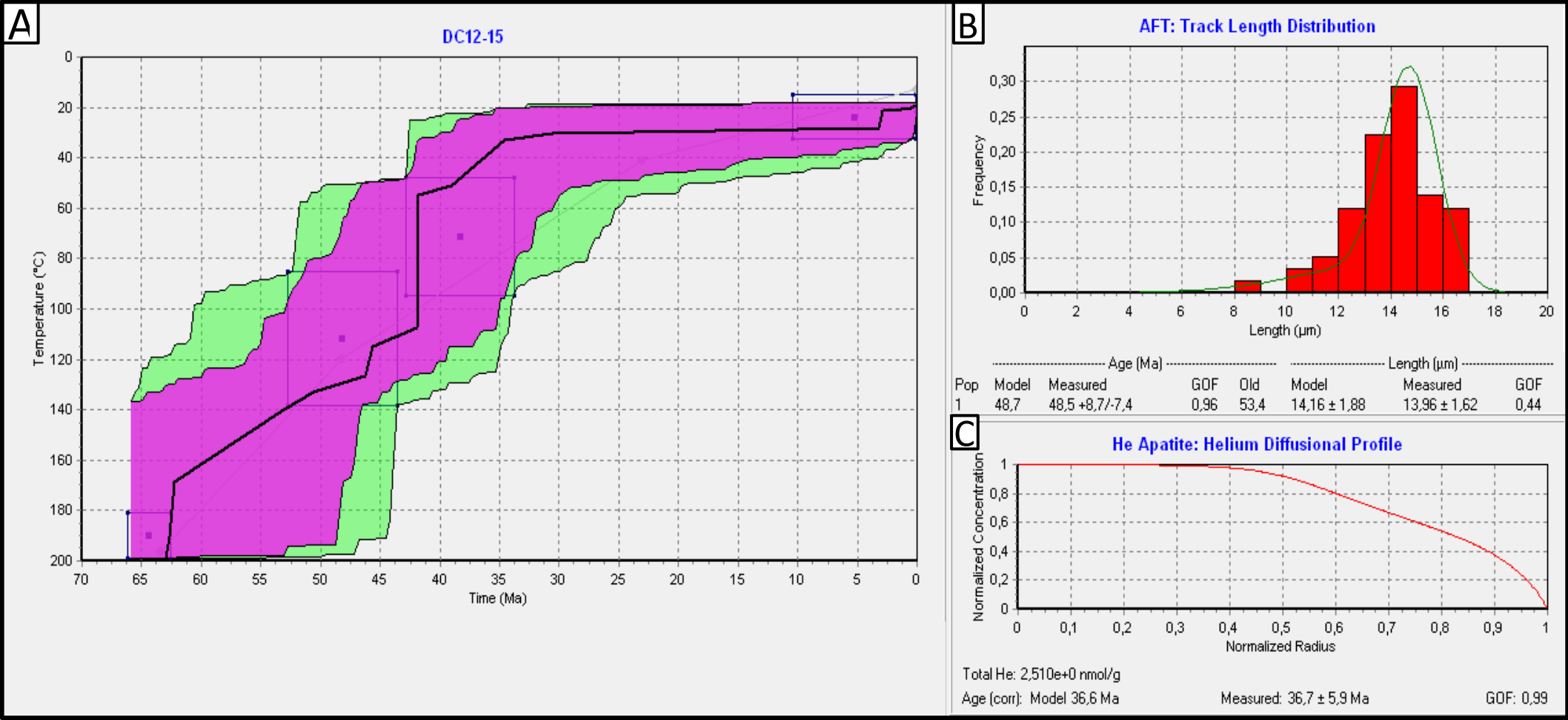
Figure A2- F. DC12-15 sample HeFty modeling.

61

62

REFERENCES

Farley, K. A. 2000. Helium diffusion from apatite: General behavior as illustrated by Durango fluorapatite. *Journal of Geophysical Research B*, **105,** 2903-2914.

Gautheron, C., Tassan-Got. L., 2010. A Monte Carlo approach to diffusion applied to noble gas/helium thermochronology. Chemical Geology, **273,** 212–224.

Hurford, A. J. 1990. Standardization of fission track dating calibration: recommendation by the Fission Track Working Group of the IUGS Subcommission on Geochronology. Chemical Geology: Isotope Geoscience Section, **80**, 171-178.

Ketcham, R. A. 2005. Forward and inverse modeling of low-temperature thermochronometry data. Reviews in mineralogy and geochemistry, **58**, 275–314.

Ketcham R. A., Carter, A., Donelick, R. A., Barbarand, J., and Hurford, A.J. 2007. Improved measurement of fission-track annealing in apatite using c-axis projection: American Mineralogist, **92**, 789–798.

Ketcham, R. A., Donelick, R. A., Balestrieri, M. L., and Zattin, M. 2009. Reproducibility of apatite fission-track length data and thermal history reconstruction. Earth and Planetary Science Letters, **284**, 504-515.

Riquelme, R., Tapia, M., Campos, E., Mpodozis, C., Carretier, S., Gonzalez, R., Muñoz, S., Fernandez-Mort, A., Sanchez, C., and Marquardt, C. Sedimentological constrains on unroofing history and geomorphologic conditions allowing supergene and exotic-Cu mineralization from porphyry coppers: the Middle Eocene to Middle Miocene Centinela Basin. Atacama Desert. *Basin Research*, Basin Research, **1**, 31.

Witt, C., Rangin, C., Andreani, L., Olaez, N., and Martinez, J. 2012. The transpressive left-lateral Sierra Madre de Chiapas and its buried front in the Tabasco plain (southern Mexico). *Journal of the Geological Society*, **169,** 143–155.

Supergene and exotic Cu mineralization occur during periods of landscape stability in the Centinela Mining District, Atacama Desert

Rodrigo Riquelme,* Miguel Tapia,*,† Eduardo Campos,* Constantino Mpodozis,‡ Sebastien Carretier,§ Rodrigo González,* Sebastian Muñoz,* Alberto Fernández-Mort,*,¶ Caroline Sanchez*,§ and Carlos Marquardt**

*Departamento de Ciencias Geológicas, Universidad Católica del Norte, Antofagasta, Chile
†Departamento de Geología, Universidad de Atacama, Copiapó, Chile
‡Antofagasta Minerals, Las Condes, Santiago, Chile
§Géosciences Environnement Toulouse, OMP, UPS, CNRS, IRD, Université Toulouse III, Toulouse, France
¶Departamento de Petrología y Geoquímica, Fac. CC. Geológicas, Universidad Complutense de Madrid, Madrid, Spain
**Departamento de Ingeniería de Minería y Grupo de Geociencias, Pontificia Universidad Católica de Chile, Santiago, Chile

ABSTRACT

The Centinela Mining District (CMD), Atacama Desert (northern Chile), includes several mid–late Eocene porphyry Cu deposits that contains supergene mineralization and provides access to a record of gravel deposits that host syn-sedimentary exotic Cu mineralized bodies. By studying these gravels, we reconstruct the unroofing history and constrain the geomorphological conditions that produced supergene and exotic Cu mineralization. We present an integrated study based on stratigraphic and sedimentological data, lithology clast counts, $^{40}Ar/^{39}Ar$ and U/Pb ages from interbedded tuff layers and U/Pb detrital zircon geochronology data. To relate the gravel deposition episodes to the timing of the supergene mineralization, we provide in-situ and exotic supergene mineral ages (40Ar/39Ar and K–Ar). Six gravel units were deposited between the mid-Eocene and the mid-Miocene. The Esperanza gravels were deposited concurrently with the emplacement of porphyry Cu deposits at depth. The subsequent Tesoro I, II and III and Atravesado gravels register the unroofing of these deposits, from the advanced argillic zone to the sericitic and prophylitic hypogene zones. The Arrieros gravels register landscape pediplanation, that is, denudational removal and wear of the landscape to base level on a relatively stable tectonic regime, occurring roughly contemporaneous with supergene activity. The supergene mineral ages of the CMD define a time span (*ca.* 25–12 Ma) during which most of the supergene ages cluster in northern Chile. This time span corresponds with a period of warm and humid climate conditions in the southern hemisphere. We conclude that landscape pediplanation favours supergene mineralization and helps preserve the former supergene mineralized zones from significant erosion. Low erosion rates during pediplanation may constitute a necessary condition for the efficiency of the supergene processes in such semi-arid climate.

INTRODUCTION

Porphyry copper deposits (porphyry Cu) are ore bodies made of hypogene sulphides deposited from hydrothermal solutions in convergent tectonic settings at a depth of about 1–2 km (e.g. Sillitoe, 2010; Yanites & Kesler, 2015;

Correspondence: Riquelme Rodrigo, Facultad de Ingeniería y Ciencias Geológicas, Universidad Católica del Norte, Avenida Angamos 0610, Antofagasta, Chile. E-mail: rriquelme@ucn.cl

Fig. 1). The hydrothermal solutions are supplied by plug-like stocks or dyke swarms and generate an alteration and hypogene mineralization pattern zoned outward from the intrusion. The Atacama Desert is known worldwide for hosting numerous world-class porphyry Cu deposits. The economic wealth of most of these ore deposits relates to the remobilization, within the weathering profile, of the copper originally contained in the hypogene sulphides (Sillitoe & McKee, 1996; Chávez, 2000; Sillitoe, 2005, 2010). Copper remobilization and reprecipitation in the

supergene environment requires enough groundwater to promote the oxidation and leaching of hypogene sulphides, the transport of copper in solution, the formation of secondary enriched sulphides and/or copper oxide minerals, and eventually the formation of gravel-hosted exotic Cu deposits related to the lateral migration of the solutions (Clark *et al.*, 1990; Münchmeyer, 1996; Chávez, 2000; Sillitoe, 2005; Fig. 1). Two conditions are seen as necessary to generate supergene minerals from the weathering of a porphyry Cu. First, a moderate precipitation rate, at the very least, is required (>100 mm year^{-1}, i.e. a semi-arid climate, Clark *et al.*, 1990), which would provide high water-to-rock ratios that favour supergene mineral generation (e.g. Vasconcelos, 1999; Chávez, 2000). Second, supergene mineralization requires a water table descent rate that allows for the hypogene sulphides to be gradually exposed to the effects of oxidative weathering (Hartley & Rice, 2005; Sillitoe, 2005; Bissig & Riquelme, 2009, 2010). Thus, the average erosion rate must be in overall balance with the water table descent rate so that the sulphides can undergo significant oxidation before they are removed mechanically (e.g. Emmons, 1917; Ransome, 1919; Brimhall *et al.*, 1985; Sillitoe, 2005). The precise climatic and geomorphologic conditions favouring the generation of supergene minerals are a matter of discussion.

The available ages obtained from supergene minerals indicate that the supergene processes affecting ore deposits in the Atacama Desert in northern Chile and southern Peru were active for a period of time between 45 Ma and 6 Ma (e.g. Gustafson & Hunt, 1975; Alpers & Brimhall, 1988; Sillitoe & McKee, 1996; Marsh *et al.*, 1997; Mote *et al.*, 2001; Bouzari & Clark, 2002; Quang *et al.*, 2003, 2005; Arancibia *et al.*, 2006; Bissig & Riquelme, 2010). Some authors postulate that most of the supergene processes began at *ca.* 30 Ma and reached a peak at 14–21 Ma. The lack of ages younger than *ca.* 9 Ma from supergene minerals suggests that supergene activity on ore deposits ended at that time (Mote *et al.*, 2001; Bouzari & Clark, 2002; Arancibia *et al.*, 2006). Other authors point out that a significant number of these ages concentrate at *ca.* 20, *ca.* 14 and *ca.* 6 Ma, which are interpreted as episodes of intense supergene activity (e.g. Alpers & Brimhall, 1988; Sillitoe & McKee, 1996; Reich *et al.*, 2009). Consequently, along with the two conditions needed to generate supergene minerals, two hypotheses have been proposed to explain these supergene episodes. First, they have been related to the prevalence of relatively wetter climate conditions that disrupted the late Cenozoic arid climate history of the Atacama Desert (e.g. Clark *et al.*, 1990; Chávez, 2000; Arancibia *et al.*, 2006). Second, they may have resulted from an episodic water
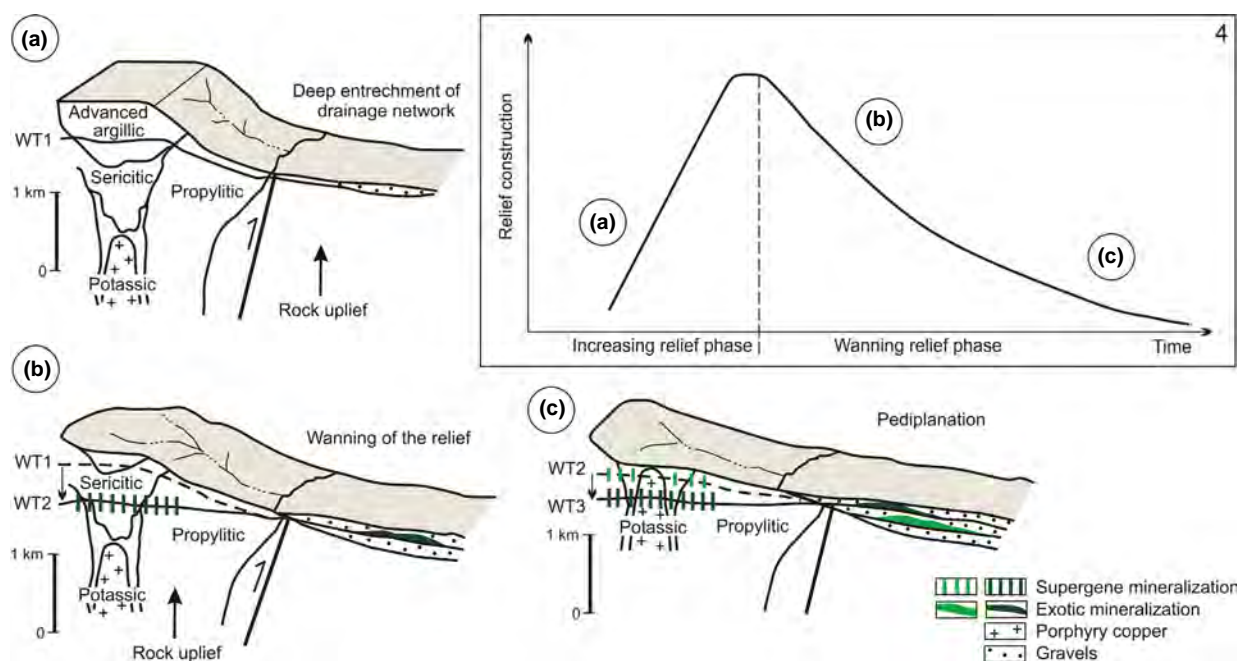
Fig. 1. Conceptual model of the co-evolution of the landscape and porphyry Cu unroofing following a rock uplift episode. The figure shows the generalized hypogene mineralization zoning pattern related to a porphyry Cu deposits and the hypothesized exhumation level in each stage of the landscape evolution. (a) increasing relief stage and deep entrenchment of the drainage network on the advanced argillic hypogene zone. (b) Beginning of the waning of the relief and river incision on the sericitic and propylitic hypogene zone. (c) Pediplanation stage. 4, geomorphological evolution cycle following a main rock uplift episode and the moment in which each mentioned stage occurs. We hypothesize that supergene and exotic Cu mineralization may result from the descent of the water table driven by river incision, or may occur later, when the landscape pediplanation allows a thick weathering profile to develop.

table descent driven by tectonically triggered unroofing episodes in porphyry Cu (Tosdal, 1978; Anderson, 1982; Brimhall *et al.*, 1985; Clark *et al.*, 1990; Bouzari & Clark, 2002; Quang *et al.*, 2003; Hartley & Rice, 2005; Sillitoe, 2005). The scarcity of supergene mineral ages older than the early Oligocene is interpreted as the result of rapid erosion linked to the Incaic tectonic phase, which precludes the preservation of supergene oxidation profiles (Arancibia *et al.*, 2006). The lack of younger supergene mineral ages is considered to be due to the middle Miocene climate change from arid to hyperarid conditions, which limited the supergene alteration processes and favoured the preservation of previously formed supergene mineralized zones (e.g. Alpers & Brimhall, 1988; Sillitoe & McKee, 1996; Bissig & Riquelme, 2009, 2010).

Although the time frame for the supergene processes is relatively well constrained, the geomorphological evolution cycle following a main rock uplift episode has not yet been considered. Unroofing occurs at different rates throughout a period of time which may encompass more than 10 Ma following the main rock uplift period, particularly in arid regions. In the Atacama Desert, this time span corresponds to the response time of mountain erosion which leads towards the formation of a smooth, gently sloping (<10°), low relief landscape surface commonly called pediplain (e.g. Mortimer, 1973; Riquelme *et al.*, 2003, 2007; Farías *et al.*, 2005; Aguilar *et al.*, 2011; Rodriguez *et al.*, 2013). Pediplains result from denudational removal and wear to near base level, acting during a period of long tectonic stability at the end of a Davis's cycle of erosion (Davis, 1905; for synthesis see Phillips, 2002; Strudley & Murray, 2007; Dohrenwend & Parsons, 2009). The landscape evolution usually begins with a deep entrenchment of the drainage network, followed by a waning of the relief due to prolonged sub-aerial erosion, eventually associated with a parallel retreat of the initial topographic front (pediplanation) (e.g. Phillips, 2002; Strudley & Murray, 2007; Carretier *et al.*, 2014; Fig. 1). The precise moment during the geomorphological evolution cycle of an uplifted landscape at which the appropriate balance between erosion rate and the water table descent rate takes place has still not been clarified (Mortimer, 1973; Alpers & Brimhall, 1988; Bouzari & Clark, 2002; Quang *et al.*, 2003; Bissig & Riquelme, 2010). Two cases favouring this type of balance exist: supergene processes may result from the descent of the water table driven by river incision, thereby exposing the underlying sulphides to the effects of oxidative weathering (e.g. Bissig & Riquelme, 2009, 2010; Fig. 1b), or it may occur much later, when the lowering of the relief reduced the erosion rate and allowed a thick weathering profile to develop (Fig. 1c). One of the main goals of the present work is to understand this issue.

The Incaic tectonic phase is an important episode of erosion and denudation in the Precordillera that occurred during and immediately after the mid-late Eocene emplacement of the porphyry Cu in northern Chile (e.g. Maksaev & Zentilli, 1999). This phase and the subsequent geomorphological evolution and paleoclimatic history of the Precordillera results in semi-consolidated gravel deposits – the Atacama Gravels (Mortimer,1973) – which cover most of the Central Depression and the Precordillera (e.g. Sáez *et al.*, 1999, 2012; Hartley & Chong, 2002; Hartley, 2003; Lamb & Davis, 2003; Dunai *et al.*, 2005; May *et al.*, 2005; Rech *et al.*, 2006, 2010; Riquelme *et al.*, 2007; Nalpas *et al.*, 2008; Amundson *et al.*, 2012; Jordan *et al.*, 2014; de Wet *et al.*, 2015; Oerter et al., 2016). We consider the Centinela Mining District (CMD), which provides unusual access to a complete record of mid-Eocene to mid–Miocene gravel deposits in which mineralized exotic Cu bodies are hosted. The district also exposes several porphyry Cu deposits affected by supergene mineralization, in which the ages of the hypogene mineralization are well constrained (Perelló *et al.*, 2010; Mpodozis & Cornejo, 2012). The gravel deposits of the CMD potentially provide a picture of the tectonic episodes, the geomorphologic and paleoclimatic conditions in which the supergene processes occurred. In this work, we describe the sedimentary facies and stratigraphy of the gravel deposits and provide geochronological constraints of the age of their deposition. Detrital zircon geochronological data combined with clast counts are used to reconstruct the unroofing sequence of the porphyry Cu deposits. To relate the supergene mineralization episodes with the timing of the gravel deposition, we provide supergene and exotic Cu mineral ages, which complement the ages previously reported in the CMD.

This study is one of the few works dedicated to understand the geomorphological condition that controls supergene mineralization, in an area where geologists are intensively searching for signals in the sedimentary record that may help find copper deposits hidden by the mid-Eocene to mid-Miocene gravel cover. The main questions addressed in this contribution are as follows: Can the unroofing history of the porphyry Cu be reconstructed from the mid-Eocene to mid-Miocene gravel record of the CMD? How did this history control the supergene mineralization episodes and exotic Cu deposition? Can the supergene mineralization be related to a specific event during the unroofing process or is it linked to a particular geomorphological setting and/or to a specific paleoclimatic episode?

GEOLOGICAL SETTING

The CMD is located in the Antofagasta Region of northern Chile, *ca.* 40 km SSW of Calama city and includes several mid-late Eocene porphyry Cu deposits (Mirador, Esperanza, Esperanza Sur, Encuentro, Penacho Blanco and Polo
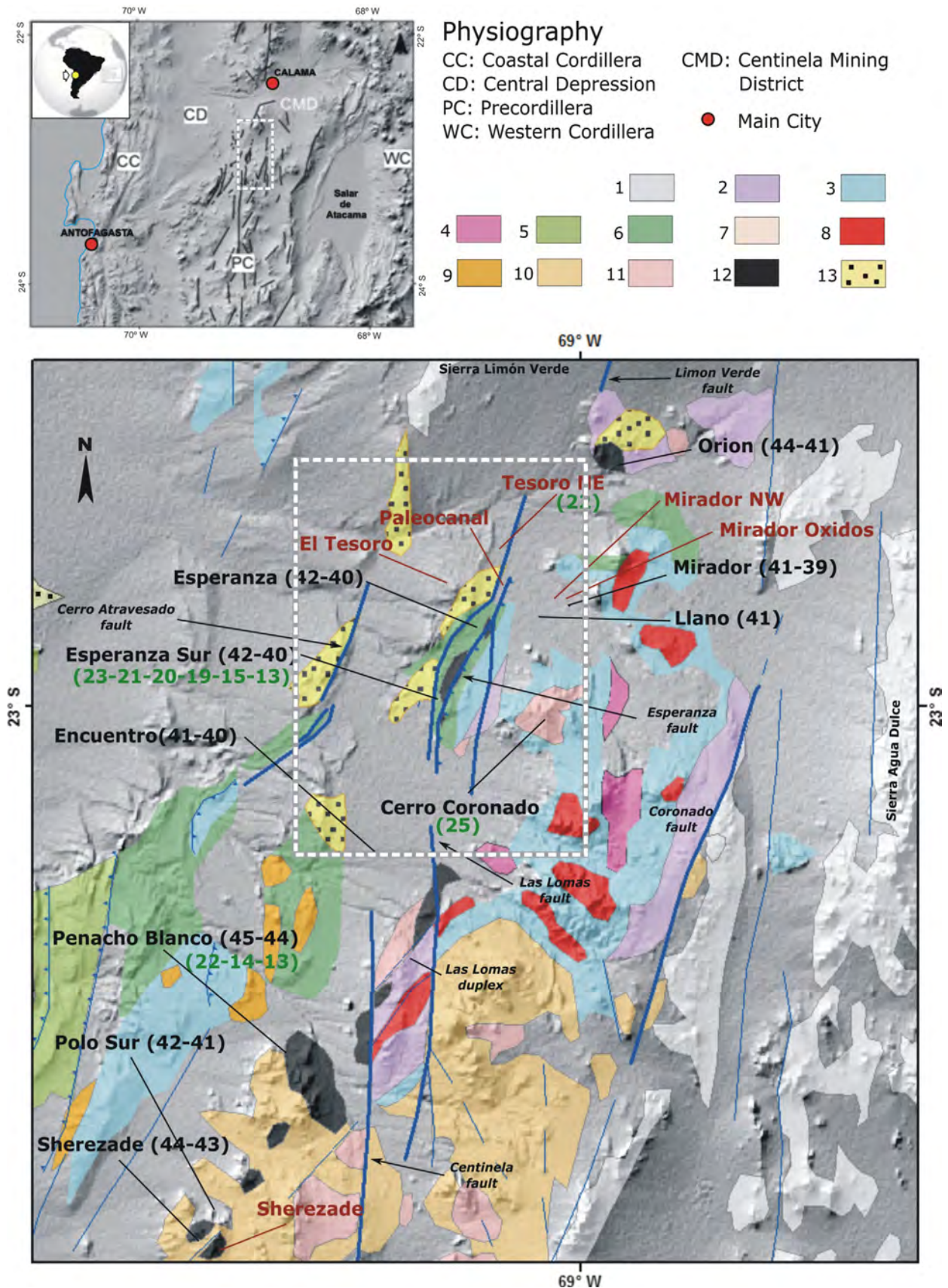
Fig. 2. (a) Location of the Centinela Mining District and the physiographic setting of the Atacama Desert in the Antofagasta Region of northern Chile. The main structures of the Domeyko Fault System in the Precordillera are shown. (b) Regional geological map of the CMD showing the main mineralized porphyry systems (taken from Mpodozis & Cornejo, 2012). 1, Upper Paleozoic (290–270 Ma) basement. 2, Upper Triassic (210–200 Ma) volcanic and sedimentary rocks. 3, Jurassic to Lower Cretaceous sedimentary and volcanic rocks. 4, Lower Cretaceous (124–100 Ma) gabbros to diorites and granodioritic porphyry intrusions. 5, Lower Cretaceous (?) volcanic rocks. 6, Upper Cretaceous (78–66 Ma) sedimentary and volcanic succession (Quebrada Mala formation).7, Undifferentiated Cretaceous granitoids. 8, Late Cretaceous (78–68 Ma) diorites and (minor) rhyolitic porphyry intrusions. 9, Lower Paleocene (65–64 Ma) diorites and dacitic porphyry intrusions. 10, Paleocene to Lower Eocene (64–53 Ma) volcanic rocks (Cinchado formation). 11, Paleocene (60–56 Ma) monzodiorites and rhyolitic porphyry intrusions. 12, Late Eocene (44–40 Ma) monzodioritic to granodioritic stocks and mineralized dacitic porphyry intrusions. 13, Upper Eocene to Oligocene gravel units (Esperanza, Tesoro I, Atravesado I and II in this work). Numbers in black corresponds to U/Pb zircon emplacement ages yielded by porphyry Cu intrusions. Numbers in green indicate the supergene mineral ages reported in this work (see Table 3).

Sur), all of which belong to the porphyry copper belt of northern Chile (Perelló *et al.*, 2010; Mpodozis & Cornejo, 2012; Fig. 2). Porphyry Cu mineralization in the district occurs along the western border of the Cordillera de Domeyko (or Precordillera), an uplifted basement range essentially formed by late Paleozoic to Triassic volcanic and intrusive rocks with ages between 320 and 200 Ma including, at Sierra Limón Verde (Fig. 2b), minor outcrops of Neoproterozoic to Paleozoic sedimentary and metamorphic units (Marinovic & García, 1999; Basso & Mpodozis, 2012; Morandé, 2014). The Cretaceous to Eocene geological evolution of the CMD records a lengthy history of magmatic activity. The oldest plutonic rocks correspond to a group of Early Cretaceous gabbros and quartz diorites, with U/Pb zircon ages between 122 and 116 Ma (Cornejo & Mpodozis, 2015). These plutonic rocks were emplaced within Upper Triassic (210–200 Ma) volcanic and sedimentary rocks (Estratos Las Lomas) and within Jurassic to Lower Cretaceous fossiliferous marine rocks and evaporites (Caracoles Group; Marinovic & García, 1999). All of the previously mentioned units are unconformably covered by an Upper Cretaceous (78–66 Ma) succession including andesitic lavas and breccias and sedimentary rocks from the Quebrada Mala Formation (Marinovic & García, 1999). This succession is in part coeval to a group of diorites to rhyolite porphyries and flow domes, with U/Pb zircon ages between 70 and 66 Ma (Mpodozis & Cornejo, 2012). Volcanism continued into Cenozoic time with the deposition of the Cinchado Formation, a volcanic succession that includes basaltic to andesitic lava flows and rhyolitic ignimbrites and domes (Mpodozis & Cornejo, 2012). These volcanic rocks derived from stratovolcanoes and small collapse calderas that were active between the early Paleocene (64 Ma) and the early Eocene (53 Ma). During this interval, a diverse group of epizonal intrusions containing quartz diorite to monzodiorite (60 Ma) and granodiorite (58–57 Ma) plus andesitic to dioritic porphyritic intrusions were emplaced in the Mesozoic units and Paleogene volcanic edifices (Mpodozis & Cornejo, 2012).

Mineralized porphyry Cu intrusions were emplaced in the CMD between 45 and 39 Ma (U/Pb zircon data; Perelló *et al.*, 2010; Mpodozis & Cornejo, 2012). The porphyries mainly correspond to hornblende-biotite dacite dike swarms that, together with several barren pyroxene-hornblende dioritic stocks and lacoliths, form a 40-km long, N to NE-trending belt, which includes at least 10 discrete intrusive complexes. The oldest porphyry Cu (45–43 Ma) deposits were emplaced on the southwestern end of the belt, with the ages decreasing northeastward, reaching 39 Ma at the northeastern edge of the porphyry belt (Fig. 2b). The hypogene mineralization in the district has been dated by $^{40}Ar/^{39}Ar$ and K-Ar hydrothermal biotite and Re-Os molybdenite ages between 45 and 40 Ma and is related to the above-mentioned dike swarms (Perelló *et al.*, 2010). Exotic Cu mineralization derived from supergene copper leaching of the hypogene sulphides contained in nearby porphyry Cu deposits can be recognized in the Paleocanal, El Tesoro and Tesoro NE deposits (Mora *et al.*, 2004; Perelló *et al.*, 2010).

The main structural feature of the CMD is a 3–5 km wide, N-S trending fault zone, which includes the Atravesado, Centinela, Las Lomas, Esperanza and Coronado faults, and that cuts obliquely across the porphyry Cu belt (Fig. 1b). This fault zone is part of the Domeyko Fault System (DFS), a major zone of tectonic deformation stretching for >1000 km along the Precordillera of northern Chile (Mpodozis *et al.*, 1993). The main episode of tectonic activity along the DFS seems to have occurred between the mid-Eocene to early Oligocene (45–33 Ma, the Incaic tectonic orogeny; Maksaev & Zentilli, 1999; Tomlinson *et al.*, 2001; Arriagada *et al.*, 2008). Porphyry Cu-related intrusions, which represent the most relevant metallogenic episode in northern Chile, are associated with the Incaic tectonic orogeny (Mpodozis & Perelló, 2003; Sillitoe & Perelló, 2005). The Incaic tectonic orogeny is also an important episode of exhumation in the Domeyko Cordillera as evidenced by fission-track data (Maksaev & Zentilli, 1999; Nalpas *et al.*, 2005; Sanchez *et al.*, 2015). However, the detailed kinematic history of the DFS is a matter of controversy as evidence for both left- and right-lateral displacement, including reversal displacements, has been documented along discrete faults that form the system (Reutter *et al.*, 1996; Tomlinson & Blanco, 1997a,b; Niemeyer & Urrutia, 2009; Dilles *et al.*, 2011).

At the CMD, the erosion and denudation of the Domeyko Cordillera in response to the Incaic tectonic orogeny resulted in the deposition, between the mid–late Eocene to the mid-Miocene, of up to *ca.* 800 m of gravel and sand deposits with scarce interbedded volcanic and evaporite layers. The upward stratigraphic sedimentary changes of these deposits are probably controlled by tectonic episodes and climatic fluctuations. Likewise, the upward stratigraphic changes in the clast composition potentially record the unroofing history for the porphyry Cu emplaced in the Domeyko Cordillera at this area. The sedimentary, clast composition and detrital zircon changes across these deposits are presented herein.

GRAVEL UNITS OF THE CMD

We identified seven gravel units along the CMD on the basis of contact relationships, sedimentary facies, lithology of clasts and the presence of interbedded volcanic layers. The surface distribution and sedimentological

information of the gravel units were collected during a 1:25.000 mapping of the CMD, which focused on the gravel record (Fig. 3). Sedimentological information was also collected from six stratigraphic columns measured on a centimetre to meter scale (Fig. 4). The sedimentary facies were described using the criteria proposed by Miall (1996) and Hogg (1982) and the modifications used for the gravel deposits in the Atacama Desert by Blanco & Tomlinson (2002) and Nalpas *et al.* (2008) have also been considered (Table 1). Once familiarized with the sedimentary facies, we were able to differentiate between the gravel units on two drill cores (>700 m of cores) that were provided by the Antofagasta Minerals S.A. mining company (Fig. 5). The sub-surface distribution was defined based on drill core logging and the sub-surface geological and structural information reported by Mpodozis & Cornejo (2012). Based on this information, geological profiles oriented across the main structural features were constructed (Fig. 6). Previous work done in the area defines an informal stratigraphy for the Tesoro mine area (Blanco & Tomlinson, 2002; Mora *et al.*, 2004; Tapia *et al.*,
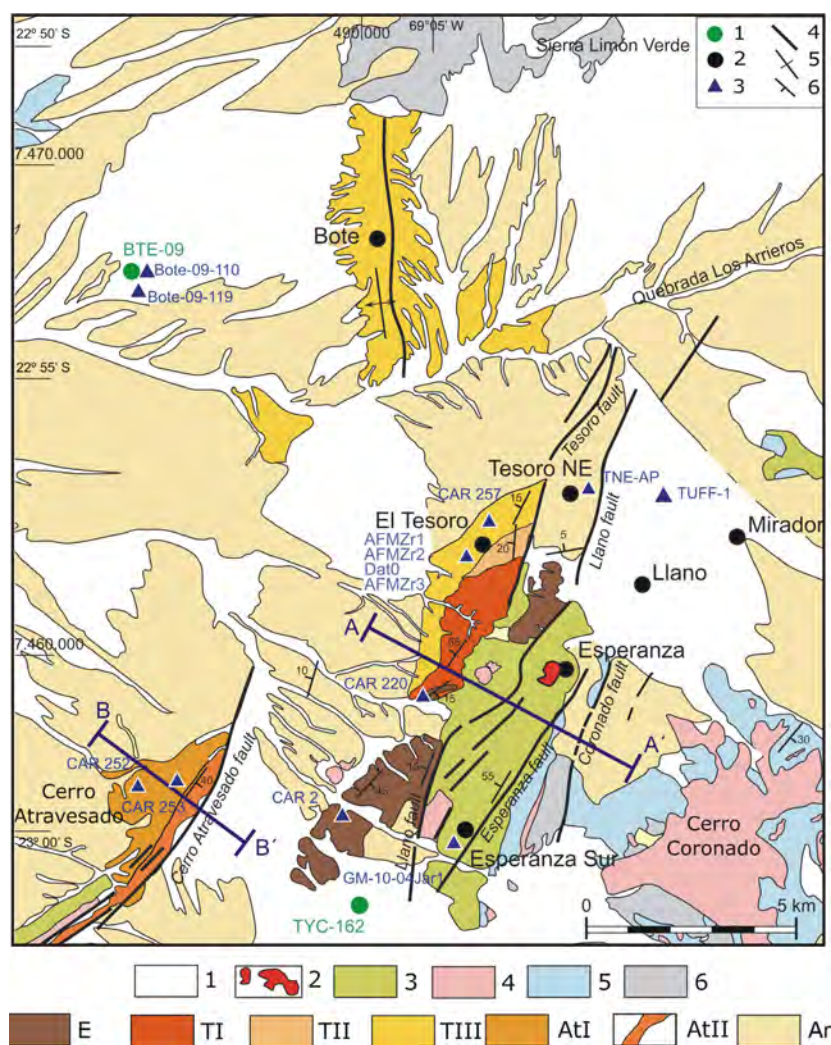
Fig. 3. Geological map focused on the mid-Eocene to mid-Miocene gravel deposits in the CMD. E: Esperanza gravels, TI, II and III: Tesoro I, II and III gravels, respectively, AtI and II: Atravesado I and II gravels, respectively, Ar: Arriero gravels. The figure shows the names of the localities and the drill holes discussed in the text. Symbols: 1: drill hole, 2: open mine pits, 3: location of the geochronological data, 4: Faults, 5: Anticline, 6: Dip bed. Legend. 1: Post-mid-Miocene poorly consolidated gravel deposits constituting the alluvial fans observed on the landscape surface. 2: Eocene (45–39 Ma) mineralized porphyry intrusions. 3: Upper Cretaceous sedimentary and volcanic rock. 4: Cretaceous and Paleocene intrusions. 5: Jurassic to Lower calcareous rocks. 6: Upper Paleozoic and Triassic basement. AA′ and BB′ show the location of the geological profile in Figure 6.
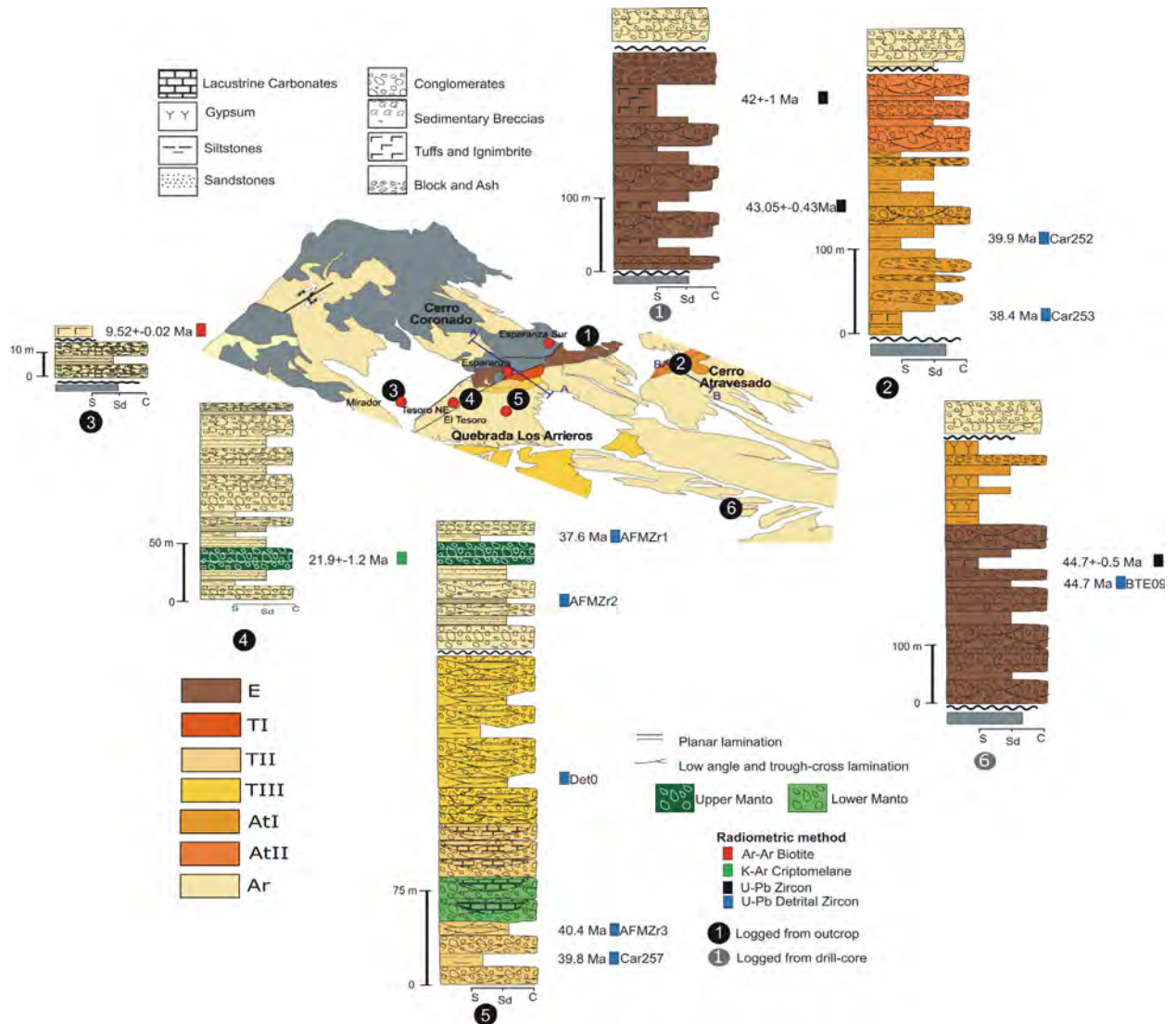
Fig. 4. Stratigraphic columns used to study the mid-Eocene to mid-Miocene gravel deposits. The columns were constructed either from outcrops or from drill core logging. The location of the columns is shown on a towards-the-south 3D view of the map presented in Fig. 3 (with the pre-Eocene rocks simplified as a grey colour). The columns also show the stratigraphic position of the geochronological data discussed in the text. The stratigraphic positions of the recognized exotic Cu mantos are shown. Note that the vertical scale changes between the columns. The abbreviations of gravel units are given in Fig. 3.

2012). The equivalence between the gravel unit names used by these authors and the names used in this work is shown in Table S1.

Esperanza gravels

Sedimentology

The Esperanza Gravels are composed of Gh and Gpt facies with sporadic intercalations of Sm, Fsm and rare Gmm facies, and abundant intercalations of volcanic layers (Fig. 5a,b). The Gh and Gpt facies are well rounded, mainly cobble grade, normally imbricated, and form tabular elongated bodies that extend by several tens of meters,

with a meter-scale thickness (2–7 m). The Sm and Fsm intercalations form tabular continuous, centimetric-scale thick bodies. The volcanic intercalations include interbedded rhyolitic and dacitic, poorly consolidated, tuff layers and block and ash deposits.

Distribution and stratigraphic relationship

The outcrops of this gravel unit are restricted to the Esperanza Sur area and the area between Esperanza and Tesoro NE. In the Esperanza Sur area, it is composed of brown-reddish coloured strata and forms an open syncline with an NE-SW-oriented axis (Fig. 3).

7

Table 1. The facies codes are modified from Miall (1996) and consider the modifications used for the gravel deposits in the Atacama Desert by Blanco & Tomlinson (2002) and Nalpas *et al.* (2008).

Facies	Description	Depositional Processes
Gmm: Matrix-supported, massive gravels.	Sub-rounded to sub-angular, ungraded and poorly sorted gravels, granule to cobble grained. Occasionally clast imbrication.	Cohesive flow deposits, sub-aerial to sub-aqueous debris flows (Smith, 1986; Miall, 1996).
Gcm: Clast-supported, massive gravels.	Rounded, sub-rounded to sub-angular, ungraded and poorly sorted gravels, granules to boulders, coarse sandy matrix.	Plastic or pseudo-plastic hyper-concentrated density flows, resulting from high sediment and water discharge floods with rapid transport and deposition (Waresback and Turbeville, 1990; Svendsen *et al.*, 2003; Smith, 1986; Horton and Schmitt, 1996).
Gh: Clast-supported, horizontally laminated gravels.	Sub-rounded to sub-angular gravels. Granules to cobble. Imbrication and flattened clast alignments	Longitudinal bar or lag deposits that result from channelized streamfloods under upper-flow regime conditions (Waresback and Turbeville, 1990; Miall, 1996). Deposited from high energy, bedload tractive, unconfined or poorly confined sheetfloods (Nemec and Steel, 1984; Horton and Schmitt, 1996; Nalpas *et al.*, 2008).
Gpt: Planar and trough cross-bedded gravels.	Clast-supported gravels. Sub-rounded to sub-angular gravels. Granules to Pebble. Imbrication.	Channel infill deposits related to transverse and lingoid bars or with 2D–3D dunes, deposited in the upper part of lower flow regime conditions (Miall, 1996; Bordy and Catuneanu, 2001; Uba *et al.*, 2005).
Sm: Massive sand.	Ungraded and unstratified fine to coarse sand with scattered gravel clasts.	Hyper-concentrate flows (Smith, 1986) or high-density turbidity currents when the sand deposition is too rapid to allow the development of bedforms (Horton and Schmitt, 1996).
Sh: horizontally laminated sand.	Fine to coarse well-sorted sand with scattered gravels. Planar or sub-planar lamination.	Deposited from high energy, sheetfloods or sheetflows in the lower part of the upper-flow-regime conditions (Collinson, 1996; Miall, 1996).
Spt: Planar and trough cross-stratified sand.	Planar and trough cross-bedded sands with scattered gravels.	Stream flow deposits associated with transverse and lingoid bars or with 2D–3D dunes, under lower flow-regime conditions (Miall, 1996; Bordy and Catuneanu, 2001; Uba *et al.*, 2005).
Fsm: Silt, mud and very fine sand,	Massive or poorly laminated, scattered sub-angular to sub-rounded gravel clasts	Confined flows in a shallow-water environment or sub-aerial waning flood flows (Miall, 1977; Horton and Schmitt, 1996).
Fl: horizontally laminated sands and silts	Well-laminated sands and silts. Occasionally soft loading features.	Suspension fallout on stagnant water bodies (Miall, 1996).
Y: massive gypsum	Massive gypsum, indurated with scattered very fine to fine sand clasts.	Salt precipitation under high evaporitic conditions
C: sandy carbonates	Poorly laminated, carbonate cemented sands. Occasionally soft loading features.	Precipitation of primary micrite in stagnant shallow lakes or pond with terrigenous inputs (Fernadez-Mort *et al.*, 2015)

The top of the exposed succession includes a massive, block and ash deposit, and biotite-hornblende-quartz lapilli and crystalline tuffs. In the southward prolongation of the syncline axis, the drill hole core TYC-162 shows that the Esperanza gravels are >300 m thick (Fig. 4, column 1). To the east, the Esperanza gravels are separate from the Upper Cretaceous strata by the sub-vertical Llano Fault. Between the Tesoro NE and Esperanza Sur areas, the Triassic-Upper Cretaceous strata form a long-wavelength asymmetric anticline, which host the 42–40 Ma Esperanza and Esperanza Sur porphyry copper intrusions (Fig. 6a). The frontal
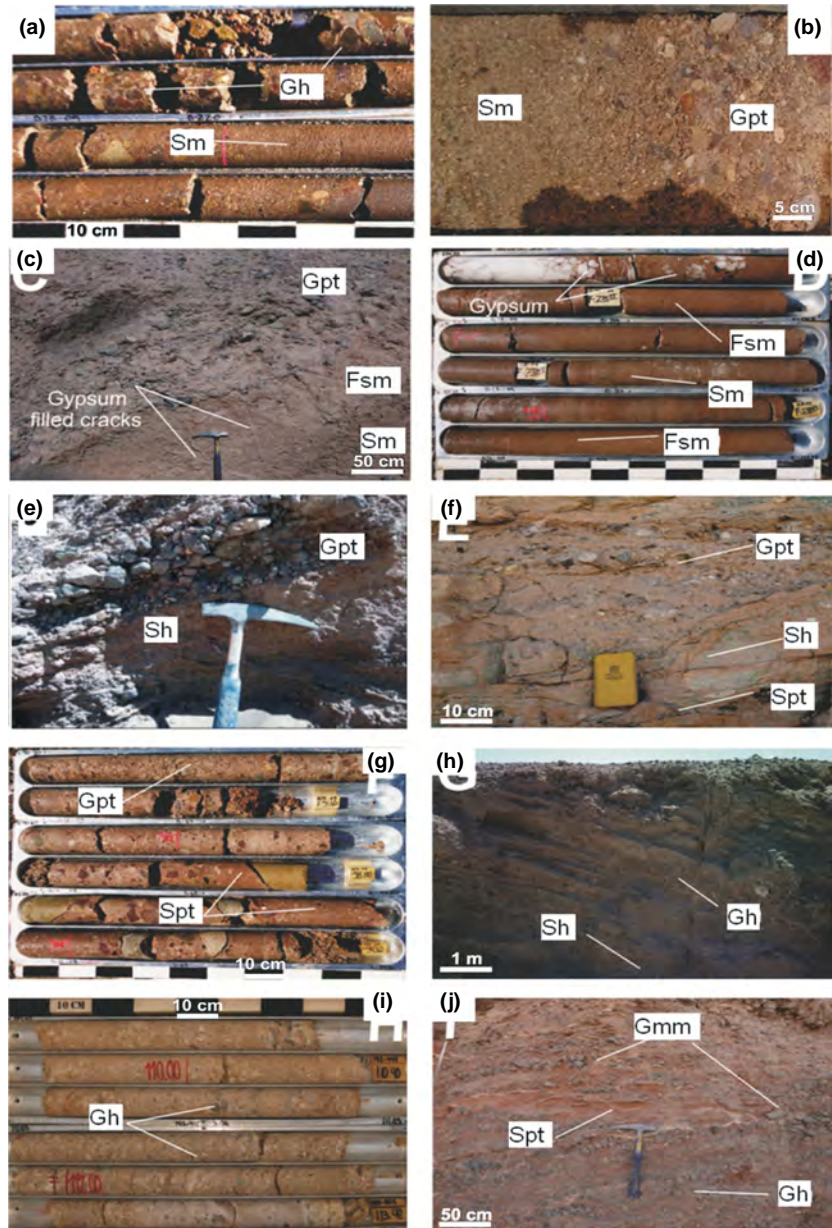
Fig. 5. Some of the main sedimentary features differentiating the gravel units (see Fig. 3 for the locations). (a, b) sedimentary features identified in the Esperanza gravels from drill core BTE-09. (c, d) Sedimentary features identified in the Atravesado I gravels in the Atravesado area and from drill core BTE-09, respectively. (e) Sedimentary features identified in the Atravesado II gravels in the Atravesado area. (f, g) Sedimentary features identified in the Tesoro II gravels from the benches of the Tesoro pit and from a drill core done at the pit bottom, respectively. (h, i) Sedimentary features identified in the Arrieros gravels from the homonymous quebrada and I from drill core BTE-09.

limb of the anticline is upthrown westward along the Telegrafo fault, over the Esperanza gravels. The hinge zone of the anticline and the Esperanza gravels are, in turn, sliced by the Llano sub-vertical fault. To the west, the logging of the drill core BTE_09 shows *ca.* 280 m of mainly Gh and Gpt facies with pyroclastic intercalations, which represents the westernmost evidence of this gravel unit (Figs 3 and 4, column 6).

The Tesoro I gravels

Sedimentolgy

This gravel unit is made of Gcm and Gmm facies, with uncommon Sm and Gh intercalations. These facies form planar to irregular, diffusely based beds measuring several meters thick (1–5 m). The Gcm facies are mainly moderately to poorly sorted and include well-rounded and imbricated clasts, commonly exposing two clast sizes (4–15 cm and 20–40 cm). The Gmm facies are poorly sorted and include sub-angular to sub-rounded, pebble to boulder clasts (large-sized clasts up 30 cm). The Sm facies are coarse-grained and commonly include granule to cobble grained clasts. The Gh facies intercalations are occasionally erosive-based.

Distribution and stratigraphic relationship

This gravel unit outcrops south of the Tesoro mine forming a 10 km long NNE-SSW trending belt in
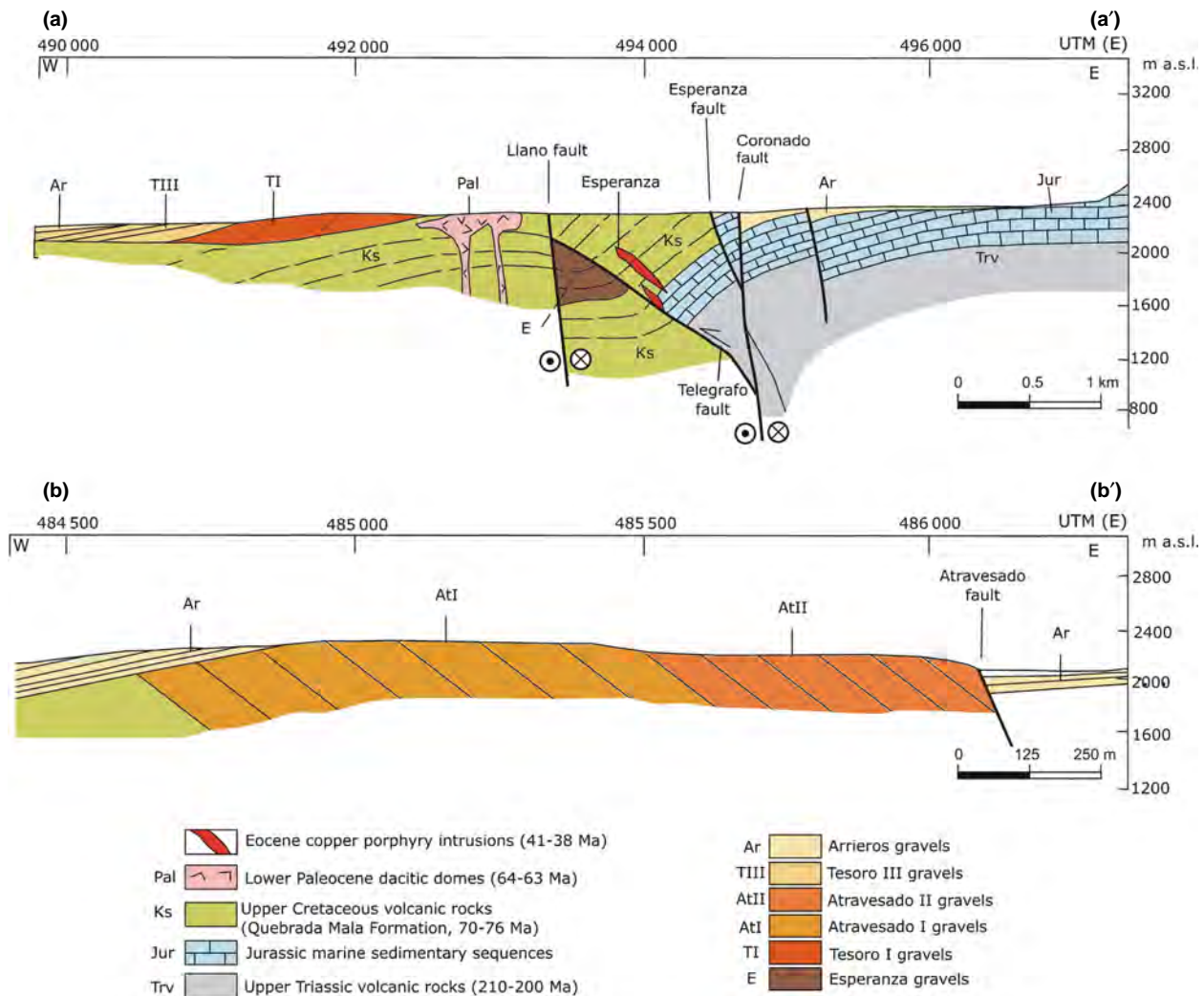
Fig. 6. Geological profiles oriented perpendicular to the main structural features of the Centinela district. Profile AA′ was published by Mpodozis & Cornejo (2012; see page 343) and was constructed from data yielded by an intensive drilling program during which the unexposed Telegrafo Fault was discovered. We slightly modified the profile only adding the gravel units. The location of the profiles is indicated in Fig. 3. Note that the horizontal scale changes between the profiles.

which the beds dip 60–65° NW. It constitutes a light brown to light grey coloured, partially lithified, sedimentary succession that reaches a thickness of *ca*. 400 m. This sedimentary succession unconformably overlays the Upper Cretaceous strata and the Esperanza gravels.

The Tesoro II gravels

Sedimentology

This gravel unit is mainly formed by Gpt facies with common Spt, Sh, Fl and minor C facies intercalations (Fig. 5f,g). The Gpt facies are sub-angular to sub-rounded and form m-scale (1–2 m) erosive-based, lenticular beds that are several meters wide. They are poorly sorted, pebble to boulder grained (2–15 cm in diameter, occasionally up to 30 cm), and locally show clast imbrications. The Spt and Sh facies are medium to coarse-grained and are disposed in lenticular to tabular beds, 0.2–0.4 m thick and several meters wide. The Fl facies forms tabular beds, 0.3–1 m thick and commonly presents cm-scale intercalations of Sh facies. The C sandy carbonate facies, which are described in detail in the work of Fernández-Mort *et al.* (2016), are present as tabular beds that are 0.5–2 m thick and several meters wide. They show very incipient parallel laminations. Carbonate is primarily represented by micrite with a high percentage of fine-grained terrigenous input. The Fl and C facies occasionally expose load casts structures, especially when they underlay coarse-grained beds.

Distribution and stratigraphic relationship

This gravel unit is a light brown coloured, carbonate cemented sedimentary succession that forms a *ca.* 1 km long NE-SW-oriented lenticular outcrop exposed in the Tesoro mine area (Fig. 3). This lenticular body is cut by the Tesoro Fault in its NE limit and is wedged towards the SW. The Tesoro II gravels unconformably overlay the Tesoro I gravels. The most complete sedimentary record of this gravel unit is observed in the Tesoro mine pit, where it reaches up to *ca.* 100 m thick and is composed by beds that dip 10°W and (Figs 3 and 4, column 5 Fig. 7b).

The Tesoro III gravels

Sedimentology

This gravel unit is almost completely formed by planar-based, medium- to coarse-grained Gh facies, which forms beds with thickness that varies between 1 and 10 meters. The bedding is mainly given by grain-size changes, occasionally related to cm-scale pebble sand intercalations or by clast alignments. The beds are poorly to moderately sorted and include angular to sub-angular, frequently imbricated clasts (2–10 cm in diameter, occasionally up to 25 cm).

Distribution and stratigraphic relationship

This gravel unit is a red to orange coloured, hematite–limonite–gypsum cemented sedimentary succession that forms a *ca.* 3.5 km long NE-SW-oriented belt that extends from the Tesoro mine towards the SW. In this area, the Tesoro III gravels reach up to 90 m thick; they unconformably overlay the Tesoro I gravels and conformably overlay the Tesoro II gravels. This facies association also forms a north-south trending ridge that extends from Quebrada Los Arrieros to the north (Fig. 3).

The Atravesado gravels

Sedimentology

The lowermost *ca.* 200 m of the column of this gravel unit is made up of Sm, Fsm and Gmm, Gcm facies, with frequent, although variable in proportion (depending on the observed section), intercalations of Gh and Sh facies (Fig. 5c,d). The Gmm, Sm and Gcm facies almost exclusively form planar to irregular, diffuse-based beds. The Sm and Fsm facies are moderately to poorly sorted, and commonly include large-sized scattered clasts (granules to cobbles, rarely boulders). The thicknesses in these facies vary from 1–3 to 18 m. Thin intercalations of Fsm beds frequently expose mudcracks and gypsum veins (Fig. 5c). The Gmm and Gcm facies are several tens of centimetres

thick, very poorly to poorly sorted, sub-angular to sub-rounded and commonly granule to cobble grained (large-sized clasts up to 30 cm). The Gh and Sh normally form 1 to 6 m thick successions, and are either on erosive paleo-channel surfaces (1–1.5 m deep, up to 4 m wide) or on diffuse planar surfaces. The Gh are commonly moderately to well sorted, sub-angular to sub-rounded, and include horizontally aligned flattened clasts.

The uppermost *ca.* 100 m of the column of this gravel unit is formed by alternations of Gh, Sh, Gpt and Spt, with minor intercalations of Sm, Fsm and Gcm beds. The Gh, Gpt, Sh and Spt facies fill paleo-channel erosive surfaces, *ca.* 1 m deep and 3–4 m wide (Fig. 5e); however more rarely, the Gh facies can reach up to 6 m thick. The Sm and Gcm facies form lenticular bodies, 50 cm thick and <1 m wide. The Gh facies are moderately to poorly sorted, sub-rounded to rounded, granule to cobble grained (4–7 cm) and commonly show horizontally aligned flattened clasts. The Gpt facies are moderately sorted, rounded to well-rounded granules (1–2 cm) or occasionally cobble grained, normally showing imbricated clasts. The Gcm facies are very poorly sorted, granule to cobble grained (larger-sized clasts of up to 20 cm) and comprise sub-angular to sub-rounded clasts embedded in a silty to fine sand grained matrix. The sand and silt facies are moderately sorted, sub-angular to sub-rounded. The Sm and Fsm facies include dispersed granules, and occasionally cobble gravel clasts.

Distribution and stratigraphic relationship

The Atravesado gravels form a red coloured, carbonate cemented, sedimentary succession exposed in the Atravesado range. It reaches a thickness of *ca.* 300 m and forms an 8 km long NNE-SSW trending belt in which the beds dip 30–40° SE (Figs 3 and 4, column 2). The Atravesado gravels unconformably overlie the Cretaceous Quebrada Mala Formation. A carbonate cemented sedimentary succession mainly formed by Sm and Fsm facies with scarce Gmm facies, which can be attributed to the Atravesado gravels, is recognized as forming the uppermost 120 m of drill core BTE-09 (Figs 3 and 4, column 6).

The Arriero gravels

Sedimentology

This gravel unit is composed of Gh, Sh and minor Gpt and Fl facies, and rarely Gmm and Y facies (Fig. 5h,i,j). The Gh and Gpt facies are composed of poorly to moderately sorted granules to fine pebbles, and angular to sub-rounded clasts. These facies, as well as the Sh facies, form tabular to very elongate lens-shaped, planar-based beds that are tens of centimetres thick. In the Gh facies, the
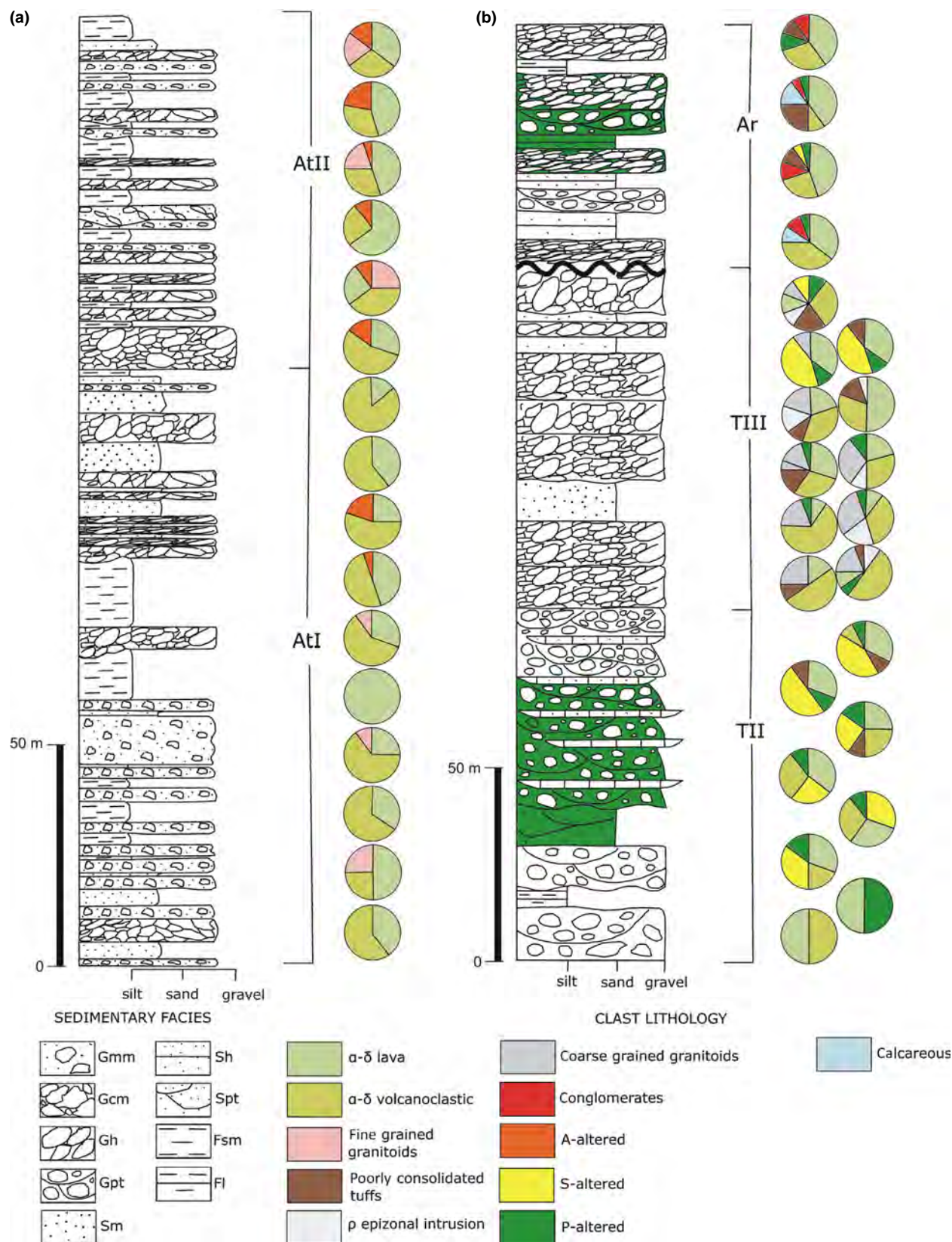
Fig. 7. High–resolution stratigraphic columns (centimetre to meter scales) showing the clast counts performed in this work. (a) col–umn logged for the Atravesado I and II gravels in the Atravesado area (column 2 in Fig. 4). (b) stratigraphic column logged for the Tesoro II and III and the Arrieros gravels in the Tesoro open pit (column 5 in Fig. 4).

lamination is given by grain-size changes or by flattened clast alignments. The Sh facies comprise fine- to coarse-grained, moderately to well sorted, angular to sub-angular sands. The Gmm facies form thick beds that can reach up to 40 cm. They include poorly sorted, granules to cobbles (2 mm–15 cm) and angular clasts. The Fl facies form fine, well-marked planar-based strata. The Y facies forms beds that are up to 3 m thick.

Distribution and stratigraphic relationship

This gravel unit is widely distributed, thereby forming most of the present-day landscape surface, not only for the studied area but also for the entire western slope of the Precordillera at this latitude (Fig. 3). It is a brown-yellow coloured, poorly consolidated, commonly gypsum cemented but occasionally carbonate cemented sedimentary succession in which the thicknesses progressively increase from the range piedmonts downstream. The thicknesses of this succession only reach several meters at the range piedmonts and progressively decrease to reach more than 100 m in the farther plains. Thus, a vertical cross-section of this succession roughly defines a wedge-shaped geometry that opens downslope from the ranges. The succession unconformably overlies all of the older stratigraphic units. To the east, it is directly deposited on an extensive bare rock surface and onlaps the range piedmonts (Fig. 3 and 6, profile AA′). In line with the change in the thicknesses, the proportion of the individual facies changes depending on the position in the landscape. Coarse-grained facies are dominant close to the ranges, whereas fine-grained facies are preponderant and Y facies are more frequent downslope. In both the Tesoro and Tesoro NE mine pit, this succession reaches *ca.* 80 m thick. In the Tesoro pit, it unconformably overlies the Tesoro III gravels and is composed by beds that dip *ca.* 5°W, whereas in the Tesoro NE pits the beds are dipping *ca.* 5°E.

CLAST COMPOSITIONS AND CLAST COUNTS

Clast counts were performed for 16 stations that are roughly homogenously distributed throughout a *ca.* 300 m thick stratigraphic column logged on the Atravesado gravels (Fig. 7, column A). Clast counts were also performed for 23 stations that are roughly homogenously distributed throughout the *ca.* 370 m thick stratigraphic column logged on the Tesoro II and III gravels and on the Arriero gravels at the Tesoro mine pit (Fig. 7, column B). One hundred clasts were counted inside a *ca.* 2 × 2 m square in each selected station. These clast counts were primarily carried out to identify lithologies that can be used to reconstruct the exhumation history of the porphyry Cu from the stratigraphic record. We paid special attention to the identification of the hypogene alteration mineralogy when performing the clast counts for two main reasons (Fig. 1). First, the hypogene mineralization zone has vertical extents of ≥2 km and presents a vertical mineralogical zoning pattern (e.g. Sillitoe, 2010). Consequently, the hypogene mineralogy can be used as relative indicator of the erosion level of a porphyry Cu. Second, the extent of the hypogene alteration (several square kilometres) is much greater than the size of the intrusive (diameters and lengths commonly of ≤1 km, respectively) that generate the porphyry Cu (e.g. Sillitoe, 2010). Therefore, it is more likely to find that this rock type constitutes a relatively large clast group. All of the clast lithologies can be linked to rock units from either the CMD and/or the immediate vicinity. Thus, the clast counts can additionally be used to perform a provenance study by comparing the clast lithology populations to the lithology of the rock units recognized in the 1:25.000 regional geological map of the district (Mpodozis & Cornejo, 2012; Antofagasta Minerals, unpublished) (Fig. 2).

The lithologies that compose the different clast groups can be divided into those that are indicative of a specific geological unit and those that are present in various geological units. Table 2 summarizes and classifies these lithologies. The α-β lava clast group is present within the entire stratigraphic record and is composed of aphanitic and porphyritic andesites and dacites. They constitute a clast group that represents between 25 and 60% (up to 100% in one case) of the clasts in the Atravesado and the Tesoro II gravels, between 10% and 35% of the clasts in the Tesoro III gravels, and between 35% and 45% of the clasts in the Arriero gravels. The fine-grained granitoids incorporate another clast group that is commonly recognized along almost all of the stratigraphic record. It is composed of medium- to fine-grained, equigranular and porphyric diorites and quarzodiorites. They make up a minor clast group (up to 25% of the clasts) in the Atravesado gravels, and is a large population along the entire stratigraphic column of the Tesoro pit: they represent between 20% and 50% of the clasts in the Tesoro II gravels, between 30% and 65% of the clasts in the Tesoro III gravels, and between 0–10% and 40% of the clasts in the Arriero gravels.

Two clast groups can be recognized as occurring only in the Atravesado gravels. One of these populations comprises the α-δ volcaniclastic clasts, which is made up of andesitic and dacitic tuffs and volcaniclastic sandstones and which commonly contain between 25 and 65% of the clasts but may include up to 85% of the clasts. Although silicified rock or residual quartz fragments, which commonly have limonite patinas and a vuggy appearance, occur in minor amounts (up to 25%), they are another distinctive clast lithology of the middle and upper part of the Atravesado gravels. These lithologies represent the advanced argillic hypogene alteration (labelled as A-altered in Table 2), which is formed by

Table 2. Clast groups determined from the clast counts performed in this work, including the clast lithology description and the geologic unit in which these lithologies can be found.

Label	Clast lithology description	Rock unit
α-δ lava	Brown, grey or slightly purple aphanitic and porphiric andesites and dacites, commonly with plagioclase, rarely with hornblende, quartz or pyroxene phenocrysts	Upper Cretaceous sedimentary and volcanic Quebrada Mala Formation and early Paleocene-early Eocene Cinchado Formation.
α-δ volcanoclastic	Andesitic and dacitic tuff and volcanoclastic sandstones	Upper Cretaceous sedimentary and volcanic Quebrada Mala Formation located on the western part of the studied area
Fine-grained granitoids	Equigranular medium to fine-grained diorites and quarzodiories and porphyric hornblende diorites and quarzodiorites, frequently with mafic crystals altered to chlorite and plagioclase altered to epidote	Early Cretaceous and Paleocene intrusions.
Poorly consolidated tuffs	Poorly consolidated light grey and white lapilli, ash and crystalline dacitic and rhyolitic tuffs with amphibole crystals	Mid-Upper Eocene sedimentary and volcanic rocks
ρ epizonal intrusion	Quartz and K-feldspar porphyric rhyolites	Epizonal Upper Cretaceous and Paleocene intrusions.
Coarse-grained granitoids	Coarse-grained granodiorites and granites	Upper Paleozoic basement
Conglomerates	Gypsum or carbonate cemented fine-grained conglomerates	Mid-Eocene-Mid-Miocene gravel deposits
A-altered	Undifferentiated silicified rock or residual quartz fragments commonly with limonite patinas and vuggy appearance	Advanced argillic hypogene alteration
S-altered	Altered porphyric rocks with abundant sericite and veins of quartz and boxworks	Sericitic hypogene alteration
P-altered	Green-grey and grey-brown-coloured clast, partially or totally altered to chlorite and epidote, with limonite and goethite and pyrolusite patinas	Propylitic hypogene alteration
Calcareous	Limestones and calcareous siltstones	Jurassic to Lower Cretaceous Caracoles Group

hydrothermal rock leaching at shallower levels (0–500 meters deep) on the roof of porphyry Cu deposits (e.g. Sillitoe, 2010; Fig. 1).

Several clast groups are observed only in the Tesoro II and III gravels and the Arriero gravels. One of these clast groups includes the poorly consolidated dacitic and rhyolitic tuffs (labelled as poorly consolidated tuffs in Table 2). They are present within the entire stratigraphic column of the Tesoro pit; they are almost absent in the Tesoro II gravels, they constitute a minor population of the clasts (5–10%) in the Tesoro III gravels, and can reach up to 25% of the clasts in the Arriero gravels.

The porphyric rhyolites clast (labelled as ρ epizonal intrusion in Table 2) constitutes a clast group restricted to the Tesoro III gravels, which constitutes between 5% and 20% of the clasts. One clast group that is mainly restricted to the Tesoro III gravels (10–30%) but which is also present in the Arriero gravels (10–15%), is made up of coarse-grained granodiorites and granites (labelled as coarse-grained granitiods in Table 2). The clasts of gypsum or carbonate cemented conglomerates (labelled as conglomerates in Table 2) are present in a proportion between 5 and 10% and are restricted to the Arriero gravels.

One key clast group includes the clasts showing prophylitic hypogene alteration (P-altered in Table 1). This alteration type is formed by hydrothermal activity at relatively deep levels, below the advanced argillic hypogene alteration, in the marginal and upper parts of the porphyry Cu-related intrusion, between 500 and >2000 m deep (Sillitoe, 2010; Fig. 1). These clasts are present along the entire column of the Tesoro open pit (Fig. 7, column B) in lower proportions (5–10%); however, they appear in large proportions (15–50%) in the Tesoro II gravels. This alteration type comprises green-grey and grey-brown coloured clasts that are partially or totally altered to chlorite and epidote, with limonite and goethite and pyrolusite patinas. Another key clast group, concentrated in the Tesoro II gravels, around the lower exotic manto (25–50%), and in the limit between the upper part of the Tesoro III gravel unit and the lower part of the Arriero gravels (5–45%), contains altered porphyric rocks with abundant sericite and veins of quartz and boxworks. This lithology represents a sericitic hypogene alteration (S-altered in Table 2), which is related to hydrothermal activity at relatively deep levels, in the upper part of the porphyry Cu deposit between 500 and 1500 m deep (Sillitoe, 2010; Fig. 1).

Additional qualitative data with regard to the clast composition based on the sedimentary deposits studied in this work have been reported by Blanco & Tomlinson (2002) around the Tesoro and Tesoro NE mines (Fig. S1). These authors indicate that the main clast group in the Tesoro I gravels is composed of α-β lava clasts (55–90%); however, the A-altered clasts also represent an important clast group (10–40%). Another minor clast group corresponds to the fine-grained granitoids. In the Tesoro II gravels, these authors report two main clast groups: ρ clasts (40–70%) and coarse-grained granitoid clasts (30–60%). The prominent clast group (up to 50%) in the Tesoro II gravels is constituted by S-altered clasts. A minor clast group (10%) is formed by P-altered clasts. Another predominant clast group (40%) in this gravel unit corresponds to α-β lava clasts. Finally, two predominant lithologies are recognized in the Arriero gravels: α-β lava clasts (50%) and limestone and calcareous siltstone clasts (40%; labelled as calcareous in Table 2). Two minor clast groups (<5%) are made up of conglomerates and coarse-grained granitoid clasts, respectively.

GEOCHRONOLOGY

Dating efforts were concentrated on constraining the ages of the different gravel units as well as the age of the supergene mineralization in the CMD. Our main objective was to relate the supergene mineralization episodes with the timing of the deposition of the gravels. Age constraints are based on three U/Pb ages and one ^{40}Ar/^{39}Ar age from the interbedded tuff layers. Due to the lack of additional volcanic rocks suitable for a more detailed geochronology analysis, we also carried out U/Pb dating on eight detrital zircon samples to estimate the maximum depositional ages and complement the tuff eruption ages obtained from the volcanic layers. We also use these data to complement the provenance study. The sampling localities for both the tuff eruption and detrital zircon ages are shown in Fig. 3 and these ages are stratigraphically positioned on the columns given in Fig. 4. See Data S1 and S2 for details regarding the geochronology data.

Two types of supergene mineralization are identified in the CMD: (a) in-situ oxide (Esperanza, Esperanza Sur, Encuentro, Llano and Mirador) or leached cap zones (Cerro Coronado) overlaying hypogene porphyry Cu mineralization; (b) roughly tabular and stratigraphic controlled exotic Cu bodies, such as at El Tesoro and Tesoro NE (Mora *et al.*, 2004; Perelló *et al.*, 2010). Five ^{40}Ar/^{39}Ar ages and one new K-Ar in-situ supergene mineral age from the CMD are reported in this study. We also report one K-Ar supergene mineral age from the exotic Cu body at the Tesoro NE pit. The sampling localities for the supergene mineral ages are shown in Fig. 3 and the

ages yielded from these samples are presented in Table 3a (^{40}Ar/^{39}Ar) and b (K-Ar).

^{40}Ar/^{39}Ar and K-Ar geochronology

Volcanic tuff

One tuff deposit (Tuff1) directly overlying the Arriero gravels in the Mirador mine pit was sampled for ^{40}Ar/^{39}Ar dating in biotite (column 3 in Fig. 4). The analysis of this sample was done at the OSU Argon Geochonology Lab, CEOAS Oregon State University (USA). The sample shows a well-defined plateau age defined by at least three consecutive steps within analytical errors of 2σ and more than 58% of ^{39}Ar released gas. Thus, the 9.52 ± 0.02 Ma plateau age is considered as the age of the tuff eruption (Data S1).

Supergene mineralization

In-situ oxide zones are characterized by chrysocolla, atacamite and paratacamite, with lesser amounts of copper clays, copper wad and copper pitch (Cu-bearing manganese oxyhydrates) and minor amounts of copper-bearing phosphates (Perelló *et al.*, 2010). These minerals frequently occur together with supergene alunite group minerals (alunite, natroalunite, jarosite), which can be dated by the ^{40}Ar/^{39}Ar or K-Ar methods to determine the ages of the supergene mineralization (Vasconcelos, 1999).

Two ^{40}Ar/^{39}Ar ages for the supergene alunite were obtained from the samples collected at the Esperanza Sur (GMC-07-221) and Penacho Blanco (CM-12.4) porphyry copper, and three other ^{40}Ar/^{39}Ar ages from the jarosite sampled at the Esperanza Sur (GM-10-04 Jar 1) and Penacho Blanco (CM-12.5B and CM-12.5A) deposits (Fig. 2; Table 3a). Following the procedure proposed by Layer (2000) and Lanphere & Dalrymple (2000), the five samples were step-heated at increased laser power with a CO_2 laser beam at the SERNAGEOMIN ^{40}Ar/^{39}Ar Geochronology Laboratory (Chile) (detailed analytical procedures are given in Arancibia *et al.* (2006). Well-defined plateau ages were obtained by at least three consecutive steps within the analytical errors of 2σ and more than 58% of ^{39}Ar released gas. The isochron ages are generally indistinguishable from the plateau ages in all of the samples. Thus, the plateau ages are considered as being more reliable, except for sample GM-10-04 Jar 1 which shows a slight excess of atmospheric Ar detected in the isochron diagram, in which case the isochron age was considered instead. One additional K-Ar age for supergene alunite was obtained from a sample collected at the Cerro Coronado alteration zone (SGCM_183.2; Fig. 2). These data are complemented with one ^{40}Ar/^{39}Ar age and three K-Ar ages previously published by Perelló *et al.* (2010) and Sillitoe & McKee (1996) for the Esperanza Sur porphyry Cu. Thus, the ages of the in-situ supergene minerals yielded

from the Esperanza Sur are 25 ± 2 Ma, 22.9 ± 0.4 Ma, 21.2 ± 0.2 Ma, 20 ± 1 Ma, 15.1 ± 1.0 Ma and 12.6 ± 2.0 Ma, the ages of in-situ supergene minerals yielded from the Penacho Blanco are 22.0 ± 0.6 Ma, 14.1 ± 0.15 Ma and 12.8 ± 0.1 Ma, whereas the Cerro Coronado alteration zone yielded an age of 25.2 ± 0.8 Ma.

Exotic Cu mineralization mainly corresponds to chrysocolla with a smaller amount of copper wad and several Mn oxides and hydroxides (Campos *et al.*, 2015; Menzies *et al.*, 2015). Atacamite, paratacamite, malachite and azurite are also present as overgrowths patinas superimposed onto the primary copper minerals, or filling open spaces in the hosting coarse-grained sediments. The copper wad includes ramsdellite and cryptomelane, the latter of which is a mineral that can be dated with the $^{40}Ar/^{39}Ar$ or K-Ar methods (Vasconcelos, 1999). Exotic Cu mineralization is hosted by roughly tabular stratigraphically controlled bodies. Two exotic Cu bodies, hosted in the Tesoro II gravels and the Arriero gravels, respectively, can be recognized in the Tesoro pit (Fig. 8a). In the Tesoro NE pit, one exotic body is hosted by the Arriero gravels. In this manto, chrysocolla occurs as angular reworked clasts and as cement filling cavities and fractures, generating coatings around non-mineralized clasts in some cases. The copper wad forms cement following the sedimentary structures and is frequently truncated by overlying barren gravel beds (Fig. 8b). These textures indicate a syn-sedimentary origin for the exotic mineralization of the exotic-body hosted by the Arriero gravels in the Tesoro NE pit. A K-Ar age from cryptomelane sampled from the copper wad from this manto (TNE-AP) (Fig. 8c; Table 3b, column 4 in Fig. 4) yielded an age of 21.9 ± 1.2 Ma.

Zircon U/Pb Geochronology

Volcanic tuff

Three tuff layers interbedded in the Esperanza gravels were sampled for U/Pb zircon dating. U/Pb geochronological analyses were done at the Geochoronology Lab of the Massachusetts Institute of Technology (USA) (Data S1). All of the samples yielded U/Pb zircon ages with an uncertainty at the 2σ level of <1.5% for a set of 18–20 analyses, representing the best estimate for the age of the tuff deposition. Sample Car2 yielded an age of 42 ± 1 Ma and was sampled from a block and ash bed interbedded in the upper part of the Esperanza gravels at the Esperanza Sur area (column 1 in Fig. 4). Sample Car220 yielded an age of 43.05 ± 0.43 Ma and was sampled from the drill hole core TYC-162, *ca.* 220 m stratigraphically downward of sample Car2 (column 1 in Fig. 4). Finally, sample Bote-09-110 yielded an age of 44.7 ± 0.5 Ma and was sampled from drill core BTE_09, *ca.* 250 m below the surface (column 6 in Fig. 4).

U-Pb detrital zircon geochronology

Sand from fine-grained beds interbedded in the Esperanza, Atravesado I, Tesoro II and III and Arriero gravels was sampled for U/Pb detrital zircon dating. The geochronological analysis of four samples (BTE09, Car253, Car252 and Car257) was done at the Radiogenic Isotope and Geochronology Laboratory, Washington State University (USA) (Fig. 9). In an attempt to constrain the age of the upper and lower exotic Cu bodies at the Tesoro pit, four additional samples (AFMZr1,2,3, and Det0) were taken from the sand matrix of conglomerates from the stratigraphic column of the Tesoro open pit (column 5 in Fig. 4). The geochronological analysis of these samples was done at the Pacific Centre for Isotopic and Geochemical Research, at the University of British Columbia (Canada). The zircon population peaks and average ages were calculated using the Isoplot software (an add-in for Excel; Ludwing, 2008) and calculation of the maximum depositional ages was based on the procedures proposed by Gehrels (2010). For each sample, we consider the 10 younger zircons ages and use the TuffZirc routine of Isoplot to differentiate within these zircons ages the largest and youngest population (made of at least three zircon ages) for which the average age has a MSWD < 1. These populations correspond to the red boxes shown in the inset of each probability plot on Fig. 9. In the case of too-young zircons, for which the scatter from the younger population is not related to their uncertainty, Pb loss is suspected and these zircon ages are rejected. Too-old zircons that increase the MSWD over 1 are also rejected. Zircon ages that were not considered are shown by the blue boxes in the inset of each probability plot on Fig. 9. The maximum depositional ages correspond to the average obtained from the red boxes ages for each sample.

The Esperanza gravels. Sample Bote-09 yielded a dominant Carboniferous-Permian population ($n = 79$) that includes zircon ages between 270 and 319 Ma, with a most common value of 296 Ma; and a second Eocene population ($n = 19$) (43–48 Ma) with a peak at 45 Ma. Four ages (59, 61, 62 and 62 Ma) define a minor Paleocene population. The maximum depositional age of the hosting sediment is 44.6 ± 0.73 Ma, yielded from the average age of the youngest coherent group of nine zircons.

The Atravesado gravels. Two samples from this gravel unit show a wide distribution of zircon ages ranging almost continuously from the Paleocene to the late Eocene. Sample Car253 corresponds to a reworked tuff. In this sample, the zircon ages ($n = 44$) range between 37 and 70 Ma with three different populations in the relative probability plot: (1) a late Eocene (37–41 Ma) population ($n = 19$), with a peak at 39 Ma; (2) a mid-late Eocene (42–44 Ma)

Table 3. $^{40}Ar/^{39}Ar$ (A) and K–Ar (B) ages of supergene minerals from the Centinela district. The geochronology analyses on the supergene minerals were carried out at the Laboratorio de Geocronología of the Servicio Nacional de Geología y Minería (SERNAGEOMIN, Chile). The additional age constraints are from Sillitoe & McKee (1996) and Perelló et al. (2010).

(A) ^{40}Ar–^{39}Ar datin

Sample	Project/Prospect	Mineral	Plateau Age (Ma ± 2s)	Steps	% ^{39}Ar in plateau	Integrated Age (Ma ± 2s)	Isochron Age (Ma ± 2δ)	Steps	Intercept $^{40}Ar/^{39}Ar$ ± 2δ	Comments
GM-10-04 Jar 1	Esperanza Sur	Jarosite	14.8 ± 0.5	6/9		14.8 ± 0.5	15.1 ± 1.0	6/8	294.8 ± 1.1	Sample with slight excess of argon, best estimation is the isochron age
GMC-07-221	Esperanza Sur	Supergene alunite	12.6 ± 2.0	8/8		13 ± 5	12.2 ± 2.4	8/8	295.6 ± 0.3	Well-defined plateau age. Sample with no excess argon
CM-12.4	Penacho Blanco	Supergene alunite	22.0 ± 0.6	4/7	58.3	17.5 ± 1.3	22.7 ± 1.6	4/7	293 ± 3	Well-defined plateau age. Sample with no excess argon
CM-12.5B	Penacho Blanco	Jarosite	14.1 ± 0.15	10/10	100	14.1 ± 0.6	14.05 ± 0.22	10/10	295.8 ± 0.9	Well-defined plateau age. Sample with no excess argon
CM-12.5A	Penacho Blanco	Jarosite	12.8 ± 0.1	5/8	88.1	12.8 ± 0.4	12.2 ± 0.6	5/8	290 ± 9	Well-defined plateau age. Sample with no excess argon
Perelló et al. (2010)	Esperanza Sur (ex-Telegrafo)	Supergene alunite	22.9 ± 0.4	4/8	64	21.49 ± 0.36	25 ± 2		284 ± 6	Supergene alunite from leached capping zone at Telégrafo

(B) K–Ar dating

Sample	Project/Prospect	Mineral	K (%)	^{40}Ar (×10^{-10} moles g^{-1})	$^{40}Ar/^{40}Ar$ total	Edad (Ma ± 2s)	Comments
SGCM_183.2[1]	Cerro Coronado	Supergene alunite	6.77	30 560	0.450	25.2 ± 0.8	Supergene alunite from the leached capping zone
TNE-AP[1]	Tesoro NE	Criptomelane	3.361	28 850		21.9 ± 1.2	Criptomelane in an exotic body of Cu in Tesoro NE
Sillitoe & McKee (1996)	Esperanza Sur (ex-Telegrafo)	Jarosite	2.55		10.4	20 ± 1	Jarositic leached capping
Perelló et al. (2010)	Esperanza Sur (ex-Telegrafo)	Supergene alunite	8.58	31 768	0.566	21.2 ± 0.2	Supergene alunite from the leached capping zone
Perelló et al. (2010)	Esperanza Sur (ex-Telegrafo)	Supergene alunite	9.54	31 961	0.824	19.2 ± 0.2	Supergene alunite from the leached capping zone
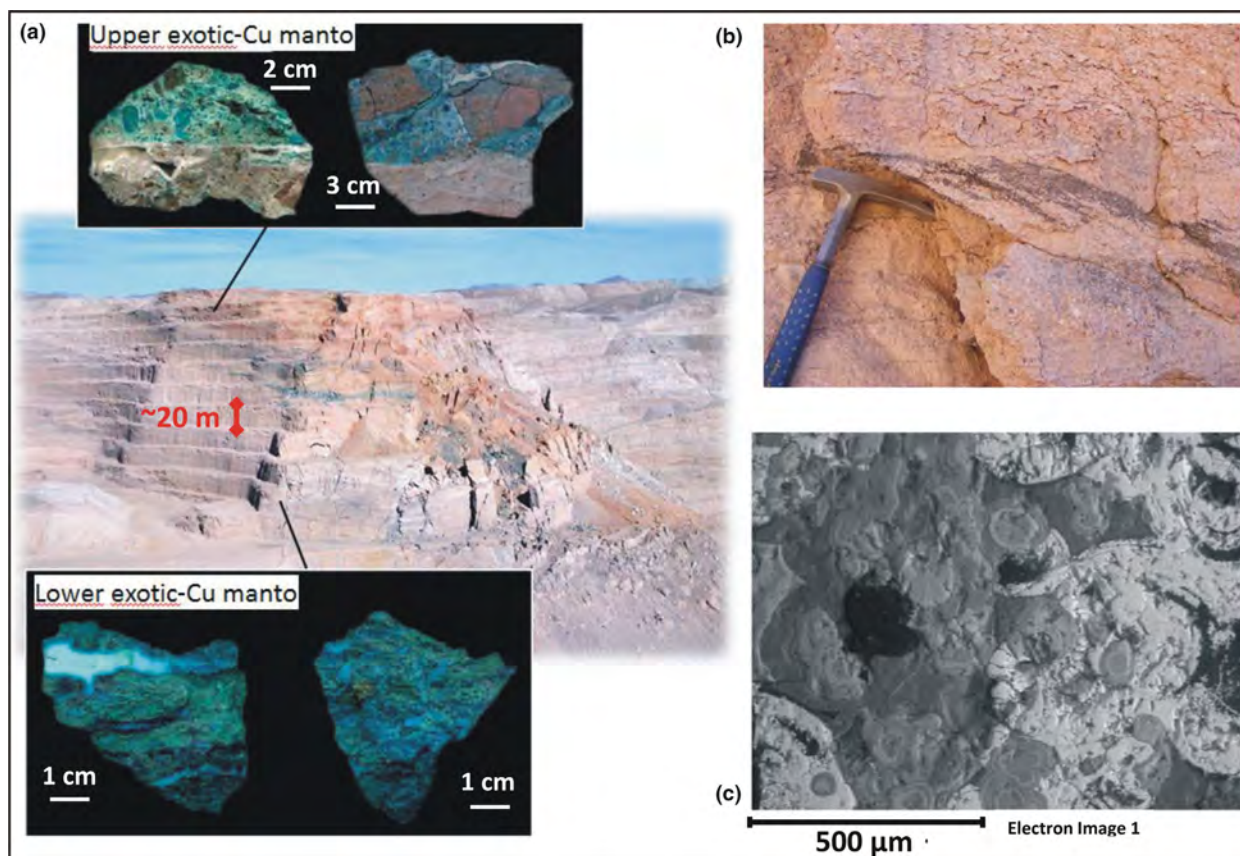
Fig. 8. (a) View of the El Tesoro open pit looking towards the southwest. The view shows the stratigraphic position of the lower and upper exotic Cu bodies. The characteristic textures of the exotic Cu mineralization in the lower and upper bodies are shown in the photographs below and over the open pit view, respectively. (b) Details of the syn-sedimentary textures shown by the copper-wad minerals exposed in the exotic Cu body at the Tesoro NE pit. (c) Scanning Electron Microscope image of the cryptomelane sampled for K–Ar dating.

population (n = 7), defining a peak at 43 Ma and (3) a late Paleocene (57–61 Ma) population (n = 14), showing a dominant value at 59 Ma. The average age yielded from the youngest coherent group of 8 zircons is 38.1 ± 0.36 Ma.

Sample Car252 shows zircon ages (n = 89) that are mainly concentrated between 39 and 70 Ma, with two large populations: one ranging between 39 and 46 Ma with a peak at 42 Ma (late Eocene, n = 76), and the other between 59 and 62 Ma with peak of 61 Ma (Paleocene, n = 5). An additional minor population (n = 4) in this sample has a mean age of 195 Ma (Sinemurian). The average age yielded from the youngest 10 zircons is 39.9 ± 0.42 Ma, which represents the maximum depositional age of the hosting sediment.

The Tesoro II gravels. Sample Car257 presents a dominant concentration of zircon ages defining a mid-late Eocene (39–46 Ma) population (n = 48) with peak at 42 Ma, a second large Paleocene (57–63 Ma) population (n = 11) at around 61 Ma, which is followed by a Late Cretaceous (68–74 Ma) population (n = 8) for which the most frequent value is around 71 Ma. The older zircon ages include two populations, a minor Jurassic (Sinemurian; 196–199 Ma) population (n = 4) with a peak around 196 Ma, and a large Carboniferous-Permian (274–309 Ma) population (n = 43) with a mean age of 292 Ma. The average age yielded from the youngest 10 zircons is 39.7 ± 0.78 Ma.

Sample AFMZr3 shows a large Eocene (35–49 Ma) population (n = 47) with a peak at around 43 Ma, followed by a Carboniferous-Permian (276–346 Ma) population (n = 35) with a mean age of 320 Ma. The maximum depositional age of the hosting sediment is 40.4 ± 1 Ma, yielded from the youngest coherent group of eight zircons.

The Tesoro III gravels. Sample Det0 presents the largest population (n = 55) of zircon ages related to the Carboniferous-Permian (266–339 Ma) with a peak around 299 Ma, followed by a second population (n = 16) with Late Cretaceous to Paleocene (58–75 Ma) ages which define two peaks, at 62 and 72 Ma, respectively. The maximum depositional age of the hosting sediment is 41.1 ± 1 Ma, yielded from the youngest coherent group of three zircons.

The Arriero gravels. Sample AFMZr2 yielded a large population ($n = 88$) of Carboniferous-Permian ages (284–342 Ma) centred at around 313 Ma. Only two zircons do not belong to this population and have younger late Eocene ages.

Finally, sample AFMZr1 contains a dominant population ($n = 33$) of late Eocene (36–43) zircon ages with a mean age of 39 Ma. In this late Eocene population, 10 individual zircon ages are younger than 39 Ma. A large Late Cretaceous-Paleocene population ($n = 16$) (58–70 Ma) with a peak at 64 Ma, followed by a large Carboniferous-Permian population (283–344 Ma) defining a peak at 329 Ma. The maximum depositional age of the hosting sediment is 37.6 ± 2.1 Ma, yielded from the youngest coherent group of nine zircons.

DISCUSSION

Timing of the sedimentation and supergene mineralization

Six gravel units with ages ranging between the mid-late Eocene and the mid-Miocene can be recognized in the CMD. The tuff eruption ages yielded from the interbedded tuff layers (45–42 Ma; Car2, Car220, BTE09-110) indicate that the deposition of the Esperanza gravels was nearly contemporaneous with the emplacement of most of the porphyry copper systems in the Centinela district (Fig. 10). On the other hand, the age for the base of the Arriero gravels is constrained by the *ca.* 22 Ma cryptomelane age (TNE-AP) yielded from the syn-sedimentary exotic Cu mineralization at the Tesoro NE open pit. It can consequently be considered as a minimum age for the base of this facies association. The minimum age for the Arriero gravels is constrained by the overlying volcanic ash that yielded 9.28 ± 0.05 Ma (SGCM_133.8, Fig. 10).

The late Eocene to Oligocene represents a magmatic and volcanic gap at the considered segment of the Central Andes (e.g. Stern, 2004; Kay *et al.*, 2005). Therefore, it is expected to find a gap in the maximum depositional age yielded from detrital zircon samples for this time span. Thus, the ages of the gravel units cannot be accurately constrained using the available detrital zircon geochronology data. In particular, the Tesoro II gravels are stratigraphically separated from the late Eocene Esperanza gravels by *ca.* 400 m of sediments that constitute the Tesoro I gravels. Thus, even if the Tesoro II gravels expose two late Eocene maximum depositional ages (*ca.* 40 Ma; Car257 and AFMZr3) intercalated at the base of the column at the Tesoro open pit, they may be much younger than *ca.* 40 Ma. On the other hand, the lowermost Atravesado gravels can be correlated to the Tesoro I gravels based on the sedimentary facies, clast compositions and stratigraphic position. Both the Tesoro I and the lowermost (*ca.* 200 m) Atravesado gravels are made

up of the same facies which differ only in the proportion of coarse-grained facies vs. the fine-grained facies: that is, the Gcm and Gmm facies are dominant in the Tesoro I unit, whereas the Sm and Fsm dominates in the Atravesado unit. The Tesoro I gravels unconformably overlie the Esperanza gravels, whereas the Atravesado gravels can be recognized directly overlying the Esperanza gravels in the drill core BTE-09. Furthermore, the Tesoro I and the Atravesado gravels are the only gravel units along the Centinela stratigraphic record to include the distinctive population of clasts showing advanced argillic alteration. The Tesoro I and, at least, the lowermost *ca.* 200 m of the Atravesado gravels can be considered as lateral variations within the same stratigraphic unit (Fig. 10). On the other hand, both the Tesoro II and the uppermost *ca.* 100 m of the Atravesado gravels show an increase in the proportion of channelized stream flow deposits (Gpt and Spt facies) with respect to their respective underlying facies association. Thus, the Tesoro II and the uppermost Atravesado gravel deposits could be a lateral variation of the same stratigraphic unit.

The age yielded from in-situ supergene minerals ranges between 25.2 ± 0.8 at Cerro Coronado and 12.6 Ma at Esperanza Sur. These ages define a time span for the supergene processes in the Centinela district that roughly overlap the time span during which the Arriero gravels were deposited. However, based on these ages, we identify a gap in the supergene activity between *ca.* 19 Ma and *ca.* 15 Ma. Thus, the supergene ages can be grouped into two episodes, *ca.* 25–19 Ma and 15–12 Ma, which can be identified from all of the available ages as well as from individual oxide zones, for example as in the Esperanza Sur and Penacho Blanco areas (Table 2). The 21.9 ± 1.2 Ma K-Ar age yielded from cryptomelane at the Tesoro NE pit is part of the first *ca.* 25–19 Ma supergene age episode.

Sediment provenances and porphyry Cu unroofing

The porphyry copper systems were emplaced possibly >2 km under the surface at the same time during which the Esperanza gravels were deposited on the surface. Thus, the relevant mid-Eocene (43–48 Ma) detrital zircon population yielded from sample BTE09 (Fig. 9) can only represent the erosion products of the volcanic rocks deposited contemporaneously with these gravels (Fig. 11a). The other large detrital zircon population is the one represented by late Paleozoic zircons. The lack of Mesozoic and Paleocene detrital zircon age populations suggests that the Paleozoic population is directly related to the erosion of the late Paleozoic basement and not the result of recycled zircon. The late Paleozoic basement is nowadays exposed to the east (Sierra Agua Dulce) and north (Sierra Limón Verde) of the Centinela district (Fig. 2).
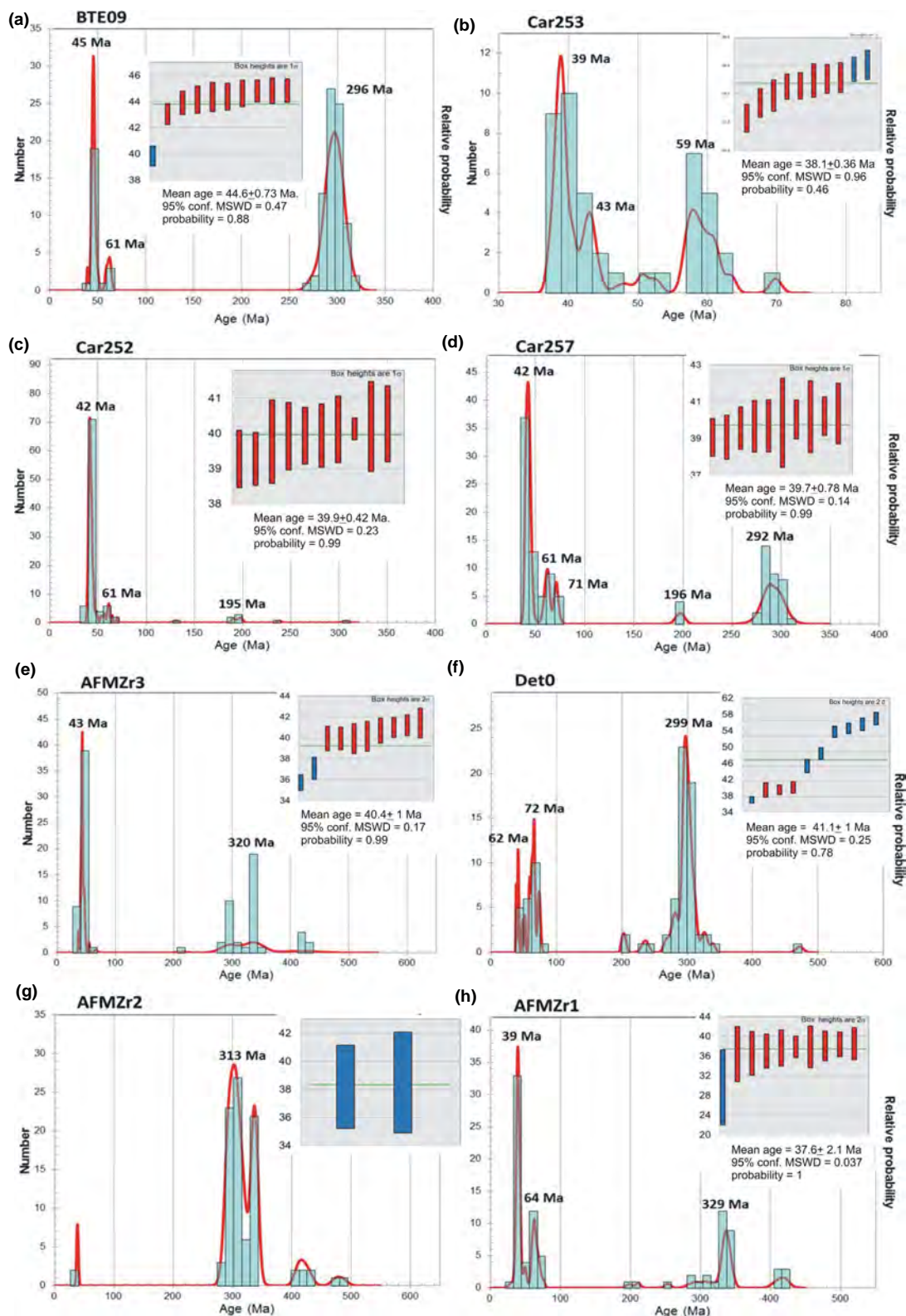
Fig. 9. Probability plots and maximum depositional ages (inset) of the detrital zircon population from samples taken from the CMD. Sample BTE-09 is sandstone from the BTE-09 drill core (column 6 in Fig. 4). Car253 (reworked tuff) and Car252 (sandstone) are samples from the Atravesado area (column 2 in Fig. 4). Sample Car257 is a sandstone bed from a drill core, taken 50 m below the base of the Tesoro open pit. See the text for explanation of the probability plots and insets.
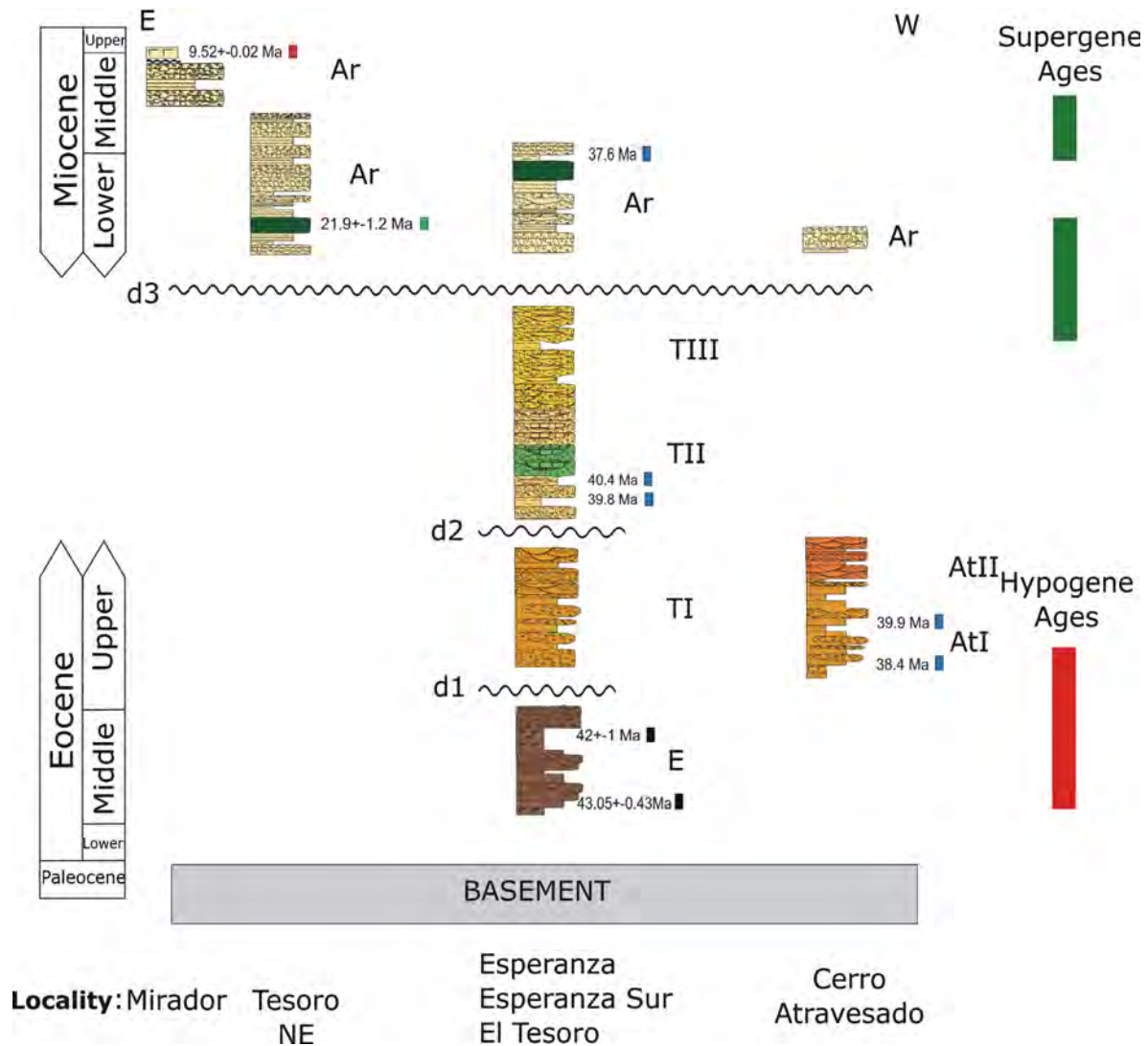
Fig. 10. Generalized stratigraphic columns arranged roughly along anEW direction including the reported geochronological data. The figure presents the stratigraphic contact and the stratigraphic relationships between the gravel units. The bars on the right side show the age ranges for hypogene (red) and supergene mineralization (green), as deduced from the hypogene ages reported by Perelló *et al.* (2010) and Mpodozis & Cornejo (2012) and the supergene ages presented in this work. The abbreviations and colours of gravel units are given in Fig. 3.

Two clast groups are present along the entire stratigraphic record from the Tesoro I gravels to the Arriero gravels. The α-β lava clasts frequently form outcrops of the Quebrada Mala Formation to the west of the studied area. Isolated outcrops of this formation are also recognized to the east covering the Jurassic-Early Cretaceous rocks. The α-β lava clast can also be recognized as composing the Paleocene Cinchado Formation, which currently outcrops to the south of the CMD (Fig. 2). Rock units that can be the source of the α-β clast are widely distributed in almost all directions in the CMD so these clasts cannot be used to infer sediment provenances. The fine-grained granitoids are a minor clast group in the Atravesado gravels and are an important population in

the Tesoro II, III and Arriero gravels. These rock types can be only from the early Cretaceous and Paleocene intrusions that outcrop in the highest reliefs located to the east of the CMD.

A predominant clast group, exclusively recognized in the Atravesado gravels, corresponds to the α-δ volcanoclastic clasts. They are common rock types widely recognized along the Upper Cretaceous Quebrada Mala Formation and the Paleocene Cinchado Formation. On the other hand, the samples Car253 and Car254 show that the Atravesado gravels comprise two large detrital zircon populations, Paleocene and Eocene, respectively (Fig. 9). Although the Paleocene zircon populations (57–61 Ma, sample Car253 and 59–62 Ma, sample Car252) can be interpreted as recycled

Paleocene zircon sourced from younger Eocene rocks, the presence of the α–δ volcanoclastic clasts indicate that, at least part of the hosting sediment came from the erosion of Paleocene rocks. Therefore, the Paleocene zircon population can be related to the erosion of the Cinchado Formation. Furthermore, considering the wide distribution of the Quebrada Mala Formation throughout the CMD and immediate vicinity, the lack of a Late Cretaceous detrital zircon population suggests that this rock unit did not undergo erosion at that time and that the α–δ volcanoclastic clasts come exclusively from the erosion of the Paleocene rocks (Fig. 11b). The Cinchado Formation nowadays only outcrops at the highest reliefs located to the south of the CMD (Fig. 2). However, this formation probably extended to the north into the CMD at the time of the Atravesado I and II gravel depositions. Thus, in this area, the Cinchado Formation was eroded, contributing sediment to these gravel units.

A clast group included in the Tesoro I unit and the upper part of the Atravesado unit corresponds to the advanced argillic altered clasts. They indicate that hydrothermally altered rocks on the roof of a porphyry Cu, at shallower depths (0–500 m deep), underwent erosion. Moreover, these gravel units do not contain clasts showing hydrothermal alteration or hypogene mineralization, indicating the erosion of a porphyry Cu–related intrusions below the advanced argillic hypogene zones. This suggests that the Eocene detrital zircon populations in samples Car253 (37–44 Ma) and Car252 (39–46) result from the erosion of the mid–late Eocene volcanic rocks, such as those intercalated in the Esperanza gravels, and not from the erosion of the porphyry Cu–related intrusions, which were probably still buried during the accumulation of these gravels (Fig. 11b). The lack of Paleozoic detrital zircon populations and clasts from Paleozoic lithologies indicates either that sediment routing systems were not connected to the Paleozoic outcrops or that these rocks were protected from erosion by the cover of Paleocene and Eocene volcanic rocks.

The clast compositions of the Tesoro II and III gravels show a wider range of clast types, which include lithologies similar to most of the rock units currently outcropping in the CMD. The same conclusion can be reached from the U–Pb detrital geochronology data (samples Car257, AFMZr3 and Det0, Fig. 9), which show a wide range of ages and a greater number of detrital zircon populations than those recorded from the underlying gravel units, indicating that most of the rock units currently exposed at the CMD underwent erosion at the time of the deposition of these gravels.

In addition to the clast groups also recognized in the underlying gravel units, the Tesoro II and III gravels include poorly consolidated tuff clasts. This rock type is exclusive of the volcanic layers intercalated in the Esperanza gravels, which currently forms the Esperanza syncline and which are recognized as being interbedded in

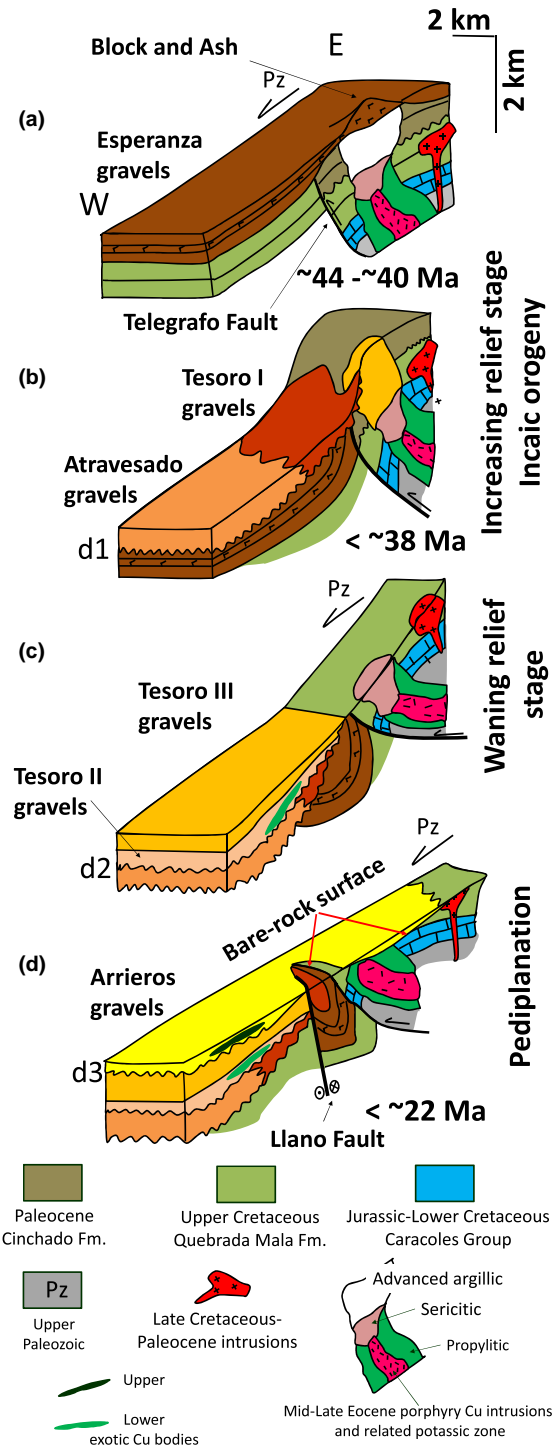Fig. 11. Schematic depiction of the landscape evolution and related porphyry Cu unroofing sequence interpreted from the stratigraphy, geochronology and sedimentology data presented in this work. The approximate location of the section is that from the profile AA′ shown in Fig. 6. The horizontal and vertical scales are approximates. The dimensions of the porphyry Cu system are greatly overdone (compare with the profile AA′ in Fig. 6).

the BTE-09 drill core (Figs 3 and 11c). The clast types that are mainly restricted to the Tesoro III gravels, but which are also recognized in the Tesoro II gravels by Blanco & Tomlinson (2002), are the coarse-grained granitoids. This rock type can be recognized in the Upper Paleozoic basement that is currently exposed immediately to the north of the CMD and *ca.* 15 km to the east, in the Agua Dulce range (Fig. 2). The sediment sourced from the Upper Paleozoic basement to the Tesoro II and III gravels is also evidenced by the Carboniferous-Permian detrital zircon populations from samples Car257, AFMZr3 and Det0. A clast group restricted to the Tesoro III gravels, which contain between 5% and 20% of the clasts, is composed of a ρ-epizonal intrusion. This lithology can be recognized as constituting the epizonal Late Cretaceous and Paleocene intrusions (Fig. 11c).

The samples from the Tesoro II and III gravels show three large detrital zircon populations: Eocene (39–46 Ma, Car257; 36–49 Ma AFMZr3), Paleocene (57–63 Ma, Car257; peak at *ca.* 62 Ma, Det0) and Late Cretaceous (68–74 Ma, Car257; peak at *ca.* 72 Ma, Det0). As a result, the volcanic and intrusive lithologies that frequently constitute the Upper Cretaceous rock also constitute important clast groups in these gravels. It is interesting to note that most of the porphyry Cu deposits recognized immediately to the south of the Tesoro mine are hosted on Upper Cretaceous rocks from the Quebrada Mala Formation. The key clast groups correspond to the sericitic and propylitic altered clasts. Both alteration types are formed by hydrothermal activity below the advanced argillic hypogene zone, in the upper and marginal parts of a porphyry Cu, respectively, between 500 and 2000 m deep (Sillitoe, 2010). Hydrothermal sericite and alunite on the clasts included in the lower exotic Cu body at the Tesoro open pit have been dated by the Ar-Ar method yielding ages of *ca.* 40 Ma (Mora *et al.*, 2004; Perelló *et al.*, 2010), confirming that relatively deep parts of a late Eocene alteration zones related to a porphyry Cu underwent erosion and supplied sediments to the Tesoro II and III gravels. Moreover, the syn-sedimentary lower exotic Cu body hosted in the Tesoro II gravels indicates that copper-bearing minerals from a porphyry Cu are being oxidized and leached (Fig. 11c).

Similarly to the Tesoro II and III gravels, both clast lithologies and detrital zircon populations indicate that almost all of the rock units outcropping in the CMD were already exposed and eroded at the time of the Arriero gravel deposition. The conglomerate clasts are a distinctive population of this gravel unit that can only result from the erosion of the underlying gravel deposits. Another distinctive clast lithology contains limestones and calcareous siltstone rock fragments, a lithology that can be recognized in the Jurassic to Lower Cretaceous Caracoles Group and which forms the country rocks of some porphyry copper located to the east of the studied area (Figs 2 and 11d). The reworked Cu mineralized clasts in the upper exotic Cu body at the Tesoro open pit corroborate that the supergene mineralized deposits were exposed and eroded at the time when the deposition of the Arriero gravels was in progress.

Factors controlling the supergene and exotic copper mineralization

Geomorphology

The Incaic tectonic phase in northern Chile is an important episode of rock exhumation (exhumation rates from 100 to 200 m Ma^{-1}, Maksaev & Zentilli, 1999). This episode is inferred to have dominated the district during porphyry Cu development between 45 and 41 Ma (Perelló *et al.*, 2010). During this episode, the porphyry Cu deposits and their country rocks were upthrown to the west along the Telegrafo Fault over the Esperanza gravels (Mpodozis & Cornejo, 2012; Fig. 11a). From the timing and stratigraphy of the gravel units in the CMD, it can be deduced that the tectonic episode allowed for porphyry Cu exhumation over the last several million years through the deposition of the Esperanza and Tesoro II gravels (Fig. 11a–c). This tectonic episode was polyphasic, as evidenced by two angular unconformities: one separating the Tesoro I gravels from the underlying Esperanza gravels (d1 in Figs 10 and 11b) and the other one which separates the Tesoro II gravels from the underlying Tesoro I gravels (d2 in the Figs 10 and 11c). The polyphasic nature of the Incaíc orogeny has been widely documented (Reutter *et al.*, 1996; Tomlinson & Blanco, 1997a,b; Niemeyer & Urrutia, 2009; Dilles *et al.*, 2011). The d1 unconformity indicates that the Esperanza gravels were deformed prior to the Tesoro I gravel deposition. However, the Tesoro I and the correlative Atravesado gravels overlie the d1 unconformity and include advanced argillic altered clasts, which indicates that the shallow parts (0–500 m) on the roof of a porphyry Cu still underwent erosion by that time. Overlying the d2 unconformity, the exotic Cu body and the sericitic and prophylitic altered clasts indicate that a porphyry Cu underwent erosion only once the Tesoro II gravel deposition was in progress (Fig. 11c).

A tectonic episode that has a minor impact in terms of relief construction and exhumation, concerning the preceding tectonic history, is reflected in the d3 unconformity (Fig. 11d). On one hand, the clast and detrital zircon populations from the Arriero gravels are essentially similar to those of the immediately underlying gravel units, which indicate that the geological units that underwent erosion essentially have not changed. On the other hand, the upper part of the porphyry Cu-related intrusion is currently recognized close to the surface and already underwent erosion during the Tesoro II deposition. Thus, after this second tectonic episode, a minor amount

of unroofing occurred. Overlying the d3 unconformity, the Arriero unit forms a regionally extensive blanket of gravels, which has a vertical cross-section that roughly defines a wedge-shaped geometry that opens downslope from the range piedmonts. To the east, it is directly deposited on an extensive, smooth, low relief and gently sloping (<10°) bare rock surface and onlaps the range piedmonts (Figs 3 and 11c). According to Dohrenwend & Parsons (2009) and Strudley & Murray (2007), these geological features constitute a pediplain: the mountainous highlands and range piedmonts corresponding to the zone of erosion and denudation, the bare rock surface representing a transitional zone of lateral corrosion and sediment transport between the high and lowlands, and the Arriero gravels resulting from up-building by alluvium deposition in the zone of aggradation (Fig. 11c). The Arriero gravels can be interpreted as the result of landscape pediplanation (i.e. the landscape evolution that leads to the pediplain formation): the underlying bare rock surface continuously forming at the topographic front and subsequently being covered as the wanning of the relief and the retreat of this topographic front is going on. Considering the age constraints of the Arriero gravels, the CMD landscape already underwent pediplanation between the late Oligocene and the mid-Miocene, before the deposition of the 9.28 ± 0.05 Ma volcanic ash.

Late Oligocene to mid-Miocene landscape planation has also been reported in the Southern Atacama Desert (Clark *et al.*, 1967; Sillitoe *et al.*, 1968; Mortimer, 1973), the northernmost Chile (Mortimer, 1980; Bouzari & Clark, 2002) and southern Peru (Quang *et al.*, 2005). In the southern Atacama Desert (26–28°, Lat.S), *ca.* 500 km north of the CMD, the Atacama Gravels deposited during this time span by alluvial fan backfilling as the piedmonts and the valley sides retreated to form the Atacama Pediplain (Mortimer, 1973; Riquelme *et al.*, 2003, 2007; Bissig & Riquelme, 2009). Similarly to what is observed at the CMD, pediplanation had ceased before the late Miocene, as indicated by a *ca.* 10 Ma ignimbrite that covers the Atacama Pediplain (Clark *et al.*, 1967; Cornejo *et al.*, 1993; Riquelme *et al.*, 2007). Likewise, the flat surfaces that compose the forearc region of northernmost Chile, between the Arica and Iquique latitude (18–20°, Lat.S), were largely formed in the mid-Miocene, before the entrenchment of the present-day canyons at *ca.* 10 Ma (e.g. Farías *et al.*, 2005; Garcia *et al.*, 2011). Landscape pediplanation seems to be a generalized geomorphic process to most of the Precordillera and Central Depression of the Atacama Desert of northern Chile and southern Peru, which operated in the course of the late Oligocene to the mid–Miocene times, upon which the landscape has not been essentially modified.

Porphyry Cu deposits are emplaced at a depth of about 2 km and their exposure at the surface can be used to track landscape exhumation (Yanites & Kesler,

2015). The geochronology data along with the clast lithology and the detrital zircon populations recorded by the gravel units of the CMD provide a useful depth-time marker of the crustal level that underwent erosion during porphyry Cu exhumation. Regardless of the particularities in the tectonic evolution, such as the polyphasic nature of the main tectonic episodes and the existence of a subsequent minor tectonic episode, the gravel units of the CMD record an entire geomorphologic cycle that includes and follows the Incaic orogeny (Fig. 1). The gravel units that underlie the d2 angular unconformity represent an important erosion and rock exhumation event that can be related to the increasing and subsequent waning relief stages of the landscape evolution (Fig. 11b,c). In the course of this time span, between 500 and 2000 meters of rocks were unroofed and the porphyry Cu intrusions were driven up close to the surface where it could be weathered and oxidized. The subsequent geomorphological evolution is recorded from the Tesoro II gravels onward and occurs without major unroofing. This stage of the landscape evolution can be related to pediplanation (Fig. 11d). The geomorphologic cycle deduced from the gravel units is also seen from thermal modelling of low temperature thermochronology data (Sanchez *et al.*, 2015). The porphyry Cu deposits in the CMD underwent a relatively rapid cooling since their emplacement at *ca.* 45–41 Ma until *ca.* 30 Ma that can be associated with the increasing stage of landscape evolution. After 30 Ma, the porphyries underwent a relatively slow cooling related to low exhumation rates, which represents the early waning relief stage of landscape evolution and the subsequent landscape pediplanation (Sanchez *et al.*, 2015). Thus, a time shift between the main post-Incaic exhumation and the supergene copper mineralization episodes of the order of 10–20 Ma can be deduced from the thermochronology data (Olivares, 2001; Sanchez *et al.*, 2015) and the supergene mineralization ages presented herein. This time shift agrees with that proposed in a review of all the thermochronology and supergene age data performed in Northern Chile (Arancibia *et al.*, 2006).

Geobarometry and geochronology data along with geochemical mass balances yielded from La Escondida porphyry Cu, also located in the Antofagasta region, suggest that *ca.* 3000 m of rocks were eroded between *ca.* 33 Ma and *ca.* 18 Ma (Alpers & Brimhall, 1988). The porphyry Cu exhumation began with the erosion of the shallow advanced argillic alteration and ended with the erosion of the deep sericitic and prophylitic alteration. This erosion sequence through the time, for the vertical zoning pattern of the hypogene mineralization, is similar to that deduced from the clast composition of the gravel units in the CMD. From the Tesoro I through the Tesoro II, the

gravel deposits of the CMD record the exhumation history of one or several mid- to late Eocene porphyry Cu deposits, located to the east of these gravels, from the depths of emplacement to position near surface, a depth at which they can be found nowadays. Similarly, after the erosion of the sericitic and prophylitic alteration zone and the beginning of supergene mineralization at *ca.* 18 Ma, the Escondida porphyry Cu remains close to the surface up to the present day (Alpers & Brimhall, 1988). In the CMD, the age distribution from the in-situ and exotic supergene minerals (*ca.* 25–12 Ma) concentrate in the time span during which the landscape underwent pediplanation and the Arriero gravels deposited. The lower exotic Cu body hosted in the Tesoro II gravels indicates that supergene mineralization occurred during the waning relief stage of the landscape evolution or relatively early during the pediplanation stage. The corresponding in-situ supergene mineralization has not been recognized because it was probably subsequently eroded.

The role of landscape peneplanation (a broader term used to define any extensive low-relief erosional surface, including the pediplains e.g. Phillips, 2002) on the formation and distribution of world-class supergene metalliferous ore deposits has been widely reported. Certainly, ancient flat landsurfaces that remained almost immune to erosion for tens of millions of years account for the widespread distribution of world-class supergene iron, manganese and aluminium ore bodies as those exposed in the southeastern Brazil, or those in the Western Australia (e.g. de Oliveira Carmo & Vasconcelos, 2006; Spier *et al.*, 2006). At Malawi, Southeast Africa, Cenozoic landscape peneplanation allowed strong chemical weathering and erosion and favoured the formation of supergene mineral deposits enriched in aluminium (Dill, 2007). In several places of the world including USA, Canada, Sweden, Iran and West Africa, diverse metalliferous deposits (copper, silver, iron, nickel, uranium, gold and REE deposits) are associated with the extensively developed sub-Cambrian surface. Many of these deposits show evidence of intense weathering that is controlled by the widespread sub-Cambrian peneplanation (Parnel *et al.*, 2014). Supergene alteration and enrichment due to oxidation not only upgrade the value of the ores, but also generate an unprecedented flushing of metals to the chemistry of the earliest Cambrian ocean, which in turn would contributed to the marked early Cambrian faunal evolution (Parnel *et al.*, 2014).

In the Atacama Desert, the relationship between pediplains and supergene activity has been investigated from the pioneer works of Clark *et al.* (1967), Sillitoe *et al.* (1968) and Mortimer (1973). In the southern Atacama Desert, the widespread supergene activity observed during the late Oligocene and early Miocene (Mote *et al.*, 2001) roughly coincides with available age constraints on the formation of the Sierra Checos del Cobre pediplain

(Mortimer, 1973). Similarly, the middle Miocene exotic copper mineralization coincides with the initial stages of the formation of the Atacama pediplain (Mote *et al.*, 2001; Riquelme *et al.*, 2007; Bissig & Riquelme, 2010). Successive episodes of renewed uplift and pediplanation are responsible of the formation of a thick (up to 450 meters depth) weathering profile at Cerro Colorado mine, in the Precordillera of northernmost Chile (Bouzari & Clark, 2002). Although these authors relate the reactivation of intense leaching to drastic fall in the water table, which would be triggered by regional uplift, no precise geochronologic constraints on the pediplains are available that allow correctly associate these landforms features to the supergene episodes. A similar statement can be postulated in the Cordillera Occidental of southern Peru. In this region, the large-scale landscape is composed of remnant pediplain surfaces disposed at different elevations. Supergene mineral ages indicate two main supergene episodes responsible of the upgrading of some ore deposits. Late Eocene supergene profiles beneath highest pediplains would result from a first episode of regional uplift and landscape entrenchment, whereas late Oligocene to early Miocene supergene profiles beneath lowest pediplains would result from renewed uplift and landscape entrenchment episode (Quang *et al.*, 2005). In general, supergene ages are used to constraint the age of the pediplains and no direct geochronologic data are available allowing to determine if supergene profile result from landscape entrenchment or from the pediplain formation. Our data shed light on this issue. The Arriero gravel deposition is clearly related to pediplain formation and evolution, and the timing in which these gravels are deposited roughly overlap the time span in which supergene mineralization took place. No landscape entrenchment can be invoked to explain the supergene age distribution across the CMD. On-going pediplanation during the Arriero gravels deposition did not only favour supergene mineralization, but also preserved the former supergene mineralized zones from significant erosion. Supergene enrichment of metalliferous ores is clearly expected to occur in landscapes that remain relatively stable for millions of years under prevailing warm and wet climatic conditions. Similarly, pediplanation can represent a geomorphologic condition favourable for protracted supergene activity in arid to semi-arid climates as those prevailing during the late Cenozoic in the Atacama Desert.

Paleoclimate

Paleoclimate apparently plays an important role in the operation of supergene processes (e.g. Clark *et al.*, 1990; Chávez, 2000; Hartley & Rice, 2005; Arancibia *et al.*, 2006; Vasconcelos *et al.*, 2015). The age distribution yielded from in-situ and exotic supergene minerals

indicate that supergene processes in the CMD were active between late Oligocene and mid-Miocene, mainly during the early Miocene, a time span that concentrates most of the supergene ages in northern Chile. Considering that supergene environments require enough groundwater to promote oxidation and leaching of hypogene sulphides (e.g. Vasconcelos, 1999; Chávez, 2000), then this time span must have been, at the very least, a time with prevailing semi-arid climate conditions (i.e. >100 mm year^{-1}, Clark *et al.*, 1990). It is interesting to note that the early Miocene has been also considered as a time of warm and humid climate conditions elsewhere in the southern hemisphere. Paleoflora records indicate that warm and humid climate condition prevailed in the Central Chile and Argentina at that time (Hinojosa, 2005; Hinojosa & Villagran, 2005). Comprehensive geochronological studies that consider the distribution of supergene Mn ages in weathering profiles from the central Queensland, Australia, indicate warm and humid conditions during the early Miocene (Li & Vasconcelos, 2002). Additional evidence for wet and relatively warm climates over much of Australia during the first part of the Miocene comes also from micro-facies analysis of carbonate sediments, paleosols clay mineralogy and the palaeontologic record (Truswell, 1993; Brachert & Dullo, 2000). On the other hand, paleoclimate records, which indicate the onset of cold and arid conditions at the mid-Miocene, are thought to be of global significance as it coincides with a major growth of the east Antarctic ice sheet (Li & Vasconcelos, 2002; Flower & Kennett, 1994; Zachos *et al.*, 2001). Furthermore, the onset of the hyperarid conditions in the Atacama Desert since mid-Miocene it is widely accepted (e.g. Sillitoe & McKee, 1996; Dunai *et al.*, 2005; Rech *et al.*, 2006, 2010; Evenstar *et al.*, 2009; Jordan *et al.*, 2014 Oerter *et al.*, 2016). It is also interesting to note that two major peaks, at 20.2 Ma and 16.5 Ma, can be deduced from the distribution of supergene Mn ages in weathering profiles from the central Queensland (Li & Vasconcelos, 2002).

The supergene minerals ages in the CMD define two supergene episodes, at 25–19 and 15–12 Ma, which overlap with the *ca*. 20 and *ca*. 14 Ma episodes of intense supergene activity that have been postulated for the Atacama Desert (e.g. Sillitoe & McKee, 1996; Arancibia *et al.*, 2006). In the CMD, these two supergene episodes are not related to unroofing episodes as has been previously proposed elsewhere in the Atacama Desert (e.g. Bouzari & Clark, 2002; Quang *et al.*, 2003; Hartley & Rice, 2005; Sillitoe, 2005). They rather result from early Miocene climate conditions in which relatively wet, weathering-prone conditions, alternate with relatively dry, erosion-prone conditions as it has been proposed to explain the major peaks in the distribution of supergene Mn ages from the central Queensland (Li & Vasconcelos, 2002).

Climate vs erosion vs time

Although pediplanation was a necessary condition to significantly enrich the copper by supergene processes in the Centinela district, we do not claim that pediplanation is a necessary condition in all of the other situations. For example, in uplifted and dissected Andean regions such as those in the Salvador, El Hueso and La Coya regions (Mote *et al.*, 2001; Bissig & Riquelme, 2009, 2010), the descent of the water table driven by incipient river incision may better explain the formation of thick Oligocene and late Miocene supergene mineralization profiles on ore deposits. These examples have been subjected to orographic rainfall and thus correspond to another climatic context. Likewise, other geomorphologic conditions must be considered to explain the thick supergene profiles formed in Pliocene porphyry Cu belts under climatic regimes of higher precipitation such as those of Papua New Guinea and Philippines (e.g. Sillitoe, 2005). The deepest known oxidation profiles (600 m thick) recognized in the Surigao district, Philippines, surely are not possible to develop under climate conditions other than those highly rainy that prevailed during the very rapid uplift and exhumation of the porphyry Cu (Braxton *et al.*, 2012). In prolonged arid areas such as the CMD, low erosion rates during pediplanation may constitute a necessary condition for the supergene enrichment of copper, as it has already been suggested by Sillitoe (2005). The appropriate balance between erosion rate and water table descent rate that allowed the development of the weathering profile seems to be promoted by a landscape evolution characterized by pediplanation. However, such a favouring geomorphologic condition also requires the prevalence of a relatively wetter climate condition (semi-arid with respect to the arid to hyperarid climatic condition prevailing in the late Cenozoic history of the Atacama Desert) to efficiently allow the supergene mineralization processes to occur. Both landscape pediplanation and semi-arid climate conditions took place during the early Miocene on the Atacama Desert.

On the other hand, time is another important factor in the development of thick supergene profiles as emphasized by Sillitoe (2005). However, the time required to form mature supergene profiles most likely depends on the balance between exhumation and precipitation rates. Thus, for example, the Surigao porphyry Cu district, in Papua New Guinea, was leached and enriched since emplacement below sea level only in the last 2.3–2.1 Ma (Braxton *et al.*, 2012). In this case, high exhumation rates (2.5 km Ma^{-1}) are balanced by high precipitation rates (2000–4000 mm year^{-1}) allowing the formation of a mature supergene profile (600 m thick) in a time span lasting for not more than few hundred thousand years (Sillitoe, 2005). In contrast, when primary ore deposits

are subjected to low exhumation rates (50 m Ma^{-1} in the Precordillera of the Atacama Desert, Maksaev & Zentilli, 1999) and low precipitation rates (e.g. 100 mm $year^{-1}$ in arid climate), the formation of mature supergene profiles may require more than 10 Ma (between *ca.* 25 and 12 Ma) as is suggested by the supergene mineralization ages of the CMD.

Implications for exploration

In recent years, exploration for copper resources around the world has shown an increasing interest for supergene-enriched deposits buried beneath piedmont gravels developed on arid to hyperarid environments, similar to those herein defined as the Arriero gravels. Traditionally, geochemical and geophysical tools have been used to locate buried ore deposits through exploration campaigns that are commonly characterized by a high investment cost and high degree of uncertainty of success. One of the main weakness of today's exploration programmes on areas covered by gravel deposits is that they do not take into consideration the long-term large-scale landscape evolution and the depositional history of the cover gravels. We propose that the integration of geomorphological and sedimentological data with provenances studies is a powerful tool to better define prospective targets, increasing the efficiency of exploration programmes that are looking for porphyry Cu deposits covered by gravels which are developed on arid to hyperarid environments.

CONCLUSION

Seven gravel units with ages ranging between the mid-late Eocene to the mid-Miocene can be recognized in the CMD. The geochronology data along with the clast lithology and the detrital zircon populations provide a useful depth-time marker that can be used to reconstruct an unroofing history for the porphyry Cu located immediately to the east of the studied gravel outcrops. This unroofing history combined with the distribution and the stratigraphic relationships between the gravel units and gravel substratum rocks can be used to interpret the landscape evolution of the CMD as the result of a geomorphological cycle that ranges from the increasing stage through the declining stage of landscape evolution, including the latest pediplanation stage, and which is triggered in the mid-late Eocene by the Incaic orogeny. The older gravel units are the Esperanza gravels that were deposited nearly contemporaneously with the emplacement of most of the porphyry copper systems. The subsequent Tesoro I to Tesoro II gravels record the unroofing of the porphyry Cu, from the advanced argillic zone to the sericitic and prophylitic hypogene zones. The porphyry Cu intrusions were exhumed sometime between the late Eocene and the

Oligocene and remain close to the surface up to the present day. After a minor tectonic episode, which has virtually no impact on the porphyry Cu unroofing, the Arriero gravels deposited and the landscape continues to evolve by pediplanation. The supergene mineral ages of the CMD define a time span (*ca.* 25–12 Ma) for the supergene processes that roughly overlap the time span during which the Arriero gravels deposited. We propose that pediplanation favours supergene mineralization and also helped preserve the former supergene mineralized zones from significant erosion. Such a favourable geomorphologic condition also requires a relatively wetter (semi-arid, >100 mm $year^{-1}$) climate condition to efficiently allow the supergene processes to occur. Low erosion rates during pediplanation may constitute a necessary requirement for the effectiveness of the supergene processes in such climatic conditions. Furthermore, most of the supergene ages are concentrated in the early Miocene, a time on which the global prevailing climate was apparently warm and humid. The supergene ages can be grouped into two episodes, *ca.* 25–19 Ma and 15–12 Ma, which overlap with the *ca.* 20 and *ca.* 14 Ma episodes of intense supergene activity that have been postulated for the Atacama Desert. In the CMD, these two supergene age episodes are not related to unroofing episodes. Therefore, the gap between 19 and 15 Ma in the supergene mineral ages can be related to a drier climatic episode which limited the supergene processes, as occurred with the onset of hyperaridity climatic condition after the mid-Miocene. Finally, the combined use of data and observations as done on this paper can be very useful on planning exploration campaigns for porphyry Cu deposits that are cover by gravels in desert environments, such as the northern Chile, southern Peru, southwest USA and Mongolia.

ACKNOWLEDGEMENTS

SUPPORTING INFORMATION

Additional Supporting Information may be found in the online version of this article:

Table S1. Table of equivalences between the stratigraphic units previously defined in the Centinela district and the gravel units presented in this work.
Fig. S1. Geologic map reported by Blanco & Tomlinson (2002). The focus is on the gravel units exposed

around the Tesoro and Tesoro NE mine and includes the qualitative data for the clast composition from these gravels. The equivalence between these gravels units and the gravel units reported in this work is presented in the Table S1.

Data S1. Volcanic tuff age geochronological data.
Data S2. Detrital Zircon geochronological data.

REFERENCES

Aguilar, G., Riquelme, R., Martinod, J., Darrozes, J. & Maire, E. (2011) Erosion rates variability on landscape's transience state in the semiarid Chilean Andes. *Earth Surface Processes and Landforms*, **36**, 1736–1748.

Alpers, C.N. & Brimhall, G.H. (1988) Middle Miocene climatic change in the Atacama Desert, northern Chile: evidence from supergene mineralization at La Escondida. *Geol. Soc. Am. Bull.*, **100**, 1640–1656.

Amundson, R., Dietrich, W., Bellugi, D., Ewing, S., Nishiizumi, K., Chong, G., Owen, J., Finkel, R., Heimsath, A., Stewart, B. & Caffee, M. (2012) Geomorphologic evidence for the late Pliocene onset of hyperaridity in the Atacama Desert. *Geol. Soc. Am. Bull.*, **124**, 1048–1070.

Anderson, J. (1982) Characteristics of leached capping and techniques of appraisal. In: *Advances in the Geology of the Porphyry Copper Deposits* (Ed. by S.R. Titley), pp. 275–296. University of Arizona Press, Tucson, AZ.

Arancibia, G., Matthews, S.J. & de Arce, C.P. (2006) K–Ar and ^{40}Ar/^{39}Ar geochronology of supergene processes in the Atacama Desert, Northern Chile: tectonic and climatic relations. *J. Geol. Soc. London*, **163**, 107–118.

Arriagada, C., Roperch, P., Mpodozis, C. & Cobbold, P.R. (2008) Paleogene building of the Bolivian orocline: tectonic restoration of the Central Andes in 2-D map view. *Tectonics*, **27**, TC6014, 14 p. https://doi.org/10.1029/2008TC002269.

Basso, M. & Mpodozis, C. (2012) Carta Cerro Quimal, Región de Antofagasta. Servicio Nacional de Geología y Minería, Carta Geológica de Chile, Serie Geología Básica, 143, 1-46. 1 mapa escala 1:100.000. Santiago, Chile.

Bissig, T. & Riquelme, R. (2009) Contrasting landscape evolution and development of supergene enrichment in the El Salvador porphyry Cu and Potrerillos-El Hueso Cu–Au districts, Northern Chile. In: *Supergene Environments, Processes and Products* (Ed. by Titley S.) *Soc. Econ. Geol. Spec. Publ.*, **14**, 59–68.

Bissig, T. & Riquelme, R. (2010) Andean uplift and climate evolution in the southern Atacama Desert deduced from geomorphology and supergene alunite-group minerals. *Earth Planet. Sci. Lett.*, **299**, 447–457.

Blanco, N. & Tomlinson, A. (2002) Estudio estratigráfico y sedimentológico del Distrito Minero El Tesoro. Unplublished report, 29 pp.

Bordy, E.M. & Catuneanu, O. (2001) Sedimentology of the upper Karoo fluvial strata in the Tuli Basin. *J. Afr. Earth Sci.*, **33**, 605–629.

Bouzari, F. & Clark, A. (2002) Anatomy, evolution, and metallogenic significance of the supergene orebody of the Cerro Colorado porphyry copper deposit, I Región, Northern Chile. *Econ. Geol.*, **97**, 1701–1740.

Brachert, T.C. & Dullo, W.C. (2000) Shallow burial diagenesis of skeletal carbonates; selective loss of aragonite shell material (Miocene to Recent, Queensland Plateau and Queensland Trough, NE Australia); implications for shallow coolwater carbonates. *Sediment. Geol.*, **136**, 169–187.

Braxton, D.P., Cooke, D.R., Dunlap, J., Norman, M., Reiners, P., Stein, H. & Waters, P. (2012) From crucible to graben in 2.3 Ma: a high-resolution geochronological study of porphyry life cycles, Boyongan-Bayugo copper-gold deposits, Philippines. *Geology*, **40**, 471–474.

Brimhall, G.H., Alpers, C.N. & Cunningham, A.B. (1985) Analysis of supergene ore-forming processes and ground water solute transport using mass balance principles. *Econ. Geol.*, **80**, 1227–1256.

Campos, E., Menzies, A., Sola, S., Hernández, V., Riquelme, R. & Barraza, M. (2015) Understanding Exotic-Cu Mineralisation: Part I – Characterization of Chrysocolla. 13th SGA Biennial Meeting, France.

Carretier, S., Tolorza, V., Rodriguez, M.P., Aguilar, G., Martinod, J., Riquelme, R., Christophoul, F., Charrier, R., Gayer, E., Farías, M., Audin, L. & Lagane, C. (2014) Erosion in the Andes between 27S and 40S: Tectonic, climatic or geomorphic control ?. In: *Geodynamic Processes in the Andes of Central Chile and Argentina* (Ed. by Sepúlveda S.A., Giambiagi L.B., Moreiras S.M., Pinto L., Tunik M., Hoke G.D. & Farías M.) *Geol. Soc. London Spec. Publ.*, **399**. https://doi.org/10.1144/sp399.16.

Chávez, W.X. (2000) Supergene oxidation of copper deposits: zoning and distribution of copper oxide minerals. *Soc. Econ. Geol. Newsletter*, **41**, 1–21.

Clark, A.H., Mortimer, C. & Sillitoe, R.H. (1967) Implications of the isotopic ages of ignimbrite flows, Southern Atacama Desert, Chile. *Nature*, **215**(5102), 723–724.

Clark, A.H., Tosdal, R.M., Farrar, E. & Plazolles, V.A. (1990) Geomorphologic environment and age of supergene enrichment of the Cuajone, Quellaveco, and Toquepala porphyry copper deposits southern Peru. *Econ. Geol.*, **85**, 1604–1628.

Cornejo, P., Mpodozis, C., Ramírez, C. F. & Tomlinson, A. (1993). Estudio geológico de la región de Potrerillos y El Salvador (26°–27° Lat. S). Servicio Nacional de Geología y Minería (SERNAGEOMIN), Santiago, Chile, Registered Report IR-93-01.

Cornejo, P. & Mpodozis, C. (2015) Aptian (122-116 Ma) silver mineralization in extensión-related magmatism in the Domeyko Cordillera: the Caracoles district, northern Chile. XIV Congreso Geológico Chileno, La Serena.

Davis, W.M. (1905) The geographical cycle in an arid climate. *J. Geol.*, **13**, 381–407.

Dill, H.G. (2007) A review of mineral resources in Malawi: with special reference to aluminum variation in mineral deposits. *J. Afr. Earth Sc.*, **47**, 153–173.

Dilles, J., Tomlinson, A., García, M. & Alcota, H. (2011) The geology of the Fortuna Granodiorite Complex, Chuquicamata district, northern Chile: Relation to porphyry

copper deposits, *SGA Biennial Meeting, 11 th*, Antofagasta, 399–401.

DOHRENWEND, J.C. & PARSONS, A.J. (2009) Pediments in arid environments. *Geomorphology of Desert Environments*, pp. 377–411. Springer Science + Business Media B.V., Amsterdam, the Netherlands.

DUNAI, T.J., GÓNZALEZ-LÓPEZ, G.A., JUEZ-LARRÉ, J. & CARRIZO, D. (2005) Oligocene/Miocene age of aridity in the Atacama Desert revealed by exposure dating of erosion sensitive landforms. *Geology*, **33**, 321–324.

EMMONS, W.H. (1917) The enrichment of ore deposits. *U.S. Geol. Surv. Bull.*, **625**, 530p.

EVENSTAR, L.A., HARTLEY, A.J., STUART, F.M., MATHER, A.E., RICE, C.M. & CHONG, G. (2009) Multiphase development of the Atacama Planation Surface recorded by cosmogenic He-3 exposure ages: implications for uplift and Cenozoic climate change in western South America. *Geology*, **37**, 658–658.

FARÍAS, M., CHARRIER, R., COMTE, D., MARTINOD, J. & HÉRAIL, G. (2005) Late Cenozoic deformation and uplift of the western flank of the Altiplano: evidence from the depositional, tectonic, and geomorphologic evolution and shallow seismic activity (northern Chile at 19°30′S). *Tectonics*, **24**. https://doi.org/10.1029/2004tc001667 (TC4001).

FERNÁNDEZ-MORT, A., ALONSO-ZARZA, A.M., RIQUELME, R. & CAMPOS, E. (2016) Origen y contexto sedimentario de depósitos de cobre exótico Cenozoicos del Desierto de Atacama, norte de Chile. *Geo-Temas*, **16**(1), 213–216.

FLOWER, B.P. & KENNETT, J.P. (1994) The middle Miocene climatic transition; East Antarctic ice sheet development, deep ocean circulation and global carbon cycling. *Palaeogeogr. Palaeoclimatol. Palaeoecol.*, **108**(1994), 537–555.

GARCIA, M., RIQUELME, R., FARIAS, M., HERAIL, G. & CHARRIER, R. (2011) Late Miocene-Holocene canyon incision in the western Altiplano, northern Chile; 11 tectonic or climatic forcing? *J. Geol. Soc.*, **168**, 1–14.

GEHRELS, G. (2010) Detrital Zircon U-Pb Geochronology: Current Methods and New Opportunities. In: *Recent Advances in Tectonics of Sedimentary Basins* (Ed. by C. Busby & A. Azor), pp. 47–62. Blackwell Publishing, Hoboken, NJ.

GUSTAFSON, L.B. & HUNT, J.P. (1975) The porphyry copper deposit at El Salvador Chile. *Econ. Geol.*, **70**, 857–912.

HARTLEY, A.J. (2003) Andean uplift and climate change. *J. Geol. Soc.*, **160**, 7–10.

HARTLEY, A.J. & CHONG, G. (2002) Late Pliocene age for the Atacama Desert: implications for the desertification of western South America. *Geology*, **30**, 43–46.

HARTLEY, A.J. & RICE, C.M. (2005) Controls on supergene enrichment of porphyry copper deposits in the Central Andes: a review and discussion. *Miner. Deposita*, **40**, 515–525.

HINOJOSA, L.F. (2005) Cambios climaticos y vegetacionales inferidos a partir de paleofloras cenozoicas del sur de Sadamerica. *Rev. Geol. Chile*, **32**(1), 95–115.

HINOJOSA, L.F. & VILLAGRAN, C. (2005) Did South American Mixed Paleofloras evolve under thermal equability or in the absence of an effective Andean barrier during the Cenozoic? *Palaeogeogr. Palaeoclimatol. Palaeoecol.*, **217**, 1–23.

HOGG, S. (1982) Sheetfloods, sheetwash, shetflow, or..? *Earth-Cience Rev.*, **18**, 59–76.

HORTON, B.K. & SCHMITT, J.G. (1996) Sedimentology of the lacustrine fan-delt'a system, Miocene Horse Camp Formation, Nevada, USA. *Sedimentology*, **43**, 133–155.

JORDAN, T.E., KIRK-LAWLOR, N., BLANCO, N., NESTER, P. & RECH, J. (2014) Landscape modification in response to repeated onset of hyperarid paleoclimate states since 14 Ma, Atacama Desert, Chile. *Geol. Soc. Am. Bull.*, **126**, B30978–B30971.

KAY, S.M., GODOY, E. & KURTZ, A. (2005) Episodic arc migration, crustal thickening, subduction erosion, and magmatism in the south-central Andes. *GSA Bull.*, **117**, 67–88.

LAMB, S. & DAVIS, P. (2003) Cenozoic climate change as a possible cause for the rise of the Andes. *Nature*, **425**, 792–797.

LANPHERE, M.A. & DALRYMPLE, G.B. (2000) First-principles calibration of 38 Ar tracers: implications for the ages of ^{40}Ar/^{39}Ar fluence monitors. U.S. Geological Survey Professional Paper, 1621, 10 pp.

LAYER, P.W. (2000) ^{40}Argon/^{39}Argon age of the El'gygytgyn impact event, Chukotka, Russia. *Meteorit. Planet. Sci.*, **35**, 591–599.

LI, J.-W. & VASCONCELOS, P. (2002) Cenozoic continental weathering and its implications for the palaeoclimate: evidence from 40 Ar/ 39 Ar geochronology of supergene K-Mn oxides in Mt Tabor, central Queensland, Australia. *Earth Planet. Sci. Lett.*, **200**, 223–239.

LUDWIG, K.R. (2008) Isoplot 3.6. *Berkeley Geochron. Ctr. Spec. Pub.*, **4**, 1–77.

MAKSAEV, V. & ZENTILLI, M. (1999) Fission track thermochronology of the Domeyko Cordillera, Northern Chile: implications for Andean tectonics and porphyry copper metallogenesis. *Explor. Min. Geol.*, **8**, 65–89.

MARINOVIC, N. & GARCÍA, M. (1999) Hoja Pampa Unión, Región de Antofagasta. Escala 1:100.000, Servicio Nacional de Geología y Minería, Mapas Geológicos, N° 9, Santiago.

MARSH, T., EINAUDI, M. & MCWILLIAMS, M. (1997) ^{40}Ar/^{39}Ar geochronology of Cu–Au and Au–Ag mineralization in the Potrerillos District, Chile. *Econ. Geol.*, **92**, 784–806.

MAY, G., HARTLEY, A., CHONG, G., STUART, F., TURNER, P. & KAPE, S. (2005) Eocene to Pleistocene lithoestratigraphy, chonostratigraphy and tectono-sedimentary evolution of the Calama Basin, northern Chile. *Rev. Geol. Chile*, **32**, 33–58.

MENZIES, A., CAMPOS, E., HERNÁNDEZ, V., SOLA, S. & RIQUELME, R. (2015) Understanding Exotic-Cu Mineralisation: Part II - Characterisation of Black Copper ("Cobre Negro"). 13th SGA Biennial Meeting, France.

MIALL, A.D. (1977) A review of the braided river depositional environment. *Earth-Sci. Rev.*, **13**, 1–62.

MIALL, A.D. (1996) *The Geology of Fluvial Deposits: Sedimentary Facies, Basin Analysis, and Petroleum Geology*, 582 pp. Springer, New York.

MORA, R., ARTAL, J., BROCKWAY, H., MARTÍNEZ, E. & MUHR, R. (2004) El Tesoro exotic copper deposit, Antofagasta Region, northern Chile. *Soc. Econ. Geol. Spec. Publ.*, **11**, 187–197.

MORANDÉ, J. (2014) El basamento pre-Mesozoico de la Sierra Limón Verde: Implicancias para la evolución tectónica del norte de Chile. M. Sc. Thesis (Unpublished), Departamento de Geología, Universidad de Chile, 121 pp.

MORTIMER, C. (1973) The Cenozoic history of the southern Atacama Desert, Chile. *Geol. Soc. London J.*, **129**, 505–526.

MORTIMER, C. (1980) Drainage evolution of the Atacama Desert of northernmost Chile. *Rev. Geol. Chile*, **11**, 3–28.

MOTE, T., BECKER, T., RENNE, P. & BRIMHALL, G. (2001) Chronology of exotic mineralization at El Salvador, Chile, by $^{40}Ar/^{39}Ar$ dating of copper wad and supergene alunite. *Econ. Geol.*, **96**, 351–366.

MPODOZIS, C. & CORNEJO, P. (2012) Cenozoic tectonics and porphyry copper systems of the Chilean Andes. *Soc. Econ. Geol. Spec. Publ.*, **16**, 329–360.

MPODOZIS, C. & PERELLÓ, J. (2003) Porphyry copper metallogeny of the middle-Eocene-early Oligocene arc of western South America. Relationships with volcanism and arc segmentation- In: X Congreso Geológico Chileno, Concepción, Extended Abstracts (CD), 1 p.

MPODOZIS, C., MARINOVIC, N., SMOJE, I. & CUITIÑO, L. (1993) Estudio geológico-estructural de la Cordillera de Domeyko entre Sierra Limón Verde y Sierra Mariposa, Región de Antofagasta. Escala 1:100.000, Santiago, Chile, Servicio Nacional de Geología y Minería, Informe Registrado, IR-93-04, 282 p., Santiago.

MÜNCHMEYER, C. (1996). Exotic deposits – products of lateral migration of supergene solutions from porphyry copper deposits. In: *Andean Copper Deposits: New Discoveries, Mineralization, Styles and Metallogeny* (Ed. by F. Camus, R. H. Sillitoe & R. Petersen) *Soc. Econ. Geol. Spec. Publ.*, **5**, 43–58.

NALPAS, T., HÉRAIL, G., MPODOZIS, C., RIQUELME, R., CLAVERO, J. & DABARD, M.P. (2005) Thermochronological data and denudation history along a transect between Chañaral and Pedernales (~26° S), North Chilean Andes: Orogenic implications. In: International Symposium on Andean Geodynamics, 6 th, Barcelona, 548−551.

NALPAS, T., DABARD, M.-P., RUFFET, G., VERNON, A., MPODOZIS, C., LOI, A. & HÉRAIL, G. (2008) Sedimentation and preservation of the Miocene Atacama Gravels in the Pedernales–Chañaral Area, Northern Chile: Climatic or tectonic control? *Tectonophysics*, **259**, 161–173.

NEMEC, W. & STEEL, R.J. (1984) Alluvial and coastal conglomerates: their significant features and some comments on gravelly mass-flow deposits. In: *Sedimentology of Gravels and Conglomerates* (Ed. by E.H. Koster & R.J. Steel), *Canadian Society of Petroleum Geologists Memoir*, **10**, 1–31.

NIEMEYER, H. & URRUTIA, C. (2009) Transcurrencia a lo largo de la Falla Sierra de Varas (Sistema de fallas de la Cordillera de Domeyko), norte de Chile. *Andean Geol.*, **36**, 37–49.

OERTER, E., AMUNDSON, R., HEIMSATH, A., JUNGERS, M., CHONG, G. & RENNE, P. (2016) Early to middle miocene climate in the atacama desert of Northern Chile. *Palaeogeogr. Palaeoclimatol. Palaeoecol.*, **441**, 890–900.

OLIVARES, B. (2001). Alzamiento, termocronometría y evolución tectónica de bloques en la Cordillera de Domeyko, Norte de Chile. M. Sc. Thesis (Unpublished), Departamento de Geología, Universidad de Chile, 70 pp.

de OLIVEIRA CARMO, I. & VASCONCELOS, P.M. (2006) 40Ar/39Ar geochronology constraints on late Miocene weathering rates in Minas Gerais, Brazil. *Earth Planet. Sci. Lett.*, **241**, 80–94.

PARNEL, J., MARK, D.F., FREI, R., FALLICK, A.E. & ELLAM, R.M. (2014) 40 Ar/ 39 Ar dating of exceptional concentration of metals by weathering of Precambrian rocks at the Precambrian–Cambrian boundary. *Precambr. Res.*, **246**, 54–63.

PERELLÓ, J., MUHR, R., MORA, R., MARTINEZ, E., BROCKWAY, H., SWANECK, T., ARTAL, J., MPODOZIS, C., MÜNCHMEYER, C., CLIFFORD, J., ACUÑA, E., VALENZUELA, D. & ARGANDOÑA, R. (2010) Wealth Creation through Exploration in a Mature Terrain: the Case History of the Centinela District, Northern Chile Porphyry Copper Belt. *Soc. Econ. Geol. Spec. Publ.*, **15**, 229–252.

PHILLIPS, J.D. (2002) Erosion, isostatic response, and the missing peneplains. *Geomorphology*, **45**(2002), 225–241.

QUANG, C.X., CLARK, A.H., LEE, J.K.W. & GUILLÉN, B.J. (2003) 40Ar–39Ar ages of hypogene and supergene mineralization in the Cerro Verde-Santa Rosa porphyry Co–Mo cluster, Arequipa, Peru'. *Econ. Geol.*, **98**, 1683–1696.

QUANG, C.X., CLARK, A.H., LEE, J.K.W. & HAWKES, N. (2005) Response of supergene process to episodic Cenozoic uplift, pediment erosion, and ignimbrite eruption in the porphyry copper province of Southern Perú. *Econ. Geol.*, **100**, 87–114.

RANSOME, F.L. (1919) The copper deposits of Ray and Miami, Arizona. *U.S. Geol. Surv. Prof. Pap.*, **115**, 192p.

RECH, J.A., CURRIE, B.S., MICHALSKI, G. & COWAN, M. (2006) Neogene climate change and uplift in the Atacama Desert, Chile. *Geology*, **34**, 761–764.

RECH, J.A., CURRIE, B.S., SHULLENBERGER, E.D., DUNAGEAN, S.P., JORDAN, T.E., BLANCO, N., TOMLINSON, A.J., ROWE, H.D. & HOUSTON, J. (2010) Evidence for the development of the Andean rain shadow from a Neogene isotopic record in the Atacama Desert, Chile. *Earth Planet. Sci. Lett.*, **292**, 371–382.

REICH, M., PALACIOS, C., VARGAS, G., LUO, S., CAMERON, E.M., LEYBOURNE, M.I., PARADA, M.A., ZÚÑIGA, A. & YOU, C.-F. (2009) Supergene enrichment of copper deposits since the onset of modern hyperaridity in the Atacama Desert, Chile. *Minerallium. Deposita*, **44**, 497–504.

REUTTER, K.-J., SCHEUBER, E. & CHONG, G. (1996) The Precordilleran fault system of Chuquicamata, northern Chile: Evidence for reversals along arc-parallel strike-slip faults. *Tectonophysics*, **259**, 213–228.

RIQUELME, R., MARTINOD, J., HÉRAIL, G., DARROZES, J. & CHARRIER, R. (2003) A geomorphological approach to determining the Neogene to Recent tectonic deformation in the Coastal Cordillera of northern Chile (Atacama). *Tectonophysics*, **361**, 255–275.

RIQUELME, R., HÉRAIL, G., MARTINOD, J., CHARRIER, R. & DARROZES, J. (2007) Late Cenozoic geomorphologic signal of Andean forearc deformation and tilting associated with the uplift and climate changes of the Southern Atacama Desert (26°S-28°S). *Geomorphology*, **86**, 283–306.

RODRIGUEZ, M.P., CARRETIER, S., CHARRIER, R., SAILLARD, M., REGARD, V., HERAIL, G., HALL, S., FARBER, D. & AUDIN, L. (2013) Geochronology of pediments and marine terraces in north-central Chile and their implications for Quaternary uplift in the Western Andes. *Geomorphology*, **180**, 33–46.

SÁEZ, A., CABRERA, L., JENSEN, A. & CHONG, G. (1999) Late Neogene lacustrine record and paleogeography in the Quillagua-Llamara basin, Central Andean fore-arc (northern Chile). *Palaeogeogr. Palaeoclimatol. Palaeoecol.*, **151**, 5–37.

SÁEZ, A., CABRERA, L., GARCÉS, M., van den BOGAARD, P., JENSEN, A. & GIMENO, D. (2012) The stratigraphic record of changing hyperaridity in the Atacama Desert over the last 10 Ma. *Earth Planet. Sci. Lett.*, **355–356**, 32–38.

SANCHEZ, C., BRICHAU, S., RIQUELME, R., LOPEZ, C., CAMPOS, E., FARIAS, M., MPODOZIS, C., REGARD, V. & HERAIL, G. (2015) Low temperature thermochronology, porphyry-Cu exhumation history and supergene enrichment in the Centinela District, Atacama Desert, Chile. XIV Congreso Geológico Chileno, La Serena, Extended Abstracts (CD), 1 pp.

SILLITOE, R. (2005) Supergene Oxidized and Enriched Porphyry Copper and related Deposits. Economic Geology 100 th Anniversary Volume, 723–768.

SILLITOE, R. (2010) Porphyry copper systems. *Econ. Geol.*, **105**, 3–41.

SILLITOE, R. & MCKEE, H. (1996) Age of supergene oxidation and enrichment in the Chilean porphyry copper province. *Econ. Geol.*, **91**, 164–179.

SILLITOE, R.H. & PERELLÓ, J. (2005) Andean copper province: Tectonomagmatic settings, deposit types, metallogeny, exploration, and discovery. Economic Geology 100 th Anniversary Volume, 845-890.

SILLITOE, R.H., MORTIMER, C. & CLARK, A.H. (1968) A chronology of landform evolution and supergene mineral alteration, southern Atacama Desert, Chile. *Trans. Inst. Min. Metall. (Sect. B: Appl. Earth sci.)*, **77**, B166–B169.

SMITH, G.A. (1986) Coarse-grained nonmarine volcaniclastic sediment: terminology and depositional process. *Geol. Soc. Am. Bull.*, **97**, 1–10.

SPIER, C.A., VASCONCELOS, P.M. & OLIVIERA, S.M.B. (2006) 40 Ar/ 39 Ar geochronological constraints on the evolution of lateritic iron deposits in the Quadrilátero Ferrífero, Minas Gerais, Brazil. *Chem. Geol.*, **234**, 79–104.

STERN, C.R. (2004) Active Andean volcanism: its geologic and tectonic setting. *Rev. Geol. Chile*, **31**, 161–206.

STRUDLEY, M.W. & MURRAY, A.B. (2007) Sensitivity analysis of pediment development through numerical simulation and selected geospatial query. *Geomorphology*, **88**, 329–351.

SVENDSEN, J., STOLLHOFEN, H., KRAPF, C.B.E. & STANISTREET, I.G. (2003) Mass and hyperconcentrated flow deposits record dune damming and catastrophic breakthrough of ephemeral rivers, Skeleton Coast Erg, Namibia. *Sediment. Geol.*, **160**, 7–31.

TAPIA, M., RIQUELME, R., MARQUARDT, C., MPODOZIS, C. & MORA, R. (2012) Estratigrafía y sedimentología de la Cuenca El Tesoro, Distrito Centinela (región de Antofagasta) y su relación con la mineralización exótica de cobre. In: XIII Congreso Geológico Chileno, Antofagasta.

TOMLINSON, A.J. & BLANCO, N. (1997a) Structural evolution and displacement history of the West fault system, Precordillera, Chile: Pt. 1. Synmineral history. In: VIII Congreso Geológico Chileno, Antofagasta, 3, 1873−1878.

TOMLINSON, A.J. & BLANCO, N. (1997b) Structural evolution and displacement history of the West fault system, Precordillera, Chile: Pt. 2. Postmineral history. In VIII Congreso Geológico Chileno, Antofagasta, 3, 1878–1882.

TOMLINSON, A.J., DILLES, J.H. & MAKSAEV, V. (2001) Application of apatite (U-Th)/He thermochronometry to the determination of the sense and amount of vertical fault displacement at the Chuquicamata porphyry copper deposit, Chile—a discussion. *Econ. Geol.*, **96**, 1307–1309.

TOSDAL, R.M. (1978) The timing of the geomorphic and tectonic evolution of the southernmost Peruvian Andes. Unpublished M.Sc. thesis, Kingston, Ontario, Queen's University, 136 pp.

TRUSWELL, E.M. (1993) Vegetation changes in the Australian Tertiary in response to climatic and phytogeographic forcing factors. *Aust. Syst. Bot.*, **6**(1993), 533–557.

UBA, C.E., HEUBECK, C. & HULKA, C. (2005) Facies analysis and basin architecture of the Neogene Subandean synorogenic wedge, southern Bolivia. *Sediment. Geol.*, **180**, 91–123.

VASCONCELOS, P.M. (1999) K–Ar and $^{40}Ar/^{39}Ar$ geochronology of weathering processes. *Annu. Rev. Earth Planet. Sci.*, **27**, 183–229.

VASCONCELOS, P.M., REICH, M. & SHUSTER, L. (2015) The paleoclimatic signatures of supergene metal deposits. *Elements*, **11**, 317–322.

WARESBACK, D.B. & TURBEVILLE, B.N. (1990) Evolution of a Plio-Pleistocene volcanogenic–alluvial fan: the Puye Formation, Jemez Mountains, NewMexico. *Geol. Soc. Am. Bull.*, **102**, 298–314.

de WET, C.B., GODFREY, L. & ANDREW, P. (2015) Sedimentology and stable isotopes from a lacustrine-to-palustrine limestone deposited in an arid setting, climatic and tectonic factors: Miocene–Pliocene Opache Formation, Atacama Desert, Chile. *Palaeogeogr. Palaeoclimatol. Palaeoecol.*, **426**, 46–67.

YANITES, B.J. & KESLER, S.E. (2015) A climate signal in exhumation patterns revealed by porphyry copper deposits. *Nat. Geosci.*, **8**, 462–465.

ZACHOS, J., PAGANI, M., SLOAN, L., THOMAS, E. & BILLUPS, K. (2001) Trends, rhythms and aberrations in global climate 65 Ma to present. *Science*, **292**, 686.

Denudation evolution and geomorphic supergene copper mineralization in Centinela district, Atacama Desert, Chile, from thermochronology and cosmogenic nuclides

Abstract:

During the Middle Eocene in the Atacama Desert region (northern Chile), the intrusion of porphyries and the synchronous deformation of the Precordillera resulted in the formation of important clusters of supergene and exotic copper ore deposits that are currently exploited. Such metal ore deposits result of the interaction of tectonics, erosion and climate, for which both timing and relations remain debated. This PhD study focuses on the quantification of geomorphological, tectonic and erosive processes to understand their relationship in the Andean western slope around 23°S in the Centinela district in the Precordillera. Twenty-nine new low-temperature thermochronological data and their modelling indicate that shallow porphyry copper emplaced during mid-Eocene were quickly exhumed near the surface by the early Oligocene. There is a five million years-long time gap between the exhumation of primary source of copper and the ~25-12 Ma range of existing $^{40}Ar/^{39}Ar$ and K/Ar ages of secondary mineralization in the District. This suggests that supergene copper related deposits occurred when the reliefs where already flattened. A syn-sedimentary exotic copper mineralization was deposited in an intra-mountainous basin in the Centinela District. We sampled sand at different depths between 135 and 13 meters in the Tesoro and Mirador open-pit mines, one of them including this exotic deposit. The ^{10}Be and ^{21}Ne concentrations of fourteen new samples were used to determine the exotic deposit age and to constrain the paleo-sedimentation rate for the last 14 Ma. The study dates the exotic deposit at ~12 Ma and suggests that this mid-Miocene exotic layer occurred during an erosive quiescence, confirming the view that supergene copper mineralization occurs during a stage of slower geomorphic activity in arid environments. The results also confirm that the erosion rates drastically dropped after 10-12 Ma, when the hyperaridity was established. This study highlights the necessary balance between exhumation and precipitation rates required to form secondary copper.

Key words: Supergene copper ore deposit, low-temperature thermochronology, Atacama Desert, cosmogenic nuclides.

Résumé :

Pendant l'Eocene Moyen, dans la région du désert d'Atacama, Nord Chili, la mise en place de porphyres et la déformation synchrone de la Précordillère aboutissent à la formation de clusters importants de dépôts de cuivre supergènes et exotiques, actuellement en cours d'exploitation. La formation de ces dépôts métallifères résulte de l'interaction entre la tectonique, l'érosion et le climat. La nature et la chronologie de ces interactions sont encore débattues. Ce travail de doctorat se concentre sur la quantification des processus géomorphologiques, tectoniques et érosifs, sur le versant ouest des Andes, autour de 23°S dans le District minier Centinela situé dans la Précordillère. Vingt-neuf nouvelles données thermochronologiques basse-température et leur modélisation indiquent que les porphyres cuprifères mis en place à faible profondeur durant l'Eocène moyen étaient déjà exhumés près de la surface à l'Oligocène moyen. Il existe un intervalle de temps de cinq millions d'années entre l'exhumation du porphyre qui constitue la source primaire de cuivre et le dépôt secondaire de cuivre dans le district de Centinela daté par les méthodes $^{40}Ar/^{39}Ar$ et K/Ar. Cette relation suggère que les dépôts de cuivre secondaires ont eu lieu lorsque les reliefs étaient déjà aplanis. Un dépôt exotique cuprifère syn-sédimentaire s'est formé dans le bassin continental du district Centinela. Des échantillons de sable ont été prélevés entre 135 et 13 mètres de profondeur dans les mines El Tesoro et Mirador. Les concentrations en ^{10}Be et ^{21}Ne de quatorze nouveaux échantillons ont permis de déterminer l'âge du dépôt et de contraindre les paléo taux de sédimentation des derniers 14 Ma. L'étude permet de dater le dépôt exotique à ~12 Ma et suggère qu'il a eu lieu lors d'une quiescence des taux d'érosion, confirmant l'idée que les dépôts supergènes de cuivre en milieu aride ont lieu après l'aplanissement des reliefs. Ces résultats confirment aussi que les taux d'érosion ont drastiquement chuté après 10-12 Ma, quand l'hyperaridité s'est établie. Ce travail de thèse illustre la balance nécessaire entre l'exhumation et les taux de précipitation pour former des minéralisations secondaires de cuivre et les conserver.

Mots-clés : Dépôt de cuivre supergène, thermochronologie basse-température, désert d'Atacama, nucléides cosmogéniques.